

JULIUS-MAXIMILIANS-UNIVERSITÄT WÜRZBURG

DISSERTATION

**Fragment Molecular Orbital Configuration Interaction
Methodology for the Description of Correlated States in
Extended Molecular Aggregates**



Dissertation zur Erlangung des naturwissenschaftlichen Doktorgrads an der Fakultät für Chemie
und Pharmazie der Julius-Maximilians-Universität Würzburg

vorgelegt von

Anurag Singh
aus Varanasi, India

December 14, 2024

Betreuer: Dr. Merle Insa Silja Röhr

Eingereicht bei der Fakultät für Chemie und Pharmazie am

Gutachter der schriftlichen Arbeit

1. Gutachter: Dr. Merle Insa Silja Röhr

2. Gutachter: _____

Prüfer des öffentlichen Promotionskolloquiums

1. Prüfer: Dr. Merle Insa Silja Röhr

2. Prüfer: _____

3. Prüfer: _____

Datum des öffentlichen Promotionskolloquiums

Doktorurkunde ausgehändigt am

List of Publications

- [1] A. Singh, A. Humeniuk, M. I. S. Röhr, Energetics and optimal molecular packing for singlet fission in BN-doped perylenes: electronic adiabatic state basis screening. *Physical Chemistry Chemical Physics*, 2021, 23, 16525-16536, <http://dx.doi.org/10.1039/D1CP01762D>
- [2] J. E. Greiner, A. Singh, M. I. S. Röhr, Functionality Optimization for Singlet Fission Rate Screening in the Full-Dimensional Molecular and Intermolecular Coordinate Space. *Physical Chemistry Chemical Physics*, 2024, 28, 19257-19265, <https://doi.org/10.1039/D4CP01274G>
- [3] A. Singh, M. I. S. Röhr, Configuration Interaction in Frontier Molecular Orbital Basis for Screening the Spin-Correlated, Spatially Separated Triplet Pair State ${}^1(T...T)$ Formation. *Journal of Chemical Theory and Computation*, 2024, (In press, Accepted on 11.09.2024), <https://doi.org/10.1021/acs.jctc.4c00473>

Contents

1	Introduction	1
1.1	Motivation	1
1.2	Singlet Fission	2
1.3	History of Singlet Fission	2
1.4	Theoretical Description of S F	3
1.4.1	Diabatic Picture	3
1.4.2	Adiabatic Picture	4
1.5	Pathways of Singlet Fission	4
1.5.1	Direct Pathway	4
1.5.2	CT/CR Mediated Singlet Fission	6
1.5.3	Excimer Role in Singlet Fission	6
1.6	Structure of Thesis	7
2	Theoretical Framework	9
2.1	Schrödinger Equation	9
2.2	Born-Oppenheimer Approximation	9
2.3	Slater Determinant	10
2.4	Hartree Fock Theory	10
2.5	Configuration Interaction Methods	13
2.6	CASPT2	14
2.6.1	MS-CASPT2	16
2.6.2	XMS-CASPT2	17
2.7	ASD/ASD-Model Hamiltonian	18
2.8	Density Functional Theories	19
2.8.1	Density Functional Theory	19
2.8.2	Time-Dependent Density Functional Theory	23
2.9	Semi-empirical Quantum Chemical Methods	25
2.10	Theoretical and Computational Approach to Singlet Fission	27
2.11	TDPT	28
2.11.1	Fermi's Golden Rule (FGR)	30
2.12	Electronic Gradients	30
2.12.1	Analytical Derivatives	31
2.13	Non-Adiabatic Coupling	32
2.14	Spin Operator And Pauli Matrices	32
2.15	Correlated Triplet Pair States in a Dimer Model	39
3	Active Space Decomposition Analysis of PDI	41
3.1	Introduction	41
3.2	Method	42
3.3	Results	44
3.3.1	Adiabatic Picture	44
3.3.2	Diabatic Picture	53
3.4	Conclusion	55
3.5	Appendix	56
3.5.1	Adiabatic Energy Plots	56
3.5.2	Total $\sum \lambda S_0 S_1\rangle$	56
3.5.3	Total $ TT\rangle$	57

3.5.4	Total $ CA\rangle$	58
3.5.5	Diabatic Energy Plots	59
4	Energetics and Optimal Molecular Packing for Singlet Fission in BN-doped Perylenes: Electronic Adiabatic State Basis Screening	61
4.1	Abstract	61
4.2	Introduction	61
4.3	Methods	64
4.3.1	The Simple Model for Singlet Fission	64
4.3.2	Singlet Fission as a Non-Adiabatic Transition	65
4.4	Results and Discussion	66
4.4.1	Comparison With <i>Ab – Initio</i> Model Hamiltonian	66
4.4.2	BN-Doped Perylene Derivatives	68
4.4.3	Singlet and Triplet Energies of Monomers	68
4.4.4	2D Scans of $ T_{RP} ^2$	70
4.4.5	Comparison of Diabatic and Non-Adiabatic Models	72
4.4.6	Selection of Best Isomers	73
4.5	Conclusion	77
5	Rotation and Functionality Optimisation of the PDI Dimer	79
5.1	Introduction	79
5.2	Method and Calculation Details	80
5.2.1	Overlap Approximation	80
5.2.2	Optimization	80
5.2.3	Dimer Structure Analysis	81
5.2.4	Diabatic Coupling Upon Rotation	82
5.3	Results	82
5.3.1	Rotation With Semi-empirical Method	82
5.3.2	Study With ASD Model Hamiltonian	84
5.3.3	Functionality Optimisation	85
5.3.4	Analysis of Different ω -Values For PDI Dimers	87
5.4	Conclusion	90
6	Tensor Modeling for Singlet Fission Using Jordan Wigner Mapping of Symbolic Qubit(Symbolic CI)	91
6.1	Introduction	91
6.2	Method	93
6.2.1	Operators	93
6.2.2	Branching Diagram	95
6.2.3	Combining Spatial Orbital With Spin Chain	100
6.2.4	Reduction of Determinant	101
6.3	Result and Discussion	102
6.3.1	Growth of Matrices	102
6.3.2	Dimer Spin Chain	102
6.3.3	Coupling Among Triplets in Dimer	106
6.3.4	Trimer Spin Chain	109
6.4	Conclusion	112
6.5	Appendix	113
6.5.1	Creation Operators	113
6.5.2	Operations to Obtain Hamiltonian	116
7	Formation Pathways of the Spin-Correlated, Spatially Separated ${}^1(T...T)$ State in the Singlet Fission Process of Perylene Diimide Stacks	119
7.1	Abstract	119
7.2	Introduction	119
7.3	Method	121
7.4	Computational Details	129
7.5	Results	129
7.5.1	Direct Pathway	130

7.5.2	Charge Transfer Mediated Pathway	130
7.5.3	Matrix Elements	131
7.5.4	${}^1(\text{TT})$ to ${}^1(\text{T...T})$ State Transition	132
7.6	Conclusion	134
7.7	Appendix	134
7.7.1	Individual Pathways	134
7.7.2	$\langle \text{LE} \hat{H} \text{CT} \rangle$ and $\langle \text{CT} \hat{H} \text{CT} \rangle$ coupling	135
8	Configuration Interaction in Frontier Molecular Orbital Basis for Screening the Spin-Correlated, Spatially Separated Triplet Pair State ${}^1(\text{T...T})$ Formation	137
8.1	Introduction	137
8.2	Method	139
8.2.1	Rate Expression	141
8.3	Computational Details	141
8.4	Results	142
8.4.1	Dexter direct transfer:	143
8.4.2	Dexter superexchange mechanism:	144
8.4.3	"One step" mechanism	145
8.5	Conclusion	147
8.6	Appendix	148
8.6.1	Wave functions	148
8.6.2	Couplings	149
8.6.3	Energy	151
8.6.4	Singlet Fission Rate	153
8.6.5	Interference	154
8.6.6	Comparison of basis sets	161
8.6.7	Energies of the Dimer System	161
8.6.8	Energy of the Trimer System	161
9	Conclusion	169
9.1	Summary	169
9.2	Outlook	170
10	Schlussfolgerung	173
10.1	Zusammenfassung	173
10.2	Ausblick	174

List of Figures

1.1	Adiabatic Picture and Diabatic Picture	4
1.2	Model for direct and CT/CR mediated pathway of singlet fission	5
2.1	Orbital categorisation schematics for a) CASCI/CASCF b) RASCI	14
2.2	Autograd Function	31
2.3	$^4S^2 = ^4S_x^2 + ^4S_y^2 + ^4S_z^2$	36
2.4	Eigen vectors of $^4S^2$ matrix	37
2.5	Eigen vectors of 4S_z matrix	38
3.1	Diabatic states in dimer base simple model of singlet fission.	43
3.2	Scan coordinate orientation with the molecular plane.	43
3.3	Adiabatic states of dimer made by 4 states of monomers of each type. LE,CT and $^1(TT)$ character of the wavefunction. a) LE character in states, b) CT character in states, c) $^1(TT)$ characters in states and d) Energy of the adiabatic states.	45
3.4	Adiabatic states of dimer made by 10 states of monomers of each type. LE,CT and $^1(TT)$ character of the wavefunction. a) LE character in states, b) CT character in states, c) $^1(TT)$ characters in states and d) Energy of the adiabatic states.	46
3.5	LE , CR character of 1 st excited state	48
3.6	LE , CR character of 2 nd excited state	53
3.7	a) LE , b) CR and c) $^1(TT)$ character in 3 rd excited state d) Sum of $^1(TT)$ character in 3 rd to 6 th excited state	54
3.8	Coupling $\langle LE H ^1(TT)\rangle$	54
3.9	a) S^+ coupling with CT b) S^- coupling with CT, c) CT with $^1(TT)$ coupling d) $ T_{RP} ^2$	55
4.1	Diabatic states in the simple model of singlet fission.	64
4.2	PBI dimer. ($\Delta X, \Delta Y$) is the parallel displacement of the center of mass of one monomer with respect to the other in the cofacially stacked homodimer (vertical distance $\Delta Z = 3.5$ Å).	67
4.3	2D scan of $ T_{RP} ^2$ for the perylene-bisimide dimer. a) Diabatic model with <i>ab initio</i> matrix elements; b) and c) semi-empirical models based on AM1 frontier orbitals. a) and b) show the perturbative contribution to $ T_{RP} ^2$ from charge-resonance mediated pathway. In c) $ T_{RP} ^2$ is approximated as the length squared of the non-adiabatic coupling vector between the adiabatic states with exciton and triplet biexciton character.	69
4.4	Numbering of atoms in perylene.	71
4.5	Representatives of singly (first row) and doubly (second row) BN-substituted perylene derivatives, which either do (left column) or do not have (right column) a Lewis structure without formal charges. In the molecules in the right column it is not possible to arrive at a resonance structure without formal charges by "flipping" electron pairs.	71
4.6	Correlation between energies of S_1 and T_1 of BN-doped perylene derivatives for different substitution levels (one or two BN groups) and the two types of resonance structures (with or without formal charges).	72
4.7	Scatter plot of the positions of the two highest local maxima in the 2D scan of $ T_{RP} ^2$. Colors denote the point group to which the isomers belong: D_{2h} - green, C_{2v} - blue, C_{2h} - red, C_s - black.	75

4.8	Selected isomers that are discussed in the text (nitrogen: blue, carbon: green, boron: pink, hydrogen: gray). BN2-112 satisfies all requirements for singlet fission.	76
4.9	AM1 frontier molecular orbitals of monomers and 2D scans of $ T_{RP} ^2 = \left \frac{(l_A \mathbf{F} l_B)(l_A \mathbf{F} h_B)}{\Delta E(CA)} - \frac{(h_A \mathbf{F} h_B)(h_A \mathbf{F} l_B)}{\Delta E(AC)} \right ^2$ (diabatic model) and $ T_{RP} _{NAC}^2 = \frac{1}{2} (\langle S^{\text{bright}*} \nabla TT^*\rangle ^2 + \langle S^{\text{dark}*} \nabla TT^*\rangle ^2)$ (non-adiabatic model).	76
5.1	Structure of PDI for the structural analysis. Along the atoms marked with the blue arrow the curvature is calculated.	81
5.2	82
5.3	The plot of coupling $\langle S_1S_0 H AC\rangle$ at a) 0 ° b) 60 ° $\langle S_1S_0 H CA\rangle$ at c) 0 ° d) 60 °	83
5.4	The plot of coupling $\langle CT H ^1(TT)\rangle$ at a) 0 ° and b) 60 ° and T_{RP} at c) 0° and d) 60°	83
5.5	Plot of coupling between $\langle CT H ^1(TT)\rangle$ using ASD	84
5.6	Plot of coupling between a) $\langle S^+ H CA\rangle$ (bright) b) $\langle S^- H CA\rangle$ (Dark) using ASD . .	84
5.7	a) Transfer probability of ${}^1(TT)$ formation from Bright exciton via CT state and b) Transfer probability of ${}^1(TT)$ formation from Dark exciton via CT	85
5.8	Plot of coupling between a) $\langle S^+ H TT\rangle$ (bright) b) $\langle S^- H TT\rangle$ (Dark) corresponding to direct pathway of singlet fission using ASD	86
5.9	Variation of parameters during optimisation: a) Increment of T_{RP} , b) Evolution of optimisation function, c) Evolution of gradient d) Evolution of gradient	89
5.10	Evolution of orbital overlap:	89
5.11	Side and top view of optimized structure by SF optimising functional	90
6.1	Branching diagram generated by the algorithm. Wave function based on S network and M network. The generated S network gives all the eigenstates of \mathbf{S}^2 for a given number of unpaired electrons. S_{points} corresponds to the number of electrons and multiplicity. $S_{pathway}$ gives the combination of multiplicities to the final multiplicity. The generated M network gives the eigenstates of \mathbf{S}_z for a given number of unpaired electrons	96
6.2	Distribution of electron in spatial orbital and construction of operators $T_1S_0T_1$. .	100
6.3	Distribution of electron in spatial orbital and construction of operators in the fragment state	101
6.4	Diabatic Hamiltonian of the trimer system, considering the HOMO and LUMO of monomers. The diabatic states involve 3 Singlet exciton states 6 Charge transfer states and 3 correlated triplet states as illustrated in Fig. 1. The matrix elements are represented in terms of the Fock operator and electron repulsion integrals in molecular orbital basis.	111
7.1	Diabatic states considered in the trimer model Hamiltonian.	121
7.2	b) CT mediated pathways of ${}^1(TT)$ and ${}^1(T...T)$ states formation.	122
7.3	Diabatic Hamiltonian of the trimer system, considering the HOMO and LUMO of monomers. The diabatic states involve 3 Singlet exciton states 6 Charge transfer states and 3 correlated triplet states as illustrated in Fig. 1. The matrix elements are represented in terms of the Fock operator and electron repulsion integrals (ERI) in molecular orbital basis.	123
7.4	PDI trimer model.	124
7.5	Matrix elements at X=2.9 Å, Y= 0.0 Å, a) only Fock matrix values, b) Only the ERI values and c)Fock + ERI	124
7.6	a) Scan of the Transition Probability for the ${}^1(TT)$ formation (Sum over all transfer probabilities from LT (Ψ) to ${}^1(TT)$ (Φ)) . b) Packing motif of the trimer system at $\Delta X = 2.9\text{\AA}$ and $\Delta Y = 0.0\text{\AA}$	126
7.7	Plots of transfer probability from individual LE to individual ${}^1(TT)$ or ${}^1(T...T)$ state, summed over all intermediate CT states. Each column has common initial LE state and each row has common final ${}^1(TT)$ state.	127
7.8	Scans of chosen individual CT-mediated pathways (in eV ²). For a) and b), CT and ${}^1(TT)$ are located on adjacent monomers. In c) and d), separated CT and ${}^1(T...T)$ states are considered.	128

7.9	Plot of coupling among LE and CT states (in eV). a) and b) illustrate matrix elements between an "edge" LE state and CT states located on adjacent monomers. In c) and d) scans of the diabatic coupling between LE to a "separate" CT state.	132
7.10	Plot of couplings (in eV) between "separate" CT state and a) joint triplet state and b) separated triplet state.	133
7.11	Scans of the absolute value of the coupling between a) the two $^1(\text{TT})$ states and b) between $^1(\text{TT})$ and $^1(\text{T...T})$ (in eV).	133
8.1	Top: Diabatic states considered in the trimer model Hamiltonian. Notice, that only singlet spin multiplicity is considered. Bottom: Structural model considered in the scans.	140
8.2	Top: Scan of transfer integral for the direct Dexter transfer mechanism. Bottom: Scan of the energy difference between $^1(\text{TT})$ state and $^1(\text{T...T})$ state.	143
8.3	Scans of couplings and transition matrix elements enrolled in the Dexter super exchange mechanism. Left box: Pathway describing initial electron transfer, followed by the transport of the hole. Right box: Initial hole and subsequent electron transfer. 144	
8.4	Top left: Scan of couplings involved in the "one step" mechanism. Bottom left: Scan of the respective transition rate expression with the energy term as arises in the denominator. The colors are shown in logarithmic scale. Top right: Scan of couplings involved in the "three step" mechanism proceeding via a CAS_0 and TCA mediated formation of TS_0T . Bottom right: Scan of absolute third order perturbation term.	146
S1	: Plots of $T_{LE_a \rightarrow ^1\text{TT}_b}$ summed over all intermediate CT states. Each column has the same initial LE state and each row has the same final ^1TT state.	155
S2	The first plot at the top shows the one-step coupling when the cation is formed on the LE, while the second plot at the top displays the one-step coupling when the anion is formed on the LE. The third plot at the top presents the sum of both couplings. Similarly, the first plot at the bottom shows the one-step perturbation term when the cation is formed on the LE, and the second plot at the bottom illustrates the one-step perturbation term when the anion is formed on the LE. The third plot at the bottom provides the sum of both perturbation terms. The plots at the bottom are shown on a logarithmic scale. To prevent numerical instability in calculations where energy differences ΔE_i are extremely small (e.g., $\Delta E_i < 10^{-16}$), we replace these problematic values with the smallest stable energy difference in the dataset. Specifically, if $\Delta E_i < \epsilon$ (with $\epsilon = 10^{-16}$), we substitute ΔE_i with ΔE_j , where $\Delta E_j = \min(\{\Delta E_k \mid \Delta E_k > \epsilon\})$. This approach ensures stable computations, particularly near points of near-degeneracy.	156
S3	Top left: Scan of couplings involved in the "one-step" mechanism. Bottom left: Scan of the transition rate expression with the energy term as arises in the denominator. Top right: Scan of couplings involved in the "two step" mechanism proceeding via a CAS_0 and TCA mediated formation of TS_0T . Bottom right: Scan of absolute third order perturbation term. The plot is shown in logarithmic scale.	157
S4	Couplings of the three-step mediated pathway $\text{S}_1\text{S}_0\text{S}_0 \rightarrow \text{CAS}_0 \rightarrow \text{TTS}_0 \rightarrow \text{TAC} \rightarrow \text{TS}_0\text{T}$	158
S5	Couplings of the three-step mediated pathway $\text{S}_1\text{S}_0\text{S}_0 \rightarrow \text{ACS}_0 \rightarrow \text{TTS}_0 \rightarrow \text{TAC} \rightarrow \text{TS}_0\text{T}$	159
S6	In the left plot, which shows the sum of the coupling terms for the three-step mediated pathway, the pathways exhibit the same signs. Upon summation, they yield a high value at $\Delta X = 0.7 \text{ \AA}$ and $\Delta Y = 0.0 \text{ \AA}$. This high value is also evident in the right plot, where a darker blue coloration is observed at $\Delta X = 0.7 \text{ \AA}$ and $\Delta Y = 0.0 \text{ \AA}$.159	

S7	Superposition of pathways in the three-step LE → TS ₀ T transfer reveals that coupling terms originating from S ₁ on the same monomer have the same sign. When these couplings, originating from the same LE source, are added together, the resulting plot resembles the one in Ref. [1]. While the couplings ⟨S ₁ S ₀ S ₀ \hat{H} ACS ₀₀ \hat{H} S ₀ TT⟩⟨S ₀ TT \hat{H} TAC⟩⟨TAC \hat{H} TS ₀ T⟩ and ⟨S ₀ S ₀ S ₁ \hat{H} S ₀ CA⟩⟨S ₀ CA \hat{H} TTS ₀₀ \hat{H} CAT⟩⟨CAT \hat{H} TS ₀ T⟩ exhibit opposite signs but similar features. This sign difference arises because ⟨CAS ₀ \hat{H} TTS ₀₀ AC \hat{H} S ₀ TT⟩ have opposite signs. Here, the cation has formed on the S ₁ fragment. Similarly, pathways where the anion is formed on the S ₁ fragment also show opposite signs. When the superposition of all four pathways is considered, the final plot shows the highest value at ΔX = 2.9 Å and ΔY = 0 Å, with other significant values observed at ΔX = 0.7 Å and ΔX = 0.0 Å. The influence of these high values is evident in the perturbation term plot, where blue coloration appears near ΔX = 0.0 Å and ΔY = 0 Å, as well as near ΔX = 2.9 Å and ΔY = 0 Å.	160
S8	Comparison of the diabatic state energy difference obtained from the 6-31G and DEF2-SVP basis sets via a line scan at ΔY = 0 Å, ΔZ = 3.4 Å, and varying ΔX from 0 Å to 4 Å for the trimer.	162
S9	Comparison of coupling terms obtained from the 6-31G and DEF2-SVP basis sets via a line scan at ΔY = 0 Å, ΔZ = 3.4 Å, and varying ΔX from 0 Å to 4 Å for the trimer.	163
S10	The adiabatic energies of states in the dimer formed by diagonalizing the diabatic Hamiltonian.	164
S11	Diabatic energy of the dimer obtained by the model CI method presented in this work.	165
S11	Diabatic state energies in the trimer relative to their respective ground states, obtained by the presented model CI methodology.	167
S11	The diabatic energy differences of the intermediate states a) CS ₀ A, b) ACT, c) CAT, d) ACS ₀ and e) CAS ₀ from TS ₀ T of the trimer.	168

Chapter 1

Introduction

1.1 Motivation

In the past few decades, global warming has stood as one of the most eminent and pressing challenges, compelling humanity to urgently reduce carbon emissions and address its far-reaching impacts. The consequences of this phenomenon have become increasingly evident as the global temperature has risen by 1.5 degrees Celsius above pre-industrial levels. To confront this crisis, there is a growing emphasis on developing technologies that can both understand and mitigate the problem. The urgency of the situation has spurred the advancement of renewable energy sources like solar, wind, and hydroelectric power.[2] Solar energy is a remarkable and sustainable form of power that harnesses the sun's vast resources to provide clean electricity and heat for various applications.

The construction of efficient light harvesting devices for the conversion of sunlight into utilisable electrical energy is one of the most promising renewable and sustainable energy sources. Solar cell materials such as semiconductors absorb photons of light and promote electrons from the valence band to the conduction band. Upon photon absorption, excited electrons and corresponding electron holes (missing electrons in the valence band) must be separated to create charge imbalances that generate an electric potential.[3, 4] Efficient electron transfer ensures that a wide range of photons across the solar spectrum are absorbed and allows these charges to be separated and prevent recombination, maximising the efficiency of solar cell energy conversion.[5, 6]

Organic photovoltaic (OPV) cells have the potential to revolutionize the energy landscape by offering a range of advantages over traditional inorganic solar cells.[7, 8, 9] One of the most significant benefits of organic solar cells is their simplicity as the material can be synthesised at room temperature and require a low-temperature vapour phase or polymer in solution processing, which are cost-effective and scalable, enabling the printing of large areas.[8, 10, 11] Researchers can tailor the bandgap, donor-acceptor (D-A) gap, and other material properties to enhance the efficiency and performance of solar cells.[12, 13, 14, 15] Despite these advantages, organic solar cells face certain limitations, including a lower photon conversion efficiency (PCE) compared to inorganic counterparts. The PCE is a measure of how efficiently a photovoltaic device can convert incident light into electricity. Due to combination of various reasons such as D-A gap, defects and thermalization losses, the PCE of organic solar cells cannot reach unity.

In an ideal single-junction photovoltaic device, in the absence of a charge carrier multiplier, the theoretical maximum PCE, lies at around 33.7%.[3, 16] This limit can be overcome by multiexciton generation, where the excess energy of the photons results into more number of electrons.[17] One of the Multiple exciton generation phenomena is called singlet fission.

Singlet fission is a process that involves at least four electrons and it is a spin-allowed, meaning the overall spin of the system remains unchanged. In this process, an initially generated singlet exciton divides into two triplet excitons. Various configurations in which the triplet pairs form and delocalize open up exciting possibilities in fields like quantum light sensing, radio wave processing, and quantum computing.[17, 18, 19, 20] For materials to be effective in storing and manipulating quantum data, they must maintain quantum coherence and entanglement for durations significantly longer than the quantum beat period of the system. Evolving states of paired triplets show non-markovian statistics in presence of magnetic fields, as observed by electron paramagnetic resonance (EPR) experiments[21]. This behaviour suggests intriguing potential in quantum appli-

cations. In singlet formation of very precise spin allowed transition (${}^1(\text{TT}) \rightarrow {}^1(\text{T...T})$) provides application in quantum computing.[20, 22, 23] ${}^1(\text{TT})$ state in the aggregate form ${}^3(\text{TT})$ and ${}^5(\text{TT})$ before becoming independent triplet $\text{T} + \text{T}$.[24, 25] These are sought to have quantum information application.

While the interaction of ${}^1(\text{TT})$ states have complex and multi-dimensional aspects. Various interpretations from different theoretical models are instrumental for complete understanding of singlet fission. The insights through various methods shed light on a broad spectrum of experimental findings.[26, 27] The current state of theoretical research has challenges of balancing accuracy with computational feasibility. As we analyse larger molecular systems and more complex electronic structures, the subtleties in the interactions between different ${}^n(\text{TT})$ states become difficult to fully comprehend. The knowledge gap between the experimentally observed aspect of singlet fission and extent of encourages ongoing exploration and innovation in both theoretical approaches for interpretation of ${}^n(\text{TT})$ and computational techniques for efficient calculation on modern machine. It is this combination of remarkable properties, intriguing challenges, and the vast potential for applications that has motivated me for pursuing this topic.

1.2 Singlet Fission

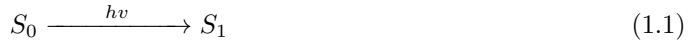
Singlet fission is considered "spin-allowed" because it follows the conservation of total electron spin angular momentum during the process. When a exciton, which has a total electron spin of singlet, undergoes fission, it splits into two triplet excitons. Importantly, the resulting triplet excitons are born coupled into a pure singlet state. Singlet fission can be regarded as a particular instance of internal conversion. In molecular crystals, singlet fission can occur extremely rapidly when the conditions are favourable.[28, 29] If the energy of the singlet fission process is nearly equal to or slightly higher than the energy of the initial singlet state (isoergic or slightly exoergic), and if the coupling between the relevant electronic states is strong, the singlet fission process becomes highly efficient. Under such circumstances, the transformation of the singlet exciton to two triplet excitons can happen within a picosecond (ps) or even sub-picosecond (sub-ps) time scale. This fast timescale allows singlet fission to compete effectively with other photophysical processes.

1.3 History of Singlet Fission

Singlet fission was first discovered in the 1960s in anthracene crystal by Singh et al. [30, 31] The concept of singlet fission gained significant momentum in 1968 as it was used to explain the low quantum yield of fluorescence in tetracene crystals. [32] A pivotal moment came in 1969 when the intricate interplay of magnetic field effects within the singlet fission process was established.[33, 34] These theories have linked singlet fission with its counterpart, triplet-triplet annihilation, incorporating the effects of magnetic fields into their interpretations. Comprehensive summaries in 1971 and 1975 encapsulated these developments.[35, 36, 37] A synthesis of these efforts culminated in comprehensive summaries of the subject matter in 1971 and 1975. [38, 39] More interests gathered in the 1980s with the observation of exciton fission in carotenoids and polymers. [40, 41] Simultaneously, significant progress has been made in the science and engineering of organic semi-conducting materials. This advancement led to the successful demonstration and optimization of various solid-state devices based on organic materials, including organic light-emitting diodes (OLEDs),[42], field effect transistors,[43, 44] photodiodes,[45] and photovoltaic cells.[46, 47, 11] Singlet fission has been shown to occur in molecular aggregates and solid-state thin films composed of a variety of conjugated molecules, with efficiencies approaching 200%. [48, 49, 50, 51] Recent years have seen theoretical breakthroughs in understanding the 'direct' and 'indirect' mechanisms of singlet fission. The 'direct' mechanism involves the formation of multiple exciton states in a single step, whereas the 'indirect' mechanism involves sequential electron transfer events through an intermediate charge-transfer state. [52, 53, 54, 28] Since the publication of Smith et al. [28] the phenomenon has gathered more interest from theoreticians and experimentalists. Casanova et al. provide a detailed review of the current state of theory and interpretation of singlet fission, highlighting recent advancements. [55] Concurrently, research has revealed numerous potential applications of singlet fission in photonics, photo-sensing, and quantum computing, unravelling new challenges and opportunities in the interpretation and formation of paired triplets. Miyata et al. thoroughly review many aspects of paired triplet formation, [56] while Guldì and coworkers discuss

the development and use of unconventional materials demonstrating singlet fission, particularly focusing on their applications in quantum computing due to the non-Markovian statistics of paired triplets.[29, 20, 22, 23]

1.4 Theoretical Description of Singlet Fission



Singlet fission is a photophysical process, in which excitation with light leads to the initial population of a singlet excited adiabatic state. Upon internal conversion, ultrafast and spin-allowed transition leads to the formation of an electronic state with singlet-spin correlated ${}^1(\text{TT})$ character. While in intramolecular singlet fission, these coupled triplets can be localized at parts of the same molecule, in intermolecular singlet fission, the triplets are localized on different molecules that are densely stacked and electronically coupled. The correlated triplet pair is then assumed to split into individual triplets by decoherence effects.[28, 53, 54]

For singlet fission to occur, the energy required to produce twice the triplet excitation energy ($2E_{T_1}$) should be lower than or close to the energy of the lowest singlet excitation E_{S_1} . In other words, there needs to be a nearly degenerate or very small energy gap between the singlet and paired triplet excited states.

However, in most organic molecules, these favourable energetics are not encountered very frequently. The energy required for twice the triplet excitation energy is typically much higher than the energy of the lowest singlet excitation. This energy mismatch results in a low probability of spontaneous singlet fission, making the process challenging to observe in these systems. When the coupling is too strong, the system effectively becomes a single chromophore, the energy splitting between the ${}^1(\text{TT})$, ${}^3(\text{TT})$ and ${}^5(\text{TT})$ levels are large, and it is not useful to think of the two triplet excitations as more or less independent.

1.4.1 Diabatic Picture

In quantum mechanics, a diabatic representation refers to a scenario where the electronic Hamiltonian is not diagonal. This implies that there is coupling within the defined states. In a diabatic state representation, it's assumed that the spatial probability density of the system remains unchanged. Therefore, the Hamiltonian exhibits coupling between these states.

Diabatic bases are not inherently unique and are formulated based on various factors, including the specific properties being analyzed, the required level of accuracy, and the computational resources available. These bases are constructed through the product of electron wave functions.

For instance, Figure 1.1 b illustrate two potential energy surfaces of diabatic states, showing a diabatic crossing at a point labelled 'M'. At points 'N' and 'O', the states exhibit minimal interference and have negligible couplings. However, near the point 'M', significant couplings between the states occur. In such regions, diabatic energies may not be accurate, whereas adiabatic energies provide a more correct description.

In the context of singlet fission, understanding the diabatic representation becomes crucial. Singlet fission involves states such as LE (local exciton), CT (charge transfer), and ${}^1(\text{TT})$ (triplet-triplet), which are critical for studying this phenomenon. These states often exist in a mixed form with adiabatic states, making the analysis of their energies and couplings essential. In this thesis, the diabatic bases are constructed using the tensor product of states representing S_0 (ground state), S_1 or S_n (excitonic states), C (cationic states), A (anionic states), and T (triplet states).

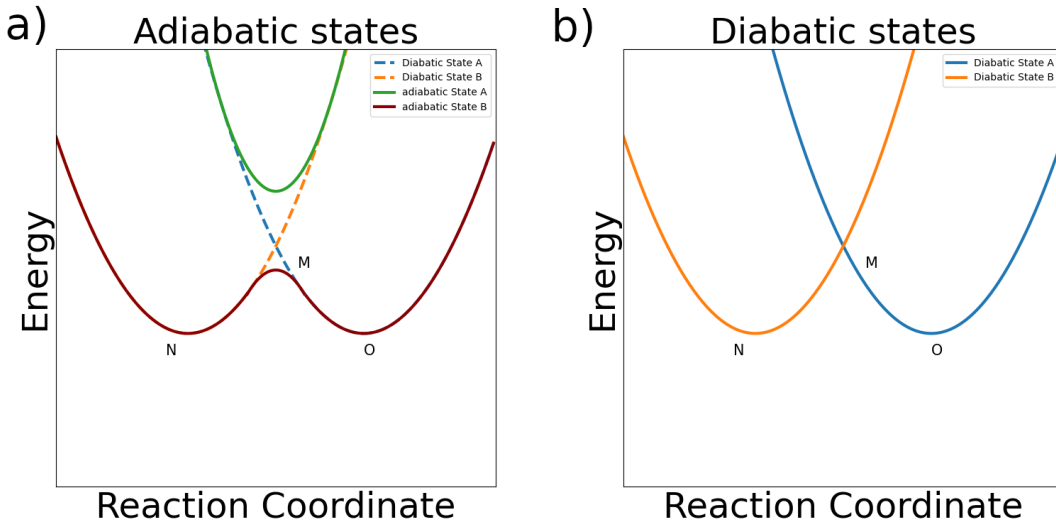


Figure 1.1: Adiabatic Picture and Diabatic Picture

1.4.2 Adiabatic Picture

Adiabatic states are defined as the eigenstates of a system's Hamiltonian, exhibiting consistent and definite energies under conditions where the external parameters change gradually. Their stability is a hallmark of their identity, ensuring minimal transitions or mixing with other states. This characteristic of adiabatic states makes them particularly reliable and predictable for describing energy levels in various physical scenarios, ranging from simple atomic systems to more complex molecular structures.

Within this framework, the phenomenon of singlet fission emerges as an example of a non-adiabatic process, that is marked by rapid transitions between different quantum states, a stark contrast to the gradual changes accommodated in adiabatic scenarios. These transitions are facilitated by non-adiabatic couplings, where interactions between states lead to swift alterations in the system's quantum state. In singlet fission, these dynamics are observed as the division of a singlet exciton into singlet paired triplet excitons. Expressing adiabatic states as a linear combination of diabatic states, as:

$$|^{Adiabatic}\Psi\rangle = \sum_i c_i^{LE} |\Psi_{LEi}\rangle + \sum_j c_j^{CT} |\Psi_{CTj}\rangle + \sum_k c_k^{1(TT)} |\Psi_{1(TT)k}\rangle, \quad (1.7)$$

helps us track and understand the transitions. The coefficients in the linear combination indicate the contributions of different diabatic states to the final adiabatic state, showing how the electronic configurations evolve.

1.5 Pathways of Singlet Fission

1.5.1 Direct Pathway

Determining the dominant mechanism for singlet fission in specific systems is essential for designing efficient singlet fission materials for various technological applications. In this mechanism, the initially formed LE directly undergoes a transition to form two correlated triplet excitons (${}^1(TT)$) without involving any intermediate charge transfer states. This mechanism relies solely on the electronic coupling between the LE and ${}^1(TT)$ states. In the 2×2 active space consisting of HOMO and LUMO on each molecule making a molecular dimer model, electronic coupling between a pair of diabatic states $\langle LE | H | {}^1(TT) \rangle$ has two-electron transfer integrals. [57, 58, 59] In acenes such as the pentacene and tetracene, singlet fission occurs through direct pathways when the vibrational or phonon degrees of freedom is absent and certain interactions between molecular orbitals can be nullified. These interactions can be present or absent based on the symmetry of

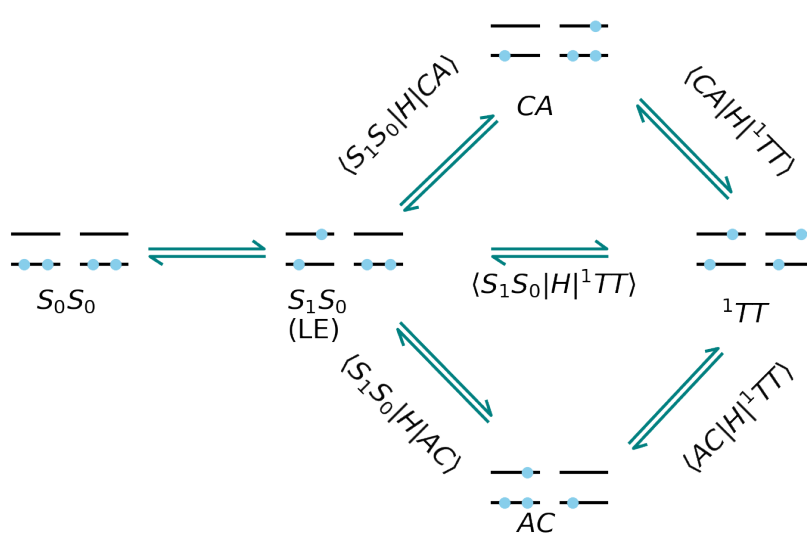


Figure 1.2: Model for direct and CT/CR mediated pathway of singlet fission

the overlap between orbitals. In many such instances, these interactions become zero because they cancel out due to symmetry considerations.

Several studies have explored the pathways of singlet fission, proposing diverse mechanisms. Zimmerman et al. suggested that motion along the intermolecular coordinate modulates the energies of LE and ^1TT states, resulting in level crossing and a conical intersection, facilitating ultrafast singlet fission despite modest electronic coupling.[13, 12] Ananth and collaborators conducted refined calculations, finding no level crossing along the intermolecular coordinate for pentacene, suggesting the singlet fission in pentacene is independence of CT states mediation.[60] In the adiabatic representation, the occurrence of singlet fission can be attributed to vibrations along phonon modes due to the vanishing electronic couplings with opposite signs. Phonon modes modulate the energetics of excitonic states through nonadiabatic couplings, influencing transitions between states. Notably, in molecular crystals, the symmetry-breaking modes, such as intermolecular symmetry breaking in acene pairs and slip-stacking in tetracene dimers, play crucial roles in singlet fission dynamics.[61, 62] Additionally, Musser et al. emphasized the significance of vibronic couplings in inducing ultrafast internal $S_1 \rightarrow ^1\text{TT}$ conversion, as observed in time-resolved spectroscopy experiments.[63] Tempelaar and Reichman provided a vibronic exciton theory treating electronic and vibrational degrees of freedom microscopically and non-perturbatively, calculating relevant energetics and oscillator strengths for singlet fission in pentacene.[64]

These derivative couplings, denoted as vibronic couplings,

$$\langle \Psi_I | \frac{d\mathcal{H}}{dQ} | \Psi_J \rangle = \frac{dE_{IJ}}{dQ} \delta_{IJ}, \quad (1.8)$$

arise due to the interaction between electronic degrees of freedom and nuclear distortions.[65] Computational studies have extensively investigated the impact of intra- and interchromophoric distortions using various electronic structure calculations and dynamical simulations [66, 67, 68, 69, 70, 71, 72, 73, 74]. While the direct expression for derivative couplings is rarely used in practical calculations, the relationship obtained through the Hellman-Feynman theorem, as shown in equation 1.8, is commonly employed.[75, 76, 77, 78, 79, 80]. Analytical expressions for nonadiabatic couplings within a Frenkel-Davydov exciton model have been developed by Morrison and Herbert and applied to investigate vibronic couplings in tetracene [81, 82, 70, 68]. Sato et al. introduced a method based on the vibronic coupling density concept, applied to a tetracene dimer model [83, 84]. Krylov and co-workers proposed a simple approach estimating nonadiabatic couplings using the reduced one-particle transition density matrix, applied to tetracene and pentacene dimers [85, 86, 87, 88, 89, 90]. Feng et al.'s nonadiabatic model employs transition state theory

and the linear free energy approach to estimate singlet fission rates, emphasizing the importance of a balanced equilibrium between triplet-triplet binding energy and the driving force for the overall process [85].

1.5.2 CT/CR Mediated Singlet Fission

In many cases, when a molecule is initially excited to its LE state upon light absorption, it relaxes to its vibronically lowest-energy singlet state before any further photo-physical processes can occur. In this relaxed LE state, the energy required for singlet fission is not readily available. The process of singlet fission from a relaxed LE state typically requires considerable thermal activation for it to happen spontaneously. In such cases, CT and charge resonance (CR) states can act as virtual intermediates that assist in the formation of ${}^1(\text{TT})$. When two chromophores are nearby, their electronic configurations can mix, leading to the formation of electron density that is partially transferred between molecules, creating a separation of positive and negative charges in CT configurations. CT states involve net charge displacement, while CR configurations describe the ionic nature of the electronic wave function without implying a permanent charge separation. The extent to which CT and CR configurations mix with LE and multiexcitons depends on various factors, including the relative energy of CT and CR states compared to other electronic states such as LE and higher singlet states (S_n) as well as electronic coupling among these states. When CT states have high energies relative to other states, their mixing with LE and ${}^1(\text{TT})$ states is weaker. When CT or CR states have relatively low energies, they can significantly mix with upper excited singlet states, affecting the overall exciton delocalization [91, 92, 93].

The larger spatial extension of LE compared to ${}^1(\text{TT})$ influences their interaction with CT configurations [71, 86, 94, 95], especially in symmetric systems where standard charge population analysis may not be suitable. Various computational techniques, such as diabatization [96, 97, 98, 99, 81, 100] or decomposition of adiabatic wave functions [101, 102, 103, 94, 104, 105]. Another widely used approach involves the construction of natural transition orbitals (NTOs) to provide a visual representation of spatial orbitals. Different methods assess the CT nature of the first excited adiabatic singlet state through standard charge population analysis or by examining the spatial overlap between ground and excited states. While NTOs are valuable for understanding charge redistribution with net charge separation, additional methods, such as attachment/detachment density analysis and other quantitative tools, contribute to a comprehensive understanding of excited states [106, 107, 108, 109, 110, 111, 112, 113, 114, 115, 116].

1.5.3 Excimer Role in Singlet Fission

An excimer is an excited electronic state that forms when two identical or nearly identical molecules come into close contact. When one of the molecules is in an excited state (e.g., a LE state), it can transfer its excitation energy to the ground-state molecule, resulting in the formation of an excimer.[117, 118] Excimer formation has several distinct properties such as photoluminescence depletion, redshift of fluorescent band and loss of vibronic resolution. In photoluminescence depletion, excimer formation is accompanied by a significant reduction in photoluminescence, which refers to the emission of light by an excited molecule when it returns to the ground state. The excimer formation process competes with photoluminescence, leading to a decrease in the emission of light from the excited state.[117] Another characteristic feature is redshift of fluorescent band where the excimer formation results in a large redshift of the fluorescent band. The fluorescent band represents the range of wavelengths at which the excited molecules emit light. The formation of an excimer alters the emission wavelength to longer wavelengths (lower energy), causing the redshift.[117] Vibronic resolution refers to the ability to distinguish fine details in the emission spectrum due to vibrational transitions. Excimer formation generally leads to a loss of vibronic resolution in the photoluminescence spectrum.[117] The role of excimers or excimer-like states in the singlet fission process is a topic of ongoing research and debate. Excimers have been proposed to play various roles in singlet fission processes, and different studies have suggested different scenarios. Some studies suggest that excimers may act as intermediates that facilitate the formation of triplet-pair states during singlet fission. In certain molecular systems like pentacene crystals,[12] derivatives of diketopyrrolopyrrole, and terrylene, excimer states have been proposed as precursor intermediates between the singlet excited state S_1 and the two triplet excitons ${}^1(\text{TT})$.[119, 120, 121] These excimers could enhance the efficiency of singlet fission by assisting the transition from S_1 to

1 (TT). The work of Walker et al. and Stern et al. signals that the formation of excimers facilitates the singlet fission process, particularly in dilute solutions of tetracene and pentacene.[122, 123] On the other hand, in face-to-face covalent dimers of tetracene and molecular packing in crystal propylene,[124] stable excimer states have been suggested to act as trap states that hinder the formation of 1 (TT), leading to suppressed singlet fission.[125, 88] In certain molecular systems like pentacene films, ultrafast excimer formation has been observed, which can compete with singlet fission. Excimers formed in these systems may compete with the singlet fission process, affecting the overall efficiency of singlet fission.[126, 127] Excimer formation has been associated with the lack of temperature dependence in the generation of the 1 (TT) state in tetracene and strong temperature dependence for the dissociation step of the triplet pair. This suggests that excimer formation might play a role in the temperature-dependent dynamics of singlet fission in some systems.[128]

1.6 Structure of Thesis

The first chapter provides an introduction to the motivation behind the research, an overview of singlet fission, its historical context, and an explanation of the singlet fission mechanism. In Chapter 2, this thesis delves into the theoretical foundations of this study, beginning with the basic principles of quantum mechanics, the formulation of the Schrödinger equation, and the Born-Oppenheimer approximation. It then proceeds to elucidate the computational and theoretical methods employed in this research, such as Hartree-Fock, CASCI, CASSCF, CASPT2, MS-CASPT2, XMS-CASPT2, DFT, TDDFT, and AM1. Furthermore, the theory of calculating derivatives of electronic wave functions, algorithmic differentiation and the concept of paired triplet wave functions are discussed within this chapter. While explaining the paired triplet system, a brief description of Pauli matrices, Jordan-Wigner transformations, and Clebsch-Gordan coefficients is provided.

In Chapter 3, the study focuses on diabatic couplings among LE, CT, and (TT) states in a cofacially stacked planar Perylenediimide (PDI) dimer using the active space decomposition method. The goal of this work was to investigate the variations in diabatic couplings when slipped stacking is considered. Additionally, the study aimed to examine the continuity and discontinuity in the adiabatic wave function. The results of this study were utilized in benchmarking the SFast method, which relies on semi-empirical approaches.

Chapter 4 delves into the theory and development of the SFast (Singlet Fission Adiabatic Basis Screening). This Python module implements two semi-empirical models (singlet fission rate constant, diabatic coupling, i.e., T_{RP} , and the norm of non-adiabatic coupling vectors) for estimating singlet fission rates in cofacially stacked homodimers to identify the optimal packing arrangement. The program constructs the cofacially stacked homodimer by duplicating the monomer and displacing the copy by a vector. The wavefunctions consist of 4 electrons distributed among the 4 frontier orbitals, which are the HOMOs and LUMOs on each monomer. Molecular orbitals of the monomer and their interactions are computed using the semi-empirical AM1 method as implemented in the PYSEQM package. The derivatives required for evaluating the non-adiabatic coupling vector are computed through automatic differentiation. In this work, 256 unique (BN)2-substituted molecules were studied, generated using the perylene scaffold by replacing two carbon atoms with B-N. The suitability of these molecules for singlet fission was studied using electronic structure methods, including TDDFT, XMS-CASPT2, SFast, and lewis structures, leading to the identification of the best candidate for singlet fission in this group of molecules.

In Chapter 5, further studies were conducted using SFast and active space decomposition by rotating a cofacially stacked PDI dimer along the z-axis. The variation in diabatic coupling was compared between both methods. Additionally, the molecular geometry of the PDI dimer was optimized for high singlet fission by utilizing T_{RP} and the ground state energy as components of the cost function. In parallel, optimization is carried out to identify the molecular geometry that results in high singlet fission. To optimize the geometry, the algorithmic differentiation technique is applied to calculate the derivative of the functional with respect to the atomic coordinates. The optimization procedure uses the L-BFGS (Limited-memory Broyden-Fletcher-Goldfarb-Shanno) algorithm to iteratively refine the molecular structure until it reaches a state that maximizes singlet fission.

In Chapter 6, a configuration interaction methodology has been developed, where the objective was to enhance the analysis method for the diabatic Hamiltonian matrix elements and apply it to aggregate systems. Simultaneously, we aimed to gain a comprehensive analytical understanding

of the intricate interactions among the states involved in singlet fission. To achieve this, the use of symbolic algebra is incorporated, enabling us to derive expressions for the Hamiltonian matrix elements in terms of electron-electron and electron-nuclear interactions. In this process, Second quantization techniques with spin-adapted creation and annihilation operators have been employed. These operators were generated using the Jordan-Wigner transformation, which involved using symbolic non-commutative variables for spin orbitals. This approach allowed us to define fermionic operators for pairing within the spin chain. The algorithm for generating the branching diagram and constructing the wave function based on the given spin configuration of subsystems have been discussed. This chapter provides valuable insights into the methodology employed for analyzing complex interactions in singlet fission systems.

In Chapter 7, The generated model to study a PDI trimer is applied. Our focus was on utilizing the transition probability of the formation from second-order perturbation terms to estimate the singlet fission rate for the correlated triplet pair state. We conducted scans along both a vertical and a longitudinal slipping mode, allowing us to investigate the electronic pathways involved in the formation of the ${}^1(T\ldots T)$ state.

In Chapter 8, the frontier molecular orbital model for singlet fission is expanded to include both separated Charge Transfer (C...A) and ${}^1(T\ldots T)$ states, as well as mixed triplet-charge transfer states. Analytic expressions for diabatic matrix elements are provided to study the perylene diimide trimer's packing dependence. The focus is on evaluating competing pathways for ${}^1(T\ldots T)$ state formation, including spatially separated triplet (T...T) and charge transfer (A...C) states, along with mixed states of type ${}^1(TAC)$. Three mechanisms are explored: the "two intermediates" scheme involving Dexter-type triplet energy transfer, and a previously unexamined "one-step" pathway that proceeds from an excited LE state directly to ${}^1(T\ldots T)$ via a charge transfer-mediated process.

Chapter 9 and Chapter 10 are the concluding chapters, comprising the summary and prospects of the research presented in this thesis, in English and German respectively.

Chapter 2

Theoretical Framework

2.1 Schrödinger Equation

Quantum chemistry aims to describe physical phenomena by considering the behaviour of electrons and nuclei. This approach begins with the hydrogen atom, comprising one nucleus and one electron, in a non-relativistic framework. At the heart of quantum chemistry are fundamental equations such as the time-dependent Schrödinger equation:

$$\hat{H}|\Psi\rangle = E|\Psi\rangle. \quad (2.1)$$

In this equation, \hat{H} represents the Hamiltonian operator. $|\Psi\rangle$ stands for the wave function characterizing the quantum state, and E denotes the associated energy eigenvalue.

The evolution of a quantum system over time is tracked by:

$$\hat{H}\Psi(\mathbf{r}, t) = i\hbar \frac{\partial\Psi(\mathbf{r}, t)}{\partial t}, \quad (2.2)$$

where $\Psi(\mathbf{r}, t)$ is the wave function dependent on position \mathbf{r} and time t , i is the imaginary unit, and \hbar is the reduced Planck's constant. Moreover, the completeness relation for a continuous basis:

$$\int_{-\infty}^{\infty} |x\rangle\langle x| dx = \mathbb{1}. \quad (2.3)$$

This relation highlights that the position states $|x\rangle$ form a comprehensive basis, with their inner products integrating to $\mathbb{1}$. It represents quantum states using a continuous position basis:

$$|\Psi(t)\rangle = \int_{-\infty}^{\infty} dx \langle x|\Phi(t)|x\rangle. \quad (2.4)$$

The equation 2.4 illustrates how the quantum state $|\Psi(t)\rangle$ can be expressed using the position basis $|x\rangle$.

2.2 Born-Oppenheimer Approximation

The total non-relativistic Hamiltonian of an electronic system can be written as the sum of nuclear-nuclear, electron-electron, and electron-nuclear interactions. It provides a framework for treating the electronic and nuclear motions in molecules as separate processes. This approximation is based on the vast difference in mass between electrons and atomic nuclei, i.e.,

$$\hat{H} = \hat{H}_e + \hat{T}_n \quad (2.5)$$

and

$$\hat{T}_n = - \sum_A \frac{1}{2M_A} \nabla_A^2, \quad (2.6)$$

which allows for their decoupling. [129] In the equations 2.5 and 2.6, \hat{T}_n represents the nuclear-nuclear Hamiltonian, where ∇ is the Laplacian operator and \hat{H}_e denotes the electronic Hamiltonian. The electronic Hamiltonian :

$$\hat{H}_e = - \sum_i \frac{1}{2} \nabla^2 - \sum_{i,A} \frac{Z_A}{R_A - \mathbf{r}_i} + \sum_{\mu < \nu} \frac{1}{\mathbf{r}_\mu - \mathbf{r}_\nu} \sum_{B > A} \frac{Z_A Z_B}{R_{AB}} \quad (2.7)$$

encompasses both the electron-electron interaction and the electron-nuclear interaction. Here, M_A represents the mass of the nucleus labeled by A . In equation 2.7, \mathbf{r} represents the electronic coordinates, corresponding to the position of each electron, while R represents the nuclear coordinates, denoting the positions of the atomic nuclei. The first term represents the kinetic energy operator for the electrons, where i indexes over all electrons in the system. The second term accounts for the attraction between each electron i and each nucleus A , where Z_A is the atomic number of nucleus A and R_A is the distance between nucleus A and the electron. The third term represents the electron-electron repulsion energy, where μ and ν index over all electrons, B indexes over all nuclei with atomic number Z_B , and R_{AB} is the distance between nuclei A and B . The total wave function is given by:

$$\Psi_{\text{tot}}(\mathbf{r}, R) = \Psi_n(R)\Psi_{\text{el}}(\mathbf{r}, R). \quad (2.8)$$

The separation of electronic and nuclear motion simplifies the Schrödinger equation for the molecular system, allowing for the treatment of the electronic and nuclear components independently. This simplification greatly streamlines calculations and makes the problem more tractable.

2.3 Slater Determinant

The Slater determinant is a mathematical construct that describes the quantum state of a multi-electron system in terms of a set of single-electron wave functions. The Slater determinant provides a systematic way to create an antisymmetric wave function for a multielectron system. It involves forming a determinant of single-electron wave functions, each corresponding to a different electron orbital. These orbitals are often taken as solutions to the Schrödinger equation for a single electron in the presence of the combined potential of the nucleus and other electrons. Suppose we have N electrons and N distinct spin orbitals $\phi_i(\mathbf{r})$ for $i = 1, 2, \dots, N$. The Slater determinant Ψ for this system is constructed as follows:

$$\Psi(\mathbf{r}_1, \mathbf{r}_2, \dots, \mathbf{r}_N) = \frac{1}{\sqrt{N!}} \begin{vmatrix} \phi_1(\mathbf{r}_1) & \phi_2(\mathbf{r}_1) & \cdots & \phi_N(\mathbf{r}_1) \\ \phi_1(\mathbf{r}_2) & \phi_2(\mathbf{r}_2) & \cdots & \phi_N(\mathbf{r}_2) \\ \vdots & \vdots & \ddots & \vdots \\ \phi_1(\mathbf{r}_N) & \phi_2(\mathbf{r}_N) & \cdots & \phi_N(\mathbf{r}_N) \end{vmatrix}, \quad (2.9)$$

here, each row corresponds to a different electron, and each column represents a different spin orbital. The determinant ensures that the resulting wave function is antisymmetric when exchanging any two electrons.

2.4 Hartree Fock Theory

Hartree fock theory encapsulates the approximations and method to solve Schrödinger equation for a set of electrons. The basic principle behind the Hartree-Fock theory is to treat each electron as moving in an average or mean field created by all the other electrons. This field is determined by the electron density, which is constructed from a set of one-electron functions called molecular orbitals. These orbitals represent the spatial distribution of electrons within the molecule. The Hartree-Fock equations, a set of coupled partial differential equations, are used to obtain these molecular orbitals. Their purpose is to minimize the total energy of the system by optimizing the orbitals. To solve these equations, the problem is transformed into an eigenvalue problem known as the Roothaan-Hall equation. Solving this equation provides the optimized molecular orbitals that best describe the electronic structure of the system. Achieving self-consistency in the Hartree-Fock method involves iterative optimization, where the molecular orbitals are updated until a stable set is obtained, corresponding to the system's minimum energy.

The Hartree-Fock description begins with the electronic Hamiltonian (Equation 2.10) in the Born-Oppenheimer approximation, consisting of the kinetic and potential energy of electrons:

$$\hat{H}_e = -\sum_i \frac{1}{2} \nabla^2 - \sum_{i,A} \frac{Z_A}{R_A - \mathbf{r}_i} + \sum_{\mu < \nu} \frac{1}{\mathbf{r}_\mu - \mathbf{r}_\nu} \sum_{B>A} \frac{Z_A Z_B}{R_{AB}}. \quad (2.10)$$

The electronic wave functions of electrons follow Pauli's exclusion principle. The two spin functions of the electron spin are orthonormal. The many-body wavefunction describing the set of electrons is antisymmetric concerning the interchange of spatial or spin coordinates of two electrons:

$$\Psi(\mathbf{r}_1 \dots \mathbf{r}_a, \dots, \mathbf{r}_b, \dots, \mathbf{r}_N) = -\Psi(\mathbf{r}_1 \dots \mathbf{r}_b, \dots, \mathbf{r}_a, \dots, \mathbf{r}_N). \quad (2.11)$$

As the time-independent Schrödinger equation is an eigenvalue equation, implying that for a given Hamiltonian, there exists an exact solution to the Schrödinger equation, where the eigenvalue refers to the energy of the system, and the eigenfunction refers to the electronic wave function:

$$\hat{H}|\Psi\rangle = \hat{E}|\Psi\rangle. \quad (2.12)$$

With the Hartree-Fock theory, we aim to reduce the problem to an eigenvalue problem of a matrix. The Hartree-Fock method assumes that any molecular orbital ψ_j is defined as a linear combination of atomic orbitals, and the wave function of the system can be approximated as a single Slater determinant formed by the product of molecular orbitals:

$$\psi_j(\mathbf{r}) = \sum_i C_{ij} \phi_i(\mathbf{r}), \quad (2.13)$$

here, C_{ij} is the coefficient of atomic orbital ϕ_i referring to the contribution of ϕ_i in orbital ψ_j . The wave function can be written in matrix representation, where C_{ij} are the matrix elements of \mathbf{C} :

$$\psi(\mathbf{r}) = \mathbf{C}\phi(\mathbf{r}). \quad (2.14)$$

The variation principle suggests that the ideal set of wave functions is the one with the minimum energy. The HF theory aims to find the coefficients that give the minimum energy. The method starts by assuming a many-body wave function $|\Psi_0\rangle$ representing the lowest energy (E_0) state. E_0 is the expectation of the Hamiltonian when a given set of molecular orbitals is occupied, giving the state $|\Psi_0\rangle$. This is illustrated as:

$$E_0 = \langle \Psi_0 | \hat{H} | \Psi_0 \rangle = \sum_a \langle a | \hat{h} | a \rangle + \frac{1}{2} \sum_a^{\text{occ}} \sum_b^{\text{occ}} (aa|bb) - (ab|ba), \quad (2.15)$$

where a and b represent orbitals belonging to occupied molecular orbitals. The one-electron operator:

$$\langle i | \hat{h} | j \rangle = \int \phi_i^*(\mathbf{r}_1) \left(-\frac{1}{2} \nabla^2 - \sum_\mu \frac{Z_\mu}{|\mathbf{r}_1 - \mathbf{R}_\mu|} \right) \phi_j(\mathbf{r}_1) d\mathbf{r}_1, \quad (2.16)$$

includes the kinetic energy and potential energy expectation between an electron and nuclei. where i and j are indices representing different orbitals, ∇ is the Laplacian operator, Z_μ represents nuclear charges, R_μ are nuclear coordinates, and ϕ_i are the orbitals. The two-electron operator $(pq|rs)$ accounts for the inter-electron repulsion energy expectation:

$$(pq|rs) = \int \int \frac{dr_1 dr_2}{|\mathbf{r}_1 - \mathbf{r}_2|} \phi_p^*(\mathbf{r}_1) \phi_q(\mathbf{r}_1) \phi_r^*(\mathbf{r}_2) \phi_s(\mathbf{r}_2). \quad (2.17)$$

Since molecular orbitals are the linear combination of atomic orbitals, by calculating the one and two-electron integrals in the atomic orbital basis and transforming them to occupied molecular orbitals, the expectation value can be calculated. However, at this point, the \mathbf{C} in equation 2.14 is unknown. The procedure for the solution can be started by assuming a trial \mathbf{C} matrix, which will provide a trial set of molecular orbitals. The expectation value with this set of molecular orbitals are calculated by evaluating the one and two-electron integrals in terms of atomic orbitals, multiplying by appropriate weights depending on the coefficients of the atomic orbitals in the given set of molecular orbitals. By tweaking the molecular orbitals through changing the coefficients, one can achieve the minimum expectation value of $\langle \Psi_0 | \hat{H} | \Psi_0 \rangle$ and obtain the needed ideal molecular orbitals.

To perform this computationally, a Fock operator ($\hat{\mathbf{F}}$) is defined to obtain the energy expectation value for an electron in an atomic orbital r and s . The expression for f_{rs} , an element of the Fock matrix, is given by:

$$f_{rs} = \langle r | \hat{h} | s \rangle + \sum_a^{\text{occ}} \left[(aa|rs) - \frac{1}{2}(ra|as) \right]. \quad (2.18)$$

here, r and s represent atomic orbitals, and a belongs to the set of occupied molecular orbitals. This expression is a consequence of the permutation symmetry in two-electron integrals, i.e., $(pq|rs) = (pq|sr) = (qp|rs) = (qp|sr) = (rs|pq) = (sr|pq) = (rs|qp) = (sr|qp)$, the anti-symmetric properties of many-electron wave functions, and spin orthogonality. The Fock operator is a one-electron operator representing the energy required for the transition of an electron from orbital r to s .

The density matrix ($\hat{\mathbf{D}}$), where the elements of the matrix (D_{kl}) are defined as:

$$D_{kl} = \sum_{a=1}^{\text{occ}} C_{ka} C_{la}, \quad (2.19)$$

here, a represents the occupied molecular orbitals, and k and l correspond to atomic orbitals.

After the Coulomb and exchange integrals have been computed using atomic orbital basis functions, the Hartree-Fock equation is reduced to an eigenvalue problem. Equation 2.18 can be expressed in terms of the density matrix and the Coulomb and exchange matrices in the atomic orbital basis as follows:

$$f_{rs} = \langle r | \hat{h} | s \rangle + \sum_a^{\text{occ}} D_{kl} \left[(kl|rs) - \frac{1}{2}(rk|ls) \right]. \quad (2.20)$$

Now, the matrices $\hat{\mathbf{F}}$ and \mathbf{C} act as proxies for the operators \hat{H} and $|\Psi\rangle$ from equation 2.12. Since molecular orbitals should be orthonormal, and the atomic orbitals basis is not orthogonal, the overlap matrix $\hat{\mathbf{S}}$ of atomic orbitals is introduced. Here, S_{ij} represents the element of the overlap matrix corresponding to the overlap between atomic orbitals ϕ_i and ϕ_j , with $\langle \phi_i | \phi_j \rangle$ denoting the overlap integral.

These formulations lead to the equation:

$$\hat{\mathbf{F}}\mathbf{C} = \hat{\mathbf{S}}\mathbf{C}\epsilon, \quad (2.21)$$

also known as the Roothaan-Hall equation. The goal is to find the coefficients \mathbf{C} and the orbital energies ϵ that satisfy these equations. The resulting coefficients represent the molecular orbitals, and the orbital energies represent the electronic energies associated with those orbitals.

The approach to solving the Roothaan-Hall equation starts with obtaining the matrix \mathbf{X} , which is the inverse square root of $\hat{\mathbf{S}}$. \mathbf{X} is calculated by diagonalizing $\hat{\mathbf{S}}$ and multiplying a diagonal matrix of the inverse square root of its eigenvalues ($\mathbf{s}^{-\frac{1}{2}}$) with the eigenvector matrix \mathbf{U} . They hold relationship as:

$$\mathbf{X} = \hat{\mathbf{S}}^{-\frac{1}{2}} = \mathbf{U}\mathbf{s}^{-\frac{1}{2}} \quad (2.22)$$

and $\mathbf{X}^{-1} = \hat{\mathbf{S}}^{\frac{1}{2}}$. After incorporating \mathbf{X} and \mathbf{X}^{-1} in equation 2.21 as:

$$\hat{\mathbf{F}}\mathbf{X}\mathbf{X}^{-1}\mathbf{C} = \hat{\mathbf{S}}\mathbf{X}\mathbf{X}^{-1}\mathbf{C}\epsilon \quad (2.23)$$

and substituting $\mathbf{X}^{-1}\mathbf{C} = \mathbf{C}'$, the expression:

$$\mathbf{X}^\dagger \hat{\mathbf{F}} \mathbf{X} \mathbf{C}' = \mathbf{X}^\dagger \hat{\mathbf{S}} \mathbf{X} \mathbf{C}' \epsilon \quad (2.24)$$

is obtained. As $\mathbf{X}^\dagger \hat{\mathbf{S}} \mathbf{X} = \mathbf{1}$ and assigning $\mathbf{X}^\dagger \hat{\mathbf{F}} \mathbf{X} = \hat{\mathbf{F}}'$, we reach a similar equation:

$$\hat{\mathbf{F}}' \mathbf{C}' = \mathbf{C}' \epsilon. \quad (2.25)$$

The obtained eigenvalues and eigenvectors by diagonalizing $\hat{\mathbf{F}}$ correspond to energy and \mathbf{C} . The SCF procedure iteratively solves these equations. It starts with an initial guess for the coefficients \mathbf{C} and orbital energies ϵ . The $\hat{\mathbf{F}}$ matrix is then constructed based on these initial orbitals. In

each iteration, new $\hat{\mathbf{D}}$, two-electron operators, and $\hat{\mathbf{F}}$ are calculated from \mathbf{C} obtained from the last diagonalization. The equations are solved, yielding new coefficients and energies. This process is repeated until self-consistency is achieved, meaning that the coefficients and energies no longer change significantly between iterations.

The molecular orbitals obtained from Hartree-Fock calculations are further used in configuration interaction, density functional theory, and perturbation correction methods.

2.5 Configuration Interaction Methods

Configuration Interaction (CI) is a quantum chemistry method that enhances the precision of wave function descriptions by accounting for electron correlation effects that go beyond the mean-field approximation. It is a post-Hartree-Fock technique designed to capture the various ways electrons can interact and move within a molecular system. In CI, the wave function is expressed as a sum of different electronic configurations, each configuration representing a specific arrangement of electrons within the molecular orbitals. This is mathematically represented as:

$$\Psi = \sum_i c_i \Phi_i, \quad (2.26)$$

where Ψ denotes the total wave function, c_i are the expansion coefficients, and Φ_i correspond to individual configurations. The number of configurations considered depends on the level of approximation and computational resources available. These configurations, Φ_i , are constructed by exciting electrons from occupied orbitals to virtual orbitals, allowing for single, double, triple, or even higher-level excitation. The coefficients c_i in this expansion are determined by solving the CI eigenvalue equation, which involves diagonalizing the Hamiltonian matrix within the chosen configuration space. The diagonal elements of this matrix correspond to the energies of individual configurations, while the off-diagonal elements represent electronic couplings between different configurations. The expansion of the CI wave function can be represented as follows:

$$|\Psi_{CI}\rangle = C_0 |\Psi_{HF}\rangle + \sum_{ma} C_m^a |\Psi_m^a\rangle + \sum_{m < n, a < b} C_{mn}^{ab} |\Psi_{mn}^{ab}\rangle + \sum_{m < n < o, a < b < c} C_{mno}^{abc} |\Psi_{mno}^{abc}\rangle + \dots, \quad (2.27)$$

here, C_0 is the coefficient of the Hartree-Fock (HF) wavefunction, which is the best single-configuration wavefunction for the molecule. $\sum_{ma} C_m^a |\Psi_m^a\rangle$ represents the single excitations, which are Slater determinants that differ from the HF wavefunction by the excitation of one electron from a closed orbital to an open orbital. $\sum_{m < n, a < b} C_{mn}^{ab} |\Psi_{mn}^{ab}\rangle$ represents the double excitations, which are Slater determinants that differ from the HF wavefunction by the excitation of two electrons from closed orbitals to open orbitals. $\sum_{m < n < o, a < b < c} C_{mno}^{abc} |\Psi_{mno}^{abc}\rangle$ represents the triple excitations, and so on.

CASCI (Complete Active Space Configuration Interaction) is a quantum chemistry approach used to investigate molecular electronic structure. It involves selecting an active space of electrons and orbitals relevant to a specific chemical phenomenon, generating all possible electronic configurations in this space, and calculating the energy while considering interactions between these configurations. The Complete Active Space Self-Consistent Field (CASSCF) wavefunction is optimized by minimizing the energy of the system using a self-consistent field (SCF) procedure. This means that the CASSCF wavefunction is calculated iteratively until the orbitals and energy converge.

Restricted Active Space Configuration Interaction (RASCI) is a computational method used in quantum chemistry for simulating the electronic structure and properties of molecular systems, particularly for molecules with complex electronic structures. It is based on the idea of dividing the orbital space into three subspaces: RAS I subspace contains the core orbitals, which are tightly bound and have low energies. RAS II subspace contains the active orbitals, which are involved in the electronic excitations of interest. RAS III subspace contains the virtual orbitals, which are high-energy and unoccupied. RASCI then calculates the CI wavefunction within the active space, subject to the restrictions that the number of holes in RAS I and the number of particles in RAS III are limited. This allows RASCI to accurately describe strongly correlated systems, while avoiding the high computational cost of full CI.

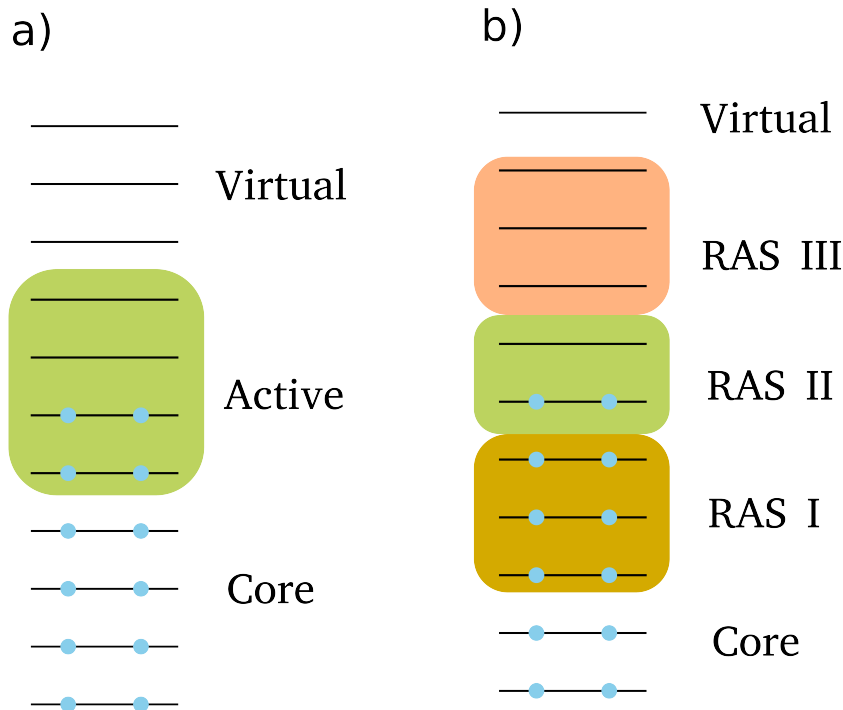


Figure 2.1: Orbital categorisation schematics for a) CASSCF b) RASCI

2.6 CASPT2

CASPT2 (Complete Active Space Second-Order Perturbation Theory) is a widely used computational method in quantum chemistry for calculating electronic structures of molecules. It combines the advantages of both multi-reference methods, such as CASSCF, and perturbation theory. It is capable of treating static and dynamic electron correlation effects, making it suitable for describing systems with strong electron correlation, such as transition metal complexes, excited states, and open-shell systems.[130] The method begins with the selection of an active space, which includes a subset of orbitals and electrons that are relevant to the electronic structure of interest. The active space is chosen based on chemical intuition and the nature of the problem being studied. Typically, it consists of a small number of orbitals and electrons, allowing for a more computationally tractable calculation compared to full configuration interaction methods. In CASPT2, the wave function is described as a linear combination of determinants, known as configuration state functions (CSFs). The CSFs are constructed by distributing the electrons among the active orbitals in different ways.[131] The expansion coefficients of the CSFs are optimized by solving the CASSCF equations, which involve variationally optimizing both the orbital and expansion coefficients. Once the CASSCF step is complete, CASPT2 applies second-order perturbation theory to incorporate dynamic electron correlation effects beyond the CASSCF reference wave function. This perturbative treatment improves the accuracy of the electronic energies and wave function. CASPT2 calculations provide valuable information about molecular properties such as ground-state energies, excited-state energies, potential energy surfaces, and transition probabilities. It can accurately describe bond breaking/formation processes, electron transfer reactions, and excited-state properties.

Perturbation theory begins by dividing the full Hamiltonian into a zeroth-order component, denoted as \hat{H}_0 , simultaneously, a perturbation operator \hat{V} is introduced to represent the difference between the full Hamiltonian and the zeroth-order part. The obtained expression looks like:

$$\hat{H} = \hat{H}_0 + \hat{V}. \quad (2.28)$$

\hat{H}_0 is associated with known eigenfunctions $\Psi_\alpha^{(0)}$ and their corresponding eigenvalues $E_\alpha^{(0)}$. CASPT2

begins with a reference state, which is defined by the CASSCF reference state denoted as $|\Psi_\alpha^{(0)}\rangle$ as zeroth-order wave functions of wave function $|\Psi_\alpha\rangle$. Within this method, a projection operator onto the reference space is introduced, represented as \hat{P} , and defined as:

$$\hat{P} = |\Psi_\alpha^{(0)}\rangle\langle\Psi_\alpha^{(0)}|. \quad (2.29)$$

The Hilbert space is partitioned into reference space and complementary space (Q). Then projection operator on complementary space is defined as $\hat{Q} = \hat{1} - \hat{P}$. To facilitate the transformation of the zeroth-order state $\Psi_\alpha^{(0)}$ into the desired state Ψ_α , a wave operator $\hat{\Omega}_\alpha$ is introduced, which is defined as :

$$\Psi_\alpha = \hat{\Omega}_\alpha \Psi_\alpha^{(0)}. \quad (2.30)$$

The commutation relationship between $\hat{\Omega}$ and the zeroth-order Hamiltonian operator \hat{H}_0 is described by the generalized Bloch equation:

$$(E_\alpha^{(0)} - \hat{H}_0)\hat{\Omega}_\alpha|\Psi_\alpha^{(0)}\rangle = \hat{Q}\hat{V}\hat{\Omega}_\alpha|\Psi_\alpha^{(0)}\rangle - \hat{Q}\hat{\Omega}_\alpha|\Psi_\alpha^{(0)}\rangle\langle\Psi_\alpha^{(0)}|\hat{V}\hat{\Omega}_\alpha|\Psi_\alpha^{(0)}\rangle. \quad (2.31)$$

In order to implement quasi degenerate perturbation theory $\hat{\Omega}_\alpha$ is expanded a series of terms:

$$\hat{\Omega}_\alpha = \hat{\Omega}_\alpha^{(0)} + \hat{\Omega}_\alpha^{(1)} + \hat{\Omega}_\alpha^{(2)} + \dots \quad (2.32)$$

As an intermediate normalization $\langle\Psi_\alpha|\Psi_\alpha^{(0)}\rangle = 1$ is introduced, it leads to first order equation for the wave operator:

$$(E_\alpha^{(0)} - \hat{H}_0)\hat{\Omega}_\alpha^{(1)}|\Psi_\alpha^{(0)}\rangle = \hat{Q}\hat{H}|\Psi_\alpha^{(0)}\rangle. \quad (2.33)$$

The second-order energy correction is computed as:

$$E_\alpha^{(2)} = E_\alpha^{(1)} + \langle\Psi_\alpha^{(0)}|\hat{H}\hat{\Omega}_\alpha^{(1)}|\Psi_\alpha^{(0)}\rangle. \quad (2.34)$$

Equation 2.35 presents the decomposition of the \hat{H}_0^α operator within the CASPT2 method. It takes the form:

$$\begin{aligned} \hat{H}_0^\alpha = & + \sum_{k \in P^\perp} |\Psi_k^{(0)}\rangle\langle\Psi_k^{(0)}|\hat{F}_\alpha|\Psi_\alpha^{(0)}\rangle\langle\Psi_\alpha^{(0)}| \\ & + \hat{Q}_{SD}^\alpha \hat{F}_\alpha \hat{Q}_{SD}^\alpha + \hat{Q}_{TQ}^\alpha \cdots \hat{F}_\alpha \hat{Q}_{TQ}^\alpha \cdots \end{aligned} \quad (2.35)$$

In this equation, P^\perp represents the set of indices orthogonal to the reference subspace. \hat{F}_α corresponds to the state-specific Fock operator, which accounts for kinetic and Coulomb interactions between electrons. \hat{Q}_{SD}^α is a subspace generated by applying double excitation operators to $|\Psi_\alpha^{(0)}\rangle$, and higher-order excitations are included as $\hat{Q}_{TQ}^\alpha \cdots$.

The Fock operator \hat{F}_α can be expressed as:

$$\hat{F}_\alpha = \sum_{pq} f_{pq}^\alpha \hat{E}_{pq}. \quad (2.36)$$

The spin-averaged excitation operators E_{pq} are defined as follows:

$$\hat{E}_{pq} = \sum_\sigma a_{q\sigma}^\dagger a_{p\sigma}. \quad (2.37)$$

The equation $\sum_\sigma a_{q\sigma}^\dagger a_{p\sigma}$ encapsulates the summation over all possible spin states (σ) and the creation (a^\dagger) and annihilation (a) operators for electrons in orbitals q and p respectively. f_{pq}^α represents the state-specific elements of the fock operator and it is defined by:

$$f_{pq}^\alpha = h_{pq} + \sum_{rs} \left((pq|rs) - \frac{1}{2}(pr|qs) \right) \quad (2.38)$$

and the density operator is expressed as:

$$D_{rs}^\alpha = h_{pq} + g_{pq}(D^\alpha). \quad (2.39)$$

The basis functions $|pqrs;\Psi_\alpha^{(0)}\rangle$ are internally contracted states that depend on the orbital indices p , q , r , and s , and are given by:

$$|pqrs; \Psi_\alpha^{(0)}\rangle = E_{pq}E_{rs}|\Psi_\alpha^{(0)}\rangle. \quad (2.40)$$

The states $|pqrs; \Psi_\alpha^{(0)}\rangle$ are characterized as nonorthogonal and linearly dependent. It's worth noting that internally contracted states involving active orbitals p, q, r , and s are not part of the \hat{Q}_{SD}^α subspace.

The application of following identities:

$$\hat{Q}\hat{H}|\Psi_\alpha^{(0)}\rangle = \hat{Q}_{SD}^\alpha \hat{H}|\Psi_\alpha^{(0)}\rangle, \quad (2.41)$$

$$\hat{Q}_{SD}^\alpha \hat{H}_0 \hat{Q}_{TQ}^\alpha = 0 \quad (2.42)$$

and

$$\hat{Q}_{SD}^\alpha \hat{H}_0 \hat{Q}_{SD}^\alpha = \hat{Q}_{SD}^\alpha \hat{F}_\alpha \hat{Q}_{SD}^\alpha \quad (2.43)$$

relate the zeroth-order Hamiltonian to the Fock operator \hat{F}_α within the \hat{Q}_{SD}^α subspace.

The CASPT2 energy equation can be expressed as:

$$(E_\alpha^{(0)} - \hat{F}_\alpha) \hat{\Omega}_\alpha^{(1)} |\Psi_\alpha^{(0)}\rangle = \hat{Q}_{SD}^\alpha \hat{H} |\Psi_\alpha^{(0)}\rangle, \quad (2.44)$$

here, $\hat{\Omega}_\alpha^{(1)}$ projects exclusively into the \hat{Q}_{SD}^α subspace,

$$\hat{\Omega}_\alpha^{(1)} = \hat{Q}_{SD}^\alpha \hat{\Omega}_\alpha^{(1)}. \quad (2.45)$$

In single-state CASPT2, a generalized Fock operator \hat{F}_α is employed. This operator is nondiagonal and depends on the one-particle density matrix of $|\Psi_\alpha^{(0)}\rangle$. The energy equation 2.44 is solved iteratively to determine $\hat{\Omega}_\alpha^{(1)}$, using states spanning the \hat{Q}_{SD}^α subspace. These states are obtained through orthogonalization, eliminating linear dependence among the $|pqrs; \Psi_\alpha^{(0)}\rangle$ states.

2.6.1 MS-CASPT2

The concept of the reference space is a fundamental aspect of Multi-State Complete Active Space Second-Order Perturbation Theory (MS-CASPT2). In this context, the multidimensional reference space (\hat{P}) represents a subspace within the broader Hilbert space, containing the reference states. Conversely, the complementary space (\hat{Q}) includes all states orthogonal to the reference space [132]. The reference space is spanned by two or more state-average CASSCF (SA-CASSCF) or CASCI states, and the projection operator is represented as:

$$\hat{P} = \sum_{\gamma \in P} |\Psi_\gamma^{(0)}\rangle \langle \Psi_\gamma^{(0)}|, \quad (2.46)$$

here, \hat{P} represents the set of indices associated with the selected reference states. $|\Psi_\gamma^{(0)}\rangle$ denotes the zeroth-order eigenfunction corresponding to the index γ , while $E_\gamma^{(0)}$ is the corresponding eigenvalue. The projector onto the complementary space is given by $\hat{Q} = 1 - \hat{P}$. In MS-CASPT2, a wave operator $\hat{\Omega}_P$, similar to CASPT2, is defined, generating the exact states of interest $|\Psi_P\rangle$ when operating on the reference states $|\Psi_P^{(0)}\rangle$:

$$|\Psi_P\rangle = \hat{\Omega}_P |\Psi_P^{(0)}\rangle. \quad (2.47)$$

The following commutation relationship describes the interplay between the wave operator $\hat{\Omega}_P$, the zeroth-order Hamiltonian operator \hat{H}_γ^0 , and the perturbation operator \hat{V}_γ :

$$(E_\gamma^0 - \hat{H}_\gamma^0) \hat{\Omega}_P |\Psi_\gamma^{(0)}\rangle = \hat{Q} \hat{V}_\gamma \hat{\Omega}_P |\Psi_\gamma^{(0)}\rangle - \hat{Q} \hat{\Omega}_P \hat{P} \hat{V}_\gamma \hat{\Omega}_P |\Psi_\gamma^{(0)}\rangle. \quad (2.48)$$

For all $\gamma \in P$, intermediate normalization $\langle \Psi_P^{(0)} | \Psi_P \rangle = 1$ is used. The perturbation Hamiltonian for each reference state indexed as γ is:

$$\hat{H} = \hat{H}_\gamma^{(0)} + \hat{V}_\gamma. \quad (2.49)$$

The order-by-order perturbative expansion of the wave operator is expressed as:

$$\hat{\Omega}_P = \hat{\Omega}_P^{(0)} + \hat{\Omega}_P^{(1)} + \hat{\Omega}_P^{(2)} + \dots \quad (2.50)$$

and the zero-order Hamiltonian is:

$$\begin{aligned}\hat{H}_\gamma^{(0)} &= \sum_{\beta \in P} |\Psi_\beta^{(0)}\rangle\langle\Psi_\beta^{(0)}| \hat{F}_\gamma |\Psi_\beta^{(0)}\rangle\langle\Psi_\beta^{(0)}| \\ &+ \sum_{k \in P^\perp} |\Psi_k^{(0)}\rangle\langle\Psi_k^{(0)}| \hat{F}_\gamma |\Psi_k^{(0)}\rangle\langle\Psi_k^{(0)}| , \\ &+ \hat{Q}_{SD}^\gamma \hat{F}_\gamma \hat{Q}_{SD}^\gamma + \hat{Q}_{TQ}^\gamma \cdots \hat{F}_\gamma \hat{Q}_{TQ}^\gamma \cdots\end{aligned}\quad (2.51)$$

where the sum over β includes all the reference states, including γ . $k \in P^\perp$ refers to states in the complete active space other than reference states. Upon substituting equation 2.50 in equation 2.48, the extracted first-order term becomes:

$$(E_\gamma^{(0)} - \hat{F}_\gamma) \hat{\Omega}_\gamma^{(1)} |\Psi_\gamma^{(0)}\rangle = \hat{Q}_{SD}^\gamma \hat{H} |\Psi_\gamma^{(0)}\rangle. \quad (2.52)$$

Similar identities from CASPT2, equations 2.41, 2.42, and 2.43, are used in equations 2.51 and 2.52. The comparison between equations 2.44 and 2.52 gives $\hat{\Omega}_P^{(1)} |\Psi_\gamma\rangle$ to be equivalent to $\Omega_\alpha^{(1)} |\Psi_\alpha\rangle$. This implies that the multistate wave operator $\hat{\Omega}_P^{(1)}$ is linear combination of a single-state wave operator:

$$\hat{\Omega}_P^{(1)} = \sum_{\gamma \in P} \hat{\Omega}_\gamma^{(1)} |\Psi_\gamma\rangle\langle\Psi_\gamma|. \quad (2.53)$$

The effective Hamiltonian of the first-order Hamiltonian is given by:

$$\hat{H}^{eff} = \hat{P} \hat{H} \hat{\Omega}_P \hat{P}. \quad (2.54)$$

When \hat{H}^{eff} operates only on reference states $|\Psi_P^{(0)}\rangle$, it results in the exact energy E_P of $|\Psi_P\rangle$. So,

$$\hat{H}^{eff} |\Psi_P^{(0)}\rangle = E_P |\Psi_P^{(0)}\rangle \quad (2.55)$$

and

$$\hat{H} |\Psi_P\rangle = E_P |\Psi_P\rangle. \quad (2.56)$$

The second-order effective Hamiltonian, denoted as H_{2nd}^{eff} , is composed of terms, including the projection operator \hat{P} , the Hamiltonian (\hat{H}), and the first-order wave operator ($\Omega_P^{(1)}$):

$$\hat{H}_{2nd}^{eff} = \hat{P} \hat{H} \hat{P} + \hat{P} \hat{H} \hat{\Omega}_P^{(1)} \hat{P}. \quad (2.57)$$

The second-order effective Hamiltonian allows for the calculation of second-order energy corrections. Specifically, for a given reference state $|\Psi_\gamma\rangle$, the expectation value of \hat{H}_{2nd}^{eff} provides the second-order energy correction, denoted as $E_\gamma^{(2)}$:

$$\langle \Psi_\gamma | \hat{H}_{2nd}^{eff} | \Psi_\gamma \rangle = E_\gamma^{(2)}. \quad (2.58)$$

Additionally, when considering interactions between different reference states $|\Psi_\alpha\rangle$ and $|\Psi_\gamma\rangle$, the matrix element of coupling takes into account both the Hamiltonian (\hat{H}) and the first-order wave operator ($\hat{\Omega}_\gamma^{(1)}$):

$$\langle \Psi_\alpha | \hat{H}_{2nd}^{eff} | \Psi_\gamma \rangle = \langle \Psi_\alpha | \hat{H} \hat{\Omega}_\gamma^{(1)} | \Psi_\gamma \rangle. \quad (2.59)$$

These equations provide a detailed understanding of how model states interact with each other and contribute to energy corrections within the quantum chemical framework.

2.6.2 XMS-CASPT2

Similar to the construction of zeroth order zeroth Hamiltonian in MS CASPT2 with same set of reference space (model space), complementary space and wave operator but with crucial difference of fock operator to be state averaged. Thus zeroth Hamiltonian is written as:

$$\begin{aligned}\hat{H}^{(0)} &= \sum_{\gamma, \delta \in P} |\Psi_\gamma^{(0)}\rangle\langle\Psi_\gamma^{(0)}| \hat{F}_{SA} |\Psi_\delta^{(0)}\rangle\langle\Psi_\delta^{(0)}| \\ &+ \sum_{k \in P^\perp} |\Psi_k^{(0)}\rangle\langle\Psi_k^{(0)}| \hat{F}_{SA} |\Psi_k^{(0)}\rangle\langle\Psi_k^{(0)}| , \\ &+ \hat{Q}_{SD} \hat{F}_{SA} \hat{Q}_{SD} + \hat{Q}_{TQ} \cdots \hat{F}_{SA} \hat{Q}_{TQ} \cdots\end{aligned}\quad (2.60)$$

The construction of the Fock operator

$$f_{pq}^{SA} = h_{pq} + g_{pq}(\mathbf{D}^{SA}) \quad (2.61)$$

is now based on the state-average density matrix. Where

$$\mathbf{D}^{SA} = \frac{1}{d} \sum_{\alpha \in P} \mathbf{D}^{\alpha}. \quad (2.62)$$

As a result, this new approach fundamentally alters the dynamics and interactions between states within the reference space. For a reference space containing d states, the non-diagonal nature of \hat{H}_0 in the zeroth-order basis introduces some complexity in solving equation 2.62 where $\mathbf{D}_{rs}^{\alpha} = \langle \tilde{\Psi}_{\alpha}^{(0)} | \hat{E}_{rs} | \tilde{\Psi}_{\alpha}^{(0)} \rangle$. However, this complexity can be effectively addressed by performing a unitary transformation of the reference states. This transformation, denoted by \hat{U} , leads to rotated wave functions:

$$\tilde{\Psi}_{\alpha}^{(0)} = \sum_{\beta \in P} \hat{U}_{\beta\alpha} \Psi_{\beta}^{(0)}, \quad (2.63)$$

here, P represents the set of indices labeling the reference states.

The primary goal of this transformation is to diagonalize the Fock operator within the reference space using the rotated wave functions. In other words, the rotated reference states satisfy the condition:

$$\langle \tilde{\Psi}_{\alpha}^{(0)} | \hat{f} | \tilde{\Psi}_{\beta}^{(0)} \rangle = 0 \quad \text{for } \alpha \neq \beta \in P \quad (2.64)$$

Thus, the Hamiltonian becomes:

$$\begin{aligned} \hat{H}_0 = & \sum_{\gamma \in P} |\tilde{\Psi}_{\gamma}^{(0)}\rangle \langle \tilde{\Psi}_{\gamma}^{(0)}| \hat{F}_{SA} |\tilde{\Psi}_{\gamma}^{(0)}\rangle \langle \tilde{\Psi}_{\gamma}^{(0)}| \\ & + \sum_{k \in P^{\perp}} |\Psi_k^{(0)}\rangle \langle \Psi_k^{(0)}| \hat{F}_{SA} |\Psi_k^{(0)}\rangle \langle \Psi_k^{(0)}| . \\ & + \hat{Q}_{SD} \hat{F}_{SA} \hat{Q}_{SD} + \hat{Q}_{TQ} \cdots \hat{F}_{SA} \hat{Q}_{TQ} \cdots \end{aligned} \quad (2.65)$$

The solution to this invariance problem was proposed independently by Granovsky for MC-QDPT and by Shiozaki et al.[133, 134] for MS-CASPT2. This solution, known as Extended Multistate CASPT2 (XMS-CASPT2), tackles the invariance issue by modifying the construction of the zeroth-order Hamiltonian. In XMS-CASPT2, the zeroth-order Hamiltonian is no longer restricted to a diagonal approximation. Instead, it takes into account both diagonal and off-diagonal interactions within the model space.

2.7 ASD/ASD-Model Hamiltonian

Electronic structure methods based on the active-space model are used to treat neutral, singly excited, doubly excited, and CT states. The complete active-space methods (CASCI/CASCF) and active-space methods with occupation restrictions (RASCI) are well suited for calculations of excitonic properties, but their factorial scaling of computational cost with respect to number of active orbitals makes calculations of excitons in molecular aggregates computationally demanding or impossible. ASD attempts to alleviate high computational demand by tailoring an active-space model especially for molecular dimers. The dimer model is immediately applicable to processes such as charge or energy transfer and exciton fission. The wave function of the system is parameterised by:

$$|\Psi\rangle = \sum_{IJ} C_{I,J}^K |\Psi_I^A\rangle \otimes |\Psi_J^B\rangle = \sum_{IJ} C_{IJ}^k |\Psi_I^A \Psi_J^B\rangle, \quad (2.66)$$

where A and B represent the fragments and I and J represent the states of the fragments, K represents the dimer status. In practice, the number of states that need to be included in simulations of molecular dimers will be shown to be fairly small. One can diagonalize the dimer Hamiltonian without forming the direct product configurations explicitly, leading to an algorithm that only requires intermediates that scale linearly with respect to the number of configurations in a monomer

calculation. Therefore, active spaces of the monomer in dimer calculations can be as large as that used in monomer calculations. The dimer Hamiltonian is written as:

$$\hat{H} = \frac{(-1)^\psi}{2} \sum_{\zeta \in \mathcal{A}} \sum_{\eta \in \mathcal{B}} \hat{E}_\zeta \hat{E}_\eta h_{\zeta, \eta}, \quad (2.67)$$

where \hat{E}_ζ and \hat{E}_η are the string of creation and annihilation operator ($\hat{a}_{p\sigma}^\dagger \hat{a}_{p\sigma}$) corresponding to orbital \mathcal{A} and \mathcal{B} .

$$\hat{E}_\zeta = \hat{a}_{p\rho}^\dagger \hat{a}_{p\sigma}^\dagger \hat{a}_{p\sigma} \quad (2.68)$$

$$\hat{E}_\eta = \hat{a}_{\bar{r}\rho} \quad (2.69)$$

$$h_{\eta, \zeta} = (pq|rs) \quad (2.70)$$

in which ρ and σ denote spins, p , q , and s label active orbitals of monomer A, and \bar{r} labels those of monomer B and $(pq|rs)$ represent two electron integral.

Different types of intermolecular interactions are classified based on their actions, including diagonal interactions, spin-flip interactions, charge-transfer interactions, and more. The matrix elements

$$\langle \Psi_I^A \Psi_J^B | \hat{H} | \Psi_I^A \Psi_J^B \rangle = \frac{(-1)^\psi}{2} \sum_{\eta\zeta} \Gamma_\zeta^{A,I^*,I} h_{\zeta, \eta} \Gamma_\eta^{B,J^*,J} \quad (2.71)$$

are computed using monomer's intermediate quantities, which are evaluated through matrix-matrix multiplications. where

$$\Gamma_\xi^{S,X,X^*} = \langle \Phi_{X^*}^S | E_\xi | \Phi_X^S \rangle, \quad (2.72)$$

and the symbols S represent the monomer and X and X^* correspond to initial and final states. The algorithm avoids the explicit construction of the dimer configuration space. The calculations are performed using the BAGEL package.[135]

2.8 Density Functional Theories

2.8.1 Density Functional Theory

Density Functional Theory (DFT) is a widely used computational approach in quantum chemistry and condensed matter physics for studying the electronic structure and properties of materials. It offers a practical way to describe many-electron systems by focusing on the electron density, making it computationally more efficient than traditional wave function-based methods. In DFT, the central quantity of interest is the electron or charge density $\rho(\mathbf{r})$ which include position and spin, which gives the probability of finding an electron at a specific point in space \mathbf{r} . Unlike wave function methods, which require solving the Schrödinger equation for each electron separately, DFT describes the behavior of all electrons through the electron density. The central challenge in DFT is accurately describing the exchange and correlation effects between electrons. The exchange-correlation functional $E_{XC}[\rho]$ captures these effects and is a crucial component of DFT. Approximations to the exchange-correlation functional are necessary, and different density functionals provide various levels of accuracy and computational efficiency. Density function theory starts from Thomas-Fermi homogeneous electron gas model .[136, 137, 138] In this model the approximation aims toward finding the electronic properties using one-electron density neglecting relativity corrections. As per that the kinetic energy and coulombic interaction energy gas is formulated as :

$$T[\rho] = C_F \int \rho^{5/3}(\mathbf{r}) d\mathbf{r} , C_F = \frac{3}{10} \left(\frac{3\pi^2}{2} \right)^{2/3} \quad (2.73)$$

and

$$J[\rho] = \frac{1}{2} \int \rho(\mathbf{r}) \rho(\mathbf{r}') \frac{1}{|\mathbf{r} - \mathbf{r}'|} d\mathbf{r} d\mathbf{r}', \quad (2.74)$$

where $T[\rho]$ represents the kinetic energy functional of ρ , and C_F is a constant. The equation calculates the kinetic energy of the charge density by integrating ρ raised to the power of 5/3 with

respect to \mathbf{r} . The exchange energy $E_X[\rho]$ represents of the charge density ρ , and constant C_X involving π , is:

$$E_X[\rho] = -C_X \int \rho^{4/3}(\mathbf{r}) d\mathbf{r} , \quad (2.75)$$

where

$$C_X = \frac{3}{4} (3\pi)^{1/2} . \quad (2.76)$$

The core principles of DFT are encapsulated in two fundamental statements formulated and proven by Hohenberg and Kohn .Regarding the electronic structure, consider a Slater determinant formed from integrally occupied orthonormal single-particle orbitals. The many particle electron density $\rho(\mathbf{r})$ is defined as:

$$\rho(\mathbf{r}) = N \int \Psi^*(\mathbf{r}_1, \mathbf{r}_2, \mathbf{r}_3, \dots) \Psi(\mathbf{r}_1, \mathbf{r}_2, \mathbf{r}_3, \dots) d\mathbf{r}_1 d\mathbf{r}_2 \dots , \quad (2.77)$$

where N is a normalization constant, and $\Psi(\mathbf{r}_1, \mathbf{r}_2, \mathbf{r}_3, \dots)$ represents the wave function of the system. The electron density within an N-body quantum system can be expressed using a set of occupied orbitals while adhering to the constraint of N-Body system is given by:

$$\rho(\mathbf{r}) = \sum_{i=1}^N |\phi_i(\mathbf{r})|^2 , \quad (2.78)$$

where

$$N = \int \rho(\mathbf{r}) d\mathbf{r} . \quad (2.79)$$

The total energy $E[\rho]$ of a quantum mechanical system is represented by the following functional expression:

$$E[\rho] = T_0[\rho] + E_{ne}[\rho] + J[\rho] + E_{XC}[\rho] . \quad (2.80)$$

It comprises several components: $T_0[\rho]$, which accounts for the kinetic energy of the non-interacting electrons; $E_{ne}[\rho]$, representing the interaction between electrons and external potentials, such as those from nuclei; $J[\rho]$, the classical Coulomb energy arising from electron-electron interactions; and $E_{XC}[\rho]$, the exchange-correlation energy functional that captures quantum mechanical exchange and correlation effects among the electrons.

The Kohn-Sham (KS) potential can be interpreted as an attempt to reconcile the perturbative changes of E_{XC} in $T_0[\rho]$ and $J[\rho]$. It is expressed as the sum of two terms:

$$E_{XC} = (T[\rho] - T_0[\rho]) + (V_{ee}[\rho] - J[\rho]), \quad (2.81)$$

where $T[\rho] - T_0[\rho]$ represents kinetic correlation energy functional, and $V_{ee}[\rho] - J[\rho]$, which accounts for the potential correlation and exchange energy.

To solve the electronic structure of a system and describe the behaviour of electrons, the system of equations incorporates the exchange-correlation potential, capturing the effects of electron-electron correlation. This leads to an eigenvalue equation that governs the behaviour of electrons. In the Kohn-Sham (KS) equation, the effective potential includes the exchange-correlation potential, which captures the effects of electron-electron correlation. This is in contrast to the Hartree-Fock equation, which considers only the classical electrostatic repulsion between electrons and neglects electron correlation effects. The Kohn-Sham equations are formulated as follows:

$$\left(-\frac{\hbar^2}{2m} \nabla^2 + v_{KS}(\mathbf{r}) \right) \phi_i(\mathbf{r}) = \varepsilon_i \phi_i(\mathbf{r}), \quad (2.82)$$

where $\phi_i(\mathbf{r})$ represents the wavefunction for the i -th electron, $v_{KS}(\mathbf{r})$ is the effective Kohn-Sham potential, ε_i is the corresponding eigenvalue. The equation 2.83 defines the Kohn-Sham potential $v_{KS}(\mathbf{r})$ as:

$$v_{KS}(\mathbf{r}) = v_{ext}(\mathbf{r}) + \int \rho(\mathbf{r}') d\mathbf{r}' \frac{1}{|\mathbf{r} - \mathbf{r}'|} + v_{XC}(\mathbf{r}), \quad (2.83)$$

in terms of various components. It showcases how the Kohn-Sham potential at a specific point \mathbf{r} is constructed through the interaction of the external potential, the charge density $\rho(\mathbf{r}')$ at different points.[139, 140] The $v_{XC}(\mathbf{r})$ is describes as:

$$v_{XC}(\mathbf{r}) = \frac{\delta E_{XC}[\rho]}{\delta \rho(\mathbf{r})}. \quad (2.84)$$

In equation 2.84, $E_{XC}[\rho]$ is the exchange-correlation energy functional, and $\frac{\delta}{\delta\rho(\mathbf{r})}$ denotes the functional derivative with respect to the charge density ρ at point \mathbf{r} . Since E_{XC} includes both exchange and correlation factors simultaneously, the approach should overcome the problem of independent particles. This is achieved by introducing the pair density.

To solve the Kohn-Sham eigenvalue problem, the computational concept of reduced density matrix and density cumulants theory is utilized. The normalized one-particle density matrix, representing the electron population of the system, is defined as:

$$\Gamma^{(1)}(\mathbf{r}_1|\mathbf{r}'_1) = N \int d\mathbf{r}_2 \dots d\mathbf{r}_N \psi^*(\mathbf{r}'_1, \mathbf{r}_2, \dots, \mathbf{r}_N) \psi(\mathbf{r}_1, \mathbf{r}_2, \dots, \mathbf{r}_N), \quad (2.85)$$

which quantifies the likelihood of finding one particle at \mathbf{r}_1 while another particle is at spin-position \mathbf{r}'_1 , with the integration encompassing the coordinates of the remaining particles. Then, equation

$$\Gamma^{(2)}(\mathbf{r}_1, \mathbf{r}_2|\mathbf{r}'_1, \mathbf{r}'_2) = N(N-1) \int d\mathbf{r}_3 \dots d\mathbf{r}_N \psi^*(\mathbf{r}'_1, \mathbf{r}'_2, \dots, \mathbf{r}_N) \psi(\mathbf{r}_1, \mathbf{r}_2, \dots, \mathbf{r}_N) \quad (2.86)$$

and

$$\Gamma^{(2)}(\mathbf{r}_1, \mathbf{r}_2|\mathbf{r}'_1, \mathbf{r}'_2) = \Gamma^{(1)}(\mathbf{r}_1|\mathbf{r}'_1)\Gamma^{(1)}(\mathbf{r}_2|\mathbf{r}'_2) - \Gamma^{(1)}(\mathbf{r}_2|\mathbf{r}'_1)\Gamma^{(1)}(\mathbf{r}_1|\mathbf{r}'_2) + \Gamma_{XC}^{(2)}(\mathbf{r}_1, \mathbf{r}_2|\mathbf{r}'_1, \mathbf{r}'_2). \quad (2.87)$$

represents expression for the two-particle reduced density matrix element. In the specific case where the positions are equal ($\mathbf{r}_1 = \mathbf{r}'_1$ and $\mathbf{r}_2 = \mathbf{r}'_2$), the equation simplifies, and the exchange-correlation contribution disappears:

$$\begin{aligned} \Gamma^{(2)}(\mathbf{r}_1, \mathbf{r}_2|\mathbf{r}_1, \mathbf{r}_2) &= \Gamma^{(2)}(\mathbf{r}_1, \mathbf{r}_2) = \Gamma^{(1)}(\mathbf{r}_1|\mathbf{r}_1)\Gamma^{(1)}(\mathbf{r}_2|\mathbf{r}_2) + \Gamma_{XC}^{(2)}(\mathbf{r}_1, \mathbf{r}_2|\mathbf{r}_1, \mathbf{r}_2) \\ &= \rho(\mathbf{r}_1)\rho(\mathbf{r}_2) + \Gamma_{XC}^{(2)}(\mathbf{r}_1, \mathbf{r}_2). \end{aligned} \quad (2.88)$$

Equation 2.88 illustrates that the total two-particle reduced density matrix element $\Gamma^{(2)}(\mathbf{r}_1, \mathbf{r}_2|\mathbf{r}_1, \mathbf{r}_2)$ can be expressed in terms of the one-particle reduced density matrices and the exchange-correlation contribution $\Gamma_{XC}^{(2)}$, which describes the correlation of the electrons due to Fermi and Coulomb interactions, thereby reducing the probability amplitude of finding them close to each other. The many-body correlation in the Density Functional Approximation (DFA) is treated approximately as a set of independent electron pairs, leading to the expression for the exchange-correlation (XC) energy. Additionally, the exchange-correlation energy is evaluated using the following equation:

$$E_{XC} = \frac{1}{2} \iint \frac{d\mathbf{r}_1 d\mathbf{r}_2}{|\mathbf{r}_1 - \mathbf{r}_2|} [\Gamma^{(2)}(\mathbf{r}_1, \mathbf{r}_2) - \rho(\mathbf{r}_1)\rho(\mathbf{r}_2)]. \quad (2.89)$$

This equation calculates the exchange-correlation energy based on the two-particle reduced density matrix $\Gamma^{(2)}$ and the charge density $\rho(\mathbf{r})$ at positions \mathbf{r}_1 and \mathbf{r}_2 . Further insight into the exchange-correlation hole comes from the equations:

$$h_{XC}(\mathbf{r}_1, \mathbf{r}_2) = \frac{\Gamma^{(2)}(\mathbf{r}_1, \mathbf{r}_2)}{\rho(\mathbf{r}_1) - \rho(\mathbf{r}_2)} \quad (2.90)$$

and

$$\int h_{XC}(\mathbf{r}_1, \mathbf{r}_2) d\mathbf{r}_2 = -1, \quad (2.91)$$

here, $h_{XC}(\mathbf{r}_1, \mathbf{r}_2)$ denotes the exchange-correlation hole, revealing the distribution of electron density around an electron positioned at \mathbf{r}_1 in response to the presence of another electron at \mathbf{r}_2 . After incorporating equation 2.90 to equation 2.89 we get the equation of exchange correlation as equation

$$E_{XC}[\rho(\mathbf{r})] = \frac{1}{2} \int \frac{\rho(\mathbf{r}_1)}{|\mathbf{r}_1 - \mathbf{r}_2|} h_{XC}(\mathbf{r}_1, \mathbf{r}_2) d\mathbf{r}_1 d\mathbf{r}_2. \quad (2.92)$$

One way to describe the exchange energy is through the concept of the exchange hole. Mathematically, the exchange hole is characterized by the equation:

$$h_X(\mathbf{r}_1|\mathbf{r}_2) = -\frac{1}{2} \frac{|\Gamma^{(1)}(\mathbf{r}_1|\mathbf{r}_2)|^2}{\rho(\mathbf{r}_1)}, \quad (2.93)$$

here, $h_X(\mathbf{r}_1|\mathbf{r}_2)$ quantifies the exchange hole, capturing the effects of electron exchange interactions. The term $\Gamma^{(1)}(\mathbf{r}_1|\mathbf{r}_2)$ represents the probability density of finding an electron at positions \mathbf{r}_1 and \mathbf{r}_2 , while $\rho(\mathbf{r}_1)$ represents the charge density at position \mathbf{r}_1 . In the context of DFT, the local density approximation (LDA) provides an approximation for the exchange energy.[141] The LDA exchange energy functional is given by:

$$E_X^{\text{LDA}}[\rho(\mathbf{r})] = -\frac{3}{4} \left(\frac{3}{\pi}\right)^{1/3} \int \rho^{4/3}(\mathbf{r}) d\mathbf{r} \quad (2.94)$$

and Local Spin Density Approximation is given as sum of individual densities:

$$E_X^{\text{LSDA}}[\rho(\mathbf{r})] = -\frac{3}{4} \left(\frac{6}{\pi}\right)^{1/3} \int \rho_{\alpha}^{4/3}(\mathbf{r}) + \rho_{\beta}^{4/3}(\mathbf{r}) d\mathbf{r}. \quad (2.95)$$

To further refine exchange energy calculations, B88 exchange energy functional was introduced. It is described as:

$$E_X^{\text{B88}}[\rho] = E_X^{\text{LDA}}[\rho] - \beta \int \rho^{4/3}(\mathbf{r}) \frac{x^2 d\mathbf{r}}{(1 + 6\beta x \sinh^{-1}(x))}. \quad (2.96)$$

It extends the LDA approach by incorporating additional terms involving parameters β and x , which consider the gradient of the charge density.[142] The B88 functional enhances the accuracy of exchange interactions. In this equation, $E_X^{\text{B88}}[\rho]$ represents the B88 exchange energy functional, which modifies the LDA exchange energy by considering the charge density and gradient-dependent terms. The derivative x quantifies the variation in electron density on the molecular scale, and its calculation is given by the equation:[142]

$$x = \frac{|\nabla \rho(\mathbf{r})|}{\rho^{4/3}(\mathbf{r})}. \quad (2.97)$$

It can be combined with LYP correlation and has no relation to the uniform electron gas. (see equation 2.98) For a closed-shell systems it reads:

$$\begin{aligned} E_C^{\text{LYP}}[\rho] = & -a \int \rho(\mathbf{r}) d\mathbf{r} \left(1 + e^{-\rho^{-1/3}(\mathbf{r})}\right) \\ & - ab \int \omega \rho^2(\mathbf{r}) \left[C_F \rho^{8/3}(\mathbf{r}) + |\nabla \rho(\mathbf{r})|^2 \left(\frac{5}{12} - \frac{\delta}{72}\right) - \frac{11}{24} |\nabla \rho(\mathbf{r})|^2\right] d\mathbf{r}. \end{aligned} \quad (2.98)$$

The equation 2.98 denoted as $E_C^{\text{LYP}}[\rho]$ embodies the LYP correlation energy functional within DFT, serving as a measure of the system's correlation effects. The equation involves two integral terms: the first term combines the charge density with a weight function $1 + e^{-\rho^{-1/3}(\mathbf{r})}$, thereby adjusting its impact. The term ω introduces an additional weighting factor, while parameters a and ab modulate the contributions from each integral term. Equation

$$\omega = \frac{\exp(-c\rho^{-1/3}(\mathbf{r}))}{1 + e^{-\rho^{-1/3}(\mathbf{r})}} \rho^{-11/3}(\mathbf{r}) \quad (2.99)$$

defines ω as a function of the charge density ρ at position \mathbf{r} . Similarly, the equation

$$\delta = c\rho^{-1/3}(\mathbf{r}) + \frac{e^{-\rho^{-1/3}(\mathbf{r})}}{(1 + e^{-\rho^{-1/3}(\mathbf{r})})}, \quad (2.100)$$

defines δ as a function of the charge density ρ at position \mathbf{r} .[143] Despite sharing the same external potential and yielding identical densities as per the first Hohenberg-Kohn theorem, the differing Hamiltonians suggest discrepant solutions.[144] This discrepancy is rectified using the adiabatic connection concept, which bridges these two extremes controlled by the interaction strength λ :

$$\hat{H}_{\lambda} = \sum_i \left(-\frac{1}{2} \Delta_i + v_{\text{ext}}^{\lambda}(\mathbf{r}) \right) + \frac{1}{2} \sum_{j \neq i} \sum_i \frac{1}{|\mathbf{r}_j - \mathbf{r}_i|}, \quad (2.101)$$

where v_{ext}^{λ} is the external potential that provides the electron density for scaled two-electron density. Exchange-correlation energy is expressed through the exchange-correlation hole integrated over the coupling constant:

$$\bar{h}_{\text{XC}}(\mathbf{r}_1, \mathbf{r}_2) = \int_0^1 h_{\text{XC}}^{\lambda}(\mathbf{r}_1, \mathbf{r}_2) d\lambda \quad (2.102)$$

or

$$\bar{\Gamma}^{(2)}(\mathbf{r}_1, \mathbf{r}_2) = \int_0^1 \Gamma^{(2)\lambda}(\mathbf{r}_1, \mathbf{r}_2) d\lambda. \quad (2.103)$$

In this equation, $\bar{h}_{\text{XC}}(\mathbf{r}_1, \mathbf{r}_2)$ represents the averaged exchange-correlation kernel within density functional theory. At the lower limit of λ , electrons exhibit no dynamic correlation to upper limit ($\lambda = 1$) representing full interaction, making it practically beneficial to evaluate the exchange energy in an exact manner:

$$E_X^{\text{HF}} = -\frac{1}{4} \iint \frac{|\Gamma^{(1)}(\mathbf{r}_1 | \mathbf{r}_2)|^2}{|\mathbf{r}_1 - \mathbf{r}_2|} d\mathbf{r}_1 d\mathbf{r}_2, \quad (2.104)$$

here, E_X^{HF} signifies the exchange component of the Hartree-Fock exchange-correlation energy in quantum chemistry computations. B3LYP is a widely used density functional theory (DFT) method that includes a combination of exchange and correlation functionals.[141, 145] The B3LYP method is named after the three different components it employs: the exchange functional of Becke (denoted by B), the correlation functional of Lee, Yang, and Parr (denoted by LYP). The B3LYP method is expressed as:

$$E_{XC}^{\text{B3LYP}} = (1 - e)E_X^{\text{LSDA}} + eE_X^{\text{HF}} + f\Delta E_X^{\text{B88}} + (1 - g)E_C^{\text{LSDA}} + gE_C^{\text{LYP}}. \quad (2.105)$$

The parameters e and g are mixing coefficients that determine the contribution of the HF exchange energy and the LYP correlation energy, respectively. The parameter f is a scaling factor for the B88 exchange energy. This method provides a good balance between accuracy and computational cost and is commonly used in electronic structure calculations for molecules and solids.

2.8.2 Time-Dependent Density Functional Theory

Time-Dependent Density Functional Theory (TDDFT) is an extension of DFT that allows for the study of electronic excitations in quantum systems. While DFT is mainly used to calculate the ground-state electronic structure of a system, TDDFT provides a framework to investigate excited states and their time evolution.

In TDDFT, the electronic dynamics are described by the time-dependent Schrödinger equation. The central quantity in TDDFT is the time-dependent density, which contains information about the electronic excitations and their behavior over time.[146, 147, 148] The TDDFT equation is described as:

$$A = \int_{t_0}^{t_1} dt \left\langle \Psi[n(\mathbf{r}, t)] \left| i \frac{\partial}{\partial t} - \hat{H}(T) \right| \Psi[n(\mathbf{r}, t)] \right\rangle \quad (2.106)$$

or

$$\hat{H}_{KS} \Psi_i(\mathbf{r}, t) = i \frac{\partial}{\partial t} \Psi_i(\mathbf{r}, t) \quad (2.107)$$

or

$$i\hbar \frac{\partial \Psi_i(\mathbf{r}, t)}{\partial t} = \left[-\frac{\hbar^2}{2m} \nabla^2 + v_s(\mathbf{r}, t) + v_{xc}[n](\mathbf{r}, t) \right] \Psi_i(\mathbf{r}, t), \quad (2.108)$$

where $v_s(\mathbf{r}, t)$ is the time-dependent external potential (including the nuclear-electron and electron-electron interactions), $v_{xc}[n](\mathbf{r}, t)$ is the time-dependent exchange-correlation potential, which accounts for the many-body effects of the interacting electrons, $n(\mathbf{r}, t)$ is the time-dependent electron density, given by the sum of squared magnitudes of the Kohn-Sham orbitals:

$$n(\mathbf{r}, t) = \sum_i |\psi_i(\mathbf{r}, t)|^2. \quad (2.109)$$

The time-dependent orbital is given by equation

$$\psi(t) = e^{-i\epsilon_i t} (\psi_i^0 + \delta\psi_i(t)), \quad (2.110)$$

where $\psi(t)$ represents the orbital at time t . ϵ_i is the energy eigenvalue associated with the orbital ψ_i^0 in the absence of perturbation. ψ_i^0 represents the unperturbed state corresponding to the energy eigenvalue ϵ_i . $\delta\psi_i(t)$ represents the perturbation-induced change in the orbital ψ_i^0 at time t as:

$$\delta\psi_i(t) = \psi_i^+ e^{-i\omega t} + \psi_i^- (r) e^{i\omega t}, \quad (2.111)$$

where ψ_i^+ and ψ_i^- are coefficients associated with the perturbation-induced change in the state ψ_i^0 . ω represents the angular frequency of the oscillation. The time-dependent behavior of the perturbation-induced change $\delta\psi_i(t)$ is separated into two terms: one term oscillating with a negative frequency $-\omega$ and another term oscillating with a positive frequency ω . The total Kohn-Sham Hamiltonian \hat{H}_{KS} can be expressed as the sum of the unperturbed Kohn-Sham Hamiltonian \hat{H}_{KS}^0 and the perturbation-induced Hamiltonian $\delta\hat{H}_{KS}$ as:

$$\hat{H}_{KS} = \hat{H}_{KS}^0 + \delta\hat{H}_{KS} \quad (2.112)$$

where

$$\delta\hat{H}_{KS} = \int d^3\mathbf{r}' \left(\frac{1}{\mathbf{r} - \mathbf{r}'} \delta n(\mathbf{r}') + \frac{\delta V_{xc}}{\delta n(\mathbf{r}')} \delta n(\mathbf{r}') \right) \quad (2.113)$$

d^3r' represents the volume element in three-dimensional space. r and r' are the spatial coordinates. $\delta n(\mathbf{r}')$ is the perturbation in the electron density at the point r' . δV_{xc} is the perturbation in the exchange-correlation potential.

After putting the quantities above in equation 2.107 and retaining only terms linear in the perturbation leads to:

$$\hat{H}_{KS}^0 \delta\psi(t) + \delta\hat{H}_{KS} \psi_i^0 = \epsilon_i \delta\psi_i(t) + i \frac{\partial}{\partial t} \delta\psi_i(t). \quad (2.114)$$

The right-hand side of the equation represents the time evolution of the perturbed wavefunction. The first term, $\epsilon_i \delta\psi_i(t)$, indicates that the perturbed wavefunction's evolution is related to its energy eigenvalue. The second term, $i \frac{\partial}{\partial t} \delta\psi_i(t)$, captures the rate of change of the perturbed wavefunction with respect to time.

Expanding the kohn sham orbitals as:

$$\delta\psi_i(t) = e^{-i\omega t} \sum_k^{virt} X_{ki} \psi_k^0(\mathbf{r}) + e^{i\omega t} \sum_k^{virt} Y_{ki} \psi_k^0(\mathbf{r}) \quad (2.115)$$

where X_{ki} and Y_{ki} are coefficients that determine the amplitudes of the contributions from the virtual orbitals to the perturbed wavefunction. The sum over virtual orbitals indicates that the perturbation involves contributions from virtual orbitals k . $\psi_k^0(\mathbf{r})$ and $\psi_k^0(\mathbf{r})$ are the spatial parts corresponding to the virtual orbital k . Upon introduction of 2.115 in 2.114 the equation lead to

$$(\epsilon_n - \epsilon_i) \begin{pmatrix} X_{ni} \\ Y_{ni} \end{pmatrix} + \sum_k^{virt} \sum_j^{occ} \left[\begin{pmatrix} Y_{kj} \\ X_{kj} \end{pmatrix} \left\langle \psi_n \psi_k \left| \frac{\partial \hat{H}_{KS}[n(\mathbf{r})]}{\partial n(\mathbf{r})} \right| \psi_j \psi_i \right\rangle, \right. \\ \left. + \begin{pmatrix} X_{kj} \\ Y_{kj} \end{pmatrix} \left\langle \psi_n \psi_j \left| \frac{\partial \hat{H}_{KS}[n(\mathbf{r})]}{\partial n(\mathbf{r})} \right| \psi_k \psi_i \right\rangle \right] = \omega \begin{pmatrix} X_{nj} \\ -Y_{nji} \end{pmatrix}, \quad (2.116)$$

where ϵ_n and ϵ_i are the energies of the virtual orbital n and the perturbed orbitals i , respectively. The term $(\epsilon_n - \epsilon_i)$ represents the energy difference between these two orbitals. $\begin{pmatrix} X_{ni} \\ Y_{ni} \end{pmatrix}$ is a column vector that contains the coefficients X_{ni} and Y_{ni} that describe the amplitudes of the perturbation for the virtual orbital n and the perturbed orbital i , respectively.

The matrix eigenvalue equation of TDDFT is derived by employing the definitions:

$$A_{ia,jb} = \delta_{ab} \delta_{ij} (\epsilon_a - \epsilon_i) + \left\langle \psi_a \psi_j \left| \frac{\partial \hat{H}_{KS}[n(\mathbf{r})]}{\partial n(\mathbf{r})} \right| \psi_b \psi_i \right\rangle \quad (2.117)$$

and

$$B_{ia,jb} = \left\langle \psi_a \psi_j \left| \frac{\partial \hat{H}_{KS}[n(\mathbf{r})]}{\partial n(\mathbf{r})} \right| \psi_b \psi_i \right\rangle, \quad (2.118)$$

where i and j are indices representing occupied Kohn-Sham orbitals, and a and b are indices representing unoccupied (virtual) Kohn-Sham orbitals. ϵ_i and ϵ_a are the energies of the occupied orbital i and the virtual orbital a , respectively. δ_{ab} and δ_{ij} are Kronecker delta functions, which are equal to 1 if the indices are the same and 0 otherwise. They ensure that terms are only present on the diagonal of the matrix A , corresponding to transitions within the same orbitals.

The equation 2.118 represents the matrix element connecting the virtual orbital a with the occupied orbital j through the derivative of the Kohn-Sham Hamiltonian with respect to the electron density $n(\mathbf{r})$. Finally this leads to

$$\begin{pmatrix} A & B \\ *B & *A \end{pmatrix} \begin{pmatrix} X \\ Y \end{pmatrix} = \omega \begin{pmatrix} -1 & 0 \\ 0 & 1 \end{pmatrix} \begin{pmatrix} \mathbf{X} \\ \mathbf{Y} \end{pmatrix}. \quad (2.119)$$

The equation is seeking solutions for $\begin{pmatrix} X \\ Y \end{pmatrix}$ and ω that satisfy the equation. The eigenvalue ω corresponds to the transition frequencies of the system and the eigenvectors \mathbf{X} and \mathbf{Y} contain the expansion coefficients for the variation of the orbitals. However, this method is not capable of describing the excitation of multi-reference states. With electron density describes as:

$$n(\mathbf{r}) = \sum_{i=1}^N \psi_i^*(\mathbf{r}) \psi_i(\mathbf{r}) \quad (2.120)$$

at a position \mathbf{r} in space. The change in the electron density at a specific position \mathbf{r} due to the perturbation is represented as:

$$\begin{aligned} \delta n(\mathbf{r}) &= \sum_i^{occ} (\delta \psi_i^* \psi_i + \psi_i^* \delta \psi_i) \\ &= \sum_i^{occ} ((\psi_i^{*+} e^{i\omega t} + \psi_i^{*-} e^{i\omega t})) \psi_i + \psi_i^* ((\psi_i^+ e^{i\omega t} + \psi_i^- e^{i\omega t})) , \\ &= \sum_k^{virt} \sum_i^{occ} ((X_{ki} \psi_k^* \psi_i + Y_{ki} \psi_i^* \psi_k) e^{i\omega t} + (X_{ki} \psi_i^* \psi_k + Y_{ki} \psi_k^* \psi_i) e^{i\omega t}) \end{aligned} \quad (2.121)$$

where $\delta \psi_i$ represents the change in the wavefunction of the i th occupied state due to the perturbation. The equation shows how the perturbation in the electron density arises from changes in the wavefunctions of occupied states. The perturbation leads to time-dependent oscillations in the electron density due to the $e^{i\omega t}$ terms.

2.9 Semi-empirical Quantum Chemical Methods

Semi-empirical quantum mechanics models have wide usage in studying ground state and excited electrocroanic structure. SEQM models use minimal basis sets and parameterize the integrals in electronic hamiltonian with experimental or *ab – intio* references. Over the years, several distinct groups of semi-empirical methods have been developed, such as modified neglect of diatomic overlap (MNDO), Austin model 1 (AM1), Parametric model 6 (PM6) and PM7.[149, 150, 151] In this thesis AM1 which is implemented in PYSEQM has been primarily been used to perform high-throughput fast calculation of electronic structure. [152] As all the electronic structure solving aims, the goal is to solve the roothan hall equation: [153]

$$\hat{\mathbf{F}}\mathbf{C} = \hat{\mathbf{S}}\mathbf{C}\epsilon, \quad (2.122)$$

where $\hat{\mathbf{F}}$ represents the Fock matrix. \mathbf{C} represents the coefficient matrix. $\hat{\mathbf{S}}$ represents the overlap matrix, ϵ represents the electronic energy of the system. The semi-empirical methods have zero differential approximation so, $\hat{\mathbf{S}} = \mathbf{1}$.[154] Thus the equation becomes

$$\hat{\mathbf{F}}\mathbf{C} = \mathbf{C}\epsilon \quad (2.123)$$

and the resultant eigenvalue equation that is solved for the molecular orbitals and electronic state. The molecular orbitals are represented as sum of atomic orbitals with coefficients $C_{i\mu}$ as:

$$\psi_i = \sum_{i\mu} C_{i\mu} \psi_\mu(\mathbf{r}). \quad (2.124)$$

The strategies to solve the equation involve several approximations. The MNDO, AM1, and PM3 methods are computational approaches that employ the Neglect of Differential Diatomic Overlap (NDDO) approximation. This approximation simplifies electronic structure calculations by considering certain integrals to be non-zero only when the involved atomic orbitals are centered on the same atom. Specifically, the integrals $\phi_\mu(r)\phi_\nu(r)dr$ are considered to be non-zero only if the atomic orbitals $\phi_\mu(r)$ and $\phi_\nu(r)$ are both centered on the same atom. This approximation greatly reduces the number of integrals that need to be computed, as it ignores all three-center and four-center integrals in the electronic structure calculation.[155] In MNDO model, along with NDDO approximation , one electron operator \hat{h} or $h_{\mu\nu}$ is further simplified to:

$$h_{\mu\nu} = \begin{cases} U_{\mu\mu} - \sum_{B \neq A} Z_B(\mu\mu, s_B s_B) & \mu = \nu \\ - \sum_{B \neq A} Z_B(\mu\nu, s_B s_B) & \mu, \nu \text{ centered on atom } A \\ \beta = \frac{(\beta_\mu + \beta_\nu)}{2} S_{\mu\nu} & \text{otherwise} \end{cases} \quad (2.125)$$

where $U_{\mu\mu}$ represents the one-electron onsite energy i.e., $U_{\mu\mu} = \langle \mu | -\frac{\nabla^2}{2} |\mu \rangle - Z_A \langle \mu | \frac{1}{R_A} |\mu \rangle$ for orbital ϕ_μ on atom A. $\sum Z_B(\mu\mu, s_B s_B)$ represents the sum over atom B of the two-center one-electron integral from the interaction with the core shell of atom B, where μ and ν are centered on the same atom i.e., $\langle \mu | \frac{1}{R_{AB}} |\nu \rangle = (\mu\nu, s_B s_B)$. μ and ν are orbital indices. s_B represents the s orbital of the valence shell for atom B. ν represents an unknown term.

The two-electron integral $(\mu\nu, \lambda\sigma)$ is not to be ignored only if both pairs of orbitals (ϕ_μ, ϕ_ν) and $(\phi_\lambda, \phi_\sigma)$ are located on the same atoms, respectively. For evaluating $(\mu\nu, \lambda\sigma)$, a classical approximation is used. $(\mu\nu, \lambda\sigma)$ describes the electron interaction energy between charge distribution $e\phi_\mu\phi_\nu$ on atom A and $e\phi_\lambda\phi_\sigma$ on atom B. $e\phi_\mu\phi_\nu$ is represented by a set of multipoles $\{M_{Alm}\}$, and each multipole is represented by a configuration of a set of point charges with:

$$(\mu\nu, \lambda\sigma) = \sum_{l_1} \sum_{l_2} \sum_m [M_{l_1, m}^A, M_{l_2, m}^B] = \frac{e^2}{2^{l_1+l_2}} \sum_{i=1}^{2^{l_1}} \sum_{j=1}^{2^{l_2}} f(R_{ij}) \quad (2.126)$$

where l is the multipole order, m is the multipole tensor index, and $f(R)$ is the Coulomb interaction between each unit point charge. To satisfy the asymptotic behavior with $R \rightarrow 0+, +\infty$, the Dewar-Sabelli-Klopman (DSK) approximation is used. [155]

The term $f(R_{ij})$ represents the Coulombic interaction between two point charges situated at a distance R_{ij} from each other. The formula for $f(R_{ij})$ is given by:

$$f(R_{ij}) = \frac{1}{\sqrt{R_{ij}^2 + (\rho_{l_{1A}} + \rho_{l_{1B}})^2}}. \quad (2.127)$$

In this formula, R_{ij} represents the distance between the two interacting charges, which could be electrons or nuclei. The terms $\rho_{l_{1A}}$ and $\rho_{l_{1B}}$ represent the charge distributions associated with the valence shell orbitals $l1$ of atoms A and B, respectively. The interaction described by $f(R_{ij})$ quantifies the electrostatic repulsion or attraction between the charges based on their separation distance and the distribution of charge around them. Here, ρ_{lA} is the additive term for atom A with the multipole order l . The value of ρ_{lA} is derived for each atomic species in the limit $R \rightarrow 0+$ for the same type of atom A and B to yield the correct direct and exchange integrals $g_{\mu\nu}$, $h_{\mu\nu}$ as:

$$\lim_{R_{AB} \rightarrow 0} (\mu_A \mu_A, \nu_B \nu_B) = (\mu_A \mu_A, \nu_A \nu_A) = g_{\mu\nu} \quad (2.128)$$

and

$$\lim_{R_{AB} \rightarrow 0} (\mu_A \nu_A, \mu_B \nu_B) = (\mu_A \nu_A, \mu_A \nu_A) = h_{\mu\nu}, \quad (2.129)$$

here, $g_{\mu\nu}$ and $h_{\mu\nu}$ are parameterized from experimental or *ab initio* calculation data, and they are smaller than the analytic values to compensate for the neglect of two- and four-center Coulomb integrals and the exclusion of electron correlation in Hartree-Fock theory.

The nuclear-nuclear interaction term for the AM1 and PM3 methods is given by:

$$E_{\text{nucl}}^{AB} = Z_A Z_B (s_A s_A, s_B s_B) [e^{-\alpha A R_{AB}} + e^{-\alpha B R_{AB}} + F_A(R_{AB}) + F_B(R_{AB})] \quad (2.130)$$

The equation 2.130 represents the nuclear-nuclear interaction term for the AM1 and PM3 methods. It calculates the energy contribution from the interaction between atomic nuclei of elements A and B. The terms involve atomic charges (Z_A, Z_B), overlap integrals ($s_{AS} s_A, s_{BS} s_B$), and Gaussian-like terms ($e^{-\alpha A R_{AB}}, e^{-\alpha B R_{AB}}, F_A(R_{AB}), F_B(R_{AB})$) and

$$F_A(R_{AB}) = \sum_i^{m_A} K_A^i e^{[L_A^i (R_{AB} - M_A^i)^2]}. \quad (2.131)$$

This equation defines the function $F_A(R_{AB})$, which is used in Equation 2.131. It's a sum of terms involving atom-type-dependent parameters (A_i, L_i, M_{Ai}) and exponential factors. This function contributes to the nuclear-nuclear interaction energy, where K_i, L_i , and M_{Ai} are sequences of atom-type-dependent parameters for the Gaussian expansion of $F_A(R_{AB})$. In AM1, the number of terms in this sum ranges from 2 to 4 depending on the element, while for PM3, there are only 2 terms.

The total energy of the system is given by:

$$E_{\text{tot}} = E_{\text{elec}} + E_{\text{nucl}} \quad (2.132)$$

combining the electronic energy (E_{elec}) and the nuclear-nuclear interaction energy (E_{nucl}), where the electronic energy (E_{elec}) is defined as:

$$E_{\text{elec}}(R, D) = \frac{1}{2} \text{Tr}[D \times (h + \hat{\mathbf{F}}(D))]. \quad (2.133)$$

Equation 2.123 is solved iteratively using an SCF loop. A trial density matrix D_0 is constructed with the valence charge of each atom evenly distributed on its valence shell orbitals. During each iterative step k , the density matrix D_{k-1} is utilized to construct the Fock matrix $\hat{\mathbf{F}}(D_{k-1})$. The subsequent step involves forming the density matrix D_k for the next iteration. This is accomplished either through the diagonalization of $\hat{\mathbf{F}}(D_{k-1})$ or by employing an expansion scheme, as referenced from a source by Pulay.[156, 157] The newly calculated density matrix D_k for the upcoming step is generated through a linear combination of multiple density matrices: D_k, D_{k-1}, D_{k-2} , and so on, up to D_{k-m} . The iterative process continues until convergence is achieved.

1. Achieving a small difference in total energy between successive iterations (ΔE_{tot}). 2. Attaining a small change in the density matrix (ΔD) between consecutive steps. 3. Ensuring that the commutator of the density matrix and the Fock matrix meets a defined threshold, denoted as

$$\epsilon = [D_k, \hat{\mathbf{F}}(D_k)] = SD_k \hat{\mathbf{F}}(D_k) - \hat{\mathbf{F}}(D_k) D_k S < \epsilon \quad (2.134)$$

This iterative loop, which involves updating the density matrix and Fock matrix, represents a fundamental approach used in quantum chemistry calculations to optimize electronic structure calculations and reach a state of convergence. the analytic gradient is automatically obtained as the total energy is computed. Automatic differentiation does not rely on finite differences to compute gradients; instead, it constructs a computational graph and saves the required intermediate variables for the backward gradient calculations, using the chain rule to calculate gradients in an efficient manner.

2.10 Theoretical and Computational Approach to Singlet Fission

Given that the adiabatic states form a complete basis for the Hilbert space, the total wave function can be represented as a linear combination of these states:

$$\Phi(\mathbf{r}, R) = \sum_I \Theta_I(R) \Psi_I(\mathbf{r}, R). \quad (2.135)$$

This equation expresses the total wave function $\Phi(\mathbf{r}, R)$ as a sum over adiabatic states $\Psi_I(\mathbf{r}, R)$, each weighted by a nuclear coefficient $\Theta_I(R)$. These adiabatic states vary with changes in nuclear coordinates R , describing the electronic structure as the nuclei move.

Alternatively, the nuclear-electron wave function can be expanded using a complete set of electronic states that are independent of the nuclear coordinates (diabatic basis $\{\Xi_I\}$):

$$\Phi(\mathbf{r}, R) = \sum_I \chi_I(\mathbf{r}) \Xi_I(R). \quad (2.136)$$

In this equation, the total wave function $\Phi(\mathbf{r}, R)$ is expressed as a sum over diabatic states $\Xi_I(R)$, each weighted by an electronic coefficient $\chi_I(\mathbf{r})$. These diabatic states represent electronic configurations that remain fixed as the nuclei move, allowing for a description of electronic structure independent of nuclear motion. This evolution is described by the time-dependent Schrödinger's equation for the total wave function:

$$i\hbar \frac{\partial \Phi}{\partial t} = \hat{H}\Phi \quad . \quad (2.137)$$

Expanding the total wave function using the adiabatic basis (equation 2.137) leads to an equation governing the time evolution of nuclear wave functions on different interacting adiabatic states:

$$\begin{aligned} i\hbar \frac{\partial}{\partial t} \Theta_I(R) &= \left(\sum_{\alpha} \frac{-\hbar^2 \nabla_{\alpha}^2}{2m_{\alpha}} + E_I(R) \right) \Theta_i(R) \\ &\quad - \sum_{J \neq I} \frac{\hbar^2}{2m_{\alpha}} (\langle \Phi_I(R) | \nabla_{\alpha}^2 | \Phi_J(R) \rangle \\ &\quad + 2 \langle \Phi_I(R) | \vec{\nabla}_{\alpha} | \Phi_J(R) \rangle \cdot \vec{\nabla}_{\alpha}) \Theta_J(R) \end{aligned} \quad . \quad (2.138)$$

The last two terms on the right side of equation 2.138, neglected in the Born-Oppenheimer approximation, are first- and second-derivative couplings responsible for mixing between adiabatic electronic potential energy surfaces. If diabatic electronic states are used instead, the derivative coupling terms vanish, resulting in equation 2.139, where diabatic states are coupled through the electronic Hamiltonian, i.e.:

$$i\hbar \frac{\partial}{\partial t} \Theta_I(R) = - \left(\sum_{\alpha} \frac{\hbar^2 \nabla_{\alpha}^2}{2m_{\alpha}} + \sum_J \langle \Xi_I(R) | H_{el} | \Xi_J(R) \rangle \right) \Theta_I(R) \quad (2.139)$$

where

$$\Xi_I = \sum_J U_{IJ} \Psi_J \quad . \quad (2.140)$$

Equations 2.138 and 2.139 underscore the significance of interstate couplings in studying photochemical dynamics involving multiple potential energy surfaces, such as singlet fission.

2.11 Time-Dependent Perturbation Theory

In time-dependent perturbation theory, the Hamiltonian of the quantum system is divided into two parts: the unperturbed Hamiltonian (\hat{H}_0), which describes the system's behavior without any external perturbation, and the perturbation Hamiltonian ($\hat{V}(t)$), which represents the time-dependent external influence on the system.[158, 159, 160, 161] Mathematically, the total Hamiltonian can be written as:

$$\hat{H} = \hat{H}_0 + \lambda \hat{V}(t). \quad (2.141)$$

The time-dependent Schrödinger equation, with the perturbation included, becomes:

$$i\hbar \frac{\partial}{\partial t} \psi(t) = (\hat{H}_0 + \lambda \hat{V}(t)) \psi(t). \quad (2.142)$$

Considering that the perturbation brought in system is weak. The value of λ is small. Thus the expression of wave function becomes:

$$|\psi(t)\rangle = e^{-\frac{i}{\hbar} \hat{H}_0(t-t_0)} |\psi_I(t)\rangle. \quad (2.143)$$

In this equation, $|\psi(t)\rangle$ represents a time-evolved state at time t starting from an initial state $|\psi_I(t)\rangle$. The evolution is determined by the exponential operator $e^{-\frac{i}{\hbar} \hat{H}_0(t-t_0)}$. Consequently the Schrodinger equation obtained after applying this simplification becomes:

$$\lambda e^{\frac{i}{\hbar} \hat{H}_0(t-t_0)} \hat{V}(t) e^{-\frac{i}{\hbar} \hat{H}_0(t-t_0)} |\psi_I(t)\rangle = i\hbar \frac{\partial \psi_I(t)}{\partial t}. \quad (2.144)$$

This equation is expanded as per Dyson series expansion as:

$$|\psi_I(t)\rangle = [1 - \frac{i\lambda}{\hbar} \int_0^t dt_1 e^{\frac{i}{\hbar} \hat{H}_0(t_1-t_0)} V(t_1) e^{-\frac{i}{\hbar} \hat{H}_0(t_1-t_0)} - \frac{\lambda^2}{\hbar^2} \int_{t_0}^t dt_1 \int_0^t dt_2 e^{\frac{i}{\hbar} \hat{H}_0(t_1-t_0)} V(t_1) e^{-\frac{i}{\hbar} \hat{H}_0(t_1-t_0)} e^{\frac{i}{\hbar} \hat{H}_0(t_2-t_0)} V(t_2) e^{-\frac{i}{\hbar} \hat{H}_0(t_2-t_0)}] . \quad (2.145)$$

When the Hamiltonian \hat{H}_0 operates on the state $|n\rangle$, it yields the energy E_n times the same state $|n\rangle$, as expressed by the equation:

$$\hat{H}_0|n\rangle = E_n|n\rangle, \quad (2.146)$$

assuming the completeness relation $\sum_n |n\rangle\langle n| = 1$.

The time evolution $|\psi_I(t)\rangle$ of the state can be expressed in terms of interactions between eigenstates of \hat{H}_0 , i.e., $|m\rangle$ and $|n\rangle$... , under the influence of a time-dependent perturbation $\hat{V}(t)$. Thus, we have:

$$|\psi_I(t)\rangle = \left[1 - \frac{i\lambda}{\hbar} \sum_m \sum_n \int_{t_0}^t dt_1 \langle m | \hat{V}(t_1) | n \rangle e^{-\frac{i}{\hbar} (E_n - E_m)(t_1 - t_0)} |m\rangle\langle n| + \dots \right] |\psi(t_0)\rangle. \quad (2.147)$$

This equation captures the expansion of the time-evolved state in terms of the perturbation parameter λ , considering the first-order contributions from various intermediate states. The unitary evolution operator with a time-independent \hat{V} is written as:

$$U(t) = 1 - \frac{i\lambda}{\hbar} \int_{t_0}^t dt_1 \sum_m \sum_n \langle m | \hat{V} | n \rangle e^{-\frac{i}{\hbar} (E_n - E_m)(t_1 - t_0)} |m\rangle\langle n| - \frac{i\lambda}{\hbar} \int_{t_0}^t dt_1 \int_{t_0}^{t_1} dt_2 \sum_m \sum_n \sum_q e^{-\frac{i}{\hbar} (E_n - E_m)(t_1 - t_0)} \langle m | \hat{V} | q \rangle \langle q | \hat{V} | n \rangle e^{-\frac{i}{\hbar} (E_n - E_q)(t_1 - t_0)} |m\rangle\langle n| \dots \quad (2.148)$$

Upon integration of intermediate time steps to infinity $t_n \rightarrow \infty$ we get the expression corresponding to evolution:

$$U(t) = 1 - \frac{i\lambda}{\hbar} \sum_n \langle n | \hat{V} | n \rangle - \frac{i\lambda^2}{\hbar} \sum_{m \neq n} \frac{\langle n | \hat{V} | n \rangle \langle n | \hat{V} | n \rangle}{E_n - E_m} t - \frac{1}{2} \frac{\lambda^2}{\hbar^2} \sum_{m,n} \langle n | \hat{V} | m \rangle \langle m | \hat{V} | n \rangle t^2 + \dots + \lambda \sum_{m \neq n} -\frac{\langle m | \hat{V} | n \rangle}{E_n - E_m} |m\rangle\langle n| + \lambda^2 \sum_{m \neq n} \sum_{q \neq n} \sum_n \frac{\langle m | \hat{V} | q \rangle \langle q | \hat{V} | n \rangle}{(E_n - E_m)(E_n - E_q)} |m\rangle\langle n| + \dots, \quad (2.149)$$

where the first half correspond the evolving terms of the state $|n\rangle$ with time. The second half of the expressions shows the static perturbation provided by all the intermediate states. In the first half of the equation, the first term ,i.e., $\frac{i\lambda}{\hbar} \sum_n \langle n | \hat{V} | n \rangle$, represents the first-order correction to the time evolution operator $U(t)$ due to the perturbation \hat{V} .

In the second half of the equation, the first term is a static correction to the time evolution operator due to the perturbation \hat{V} . It calculates the matrix element $\langle m | \hat{V} | n \rangle$ and divides it by the energy difference $E_n - E_m$. This serves as direct coupling term referring to the transition from state $|n\rangle$ to state $|m\rangle$ bringing charactersitics of state $|m\rangle$ in $|n\rangle$. The second term represents a static second-order correction to the time evolution operator. It involves a triple sum over quantum states m , n , and q , with each of them being distinct. For each combination of m , n , and q . This serves as mediated coupling term referring to the transition from state $|n\rangle$ to state $|m\rangle$ via an intermediate state $|q\rangle$ implying extent of facilitation of state $|q\rangle$ in bringing $|m\rangle$ character in state $|n\rangle$.

Various models utilize diabatic and adiabatic wave functions for the states involved in singlet fission and evaluate the coupling between these wave functions to estimate the reaction rate.

2.11.1 Fermi's Golden Rule (FGR)

Fermi's Golden Rule is a fundamental principle in quantum mechanics that describes the transition rate between quantum states due to the interaction between them. In the context of singlet fission, FGR provides a way to calculate the rate constant (k_{SF}) for the process. The rate constant is proportional to the square of the electronic coupling (V) between the initial singlet state (S_1) and the final multiexciton state, and it is multiplied by the Franck-Condon weighted density of states (FCWD), which accounts for the energy conservation during the process. The FCWD reflects the vibrational overlap between the initial and final states, which influences the efficiency of the singlet fission process.

$$k_{SF} = \frac{2\pi}{\hbar} |\hat{V}|^2 \delta(E_i - E_j) \quad (2.150)$$

where V is the coupling between initial and final states, and $\delta(E_i - E_j)$ guarantees energy conservation along the process, typically formulated as the Franck-Condon weighted density of states. This rate expression has been discussed in detail regarding the importance of electronic coupling within the diabatic basis in seminal reviews by Smith and Michl [28, 53].

The diabatic wave function approach, pioneered by Michl and colleagues, describes bichromophoric systems using single Slater determinants under the frozen orbital approximation. This method has been widely used to explore optimal couplings for singlet fission and construct effective Hamiltonians to study fission dynamics. While it offers a useful starting point, it assumes the frozen orbital approximation, which neglects correlation effects and orbital relaxation, potentially limiting its accuracy in describing more complex systems.[162]

The diabatic coupling scheme calculates electronic couplings between localized excited states without assuming any specific wave function form. It is based on the notion that electronic eigenstates can be represented as linear combinations of initial and final diabatic wave functions. By computing overlap integrals and electronic Hamiltonian matrix elements, this approach yields an estimate of the couplings. However, it may not fully capture correlation effects and orbital relaxation within each diabatic state, and more advanced computational techniques, such as CASSCF CASPT2, have been applied to refine the calculations.

Diabatization of adiabatic excited states involves constructing diabatic states expressed as linear combinations of adiabatic states using a unitary transformation. This approach allows for a more accurate representation of the couplings, as it considers the correlations and relaxation within each diabatic state. It has been applied to study pairwise couplings in π -conjugated molecular crystals, providing valuable insights into singlet fission processes in such systems.

2.12 Electronic Gradients

The derivative of the electronic structure, represents how the total energy of a quantum mechanical system changes concerning some external parameter or coordinate, R_a . It's a crucial concept in quantum chemistry and molecular physics, where researchers frequently need to assess how the electronic energy varies as atomic positions change (molecular geometry optimization) or as an external field is applied.

The derivative of the electronic structure has several applications in quantum chemistry and physics:

(1) Geometry Optimization: In molecular structure calculations, it's crucial to find the equilibrium geometry of molecules by minimizing the energy. This involves computing $\frac{dE}{dR_a}$ and adjusting nuclear coordinates to reach the minimum energy configuration. (2) Vibrational Spectroscopy: The second derivative of the electronic energy with respect to nuclear coordinates ($\frac{d^2E}{dR_a^2}$) is used to calculate vibrational frequencies and intensities in infrared and Raman spectroscopy. (3) Reaction Pathways: $\frac{dE}{dR_a}$ helps in studying reaction pathways and transition states in chemical reactions, such as barrier heights and reaction mechanisms. (4) Property Predictions: The electronic structure derivative can be used to compute various molecular properties, such as the rate of a process and non-adiabatic couplings. The electronic gradients, defined as:

$$\frac{dE}{dR_a} = \frac{\partial E}{\partial R_a} + \sum_i \frac{\partial E}{\partial C_i} \frac{C_i}{R_a}, \quad (2.151)$$

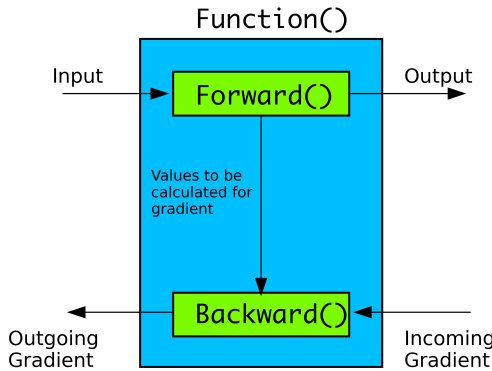


Figure 2.2: Autograd Function

represents the derivative of the energy E with respect to a nuclear coordinate R_a , involving partial derivatives with respect to both R_a and the coefficients C_i of certain functions. It can be broken down as:

$$\frac{\partial E}{\partial R_a} = \left\langle \Psi \left| \frac{\partial \hat{H}}{\partial R_a} \right| \Psi \right\rangle + 2Re \left\langle \frac{\partial \Psi}{\partial R_a} \left| \hat{H} \right| \Psi \right\rangle, \quad (2.152)$$

where the two terms are:

- $\left\langle \Psi \left| \frac{\partial \hat{H}}{\partial R_a} \right| \Psi \right\rangle$: This term involves the expectation value of the derivative of the Hamiltonian operator (\hat{H}) with respect to the nuclear coordinate R_a in the quantum state Ψ . This is hellmann Feynman's force. It is valuable when the wave function is not changing significantly with changes in nuclear coordinate. Most of the work in this thesis have been analysis related to hellmann Feynman's force. [163, 164, 165, 166]
- $2Re \left\langle \frac{\partial \Psi}{\partial R_a} \left| \hat{H} \right| \Psi \right\rangle$: This term involves the real part of the expectation value of the derivative of the wave function (Ψ) with respect to R_a and the Hamiltonian operator. This is called Pulay force. When the wave function is changing with change nuclear coordinate.[167, 168]

2.12.1 Analytical Derivatives

Analytical derivatives involve computing the gradient directly from mathematical expressions for the energy in terms of the nuclear coordinates, rather than approximating the derivatives numerically. This can be more efficient computationally, as it avoids the need for numerical differentiation methods that require multiple energy calculations for small displacements along each coordinate direction. [169, 170]

Alternative to the tedious implementation of analytical gradient, autograd provides automatic analytical differentiation, which allows you to compute gradients with respect to input tensors without explicitly deriving or calculating the gradients manually. Automatic differentiation is a technique used to compute the derivatives of functions with respect to their input variables.[171] It is a key tool in numerical optimization, machine learning, and scientific computing. Traditional methods for computing derivatives, such as symbolic differentiation and numerical approximation, have limitations in terms of computational efficiency and accuracy. Automatic differentiation addresses these limitations by providing an efficient and accurate way to compute derivatives based on the chain rule of differentiation. In automatic differentiation, a function is decomposed into a sequence of elementary operations, such as addition, multiplication, logarithm, etc., and each operation is associated with a derivative rule. During the computation, the derivatives of the intermediate results are computed simultaneously with the function evaluation.

In deep learning frameworks like PyTorch or TensorFlow, gradient tracking is typically implemented using computational graphs. A computational graph is a data structure that represents the flow of operations and their dependencies. It allows the framework to automatically compute the gradients using the chain rule of calculus.

When a variable is involved in a computation, such as addition, multiplication, or more complex operations like neural network layers, the framework records the operations and their inputs to build a computational graph. The graph consists of nodes representing the operations and edges representing the dependencies between the variables.

1. Forward Mode : During forward propagation, the framework evaluates the computation graph by applying the operations to the input variables and producing an output. At the same time, it keeps track of the operations and their inputs for each variable.

2. Backward Mode : During backward propagation, the framework traverses the computational graph in reverse order. It uses the chain rule to compute the gradients of the output with respect to the input variables. The chain rule states that the derivative of a composition of functions is the product of the derivatives of the individual functions.

By tracking the operations and dependencies in the computational graph, the framework can efficiently compute the gradients by applying the chain rule recursively. This allows for gradient-based optimization algorithms, such as stochastic gradient descent, to update the model's parameters and optimize the objective function.

2.13 Non-Adiabatic Coupling

Non-adiabatic processes represent scenarios where a quantum system's electronic energy states change too rapidly for the system to maintain its equilibrium state. Unlike adiabatic processes, where transitions between energy levels are negligible, non-adiabatic processes entail quantum state transitions. This occurs when the energy landscape evolves quickly, making it impossible for the system to adapt in real-time. These transitions, called non-adiabatic transitions, often involve shifts between different electronic states, leading to energy exchange. In such cases, the Born-Oppenheimer approximation, which assumes that nuclear and electronic motions can be separated, may no longer be valid. This departure from adiabatic behavior can lead to phenomena like internal conversion (IC) and intersystem crossing (ISC), depending on the nature of the electronic states and their couplings. Mathematically, non-adiabatic coupling can be expressed as:

$$V_{ij}(R) = \langle \Psi_i | \nabla_R \Psi_j \rangle \quad (2.153)$$

here, $V_{ij}(R)$ represents the non-adiabatic coupling between electronic states i and j as a function of nuclear coordinates R . Ψ_i and Ψ_j are the wavefunctions corresponding to states i and j , respectively. The term ∇_R represents the gradient operator with respect to nuclear coordinates.

2.14 Spin Operator And Pauli Matrices

In quantum mechanics, the spin operator is a mathematical representation of the intrinsic angular momentum of particles, such as electrons. It characterizes the spin degree of freedom, which is a fundamental property of particles beyond their orbital motion. The spin operator allows us to describe and manipulate the spin state of particles.[172]

The Pauli matrices, denoted as σ_x , σ_y , and σ_z , are a set of three 2×2 matrices that serve as the mathematical operators corresponding to spin measurements along x -axis, y -axis and z -axis respectively. The Pauli matrices are defined as follows:

$$\sigma_x = \frac{1}{2} \begin{bmatrix} 0 & 1 \\ 1 & 0 \end{bmatrix}, \quad (2.154)$$

$$\sigma_y = \frac{1}{2} \begin{bmatrix} 0 & -i \\ i & 0 \end{bmatrix} \quad (2.155)$$

and

$$\sigma_z = \frac{1}{2} \begin{bmatrix} 1 & 0 \\ 0 & -1 \end{bmatrix}. \quad (2.156)$$

These matrices have several important properties. Each Pauli matrix is Hermitian, meaning it is equal to its own conjugate transpose. The square of each Pauli matrix is equal to the 2×2 identity matrix, I :

$$\sigma_x^2 = \sigma_y^2 = \sigma_z^2 = I \quad (2.157)$$

The Pauli matrices satisfy specific commutation and anticommutation relationships:

$$[\sigma_i, \sigma_j] = 2i\epsilon_{ijk}\sigma_k \quad (\text{for } i \neq j) \quad (2.158)$$

$$\{\sigma_i, \sigma_j\} = 2\delta_{ij}\mathbb{1} \quad (\text{for } i = j) \quad (2.159)$$

Here, $[\cdot, \cdot]$ denotes the commutator, $\{\cdot, \cdot\}$ denotes the anticommutator, ϵ_{ijk} is the Levi-Civita symbol, and δ_{ij} is the Kronecker delta[173, 174].

The spin operator, represented by a vector operator $S = (\sigma_x, \sigma_y, \sigma_z)$, can be expressed in terms of the Pauli matrices. The spin operator acts on the spin state of a particle, allowing us to measure or manipulate its spin angular momentum. The relationships involving the square of the total spin angular momentum operator S and the components of the spin angular momentum operator S_x , S_y , and S_z are:

$$S^2 = S_x^2 + S_y^2 + S_z^2. \quad (2.160)$$

The equation 2.161 states that the square of the total spin angular momentum operator S^2 is the sum of the squares of its components S_x^2 , S_y^2 and S_z^2 . Additionally

$$S = S_x + S_y + S_z \quad (2.161)$$

represents the total spin angular momentum operator S as the sum of its components S_x , S_y , and S_z . The total spin angular momentum operator of the composite system consisting of subsystems A and B

$${}^{A,B}S = {}^A S \otimes {}^B \mathbb{1} + {}^A \mathbb{1} \otimes {}^B S \quad (2.162)$$

where ${}^A S$ represents the spin angular momentum operator of subsystem A. ${}^B S$ represents the spin angular momentum operator of subsystem B. $\mathbb{1}$ represents the identity operator. This equation states that the total spin angular momentum operator of the composite system is the sum of two terms. The first term (${}^A S \otimes {}^B \mathbb{1}$) represents the spin angular momentum of subsystem A combined with the identity operator of subsystem B. The second term (${}^A \mathbb{1} \otimes {}^B S$) represents the identity operator of subsystem A combined with the spin angular momentum of subsystem B.

This thesis dealt with the spin of electrons, which is described as follows:

$$\left| \frac{1}{2}, -\frac{1}{2} \right\rangle = |\downarrow\rangle = \begin{bmatrix} 0 \\ 1 \end{bmatrix} \quad (2.163)$$

and

$$\left| \frac{1}{2}, \frac{1}{2} \right\rangle = |\uparrow\rangle = \begin{bmatrix} 1 \\ 0 \end{bmatrix} \quad (2.164)$$

Utilising Pauli matrices described in equation 2.154, 2.155 and 2.155 and the principle of spin addition (equation 2.162) at 2 sites, the extended Pauli matrices becomes:

$${}^2S_x = \frac{1}{2} \begin{bmatrix} 0 & 1 & 1 & 0 \\ 1 & 0 & 0 & 1 \\ 1 & 0 & 0 & 1 \\ 0 & 1 & 1 & 0 \end{bmatrix}, \quad (2.165)$$

$${}^2S_y = \frac{1}{2} \begin{bmatrix} 0 & -i & -i & 0 \\ i & 0 & 0 & -i \\ i & 0 & 0 & -i \\ 0 & i & i & 0 \end{bmatrix} \quad (2.166)$$

and

$${}^2S_z = \begin{bmatrix} 1 & 0 & 0 & 0 \\ 0 & 0 & 0 & 0 \\ 0 & 0 & 0 & 0 \\ 0 & 0 & 0 & -1 \end{bmatrix}. \quad (2.167)$$

Thus,

$${}^2S_x^2 = \frac{1}{2} \begin{bmatrix} 1 & 0 & 0 & 1 \\ 0 & 1 & 1 & 0 \\ 0 & 1 & 1 & 0 \\ 1 & 0 & 0 & 1 \end{bmatrix}, \quad (2.168)$$

$${}^2S_y^2 = \frac{1}{2} \begin{bmatrix} 1 & 0 & 0 & -1 \\ 0 & 1 & 1 & 0 \\ 0 & 1 & 1 & 0 \\ -1 & 0 & 0 & 1 \end{bmatrix}, \quad (2.169)$$

and

$${}^2S_z^2 = \begin{bmatrix} 1 & 0 & 0 & 0 \\ 0 & 0 & 0 & 0 \\ 0 & 0 & 0 & 0 \\ 0 & 0 & 0 & 1 \end{bmatrix} \quad (2.170)$$

Upon addition of ${}^2S_x^2$, ${}^2S_y^2$, and ${}^2S_z^2$, the resulting total spin operator ${}^2S_{total}^2$ is represented by the matrix:

$${}^2S_{total}^2 = \begin{bmatrix} 2 & 0 & 0 & 0 \\ 0 & 1 & 1 & 0 \\ 0 & 1 & 1 & 0 \\ 0 & 0 & 0 & 2 \end{bmatrix} \quad (2.171)$$

Upon diagonalisation, matrix ${}^2S_{total}^2$ has 2 unique eigenvalues: 2 and 0. The eigenvalue matrix is $[0, 2, 2, 2]$. The row in the matrix:

$$\begin{bmatrix} 2S + 1 = 1 : j(j+1) = 0 & | & 0 & -\frac{1}{\sqrt{2}} & \frac{1}{\sqrt{2}} & 0 \\ 2S + 1 = 3 : j(j+1) = 2 & | & 0 & \frac{1}{\sqrt{2}} & \frac{1}{\sqrt{2}} & 0 \\ 2S + 1 = 3 : j(j+1) = 2 & | & 1 & 0 & 0 & 0 \\ 2S + 1 = 3 : j(j+1) = 2 & | & 0 & 0 & 0 & 1 \end{bmatrix}, \quad (2.172)$$

represent the eigenvectors corresponding to different configurations of the system with respect to the total spin angular momentum ($2S + 1$) and the total angular momentum quantum number j , where $j(j+1)$ represents the eigenvalue of the operator ${}^2S_{total}^2$. Each row corresponds to a different configuration, and the columns represent the coefficients of the basis states in each configuration. Similarly, the diagonalization of ${}^2S_{z,paired}$ gives 3 unique eigenvalues: 1, 0, and -1, i.e., $[-1, 0, 0, 1]$. These eigenvalues correspond to the high spin state of the electronic configuration. The corresponding eigenvectors corresponding to the electronic configuration are given by:

$$\begin{bmatrix} m_s = 1 : |\uparrow\uparrow\rangle & | & 0 & 0 & 0 & 1 \\ m_s = 0 : |\uparrow\downarrow\rangle & | & 0 & 1 & 0 & 0 \\ m_s = 0 : |\downarrow\uparrow\rangle & | & 0 & 0 & 1 & 0 \\ m_s = -1 : |\downarrow\downarrow\rangle & | & 1 & 0 & 0 & 0 \end{bmatrix}. \quad (2.173)$$

In this matrix, each column represents an eigenvector corresponding to the electronic configurations: $|\uparrow\uparrow\rangle$, $|\uparrow\downarrow\rangle$, $|\downarrow\uparrow\rangle$, and $|\downarrow\downarrow\rangle$. The non-zero values in the eigenvectors indicate the coefficients of the corresponding electronic configurations in the eigenstates.

By combining the information from matrices 2.172 and 2.173 the wave function of the desired system can be obtained. By performing a dot product of this row vector with the columns in the matrix described above, the choice of electronic configurations along with their respective coefficients is made. For example, for $2S + 1 = 1$ (singlet state) where $j(j+1) = 0$,

$$S_1 = |0, 0\rangle = \frac{1}{\sqrt{2}}(|\uparrow\downarrow\rangle - |\downarrow\uparrow\rangle), \quad (2.174)$$

the coefficients for the basis states $|\uparrow\downarrow\rangle$ and $|\downarrow\uparrow\rangle$ are $-\frac{1}{\sqrt{2}}$ and $\frac{1}{\sqrt{2}}$ respectively. Similarly the wavefunction of triplet state $2S + 1 = 3$ (triplet state), $j(j+1) = 2$: These rows represent configurations with total spin angular momentum equal to 3 and total angular momentum quantum

number j satisfying $j(j+1) = 2$. The coefficients for the basis states $|\uparrow\uparrow\rangle$, $|\uparrow\downarrow\rangle$, $|\downarrow\uparrow\rangle$, and $|\downarrow\downarrow\rangle$ indicate different combinations of these states in the triplet configuration as:

$$T^0 = |1, 0\rangle = \frac{1}{\sqrt{2}}(|\uparrow\downarrow\rangle + |\downarrow\uparrow\rangle), \quad (2.175)$$

$$T^{+1} = |1, 1\rangle = |\uparrow\uparrow\rangle, \quad (2.176)$$

and

$$T^{-1} = |1, -1\rangle = |\downarrow\downarrow\rangle. \quad (2.177)$$

Four electron operator system is made using equation 2.162 by addition of operator of 2 electron:

$${}^4S = {}^{2A}S \otimes {}^{2B}\mathbb{1} + {}^{2A}\mathbb{1} \otimes {}^{2B}S \quad (2.178)$$

where the super script 4S represents 4 electron in the combined system. ${}^4S_x, {}^4S_y, {}^4S_z$ and 4S operators are 16×16 matrix. ${}^4S^2$ is show in the figure 2.3. Up on digonalisation of ${}^4S^2$ one get 3 unique eigen values of the combined matrix. Five 6, Nine 2, and two 0 this will cause thus the possible J will be 2, 1 and 0. Thus we get 5 quintet, 9 triplets (3 kind of triplet) and 2 singlets. The eigenvalues and eigenvectors of different states are shown in Figure 2.4. Digonalisation of S_z gives eigenvalue corresponding to m_s and eigen vectors correspond to the spin configuration of state shown in the figure 2.5. In the figure 2.5 the columns correspond to the coefficients of the electronic configuration with m_s .

Due to the presence of many states with the same eigenvalues, the eigenvectors obtained from calculations can sometimes be non-orthogonal and may not accurately represent the true eigenstates. This can result in incorrect wavefunction estimations. To address these numerical limitations, we use analytical methods such as the Jordan-Wigner transformation and the Wigner-Eckart theorem. These methods help to derive the wavefunctions more accurately. The programming principles to obtain wave functions of state and hamiltonian analytically is discussed in chapter 7.

In the Jordan-Wigner transformation, spin operators are represented in terms of fermionic creation and annihilation operators. This transformation allows one to connect quantum spin models with models of non-interacting fermions, which are often easier to solve analytically.[175] The spin raising and lowering operators σ_j^+ and σ_j^- are mapped onto fermionic creation and annihilation operators c_j^\dagger and c_j , respectively, along with an additional phase factor. Specifically, σ_j^+ and σ_j^- are given by

$$\sigma_j^+ = c_j^\dagger e^{-i\pi \sum_{l=1}^{j-1} c_l^\dagger c_l} \quad (2.179)$$

and

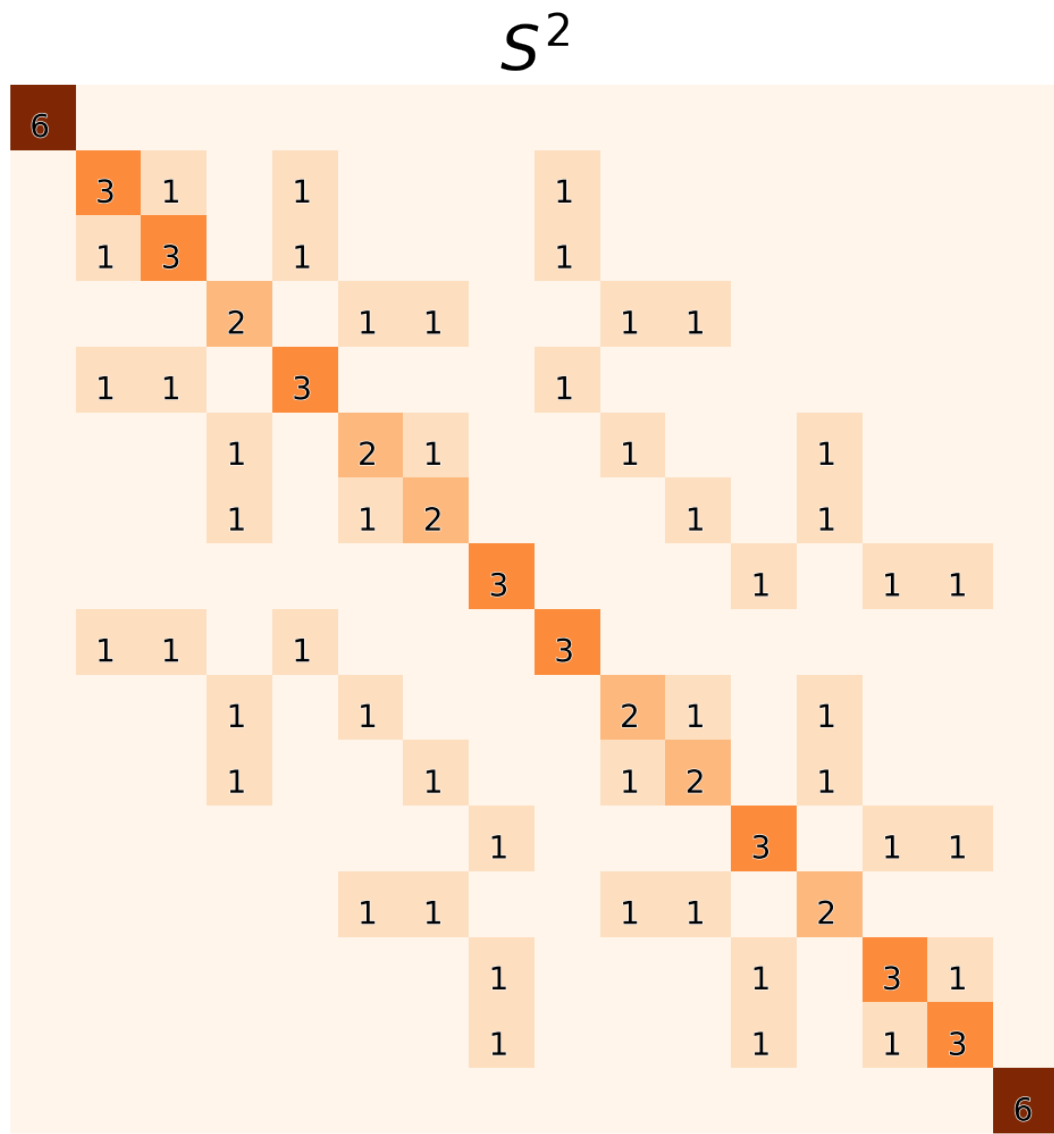
$$\sigma_j^- = e^{i\pi \sum_{l=1}^{j-1} c_l^\dagger c_l} c_j, \quad (2.180)$$

where c_j^\dagger and c_j create and annihilate a fermion at site j , respectively. The z-component of the spin operator S_j^z is also transformed, becoming $\sigma_j^z = 1 - 2c_j^\dagger c_j$. These transformations allow for the translation of spin Hamiltonians into fermionic language, facilitating analytical solutions.

The Wigner-Eckart theorem relates matrix elements of tensor operators within the same irreducible representation of a group. This theorem provides a way to simplify the calculation of certain expectation values involving tensor operators and is widely used in the study of angular momentum and other symmetries in quantum systems.[176] The Wigner-Eckart theorem states that the matrix element of a tensor operator $T_q^{(k)}$ between states $|j_1, m_1\rangle$ and $|j_2, m_2\rangle$ can be expressed in terms of a reduced matrix element and a Clebsch-Gordan coefficient:

$$\langle j_1, m_1 | T_q^{(k)} | j_2, m_2 \rangle = (-1)^{j_1 - m_1} \sqrt{2j_2 + 1} \begin{pmatrix} j_1 & k & j_2 \\ -m_1 & q & m_2 \end{pmatrix} \langle j_1 || T^{(k)} || j_2 \rangle, \quad (2.181)$$

where $T_q^{(k)}$ is the tensor operator of rank k with a component q . $|j_1, m_1\rangle$ and $|j_2, m_2\rangle$ are states with angular momenta j_1 and j_2 and their respective magnetic quantum numbers m_1 and m_2 . $\begin{pmatrix} j_1 & k & j_2 \\ -m_1 & q & m_2 \end{pmatrix}$ is a Clebsch-Gordan coefficient. $\langle j_1 || T^{(k)} || j_2 \rangle$ is the reduced matrix element.

Figure 2.3: ${}^4S^2 = {}^4S_x^2 + {}^4S_y^2 + {}^4S_z^2$

$2S+1$	$j(j+1)$	-2	-1	-1	-1	-1	0	0	0	0	0	0	1	1	1	1	2
1.00	0.00 :	-0.00	-0.00	0.00	0.00	0.00	-0.50	0.50	0.00	-0.00	0.50	-0.50	-0.00	-0.00	-0.00	-0.00	0.00
1.00	0.00 :	0.00	-0.00	-0.00	0.58	0.00	-0.29	-0.29	0.00	-0.00	-0.29	-0.29	0.00	0.58	0.00	0.00	0.00
3.00	2.00 :	0.00	-0.42	-0.51	0.27	0.46	0.00	0.00	0.00	0.46	0.00	0.00	0.00	-0.27	0.00	0.00	0.00
3.00	2.00 :	0.00	0.00	0.00	-0.04	0.59	0.10	-0.37	0.04	-0.10	-0.59	0.36	0.00	0.03	-0.02	0.00	0.00
3.00	2.00 :	0.00	0.00	0.00	0.00	0.16	0.12	-0.30	0.11	-0.16	0.30	-0.12	0.02	-0.00	-0.66	0.53	0.00
3.00	2.00 :	0.00	0.00	0.00	0.00	0.35	0.13	0.45	0.47	-0.35	-0.45	-0.13	-0.09	0.00	-0.24	-0.15	0.00
3.00	2.00 :	-0.00	-0.28	-0.10	-0.65	0.19	-0.00	0.00	0.00	0.19	0.00	0.00	0.00	0.65	0.00	0.00	0.00
3.00	2.00 :	-0.00	-0.00	-0.00	-0.00	-0.33	-0.01	0.38	-0.15	0.33	-0.38	0.01	-0.36	0.00	-0.07	0.58	0.00
3.00	2.00 :	0.00	0.00	0.00	-0.00	-0.47	0.17	-0.09	0.57	0.47	0.09	-0.17	-0.02	0.00	-0.23	-0.31	0.00
3.00	2.00 :	0.00	0.71	-0.69	-0.10	-0.01	0.00	0.00	0.00	-0.01	0.00	0.00	0.00	0.10	0.00	0.00	0.00
3.00	2.00 :	0.00	0.00	0.00	0.00	-0.13	-0.30	0.20	-0.17	0.13	-0.20	0.30	0.69	0.00	-0.44	-0.09	0.00
5.00	6.00 :	0.00	0.00	0.00	-0.00	-0.00	0.00	0.00	-0.50	0.00	-0.00	-0.00	-0.50	0.00	-0.50	-0.50	0.00
5.00	6.00 :	-0.00	-0.00	0.00	0.41	-0.00	0.41	0.41	0.00	-0.00	0.41	0.41	0.00	0.41	0.00	0.00	0.00
5.00	6.00 :	1.00	0.00	0.00	0.00	0.00	0.00	0.00	0.00	0.00	0.00	0.00	0.00	0.00	0.00	0.00	0.00
5.00	6.00 :	0.00	0.00	0.00	0.00	0.00	0.00	0.00	0.00	0.00	0.00	0.00	0.00	0.00	0.00	1.00	0.00
5.00	6.00 :	0.00	0.50	0.50	0.00	0.50	0.00	0.00	0.00	0.50	0.00	0.00	0.00	0.00	0.00	0.00	0.00

Figure 2.4: Eigen vectors of ${}^4S^2$ matrix

m	Spin Configuration	Eigen Vectors
-2 :	$ \uparrow \uparrow \uparrow \uparrow \rangle$	1
-1 :	$ \downarrow \uparrow \uparrow \uparrow \rangle$	1
-1 :	$ \uparrow \downarrow \uparrow \uparrow \rangle$	1
-1 :	$ \uparrow \uparrow \downarrow \uparrow \rangle$	1
-1 :	$ \uparrow \uparrow \uparrow \downarrow \rangle$	1
0 :	$ \downarrow \uparrow \downarrow \uparrow \rangle$	1
0 :	$ \downarrow \uparrow \uparrow \downarrow \rangle$	1
0 :	$ \uparrow \downarrow \downarrow \uparrow \rangle$	1
0 :	$ \uparrow \downarrow \uparrow \downarrow \rangle$	1
0 :	$ \uparrow \uparrow \downarrow \downarrow \rangle$	1
0 :	$ \downarrow \uparrow \uparrow \downarrow \rangle$	1
1 :	$ \downarrow \downarrow \uparrow \downarrow \rangle$	1
1 :	$ \downarrow \downarrow \downarrow \uparrow \rangle$	1
1 :	$ \uparrow \downarrow \downarrow \downarrow \rangle$	1
1 :	$ \downarrow \uparrow \downarrow \downarrow \rangle$	1
2 :	$ \downarrow \downarrow \downarrow \downarrow \rangle$	1

Figure 2.5: Eigen vectors of 4S_z matrix

2.15 Correlated Triplet Pair States in a Dimer Model

The correlated triplet pair state with singlet multiplicity, denoted as $^1(\text{TT})$, is the lowest energy state and plays a key role in singlet fission. The other correlated pair state, $^1(S_1S_1)$, is higher in energy.[177] The $^1(\text{TT})$, $^3(\text{TT})$ and $^5(\text{TT})$ state are significant in singlet fission.[177] Two of the three triplet correlated pair states, $^3(\text{TT})$, have mixed triplet and singlet-triplet pair character, while the third state, $^3(\text{TS}_1)$, represents a correlated singlet-triplet pair state. Additionally, there are quintet states described as the correlated triplet pair $^5(\text{TT})$ states, degenerate with $^1(\text{TT})$.[178] In a simplified description, the electron spin properties of the correlated triplet pair state are understood as the linear combination of the spin angular momenta of both isolated triplet entities, resulting in one singlet state, three triplet states, and nine quintet states $^{2S+1}(\text{TT})$.[179, 35, 37] This approach works well in cases without significant inter-triplet interactions, such as in tetracene or triplet-triplet annihilation.[180, 181, 182] However, when inter-triplet interactions are important, a "sixteen spin state" representation is more appropriate.[183, 184, 178] Two different correlated triplet pair states: one with inter-triplet electronic coupling and spin coherence $^1(\text{TT})$, and another without electronic coupling but still maintaining spin coherence $^1(\text{T...T})$.[178] The correlated triplet pair with inter-triplet interaction $^1(\text{TT})$ can form through either a coherent or an incoherent pathway.[185] In the last step of singlet fission, the correlated triplet pair state undergoes a transition where it loses its spin coherence and transforms into two independently acting triplet excited states, denoted as $\text{T} + \text{T}$. This step is considered as the elementary process of singlet fission. [186, 187, 188, 189, 190, 191, 192, 193] The wave function is expanded as a linear combination of these independent triplet states:

$$|\chi_i\rangle = \sum_{m_{sA}} \sum_{m_{sB}} c_{m_{sA}, m_{sB}}^i |T_{mA}^{m_{sA}} T_{mB}^{m_{sB}}\rangle, \quad (2.182)$$

here, $c_{m_{sA}, m_{sB}}^i$ are the coefficients for the independent triplet microstates with local magnetic spin quantum number m_s of the corresponding chromophore X (A or B). To understand the process of spin decoherence in the correlated triplet pair state $^1(\text{TT})$, it's necessary to consider the time evolution of the initial spin density matrix ($\rho(0)$).[194] This density matrix represents the probabilities of different spin configurations. Off-diagonal elements of the matrix

$$\rho(0) = |\chi_i\rangle \langle \chi_i| \quad (2.183)$$

indicate the quantum coherence or spin entanglement between the triplet entities.

Several factors contribute to spin decoherence in the correlated triplet pair state. These include interactions with the environment, such as coupling to the phonon bath, nuclear spins, temperature, or energetic disorder.[189, 190, 191, 192, 193] Spin-flip processes induced by spin-orbit coupling also contribute to decoherence. As the system interacts with its surroundings, spontaneous spin transitions occur, leading to the loss of spin coherence. Experimental studies, including optical spectroscopy, have provided evidence that the two triplets in $^1(\text{TT})$ are bound relative to the $(\text{T} + \text{T})$ configuration.[186, 195, 196, 197] The binding energy (E_B) of $^1(\text{TT})$ can be calculated using the energy differences between the triplet pair state and the separated triplets:

$$E_B = 2E_{T_1} - E_{^1(T_1T_1)} \quad (2.184)$$

Chapter 3

Active Space Decomposition Analysis of PDI

3.1 Introduction

Although both the diabatic and adiabatic pictures are considered equally valid in the context of singlet fission, they often present different perspectives, and their adequacy is subjected to the mechanism through which singlet fission is occurring. Computational limitations to simulate the molecule with the required level of complexity to calculate the energy levels pose another challenge when analyzing singlet fission. *Ab – initio* calculations require a significant amount of computational resources, making high-throughput analysis difficult and impractical on a large scale. To address this, we have developed an efficient screening methodology in adiabatic basis which relies on the Simple Model by Michl, which allows for high-throughput analysis. In this chapter, the primary objective is to study the adiabatic and diabatic picture of singlet fission analysis and use the results to benchmark our developed "SFast" methodology for singlet fission analysis.[198, 199] The details of the theory and implementation of SFast are discussed in the next chapter.

The chosen mechanism for the study of singlet fission is the charge transfer (CT) mediated route. This process involves a sequence of successive one-electron and/or two-electron transfer connecting the Local Exciton (LE) state to a CT state, and subsequently, the CT state to the triplet exciton pair ${}^1\text{(TT)}$ state. Eventually, the emerging triplet pair undergoes dissociation into separate, harvestable triplets.

To evaluate the validity of the developed method, Active Space Decomposition (ASD) and ASD model Hamiltonian calculations are conducted to study the variation of Adiabatic and Diabatic wave functions of the Perylenediimide (PDI) dimer[200, 201]. We have chosen the PDI molecule for benchmarking because PDI and its derivative have attracted a lot of interest for their potential applications as visible light-absorbing electron acceptors. In the last decade, PDI has been actively studied for charge transport and singlet fission. In PDI, singlet fission occurs mainly through a CT mediated mechanism, making it a prominent molecule to explore the relation between CT and ${}^1\text{(TT)}$ in the adiabatic states. In previous theoretical research on PDI by Ratner and Grozema and coworkers involves a 2D scan using a Markus theory to evaluate rate of singlet fission in cofacially stacked PDI dimer.[1, 202, 203] Farag et al. employed a non-adiabatic coupling model to perform 2D scan to study ${}^1\text{(TT)}$ character to comment on endoergic singlet fission in PDI.[204] The use of proprietary software in these research limited the independent study related to methodologies.

In the ASD analysis, dimer states are formed by linear combinations of direct products involving localized orthogonal monomer states. Notably, this technique allows for the computation of Hamiltonian matrix elements directly, bypassing the explicit construction of the often high-dimensional product space. This decomposition methodology holds the promise of being potentially exact, especially when a set of monomer states is included in the calculations. Subsequently, the adiabatic states are determined by diagonalizing the dimer Hamiltonian matrix. All the calculations shown in this chapter are performed using the open-source BAGEL package. [135, 200, 201]

The chapter outlines two procedures employed in the ASD analysis. Firstly, it involves the decomposition of the adiabatic states of the dimer. This decomposition is carried out in terms of the direct product states of the monomer, revealing the relationships between the dimer's adiabatic

states and those of its monomers. Secondly, the research focuses on constructing a model diabatic Hamiltonian using the direct product states of the modeled monomer states. This model Hamiltonian is constructed in terms of product states consisting of the ground state product (S_0S_0), LE states (S_1S_0), CT states (CA) and $^1(\text{TT})$. The study includes line scan computations by ASD to calculate dimer states by forming combinations of localized monomer states. Additionally, model Hamiltonian analysis is conducted with a set of reference dimer adiabatic states decomposed into model monomer states and get the diabatic couplings among these model states. To accomplish this, two distinct methods have been employed for the ASD calculations, namely, CASSCF (for ASD decomposition) and RASCI (for ASD model Hamiltonian) calculations based on computation cost, because the latter is computationally lighter. [205, 206] Initially, the research began with a line scan, investigating the computational resource requirements and the information yielded by these methods. Subsequently, based on the findings, the parameters and procedures for further calculations were chosen to benchmark the process to evaluate singlet fission rates.

3.2 Method

The diabatic model Hamiltonians are computed by identifying model states and then computing the exact matrix elements in the basis function of these model states. The basis states in which we expand the dimer wave function are, by construction, diabatic in the sense that each monomer state in each dimer basis has a well-defined charge and spin. The model dimer Hamiltonian for singlet fission includes the low-lying single-exciton states ($S+$ and $S-$, which are linear combinations of $|S_0S_1\rangle \pm |S_1S_0\rangle$), the paired triplet state ($|^1(\text{TT})\rangle$), and charge-transfer states ($|AC\rangle$ and $|CA\rangle$) illustrated in figure 3.1. The is written as:

$$\begin{bmatrix} H_{S-,S-} & H_{S-,S+} & H_{S-,^1(\text{TT})} & H_{S-,CA} & H_{S-,AC} \\ H_{S+,S-} & H_{S+,S+} & H_{S+,^1(\text{TT})} & H_{S+,CA} & H_{S+,AC} \\ H_{^1(\text{TT}),S-} & H_{^1(\text{TT}),S+} & H_{^1(\text{TT}),^1(\text{TT})} & H_{^1(\text{TT}),CA} & H_{^1(\text{TT}),AC} \\ H_{CA,S-} & H_{CA,S+} & H_{CA,^1(\text{TT})} & H_{CA,CA} & H_{CA,AC} \\ H_{AC,S-} & H_{AC,S+} & H_{AC,^1(\text{TT})} & H_{AC,CA} & H_{AC,AC} \end{bmatrix}, \quad (3.1)$$

where $H_{X,Y} = \langle X|\hat{H}|Y\rangle$. In the equation 3.1, $H_{IJ,I'J'} = \langle \Phi_I^A \Phi_J^B | H | \Phi_{I'}^A \Phi_{J'}^B \rangle$ where A and B are labels of monomer units and I and J represent the states of monomer. The singlet fission rate is calculated as per the Fermi golden rule, is expressed as follows:

$$W(\text{SF}) = \frac{2\pi}{\hbar} |T_{RP}|^2 \rho(E), \quad (3.2)$$

where $W(\text{SF})$ represents the rate of singlet fission, where \hbar is the reduced Planck's constant. The key factor in determining this rate is the matrix element $|T_{RP}|^2$, and it is influenced by the vibrational structure as represented by the density of states $\rho(E)$ is approximated to 1.

The matrix element $|T_{RP}|^2$ is central to our analysis, and it can be split into two pathways: the direct path and the charge-resonance mediated path. First, let's consider the direct path, which involves the matrix element $\langle LE|H|^1(\text{TT})\rangle$. However, this element is typically small and can often be neglected in calculations as it is very low (see figure 3.8). The more significant contribution comes from the charge-resonance mediated path, and its matrix element can be expressed as follows:

$$T_{RP} = \frac{\langle LE|\mathbf{H}|CA\rangle\langle CA|\mathbf{H}|^1(\text{TT})\rangle}{\Delta E(CA)} + \frac{\langle LE|\mathbf{H}|AC\rangle\langle AC|\mathbf{H}|^1(\text{TT})\rangle}{\Delta E(AC)} \quad (3.3)$$

here, $\Delta E(CA)$ and $\Delta E(AC)$ represent the energy differences between states CA and LE and between states AC and LE , respectively. Notably, after careful consideration, it was determined that $\Delta E(AC)$ has no significant influence on the qualitative behavior of T_{RP} , allowing us to simplify the equation as follows:

$$T_{RP} = |\langle LE|\mathbf{H}|CA\rangle\langle CA|\mathbf{H}|^1(\text{TT})\rangle + \langle LE|\mathbf{H}|AC\rangle\langle AC|\mathbf{H}|^1(\text{TT})\rangle|^2. \quad (3.4)$$

This approximation provides an efficient way to calculate the matrix element $|T_{RP}|^2$ for the charge-resonance mediated path, which plays a crucial role in understanding the rate of singlet fission.

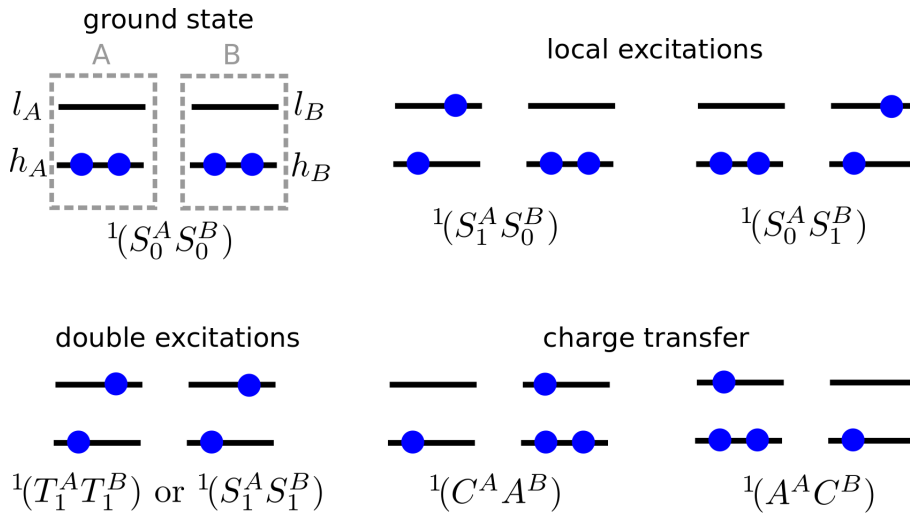


Figure 3.1: Diabatic states in dimer base simple model of singlet fission.

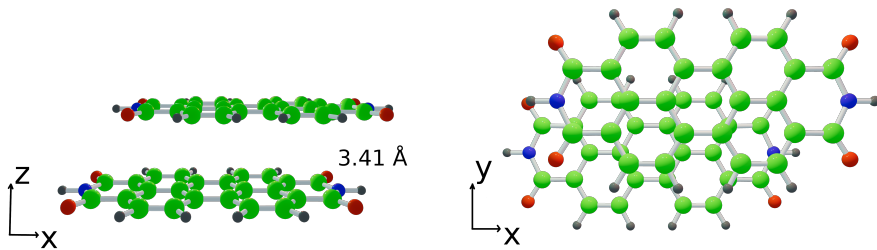


Figure 3.2: Scan coordinate orientation with the molecular plane.

Localization procedure was applied separately to the sets of canonical occupied and virtual orbitals arising from a dimer Hartree–Fock calculation in order to define monomer orbitals. First, the canonical orbitals were localized and assigned to each fragment using the Pipek–Mezey algorithm by maximizing the sum of orbital-dependent partial charges on the nuclei:

$$L = \sum_i [(P_{iA})^2 + (P_{iB})^2] \quad (3.5)$$

where P_{iX} is the Löwdin population of orbital i on fragment X .[207] Diagonalizing the Fock matrix within each block of orbitals belonging to the same monomer yields a full set of molecular orbitals that are localized to each monomer, and the resulting orbitals resemble isolated monomer molecular orbitals. Finally, the orbitals that have the greatest overlap with reference active orbitals obtained from minimal-basis calculations on isolated monomers are chosen to be part of active space. The model Hamiltonians is constructed by computing model states and evaluating the exact Hamiltonian matrix elements in the basis function of those model states. The model states are chosen by diagonalizing the sub-blocks of the dimer Hamiltonian with the desired diabatic character and extracting the relevant low-lying block eigenstates.

Monomer states are computed using the RAS model [206], in which the active orbitals are split into three subsets (referred to as I, II, and III), and the configuration space is restricted such that subset I has a minimum occupation number (or a maximum number of holes), subset III has a maximum occupation, while subset II has no restrictions on occupations. A specific RAS model is defined by assigning active orbitals to each subset and choosing the allowed number of holes in subset I, denoted as h , and the allowed number of particles in subset III, denoted as p . Consequently, this model fully correlates the electrons in the RAS II space while allowing selective interactions with the RAS I and III spaces, depending on the chosen values of h and p . Due to these restrictions, the number of active orbitals used in RAS can be significantly larger than what is feasible for the complete active space model. A RAS model is delineated by the notation RAS(l, m, n) $[h, p]$, where l , m , and n are the numbers of orbitals in the subsets I, II, and III,

respectively, and h and p are the maximum numbers of allowed holes and particles in subsets I and III, respectively.

3.3 Results

3.3.1 Adiabatic Picture

Line Scan

The geometry of the PDI monomer was optimized using the CAMB3LYP/def2-svp method.[208, 209] ASD calculations using CASCI were conducted on the PDI molecule. To perform these calculations, the cc-pVDZ basis set was chosen.[205, 210] The ASD approach involves the construction of monomer states. These include singlet states ($|S_0\rangle$, $|S_1\rangle$, and so on), triplet states ($|T_1\rangle$, $|T_2\rangle$, and so forth), cationic states ($|C_1\rangle$, $|C_2\rangle$, and more), and anionic states ($|A_1\rangle$, $|A_2\rangle$, and beyond). Though many states of give types to get a smooth functional variation of states, in this work we focus on the lowest local exciton, cationic, anionic, and triplet states.

To investigate how the choice of the number of monomer states influences the results, two line scan of ASD calculations was performed using 4 monomer states and 10 monomer states, from $\Delta X = 0 \text{ \AA}$ to 4 \AA at $\Delta Y = 0 \text{ \AA}$ and $\Delta z = 3.5 \text{ \AA}$ with grid size of 0.04 \AA . The molecular structure used in the scan is shown in the figure 3.1. With the monomer states 8 adiabatic states of dimer were calculated and compared as the number of monomer states changed. This comparative analysis allowed us to assess the impact of the number of monomer states on the outcomes of the study. For the monomer calculations, an active space consisting of 8 orbitals with 8 electrons (8o,8e) was selected. This choice results in a total of (16o,16e) when considering the dimer system. The chosen states combine to make states present in the dimer system.

The plot of LE, CT and $^1(\text{TT})$ characters along with adiabatic energies of ground state and 7 excited states of the dimer system, from $\Delta X = 0 \text{ \AA}$ to $\Delta X = 4 \text{ \AA}$ is shown in the figure 3.3 and 3.4 where figure 3.3 d) is showing the energies when the 4 monomer states were chosen, along with the characteristics of the states and figure 3.4 d) shows the dimer system energies build from 10 monomer states. The adiabatic energy of the ground state is highest at $\Delta X = 0 \text{ \AA}$ and as ΔX increases the ground state energy decreases and reaches a minimum at 3.2 \AA . The energies of excited states from the ground state, at the selected key positions are shown in the tables 3.1, 3.2, 3.3, 3.4, 3.5, 3.6, 3.7, 3.8 and 3.9. The first excited state has an excimer character at $\Delta X = 0 \text{ \AA}$ with 67% of S^+ character and 32% of CR character. The coefficients of CA and AC are equal. The second excited state has mostly S^- character (95%) and slight (4%) of CR character. As ΔX increases S^+ character increases in the first excited state and S^- character decreases in the second excited state. Whereas CR character in the first excited state decreases and it increases in CR character. This trend continues till $\Delta X = 1.7 \text{ \AA}$. At $\Delta X = 1.7 \text{ \AA}$ first excited state becomes purely consisting of S^+ type of exciton whereas the Second excited state has S^- and CR character. The first excited state and the second excited state become degenerated at $\Delta X = 2.3 \text{ \AA}$ and $\Delta X = 3.2 \text{ \AA}$. At $\Delta X = 2.3 \text{ \AA}$ character of the first excited state and second excited state switched. Between $\Delta X = 2.3 \text{ \AA}$ and $\Delta X = 3.2 \text{ \AA}$ first excited state has S^- and CR character and second excited state has mostly S^+ . After $\Delta X = 3.2 \text{ \AA}$ the wave function makes a swap again.

Among these states lowest state that has triplet states is 3^{rd} excited state. In this analysis, 3^{rd} excited state is the lowest state with significant $^1(\text{TT})$ character. As inferred from Figure 3.4 c) and figure 3.4 d), the 3^{rd} excited state has high CR character at full stacking. As the monomer is slipped along the x-axis the CR character decreases and the $^1(\text{TT})$ character function increases, the $^1(\text{TT})$ coefficients reduce but at the same time, it goes on contributing to lower energy states. At a slipped stack of $\Delta X = 1.2 \text{ \AA}$ it starts defining 3^{rd} excited state. But it reduces to 0 at $\Delta X = 1.7 \text{ \AA}$. After $\Delta X = 2.3 \text{ \AA}$ the $^1(\text{TT})$ coefficients start increasing. In 3^{rd} excited state the highest triplet admixture is at $\Delta X = 3.75 \text{ \AA}$ of 22%. 3^{rd} excited state has a high CR character. It is almost equal to 100% at full stacking but reduces to 60% at $\Delta X = 1.2 \text{ \AA}$ and increases to 100% $\Delta X = 2.0 \text{ \AA}$. After $\Delta X = 2.0 \text{ \AA}$ CR character decreases. The decreasing of CR character in 3^{rd} excited state is accompanied by increasing $^1(\text{TT})$ character.

4^{th} excited state has triplet fragments from $\Delta X = 0.8 \text{ \AA}$ to 1.2 \AA but its amount of contribution decreases after there it is exchanged with 3^{rd} excited state. CR character increases between $\Delta X = 0.8 \text{ \AA}$ to 1.2 \AA and remains stagnant to 60% upon further slipping. 5^{th} , 6^{th} and 7^{th} state

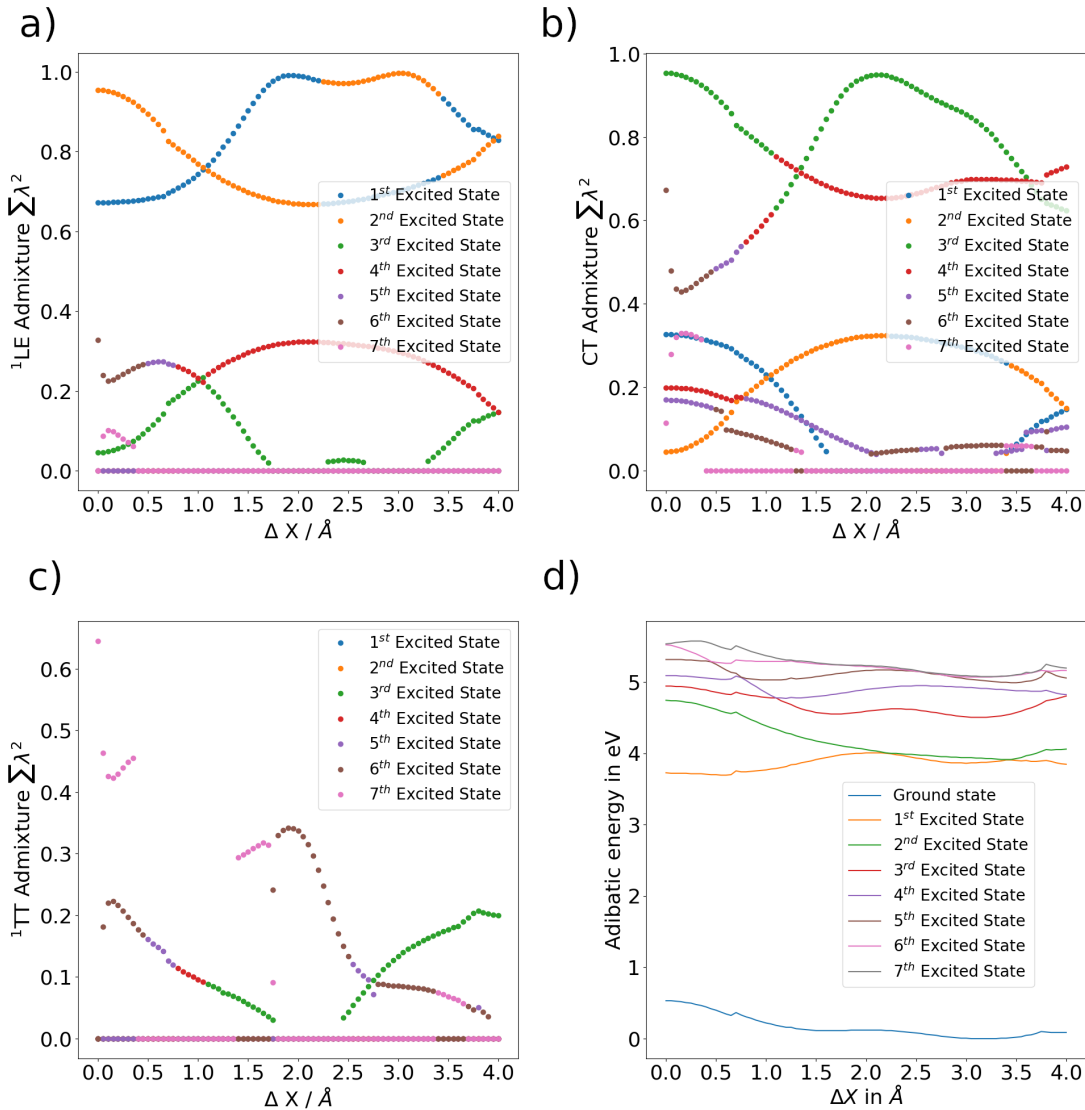


Figure 3.3: Adiabatic states of dimer made by 4 states of monomers of each type. LE, CT and ${}^1\text{(TT)}$ character of the wavefunction. a) LE character in states, b) CT character in states, c) ${}^1\text{(TT)}$ characters in states and d) Energy of the adiabatic states.

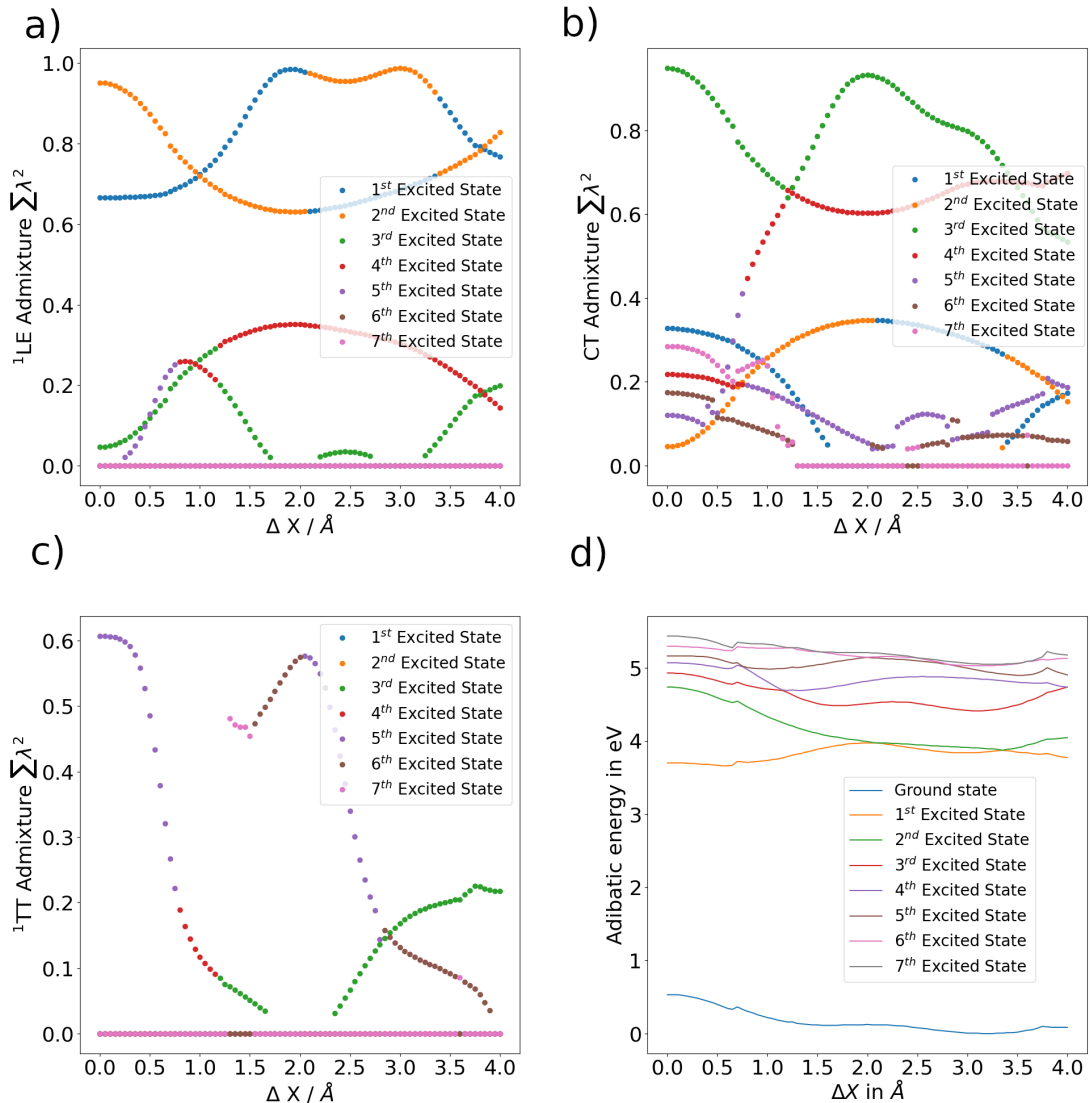


Figure 3.4: Adiabatic states of dimer made by 10 states of monomers of each type. LE, CT and ^1TT character of the wavefunction. a) LE character in states, b) CT character in states, c) ^1TT characters in states and d) Energy of the adiabatic states.

State	electronic structure	coefficient	energy
G S	$-\alpha S_{0,0}S_{0,0}\rangle$	$\alpha = 0.99911,$	0.000 eV
1 st	$-\alpha S_{0,0}S_{1,0}\rangle - \beta S_{1,0}S_{0,0}\rangle - \gamma A_{1,-1}C_{1,1}\rangle + \epsilon A_{1,1}C_{1,-1}\rangle - \kappa C_{1,-1}A_{1,1}\rangle + \lambda C_{1,1}A_{1,-1}\rangle$	$\alpha = 0.57727, \beta = 0.57727, \gamma = 0.28631, \epsilon = 0.28631, \kappa = 0.28631, \lambda = 0.28631,$	3.166 eV
2 nd	$+ \alpha S_{0,0}S_{1,0}\rangle - \beta S_{1,0}S_{0,0}\rangle - \gamma A_{1,-1}C_{1,1}\rangle + \epsilon A_{1,1}C_{1,-1}\rangle + \kappa C_{1,-1}A_{1,1}\rangle - \lambda C_{1,1}A_{1,-1}\rangle$	$\alpha = 0.68967, \beta = 0.68967, \gamma = 0.10714, \epsilon = 0.10714, \kappa = 0.10714, \lambda = 0.10714,$	4.201 eV
3 rd	$+ \alpha S_{0,0}S_{1,0}\rangle - \beta S_{1,0}S_{0,0}\rangle + \gamma A_{1,-1}C_{1,1}\rangle - \epsilon A_{1,1}C_{1,-1}\rangle - \kappa C_{1,-1}A_{1,1}\rangle + \lambda C_{1,1}A_{1,-1}\rangle$	$\alpha = 0.15169, \beta = 0.15169, \gamma = 0.48707, \epsilon = 0.48707, \kappa = 0.48707, \lambda = 0.48707,$	4.396 eV
4 th	$+ \alpha S_{0,0}S_{2,0}\rangle - \beta S_{2,0}S_{0,0}\rangle - \gamma A_{2,-1}C_{1,1}\rangle + \epsilon A_{2,1}C_{1,-1}\rangle + \kappa C_{1,-1}A_{2,1}\rangle - \lambda C_{1,1}A_{2,-1}\rangle$	$\alpha = 0.61506, \beta = 0.61506, \gamma = 0.23343, \epsilon = 0.23343, \kappa = 0.23343, \lambda = 0.23343,$	4.536 eV
5 th	$+ \alpha S_{0,0}S_{3,0}\rangle + \beta S_{3,0}S_{0,0}\rangle - \gamma T_{1,-2}T_{1,2}\rangle + \epsilon T_{1,0}T_{1,0}\rangle - \kappa T_{1,2}T_{1,-2}\rangle + \lambda A_{1,-1}C_{5,1}\rangle - \nu A_{5,-1}C_{1,1}\rangle - \varphi A_{1,1}C_{5,-1}\rangle + \sigma A_{5,1}C_{1,-1}\rangle - \varpi C_{1,-1}A_{5,1}\rangle - \delta C_{5,-1}A_{1,1}\rangle + \omega C_{1,1}A_{5,-1}\rangle + \sigma C_{5,1}A_{1,-1}\rangle$	$\alpha = 0.30418, \beta = 0.30418, \gamma = 0.44972, \epsilon = 0.44972, \kappa = 0.44972, \lambda = 0.12840, \nu = 0.11703, \varphi = 0.12840, \sigma = 0.11703, \varpi = 0.11702, \delta = 0.12840, \omega = 0.11702, \sigma = 0.12840,$	4.624 eV
6 th	$- \alpha S_{0,0}S_{3,0}\rangle + \beta S_{3,0}S_{0,0}\rangle + \gamma A_{1,-1}C_{2,1}\rangle - \epsilon A_{4,-1}C_{1,1}\rangle - \kappa A_{1,1}C_{2,-1}\rangle + \lambda A_{4,1}C_{1,-1}\rangle + \nu C_{1,-1}A_{4,1}\rangle - \varphi C_{2,-1}A_{1,1}\rangle - \sigma C_{1,1}A_{4,-1}\rangle + \varpi C_{2,1}A_{1,-1}\rangle$	$\alpha = 0.63792, \beta = 0.63792, \gamma = 0.11379, \epsilon = 0.17503, \kappa = 0.11379, \lambda = 0.17503, \nu = 0.17503, \varphi = 0.11379, \sigma = 0.17503, \varpi = 0.11379,$	4.758 eV
7 th	$+ \alpha S_{0,0}S_{5,0}\rangle + \beta S_{5,0}S_{0,0}\rangle + \gamma A_{3,-1}C_{1,1}\rangle - \epsilon A_{3,1}C_{1,-1}\rangle - \kappa C_{1,-1}A_{3,1}\rangle + \lambda C_{1,1}A_{3,-1}\rangle$	$\alpha = 0.59348, \beta = 0.59348, \gamma = 0.26705, \epsilon = 0.26705, \kappa = 0.26705, \lambda = 0.26705,$	4.903 eV

Table 3.1: ASD at 0.0000 Å

are very degenerate . And the characteristics of these states are being exchanged very frequently.

In the analysis of the ¹(TT) state, it was observed that performing the scan using 10 monomer states of the types LE , CT , and ¹(TT) resulted in smoother plots. This indicates that a more comprehensive set of monomer states contributes to a more accurate representation of the ¹(TT) state's properties.

2D Scan

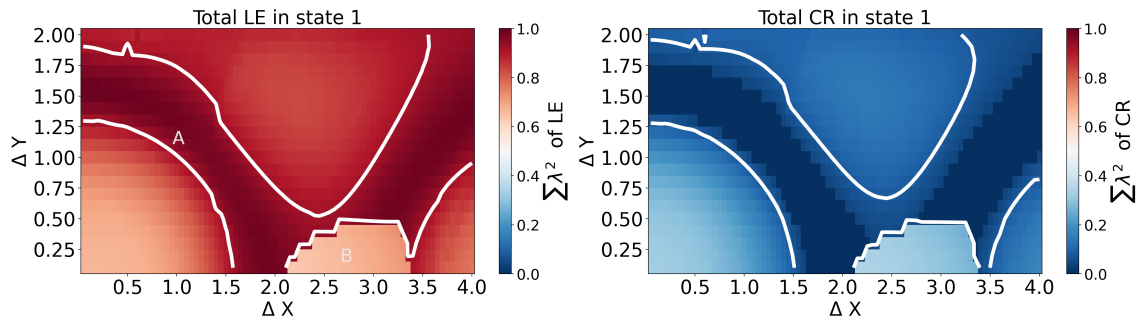
To delve deeper into the wave function characteristics of the PDI states, a two-dimensional (2D) scan was conducted. The chosen active space for this extended study comprised (16o,16e), with each monomer containing (8o,8e). Additionally, 10 monomer states of types LE, CT, and ¹(TT), along with 8 dimer states, were obtained in the calculations. For the 2D scan, ASD calculations employed the CASCI/cc-pVDZ method for monomer calculation. The scan covered a range from $\Delta X = 0 \text{ \AA}$ to $\Delta X = 4 \text{ \AA}$ and $\Delta Y = 0 \text{ \AA}$ to $\Delta Y = 2 \text{ \AA}$ at a fixed ΔZ coordinate of 3.5 Å . The grid size used for the scan was 0.1 Å along the Y axis and 0.05 Å along the X axis. The ground state exhibited a minimum energy E_0^{\min} at coordinates $\Delta X = -3.3 \text{ \AA}$ and $\Delta Y = -1.6 \text{ \AA}$, while the maximum energy E_0^{\max} occurred at $\Delta X = 0 \text{ \AA}$ and $\Delta Y = 0 \text{ \AA}$. Importantly, this ground state (E_0^{\min}) was found to consist solely of $|S_0S_0\rangle$ character.

In ASD first excited state has minimum energy at $\Delta X = 2.0 \text{ \AA}$ $\Delta Y = 2 \text{ \AA}$ (3.18 eV) and maximum at $\Delta X = 2 \text{ \AA}$, $\Delta Y = 0.25 \text{ \AA}$ 3.94 eV. In figure 3.5, the variation of LE and CT characters in first excited state are shown. Similar to previous discussion in the line scan, the region around the full stacking has 60% LE character and 25% CR character thus have good excimer type character. In this figure the region A has very high LE contribution and negligible CR admixture. The region between the points of degeneracy $\Delta X = 2.3 \text{ \AA}$ and $\Delta X = 3.2 \text{ \AA}$ expand into the region designated as B it has 60%LE and 40% CT character.

In Figure 3.6, the variations of LE and CT characters in the second excited state are shown.

State	electronic structure	coefficient	energy
G S	$-\alpha S_{0,0}S_{0,0}\rangle$	$\alpha = 0.99504,$	0.000 eV
1 st	$-\alpha S_{0,0}S_{1,0}\rangle + \beta S_{1,0}S_{0,0}\rangle - \gamma A_{1,-1}C_{1,1}\rangle + \epsilon A_{1,1}C_{1,-1}\rangle + \kappa C_{1,-1}A_{1,1}\rangle - \lambda C_{1,1}A_{1,-1}\rangle$	$\alpha = 0.58835, \beta = 0.58835, \gamma = 0.26102, \epsilon = 0.26102, \kappa = 0.26102, \lambda = 0.26102,$	3.402 eV
2 nd	$+\alpha S_{0,0}S_{1,0}\rangle + \beta S_{1,0}S_{0,0}\rangle - \gamma A_{1,-1}C_{1,1}\rangle + \epsilon A_{1,1}C_{1,-1}\rangle - \kappa C_{1,-1}A_{1,1}\rangle + \lambda C_{1,1}A_{1,-1}\rangle$	$\alpha = 0.61906, \beta = 0.61906, \gamma = 0.23163, \epsilon = 0.23163, \kappa = 0.23163, \lambda = 0.23163,$	4.156 eV
3 rd	$+\alpha S_{0,0}S_{1,0}\rangle + \beta S_{1,0}S_{6,0}\rangle + \gamma S_{1,0}S_{0,0}\rangle + \epsilon S_{6,0}S_{0,0}\rangle + \kappa A_{1,-1}C_{1,1}\rangle - \lambda A_{1,1}C_{1,-1}\rangle + \nu C_{1,-1}A_{1,1}\rangle - \varphi C_{1,1}A_{1,-1}\rangle$	$\alpha = 0.33124, \beta = 0.11217, \gamma = 0.33124, \epsilon = 0.11217, \kappa = 0.43107, \lambda = 0.43107, \nu = 0.43107, \varphi = 0.43107,$	4.451 eV
4 th	$-\alpha S_{0,0}S_{1,0}\rangle - \beta S_{0,0}S_{3,0}\rangle + \gamma S_{1,0}S_{0,0}\rangle + \epsilon S_{3,0}S_{0,0}\rangle + \kappa T_{1,-2}T_{1,2}\rangle - \lambda T_{1,0}T_{1,0}\rangle + \nu T_{1,2}T_{1,-2}\rangle + \varphi A_{1,-1}C_{1,1}\rangle - \sigma A_{1,1}C_{1,-1}\rangle - \varpi C_{1,-1}A_{1,1}\rangle + \delta C_{1,1}A_{1,-1}\rangle$	$\alpha = 0.35929, \beta = 0.20406, \gamma = 0.35929, \epsilon = 0.20407, \kappa = 0.25098, \lambda = 0.25098, \nu = 0.25098, \varphi = 0.33468, \sigma = 0.33468, \varpi = 0.33468, \delta = 0.33468,$	4.671 eV
5 th	$+\alpha S_{0,0}S_{2,0}\rangle - \beta S_{2,0}S_{0,0}\rangle - \gamma A_{2,-1}C_{1,1}\rangle + \epsilon A_{2,1}C_{1,-1}\rangle - \kappa C_{1,-1}A_{2,1}\rangle + \lambda C_{1,1}A_{2,-1}\rangle$	$\alpha = 0.62123, \beta = 0.62123, \gamma = 0.21916, \epsilon = 0.21916, \kappa = 0.21916, \lambda = 0.21916,$	4.699 eV
6 th	$+\alpha S_{0,0}S_{3,0}\rangle + \beta S_{3,0}S_{0,0}\rangle - \gamma A_{4,-1}C_{1,1}\rangle + \epsilon A_{4,1}C_{1,-1}\rangle - \kappa C_{1,-1}A_{4,1}\rangle + \lambda C_{1,1}A_{4,-1}\rangle$	$\alpha = 0.65554, \beta = 0.65554, \gamma = 0.15578, \epsilon = 0.15578, \kappa = 0.15578, \lambda = 0.15578,$	4.968 eV
7 th	$+\alpha S_{0,0}S_{2,0}\rangle + \beta S_{0,0}S_{4,0}\rangle + \gamma S_{0,0}S_{5,0}\rangle + \epsilon S_{2,0}S_{0,0}\rangle + \kappa S_{4,0}S_{0,0}\rangle + \lambda S_{5,0}S_{0,0}\rangle - \nu A_{3,-1}C_{1,1}\rangle + \varphi A_{3,1}C_{1,-1}\rangle + \sigma C_{1,-1}A_{3,1}\rangle - \varpi C_{1,1}A_{3,-1}\rangle$	$\alpha = 0.19422, \beta = 0.31161, \gamma = 0.47854, \epsilon = 0.19423, \kappa = 0.31161, \lambda = 0.47854, \nu = 0.24332, \varphi = 0.24332, \sigma = 0.24332, \varpi = 0.24332,$	5.027 eV

Table 3.2: ASD at 0.8000 Å

Figure 3.5: LE , CR character of 1st excited state

State	electronic structure	coefficient	energy
G S	$+\alpha S_{0,0}S_{0,0}\rangle$	$\alpha = 0.99338,$	0.000 eV
1 st	$-\alpha S_{0,0}S_{1,0}\rangle + \beta S_{1,0}S_{0,0}\rangle + \gamma A_{1,-1}C_{1,1}\rangle - \epsilon A_{1,1}C_{1,-1}\rangle - \kappa C_{1,-1}A_{1,1}\rangle + \lambda C_{1,1}A_{1,-1}\rangle$	$\alpha = 0.62220, \beta = 0.62220, \gamma = 0.21792, \epsilon = 0.21792, \kappa = 0.21792, \lambda = 0.21792,$	3.623 eV
2 nd	$-\alpha S_{0,0}S_{1,0}\rangle - \beta S_{1,0}S_{0,0}\rangle - \gamma A_{1,-1}C_{1,1}\rangle + \epsilon A_{1,1}C_{1,-1}\rangle - \kappa C_{1,-1}A_{1,1}\rangle + \lambda C_{1,1}A_{1,-1}\rangle$	$\alpha = 0.58473, \beta = 0.58473, \gamma = 0.26954, \epsilon = 0.26954, \kappa = 0.26954, \lambda = 0.26954,$	4.064 eV
3 rd	$-\alpha S_{0,0}S_{1,0}\rangle - \beta S_{0,0}S_{3,0}\rangle + \gamma S_{1,0}S_{0,0}\rangle - \epsilon S_{3,0}S_{0,0}\rangle + \kappa T_{1,-2}T_{1,2}\rangle - \lambda T_{1,0}T_{1,0}\rangle + \nu T_{1,2}T_{1,-2}\rangle - \varphi A_{1,-1}C_{1,1}\rangle + \sigma A_{1,1}C_{1,-1}\rangle + \varpi C_{1,-1}A_{1,1}\rangle - \delta C_{1,1}A_{1,-1}\rangle$	$\alpha = 0.31641, \beta = 0.16311, \gamma = 0.31641, \epsilon = 0.16311, \kappa = 0.16806, \lambda = 0.16806, \nu = 0.16806, \varphi = 0.39999, \sigma = 0.39999, \varpi = 0.39998, \delta = 0.39998,$	4.500 eV
4 th	$-\alpha S_{0,0}S_{1,0}\rangle + \beta S_{0,0}S_{6,0}\rangle - \gamma S_{1,0}S_{0,0}\rangle + \epsilon S_{6,0}S_{0,0}\rangle + \kappa A_{1,-1}C_{1,1}\rangle - \lambda A_{1,1}C_{1,-1}\rangle + \nu C_{1,-1}A_{1,1}\rangle - \varphi C_{1,1}A_{1,-1}\rangle$	$\alpha = 0.38655, \beta = 0.11963, \gamma = 0.38654, \epsilon = 0.11963, \kappa = 0.40561, \lambda = 0.40561, \nu = 0.40561, \varphi = 0.40561,$	4.527 eV
5 th	$-\alpha S_{0,0}S_{2,0}\rangle - \beta S_{2,0}S_{0,0}\rangle - \gamma A_{2,-1}C_{1,1}\rangle + \epsilon A_{2,1}C_{1,-1}\rangle - \kappa C_{1,-1}A_{2,1}\rangle + \lambda C_{1,1}A_{2,-1}\rangle$	$\alpha = 0.63921, \beta = 0.63921, \gamma = 0.19688, \epsilon = 0.19688, \kappa = 0.19688, \lambda = 0.19688,$	4.833 eV
6 th	$-\alpha S_{0,0}S_{2,0}\rangle - \beta S_{0,0}S_{3,0}\rangle + \gamma S_{2,0}S_{0,0}\rangle + \epsilon S_{3,0}S_{0,0}\rangle + \kappa A_{4,-1}C_{1,1}\rangle - \lambda A_{4,1}C_{1,-1}\rangle + \nu C_{1,-1}A_{4,1}\rangle - \varphi C_{1,1}A_{4,-1}\rangle$	$\alpha = 0.11818, \beta = 0.66292, \gamma = 0.12541, \epsilon = 0.66419, \kappa = 0.12332, \lambda = 0.12332, \nu = 0.12312, \varphi = 0.12312,$	5.112 eV
7 th	$+\alpha S_{0,0}S_{2,0}\rangle - \beta S_{0,0}S_{3,0}\rangle - \gamma S_{0,0}S_{5,0}\rangle - \epsilon S_{2,0}S_{0,0}\rangle + \kappa S_{3,0}S_{0,0}\rangle - \lambda S_{5,0}S_{0,0}\rangle + \nu A_{3,-1}C_{1,1}\rangle - \varphi A_{3,1}C_{1,-1}\rangle - \sigma C_{1,-1}A_{3,1}\rangle + \varpi C_{1,1}A_{3,-1}\rangle$	$\alpha = 0.62299, \beta = 0.13310, \gamma = 0.24875, \epsilon = 0.62158, \kappa = 0.12663, \lambda = 0.24872, \nu = 0.11043, \varphi = 0.11043, \sigma = 0.11046, \varpi = 0.11046,$	5.112 eV

Table 3.3: ASD at 1.2000 Å

State	electronic structure	coefficient	energy
G S	$+\alpha S_{0,0}S_{0,0}\rangle$	$\alpha = 0.99368,$	0.000 eV
1 st	$+\alpha S_{0,0}S_{1,0}\rangle + \beta S_{1,0}S_{0,0}\rangle$	$\alpha = 0.69291, \beta = 0.69291,$	3.823 eV
2 nd	$-\alpha S_{0,0}S_{1,0}\rangle + \beta S_{1,0}S_{0,0}\rangle - \gamma A_{1,-1}C_{1,1}\rangle + \epsilon A_{1,1}C_{1,-1}\rangle - \kappa C_{1,-1}A_{1,1}\rangle + \lambda C_{1,1}A_{1,-1}\rangle$	$\alpha = 0.56398, \beta = 0.56398, \gamma = 0.29111, \epsilon = 0.29111, \kappa = 0.29111, \lambda = 0.29111,$	3.934 eV
3 rd	$-\alpha S_{0,0}S_{1,0}\rangle - \beta S_{0,0}S_{3,0}\rangle - \gamma S_{1,0}S_{0,0}\rangle - \epsilon S_{3,0}S_{0,0}\rangle - \kappa A_{1,-1}C_{1,1}\rangle + \lambda A_{1,1}C_{1,-1}\rangle + \nu C_{1,-1}A_{1,1}\rangle - \varphi C_{1,1}A_{1,-1}\rangle$	$\alpha = 0.10430, \beta = 0.15038, \gamma = 0.10430, \epsilon = 0.15038, \kappa = 0.46891, \lambda = 0.46891, \nu = 0.46891, \varphi = 0.46891,$	4.366 eV
4 th	$-\alpha S_{0,0}S_{1,0}\rangle - \beta S_{0,0}S_{6,0}\rangle + \gamma S_{1,0}S_{0,0}\rangle + \epsilon S_{6,0}S_{0,0}\rangle + \kappa A_{1,-1}C_{1,1}\rangle - \lambda A_{1,1}C_{1,-1}\rangle + \nu C_{1,-1}A_{1,1}\rangle - \varphi C_{1,1}A_{1,-1}\rangle$	$\alpha = 0.41598, \beta = 0.10687, \gamma = 0.41598, \epsilon = 0.10687, \kappa = 0.39021, \lambda = 0.39021, \nu = 0.39022, \varphi = 0.39022,$	4.632 eV
5 th	$-\alpha S_{0,0}S_{2,0}\rangle + \beta S_{2,0}S_{0,0}\rangle - \gamma A_{2,-1}C_{1,1}\rangle + \epsilon A_{2,1}C_{1,-1}\rangle - \kappa C_{1,-1}A_{2,1}\rangle + \lambda C_{1,1}A_{2,-1}\rangle$	$\alpha = 0.66738, \beta = 0.66738, \gamma = 0.14938, \epsilon = 0.14938, \kappa = 0.14938, \lambda = 0.14938,$	4.971 eV
6 th	$+\alpha S_{0,0}S_{3,0}\rangle + \beta S_{3,0}S_{0,0}\rangle + \gamma T_{1,-2}T_{1,2}\rangle - \epsilon T_{1,0}T_{1,0}\rangle + \kappa T_{1,2}T_{1,-2}\rangle$	$\alpha = 0.45382, \beta = 0.45382, \gamma = 0.41239, \epsilon = 0.41239, \kappa = 0.41239,$	5.069 eV
7 th	$-\alpha S_{0,0}S_{2,0}\rangle - \beta S_{0,0}S_{5,0}\rangle - \gamma S_{2,0}S_{0,0}\rangle - \epsilon S_{5,0}S_{0,0}\rangle$	$\alpha = 0.67489, \beta = 0.14846, \gamma = 0.67489, \epsilon = 0.14846,$	5.095 eV

Table 3.4: ASD at 1.7000 Å

State	electronic structure	coefficient	energy
G S	$+\alpha S_{0,0}S_{0,0}\rangle$	$\alpha = 0.99450,$	0.000 eV
1^{st}	$-\alpha S_{0,0}S_{1,0}\rangle - \beta S_{1,0}S_{0,0}\rangle$	$\alpha = 0.70074, \beta = 0.70074,$	3.850 eV
2^{nd}	$-\alpha S_{0,0}S_{1,0}\rangle + \beta S_{1,0}S_{0,0}\rangle + \gamma A_{1,-1}C_{1,1}\rangle - \epsilon A_{1,1}C_{1,-1}\rangle - \kappa C_{1,-1}A_{1,1}\rangle + \lambda C_{1,1}A_{1,-1}\rangle$	$\alpha = 0.56186, \beta = 0.56186, \gamma = 0.29467, \epsilon = 0.29467, \kappa = 0.29467, \lambda = 0.29467,$	3.868 eV
3^{rd}	$+\alpha S_{0,0}S_{3,0}\rangle + \beta S_{3,0}S_{0,0}\rangle - \gamma A_{1,-1}C_{1,1}\rangle + \epsilon A_{1,1}C_{1,-1}\rangle - \kappa C_{1,-1}A_{1,1}\rangle + \lambda C_{1,1}A_{1,-1}\rangle$	$\alpha = 0.13705, \beta = 0.13705, \gamma = 0.48281, \epsilon = 0.48281, \kappa = 0.48281, \lambda = 0.48281,$	4.387 eV
4^{th}	$+\alpha S_{0,0}S_{1,0}\rangle - \beta S_{1,0}S_{0,0}\rangle + \gamma A_{1,-1}C_{1,1}\rangle - \epsilon A_{1,1}C_{1,-1}\rangle - \kappa C_{1,-1}A_{1,1}\rangle + \lambda C_{1,1}A_{1,-1}\rangle$	$\alpha = 0.41873, \beta = 0.41873, \gamma = 0.38816, \epsilon = 0.38816, \kappa = 0.38816, \lambda = 0.38816,$	4.694 eV
5^{th}	$-\alpha S_{0,0}S_{2,0}\rangle + \beta S_{2,0}S_{0,0}\rangle + \gamma A_{2,-1}C_{1,1}\rangle - \epsilon A_{2,1}C_{1,-1}\rangle + \kappa C_{1,-1}A_{2,1}\rangle - \lambda C_{1,1}A_{2,-1}\rangle$	$\alpha = 0.67916, \beta = 0.67916, \gamma = 0.11703, \epsilon = 0.11703, \kappa = 0.11703, \lambda = 0.11703,$	5.019 eV
6^{th}	$-\alpha S_{0,0}S_{3,0}\rangle - \beta S_{3,0}S_{0,0}\rangle - \gamma T_{1,-2}T_{1,2}\rangle + \epsilon T_{1,0}T_{1,0}\rangle - \kappa T_{1,2}T_{1,-2}\rangle$	$\alpha = 0.40248, \beta = 0.40248, \gamma = 0.43757, \epsilon = 0.43757, \kappa = 0.43757,$	5.019 eV
7^{th}	$-\alpha S_{0,0}S_{2,0}\rangle - \beta S_{0,0}S_{5,0}\rangle - \gamma S_{2,0}S_{0,0}\rangle - \epsilon S_{5,0}S_{0,0}\rangle$	$\alpha = 0.67815, \beta = 0.12406, \gamma = 0.67815, \epsilon = 0.12406,$	5.083 eV

Table 3.5: ASD at 2.0000 Å

State	electronic structure	coefficient	energy
G S	$-\alpha S_{0,0}S_{0,0}\rangle$	$\alpha = 0.99495,$	0.000 eV
1^{st}	$-\alpha S_{0,0}S_{1,0}\rangle + \beta S_{1,0}S_{0,0}\rangle + \gamma A_{1,-1}C_{1,1}\rangle - \epsilon A_{1,1}C_{1,-1}\rangle - \kappa C_{1,-1}A_{1,1}\rangle + \lambda C_{1,1}A_{1,-1}\rangle$	$\alpha = 0.56543, \beta = 0.56543, \gamma = 0.29299, \epsilon = 0.29299, \kappa = 0.29299, \lambda = 0.29299,$	3.826 eV
2^{nd}	$-\alpha S_{0,0}S_{1,0}\rangle - \beta S_{1,0}S_{0,0}\rangle$	$\alpha = 0.69267, \beta = 0.69267,$	3.855 eV
3^{rd}	$-\alpha S_{0,0}S_{1,0}\rangle + \beta S_{0,0}S_{3,0}\rangle - \gamma S_{1,0}S_{0,0}\rangle + \epsilon S_{3,0}S_{0,0}\rangle - \kappa A_{1,-1}C_{1,1}\rangle + \lambda A_{1,1}C_{1,-1}\rangle - \nu C_{1,-1}A_{1,1}\rangle + \varphi C_{1,1}A_{1,-1}\rangle$	$\alpha = 0.12255, \beta = 0.11015, \gamma = 0.12255, \epsilon = 0.11015, \kappa = 0.47392, \lambda = 0.47392, \nu = 0.47392, \varphi = 0.47392,$	4.425 eV
4^{th}	$+\alpha S_{0,0}S_{1,0}\rangle - \beta S_{0,0}S_{3,0}\rangle - \gamma S_{1,0}S_{0,0}\rangle + \epsilon S_{3,0}S_{0,0}\rangle + \kappa A_{1,-1}C_{1,1}\rangle - \lambda A_{1,1}C_{1,-1}\rangle - \nu C_{1,-1}A_{1,1}\rangle + \varphi C_{1,1}A_{1,-1}\rangle$	$\alpha = 0.41366, \beta = 0.10139, \gamma = 0.41366, \epsilon = 0.10139, \kappa = 0.39073, \lambda = 0.39073, \nu = 0.39073, \varphi = 0.39073,$	4.757 eV
5^{th}	$+\alpha S_{0,0}S_{3,0}\rangle + \beta S_{3,0}S_{0,0}\rangle - \gamma T_{1,-2}T_{1,2}\rangle + \epsilon T_{1,0}T_{1,0}\rangle - \kappa T_{1,2}T_{1,-2}\rangle + \lambda A_{1,-1}C_{1,1}\rangle + \nu A_{4,-1}C_{1,1}\rangle - \varphi A_{1,1}C_{1,-1}\rangle - \sigma A_{4,1}C_{1,-1}\rangle + \varpi C_{1,-1}A_{1,1}\rangle + \delta C_{1,-1}A_{4,1}\rangle - \omega C_{1,1}A_{1,-1}\rangle - \sigma C_{1,1}A_{4,-1}\rangle$	$\alpha = 0.41709, \beta = 0.41709, \gamma = 0.40761, \epsilon = 0.40761, \kappa = 0.40761, \lambda = 0.10397, \nu = 0.11166, \varphi = 0.10397, \sigma = 0.11166, \varpi = 0.10397, \delta = 0.11166, \omega = 0.10397, \sigma = 0.11166,$	5.007 eV
6^{th}	$-\alpha S_{0,0}S_{2,0}\rangle - \beta S_{2,0}S_{0,0}\rangle$	$\alpha = 0.68481, \beta = 0.68482,$	5.042 eV
7^{th}	$+\alpha S_{0,0}S_{2,0}\rangle + \beta S_{0,0}S_{5,0}\rangle - \gamma S_{2,0}S_{0,0}\rangle - \epsilon S_{5,0}S_{0,0}\rangle$	$\alpha = 0.67752, \beta = 0.10929, \gamma = 0.67751, \epsilon = 0.10929,$	5.068 eV

Table 3.6: ASD at 2.3000 Å

State	electronic structure	coefficient	energy
G S	$-\alpha S_{0,0}S_{0,0}\rangle$	$\alpha = 0.99448,$	0.00000 eV
1 st	$+\alpha S_{0,0}S_{1,0}\rangle + \beta S_{1,0}S_{0,0}\rangle + \gamma A_{1,-1}C_{1,1}\rangle - \epsilon A_{1,1}C_{1,-1}\rangle - \kappa C_{1,-1}A_{1,1}\rangle + \lambda C_{1,1}A_{1,-1}\rangle$	$\alpha = 0.57882, \beta = 0.57882, \gamma = 0.28188, \epsilon = 0.28188, \kappa = 0.28188, \lambda = 0.28188,$	3.815 eV
2 nd	$-\alpha S_{0,0}S_{1,0}\rangle + \beta S_{1,0}S_{0,0}\rangle$	$\alpha = 0.69825, \beta = 0.69825,$	3.892 eV
3 rd	$+\alpha T_{1,-2}T_{1,2}\rangle - \beta T_{1,0}T_{1,0}\rangle + \gamma T_{1,2}T_{1,-2}\rangle - \epsilon A_{1,-1}C_{1,1}\rangle + \kappa A_{1,1}C_{1,-1}\rangle - \lambda C_{1,-1}A_{1,1}\rangle + \nu C_{1,1}A_{1,-1}\rangle$	$\alpha = 0.21312, \beta = 0.21312, \gamma = 0.21312, \epsilon = 0.45132, \kappa = 0.45132, \lambda = 0.45133, \nu = 0.45133,$	4.417 eV
4 th	$+\alpha S_{0,0}S_{1,0}\rangle + \beta S_{1,0}S_{0,0}\rangle - \gamma A_{1,-1}C_{1,1}\rangle + \epsilon A_{1,1}C_{1,-1}\rangle + \kappa C_{1,-1}A_{1,1}\rangle - \lambda C_{1,1}A_{1,-1}\rangle$	$\alpha = 0.39855, \beta = 0.39855, \gamma = 0.40478, \epsilon = 0.40478, \kappa = 0.40478, \lambda = 0.40478,$	4.839 eV
5 th	$+\alpha S_{0,0}S_{2,0}\rangle + \beta S_{0,0}S_{3,0}\rangle + \gamma S_{2,0}S_{0,0}\rangle + \epsilon S_{3,0}S_{0,0}\rangle + \kappa T_{1,-2}T_{1,2}\rangle - \lambda T_{1,0}T_{1,0}\rangle + \nu T_{1,2}T_{1,-2}\rangle + \varphi A_{1,-1}C_{1,1}\rangle - \sigma A_{4,-1}C_{1,1}\rangle - \varpi A_{1,1}C_{1,-1}\rangle + \delta A_{4,1}C_{1,-1}\rangle + \omega C_{1,-1}A_{1,1}\rangle - \sigma C_{1,-1}A_{4,1}\rangle - a C_{1,1}A_{1,-1}\rangle + b C_{1,1}A_{4,-1}\rangle$	$\alpha = 0.27043, \beta = 0.52296, \gamma = 0.27044, \epsilon = 0.52296, \kappa = 0.21875, \lambda = 0.21875, \nu = 0.21875, \varphi = 0.10204, \sigma = 0.11531, \varpi = 0.10204, \delta = 0.11531, \omega = 0.10204, \sigma = 0.11531, a = 0.10204, b = 0.11531,$	5.019 eV
6 th	$-\alpha S_{0,0}S_{2,0}\rangle + \beta S_{0,0}S_{3,0}\rangle + \gamma S_{0,0}S_{5,0}\rangle - \epsilon S_{2,0}S_{0,0}\rangle + \kappa S_{3,0}S_{0,0}\rangle + \lambda S_{5,0}S_{0,0}\rangle + \nu A_{3,-1}C_{1,1}\rangle - \varphi A_{3,1}C_{1,-1}\rangle + \sigma C_{1,-1}A_{3,1}\rangle - \varpi C_{1,1}A_{3,-1}\rangle$	$\alpha = 0.60366, \beta = 0.23514, \gamma = 0.12004, \epsilon = 0.60367, \kappa = 0.23515, \lambda = 0.12004, \nu = 0.11218, \varphi = 0.11218, \sigma = 0.11218, \varpi = 0.11218,$	5.021 eV
7 th	$-\alpha S_{0,0}S_{2,0}\rangle + \beta S_{2,0}S_{0,0}\rangle$	$\alpha = 0.69019, \beta = 0.69018,$	5.058 eV

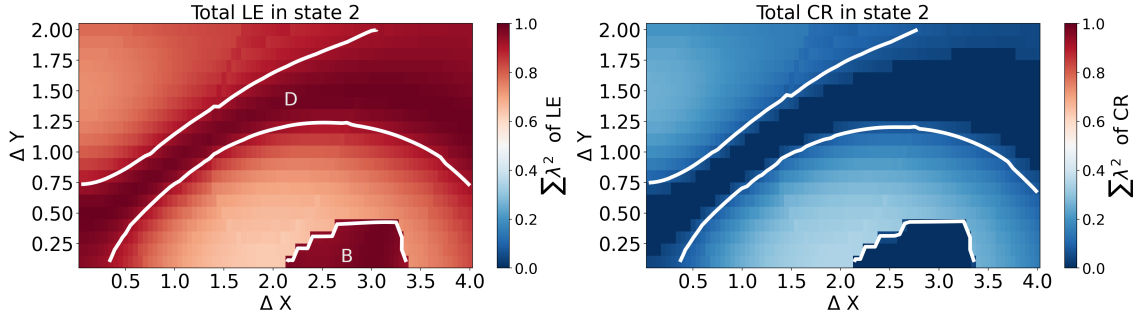
Table 3.7: ASD at 2.8000 Å

State	electronic structure	coefficient	energy
G S	$-\alpha S_{0,0}S_{0,0}\rangle$	$\alpha = 0.99392,$	0.000 eV
1 st	$-\alpha S_{0,0}S_{1,0}\rangle + \beta S_{1,0}S_{0,0}\rangle - \gamma A_{1,-1}C_{1,1}\rangle + \epsilon A_{1,1}C_{1,-1}\rangle + \kappa C_{1,-1}A_{1,1}\rangle - \lambda C_{1,1}A_{1,-1}\rangle$	$\alpha = 0.59337, \beta = 0.59337, \gamma = 0.26650, \epsilon = 0.26650, \kappa = 0.26650, \lambda = 0.26650,$	3.848 eV
2 nd	$-\alpha S_{0,0}S_{1,0}\rangle - \beta S_{1,0}S_{0,0}\rangle$	$\alpha = 0.69590, \beta = 0.69590,$	3.893 eV
3 rd	$-\alpha T_{1,-2}T_{1,2}\rangle + \beta T_{1,0}T_{1,0}\rangle - \gamma T_{1,2}T_{1,-2}\rangle + \epsilon A_{1,-1}C_{1,1}\rangle - \kappa A_{1,1}C_{1,-1}\rangle + \lambda C_{1,-1}A_{1,1}\rangle - \nu C_{1,1}A_{1,-1}\rangle$	$\alpha = 0.25026, \beta = 0.25026, \gamma = 0.25026, \epsilon = 0.43646, \kappa = 0.43646, \lambda = 0.43646, \nu = 0.43646,$	4.415 eV
4 th	$-\alpha S_{0,0}S_{1,0}\rangle + \beta S_{1,0}S_{0,0}\rangle + \gamma A_{1,-1}C_{1,1}\rangle - \epsilon A_{1,1}C_{1,-1}\rangle - \kappa C_{1,-1}A_{1,1}\rangle + \lambda C_{1,1}A_{1,-1}\rangle$	$\alpha = 0.37633, \beta = 0.37633, \gamma = 0.41220, \epsilon = 0.41220, \kappa = 0.41220, \lambda = 0.41220,$	4.838 eV
5 th	$+\alpha S_{0,0}S_{2,0}\rangle - \beta S_{0,0}S_{5,0}\rangle + \gamma S_{2,0}S_{0,0}\rangle - \epsilon S_{5,0}S_{0,0}\rangle + \kappa A_{3,-1}C_{1,1}\rangle - \lambda A_{3,1}C_{1,-1}\rangle + \nu C_{1,-1}A_{3,1}\rangle - \varphi C_{1,1}A_{3,-1}\rangle$	$\alpha = 0.62512, \beta = 0.20081, \gamma = 0.62513, \epsilon = 0.20081, \kappa = 0.14165, \lambda = 0.14165, \nu = 0.14165, \varphi = 0.14165,$	4.943 eV
6 th	$-\alpha S_{0,0}S_{3,0}\rangle - \beta S_{3,0}S_{0,0}\rangle - \gamma T_{1,-2}T_{1,2}\rangle + \epsilon T_{1,0}T_{1,0}\rangle - \kappa T_{1,2}T_{1,-2}\rangle - \lambda A_{4,-1}C_{1,1}\rangle + \nu A_{4,1}C_{1,-1}\rangle - \varphi C_{1,-1}A_{4,1}\rangle + \sigma C_{1,1}A_{4,-1}\rangle$	$\alpha = 0.61117, \beta = 0.61117, \gamma = 0.19413, \epsilon = 0.19413, \kappa = 0.19413, \lambda = 0.13395, \nu = 0.13395, \varphi = 0.13395, \sigma = 0.13395,$	5.025 eV
7 th	$-\alpha S_{0,0}S_{2,0}\rangle + \beta S_{2,0}S_{0,0}\rangle$	$\alpha = 0.68662, \beta = 0.68662,$	5.047 eV

Table 3.8: ASD at 3.2000 Å

State	electronic structure	coefficient	energy
G S	$+\alpha S_{0,0}S_{0,0}\rangle$	$\alpha = 0.99452,$	0.000 eV
1 st	$-\alpha S_{0,0}S_{1,0}\rangle - \beta S_{1,0}S_{0,0}\rangle + \gamma A_{1,-1}C_{1,1}\rangle - \epsilon A_{1,1}C_{1,-1}\rangle - \kappa C_{1,-1}A_{1,1}\rangle + \lambda C_{1,1}A_{1,-1}\rangle$	$\alpha = 0.63062, \beta = 0.63062, \gamma = 0.18997, \epsilon = 0.18997, \kappa = 0.18997, \lambda = 0.18997,$	3.724 eV
2 nd	$+\alpha S_{0,0}S_{1,0}\rangle - \beta S_{1,0}S_{0,0}\rangle + \gamma A_{1,-1}C_{1,1}\rangle - \epsilon A_{1,1}C_{1,-1}\rangle + \kappa C_{1,-1}A_{1,1}\rangle - \lambda C_{1,1}A_{1,-1}\rangle$	$\alpha = 0.62209, \beta = 0.62209, \gamma = 0.22829, \epsilon = 0.22829, \kappa = 0.22829, \lambda = 0.22829,$	3.910 eV
3 rd	$+\alpha S_{0,0}S_{1,0}\rangle + \beta S_{1,0}S_{0,0}\rangle - \gamma T_{1,-2}T_{1,2}\rangle + \epsilon T_{1,0}T_{1,0}\rangle - \kappa T_{1,2}T_{1,-2}\rangle + \lambda A_{1,-1}C_{1,1}\rangle - \nu A_{1,1}C_{1,-1}\rangle - \varphi C_{1,-1}A_{1,1}\rangle + \sigma C_{1,1}A_{1,-1}\rangle$	$\alpha = 0.29425, \beta = 0.29425, \gamma = 0.27431, \epsilon = 0.27431, \kappa = 0.27431, \lambda = 0.37593, \nu = 0.37593, \varphi = 0.37593, \sigma = 0.37593,$	4.524 eV
4 th	$-\alpha S_{0,0}S_{1,0}\rangle - \beta S_{0,0}S_{3,0}\rangle + \gamma S_{1,0}S_{0,0}\rangle + \epsilon S_{3,0}S_{0,0}\rangle + \kappa A_{1,-1}C_{1,1}\rangle - \lambda A_{1,1}C_{1,-1}\rangle + \nu C_{1,-1}A_{1,1}\rangle - \varphi C_{1,1}A_{1,-1}\rangle$	$\alpha = 0.31449, \beta = 0.22810, \gamma = 0.31449, \epsilon = 0.22810, \kappa = 0.40869, \lambda = 0.40869, \nu = 0.40869, \varphi = 0.40869,$	4.693 eV
5 th	$+\alpha S_{0,0}S_{2,0}\rangle + \beta S_{0,0}S_{5,0}\rangle + \gamma S_{2,0}S_{0,0}\rangle + \epsilon S_{5,0}S_{0,0}\rangle - \kappa A_{2,-1}C_{1,1}\rangle + \lambda A_{3,-1}C_{1,1}\rangle + \nu A_{2,1}C_{1,-1}\rangle - \varphi A_{3,1}C_{1,-1}\rangle - \sigma C_{1,-1}A_{2,1}\rangle + \varpi C_{1,-1}A_{3,1}\rangle + \delta C_{1,1}A_{2,-1}\rangle - \omega C_{1,1}A_{3,-1}\rangle$	$\alpha = 0.57479, \beta = 0.25833, \gamma = 0.57479, \epsilon = 0.25833, \kappa = 0.11706, \lambda = 0.17137, \nu = 0.11706, \varphi = 0.17137, \sigma = 0.11706, \varpi = 0.17138, \delta = 0.11706, \omega = 0.17138,$	4.859 eV
6 th	$+\alpha S_{0,0}S_{3,0}\rangle + \beta S_{3,0}S_{0,0}\rangle - \gamma T_{1,-2}T_{1,2}\rangle + \epsilon T_{1,0}T_{1,0}\rangle - \kappa T_{1,2}T_{1,-2}\rangle - \lambda A_{4,-1}C_{1,1}\rangle + \nu A_{4,1}C_{1,-1}\rangle + \varphi C_{1,-1}A_{4,1}\rangle - \sigma C_{1,1}A_{4,-1}\rangle$	$\alpha = 0.64359, \beta = 0.64359, \gamma = 0.15114, \epsilon = 0.15114, \kappa = 0.15114, \lambda = 0.13071, \nu = 0.13071, \varphi = 0.13071, \sigma = 0.13071,$	5.020 eV
7 th	$+\alpha S_{0,0}S_{2,0}\rangle - \beta S_{2,0}S_{0,0}\rangle$	$\alpha = 0.68918, \beta = 0.68918,$	5.052 eV

Table 3.9: ASD at 3.7500 Å

Figure 3.6: LE , CR character of 2nd excited state

In the second excited state, region D exhibits very high LE character and low CT character, whereas region C displays mixed LE/CT character. The LE character of the 2nd excited state is mostly comprised of S^- in regions C and D. The energy of this state is highest when fully stacked and minimum when $\Delta X = -3.2 \text{ \AA}$, $\Delta Y = -0.25 \text{ \AA}$. In region B of the first excited state, has predominantly S^+ character, while in the second excited state has predominantly S^- character.”

The 3rd, 4th, 5th, and 6th excited states exhibit varying degrees of charge-transfer (CT) character, with the 3rd and 4th states showing a significant CT character, while the 5th and 6th states have very little CT character. These excited states are discussed together because the potential energy surface intersects at various points, and the ¹(TT) state is shared among them. It is inferred from the line scan that at $\Delta X = 1.2 \text{ \AA}$, at $\Delta Y = 0 \text{ \AA}$ the 3rd and 4th excited states become degenerate, and from this point, the roles of the wave functions contributing to the 3rd and 4th excited states are exchanged. The 4th excited state exhibits triplet character from $\Delta X = -1.2 \text{ \AA}$ to -0.8 \AA at $\Delta Y = 0 \text{ \AA}$; afterward, it is exchanged with the 5th excited state. Also, at $\Delta X = -1.90 \text{ \AA}$ and $\Delta X = -3.8 \text{ \AA}$, at $\Delta Y = 0 \text{ \AA}$, the 5th and 6th states interchange. One notable aspect is the merging of the ¹(TT) contributions from various excited states. This merging is achieved by adding the squares of the coefficients associated with the ¹(TT) states. Upon merging the ¹(TT) states, a continuous variation of ¹(TT) is obtained. There are two regions of interest: one at a stacking distance of approximately at $\Delta X = 2.1 \text{ \AA}$ with no displacement along the Y axis and another at a fully stacked conformation ($\Delta X = 0 \text{ \AA}$ and $\Delta Y = 0 \text{ \AA}$). Additionally, there is a region of significant ¹(TT) character between $\Delta X = -1.5 \text{ \AA}$ to -2.5 \AA , at $\Delta Y = 0 \text{ \AA}$ and another between $\Delta X = 0.0 \text{ \AA}$ to 0.7 \AA . The excitation energy of the 3rd, 4th, 5th, and 6th states is high when fully stacked. The 3rd excited state has low energy at $\Delta X = -3.25 \text{ \AA}$, $\Delta Y = -0.75 \text{ \AA}$, with an energy of 4.57 eV. It is also the lowest state that exhibits triplet character.

6th and 7th excited states are very close to each other and cross multiple times, as seen in the line plot. This gives rise to the art effect in 6th excited state’s plots especially in ¹(TT) plot. 7th state is not included because it has lots of art effects. Other higher states have too much mixing with it and giving lots of art effects. 7th state has a very low CT character.

3.3.2 Diabatic Picture

In the calculation of the ASD model Hamiltonian, for the RAS-CI/cc-pVDZ calculation, the monomer active space was chosen to be HOMO-1, HOMO, LUMO and LUMO +1 as RAS-II type of orbitals. (This space acts as full active space), 11 orbitals from HOMO-2 to HOMO-12 (including HOMO-12) were chosen to be of type RAS-I where only excitation of one particle is allowed. Likewise, 11 orbitals from LUMO+2 to LUMO+13 were chosen to be of type RAS-III where excitation of one electron is allowed. Adiabatic states of the dimer were constructed by the product of monomer states. These dimer states were decomposed into the product of monomer fragment states. [206, 211, 200, 201] The quasi-diabatic mode states formed are the ground state ($|S_0S_0\rangle$), LE states ($S^+ = |S_1S_0\rangle + |S_0S_1\rangle$ and $S^- = |S_1S_0\rangle - |S_0S_1\rangle$), CT states (CA and AC), and triplet states ¹(TT). The energies of diabatic states are shown in the appendix. In Figure 3.8, the coupling $\langle LE|H|^1(TT)\rangle$ is shown with maxima at $\Delta X = 2.8 \text{ \AA}$ with a value of 9×10^{-4} , which is low. Figure 3.9 shows the coupling between the bright singlet exciton $|S^+\rangle$ and CT states. Since both monomers are alike due to symmetry, the CT states CA and AC are alike. We show the sum of the absolute value of $|\langle S^+|H|CA\rangle| + |\langle S^+|H|AC\rangle|$. The LE (bright) coupling with CT state is high at $\Delta X = 0 \text{ \AA}$ with a value of 1.1 eV. Figure 3.9 also shows the coupling between the dark

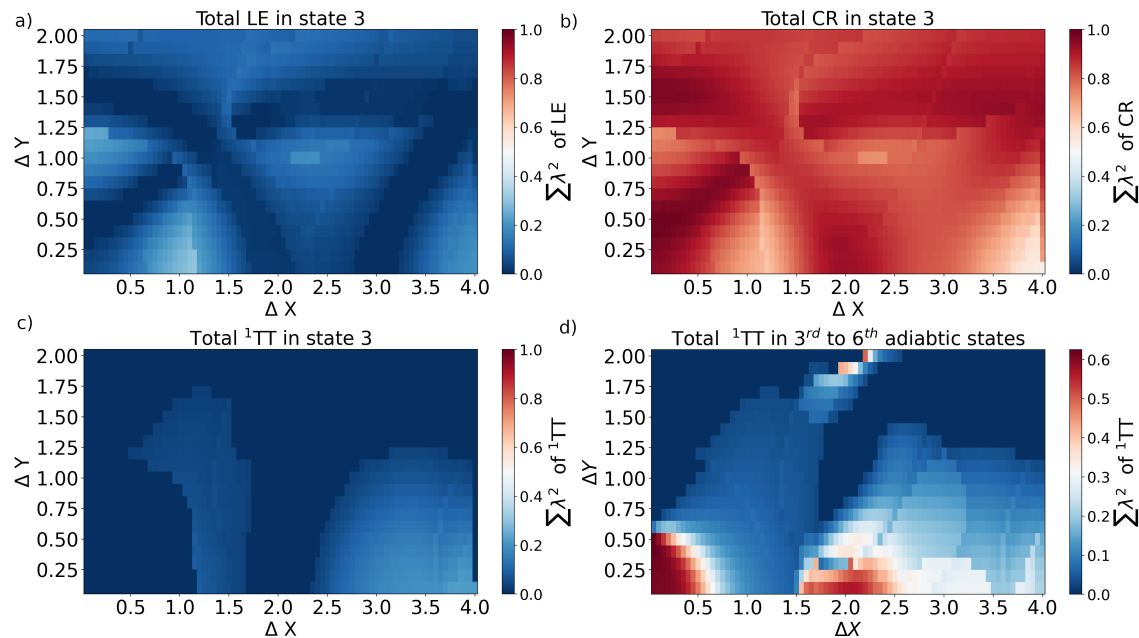


Figure 3.7: a) LE , b) CR and c) ^1TT character in 3rd excited state d) Sum of ^1TT character in 3rd to 6th excited state

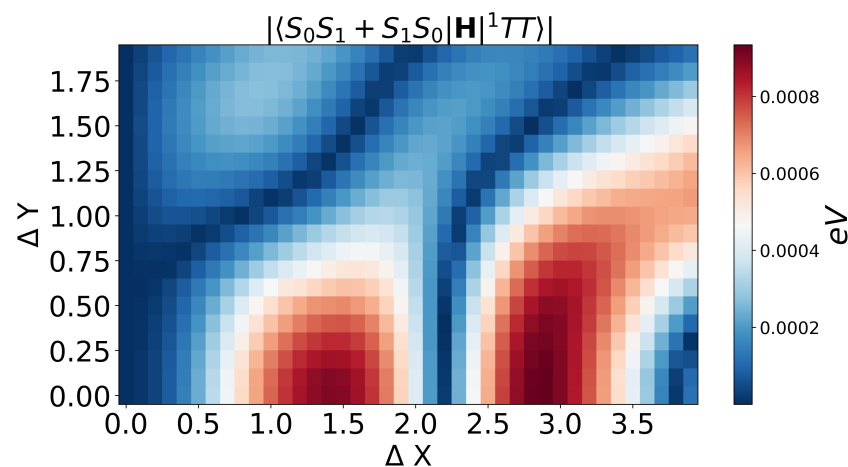


Figure 3.8: Coupling $\langle LE|H|^1(\text{TT})\rangle$

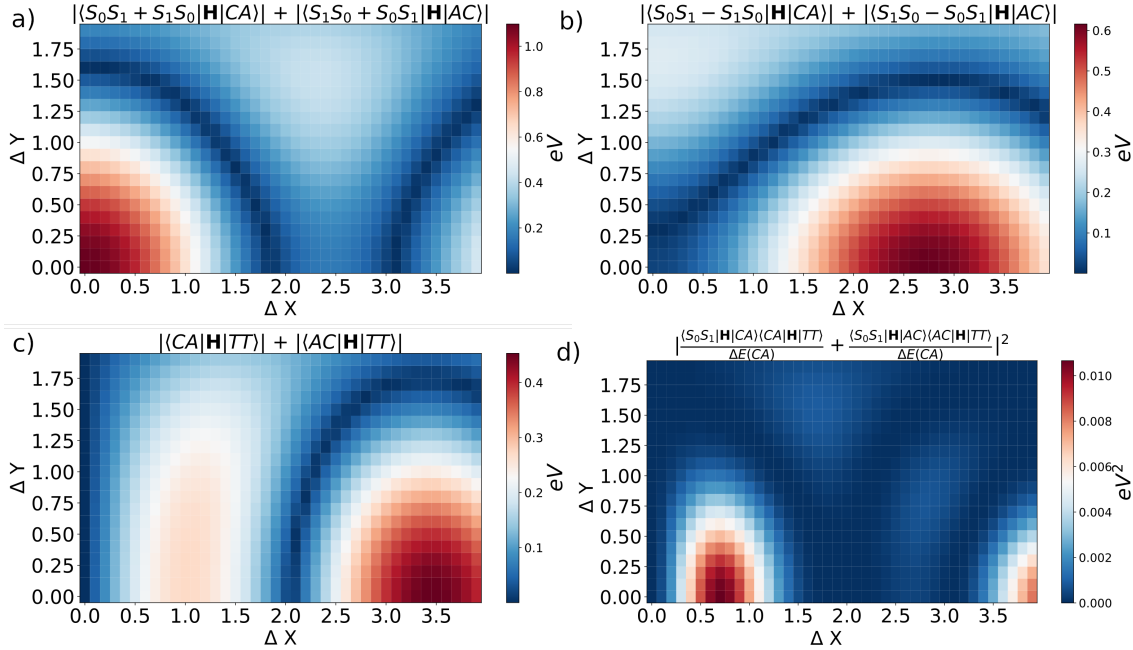


Figure 3.9: a) S^+ coupling with CT b) S^- coupling with CT, c) CT with ${}^1(TT)$ coupling d) $|T_{RP}|^2$

singlet exciton $|S^- \rangle$ and CT states. The yield of $|\langle S^- | H | CA \rangle| + |\langle S^- | H | AC \rangle|$ at $\Delta X = 2.8 \text{ \AA}$ of stacking will be high with a value of 0.6 eV. Then coupling between CT states and ${}^1(TT)$ states is shown in Figure 3.9c, in which the coupling value is highest at $\Delta X = 3.5 \text{ \AA}$. The overall $|T_{RP}|^2$ is given by the bright LE states at $\Delta X = 0.7 \text{ \AA}$ with a value of 0.08 eV², whereas dark LE gives negligible values of $|T_{RP}|^2$. The variation of $|T_{RP}|^2$ thus produced matches with the published work. This data is used to benchmark the results of $|T_{RP}|^2$ calculation from AM1 in the next chapter.

3.4 Conclusion

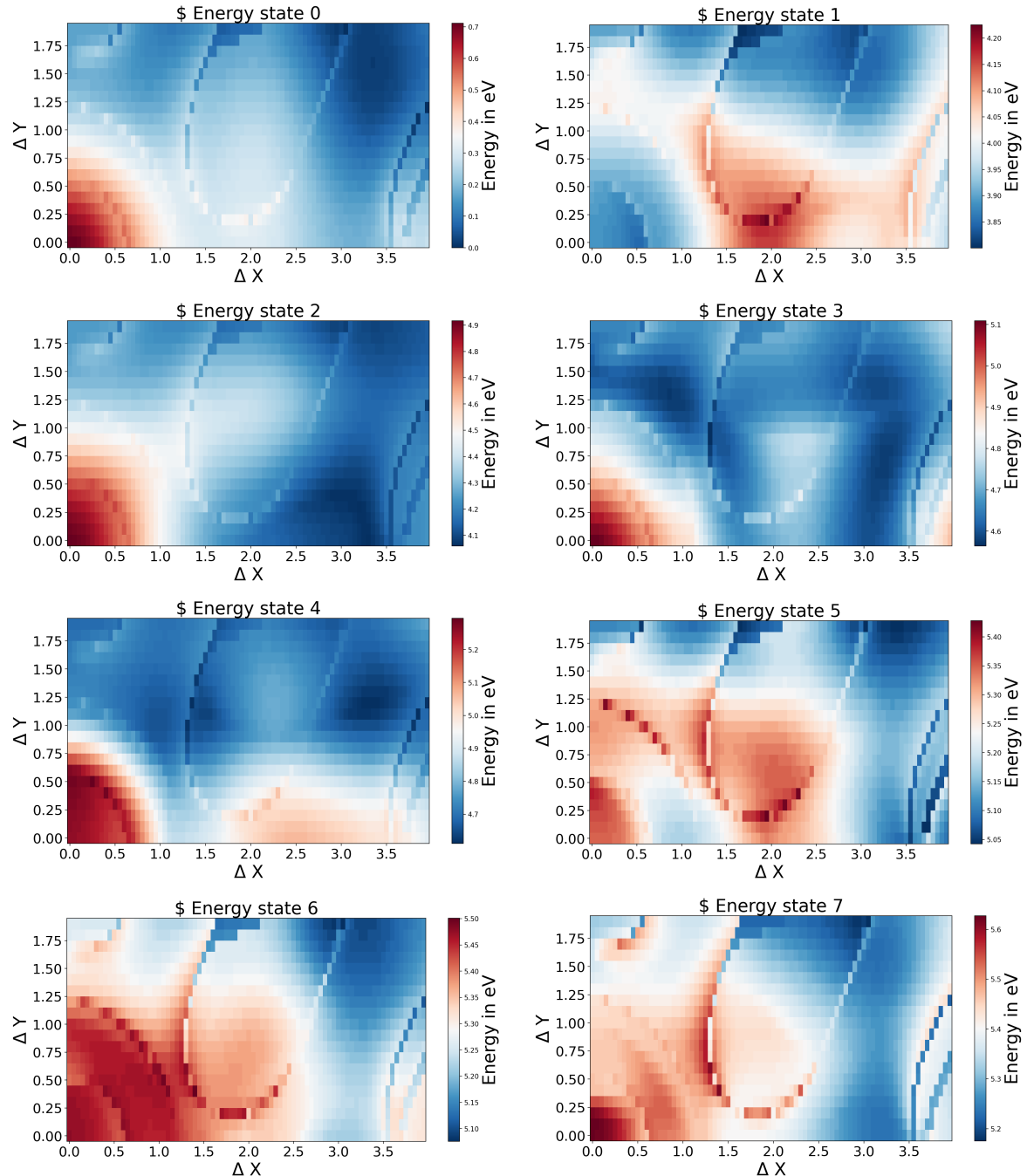
In summary, this study began by conducting scans on cofacially stacked PDI dimers at a fixed Z-coordinate of 3.4 \AA using ASD. Initially, a 1D scan along the X-axis was performed, followed by a comprehensive 2D scan along both the X and Y axes. During these scans, adiabatic energies were computed using ASD, utilizing the adiabatic states of the monomers. Increasing the number of monomer states to make the diabatic wave functions of the dimer, give continuous variation of adiabatic wave function, for decomposition in LE, CT and ${}^1(TT)$ states. Within the adiabatic states of the dimers, the study investigated the characteristics of LE, CT, and ${}^1(TT)$ states. It was observed that the first and second excited states exhibited some CT character, while the third and higher excited states displayed high CT character and significant ${}^1(TT)$ character. Notably, the plot of the first and second excited states intersected at two points, indicating a change in the roles of the wave functions contributing to these states. Notice that the energy of the adiabatic states obtained in this analysis is overestimated. The ASD method overestimates the energy, yet it is been shown in recent publications the comparable methods such as NOCI-CASSCF also overestimates the excited states of PDI. [212]

Expanding the scan into two dimensions along the Y-axis revealed additional features and insights into these states. Subsequently, these states were employed to construct a diabatic Hamiltonian. With the diabatic Hamiltonian in hand, the study delved into analyzing the couplings among LE/ ${}^1(TT)$, LE/CT, and CT/ ${}^1(TT)$ states. The bright exciton and CT coupling was found to be highest at $\Delta X = 0.0 \text{ \AA}$, while the LE/CT coupling peaked at $\Delta X = 2.8 \text{ \AA}$, and the CT/ ${}^1(TT)$ coupling reached its maximum at $\Delta X = 3.5 \text{ \AA}$. The diabatic coupling variation observed has a continuous and differentiable pattern implying reduced chances of failure of calculation of derivative. The differentiability of a function is an indispensable criterion for calculating non-adiabatic coupling and performing optimisation operations, which are discussed in upcoming chapters. Overall, this study successfully reproduced the scanning patterns and provided valuable insights into

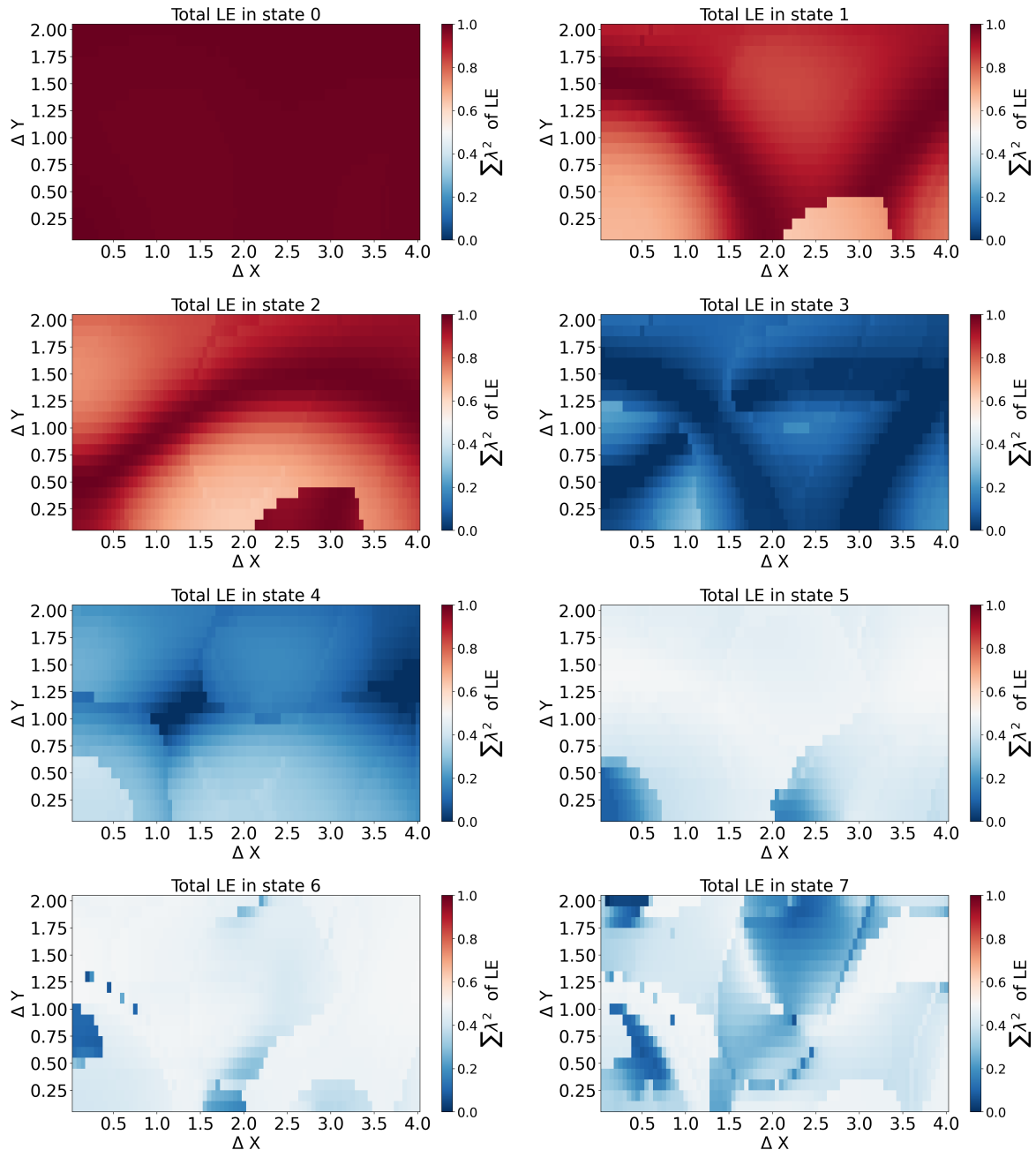
the electronic characteristics and couplings of LE, CT, and ${}^1\text{TT}$ states in cofacially stacked PDI dimers, shedding light on their roles in singlet fission processes.

3.5 Appendix

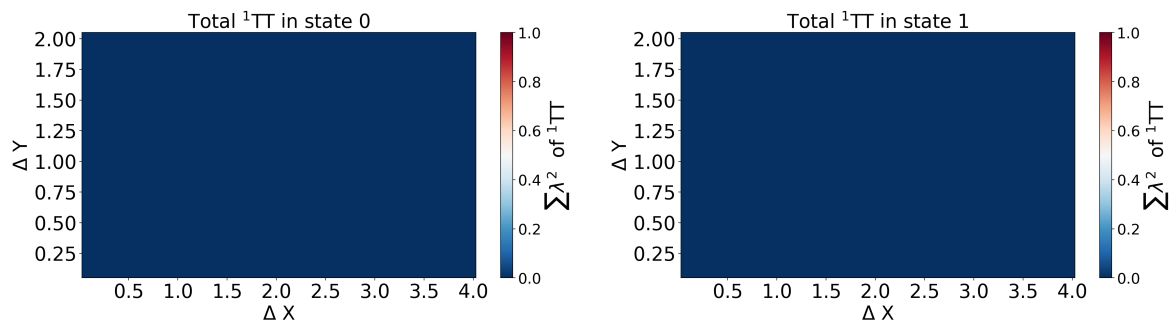
3.5.1 Adiabatic Energy Plots

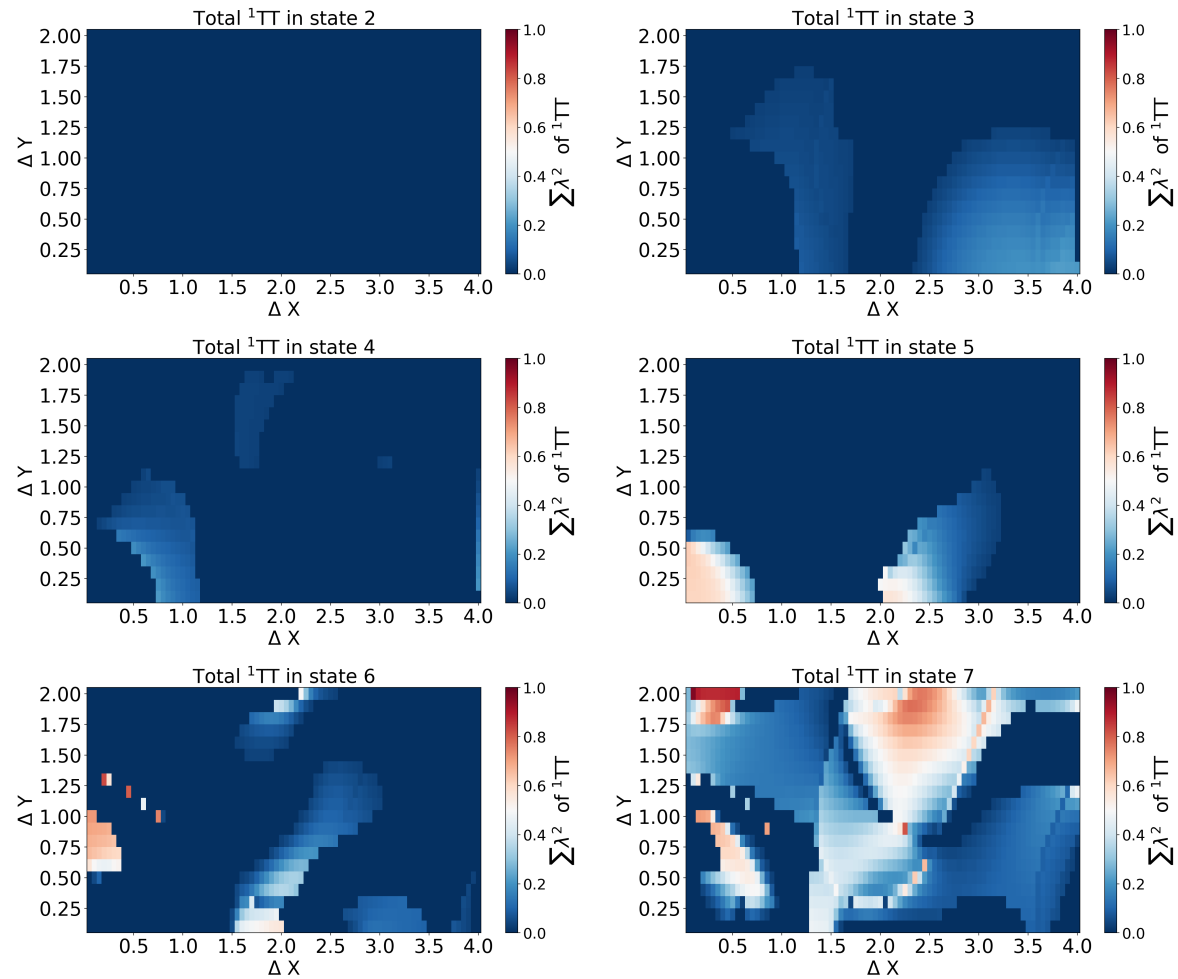


3.5.2 Total $\sum \lambda |S_0 S_1\rangle$

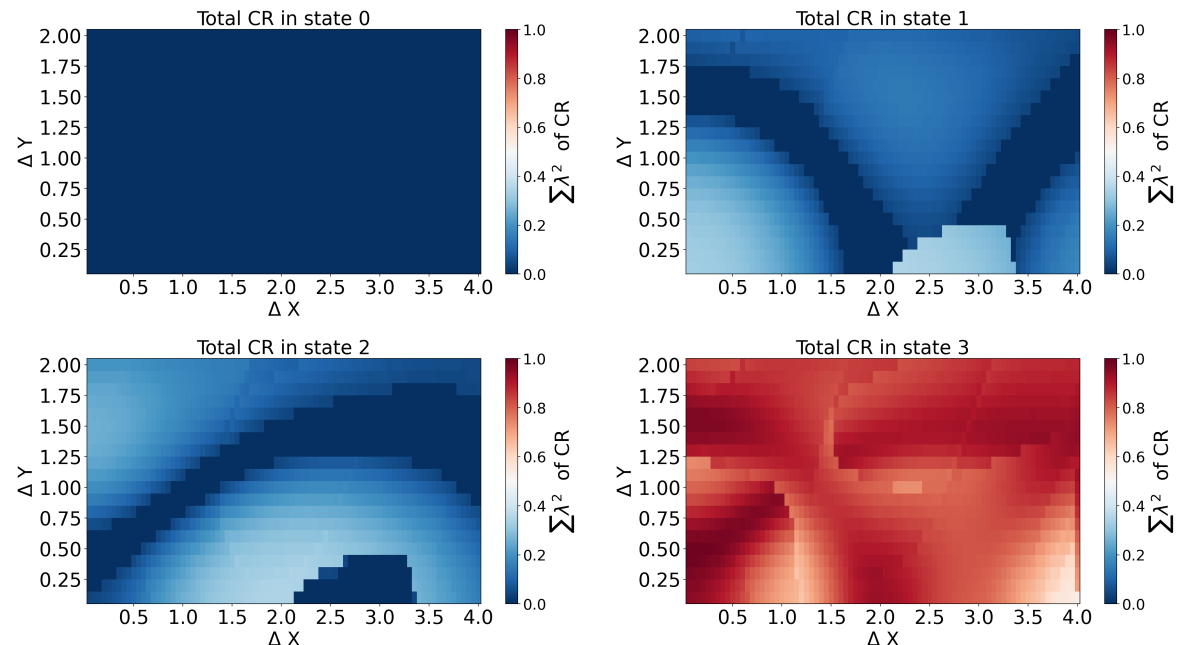


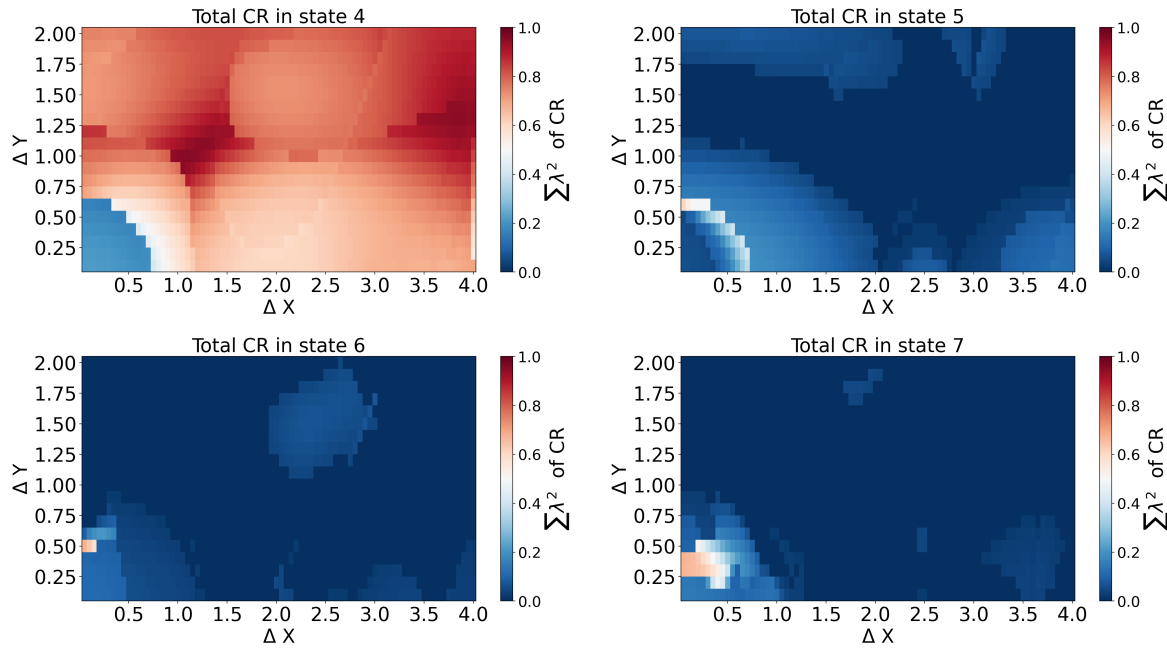
3.5.3 Total $|TT\rangle$



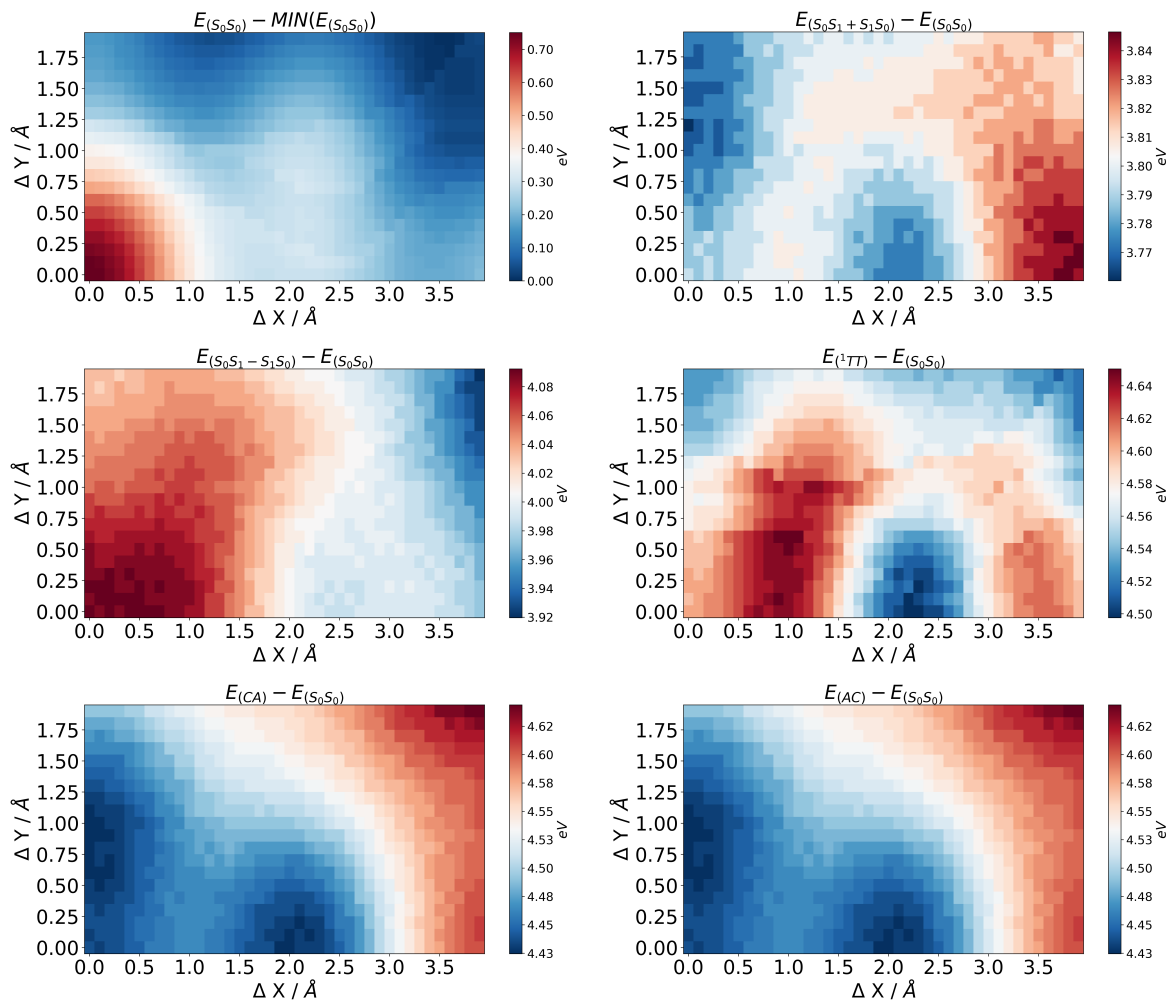


3.5.4 Total $|CA\rangle$





3.5.5 Diabatic Energy Plots



Chapter 4

Energetics and Optimal Molecular Packing for Singlet Fission in BN-doped Perylenes: Electronic Adiabatic State Basis Screening

4.1 Abstract

Singlet fission has the potential to increase the efficiency of photovoltaic devices, but the design of suitable chromophores is notoriously difficult. Both the electronic properties of the monomer and the packing motif in the crystal have a big impact on the singlet fission efficiency. Using perylene as an example, it is shown that doping with boron and nitrogen not only helps to align the energy levels but also shifts the stacking position that is optimal for singlet fission. Among all perylene derivatives doped with one or two BN groups, we identify the most suitable isomer for singlet fission with the help of TD-DFT and CASPT2 calculations. The optimal relative disposition of the two monomer units in a cofacially stacked homodimer is explored using two semi-empirical models for the singlet fission rate: The first one is the well-known diabatic frontier orbital model, while the second treats singlet fission as a non-adiabatic transition and approximates the rate as the length squared of the non-adiabatic coupling vector between eigenfunctions of the diabatic Hamiltonian.

4.2 Introduction

Singlet fission [28] is a photophysical process in the condensed phase where a singlet exciton splits into two triplet excitons of half the energy, which can diffuse independently. Organic photovoltaics has rekindled the interest in this phenomenon, since it allows in principle to increase the efficiency of organic solar cells: The number of charge carrier per absorbed solar photon is doubled (at lower voltage and losing less energy to heat) and the triplet excitons are less likely to be lost on their way to the electrodes, since transitions to the ground state are spin-forbidden. Progress has been hampered by the dearth of suitable molecules that undergo singlet fission. Many reviews have been published suggesting design guidelines for singlet fission chromophores [28, 213] [214, 215, 55, 202], mostly focussing on properties of the monomer and model dimers.

The singlet and triplet states of the monomer unit have to satisfy two energetic conditions [216]: The singlet state should be slightly higher in energy than twice the energy of the triplet ground state, so that the process $S_0 + S_1 \rightarrow T_1 + T_1$ is (slightly) exoergic:

$$\Delta E_{ST} = 2E(T_1) - E(S_1) \leq 0 \quad (4.1)$$

Furthermore, higher excited triplet states should lie above $2E(T_1)$, so that the newly formed spin-uncorrelated pair of triplets cannot annihilate to form an excited triplet. Therefore, to ensure that the process $T_1 + T_1 \rightarrow S_0 + T_2$ and intersystem crossing from S_1 to T_2 are energetically unfavourable, the second condition

$$\Delta E_{TT} = 2E(T_1) - E(T_2) < 0 \quad (4.2)$$

has to be fulfilled, although this condition is less important than the first [213]. Apart from this, a good singlet fission material should be stable both in the ground and excited state and have a high absorption coefficient at ≈ 2 eV [216].

Most dyes do not satisfy the above energetic conditions, as the T_1 state usually lies closely below the S_1 state. In the self-consistent field approximation the gap between T_1 and S_1 equals $2K = 2 \int \int h(r_1)l(r_1)e/r_{12}h(r_2)l(r_2)dr_1dr_2$, twice the exchange integral between HOMO and LUMO [216]. K is large in alternant hydrocarbons, where HOMO and LUMO have large amplitudes on the same carbons, which are therefore good starting points for designing singlet fission materials. In addition, because of the large size of their π -systems, alternant hydrocarbons such as tetracene and perylene have relatively low excitation energies lying in the desired range around 2 eV [216].

Another approach for designing energy levels suited for singlet fission, is to start with an open-shell biradical and stabilize it by captodative substitution, so that the singlet ground state is lowered. [217] This strategy for increasing the singlet-triplet gap by doping small molecules with pairs of boron and nitrogen was explored by Zeng et al. [218] and Pinheiro et al. [219]. The substituted BN-derivatives are isoelectronic to the original molecules, but admit resonance structures with unpaired electrons and satisfy $E(S_1) \approx 2E(T_1)$. Zeng et al. [220] employed these ideas to explain why a recently synthesized $(BN)_2$ -substituted pyrene is suitable for singlet fission. Their study suggests that azaborine substitution is a viable route to align the energy levels. Doping of organic molecules and polycyclic aromatic hydrocarbons (PAHs) with BN causes drastic changes of the optical and electronic properties, often without pronounced structural effects: Replacement of a C=C bond by an isoelectronic B-N unit leads to structurally similar species but strongly alters the π electron distribution. [221] BN doping in acenes stabilizes the HOMO while the optical band gap is maintained. [222]

The conditions on ΔE_{ST} and ΔE_{TT} for the monomer energies are only rough guidelines, since singlet fission involves multiple molecules, whose states interact and form delocalized exciton bands that are spread over many units. The simplest model, which neglects much of this complexity, is the homodimer.

The second factor determining the efficiency of singlet fission is the packing motif in the crystal, which is very difficult to predict.

In perylene and 1,3-diphenylisobenzofuran, which can each crystallize in more than one structure, a morphology dependence of the singlet fission yield has been observed. [223, 224]

The relative disposition of neighbouring molecules in the crystal modifies not only the energetics, but most importantly it determines the coupling between monomer states through orbital interactions, which are very sensitive to shifts in the orbital patterns. The slip-stacked motif, which occurs in crystalline perylene bisimide, has been shown to be favourable for singlet fission [204]. Once a favourable arrangement has been identified, it is still a difficult task to realize it in a crystal structure by attaching the right substituents.

Substitution with BN modulates the amplitudes of the HOMO and LUMO and can even change the pattern of the nodes. Since the singlet fission rate is very sensitive to the orbital overlap, the optimal arrangement for singlet fission will be shifted upon substitution. Doping can thus not only help to align the energy levels but also to shift the relative disposition of the molecule for which singlet fission should be most effective to a position that might be easier to realize in the crystal structure.

Singlet fission chromophores often contain aromatic rings that have a tendency for pi-stacking. Therefore, studies focusing on the impact of intermolecular stacking on the SF rate were usually limited to 2D scans of the parallel displacement in a molecular dimer at a constant inter-plane distance [225, 226]. In the case of perylene bisimide (PBI) two studies [203, 204] using a different theoretical method came to the conclusion that the singlet fission rate is highest if one of the PBI molecules is shifted by 3 Å along the long molecular axis. This packing arrangement was realized in thin films by adding certain functional groups at the imide position [227] and showed a high triplet yield of 178% close to the theoretical maximum of 200%. The rotation of perylene bisimides perpendicular to the molecular plane has also been investigated recently [228]. Buchanan [229, 162] performed an exhaustive search in the six-dimensional space of all relative translations and rotations between two chromophores to identify local maxima of the electronic matrix element relevant for singlet fission. Since even a grid with modest resolution in each dimensions leads to billions of electronic structure calculations, the level of theory was necessarily limited to the simple frontier orbital model popularized by Michl and coworkers [28]. This model is still at the heart of

more sophisticated diabatic models for singlet fission such as presented in Ref. [230].

For simplicity, the influence of the environment on the singlet fission rate is often neglected, although it may be significant for at least two reasons: (1) A polarizable environment stabilizes the charge resonances, through which the exciton and triplet biexciton states are indirectly coupled. (2) The initial exciton is delocalized over multiple units, not just a pair of chromophores, and the spatial extent of the singlet and triplet excitons may be different [231]. Aguilar Suarez et. al [232] went one step beyond the gas-phase approximation by including the surrounding chromophores as point charges in a QM/MM scheme. Others have incorporated the environment using Redfield theory, where the system-bath coupling is a weak perturbation. [202, 72, 203] However, atomistic high level quantum-mechanical calculations with more than two units are still out of reach, since the monomers of singlet fission materials are quite large.

The aim of the present work is to further explore how BN-doping affects the energy levels and optimal molecular packing. We use perylene as a simplified model for perylene bisimide. Both share the same core and have very similar frontier orbitals. It has been shown for perylene-bisimide that the crystal packing can be modified by attaching different substituents at the imide positions [227]. Starting from perylene we generate all structural isomers in which one or two pairs of neighbouring carbon atoms are substituted by the isoelectric BN group. We make the assumption that the crystal structure is not drastically changed by the BN substitutions and can be mostly controlled via the imide substituents. Questions of synthetic feasibility of the perylene derivatives are left aside. However, it is noted that BN isosteres have been synthesized for a number of polycyclic aromatic hydrocarbons [222]. A recently synthesized pyrene derivative [220] contains one of the envisioned BN substitution patterns.

In the present contribution, two semi-empiricalmodels are tested for estimating the SF rate as a function of the molecular packing. The first one is the "simple" frontier orbital model extensively used by the Michl group [28] and others. It contains diabatic states constructed for four electrons in the four monomer frontier orbitals. The rate for singlet fission is taken to be proportional to the square of the matrix element of the diabatic Hamiltonian between the exciton and the triplet biexciton states. The direct coupling between the two states is often negligible, while the indirect coupling via higher-lying charge transfer states that mix both with the singlet exciton and the paired-triplet state makes the dominant contribution. [162] Although the model provides valuable insights, it is somewhat unsatisfactory, since truly diabatic states, that is to say electronic wavefunctions which are independent of the nuclear coordinates, do not exist. The diabatic model ignores that, being a non-adiabatic transition, singlet fission cannot occur without nuclear motion. In the Born-Oppenheimer approximation absorption of a photon creates a wavepacket on the excited state potential energy surface, which is out of equilibrium and starts to move downhill. The wavepacket momentum parallel to the non-adiabatic coupling vector can induce a non-adiabatic transition from the exciton state to the biexcition state, which is a doubly excited singlet state composed of two triplet states paired into a singlet. In other words, the electronic excitation is accompanied by the excitation of phonons and it is the coupling between phonons and electrons which leads to the population of the dark biexciton state, which cannot be excited directly due to its low oscillator strength.

To account for these considerations at least in an approximate manner, singlet fission should be treated as a transition between adiabatic states mediated by the nuclear kinetic energy. When studying singlet fission in the adiabatic picture, the norm of the one-particle transition density matrix has been used widely as a substitute for the length of the coupling vector [233, 204, 27]. Here another simple semi-empiricalmodel for singlet fission in the adiabatic picture is proposed:

The diabatic Hamiltonian of the frontier orbital model is diagonalized to yield adiabatic wavefunctions. The non-adiabatic coupling vector between states of predominantly excitonic and biexcitonic character is then calculated as the gradient of the wavefunction coefficients with respect to all nuclear coordinates. The length of the non-adiabatic coupling vector, which varies strongly with relative disposition of the two monomers, is taken as a measure of the singlet fission rate.

2D scans of cofacially stacked perylene derivatives are performed using both models to identify the optimal packing for singlet fission. Even when only considering rigid shifts in a plane, the maxima of the SF matrix elements can be shifted by several Å relative to undoped perylene depending on the atoms are substituted.

Brief outline of the article: First the semi-empiricaldiabatic and non-adiabatic models for singlet fission are sketched in section 4.3. Then the semi-empiricalversions of the diabatic model is benchmarked against a diabatic model constructed from high-level CASSCF wavefunctions, to as-

sess the influence of semi-empirical integral approximations on the positions of the maxima (section 4.4.1). The effect of doping with BN on the singlet-triplet gap in perylene derivatives is investigated in section 4.4.3 and rationalized in terms of resonance structures. In sections 4.4.4 and 4.4.5 the optimal packing arrangements resulting from 2D scans are compared for the two models. Finally, in section 4.4.6 the selection is narrowed down to a single isomer having suitable properties for singlet fission.

4.3 Methods

4.3.1 The Simple Model for Singlet Fission

In this section the simple model for singlet fission by Smith and Michl [28] is briefly recapitulated. It presupposes that the bright S_1 is dominated by a HOMO \rightarrow LUMO transition, so that only two frontier orbitals have to be included. This limits its applicability to chromophores of class I in the nomenclature of Ref. [28].

The system consists of two chromophores A and B . Only the highest occupied and lowest unoccupied orbitals on each monomer are considered, so that one has to deal with 4 electrons in the 4 orbitals h_A, l_A, h_B, l_B . The orbitals are assumed to be real, normalized and orthogonal to each other. Each monomer $I = A, B$ has 3 electronic states, the ground state S_0^I , the singlet excited state S_1^I and a triplet state, T_1^I . By removing or adding an electron to a monomer, the radical cation C^I or anion A^I is formed.

The seven lowest electronic singlet states of the combined system that can be constructed by distributing the electrons over the four orbitals as shown in Fig. 4.1. They can be classified as the ground state ${}^1(S_0^A S_0^B)$, two singly excited states ${}^1(S_1^A S_0^B)$ and ${}^1(S_0^A S_1^B)$, two charge transfer states ${}^1(C^A A^B)$ and ${}^1(A^A C^B)$ and two doubly excited states ${}^1(T_1^A T_1^B)$ and ${}^1(S_1^A S_1^B)$. The last state is excluded from further consideration because the energy of two localized singlet excitations are much higher than that of two localized triplet ground states paired into a singlet.

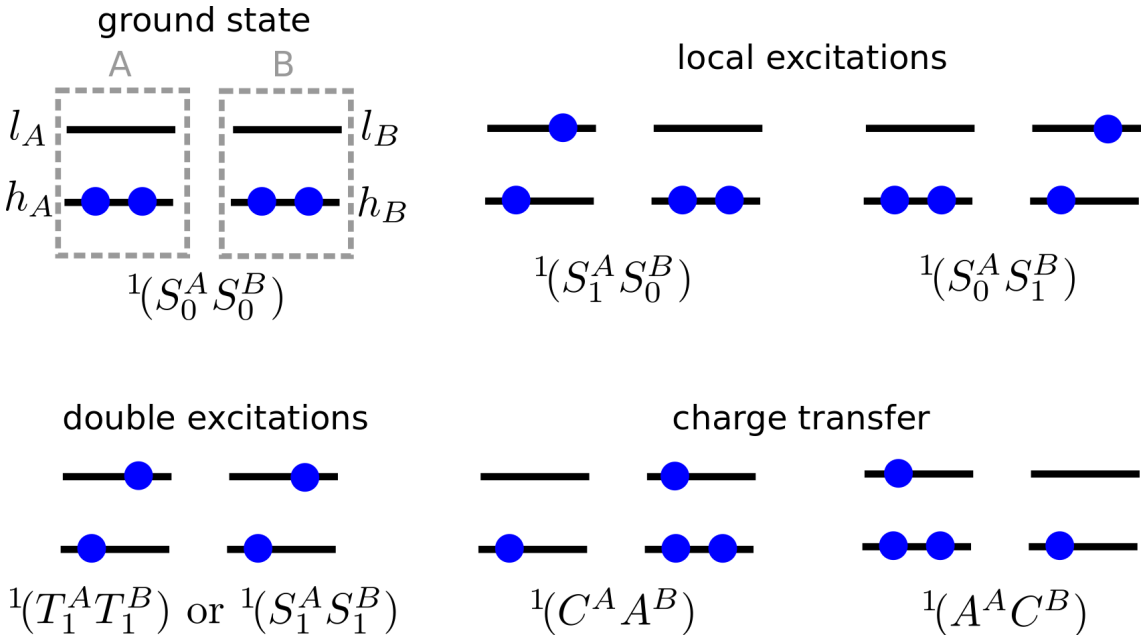


Figure 4.1: Diabatic states in the simple model of singlet fission.

The rate of singlet fission is approximated by Fermi's Golden rule. For simplicity and because the excitation might localize to one of the monomers, the initial reactant state is taken as ${}^1(S_0 S_1)$. The final product state which consists predominantly of ${}^1(TT)$ but also mixes with the charge transfer states, is denoted by \tilde{TT} . According to first-order perturbation theory

$$\left| \tilde{TT} \right\rangle = |TT\rangle + \frac{\langle CA| \mathbf{H} |TT\rangle}{\Delta E(CA)} |CA\rangle + \frac{\langle AC| \mathbf{H} |TT\rangle}{\Delta E(AC)} |AC\rangle. \quad (4.3)$$

The rate for singlet fission is

$$W(\text{SF}) = \frac{2\pi}{\hbar} |T_{RP}|^2 \rho(E) \quad (4.4)$$

with the matrix element $|T_{RP}|^2 = |\langle S_0S_1 | H | \tilde{TT} \rangle|^2$ (R stands for reactant state and P for product state). The density of states $\rho(E)$, which depends on the vibrational structure, is ignored in this expression.

The matrix element for the direct path, $\langle S_0S_1 | H | TT \rangle$ is small and can be neglected. The electronic matrix element for the charge-resonance mediated path is:

$$|T_{RP}|^2 = \left| \frac{\langle S_0S_1 | \mathbf{H} | CA \rangle \langle CA | \mathbf{H} | TT \rangle}{\Delta E(CA)} + \frac{\langle S_0S_1 | \mathbf{H} | AC \rangle \langle AC | \mathbf{H} | TT \rangle}{\Delta E(AC)} \right|^2 \quad (4.5)$$

with $\Delta E(AC) = E(AC) - E(S_0S_1)$.

Approximations for $|T_{RP}|^2$ of increasing complexity were presented by Buchanan et al. [162]. In the simple frontier orbital model combined with the zero differential overlap approximation, eqn. 4.5 reduces to

$$|T_{RP}|^2 = \left| \frac{(l_A | \mathbf{F} | l_B)(l_A | \mathbf{F} | h_B)}{\Delta E(CA)} - \frac{(h_A | \mathbf{F} | h_B)(h_A | \mathbf{F} | l_B)}{\Delta E(AC)} \right|^2 \quad (4.6)$$

where \mathbf{F} is the Fock matrix.

It should be noted that eqn. 4.5 is much more general than the simple model, since the diabatic many-electron states that enter the expression can be constructed using high-level first principles electronic structure methods such as the active subspace decomposition (ASD) method [234]. ASD produces diabatic model Hamiltonians in the basis of CASSCF monomer states with well-defined spin and charge.

Expression 5.1 on the other hand is suitable for rapidly screening many chromophores and scanning their relative orientation. In this study we employ the semi-empirical AM1 method implemented in the code PYSEQM [152] to compute the Fock matrix elements between monomer orbitals. The semi-empirical code is fast and allows us to scan large numbers of molecules. In this sense it is similar to Zaykov's "Simple" code [235]; although slower, it is in principle not restricted to rigid translations and rotations of the monomer.

Taking perylene bisimide (PBI) as an example, we will show that the frontier orbital model (eqn. 5.1) does an excellent job in predicting the positions of the maxima of the electronic coupling $|T_{RP}|^2$, although the absolute magnitudes are underestimated as compared to ASD.

4.3.2 Singlet Fission as a Non-Adiabatic Transition

Singlet fission is a special case of internal conversion between exciton states, which are dominated by single excitations, and paired triplet states, which are dominated by double excitations. The adiabatic states are obtained by diagonalizing the Hamiltonian given in eqn. 6.28 below.

For a parallel-stacked homo-dimer there are two exciton states built from the in-phase and out-of-phase combinations of $|S_0^A S_1^B\rangle$ and $|S_1^A S_0^B\rangle$:

$$|S^{\text{bright}}\rangle = \frac{1}{\sqrt{2}} (|S_0S_1\rangle + |S_1S_0\rangle) \quad (4.7)$$

$$|S^{\text{dark}}\rangle = \frac{1}{\sqrt{2}} (|S_0S_1\rangle - |S_1S_0\rangle) \quad (4.8)$$

A general adiabatic state $|X\rangle$ is a linear combination of all diabatic states:

$$|X\rangle = C_{S_0S_1} |S_0S_1\rangle + C_{S_1S_0} |S_1S_0\rangle + C_{CA} |CA\rangle + C_{AC} |AC\rangle + C_{TT} |TT\rangle \quad (4.9)$$

The coefficients C are the eigenvectors of the diabatic Hamiltonian for the frontier orbital model. Making the zero-differential overlap approximation and neglecting two-electron integrals

between charge distributions on different monomers, $(h_A l_A | h_B l_B) \approx 0$, the Hamiltonian reads

$$\mathbf{H} = \begin{pmatrix} {}^1(S_0^A S_1^B) & {}^1(S_1^A S_0^B) & {}^1(A^A C^B) & {}^1(C^A A^B) & {}^1(T^A T^B) \\ {}^1(S_0^A S_1^B) & \epsilon_S(A) & 0 & (l_A |\mathbf{F}| l_B) & -(h_A |\mathbf{F}| h_B) & 0 \\ {}^1(S_1^A S_0^B) & \epsilon_S(B) & - (h_A |\mathbf{F}| h_B) & (l_A |\mathbf{F}| l_B) & 0 & 0 \\ {}^1(A^A C^B) & & \epsilon_{AC} & 0 & \sqrt{\frac{3}{2}} (h_A |\mathbf{F}| l_B) & \\ {}^1(C^A A^B) & & & \epsilon_{CA} & \sqrt{\frac{3}{2}} (h_B |\mathbf{F}| l_A) & \\ {}^1(T^A T^B) & & & & \epsilon_T(A) + \epsilon_T(B) & \end{pmatrix} \quad (4.10)$$

The diagonal elements are held constant. It is assumed that the ${}^1(TT)$ state is resonant with the exciton states, $\epsilon_S(A) = \epsilon_S(B) = \epsilon_T(A) + \epsilon_T(B) = 0$, while the charge transfer states are higher in energy by $\epsilon_{CA} = \epsilon_{AC} = 1$ eV. (Estimating the energies of the charge transfer states accurately is complicated, because they depend strongly on the dielectric environment.) The off-diagonal elements of the diabatic Hamiltonian are computed from semi-empirical orbitals at the AM1 level of theory with PYSEQM [152].

Let us denote by $|S^*\rangle$ and $|TT^*\rangle$ the adiabatic states which are most similar to one of the exciton states in eqns. 4.7 or 4.8 and the biexciton state $|T_1 T_1\rangle$ respectively. The singlet-fission rate should then be roughly proportional to the length squared of the first order derivative coupling vector:

$$\vec{\tau} = \langle S^* | \nabla | TT^* \rangle = \sum_{i=S_0 S_1, S_1 S_0, \dots, TT} C_i^{\text{exciton}} \nabla C_i^{\text{triplet}} \quad (4.11)$$

We have assumed that the gradients of the quasi-diabatic states can be neglected so that we only have to consider the gradient of the coefficients. The scalar product 4.11 can be calculated efficiently using automatic differentiation and PYSEQM [152]. The derivatives on the density matrix matrix are neglected, since back propagation of derivatives through the self-consistent field cycles increases the computational cost enormously. The validity of this approximation is tested in the supporting information.

Since one does not know for certain if singlet fission happens from the dark or the bright exciton state, we take the average:

$$|T_{RP}|_{\text{NAC}}^2 = \frac{1}{2} \left(| \langle S^{\text{bright}*} | \nabla | TT^* \rangle |^2 + | \langle S^{\text{dark}*} | \nabla | TT^* \rangle |^2 \right) \quad (4.12)$$

This approach automatically includes the direct and mediated pathways. The second one becomes more important if the initial and final adiabatic states have partial charge transfer character. It can also be extended to more than two molecules. In that case one has to diagonalize a larger Hamiltonian matrix and sum over all internal conversion channels, where the initial state has exciton character and the final state has triplet biexciton character.

The python code for reproducing calculations with the two semi-empirical models is available online [199].

4.4 Results and Discussion

4.4.1 Comparison With *Ab – Initio* Model Hamiltonian

The first question we wish to address is how accurate the frontier orbital model is as compared to diabatic model Hamiltonians constructed from first principles. The characters of the diabatic states included in the model remain the same, however the monomer states are obtained *ab – initio* and no approximation is made in the evaluation of the matrix elements between diabatic states.

Perylene bisimide (PBI) serves as a test case, since this molecule has been the objective of numerous studies on singlet fission [204, 228]. To construct a model Hamiltonian for singlet fission, we follow the approach pioneered by Parker et al. [230] using the methods implemented in BAGEL [135].

The monomer basis consists of states with different total spin S and charge Q , which can be combined to form dimer states that are overall neutral and singlets: These states are the neutral singlets S ($S = 0, Q = 0$), triplets T ($S = 1, Q = 0$) and singly charged cations C ($S = 1/2, Q = +1$) and anions A ($S = 1/2, Q = -1$). In each manifold with fixed spin and charge

the lowest 10 monomer states are calculated using the restricted active space (RAS) configuration interaction method [206] together with the cc-pVDZ [211] basis set. The restricted active space is RAS(11,4,11)[1,1] using the notation RAS(a,b,c)[i,j] where a,b,c are the numbers of orbitals in the subsets RAS **I**, **II** and **III** and i and j are the maximum number of allowed holes and particles [230] in **I** and **III**, respectively. Subspace **II** consists of the frontier orbitals h_A , h_B , l_A and l_B .

The dimer Hamiltonian is formally constructed using the direct product of monomer states as a basis. Matrix elements between dimer states can be evaluated efficiently without having to construct wave functions of the dimer explicitly using the active subspace decomposition (ASD) method [230]. A model Hamiltonian is extracted from the dimer Hamiltonian by diagonalizing sub-blocks with the desired diabatic character; the lowest three states are taken from the *SS* sub-block, in addition the lowest state each from the *TT*, *AC* and *CA* blocks are included. The model Hamiltonian thus obtained has the terms $\langle SS|H|TT\rangle$, $\langle SS|H|CA\rangle$, $\langle SS|H|AC\rangle$, $\langle TT|H|CA\rangle$ and $\langle TT|H|AC\rangle$ required by Michl's Simple Model. The *SS* manifold contains three states: the ground state S_0S_0 , which does not participate in singlet fission, and the two exciton states $S^{\text{bright/dark}*} \approx \frac{1}{\sqrt{2}}(S_0S_1 \pm S_1S_0)$. In the parallel stacked dimer (H-type coupling) the lower exciton state ("−" combination) is dark in absorption and the higher ("+" combination) is bright. It is assumed that singlet fission happens from the lower exciton state. $|T_{RP}|^2$ is calculated according to eqn. 4.5 with $SS = S^{\text{dark}*}$. (We also computed $|T_{RP}|^2$ for the bright exciton state, but the coupling matrix element is negligible, $\approx 10^{-10}$ eV²).

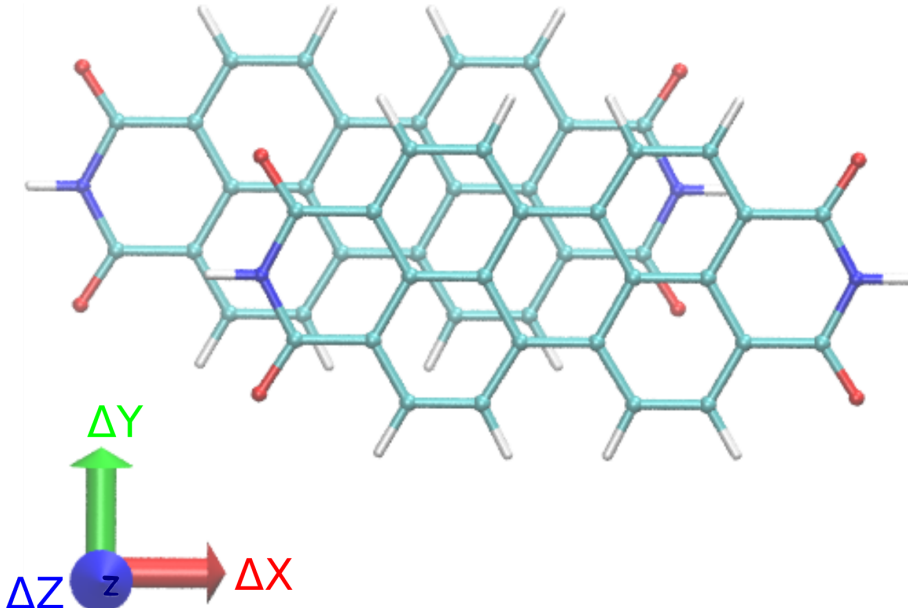


Figure 4.2: PBI dimer. $(\Delta X, \Delta Y)$ is the parallel displacement of the center of mass of one monomer with respect to the other in the cofacially stacked homodimer (vertical distance $\Delta Z = 3.5$ Å).

With the procedure just outlined we performed scans of $|T_{RP}|^2$ as a function of the parallel displacement of two perylene bisimide molecules. The geometry with the displacement vectors is shown in Fig. 4.2. The scan covers the region from $\Delta X = 0$ to 4 Å and from $\Delta Y = 0$ to 2 Å with a step size of 0.1 Å at an interplanar distance of $\Delta Z = 3.5$ Å. Figure 4.3 a) shows the plot of $|T_{RP}|^2$ as calculated with ASD. $|\langle S_0S_1|H|TT\rangle|$ is reported in Figure 1 of the supplementary information. Since it is on the order of 10^{-4} eV, it can be neglected. This is in accordance with previous work [203] [1], in which the electronic couplings were estimated from the one-electron and Coulomb interactions between the HOMO and the LUMO. Note, however, that the ASD couplings are computed from correlated many-electron wavefunctions.

Similar scans were performed with the semi-empirical approximations based on AM1 frontier orbitals. First we show in Fig. 4.3 b) the scan of $|T_{RP}|^2$ according to approximation 5.1, which is based on the matrix elements of the Fock matrix between HOMO and LUMO. The resemblance with the *ab initio* plot in Fig. 4.3 a) is perfect, yet the magnitude of $|T_{RP}|^2$ is much smaller. In the π -stacked dimer, only the tails of the monomer orbitals interact. The minimal basis set used in AM1 is not diffuse enough to account for this interaction quantitatively, but the pattern

is reproduced correctly. In Figure 2 and Figure 3 of the supplementary information $|\langle l_A | \mathbf{F} | l_B \rangle|$ (from AM1 orbitals) and $|\langle S_0 S_1 | \mathbf{H} | CA \rangle|$ (from ASD many-electron wavefunctions) are compared. $|\langle S_0 S_1 | \mathbf{H} | CA \rangle|$ is larger than $|\langle l_A | \mathbf{F} | l_B \rangle|$ by a factor of 10, but the positions of the maxima agree very well.

Next we show the scan of the non-adiabatic coupling $|T_{RP}|_{NAC}^2$ according to eqn. 4.12 in Fig. 4.3 c). The positions of the maxima of the non-adiabatic couplings agree roughly with those of the diabatic couplings. In both cases there are two maxima at a slipped-stacked position, one around $\Delta X = 0.8 \text{ \AA}$ and a second less pronounced one at $\Delta X = 4.0 \text{ \AA}$. The plot shares characteristic features with the coupling $||\gamma||^2$ shown in the supplementary information of Ref. [204] ($||\gamma||$ is the norm of the transition density matrix between the states which in our notation would be called $S_0 S_1$ and TT).

These comparisons demonstrate that the semi-empirical approximations, while underestimating the coupling between the exciton states and the paired-triplet state, can correctly predict the positions where the coupling is maximized. This is sufficient for the purpose of identifying those relative dispositions of doped perylene dimers, which are optimal for singlet fission. The low computational cost of the semi-empirical approach gives the opportunity to rapidly explore a large number of molecules and identify the best packing arrangements.

4.4.2 BN-Doped Perylene Derivatives

Perylene is highly fluorescing and its electron accepting properties make it suitable for photovoltaic applications. [236][237] The experimentally observed lowest excited state S_1 has an energy of 2.86 eV and the triplet state lies at 1.51 eV. [238][239] However, singlet fission occurs from the upper excited states in perylene. [240][241] Theoretically the most accurate energies have been reported using the density matrix renormalization group method. [242]

Doping with BN. Starting from the perylene scaffold we enumerated all substitutions where two adjacent carbon atoms are replaced by B-N. The resulting molecules are labelled as perylene-(BN) $_n$ - i with the integer n indicating the number of BN substitutions and $i = 0, 1, 2, \dots$ enumerating the structural isomers. To eliminate duplicate molecules, which are related to each other by symmetry, the geometries were converted to canonical smiles strings. This resulted in 13 unique (BN) $_1$ -substituted and 256 unique (BN) $_2$ -substituted molecules. The geometries and names of all isomers are listed in the supporting information.

All molecules were optimized with the semi-empirical PM6 method using MOPAC [243] and most remained planar with all eigenvalues of the Hessian matrix positive (with the exception of six isomers which developed a twist at the bay region). For these optimized monomer geometries vertical singlet and triplet excitation energies were calculated at the CASPT2 and TD-DFT level of theory to identify good candidates for singlet fission.

4.4.3 Singlet and Triplet Energies of Monomers

Since the quantities ΔE_{ST} and ΔE_{TT} are differences of excitation energies (which themselves are differences of energies), special care was taken to minimize the errors which might result from subtracting energies calculated at different levels of theory. Four types of calculations were performed with the software package BAGEL [135]: (1) CASPT2 [130] for the singlet ground state S_0 , (2) CASPT2 for the triplet ground state T_1 , (3) XMS-CASPT2 [133] for the lowest two singlet states S_0 and S_1 and (4) XMS-CASPT2 for the lowest two triplet states T_1 and T_2 . In (1)-(3) the active space consists of 2 electrons in the HOMO and LUMO, but calculation (4) was done with 4 electrons in the 4 frontier orbitals HOMO-1 to LUMO+1. In all calculations the basis set cc-pVDZ [211] was used. The excitation energies of the states S_1 , T_1 and T_2 relative to the singlet ground state were calculated as follows:

$$\begin{aligned} E(S_1) &= E(\text{XMS-CASPT2}, S_1) - E(\text{XMS-CASPT2}, S_0) \\ E(T_1) &= E(\text{CASPT2}, T_1) - E(\text{CASPT2}, S_0) \\ E(T_2) &= E(T_1) + E(\text{XMS-CASPT2}, T_2) - E(\text{XMS-CASPT2}, T_1) \end{aligned}$$

This ensures that energy differences are taken between (XMS)-CASPT2 calculations with the same number of states and same active spaces.

Fine tuning the biradical character [244] [245] can enhance the singlet fission rate.[246, 247, 248, 249] It is a prime property to be looked at while designing singlet fission molecules. The

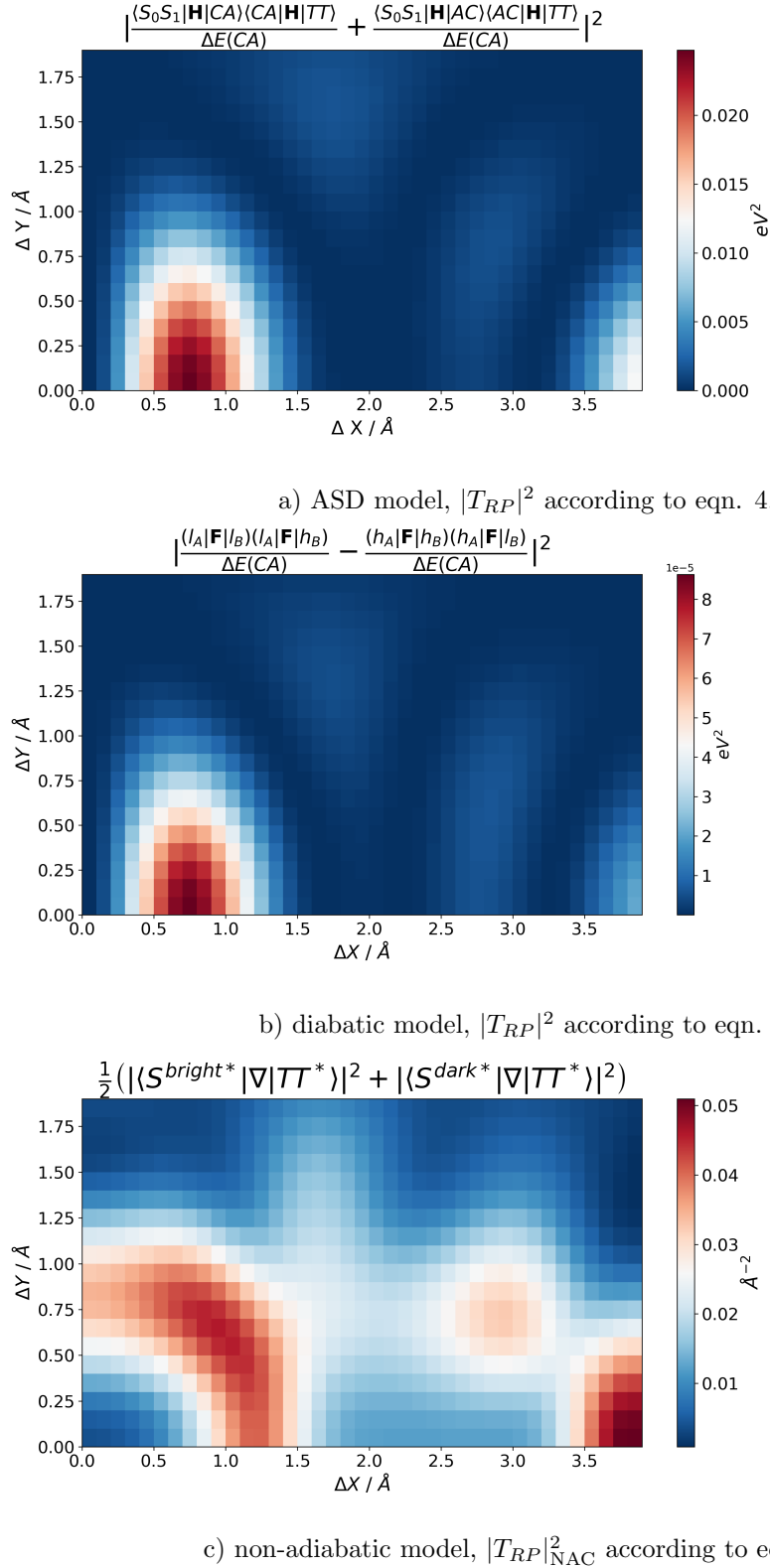


Figure 4.3: 2D scan of $|T_{RP}|^2$ for the perylene-bisimide dimer. **a)** Diabatic model with *ab initio* matrix elements; **b)** and **c)** semi-empirical models based on AM1 frontier orbitals. **a)** and **b)** show the perturbative contribution to $|T_{RP}|^2$ from charge-resonance mediated pathway. In **c)** $|T_{RP}|^2$ is approximated as the length squared of the non-adiabatic coupling vector between the adiabatic states with exciton and triplet biexciton character.

biradical character was estimated from the natural orbital occupation numbers of the highest occupied (HONO) and lowest unoccupied (LUNO) natural orbitals for the ground state CASPT2 wavefunctions

$$y_0 = 1 - \frac{1}{2} (n_{\text{HONO}} - n_{\text{LUNO}}) \quad (4.13)$$

Closed-shell molecules ($y \approx 0$) are preferable to biradicaloids ($y \approx 1$), since they are expected to be less reactive.

The lowest singlet and triplet TD-DFT excitation energies were also calculated with the PBE [250] functional and the cc-pVDZ [211] basis set using Gaussian 16 [251]. T_1 and T_2 were obtained as triplet excited states from the closed-shell reference state S_0 .

Table S1 in the supporting information lists the excitation energies for all BN-doped derivatives of perylene.

Resonance structures. Perylene is an alternant hydrocarbon, which means that the carbon atoms can be divided into two sublattices such that double bonds exist only between atoms from different lattices. When replacing neighbouring carbons with boron and nitrogen, the Lewis structure of perylene can be maintained but formal charges of -1 on boron and $+1$ on nitrogen have to be introduced. If only secondary carbons are substituted, a resonance structure without formal charges can be drawn, in which nitrogen has a lone electron pair and boron has only six electrons in its valence shell [219]. This suggests that placing nitrogen next to boron (and creating 6-membered rings that resemble azaborine) will produce relatively stable structures, which is reflected in the moderate biradical character y_0 of all derivatives. $(\text{BN})_n$ substituted derivatives can be grouped based on their resonance structures: Derivatives that admit a neutral Lewis structure form one group (called $B\bar{N}$), while those that only admit resonance structures with formal charges or unpaired electrons form the other group (called B^-N^+). The first group should have a lower biradical character than the second. Nitrogen is more electronegative than boron, so that the formal charges on B^- and N^+ in the second group indicate an unstable isomer [220]. The Lewis structures are assigned automatically using the linear programming approach from [252] and checked manually. Fig. 4.5 shows the Lewis structures of representatives of each group.

There is a clear connection between the type of the most important resonance structure and the T_1 and S_1 excitation energies as evidenced in Fig. 4.6 a) (TD-DFT) and Fig. 4.6 b) (CASPT2). Among the perylene derivatives with a single BN unit only perylene-(BN)₁-7 does not have any Lewis structure without formal charges on B and N (cf. Fig. 4.5). It is also the molecule with by far the lowest TD-DFT excitation energy in the group, 1.67 eV for S_1 and 0.72 eV for T_1 . All other perylene derivatives in (BN)₁ have excitation energies above 2.3 eV for S_1 and above 1.2 eV for T_1 . Adding a second BN unit lowers the excitation energies considerably, provided the resonance structures fall into the group B^-N^+ . $E(T_1)$ depends approximately linearly on $E(S_1)$, however the slope is steeper than $1/2$. Therefore there is an intersection with the ideal line $2E(T_1) = E(S_1)$ at a $E(S_1) \approx 1.8$ eV. Molecules from the group B^-N^+ , whose excitation energies are not too low, are better candidates, because for them singlet fission is isoergic or slightly exoergic. This is in line with the finding of Ref. [220] that chromophores with $\Delta E_{ST} \leq 0$ can be identified by looking at their resonance structures. There is also a connection with the biradical character y_0 . Molecules from group B^-N^+ have ground states with larger biradical character as compared to molecules from the group $B\bar{N}$. In fact all isomers with $y_0 > 0.1$ belong to the group B^-N^+ .

4.4.4 2D Scans of $|T_{RP}|^2$

Symmetry Considerations. Perylene has D_{2h} symmetry. When stacked in a perfectly parallel arrangement ($\Delta X = \Delta Y = 0$), the matrix elements between the HOMO (a_u) on one monomer and the LUMO (b_{3g}) on the other one vanish because of symmetry ($a_u \times b_{3g} = b_{3u} \neq a_g$), $(l_A|\mathbf{F}|h_B) \propto (l_A|h_B) = 0$ and $(h_A|\mathbf{F}|l_B) \propto (h_A|l_B) = 0$. According to eqn. 5.1, the matrix element for singlet fission is zero at this geometry. By substitution with BN the molecular symmetry is lowered. Only two isomers retain D_{2h} symmetry. In all other cases the symmetry is reduced to C_{2v} (for example BN1-100 and BN2-112), C_{2h} , C_s (most molecules) or C_1 for those derivatives that are twisted. Non-planar molecules are excluded, since atoms from twisted monomers would collide during the scan.

Maxima of $|T_{RP}|^2$. For all isomers the parallel displacement ($\Delta X, \Delta Y$) in the cofacially stacked homodimer was scanned on the grid described in section 4.4.1 above. The local maxima of $|T_{RP}|^2$ in the two-dimensional scans, which are the optimal packing arrangements, were identified with the help of a maximum filter of size 20×20 pixels. The highest two local maxima of all

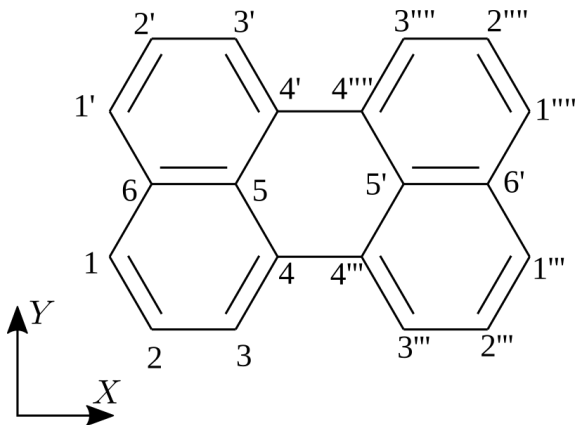


Figure 4.4: Numbering of atoms in perylene.

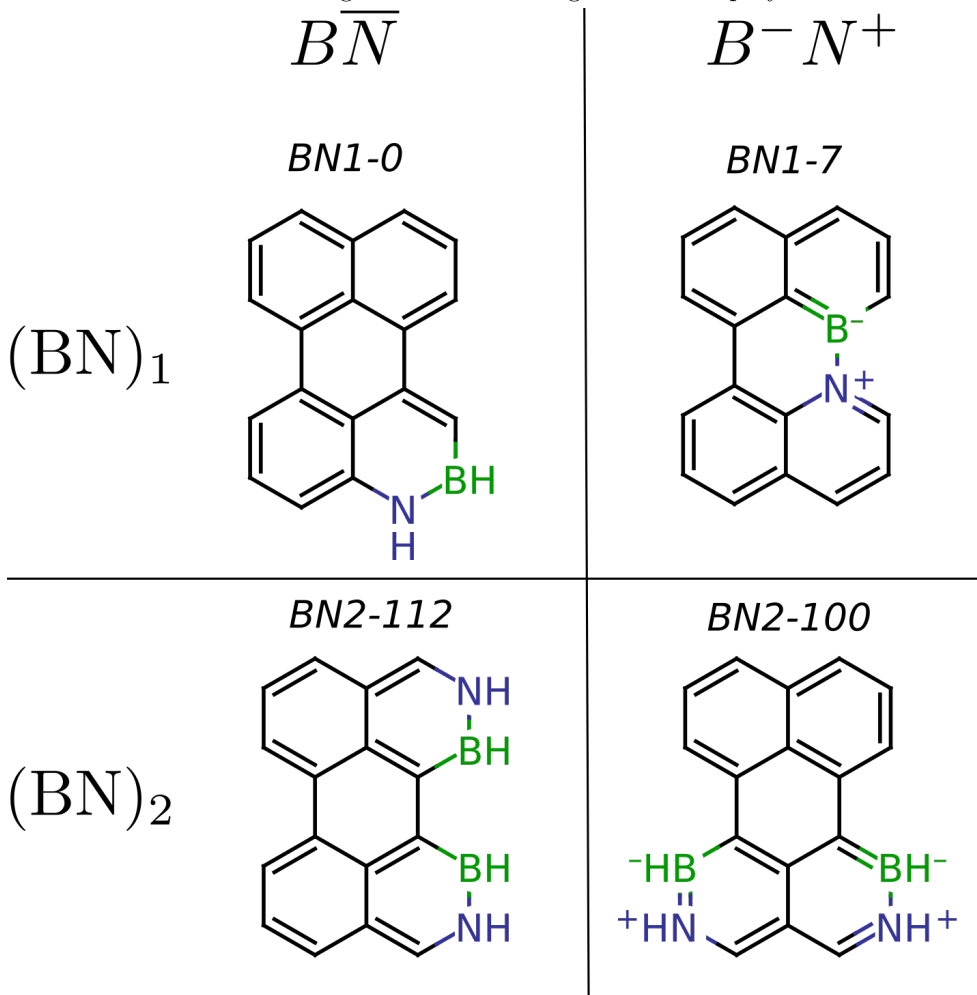
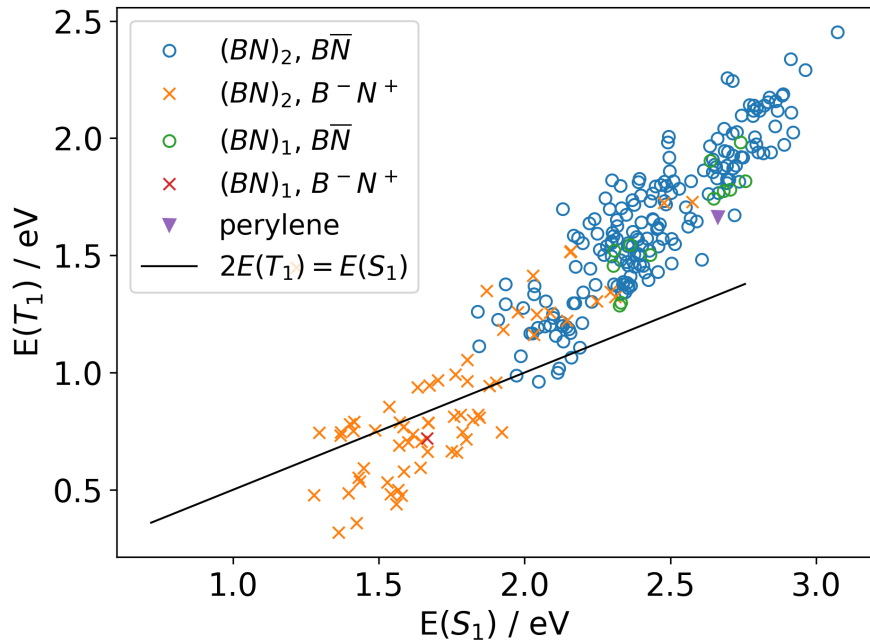
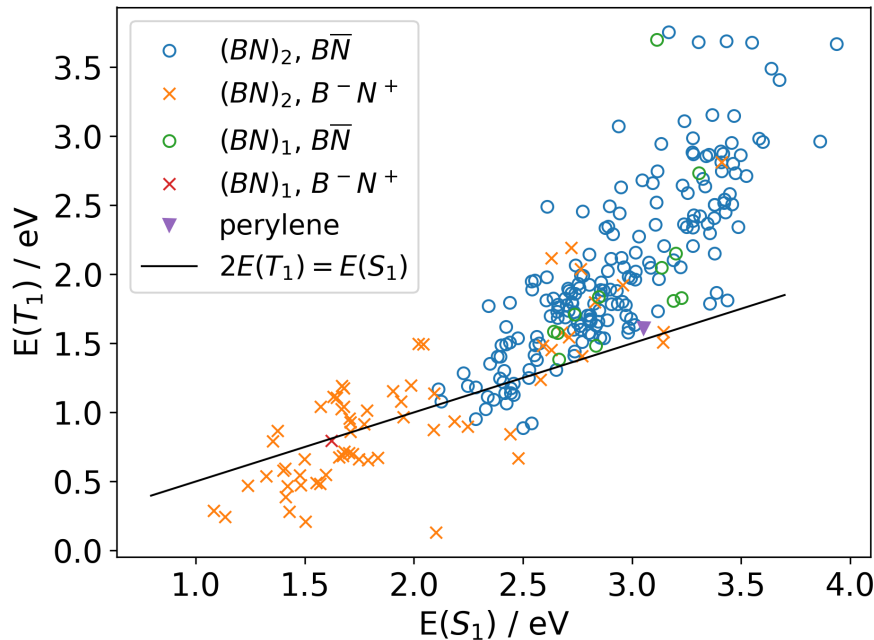


Figure 4.5: Representatives of singly (first row) and doubly (second row) BN-substituted perylene derivatives, which either do (left column) or do not have (right column) a Lewis structure without formal charges. In the molecules in the right column it is not possible to arrive at a resonance structure without formal charges by "flipping" electron pairs.

isomers are shown in Figs. 4.7a) and b) for the diabatic and the non-adiabatic model, respectively. With both models the maxima are scattered in the XY plane in a cross-like pattern parallel to the axes. By choosing an appropriate isomer the optimal stacking arrangement can be shifted to



a) TD-DFT energies



b) CASPT2 energies

Figure 4.6: Correlation between energies of S_1 and T_1 of BN-doped perylene derivatives for different substitution levels (one or two BN groups) and the two types of resonance structures (with or without formal charges).

a wide range of positions along the x- or y-axis.

4.4.5 Comparison of Diabatic and Non-Adiabatic Models

Although the distribution of the maxima in Figs. 4.7 a) and 4.7 b) looks somewhat similar, the two models give different 2D scans for some isomers. This discrepancy as well as the influence

of BN-doping on the maxima of $|T_{RP}|^2$ will be illustrated on three isomers. In addition to the best candidate BN2-112 (the criteria for selecting this isomer will be expounded in section 4.4.6), two more isomers (BN2-100 and BN2-150, see Fig. 4.8) are included, which stand out because for them the pattern of the 2D scan differs significantly from that of perylene.

For perylene, the diabatic model (Fig. 4.9a, 3rd column) predicts that the highest singlet fission rate should be achieved if the monomers are slip-stacked in the direction of the long molecular axis at $\Delta X = \pm 0.8 \text{ \AA}$ and $\Delta Y = 0 \text{ \AA}$. This shift by approximately half a C-C bond length maximizes the overlap between HOMO and LUMO. To have a high singlet fission rate, $(l_A|\mathbf{F}|l_B)(l_A|\mathbf{F}|h_B)$ and $(h_A|\mathbf{F}|h_B)(h_A|\mathbf{F}|l_B)$ in eqn. 5.1 should differ greatly. Upon complete stacking the matrix element $(h_{A/B}|\mathbf{F}|l_{B/A})$ vanishes because of symmetry and a low singlet fission rate results. The non-adiabatic model, on the other hand, predicts that the maxima occur for a shift along the short molecular axis at $\Delta X = 0 \text{ \AA}$, $\Delta Y = \pm 0.9 \text{ \AA}$ (Fig. 4.9a 4th column). The large size of the dimer together with the doubly excited character of the biexciton state, which cannot be described with conventional TD-DFT, precludes us from computing *ab initio* non-adiabatic coupling vectors to check which model is more realistic.

In BN2-100 (Fig. 4.9b) both BN-groups are placed on the same naphthalene subunit. As a consequence the LUMO becomes more localized in the substituted half of the molecule. The best arrangement for singlet fission occurs at a slip-stacking of $\Delta X = -3 \text{ \AA}$, when atoms 1 and 1' on one monomer are aligned with atoms 4 and 4' on the second monomer (see Fig. 4.4 for numbering of atoms), so that the overlap of HOMO and LUMO is maximized. By comparing $|T_{RP}|^2$ with $|T_{RP}|_{\text{NAC}}^2$ for the BN2-100 isomer it is apparent that the diabatic model is not symmetric and has only a single maximum at $\Delta X = -3 \text{ \AA}$. This is because in the diabatic model the initial exciton state is $|S_0 S_1\rangle$, where the excitation is localized on the second monomer. If the excitation is placed on the other monomer ($|S_1 S_0\rangle$) instead, the maximum is found to lie at $\Delta X = 3 \text{ \AA}$. As opposed to this, the adiabatic wavefunctions, which are used in the non-adiabatic model, have the full symmetry of the molecular geometry and are delocalized over both monomers. Therefore the 2D scan of $|T_{RP}|_{\text{NAC}}^2$ is symmetric with two maxima at $\Delta X = \pm 3 \text{ \AA}$.

The pattern of BN2-112 (Fig. 4.9c) is almost identical to that of perylene, with two symmetric maxima at $\Delta X = \pm 0.8 \text{ \AA}$. BN2-100 and BN2-112 both have C_{2v} symmetry, however, in BN2-112 the C_2 axis is parallel to the Y-axis, while in BN2-100 it is parallel to the X-axis. Therefore the scan of $|T_{RP}|^2$ for BN2-112 is symmetric under reflection about the Y-axis but not the X-axis. Interestingly the scan of $|T_{RP}|_{\text{NAC}}^2$ still has the full D_{2h} symmetry as for perylene.

For BN2-150 (Fig. 4.9d) the positions of the maxima agree reasonably well between the two models. The main difference is that the diabatic model predicts the rate to be exactly zero at the perfectly stacked position because of symmetry, while the NAC vector does not completely vanish at this position. The NAC vector has as many components as there are cartesian coordinates, but only certain linear combinations of displacements belong to the irreducible representation for which the non-adiabatic coupling vanishes in the symmetric arrangement.

Six lobes of the HOMO of BN2-150 are aligned parallel to the bond between carbons 5 and 4', which makes an angle of 60° with the longitudinal axis. Upon shifting one monomer along a vector that makes an angle of 30° with the x-axis, according to the diabatic model $|T_{RP}|^2$ attains a maximum at $\Delta X = 0.7 \text{ \AA}$ and $\Delta Y = 0.4 \text{ \AA}$ and symmetrically at $\Delta X = -0.7 \text{ \AA}$ and $\Delta Y = -0.4 \text{ \AA}$.

In all these examples, the nodal pattern of the perylene frontier orbitals is essentially retained. Doping with BN introduces a small perturbation, which increases or reduces the orbital lobes in the vicinity of the boron or nitrogen, thus making the orbitals less symmetric. Since in the diabatic model, $|T_{RP}|^2$ depends delicately on the cancellation of two matrix products, the positions of the maxima are very sensitive to the substitution pattern.

4.4.6 Selection of Best Isomers

In order to filter out the best candidates for singlet fission, the following criteria were applied. These narrow the selection down to just two molecules, which are then proposed as interesting targets for synthesis: (1) The S_1 excitation energy at the CASPT2 level should lie in the range $1.8 \text{ eV} \leq E(S_1, \text{CASPT2}) \leq 3.0 \text{ eV}$. This ensures that the molecule absorbs in the energy region where the solar spectrum has high intensity. (2) The energy of the T_1 state, which limits the maximum voltage of a solar cell operating with a singlet fission layer, should satisfy $0.8 \text{ eV} < E(T_1, \text{TD-DFT})$. A very low-lying triplet state indicates that the molecule might be a biradicaloid with high reactivity. (3) The most important condition is that singlet fission has to be exoergic or

Molecule	PG	LS	CASPT2					TD-DFT					diabatic		
			$E(S_1)$ (eV)	$E(T_1)$ (eV)	ΔE_{ST} (eV)	ΔE_{TT} (eV)	y_0	$E(S_1)$ (eV)	$E(T_1)$ (eV)	ΔE_{ST} (eV)	ΔE_{TT} (eV)	f	ΔX (Å)	ΔY (Å)	$ T_{RP} ^2$ (eV ²)
BN2-112 perylene	C_{2v} D_{2h}	$B\bar{N}$	2.33 3.05	1.02 1.61	-0.28 0.17	-0.44 0.43	0.06 0.02	2.05 2.66	0.96 1.66	-0.13 0.67	-0.48 0.30	0.27 0.28	± 0.7 ± 0.7	0.0 0.0	5×10^{-5} 6×10^{-5}

Table 4.1: Properties of the best BN-doped perylene isomer and undoped perylene. PG: point group, LS: type of Lewis structure, y_0 : biradical character, f : $S_0 \rightarrow S_1$ oscillator strength, diabatic: position and value of maximum of the diabatic coupling $|T_{RP}|^2$ in a scan of the relative displacement of two cofacially stacked dimers (vertical separation $\Delta Z = 3.5$ Å).

at most slightly endoergic. As there is some uncertainty in the energy predictions from different *ab initio* methods, only those molecules pass this test for which both the CASPT2 and TD-DFT energies fulfill -0.3 eV $< \Delta E_{ST}(\text{CASPT2}), \Delta E_{ST}(\text{TD-DFT}) < 0.2$ eV. (4) Finally the T_2 state should be above the S_1 state so that intersystem crossing can be excluded as a loss channel competing with singlet fission. Requiring $\Delta E_{TT}(\text{CASPT2}), \Delta E_{TT}(\text{TD-DFT}) < -0.2$ eV leaves only two isomers: BN2-112 and BN2-171. Their molecular structures are shown in Figs. 4.8b) and 4.8d). In both isomers the same pairs of carbon are substituted, however in one isomer the positions of B and N are exchanged relative to the other. Optimization of the two isomers with the CAM-B3LYP [208] functional and the def-SVP [253] basis set using Q-Chem [254] eliminates isomer BN2-171, which does not remain planar, presumably because of the repulsion between the lone electron pairs on the two nitrogen atoms in the bay positions. Therefore only a single candidate remains, BN2-112. The selected candidate has other desirable properties, too: It has a Lewis structure without formal charges and consequently a moderate biradical character of $y_0 = 0.06$, whereas the full set of isomers has y_0 in the range 0.01 to 0.66. The oscillator strength $f(S_0 \rightarrow S_1) = 0.27$ is close to that of undoped perylene (0.30) and among the highest of all isomers, for which f takes on values in the range 0.0 to 0.33. The diabatic and non-adiabatic couplings, which are taken as an indicator of the singlet fission rate, however have only low or intermediate values as compared to the other isomers: For BN2-112, the maximum diabatic coupling matrix element is $|T_{RP}|^2 = 5 \times 10^{-5}$ eV², and the maximum length squared of the non-adiabatic coupling vector amounts to $|T_{RP}|_{\text{NAC}}^2 = 3 \times 10^{-2}$ Å⁻². These values fall into the lower end of the coupling strengths observed for all isomers, $|T_{RP}|^2$ ranges from 4×10^{-6} to 1×10^{-3} eV², while $|T_{RP}|_{\text{NAC}}^2$ ranges from 3×10^{-2} to 4.0 Å⁻². The positions of the maxima and magnitude of the couplings are almost identical to undoped perylene, however, the energetic conditions are better. Table 4.1 collects the electronic properties of the selected isomer. In the supporting information we show scans of $|T_{RP}|^2$ for the dimer of BN2-112, wherein one unit is rotated by 180°.

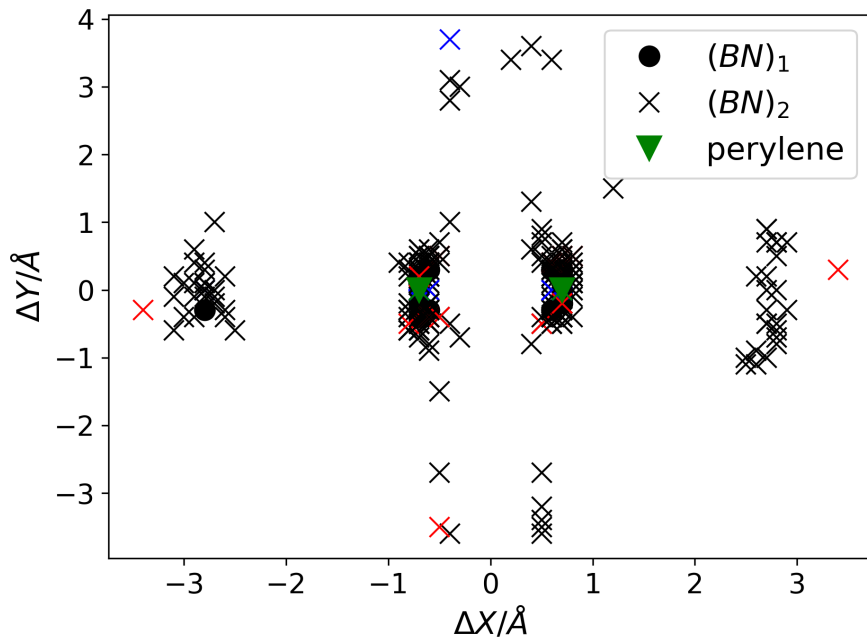
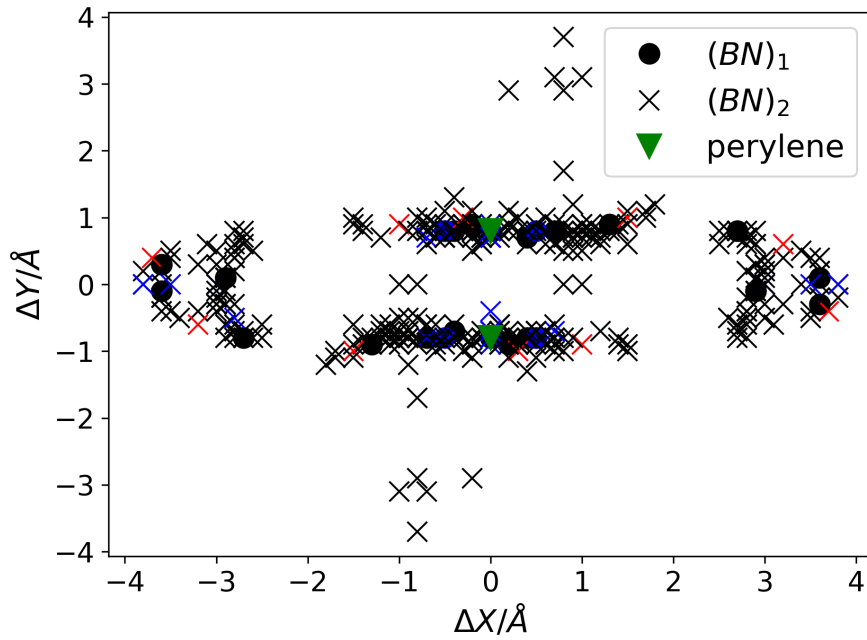
a) Maxima of $|T_{RP}|^2$ (eqn. 5.1).b) Maxima of $|T_{RP}|^2_{NAC}$ (eqn. 4.12)

Figure 4.7: Scatter plot of the positions of the two highest local maxima in the 2D scan of $|T_{RP}|^2$. Colors denote the point group to which the isomers belong: D_{2h} - green, C_{2v} - blue, C_{2h} - red, C_s - black.

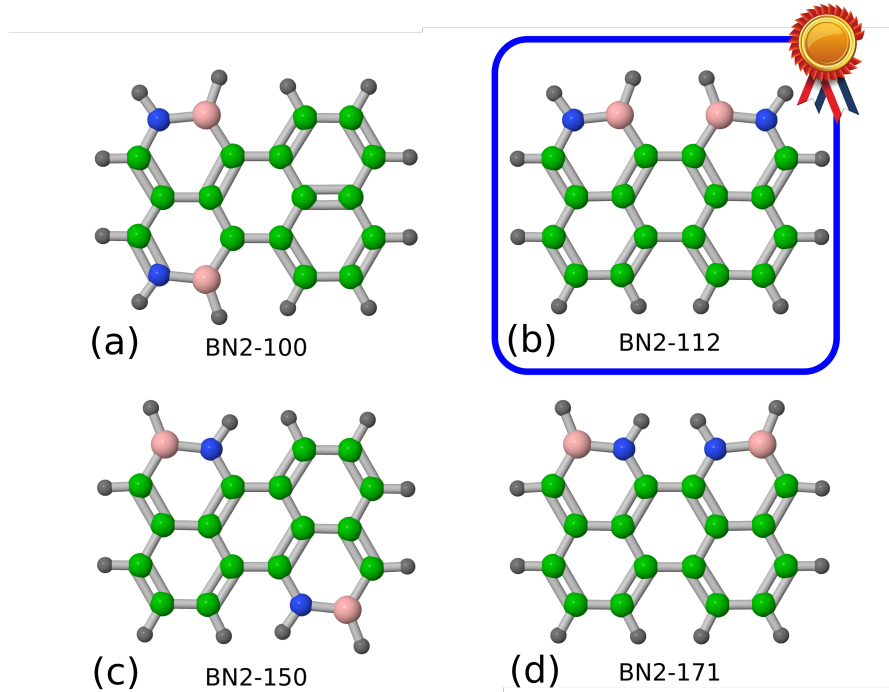


Figure 4.8: Selected isomers that are discussed in the text (nitrogen: blue, carbon: green, boron: pink, hydrogen: gray). BN2-112 satisfies all requirements for singlet fission.

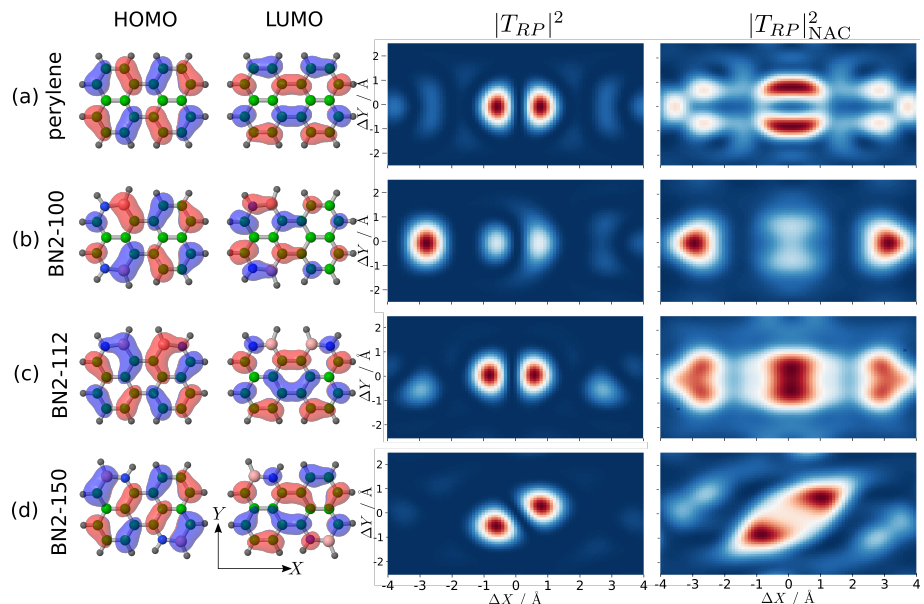


Figure 4.9: AM1 frontier molecular orbitals of monomers and 2D scans of $|T_{RP}|^2 = \left| \frac{(l_A|\mathbf{F}|l_B)(l_A|\mathbf{F}|h_B)}{\Delta E(C'A)} - \frac{(h_A|\mathbf{F}|h_B)(h_A|\mathbf{F}|l_B)}{\Delta E(AC)} \right|^2$ (diabatic model) and $|T_{RP}|_{NAC}^2 = \frac{1}{2} (|\langle S^{\text{bright}*} | \nabla |TT^*\rangle|^2 + |\langle S^{\text{dark}*} | \nabla |TT^*\rangle|^2)$ (non-adiabatic model).

4.5 Conclusion

Doping of polycyclic aromatic hydrocarbons with isoelectronic BN groups was explored as a means to expand the range of molecules that might undergo singlet fission. Using perylene as a template all isomers containing one or two BN groups were systematically enumerated and investigated by TD-DFT and CASPT2 calculations. Those isomers for which no Lewis structure without formal charges can be found have lower excitation energies and satisfy the energy condition for exoergic or slightly endoergic singlet fission. However, they have a higher biradical character and are expected to be less stable. One particular isomer of $(BN)_2$ -substituted perylene was proposed, which from a computational perspective satisfies all conditions for a reasonable singlet fission chromophore. In this isomer the opposite carbon atoms in the bay position are substituted by boron and the adjacent carbon atoms in the ortho positions are replaced by nitrogen. Two inexpensive, semi-empirical models were tested for predicting the optimal packing arrangement in BN-doped perylene derivatives. The models based on the diabatic and adiabatic picture sometimes give conflicting results regarding the positions of maximum singlet fission rate. More accurate models are required to resolve these issues. However, both models suggest that the optimal cofacial packing arrangement is very sensitive to the substitution pattern. On the methodological level, we could confirm that automatic differentiation is a versatile tool for obtaining derivatives of quantum chemical properties, without having to go through the tedious implementation of analytic gradients.

Chapter 5

Rotation and Functionality Optimisation of the PDI Dimer

5.1 Introduction

Expanding beyond a two-dimensional scan for singlet fission rate, the investigation delves into exploring the impact of rotational symmetry on this process. Researchers are actively synthesizing rotated slipped stacked aggregates using Perylene Diimide (PDI), which has the potential to enhance singlet fission rates. Many studies have pointed out PDI as an important photoactive functional base molecule. Several studies have underscored the significant impact of PDI morphology on singlet fission (SF) efficiency.[255, 256, 257, 258] These investigations have involved interdisciplinary collaborations between organic chemistry, spectroscopy, and quantum chemistry.[259, 258, 260, 203, 261, 15, 262] Notably, they have demonstrated that efficient SF can be achieved in well-designed dimeric PDI systems in solution by modulating charge transfer (CT) and coulomb couplings.[263] Studies have highlighted while PDIs with distinct substituents at their imide positions share similar electronic structures, their packing arrangements exhibit substantial variations. Notably, the study observed a highly promising outcome of high triplet generation upon single-photon absorption for a $\pi - \pi$ stacking configuration characterized by rotation along the axis perpendicular to the plane of PDI. These findings emphasize the need for theoretical investigations to elucidate the impact of rotation along Z-axis on SF efficiency. [262, 264]

Quantum chemical simulations have shown that a rotation in the orientation of two parallel PDIs can enhance SF efficiency. [265] Additionally, the simulations have indicated that ME generation is unlikely to occur due to highly endothermic energetics at the slightly rotated Franck–Condon geometry. This prediction aligns with experimental observations of significantly slower SF rates in viscous solvents.[263] Thus, these findings suggest that the rotation of chromophores may play a pivotal role in modifying electronic structures relevant to SF. Modulation of singlet fission through rotation of terrylene is demonstrated by Hariharan and coworker [266].

In real-world scenarios, molecular structures are often subject to constraints in terms of translation and rotation, but it's crucial to recognize that all degrees of freedom can impact the singlet fission (SF) efficiency of a molecule. For instance, structural distortions in pentacene play a pivotal role in bringing the Franck-Condon region closer to the conical intersection between the S_1 and 1TT states, ultimately leading to efficient singlet fission processes, as demonstrated in the work by Miyata et al.[267]. The nature of coupling among the Local Exciton (LE), CT, and triplet-triplet $^1(TT)$ states has also been employed in the study of structural distortions induced by molecular vibrations in pentacene, as explored by Schnedermann et al. [268].

The pursuit of enhanced singlet fission efficiency through molecular structural contortion has yielded promising results, particularly in molecules like perylene and PDI. Researchers have achieved success in this endeavour, as exemplified by the works of Conrad-Burton et al. [269] and Sun et al. [270]. These studies have showcased the potential for manipulating molecular structures to optimize singlet fission processes. Research efforts in our lab, made by previous colleagues, have been dedicated to exploring, searching, and optimizing functional properties in molecules. This includes investigations into biradical character and conical intersections within the energy landscape of molecules using metadynamics, as documented in works by Lindner et al. [271, 272] One of the key advantages of SFast is that it leverages semi-empirical methods, bringing a balance

between accuracy and computational demands. It also harnesses machine learning principles and is implemented using Python's Pyseqm and PyTorch library. [152]

The study places particular emphasis on understanding CT states. This research promises insights into how the rotation of stacked aggregates can influence singlet fission and the behavior of CT states. In this chapter, results are presented in three sections: the rotation scan with the empirical method, the rotation scan with ASD, and the optimization of PDI dimers.

5.2 Method and Calculation Details

5.2.1 Overlap Approximation

In the study, the singlet fission rate (T_{RP}) was investigated within the framework of the singlet fission process. Simplifying the expression within the simple frontier orbital model and zero differential overlap approximation, Equation 4.5 reduces to

$$Fock T_{RP} = \left| \frac{\langle l_A | \hat{\mathbf{F}} | l_B \rangle \langle l_A | \hat{\mathbf{F}} | h_B \rangle}{\Delta E(\text{CA})} - \frac{\langle h_A | \hat{\mathbf{F}} | h_B \rangle \langle h_A | \hat{\mathbf{F}} | l_B \rangle}{\Delta E(\text{AC})} \right|. \quad (5.1)$$

where $\hat{\mathbf{F}}$ is the Fock matrix. The rate expression (T_{RP}) was approximated by transitioning from Fock matrix elements to overlap matrix elements, represented as $\langle \phi | \hat{\mathbf{F}} | \psi \rangle = \epsilon \langle \phi | \psi \rangle$, where ϵ is constant. The obtained equation is:

$$Overlap T_{RP} = \left| \frac{\langle l_A | l_B \rangle \langle l_A | h_B \rangle}{\Delta E(\text{CA})} - \frac{\langle h_A | h_B \rangle \langle h_A | l_B \rangle}{\Delta E(\text{AC})} \right|. \quad (5.2)$$

Also, $\Delta E(\text{CA})$ and $\Delta E(\text{AC})$ are approximated to be one, which gives the final approximated version as:

$$T_{RP} = |\langle l_A | l_B \rangle \langle l_A | h_B \rangle - \langle h_A | h_B \rangle \langle h_A | l_B \rangle|. \quad (5.3)$$

5.2.2 Optimization

In the rigid scan model, the analysis was limited to considering only four degrees of freedom in the context of singlet fission. However, to gain a more comprehensive understanding of this intricate process, we decided to explore all possible degrees of freedom involved. To accomplish this, we integrated the "SFast" method with the Limited memory Broyden-Fletcher-Goldfarb-Shanno (L-BFGS) optimization procedure. In any structural optimization, it's crucial to have the gradient of the function with respect to atomic coordinates. The gradient guides the optimization process by indicating how the function changes as atomic positions are adjusted. In this study, the gradient of the functional was calculated analytically using automatic differentiation. This approach involves keeping track of the operations performed during the calculation of functions and then using this information to calculate derivatives.

Within the framework, a custom-defined objective function is shown in equation 5.4. It incorporates T_{RP} such that the singlet fission rate is enhanced upon optimisation. This optimization involves minimizing an objective function, which can be expressed as:

$$L(x) = E(x) - \omega \cdot \log(|T_{RP}|^2(x)) \quad (5.4)$$

Here, $E(x)$ represents the total energy of the system, $|T_{RP}|^2(x)$ quantifies the magnitude of the singlet fission rate, and w is a weighting factor that determines the trade-off between energy and singlet fission rate. By finding the minimum of $L(x)$, it is possible to identify specific molecular geometries that lead to optimal singlet fission rates. The main idea behind the L-BFGS algorithm is to approximate the inverse Hessian matrix \mathbf{H}_k without explicitly forming or storing it. Instead, it maintains a limited memory of the past gradient and parameter changes to build this approximation incrementally. The update in the L-BFGS algorithm can be described using the following equations:

$$\mathbf{q}_k = \nabla f(\mathbf{x}_k), \quad (5.5)$$

which describes gradient at the current point,

$$\mathbf{y}_k = \nabla f(\mathbf{x}_{k+1}) - \nabla f(\mathbf{x}_k), \quad (5.6)$$

which describes Change in gradient,

$$\rho_k = \frac{1}{\mathbf{y}_k^T \cdot \mathbf{s}_k}, \quad (5.7)$$

which describes scalar factor,

$$\alpha_k = \rho_k \cdot \mathbf{s}_k^T \cdot \mathbf{q}_k, \quad (5.8)$$

which describes step length,

$$\beta_k = \rho_k \cdot \mathbf{y}_k^T \cdot \mathbf{q}_k, \quad (5.9)$$

which describes curvature parameter and

$$\mathbf{r}_k = \alpha_k \cdot \mathbf{s}_k - \beta_k \cdot \mathbf{y}_k, \quad (5.10)$$

which describes update direction. These equations are used to update the search direction at each iteration, and the L-BFGS algorithm iteratively refines this direction to find the minimum of the objective function. The algorithm combines this direction with a line search to determine the step size and update the current solution \mathbf{x}_k .

5.2.3 Dimer Structure Analysis

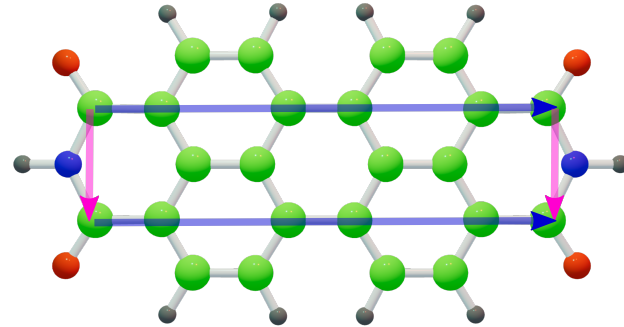


Figure 5.1: Structure of PDI for the structural analysis. Along the atoms marked with the blue arrow the curvature is calculated.

To analyze the optimized dimer structure, we establish parameters characterizing the geometry of the dimer. These parameters include the relative translations and rotations between monomers, as well as the curvature and twisting within each monomer. To achieve this, we define a coordinate frame for each monomer using a set of guidance atoms. These atoms enable us to generate vectors along the long (X-axis) and short (Y-axis) axes of the original planar molecule (depicted in blue and orange in Figure 5.1). Through the Gram-Schmidt orthogonalization process, we ensure the orthogonality of these vectors and determine the vector normal to the plane (Z-axis).

Relative translations are calculated by projecting the vector connecting the center of mass of both monomers onto the internal coordinate system of a monomer. Relative rotations follow a similar approach. For instance, the Z-rotation is determined by projecting the X-vector of one molecule onto the XY-plane of the other molecule and calculating the angle between the projected vector and the X-vector.

Curvature is computed by projecting the guidance atoms of each long side (illustrated by blue arrows in Figure 5.1) onto the XZ plane of the monomer's coordinate frame and fitting these points to the parabola $z(x) = ax^2 + bx + c$. The curvature, defined as the second derivative of Z, is then obtained as $2a$. As both sides are fitted independently, the mean curvature of a monomer is determined.

The twisting angle of a monomer is defined as the angle between the two short axes vectors (pink arrows in Figure 5.1) of the molecule.

5.2.4 Diabatic Coupling Upon Rotation

In the semi-empirical model Hamiltonian study, a detailed rotational scan was conducted, by rotating one of the cofacially stacked monomer, ranging from 0° to 90° , along Z-axis. The PDI monomer was translated along the X-axis, spanning from -5 \AA to 5 \AA , and along the Y-axis, varying from -2.5 \AA to 2.5 \AA , while maintaining a fixed distance of 3.41 \AA in the Z-axis direction. The grid for this scan had a step size of 0.1 angstroms. Additionally, for each point on the grid, the monomer underwent rotation, with the rotation angle incrementing by 0.5° . The model Hamiltonian is constructed using active space decomposition implemented in the BAGEL package.[135] It comprises specific terms, such as $\langle S_1S_0 + S_0S_1 | \hat{H} | TT \rangle$, $\langle S_1S_0 - S_0S_1 | \hat{H} | TT \rangle$, $\langle S_1S_0 + S_0S_1 | \hat{H} | CA/AC \rangle$, $\langle S_1S_0 + S_0S_1 | \hat{H} | AC/CA \rangle$, $\langle TT | \hat{H} | CA/AC \rangle$, and $\langle TT | \hat{H} | AC/CA \rangle$, which are essential components in Michl's Simple Model for singlet fission rate calculation.[28] To investigate the behaviour of this system, a scan was conducted, spanning from $\Delta X = 0.0 \text{ \AA}$ to $\Delta X = 4.0 \text{ \AA}$, while ΔY remained at 0.0 \AA . The rotation was executed along the Z-axis, ranging from $\Delta\theta = 0^\circ$ to 90° , with a rotational grid size of $\frac{90^\circ}{20^\circ}$. This study involved the use of 10 monomer states in each manifold, and RAS-CI with cc-pVDZ basis set calculations were carried out with an RAS(11,4,11)[1,1] configuration.

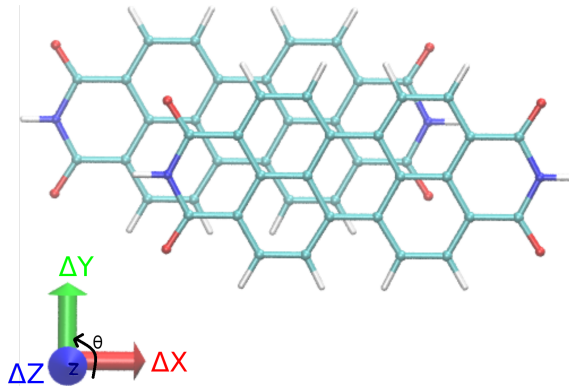


Figure 5.2

5.3 Results

5.3.1 Rotation With Semi-empirical Method

The coupling elements $\langle S_1S_0 | \hat{H} | AC \rangle$, specifically $\langle h_A | \hat{F} | h_B \rangle$ when the anion forms on the singlet exciton fragment, exhibit distinctive behaviour depending on the dimer's configuration. These coupling elements demonstrate high values both at full stacking (0° rotation) and at the fully slipped position ($\Delta X = 1.5 \text{ \AA}$, $\Delta Y = 0 \text{ \AA}$). However, at the slipped stacked position, the coupling reduces to 0 eV and changes sign. The minimum coupling value is reached at $\Delta X = 3 \text{ \AA}$, $\Delta Y = 0 \text{ \AA}$. Remarkably, as the monomer undergoes rotation, the coupling value decreases until it reaches a minimum at 30° of rotation. Subsequently, it starts increasing and attain their maximum at 60° of rotation. At this point, the LE/CT coupling reaches its peak, with maximum values observed at positions such as $\Delta X = \pm 2 \text{ \AA}$, $\Delta Y = \mp 1 \text{ \AA}$, and $\Delta X = \pm 1 \text{ \AA}$, $\Delta Y = \pm 1.5 \text{ \AA}$, where it reaches -0.008 eV .

Conversely, when the cation forms on the singlet exciton fragment, as indicated by the coupling elements $\langle S_1S_0 | \hat{H} | CA \rangle$, specifically $\langle l_A | \hat{F} | l_B \rangle$, a similar pattern is observed. These coupling elements also display high values at full stacking (0° rotation) and follow a rotation-dependent trend. The maximum coupling values are encountered at positions akin to $\Delta X = \pm 2 \text{ \AA}$, $\Delta Y = \mp 1 \text{ \AA}$, and $\Delta X = \pm 1 \text{ \AA}$, $\Delta Y = \pm 1.5 \text{ \AA}$, with particular emphasis on the 60° rotation configuration, where the coupling reaches -0.008 eV .

The coupling element $\langle CT | \hat{H}^1 | TT \rangle$ exhibits intriguing characteristics depending on the molecular geometry and rotation angle along the Z-axis. Initially, at the fully stacked position (0° rotation), this coupling element has a zero value, consistent across all rotation angles along the Z-axis. However, as the dimer is rotated, a distinct pattern emerges in the coupling plot. At 0° of rotation,

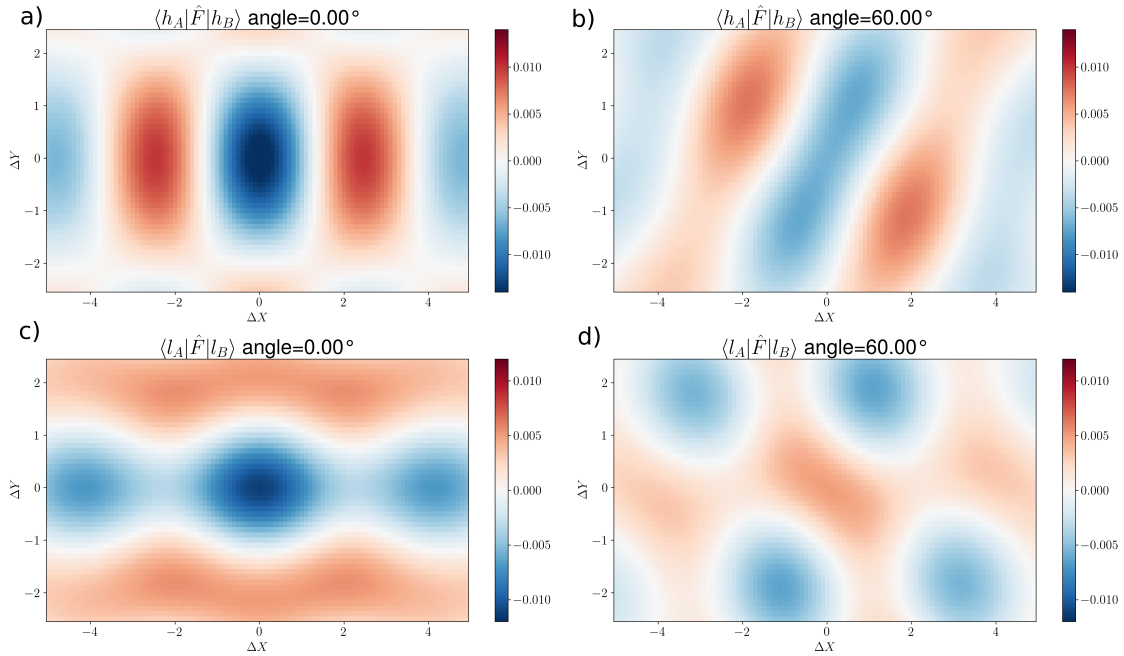


Figure 5.3: The plot of coupling $\langle S_1S_0|H|AC\rangle$ at a) 0° b) 60° $\langle S_1S_0|H|CA\rangle$ at c) 0° d) 60°

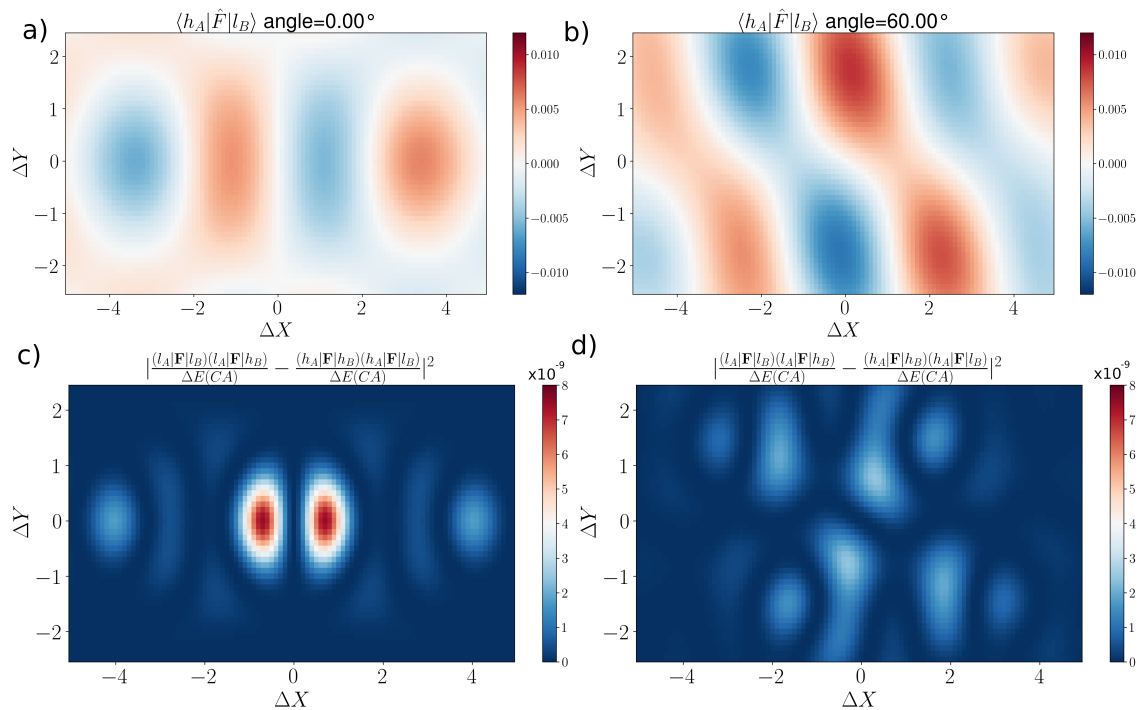


Figure 5.4: The plot of coupling $\langle CT|H|^{1(TT)}\rangle$ at a) 0° and b) 60° and T_{RP} at c) 0° and d) 60°

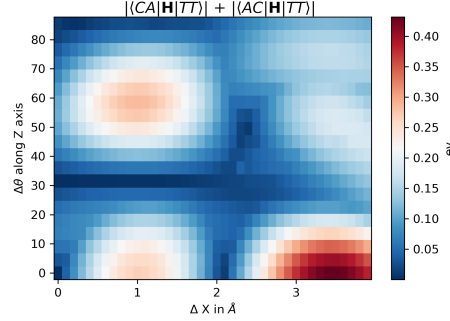


Figure 5.5: Plot of coupling between $\langle CT|H|^1(TT)\rangle$ using ASD

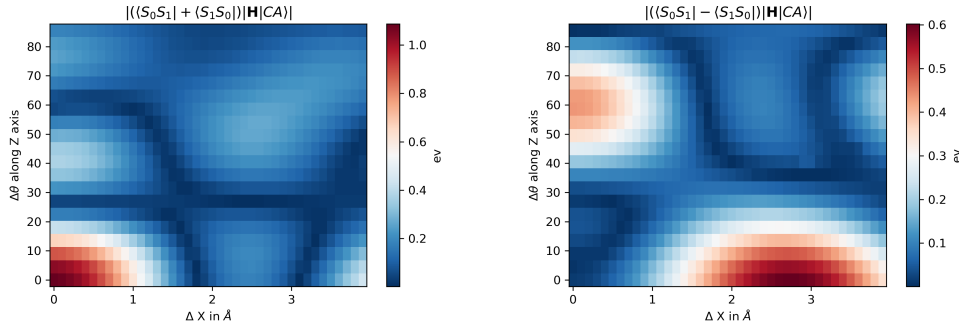


Figure 5.6: Plot of coupling between a) $\langle S^+|H|CA\rangle$ (bright) b) $\langle S^-|H|CA\rangle$ (Dark) using ASD

the plot displays four regions with notably high coupling values. The coupling strength reaches its maximum value, measuring 0.005 eV, at positions such as $\Delta X = \pm 1 \text{ \AA}$ and $\Delta Y = 0 \text{ \AA}$, as well as $\Delta X = \pm 3.5 \text{ \AA}$ and $\Delta Y = 0 \text{ \AA}$. Interestingly, as the dimer undergoes further rotation, the coupling values decrease until reaching a rotation angle of 30 °.

When the rotation angle reaches 60 °, the $\langle CT|\hat{H}|^1(TT)\rangle$ coupling element exhibits significantly high values, approximately $\pm 0.008 \text{ eV}$, at positions like ($\Delta X = 0 \text{ \AA}$ and $\Delta Y = 1.5 \text{ \AA}$), ($\Delta X = -2 \text{ \AA}$ and $\Delta Y = 1.5 \text{ \AA}$), ($\Delta X = 2 \text{ \AA}$ and $\Delta Y = -1.5 \text{ \AA}$), and ($\Delta X = 0 \text{ \AA}$ and $\Delta Y = 1.5 \text{ \AA}$). Though, these values at 60 ° do not exceed the maxima observed at 0 ° of rotation.

During the rotational scan, it was observed that the maximum value of the singlet fission rate, denoted as $|T_{RP}|^2$, was achieved at a slipped stacked position of $\Delta X = 0.7 \text{ \AA}$. The magnitude of $|T_{RP}|^2$ at this point was approximately $8.629 \times 10^{-5} \text{ eV}^2$. Initially, as the rotation scan started from 0 °, the singlet fission rate was highest. However, as the rotation angle increased up to 30 °, the singlet fission rate gradually decreased, indicating a fading out of this process.

Interestingly, the singlet fission rate started to increase again as the rotation angle reached 60 °. At this point, it reached a local maximum with a value of $3.5027 \times 10^{-5} \text{ eV}^2$. This local maximum was located at coordinates $\Delta X = 0.3 \text{ \AA}$ and $\Delta Y = 0.7 \text{ \AA}$ on the grid. Subsequently, as the rotation angle continued to increase to 90 °, the singlet fission rate once again began to fade out.

5.3.2 Study With ASD Model Hamiltonian

In the analysis with ASD Model Hamiltonian various features of the coupling among LE/CT, LE/¹(TT) and CT/¹(TT) has been observed. The coupling between CT and ¹(TT) states is illustrated in Figure 5.5. Notably, the highest CT to ¹(TT) coupling is observed at a distance of 3.5 Å with no rotational deviation (0° rotation). This optimal coupling indicates efficient CT mediation between the states. Furthermore, there are distinct regions with high CT to ¹(TT) coupling. One such region is located at coordinates $\Delta X = 1.0 \text{ \AA}$, $\Delta Y = 0 \text{ \AA}$, and $\theta = 0^\circ$, where the coupling energy is 0.32 eV. Another region is situated at coordinates $\Delta X = 1.2 \text{ \AA}$, $\Delta Y = 0 \text{ \AA}$, and $\theta = 55^\circ$, with a coupling energy of 0.32 eV.

In Figure 5.6a, the coupling between the bright exciton state and CT states is showcased. This coupling reaches its maximum intensity when the stacking is complete, corresponding to $\Delta X = 0$

\AA and $\theta = 0^\circ$, with a coupling energy of 1.0 eV. Additionally, there is a region with high coupling values situated at coordinates $\Delta X = 0 \text{ \AA}$, $\Delta Y = 0 \text{ \AA}$, and $\theta = 40^\circ$, where the coupling energy is 0.5 eV. In Figure 5.6b, the coupling between the dark exciton state and CT states is showcased. This coupling reaches its maximum at the slipped stacked position of $\Delta X = 2.7 \text{ \AA}$ and $\theta = 0^\circ$, with a coupling energy of 0.6 eV. Additionally, there is a region with high coupling values situated at coordinates $\Delta X = 0 \text{ \AA}$, $\Delta Y = 0 \text{ \AA}$, and $\theta = 60^\circ$, where the coupling energy is 0.4 eV.

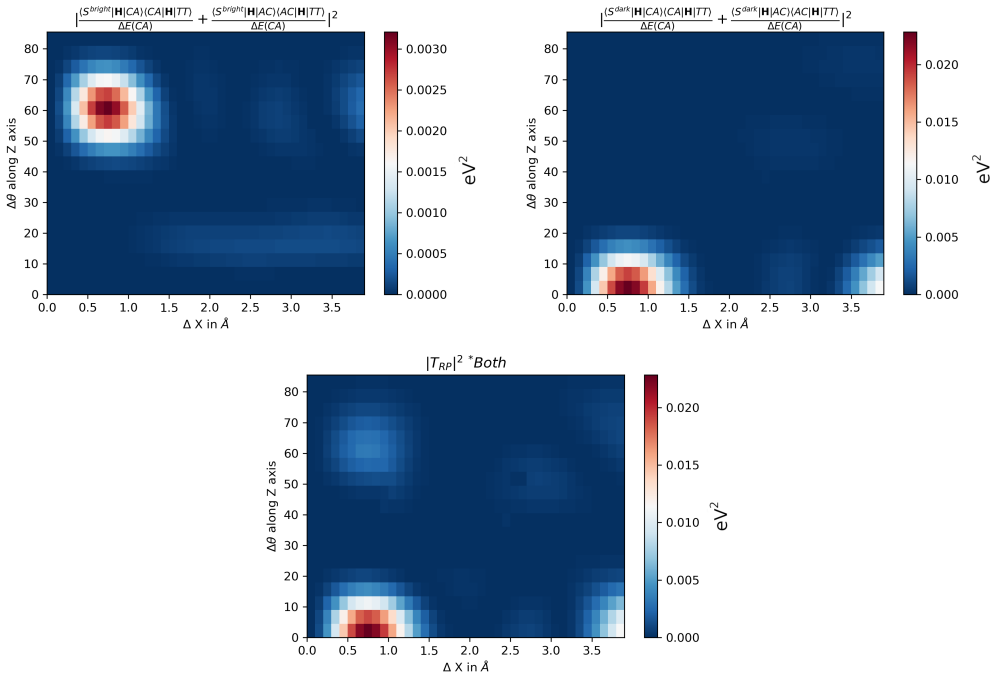


Figure 5.7: a) Transfer probability of ${}^1(\text{TT})$ formation from Bright exciton via CT state and b) Transfer probability of ${}^1(\text{TT})$ fromation from Dark exciton via CT

At fully stacked position, upon rotation along the Z-axis, the $\langle S^+|\hat{H}|CA\rangle$ shows damped oscillatory behaviour and diminishes whereas $\langle S^-|\hat{H}|CA\rangle$ reaches maxima at 60° . At $\Delta X = 0.0 \text{ \AA}$, as rotation increases, the dark exciton to CT coupling decreases and bright exciton to CT coupling increases and reaches the local maximum at 60° , whereas at slipped position of $\Delta X = 1.0 \text{ \AA}$ CT/ ${}^1(\text{TT})$ coupling decreases upon rotation from $\Delta\theta = 0^\circ$ to $\Delta\theta = 30^\circ$ and increases from $\Delta\theta = 30^\circ$ to $\Delta\theta = 60^\circ$ and then decreases again. Thus, as combination of these situation as maxima is observed at $\Delta X = 0.7 \text{ \AA}$, $\Delta\theta = 0^\circ$ ($T_{RP} = 0.024 \text{ eV}^2$) and a local maxima at $\Delta X = 0.7 \text{ \AA}$, $\Delta\theta = 60^\circ$ ($T_{RP} = 0.005 \text{ eV}^2$). Please refer to the plot show in the figure 5.7. Also because of bright $\langle S^+|\hat{H}|CA\rangle$ and CT/ ${}^1(\text{TT})$ coupling another local maxima is observed at $\Delta X = 4.0 \text{ \AA}$, $\Delta\theta = 0^\circ$ ($T_{RP} = 0.01 \text{ eV}^2$). At fully stacked position the $\langle CA|\hat{H}|TT\rangle$ is zero through out rotation scan so T_{RP} is zero.

In Figure 5.8a, the plot represents the coupling between the bright exciton and the ${}^1(\text{TT})$ state. The plot shows two distinct maxima, where the coupling is equally strong. The first maximum occurs at $\Delta X = 1.5 \text{ \AA}$, the bright exciton has a high probability of transitioning to a triplet state. The second maximum is at $\Delta X = 0.8 \text{ \AA}$ and $\Delta\theta = 25^\circ$. Both of these maxima are of the order of approximately 1.0×10^{-3} .

Figure 5.8b, focuses on the coupling between the dark exciton and the triplet state. The plot reveals two local maxima. The first maximum is observed at an 18° rotation angle and $\Delta X = 2.5 \text{ \AA}$. The second maximum occurs at a 55° rotation angle and $\Delta X = 0.5 \text{ \AA}$, indicating another region where the coupling between the dark exciton and the ${}^1(\text{TT})$ state is significant.

5.3.3 Functionality Optimisation

To initiate the optimization process, we used a planar PDI dimer structure as the initial configuration. The goal was to optimize the molecular structure to maximize the singlet fission rate. In this context, the rate expression (T_{RP}) was approximated by transitioning from fock matrix

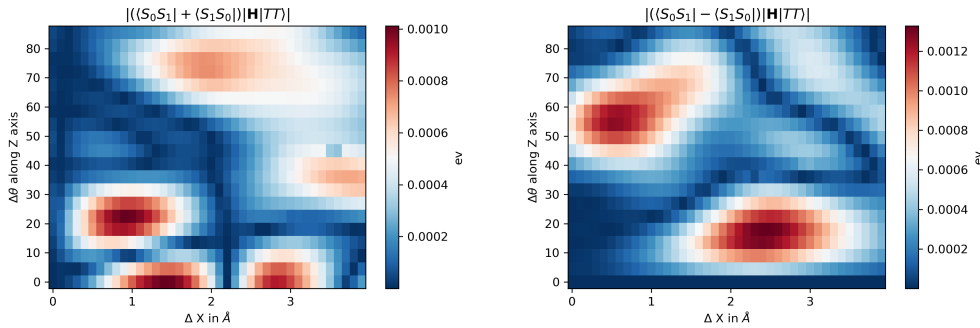


Figure 5.8: Plot of coupling between a) $\langle S^+ | H | TT \rangle$ (bright) b) $\langle S^- | H | TT \rangle$ (Dark) corresponding to direct pathway of singlet fission using ASD

elements to overlap matrix elements. This approximation aligns with the further simplification of Michl's model [162]. The optimization process involved a total of 30 steps. Convergence of the optimization was deemed successful when the norm of the gradient reached a value lower than 10^{-2} . Following the convergence, energy calculations were performed, taking into account dispersion corrections. In this optimization procedure, the weight assigned to the objective function was set to 1.0. As the optimization progressed, the value of T_{RP} (representing certain properties or characteristics) increased significantly, transitioning from an initial value of 1.14×10^{-11} to a final value of 5.34×10^{-6} . This increase in T_{RP} suggests that the optimization process was effective in achieving its objectives. Moreover, during the optimization process, the ground state energy of the molecule experienced a slight elevation, specifically by an increment of 0.01 eV. As a result of the functional optimization, the molecular structure underwent a noticeable transformation, leading to a distinctive bowed shape, as visually depicted in figure 5.11. The alteration in the molecular structure is indicative of the optimization process aiming to enhance singlet fission rates. Initially, the matrix elements $\langle h_A | h_B \rangle$ and $\langle l_A | l_B \rangle$ had the same sign, but as the optimization progressed, they became opposite to each other. Meanwhile, the overlap matrix elements corresponding to CT and ${}^1(TT)$ coupling, i.e., $\langle l_A | h_B \rangle$ and $\langle h_A | l_B \rangle$, also changed in sign, and eventually, these two terms became of the same sign. This change in the signs of matrix elements and their combination had a significant effect on the rate expression. Initially, the rate expression had subtractive terms, but due to the evolving signs, it became accumulative.

To study the effect of various features, a series of optimizations is performed, and the structural properties are studied.

5.3.4 Analysis of Different ω -Values For PDI Dimers

Table 5.1: PDI dimer configurations optimized with different ω values. ω : free optimizsation paramter. **id**: index of the original trajectory. **translation (x,y,z)**: Relative translation of the dimers in Å. **rotation (x,y,z)**: Relative rotation of the dimers in degree (due to symmetry the angle is always positive and lower than 180°). **curvature (A,B)**: mean curvature measured along two parallel lines along the long axis of PDI in $1 \times 10^{-3} \text{ \AA}^{-2}$. **twist (A,B)**: dihedral angle between outer carbons along the long axis of PDI in degrees. **rate**: SF rate calculated with the overlap approximation. ΔE : AM1 stabilization energy of the dimer with the reference of two non-interacting monomers. **steps**: Optimisation steps until convergence. Maximal steps are set to 300.

ω	translation			rotation			curvature		twist		rate	ΔE	steps
	x	y	z	x	y	z	A	B	A	B			
0.1	-1.15	0.52	3.62	11.3	9.4	5.3	-8.6	8.5	3.7	15.8	2.01×10^{-8}	-0.16	40
0.2	-1.03	0.18	3.43	7.5	8.6	0.0	-17.1	21.3	5.9	10.5	1.44×10^{-7}	0.12	20
0.3	-1.00	0.14	3.34	6.4	7.8	0.1	-20.3	25.8	5.2	9.3	3.48×10^{-7}	0.33	23
0.4	-0.88	-0.02	3.21	0.2	4.6	0.1	-26.8	31.3	0.7	1.4	8.41×10^{-7}	0.66	22
0.5	-0.86	-0.03	3.16	0.6	4.1	0.2	-27.7	32.0	1.2	0.4	1.37×10^{-6}	0.88	23
0.6	-0.85	-0.03	3.12	0.7	3.9	0.3	-28.3	32.6	1.2	0.1	2.00×10^{-6}	1.09	23
0.7	-0.85	-0.03	3.08	0.8	3.7	0.3	-28.7	33.0	1.1	0.1	2.71×10^{-6}	1.29	24
0.8	-0.84	-0.02	3.05	0.8	3.6	0.3	-29.1	33.4	1.0	0.1	3.52×10^{-6}	1.48	21
0.9	-0.84	-0.02	3.02	0.7	3.5	0.3	-29.4	33.6	0.9	0.1	4.40×10^{-6}	1.67	32
1.0	-0.84	-0.02	3.00	0.6	3.4	0.3	-29.5	33.7	0.8	0.1	5.34×10^{-6}	1.85	30
1.1	-0.84	-0.02	2.98	0.6	3.3	0.3	-29.6	33.6	0.8	0.1	6.34×10^{-6}	2.03	32
1.2	-0.83	-0.02	2.96	0.6	3.3	0.3	-29.6	33.4	0.7	0.1	7.38×10^{-6}	2.21	37
1.3	-0.83	-0.02	2.94	0.5	3.2	0.3	-29.5	33.2	0.7	0.2	8.47×10^{-6}	2.38	39

In the provided table 5.1, it is observed that as the value of ω increases, the optimization rate also increases. At $\omega = 1.3$, the rate reaches its peak with a value of 8.47×10^{-6} , while at $\omega = 0.1$, the rate hits its lowest point at 2.01×10^{-8} . Interestingly, when we analyze the twist of the molecular fragments, we notice that as ω increases to boost the rate, the twist in the molecule decreases. Specifically, the dimer with the lowest twist achieves the highest rate. Furthermore, as the optimization rate increases, the curvature of the optimised molecule also increases. During the optimization process, it's observed that the two fragments exhibit opposite curvature, leading to opposite signs. For instance, the curvature of the molecule optimized with $\omega = 0.1$ is -8.6 and 8.5 for fragments A and B, respectively. In contrast, the curvature of the molecule optimized with $\omega = 1.3$ is significantly higher, with values of -29.5 and 33.2 for fragments A and B, respectively, reflecting its higher rate. Additionally, it's noteworthy that as ω increases, the energy difference (ΔE) also increases. Lastly, the convergence behaviour of the optimization process is influenced by the choice of ω . When ω is low, a higher number of steps is required to achieve convergence, whereas with high ω , the convergence rate of optimization is slower. The highest convergence rate is attained at $\omega = 0.8$, accomplished within 21 steps. Overall, the optimization performed with $\omega = 0.8$ stands out as the most successful. With a rate of 3.52×10^{-6} , this configuration demonstrates the highest optimization efficiency. Moreover, the resulting molecular twist is with values of 1.0° for fragment A and 0.1° for fragment B. Additionally, the curvature of the optimized structure is high, with fragment A exhibiting a curvature of -29.4 and fragment B with 33.6.

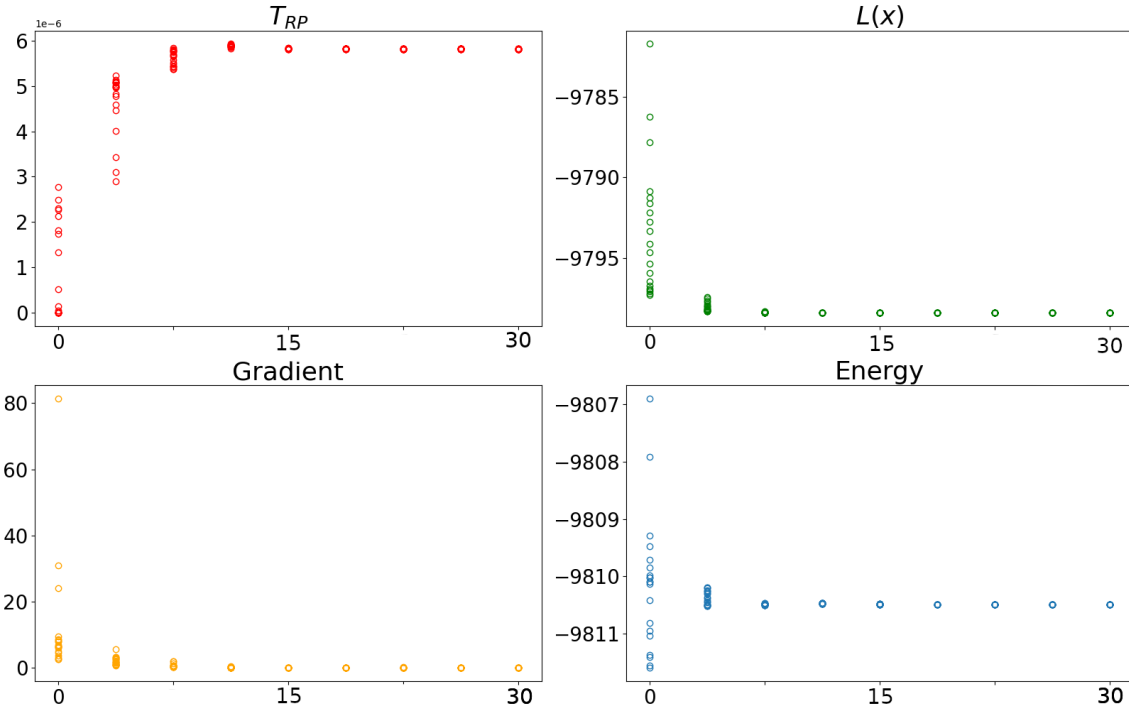


Figure 5.9: Variation of parameters during optimisation: a) Increment of T_{RP} , b) Evolution of optimisation function, c) Evolution of gradient d) Evolution of energy

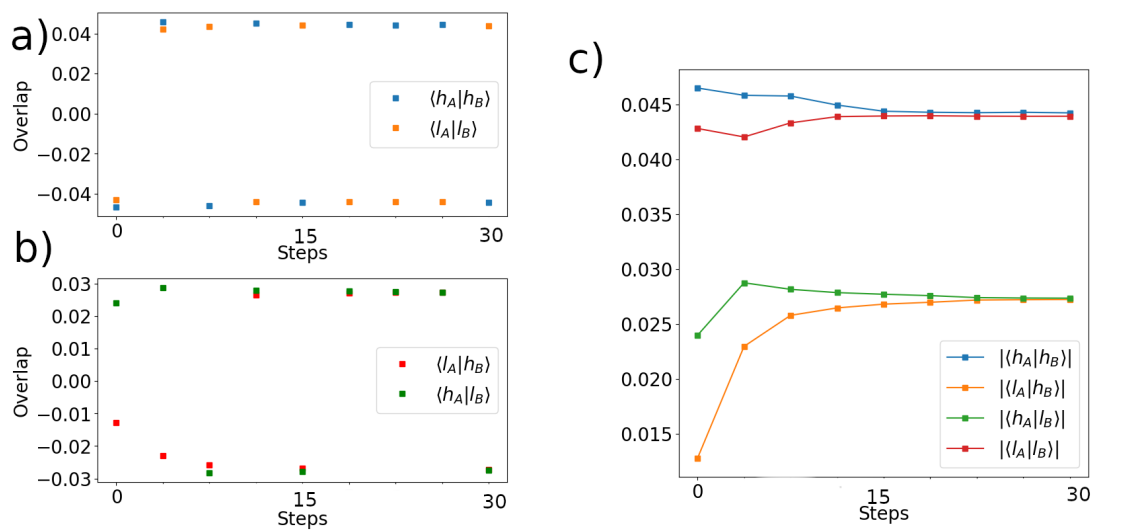


Figure 5.10: Evolution of orbital overlap:

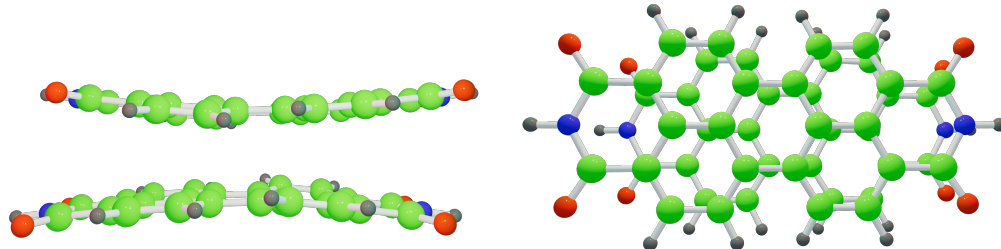


Figure 5.11: Side and top view of optimized structure by SF optimising functional

5.4 Conclusion

In this chapter, we investigate variations in electronic coupling within cofacially stacked PDI dimers as a function of rotation along an axis orthogonal to the facial plane. We employed the semi-empirical SFast method and active space decomposition model Hamiltonian analysis for this study.

The SFast method offers computational efficiency, enabling the exploration of 2D translation and rotation of the monomers. In contrast, the ASD model Hamiltonian analysis involved translating one of the monomers in the x-direction and rotating it along the Z-axis. These manipulations of molecular geometry aimed to explore how changes in the relative orientations of the dimers affect electronic couplings between different diabatic electronic states.

Our observations revealed that electronic couplings are generally higher when rotation is at 0 °, particularly evident for CT⁻¹(TT) and LE-CT transitions. However, notable enhancements in coupling values were observed at rotation angles between 50° and 60°, particularly in the slipped stack position $\Delta X = 0.7 \text{ \AA}$, $\Delta Y = 0.0 \text{ \AA}$.

Although the coupling corresponding to LE⁻¹(TT) transitions is lower compared to LE-CT and CT⁻¹(TT) transitions, we observed an increase in coupling values upon rotation. This suggests that changes in molecular orientation, especially for the dark LE state, can enhance singlet fission processes. High coupling of CT⁻¹(TT), where LE-CT coupling is also high, whereas LE⁻¹(TT) coupling is low, suggests a preference for both mediated and excimer-mediated pathways. Subsequently, we devised a function to enhance the singlet fission efficiency of the dimer, considering all degrees of freedom. We obtained molecular structures with a bow-shaped conformation and with a twisted molecular structure.

The analysis of structural features was conducted by varying the value of ω to achieve a higher singlet T_{RP} . It was observed that increasing the value of ω led to a higher singlet fission rate. This increase was accompanied by an increase in the curvature of the PDI along its long axis. This observation qualitatively aligns with experimental findings reported in reference [269].

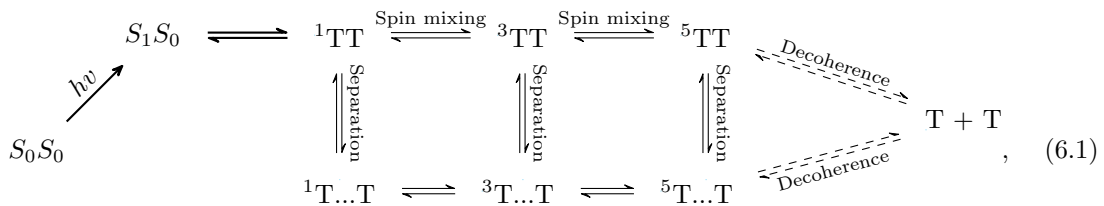
We have employed a semi-classical approach based on Marcus' theory to compute SF rates for parallel PDI dimers, systematically altering their relative displacement along both the short and long axes. Through these calculations, SF rates were determined for two distinct pathways: the direct and mediated two-step mechanisms. Importantly, the results revealed a strong correlation between the total triplet yield and the value of two-electron coupling. Furthermore, electronic structure calculations have demonstrated that the electronic properties of PDIs are highly dependent on the rotation along the Z-axis between two PDI monomers. In conjunction with experimental observations, these insights have motivated the exploration of SF efficiency in dimeric PDI systems with varying rotation along the Z-axis.

Chapter 6

Tensor Modeling for Singlet Fission Using Jordan Wigner Mapping of Symbolic Qubit(Symbolic CI)

6.1 Introduction

Singlet fission is a process in which a singly excited singlet exciton converts into two triplets upon interaction with ground states of neighboring molecules [273, 56]. Despite being a very promising process for highly efficient organic and inorganic solar cells, electronics, photonics, and quantum computing applications, it is complex to study and implement [29, 21]. The phenomenon is elucidated as shown in Equation 6.1, where an electron in the ground state gets excited by photons to S_1 , forming a spin-allowed correlated triplet pair ${}^1\text{TT}$. This triplet state further goes on to form many other possibilities, including separated correlated ${}^1(\text{T...T})$, uncorrelated T+T , and triplet pairs of higher multiplicities ${}^3(\text{TT})$, ${}^5(\text{TT})$. Time-resolved electron paramagnetic resonance has been utilized to observe the transportation of singlet and quintet characters.[274, 21, 275] EPR experiments traverse magnetization depending on \mathbf{S} and \mathbf{S}_z . \mathbf{S} represent spin angular momentum and \mathbf{S}_z represent the high spin state. EPR signal intensity ${}^1(\text{TT}) \longleftrightarrow {}^s(\text{TT})$ is proportional to the corresponding transition character [275]. The triplet-triplet dissociation process representation:



provides insight into the energy manifold of the different multiplicity (s) of biexcitonic ${}^s(\text{TT})$ character.

Usually, the close packing in molecular aggregates increases the electronic coupling between the initial singlet state and ${}^1(\text{TT})$, which hint to high yeild of ${}^1(\text{TT})$ but can lead to decoherence via triplet-triplet annihilation depending on the energy level of the initial bright state and the ${}^1(\text{TT})$ state [276, 277]. For ${}^s(\text{TT})$ state that are energetically favorable, it has been shown that lowering this coupling can lead to higher yields of the separated triplets (T+T) from ${}^1(\text{TT})$ in the case of intramolecular singlet fission. [25]

The formation of ${}^1(\text{T...T})$ has recently been shown to improve the final triplet yield in covalently linked tetracene trimers and tetramers [278](41). Spatially separated yet spin-entangled ${}^1(\text{T...T})$ states have been proposed as a possible intermediate [279] and have subsequently been characterized experimentally [280, 281]. The transition model among ${}^s(\text{TT})$ s have been proposed for the formation of these states [280, 281, 88, 282]. Also, the formation of ${}^s(\text{TT})$ and ${}^s(\text{T...T})$ proceed with a charge transfer intermediate process [185, 53]. This complex interplay among the

states provides numerous utilities. On one hand, the long-lived T+T on different monomers is desirable for photovoltaic applications; on the other hand, the kinetically stabilized ${}^1(T\ldots T)$ bears quantum entanglement and highly suitable for quantum computing applications [20, 22, 23]. Organic materials showing singlet fission have potential utilization in ultra-fast switching and data storage [283]. Transformation of ${}^1(TT)$ to ${}^1(T\ldots T)$ happens without involving spin-orbit coupling, whereas spin-spin coupling becomes inevitable for interchange among ${}^1(TT)$, ${}^3(TT)$, and ${}^5(TT)$ (similarly among ${}^1(T\ldots T)$, ${}^3(T\ldots T)$, and ${}^5(T\ldots T)$ [284, 285]. To study the interplay of various ${}^s(TT)$ states and explore their utility in different fields, an effective model is required.

The widely adopted Merrifield model for singlet fission is reverse of the model proposed for the triplet-triplet annihilation process. It uses 9 spin state expressions to study the kinetics as three types of triplet pairs in triplet multiplicity get annihilated to form a singlet.[38] The model has been used to explain many experimental observations. It just assumes the degeneracy of orbitals and electrons are considered unpaired thus considering only spin perturbation and neglecting the spatial portion. Thus reducing adequacy for singlet fission study [56, 17] Later on, a complete 16-state model was derived by Scholes et al. where he discussed all the possible spin states by a combination of 4 electrons using a branching diagram that includes the presence of entanglement of triplet pair state ${}^1(TT)$ as they get separated with density operators[178]. G. Tao and Y Tan propose a modular tensor diagram for 16 spin states models of exciton pair for computation of diabatic energy of all the possible spin states and show the hierarchical symmetry[23]. The work discussed the energies of the 16 spin eigenstates in the context HOMO and LUMO. Again Tao and Tan used the same approach to get the many-body wave function of the spin state of singlet fission for a 6 electron in 6 orbitals system and further derived the expression for energy of all the 64 states. They identified 64 states to represent all the possible multiplicities. They formulated the expression for energy and gave the expression for the transition density operator using the quantum Liouville equation to calculate the transition rate among the states. [286]. Though the model was meticulously crafted for all states formed in the trimer system, the branching diagram model generates spin-only configuration functions Slater determinant and the model considers unpaired electrons. Since electrons in the same spatial orbital should be in an antisymmetric configuration, G D Scholes suggested a modified permutation operator for pairing the electron[178]. In most cases, singlet fission is facilitated by charge transfer states and excimer formation. [265]. To properly study the relationships of the states involved in singlet fission a model comprising properly distributed electrons in spatial orbitals and suitable permutation operators should be used, which provides proper perturbation operators as per the nature of interaction of LE, CT or multi-exiton states.

A simple model involving the charge transfer state in dimers is given by Josef Michl and coworkers [287, 162]. In the dimer model, there are only 2 charge transfer states and the coupling between the charge transfer state is low. The charge transfer states are combined states of cation and anion monomers formed by the lack and access of electrons in the spatial orbitals, respectively. In aggregates, multiple possibilities of charge transfer states are formed, and coupling among these influences the rate of formation ${}^1(TT)$. As the number of monomers and electrons increases, automation is needed for the generation of expression of energy and coupling to analyse the transition rate. The second quantisation protocol uses creation and annihilation operators for the calculation of elements of Hamiltonian. It allows, the study of processes, such as electronic transitions, quantum interference, and population transfer between electronic states. Burton et al. used the Wicks theorem for the second quantisation to generate the matrix element of the Hamiltonian [288, 289]. Another approach to perform the second quantisation is using the Jordan Wigner transformation. Jordan Wigner transformation uses Paulie's matrix to represent the creation and annihilation operators to incorporate Paulie's exclusion principle for entangled electrons[175] The creation and annihilation operators formed by Jordan Wigner transformation are widely used in tensor method for entangled electrons.[290, 291, 292, 293, 294] Though these methods are very efficient in calculating the electronic structure. Our goal was to develop an analytical understanding of the complexity of interacting states involved in singlet fission. Thus, we adapted the use of symbolic algebra to obtain the expressions of Hamiltonian matrix elements. Spin-adapted creation and annihilation operators created as per Jordan Wigner's transformation using a symbolic non-commutative variable for spin orbitals give the fermionic operators for the pairing of the spin chain. We are presenting descriptive educational tools to understand the complexity of the spin state of the wave function as well as all second quantisation approaches automatically generate the wave function and diabatic Hamiltonian operator [295, 296]. The diabatic Hamiltonian provides a convenient representation for describing the coupling between different electronic states in terms

of electron-electron and electron-nuclear interaction.

6.2 Method

6.2.1 Operators

It is convenient to use the language of second quantization when treating a general many-body problem. In the second quantization, we assume that a complete set of one-particle operators with corresponding eigenvalues generates a complete set of one-particle states for the system under consideration. We can generate the states in the Fock space by use of creation operators. The general state in Fock space may be constructed by applying a succession of creation operators to the vacuum state. Application of an annihilation operator to the given state yields state representation without the electron corresponding to the annihilation operator. The creation and annihilation operators for fermions satisfy anticommutation relations. This reflects the fact that fermions cannot occupy the same quantum state simultaneously. The creation and annihilation operators are made using Jordan Wigner [175] Transform. Equation 6.2 and 6.3 gives the creation and annihilation operator for an electron at site n as:

$$a_n^\dagger = s \otimes s \otimes \dots \otimes s \otimes a^\dagger \otimes 1 \otimes \dots \otimes 1 \otimes 1 \quad (6.2)$$

and

$$a_n = s \otimes s \otimes \dots \otimes s \otimes a \otimes 1 \otimes \dots \otimes 1 \otimes 1, \quad (6.3)$$

where a^\dagger and a are the creation and annihilation operators of single spinless particles respectively. Where $a^\dagger = \sigma_x - i\sigma_y$ and $a = \sigma_x + i\sigma_y$ and $s = \sigma_z$. σ_x, σ_y and σ_z are the Pauli matrices and represent a projection of the spin of one electron on x, y, z axis respectively. The operators are spin-adapted as per the equation shown below:

$$a_{\uparrow n}^\dagger = \mathbf{s} \otimes \dots \otimes \mathbf{s} \otimes a_\uparrow^\dagger \otimes 1^2 \otimes \dots \otimes 1^2, \quad (6.4)$$

$$a_{\downarrow n}^\dagger = \mathbf{s} \otimes \dots \otimes \mathbf{s} \otimes a_\downarrow^\dagger \otimes 1^2 \otimes \dots \otimes 1^2 \quad (6.5)$$

and

$$a_\uparrow^\dagger |-\rangle = |\uparrow\rangle, \quad (6.6)$$

where \uparrow represent α electrons and $a_\uparrow^\dagger = a^\dagger \otimes 1$. \downarrow represents the β electrons and $a_\downarrow^\dagger = s \otimes a^\dagger$. Here $\mathbf{s} = s \otimes s$ and $1^2 = 1 \otimes 1$. Similarly, the annihilation operators can be made using $(a^\dagger)^\top$. Operators for an electron of spin σ in spatial orbital ψ are made as per equation 6.7:

$$\mathbf{a}_{\sigma\psi}^\dagger = (\mathbf{s} \otimes \dots \otimes \mathbf{s} \otimes a_\sigma^\dagger \otimes 1^2 \otimes \dots \otimes 1^2)\psi. \quad (6.7)$$

We are employing two different representations of operators for automation purposes. 1) The creation operators used to represent the operators in the Hamiltonian called here symbolic operators, are presented by multiplying the symbol representing the molecular orbital, as shown in Equation 6.7. We have used a bold character for a symbolic operator, $\mathbf{a}_{\uparrow h_1}^\dagger$. 2) The creation operator called here numerical operator, is used for the wave function of a state and is not multiplied with a symbol. The operator employed in the wave function is presented in normal script, $a_{\uparrow h_1}^\dagger$.

For an example, let's consider a system characterized by 2 electrons distributed across 2 spin sites within a single spatial orbital. The numerical creation operators are constructed according to equations 6.4 and 6.5. These spin sites are designated as $h_{1\uparrow}$ and $h_{1\downarrow}$, and the numerical creation operator are

$$c_{\uparrow h_1}^\dagger = \begin{bmatrix} 0 & 0 & 0 & 0 \\ 0 & 0 & 0 & 0 \\ 1 & 0 & 0 & 0 \\ 0 & 1 & 0 & 0 \end{bmatrix} \quad (6.8)$$

and

$$c_{\downarrow h_1}^\dagger = \begin{bmatrix} 0 & 0 & 0 & 0 \\ 1 & 0 & 0 & 0 \\ 0 & 0 & 0 & 0 \\ 0 & 0 & -1 & 0 \end{bmatrix}. \quad (6.9)$$

For the $h_{1\uparrow}$ spin site, $\mathbf{c}_{\uparrow h_1}^\dagger$ is a 4×4 matrix given by

$$\mathbf{c}_{\uparrow h_1}^\dagger = \begin{bmatrix} 0 & 0 & 0 & 0 \\ 0 & 0 & 0 & 0 \\ h_{1\uparrow} & 0 & 0 & 0 \\ 0 & h_{1\uparrow} & 0 & 0 \end{bmatrix}, \quad (6.10)$$

indicating off-diagonal elements for the $h_{1\uparrow}$ orbital with an up-spin electron and spatial orbital h . Similarly, for the $h_{1\downarrow}$ spin site, $\mathbf{c}_{\downarrow h_1}^\dagger$ is a 4×4 matrix from

$$\mathbf{c}_{\downarrow h_1}^\dagger = \begin{bmatrix} 0 & 0 & 0 & 0 \\ h_{1\downarrow} & 0 & 0 & 0 \\ 0 & 0 & 0 & 0 \\ 0 & 0 & -h_{1\downarrow} & 0 \end{bmatrix}, \quad (6.11)$$

with off-diagonal components representing the $h_{1\downarrow}$ orbital and a down-spin electron and same spatial orbital.

Now, turning to the state vector manipulations:

$$|-\rangle = \begin{bmatrix} 1 \\ 0 \\ 0 \\ 0 \end{bmatrix} \quad (6.12)$$

represents a vacuum state vector. Upon application of a set of numerical operators in a vacuum state, gives ± 1 non-zero element,

$$c_{\uparrow h_1}^\dagger c_{\downarrow h_1}^\dagger |-\rangle = \begin{bmatrix} 0 \\ 0 \\ 0 \\ 1 \end{bmatrix} \quad (6.13)$$

and

$$c_{\downarrow h_1}^\dagger c_{\uparrow h_1}^\dagger |-\rangle = \begin{bmatrix} 0 \\ 0 \\ 0 \\ -1 \end{bmatrix}. \quad (6.14)$$

Applying the symbolic creation operator $\mathbf{c}_{\downarrow h_1}^\dagger$ to $|-\rangle$:

$$\mathbf{c}_{\uparrow h_1}^\dagger |-\rangle = \begin{bmatrix} 0 \\ 0 \\ h_{1\uparrow} \\ 0 \end{bmatrix} \quad (6.15)$$

yields a new state vector in which the third component corresponds to the orbital $h_{1\uparrow}$, which means the addition of a down spin electron. The other components remain unchanged. On the other hand, the application of $\mathbf{c}_{\uparrow h_1}^\dagger$ on $|-\rangle$:

$$\mathbf{c}_{\downarrow h_1}^\dagger |-\rangle = \begin{bmatrix} 0 \\ h_{1\downarrow} \\ 0 \\ 0 \end{bmatrix} \quad (6.16)$$

leads to a state vector in which the second component corresponds to the $h_{1\downarrow}$ orbital, indicating the inclusion of an up-spin electron. Further exploration involves applying both creation operators sequentially: $\mathbf{c}_{\uparrow h_1}^\dagger \mathbf{c}_{\downarrow h_1}^\dagger |-\rangle$:

$$\mathbf{c}_{\uparrow h_1}^\dagger \mathbf{c}_{\downarrow h_1}^\dagger |-\rangle = \begin{bmatrix} 0 \\ 0 \\ 0 \\ h_{1\uparrow} h_{1\downarrow} \end{bmatrix} \quad (6.17)$$

leads to a new state vector where the fourth component represents a combined symbol of both $h_{1\uparrow}$ and $h_{1\downarrow}$, indicating the presence of 2 electrons in the orbitals. Interestingly, the reversed order, $\mathbf{c}_{\downarrow h_1}^\dagger \mathbf{c}_{\uparrow h_1}^\dagger |-\rangle$,

$$\mathbf{c}_{\downarrow h_1}^\dagger \mathbf{c}_{\uparrow h_1}^\dagger |-\rangle = \begin{bmatrix} 0 \\ 0 \\ 0 \\ -h_{1\downarrow} h_{1\uparrow} \end{bmatrix} \quad (6.18)$$

shows similar combined symbols but with a negative sign, illustrating the anti-commutation behaviour of fermionic operators. One electron operator for one electron integral (i,j) is:

$$\mathbf{T}_{(i,j)} = \sum_{o_i, j, s} \mathbf{a}_{o_i, s}^\dagger \mathbf{a}_{o_j, s}. \quad (6.19)$$

Similarly Electron Repulsion operator for the two elctron integral $\langle ij|lk\rangle$:

$$\mathbf{V}_{\langle ij|lk\rangle} = \frac{1}{2} \sum_{o_i, j, k, l, s} \mathbf{a}_{o_i, s}^\dagger \mathbf{a}_{o_j, s}^\dagger \mathbf{a}_{o_k, s} \mathbf{a}_{o_l, s}. \quad (6.20)$$

A schematic of the one-electron operator and its interaction with many-electron states is demonstrated in Appendix. We are utilising the second quantisation for the formulation of Hamiltonian for the aggregates as:

$$H = \sum_{i,j=1}^d \sum_{s_i, s_j = \uparrow, \downarrow} T_{ij} \mathbf{a}_{i, s_i}^\dagger \mathbf{a}_{j, s_j} + \frac{1}{2} \sum_{i,j,k,l=1}^d \sum_{s_i, s_j, s_k, s_l = \uparrow, \downarrow} V_{ijkl} \mathbf{a}_{i, s_i}^\dagger \mathbf{a}_{j, s_j}^\dagger \mathbf{a}_{k, s_k} \mathbf{a}_{l, s_l} \quad (6.21)$$

and

$$\langle \Psi_m | \hat{H} | \Psi_n \rangle = \sum_{i,j=1}^d \sum_{s_i, s_j = \uparrow, \downarrow} T_{ij} \langle \Psi_m | \mathbf{a}_{i, s_i}^\dagger \mathbf{a}_{j, s_j} | \Psi_n \rangle + \frac{1}{2} \sum_{i,j,k,l=1}^d \sum_{s_i, s_j, s_k, s_l = \uparrow, \downarrow} V_{ijkl} \langle \Psi_m | \mathbf{a}_{i, s_i}^\dagger \mathbf{a}_{j, s_j}^\dagger \mathbf{a}_{k, s_k} \mathbf{a}_{l, s_l} | \Psi_n \rangle, \quad (6.22)$$

here, T_{ij} is an electron integral and adjacent set of operators $|\mathbf{a}_{i, s_i}^\dagger \mathbf{a}_{j, s_j}|$ are the one electron integral operator \mathbf{T} . V_{ijkl} is two electron integral of the molecular orbitals (i, j, k, l) and adjacent set of operators, $|\mathbf{a}_{i, s_i}^\dagger \mathbf{a}_{j, s_j}^\dagger \mathbf{a}_{k, s_k} \mathbf{a}_{l, s_l}|$ are the two electron integral operators or electron repulsion operator \mathbf{V} . $\mathbf{a}_{i, s_i}^\dagger$ and \mathbf{a}_{i, s_i} are the symbolic creation and annihilation operators respectively for orbital i with spin s_i . The integrals, T_{ij} and V_{ijkl} are calculated by transforming the atomic orbital integral molecular orbital integrals. The wave functions Ψ_m and Ψ_n are made using numerical operators. Upon utilisation of equation 8.3 for a given pair of wave function configuration expressions, the coupling expression is extracted from the $(0,0)$ index of the Hamiltonian matrix upon application of given wave functions. These equations are implemented in code using the sympy library for symbolic math operations in Python.

6.2.2 Branching Diagram

The multi-configuration representation of an N -electron wave function is a linear combination of all possible N -electron determinants formed from a complete set of spin orbitals. The electron addition sequence of a determinant is the sequence of spin orbitals that are added to the vacuum state to create the determinant. One way to obtain the electron addition sequence of a determinant is to use a branching diagram. A branching diagram is a network structure, with the root node representing the vacuum state. Each node in the network represents a determinant with S^2 or S_z when a certain number of electrons are added. To construct a branching diagram, we start at the root node and add the electrons to the vacuum state. At each step, we consider all possible

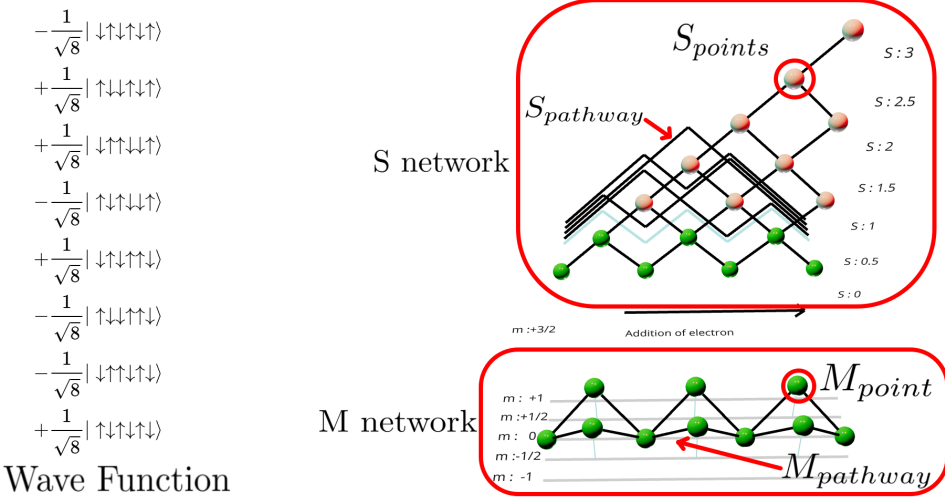


Figure 6.1: Branching diagram generated by the algorithm. Wave function based on S network and M network. The generated S network gives all the eigenstates of \mathbf{S}^2 for a given number of unpaired electrons. S_{points} corresponds to the number of electrons and multiplicity. $S_{pathway}$ gives the combination of multiplicities to the final multiplicity. The generated M network gives the eigenstates of \mathbf{S}_z for a given number of unpaired electrons

ways to add the next electron and create a new node for each possibility. The branching diagram terminates when all N electrons have been added. It is computationally efficient and avoids the construction of whole \mathbf{S} and \mathbf{S}_z matrix. We initiate the construction of a branching diagram using the class \mathbf{S} , representing multiplicity as y with the addition of x electrons. The third attribute called the `connection_list`, retains references to previous multiplicities from which the current multiplicity y can be reached by adding one electron. To form connections among these \mathbf{S} objects and track multiplicity evolution, we create a \mathbf{S} network. This network links existing \mathbf{S} objects, representing \mathbf{S} states formed by electron additions. The result is a network of interconnected \mathbf{S} objects, representing diverse electron addition sequences leading to desired multiplicities. Our objective with the \mathbf{S} diagram is to trace these connections and identify the electron addition sequences achieving the desired overall multiplicity.

```
class S {
    int x = 0; # electron chain
    int y = 0; # multiplicity
    list connection_list = [...]
}
```

The algorithm presented as Algorithm 1 is used in the generation of S points. This algorithm follows the concept outlined in [131]. In Algorithm 1, the variable i represents the number of electrons, while j corresponds to 2 times the value of $\mathbf{S}.y$. The algorithm begins by initializing an empty array called S_{points} , which serves as a container for the generated \mathbf{S} object. For each value of i from 0 to $n_electrons + 1$, a new blank array is added to the at $S_{points}[i]$. This array will hold the class \mathbf{S} objects corresponding to the specific electron configuration and multiplicity. Within a nested loop structure, the variable j ranges from 0 to $i + 1$. During each iteration, the algorithm checks if the difference between i and j is an even number. When this condition is met, it signifies that the corresponding \mathbf{S} object, with attributes ($x = i, y = j$), should be included in the S network. The choice of j is based on the understanding that $2S$ reflects the number of unpaired electrons in the system. By subtracting the count of unpaired electrons from the total number of electrons, we obtain the count of paired electrons, which should thus be an even number. Consequently, the algorithm appends this \mathbf{S} object to the end of the array associated with the S_{points} at index i . The resulting array within $S_{points}[i]$ contains all the \mathbf{S} objects representing the electron configurations that lead to a particular multiplicity. The S network is represented as a triangular 2D array, where each S_{point} corresponds to a specific electron configuration and multiplicity. Within the S network, consecutive pairs of S points, $S_{point}[2n]$ and $S_{point}[2n+1]$, have the same number of elements, each representing a distinct multiplicity value. This arrangement facilitates the subsequent connection

Algorithm 1 S_{points} generation Algorithm

Require: $n \geq 2$

- 1: $S_{points} \leftarrow [...]$ ▷ Blank array
- 2: $n_electrons \leftarrow n$
- 3: **for** $i \leftarrow 0$ to $n_electrons + 1$ **do**
- 4: Add [...] at $S_{point}[i]$ ▷ add blank array in the end
- 5: **for** $j \leftarrow 0$ to $i + 1$ **do**
- 6: **if** $i - j$ is even **then**
- 7: Add object $S(x=i,y=j)$ to end of $S_{points}[i]$
- 8: **end if**
- 9: **end for**
- 10: **end for**

process.

Algorithm 2 systematically establishes connections between the S object based on the value of y . It iterates over the S object, considering each point represented by $S_{point}[i][j]$. The algorithm then examines the neighboring S object in the previous electron multiplicity, namely $S_{point}[i-1][j]$, $S_{point}[i-1][j-1]$, and $S_{point}[i-1][j+1]$, and creates connections accordingly.

These connections are made by adding the corresponding S objects to the *connection_list* attribute of the current S object. The *connection_list* attribute is an array associated with each S object, serving as a repository for storing the S objects to which the current S objects are connected. By populating the *connection_list* of each S object, the algorithm establishes the links between S objects, thereby completing the construction of the network of interconnected S_{points} . The execution of Algorithm 2 ensures that all relevant connections are established within the S network.

Algorithm 2 S network Creation

```

for  $i \leftarrow 0$  to length of  $S_{points}$  do
    for  $j \leftarrow 0$  to length of  $S_{points}[i]$  do
        if  $i > 0$  then
            if  $j < \text{length of } S_{points}[i - 1]$  then
                add  $S_{points}[i - 1][j]$  to end of  $S_{points}[i][j].connection\_list$ 
            end if
        end if
        if  $j > 0$  then
            if  $i$  is even then
                add  $S_{points}[i - 1][j - 1]$  to end of  $S_{points}[i][j].connection\_list$ 
            end if
        end if
        if  $j + 1 < \text{length of } S_{points}[i - 1]$  then
            if  $i$  is odd then
                add  $S_{points}[i - 1][j + 1]$  to end of  $S_{points}[i][j].connection\_list$ 
            end if
        end if
    end for
end for

```

Once the fully formed S_{point} network is generated, it serves as the basis for constructing the chain of S configuration states. This chain represents the sequence of multiplicities that form within the system as electrons are added. To generate this chain, one selects a desired final multiplicity and begins from the corresponding S_{point} element. By following the connections between S_{point} elements and their associated previous connections, a list of S object chains is obtained.

Algorithm 3 generates the S object chains by recursively and dynamically executing the necessary operations. The algorithm utilizes a utility array named $S_{pathway}$, which is initially set with an unreachable value of S (ie., -1). This array keeps track of the sequence of multiplicities encountered during the exploration of the S network.

The function FOLLOW PREVIOUS is at the heart of Algorithm 3. It takes as input the current

S_{point} element and the $S_{pathway}$ array. The function follows the connections between \mathbf{S} that lie at the $(i - 1)$ of S_{point} and are connected to the current S_{point} element at index (i, j) . To do so, the function calls itself recursively for each S_{point} element in the *connection_list* of the current S_{point} element. This recursive process continues until the end of the network is reached.

During the recursive execution of FOLLOW PREVIOUS, the algorithm records the multiplicities of the S_{point} elements encountered in the $S_{pathway}$ array. When the end of the network is reached, indicated by all values in the $S_{pathway}$ array being set, a copy of the $S_{pathway}$ array is added to the collection $ALL_S_{pathways}$. This collection contains all the distinct electron addition sequences of multiplicities that lead to the desired final multiplicity.

Algorithm 3 can systematically explore and analyze the various electron addition sequences within the \mathbf{S} network. This algorithm efficiently generates the \mathbf{S} object chain by traversing the network, recording the multiplicities encountered along the way, and storing them in the $ALL_S_{pathways}$ collection. This allows for a comprehensive understanding of the possible electron configurations and multiplicities that arise during the addition of electrons to the system.

Algorithm 3 Make chain of \mathbf{S}

Require: \mathbf{S} ▷ Final S_{point}

- 1: $S_{pathway} \leftarrow [-1, -1, -1, \dots]$ ▷ Initialize the array of electron addition sequences with -1
- 2: $ALL_S_{pathways} \leftarrow [\dots]$
- 3: **function** FOLLOW PREVIOUS($S, S_{pathway}$)
- 4: **if** length of $S.list = 0$ **then**
- 5: $S_{pathway}[S.x] \leftarrow S.y$
- 6: **if** $-1 \notin S_{pathway}$ **then**
- 7: add a copy of $S_{pathway}$ to $ALL_S_{pathways}$
- 8: **end if**
- 9: **end if**
- 10: **for** $k \leftarrow 0$ to length of $S.connection_list$ **do**
- 11: $S_{pathway}[S.x] \leftarrow S.y$
- 12: FOLLOW PREVIOUS($S.connection_list[k], S_{pathway}$)
- 13: **end for**
- 14: **end function**

```
class M {
    int x = 0;  # electron chain
    int y = 0;  # M
    list connection_list = [...]
}
```

In the exploration of the configuration state function, a particular electron addition sequence from $ALL_S_{pathway}$ is chosen to create the corresponding \mathbf{M} network. In this context, m represents the high spin state $\hat{\mathbf{S}}_z$. The \mathbf{M} network is constructed as a non-rectangular 2D array called M_{points} . The elements in the M_{points} are \mathbf{M} objects. The range of m spans from - S to S , with a difference of 1 between consecutive points. The class named \mathbf{M} is defined, where the y attribute refers to the value of m after the addition of x electrons in the spin chain of \mathbf{S} . The *connection_list* of \mathbf{M} object in the \mathbf{M} network establishes connections to the previous points in the network that were formed by the addition of previous electrons. This creation of the \mathbf{M} network enables the construction of the Configuration state function using m as per the \mathbf{S} chain. The algorithm presented as Generate M_{points} utilizes the information from the \mathbf{S} in $S_{pathway}$ to determine the maximum and minimum values of m (denoted as M_{max} and M_{min} respectively). It then constructs the \mathbf{M} network by iterating through the elements of the $S_{pathway}$ and creating \mathbf{M} objects within the appropriate range of m . These \mathbf{M} objects are added to the corresponding M_{points} element, resulting in the formation of the \mathbf{M} object points in the \mathbf{M} network.

The creation of the \mathbf{M} network involves establishing connections between the M_{points} that are generated by the addition of n electrons and the \mathbf{M} points that are created by the addition of $n - 1$ electrons. The addition of a single electron can lead to a change in the value of y of \mathbf{M} by either $+\frac{1}{2}$ or $-\frac{1}{2}$. Therefore, to connect the M_{points} , we examine the difference between their

Algorithm 4 Generate M_{points}

Require: $S_{pathway}$ ▷ List of S in the chain

```

 $M\_max \leftarrow S_{pathway}$ 
 $M\_min \leftarrow -1 \times S_{pathway}$ 
 $M_{Points} \leftarrow [...]$ 
for  $i \leftarrow 0$  to length of  $S_{pathway}$  do
    Add [...] to  $M_{Points}$ 
    for  $j \leftarrow M\_min[i]$  to  $M\_max[i] + 1$  with step size = 1 do
        Add object  $M(i, j)$  to  $M_{Points}[i]$ 
    end for
end for
end for

```

Algorithm 5 Make point M_{point} connections

```

for  $i \leftarrow 0$  to length of  $M_{point}$  do
    for  $j \leftarrow 0$  to length of  $M_{point}[i]$  do
        if  $i > 0$  then
            for  $k \leftarrow 0$  to length of  $M_{point}[i - 1]$  do
                if  $|M_{point}[i - 1][k].y - M_{point}[i][j].y| = \frac{1}{2}$  then
                    Add  $M_{point}[i-1][k]$  to end of  $M_{point}[i][j].connection\_list$ 
                end if
            end for
        end if
    end for
end for

```

respective values of y of M . If the difference is equal to $\frac{1}{2}$, the M_{points} are connected, representing the transition between neighbouring spin states.

To implement this connectivity, the algorithm "Make point M_{point} connections" is employed. It iterates through each element in the M_{point} array, starting from the first M in the network and progressing to subsequent M_{point} elements. For each element, it checks if there is a preceding electron chain (i.e., $i > 0$). If so, it further iterates through the M points in the preceding electron chain. For each pair of M_{points} from the current and preceding chains, it compares the absolute difference in their values of y of M . If the absolute difference is equal to $\frac{1}{2}$, indicating a change of $+\frac{1}{2}$ or $-\frac{1}{2}$ in y , the two M_{points} elements are connected. The M from the preceding chain is added to the *connection_list* of the M in the current chain.

Algorithm 6 Clebsch-Gordan of spin chain

Require: $S_{pathway}$: numpy array of a desired $S_{pathway}$ to the final multiplicity $S \in [s_0, s_1, s_2, s_3, \dots]$

Require: M : a 2D array of all the $M_{pathway}$ for a given $S_{pathway}$, $m \in [[{}^0m_0, {}^0m_1, \dots], [{}^1m_0, {}^1m_1, \dots], \dots]$

Require: CG : [...]

- 1: **for** j^{th} pathway in M **do**
- 2: $s_0 \leftarrow S_{pathway}[0]$
- 3: $m_0 \leftarrow M_{pathway}[j, 0]$
- 4: $s_1 \leftarrow S_{pathway}[1]$
- 5: $m_1 \leftarrow M_{pathway}[j, 1]$
- 6: $cg \leftarrow \text{ClebschGordan}(|s_0, m_0\rangle \otimes |{}^{\frac{1}{2}}(m_1 - m_0)\rangle, |s_1, m_1\rangle)$
- 7: **for** i in 1 to (length of $S_{pathway} - 1$) **do**
- 8: $cg \leftarrow cg \times \text{ClebschGordan}(|s_i, {}^j m_i\rangle \otimes |{}^{\frac{1}{2}}({}^j m_{i+1} - {}^j m_i)\rangle, |s_{i+1}, {}^j m_{i+1}\rangle)$
- 9: **end for**
- 10: **Add** cg to CG
- 11: **end for**
- 12: **return**(CG) ▷ return Clebsch-Gordan coefficient for the current pathway

The provided algorithm computes Clebsch-Gordan coefficients for a spin chain state, tailored

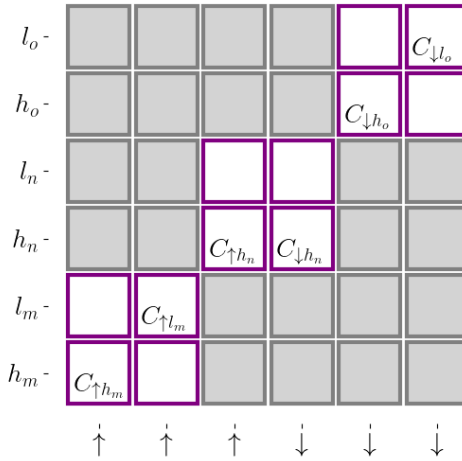


Figure 6.2: Distribution of electron in spatial orbital and construction of operators $T_1S_0T_1$

for a specific pathway to the final multiplicity S . It takes as input a numpy array $S_{pathway}$ representing the desired quantum numbers for the pathway to S , a 2D array M containing the associated magnetic quantum numbers m for each spin, and initializes an array CG to store the Clebsch-Gordan coefficients for each chain of M .

The algorithm iterates through each $M_{pathway}$, extracting the quantum numbers s_i and m_i for each spin in the process. It then initializes a Clebsch-Gordan coefficient (cg) to the Clebsch-Gordan coefficient between the first two spins. Using a loop, the algorithm iteratively calculates the Clebsch-Gordan coefficients for subsequent spins in the pathway, updating cg accordingly. The computed coefficients are added to the array CG for the current pathway.

The final output is the array CG , containing the Clebsch-Gordan coefficients for each pathway. This algorithm offers a specialized approach for efficiently obtaining Clebsch-Gordan coefficients, specifically tailored for spin chain states with a designated pathway to a desired final multiplicity.

6.2.3 Combining Spatial Orbital With Spin Chain

Once the branching diagram is constructed, we can obtain the electron addition sequence for a given determinant by tracing a path from the root node to the node representing the determinant. The electron addition sequence is simply the sequence of spin-orbital labels that we encounter along the path. The obtained wave function shown in equation 6.23 with spin only information is transformed to equation 8.6 upon the assignment of creation/annihilation operators with given spatial orbital and spin as per figure 6.2. Figure 6.2 shows how the spin and spatial orbital are merged to make creation operators. Each creation/annihilation operator is unique with its combination of spin and spatial term. One electron operator and Two electron operator is constructed with equation 6.19 and 6.20 respectively.

$$|\Psi_{(i)s}^{S_{pathway}}\rangle = \sum_k^{M_{pathways}} CG_k |s_1, m_1\rangle \otimes \dots \otimes |s_i, m_i\rangle \dots \otimes |s_n, m_n\rangle \quad (6.23)$$

$$|\Psi_{(i)s}^{S_{pathway}}\rangle = \sum_k^{M_{pathways}} \sum_k CG_k C^{\dagger \psi_i}_{|s,m\rangle_j} C^{\dagger \psi_i}_{|s,m\rangle_j} \dots |-\rangle \quad (6.24)$$

Where $s_i \in S_{pathway}$ and $m_i \in M_{pathway}$, $|\Psi_{(i)s}\rangle$ is the wave function operator of the desired state with overall multiplicity s and high spin state m , CG_k is the coefficient of the determinant $|\Phi_{(j,s,jm)}\rangle$, $|\Phi_{(j,s,jm)}\rangle$ is the operator of the determinant, $C^{\dagger \psi_i}_{|s,m\rangle_j}$ is the creation operator for an electron with spin label (s_i, m_i) in spatial orbital ψ_i . The operation shown in equation 6.25,

$$\langle \Phi | O | \Psi \rangle = \sum_i \sum_j CG_i CG_j C^{\phi_i} C^{\phi_j} \dots [C^{\dagger \psi_i} \dots C^{\psi_j}] C^{\dagger \psi_i} C^{\dagger \psi_j} \quad (6.25)$$

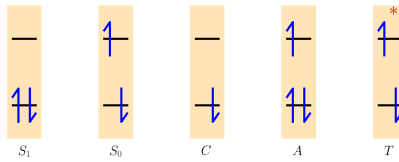


Figure 6.3: Distribution of electron in spatial orbital and construction of operators in the fragment state

is performed for all the sets of One electron operator and Two electron operator that are possible in the system. The coupling expression is extracted from (0,0) index of the resultant matrix after the application of state operators on the one electron operator and electron repulsion operators. Examples of constructed operators and evaluated couplings are shown in Appendix.

We distribute electrons while adhering to a specific spin sequence to achieve the desired multiplicity, thereby creating the wave function for a given state. This distribution precisely aligns with the requirements of each state under consideration. In the model of singlet fission. The model monomer system comprises the HOMO and LUMO orbitals of each monomer. Electrons in the HOMO of the i^{th} monomer are represented as $h_{i\uparrow}$ and $h_{i\downarrow}$, while electrons in the LUMO are represented as $l_{i\uparrow}$ and $l_{i\downarrow}$. These orbitals are assumed to be real, orthogonal, and normalized.

States of individual monomers are symbolized using single alphabets, with the ground state denoted as S_0 , the first singlet excited state as S_1 , and the lowest triplet state as T_1 . In the ground state of each monomer, both electrons occupy the lowest-energy orbitals. A singlet singly excited state, represented as S_1 , is characterized by one electron occupying higher-energy orbitals while the other remains in the lowest orbital. States arising from the loss or gain of electrons are labelled as C (cat-ionic) and A (anionic). Cationic states are formed when electrons are removed from the fragments, while anionic states result from the addition of electrons to the fragments shown in figure 6.3.

In our approach, we consider the cationic and anionic states together as collectively forming a singlet state, despite the possibility of higher multiplicities. For charge transfer states, we specifically opt for a singlet multiplicity, while maintaining a doublet multiplicity for the fragments within the charge transfer state. This choice ensures that the charge transfer system remains in a non-multiexciton state.

To represent states formed by combining monomer states, we concatenate the alphabet symbols corresponding to their respective states, following the order of the monomers they represent. For example, the state $T_1S_0T_1$ signifies a triplet state on the first monomer, a singlet ground state on the second monomer, and another triplet state on the third monomer (figure 6.3). In the case of a monomer with HOMO and LUMO orbitals, we have 4 sites available to accommodate 2 electrons. When evaluating energy expressions, n sites prove sufficient for n electrons. However, for assessing expressions related to transitions, we introduce empty sites to facilitate the transition process. This step is essential for handling electron transitions effectively.

6.2.4 Reduction of Determinant

$$f(N, n, S) = \frac{2s+1}{n+1} \binom{n+1}{\frac{N}{2}-S} \binom{n+1}{n-\frac{N}{2}-S} \quad (6.26)$$

The total number of states that can be generated with a given number of electrons in a spin basis is given by the Weyl-Paldus dimension expression (eq. 6.26). [297] The Number of states for a given number of unpaired electrons is shown in table 6.1. Upon distribution of electrons in spatial orbitals many determinants become identical or completely overlapped. It is identified and the number of determinants in a wavefunction is reduced by evaluating the overlap between determinants. which reduces the required computational resources.

$$V = \langle \Psi_{M_{pathways(i)}} | \Phi_{M_{pathways(j)}} \rangle \quad (6.27)$$

When V is a zero matrix, the two determinants are orthogonal, and when they are non-zero, they are non-orthogonal. In this case, the inner product of the state will be either 1 or -1. When

No. of electrons	No. of singlet Eigen state	No. of non-vanishing terms
4	2	10
6	5	70
8	14	588
10	42	5 544
12	132	56 628
14	429	613 470
16	1430	6 952 660
18	4862	81 662 152

Table 6.1: Number of states that can be generated with a given number of electrons in a spin basis

it is 1 or -1, both determinants can be replaced with either determinant. Their coefficients are multiplied. This reduces the number of determinants to be used in the derivation. The reduction of determinants in the wave functions of the dimer and trimer is discussed in the next section.

6.3 Result and Discussion

6.3.1 Growth of Matrices

Each electron in the system possesses two possible spin states: α (\uparrow) or β (\downarrow). The creation and annihilation operators for an electron within a spatial orbital are mathematically represented by 4x4 matrices. When dealing with a pair of spatial orbitals, the corresponding matrices become 16x16 in size.

As the system becomes more complex and involves multiple fragments, the size of the matrices grows significantly. Specifically, the matrix size scales exponentially with the number of fragments. For each additional fragment introduced, the matrix size increases by a factor of 16^n , where "n" signifies the number of fragments. As each determinant in the initial state can interact with every determinant in the final state, the computational load for coupling evaluations escalates due to the multiplication rate of matrices ($N_i \times N_j$, where N_i and N_j denote the number of determinants in the initial and final state, respectively).

Similarly, building all one-electron operators requires one matrix multiplication for each available pair of spin-orbital sites. Thus, $N_e \times (N_e - 1)$ ie $N_e^2 - N_e$ matrix multiplication is performed for one electron operator, where N_e represents the number of all the possible sites that an electron can occupy. For all two-electron operators, the $N_e^4 - 2N_e^3 + N_e$ matrix multiplication operation is performed.

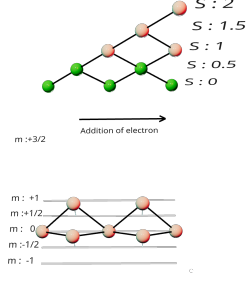
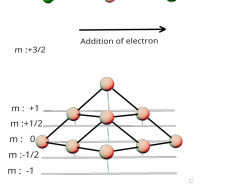
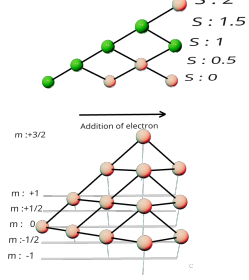
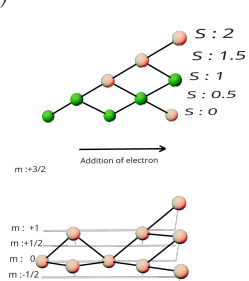
Taking all these considerations into account, the total number of operations required for the entire process becomes a composition of these factors. $N_i \times N_j \times (N_e^2 - N_e)$ matrix multiplication is performed for evaluation one electron operators and $N_i \times N_j \times (N_e^4 - 2N_e^3 + N_e)$ matrix multiplication is performed for evaluation Two electron operators to evaluate coupling between two states.

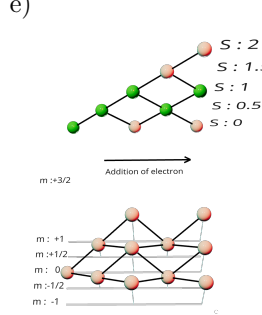
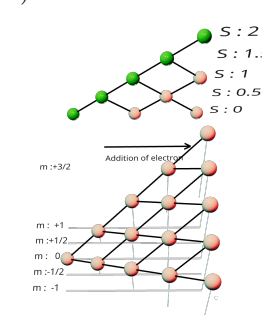
6.3.2 Dimer Spin Chain

The dimer spin chain for singlet fission is established based on a system comprising 4 electrons distributed across 4 orbitals. The resulting 16-state diagram encompasses various states: 2 singlet states, 3 S_{pathway} states for triplet multiplicities (each with 3 states, totalling 9 triplet states), and additionally, 1 quintet state with 5 distinct M states, resulting in a total of 16 states. Configuration branch diagrams depicting these states are shown in table 6.2.

In table 6.2, panel a) illustrates a branching diagram for a singlet state, where the subsystems themselves are in singlet states. When the 4 electrons within this spin configuration are distributed among 4 separate orbitals, the state representation is comprised of 4 determinants, analogous to the S_1S_1 arrangement. In scenarios where distribution occurs across 3 spatial orbitals, the state is represented by 2 determinants, akin to S_0S_1 . Alternatively, when these electrons are allocated to 2 spatial orbitals, a single determinant suffices to represent the state, as seen in S_0S_0 . This specific spin configuration state serves as the basis for constructing charge transfer states.

Table 6.2: Dimer Spin Chain, The equations of wave functions are represented in the form ${}^x|I : J\rangle$. Here, superscript x is index of the electron addition chain that has been followed to reach the final spin states. I represent $2\mathbf{S}$ and J represent $2\mathbf{S}_z$.

Branching Diagram	Spin only wave functions
a)	 ${}^1 0 : 0\rangle = +\frac{1}{2} \downarrow\uparrow\downarrow\uparrow\rangle - \frac{1}{2} \uparrow\downarrow\uparrow\downarrow\rangle - \frac{1}{2} \downarrow\uparrow\uparrow\downarrow\rangle + \frac{1}{2} \uparrow\downarrow\uparrow\downarrow\rangle$
b)	 ${}^2 0 : 0\rangle = +\frac{1}{\sqrt{3}} \downarrow\downarrow\uparrow\uparrow\rangle - \frac{1}{\sqrt{12}} \downarrow\uparrow\downarrow\uparrow\rangle - \frac{1}{\sqrt{12}} \uparrow\downarrow\downarrow\uparrow\rangle - \frac{1}{\sqrt{12}} \downarrow\uparrow\uparrow\downarrow\rangle - \frac{1}{\sqrt{12}} \uparrow\downarrow\uparrow\downarrow\rangle + \frac{1}{\sqrt{3}} \uparrow\uparrow\downarrow\downarrow\rangle$
c)	 ${}^1 1 : -1\rangle = -\frac{\sqrt{3}}{2} \downarrow\downarrow\downarrow\uparrow\rangle + \frac{1}{\sqrt{12}} \downarrow\downarrow\uparrow\downarrow\rangle + \frac{1}{\sqrt{12}} \uparrow\downarrow\downarrow\downarrow\rangle + \frac{1}{\sqrt{12}} \uparrow\downarrow\downarrow\downarrow\rangle$ ${}^1 1 : 0\rangle = -\frac{1}{\sqrt{6}} \downarrow\downarrow\uparrow\uparrow\rangle - \frac{1}{\sqrt{6}} \downarrow\uparrow\downarrow\uparrow\rangle - \frac{1}{\sqrt{6}} \uparrow\downarrow\downarrow\uparrow\rangle + \frac{1}{\sqrt{6}} \downarrow\uparrow\uparrow\downarrow\rangle + \frac{1}{\sqrt{6}} \uparrow\downarrow\uparrow\downarrow\rangle + \frac{1}{\sqrt{6}} \uparrow\uparrow\downarrow\downarrow\rangle$ ${}^1 1 : 1\rangle = -\frac{1}{\sqrt{12}} \downarrow\uparrow\uparrow\uparrow\rangle - \frac{1}{\sqrt{12}} \uparrow\downarrow\uparrow\uparrow\rangle - \frac{1}{\sqrt{12}} \uparrow\uparrow\downarrow\uparrow\rangle + \frac{\sqrt{3}}{2} \uparrow\uparrow\uparrow\downarrow\rangle$
d)	 ${}^2 1 : -1\rangle = -\frac{1}{\sqrt{2}} \downarrow\uparrow\downarrow\downarrow\rangle + \frac{1}{\sqrt{2}} \uparrow\downarrow\downarrow\downarrow\rangle$ ${}^2 1 : 0\rangle = -\frac{1}{2} \downarrow\uparrow\downarrow\uparrow\rangle + \frac{1}{2} \uparrow\downarrow\downarrow\uparrow\rangle - \frac{1}{2} \downarrow\uparrow\uparrow\downarrow\rangle + \frac{1}{2} \uparrow\downarrow\uparrow\downarrow\rangle$ ${}^2 1 : 1\rangle = -\frac{1}{\sqrt{2}} \downarrow\uparrow\uparrow\uparrow\rangle + \frac{1}{\sqrt{2}} \uparrow\downarrow\uparrow\uparrow\rangle$

	${}^3 1 : -1\rangle = -\sqrt{\frac{2}{3}} \downarrow\downarrow\uparrow\downarrow\rangle + \frac{1}{\sqrt{6}} \downarrow\uparrow\downarrow\downarrow\rangle + \frac{1}{\sqrt{6}} \uparrow\downarrow\downarrow\downarrow\rangle$ ${}^3 1 : 0\rangle = -\frac{1}{\sqrt{3}} \downarrow\downarrow\uparrow\uparrow\rangle + \frac{1}{\sqrt{12}} \downarrow\uparrow\downarrow\uparrow\rangle + \frac{1}{\sqrt{12}} \uparrow\downarrow\downarrow\uparrow\rangle - \frac{1}{\sqrt{12}} \downarrow\uparrow\uparrow\downarrow\rangle - \frac{1}{\sqrt{12}} \uparrow\downarrow\uparrow\downarrow\rangle + \frac{1}{\sqrt{3}} \uparrow\uparrow\downarrow\downarrow\rangle$ ${}^3 1 : 1\rangle = -\frac{1}{\sqrt{6}} \downarrow\uparrow\uparrow\uparrow\rangle - \frac{1}{\sqrt{6}} \uparrow\downarrow\uparrow\uparrow\rangle + \sqrt{\frac{2}{3}} \uparrow\uparrow\downarrow\uparrow\rangle$
	${}^1 2 : -2\rangle = \downarrow\downarrow\downarrow\downarrow\rangle$ ${}^1 2 : -1\rangle = +\frac{1}{2} \downarrow\downarrow\downarrow\uparrow\rangle + \frac{1}{2} \downarrow\downarrow\uparrow\downarrow\rangle + \frac{1}{2} \downarrow\uparrow\downarrow\downarrow\rangle + \frac{1}{2} \uparrow\downarrow\downarrow\downarrow\rangle$ ${}^1 2 : 0\rangle = +\frac{1}{\sqrt{6}} \downarrow\downarrow\uparrow\uparrow\rangle + \frac{1}{\sqrt{6}} \downarrow\uparrow\uparrow\uparrow\rangle + \frac{1}{\sqrt{6}} \uparrow\downarrow\downarrow\uparrow\rangle + \frac{1}{\sqrt{6}} \uparrow\uparrow\downarrow\uparrow\rangle + \frac{1}{\sqrt{6}} \uparrow\uparrow\uparrow\downarrow\rangle$ ${}^1 2 : 1\rangle = +\frac{1}{2} \downarrow\uparrow\uparrow\uparrow\rangle + \frac{1}{2} \uparrow\downarrow\uparrow\uparrow\rangle + \frac{1}{2} \uparrow\uparrow\downarrow\uparrow\rangle + \frac{1}{2} \uparrow\uparrow\uparrow\downarrow\rangle$ ${}^1 2 : 2\rangle = \uparrow\uparrow\uparrow\uparrow\rangle$

The branching diagram in Table 6.2 row b) shows the second electron addition sequence ($S_{pathway}$) with a singlet final spin. In this diagram, the first 2 electrons pair to form triplets, and the second electron pair reduces the singlet multiplicity. Therefore, this set of branching diagrams consists of two triplets merged into a singlet. The state is represented by a configuration of 6 determinants. For this configuration, the electrons must be distributed in 4 spatial orbitals, giving ${}^1(TT)$.

The spin configurations leading to the triplet overall spin are shown in Figures in Table 6.2 Rows c), d), and e). These are described in great detail in the next section.

Table 6.2 row f) shows the quintet state diagram formed by 4 electrons, and the wave functions of 5 high spin states are shown in the row. These spin states require 4 spatial orbitals.

The full system is formed with four electrons, which can be distributed among four spatial orbitals. This results in 16 possible electron configurations in 8 spin sites. However, only singlet multiplicity states with lower energy are important for the initiation of singlet fission. The model Hamiltonian for this system is constructed using wave functions from the 1st electron addition sequence for the singlet states, and the second electron addition sequence for the ${}^1(TT)$ state. There are 2 single-excited states S_1S_0 and S_0S_1 , 2 charge-transfer states CA and AC , and 1 singlet pair of triplets ${}^1(TT)$. The wave functions obtained by distributing the electrons in spatial orbitals are illustrated in Table 6.3.

The coupling between the singlet exciton states S_1S_0 and S_0S_1 involves only two-electron integrals. The coupling between the singlet exciton and charge transfer states involves both one-electron and two-electron integral terms. The coupling between charge transfer states involves only two-electron integrals. When states are derived from wave functions using different $S_{pathways}$, additional coefficients come into play. For example, the coefficient for the configuration state function derived from $S_{pathway}$ 1 to $S_{pathway}$ 2 is $\sqrt{\frac{3}{2}}$. The coupling between the singlet exciton and triplet state involves two-electron integral terms. The coupling between charge transfer states and the ${}^1(TT)$ state includes both one-electron terms and two-electron integrals.

Table 6.3: The wave functions are obtained by distributing the electrons in spatial orbitals. Here the states are represented as $|^{i:j:k}\Psi^m\Psi^n\rangle$ where i is index of the $S_{pathway}$, j represent $2\mathbf{S}$ and k represent $2\mathbf{S}_z$

States	wave functions
$ ^{1:0:0}S_0S_0\rangle =$	$+\frac{1}{2} h_{m\uparrow}h_{m\downarrow}h_{n\uparrow}h_{n\downarrow}\rangle - \frac{1}{2} h_{m\downarrow}h_{m\uparrow}h_{n\uparrow}h_{n\downarrow}\rangle - \frac{1}{2} h_{m\uparrow}h_{m\downarrow}h_{n\downarrow}h_{n\uparrow}\rangle + \frac{1}{2} h_{m\downarrow}h_{m\uparrow}h_{n\downarrow}h_{n\uparrow}\rangle$
$ ^{1:0:0}S_1S_0\rangle =$	$+\frac{1}{2} h_{m\uparrow}l_{m\downarrow}h_{n\uparrow}h_{n\downarrow}\rangle - \frac{1}{2} h_{m\downarrow}l_{m\uparrow}h_{n\uparrow}h_{n\downarrow}\rangle - \frac{1}{2} h_{m\uparrow}l_{m\downarrow}h_{n\downarrow}h_{n\uparrow}\rangle + \frac{1}{2} h_{m\downarrow}l_{m\uparrow}h_{n\downarrow}h_{n\uparrow}\rangle$
$ ^{1:0:0}CA\rangle =$	$+\frac{1}{2} h_{m\uparrow}l_{n\downarrow}h_{n\uparrow}h_{n\downarrow}\rangle - \frac{1}{2} h_{m\downarrow}l_{n\uparrow}h_{n\uparrow}h_{n\downarrow}\rangle - \frac{1}{2} h_{m\uparrow}l_{n\downarrow}h_{n\downarrow}h_{n\uparrow}\rangle + \frac{1}{2} h_{m\downarrow}l_{n\uparrow}h_{n\downarrow}h_{n\uparrow}\rangle$
$ ^{1:0:0}S_1S_1\rangle =$	$+\frac{1}{2} h_{m\uparrow}l_{m\downarrow}h_{n\uparrow}l_{n\downarrow}\rangle - \frac{1}{2} h_{m\downarrow}l_{m\uparrow}h_{n\uparrow}l_{n\downarrow}\rangle - \frac{1}{2} h_{m\uparrow}l_{m\downarrow}h_{n\downarrow}l_{n\uparrow}\rangle + \frac{1}{2} h_{m\downarrow}l_{m\uparrow}h_{n\downarrow}l_{n\uparrow}\rangle$
$ ^{2:0:0}TT\rangle =$	$+\frac{1}{\sqrt{3}} h_{m\uparrow}l_{m\uparrow}h_{2\downarrow}l_{2\downarrow}\rangle - \frac{1}{\sqrt{12}} h_{m\uparrow}l_{m\downarrow}h_{2\uparrow}l_{2\downarrow}\rangle - \frac{1}{\sqrt{12}} h_{m\downarrow}l_{m\uparrow}h_{2\uparrow}l_{2\downarrow}\rangle$ $- \frac{1}{\sqrt{12}} h_{m\uparrow}l_{m\downarrow}h_{2\downarrow}l_{2\uparrow}\rangle - \frac{1}{\sqrt{12}} h_{m\downarrow}l_{m\uparrow}h_{2\downarrow}l_{2\uparrow}\rangle + \frac{1}{\sqrt{3}} h_{m\downarrow}l_{m\downarrow}h_{2\uparrow}l_{2\uparrow}\rangle$
$ ^{1:1:-1}TT\rangle =$	$-\frac{\sqrt{3}}{2} h_{m\downarrow}l_{m\downarrow}h_{n\downarrow}l_{m\uparrow}\rangle + \frac{1}{\sqrt{12}} h_{m\downarrow}l_{m\downarrow}h_{n\uparrow}l_{m\downarrow}\rangle + \frac{1}{\sqrt{12}} h_{m\downarrow}l_{m\uparrow}h_{n\downarrow}l_{m\downarrow}\rangle$ $+ \frac{1}{\sqrt{12}} h_{m\uparrow}l_{m\downarrow}h_{n\downarrow}l_{m\downarrow}\rangle$
$ ^{1:1:0}TT\rangle =$	$-\frac{1}{\sqrt{6}} h_{m\downarrow}l_{m\downarrow}h_{n\uparrow}l_{n\uparrow}\rangle - \frac{1}{\sqrt{6}} h_{m\downarrow}l_{m\uparrow}h_{n\downarrow}l_{n\uparrow}\rangle - \frac{1}{\sqrt{6}} h_{m\uparrow}l_{m\downarrow}h_{n\downarrow}l_{n\uparrow}\rangle$ $+ \frac{1}{\sqrt{6}} h_{m\downarrow}l_{m\uparrow}h_{n\uparrow}l_{n\downarrow}\rangle + \frac{1}{\sqrt{6}} h_{m\uparrow}l_{m\downarrow}h_{n\uparrow}l_{n\downarrow}\rangle + \frac{1}{\sqrt{6}} h_{m\uparrow}l_{m\uparrow}h_{n\downarrow}l_{n\downarrow}\rangle$
$ ^{1:1:1}TT\rangle =$	$-\frac{1}{\sqrt{12}} h_{m\downarrow}l_{m\uparrow}h_{n\uparrow}l_{n\uparrow}\rangle - \frac{1}{\sqrt{12}} h_{m\uparrow}l_{m\downarrow}h_{n\uparrow}l_{n\uparrow}\rangle - \frac{1}{\sqrt{12}} h_{m\uparrow}l_{m\uparrow}h_{n\downarrow}l_{n\uparrow}\rangle$ $+ \frac{\sqrt{3}}{2} h_{m\uparrow}l_{m\uparrow}h_{n\uparrow}l_{n\downarrow}\rangle$
$ ^{1:1:-1}S_0T\rangle =$	$-\frac{\sqrt{3}}{2} h_{m\downarrow}h_{m\downarrow}h_{n\downarrow}l_{m\uparrow}\rangle + \frac{1}{\sqrt{12}} h_{m\downarrow}h_{m\downarrow}h_{n\uparrow}l_{m\downarrow}\rangle + \frac{1}{\sqrt{12}} h_{m\downarrow}h_{m\uparrow}h_{n\downarrow}l_{m\downarrow}\rangle$ $+ \frac{1}{\sqrt{12}} h_{m\uparrow}h_{m\downarrow}h_{n\downarrow}l_{m\downarrow}\rangle$
$ ^{1:1:0}S_0T\rangle =$	$-\frac{1}{\sqrt{6}} h_{m\downarrow}h_{m\downarrow}h_{n\uparrow}l_{n\uparrow}\rangle - \frac{1}{\sqrt{6}} h_{m\downarrow}h_{m\uparrow}h_{n\downarrow}l_{n\uparrow}\rangle - \frac{1}{\sqrt{6}} h_{m\uparrow}h_{m\downarrow}h_{n\downarrow}l_{n\uparrow}\rangle$ $+ \frac{1}{\sqrt{6}} h_{m\downarrow}h_{m\uparrow}h_{n\uparrow}l_{n\downarrow}\rangle + \frac{1}{\sqrt{6}} h_{m\uparrow}h_{m\downarrow}h_{n\uparrow}l_{n\downarrow}\rangle + \frac{1}{\sqrt{6}} h_{m\uparrow}h_{m\uparrow}h_{n\downarrow}l_{n\downarrow}\rangle$
$ ^{1:1:1}S_0T\rangle =$	$-\frac{1}{\sqrt{12}} h_{m\downarrow}h_{m\uparrow}h_{n\uparrow}l_{n\uparrow}\rangle - \frac{1}{\sqrt{12}} h_{m\uparrow}h_{m\downarrow}h_{n\uparrow}l_{n\uparrow}\rangle - \frac{1}{\sqrt{12}} h_{m\uparrow}h_{m\uparrow}h_{n\downarrow}l_{n\uparrow}\rangle$ $+ \frac{\sqrt{3}}{2} h_{m\uparrow}h_{m\uparrow}h_{n\uparrow}l_{n\downarrow}\rangle$
$ ^{2:1:-1}TT\rangle =$	$-\frac{1}{\sqrt{2}} h_{m\downarrow}l_{m\uparrow}h_{n\downarrow}l_{n\downarrow}\rangle + \frac{1}{\sqrt{2}} h_{m\uparrow}l_{m\downarrow}h_{n\downarrow}l_{n\downarrow}\rangle$
$ ^{2:1:0}TT\rangle =$	$-\frac{1}{2} h_{m\downarrow}l_{m\uparrow}h_{n\downarrow}l_{n\uparrow}\rangle + \frac{1}{2} h_{m\uparrow}l_{m\downarrow}h_{n\downarrow}l_{n\uparrow}\rangle - \frac{1}{2} h_{m\downarrow}l_{m\uparrow}h_{n\uparrow}l_{n\downarrow}\rangle$ $+ \frac{1}{2} h_{m\uparrow}l_{m\downarrow}h_{n\uparrow}l_{n\downarrow}\rangle$
$ ^{2:1:1}TT\rangle =$	$-\frac{1}{\sqrt{2}} h_{m\downarrow}l_{m\uparrow}h_{n\uparrow}l_{n\uparrow}\rangle + \frac{1}{\sqrt{2}} h_{m\uparrow}l_{m\downarrow}h_{n\uparrow}l_{n\uparrow}\rangle$
$ ^{3:1:-1}TT\rangle =$	$-\sqrt{\frac{2}{3}} h_{m\downarrow}l_{m\downarrow}h_{n\uparrow}l_{n\downarrow}\rangle + \frac{1}{\sqrt{6}} h_{m\downarrow}l_{m\uparrow}h_{n\downarrow}l_{n\downarrow}\rangle + \frac{1}{\sqrt{6}} h_{m\uparrow}l_{m\downarrow}h_{n\downarrow}l_{n\downarrow}\rangle$

$ ^{3:1:0}TT\rangle =$	$-\frac{1}{\sqrt{3}} h_{m\downarrow}l_{m\downarrow}h_{n\uparrow}l_{n\uparrow}\rangle + \frac{1}{\sqrt{12}} h_{m\downarrow}l_{m\uparrow}h_{n\downarrow}l_{n\uparrow}\rangle + \frac{1}{\sqrt{12}} h_{m\uparrow}l_{m\downarrow}h_{n\downarrow}l_{n\uparrow}\rangle - \frac{1}{\sqrt{12}} h_{m\downarrow}l_{m\uparrow}h_{n\uparrow}l_{n\downarrow}\rangle - \frac{1}{\sqrt{12}} h_{m\uparrow}l_{m\downarrow}h_{n\uparrow}l_{n\downarrow}\rangle + \frac{1}{\sqrt{3}} h_{m\uparrow}l_{m\uparrow}h_{n\downarrow}l_{n\downarrow}\rangle$
$ ^{3:1:1}TT\rangle =$	$-\frac{1}{\sqrt{6}} h_{m\downarrow}l_{m\uparrow}h_{n\uparrow}l_{n\uparrow}\rangle - \frac{1}{\sqrt{6}} h_{m\uparrow}l_{m\downarrow}h_{n\uparrow}l_{n\uparrow}\rangle + \sqrt{\frac{2}{3}} h_{m\uparrow}l_{m\uparrow}h_{n\downarrow}l_{n\uparrow}\rangle$

$$\hat{H} \left(\begin{array}{ccccc} 1:0:0 S_0 S_1 & 1:0:0 S_1 S_0 & 1:0:0 AC & 1:0:0 CA & 2:0:0 TT \\ \begin{array}{c} 2.0\langle h_n|\hat{\mathbf{F}}|h_n\rangle \\ +\langle l_m|\hat{\mathbf{F}}|l_m\rangle+\langle h_m|\hat{\mathbf{F}}|h_m\rangle \\ -1.0(h_m,h_m|l_m,l_m) \\ +2.0(h_m,l_m|l_m,h_m) \end{array} & \begin{array}{c} -(h_m,h_n|l_n,l_m) \\ +2(h_m,l_m|l_n,h_n) \end{array} & \begin{array}{c} (l_m|\hat{\mathbf{F}}|l_n) \\ -(h_m,h_m|l_m,l_n) \\ +2(h_m,l_m|l_n,h_n) \end{array} & \begin{array}{c} -(h_m|\hat{\mathbf{F}}|h_n) \\ -(h_m,h_n|l_m,l_m) \\ +2(h_m,l_m|l_n,h_n) \end{array} & \begin{array}{c} \sqrt{\frac{3}{2}}(-(h_m,l_m|h_n,h_m) \\ +(l_n,l_m|h_n,l_n)) \end{array} \\ 1:0:0 S_1 S_0 & \begin{array}{c} 2.0*\langle h_m|\hat{\mathbf{F}}|h_m\rangle \\ +\langle l_n|\hat{\mathbf{F}}|l_n\rangle+\langle h_n|\hat{\mathbf{F}}|h_n\rangle \\ -1.0(h_n,h_n|l_n,l_n) \\ +2.0(h_n,l_n|l_n,h_n) \end{array} & \begin{array}{c} -\langle h_n|\hat{\mathbf{F}}|h_m\rangle \\ -(h_n,h_m|l_n,l_n) \\ +2(h_n,l_n|l_n,h_m) \end{array} & \begin{array}{c} \langle l_n|\hat{\mathbf{F}}|l_m\rangle \\ -(h_n,h_n|l_n,l_m) \\ +2(h_n,l_n|l_m,h_n) \end{array} & \begin{array}{c} \sqrt{\frac{3}{2}}(-(h_n,l_n|h_m,h_n) \\ +(l_m,l_n|h_m,l_m)) \end{array} \\ 1:0:0 AC & \begin{array}{c} 2.0*\langle h_n|\hat{\mathbf{F}}|h_n\rangle \\ +\langle h_m|\hat{\mathbf{F}}|h_m\rangle+\langle l_n|\hat{\mathbf{F}}|l_n\rangle \\ -1.0(h_m,h_m|l_n,l_n) \\ +2.0(h_m,l_n|h_m,l_n) \end{array} & \begin{array}{c} -(h_m,h_n,l_n,l_m) \\ +2(h_m,l_m,l_n,h_n) \end{array} & \begin{array}{c} -(h_m,h_n,l_n,l_m) \\ +2(h_m,l_m,l_n,h_n) \end{array} & \begin{array}{c} \sqrt{\frac{3}{2}}\langle h_m|\hat{\mathbf{F}}|l_n\rangle \\ +(h_m,l_n|l_m,l_m) \\ -(h_m,l_n|h_m,h_m) \end{array} \\ 1:0:0 CA & \begin{array}{c} 2.0*\langle h_m|\hat{\mathbf{F}}|h_m\rangle \\ +\langle h_n|\hat{\mathbf{F}}|h_n\rangle+\langle l_m|\hat{\mathbf{F}}|l_m\rangle \\ -1.0(h_n,h_n|l_m,l_m) \\ +2.0(h_n,l_m|h_n,l_m) \end{array} & \begin{array}{c} +\langle h_n|\hat{\mathbf{F}}|l_m\rangle \\ -(h_n,l_m|l_n,l_n) \\ +2(h_n,l_m|h_n,h_n) \end{array} & \begin{array}{c} \sqrt{\frac{3}{2}}\langle h_n|\hat{\mathbf{F}}|l_n\rangle \\ -(h_n,l_m|h_n,h_n) \\ +(h_n,l_m|h_n,h_n) \end{array} & \begin{array}{c} \langle l_m|\hat{\mathbf{F}}|l_m\rangle \\ +\langle h_m|\hat{\mathbf{F}}|h_m\rangle \\ +\langle l_n|\hat{\mathbf{F}}|l_n\rangle+\langle h_n|\hat{\mathbf{F}}|h_n\rangle \\ -1.0(h_m,h_m|l_m,l_m) \\ -1.0(h_n,h_n|l_n,l_n) \end{array} \\ 2:0:0 TT & \end{array} \end{array} \right) \quad (6.28)$$

6.3.3 Coupling Among Triplets in Dimer

The spin configuration that leads to the triplet overall spin is shown in the figure of table 6.2 row c),d), and e) These are three different electron addition sequences ($S_{pathways}$) that are found in the branching diagram of S. Thus, we get an overall 9 states. In the diagrams of table 6.2 row c), the first electron pair forms a triplet, the third electron increases the multiplicity to 1.5 and the 4th electron reduces the multiplicity again to 1 making an overall triplet. This configuration requires 4 spatial orbitals. In the second set of triplet electron addition sequences in table 6.2 row d), the first 2 electrons form a singlet and the second pair forms a triplet. This configuration can be formed into 3 or 4 spatial orbitals giving S_0T_1 and S_1T_1 . In the third set of triplets shown in table 6.2 row e). The first two electrons of the triplet increase the multiplicity, the third electron reduces the multiplicity of the system to the doublet, and the fourth electron takes the multiplicity back to the triplet. These Slater determinants require 4 spatial orbitals. The wave functions obtained by distributing the electrons in spatial orbitals are illustrated in table 6.3.

Table 6.4 and 6.5 illustrate the excitation coupling from various S_0T to $^3(TT)$ and among various kind of $^3(TT)$ respectively. There are three categories of coupling within this scenario: 1) In the provided equation, there are three types of couplings mentioned, each involving different elements: This type of coupling involves both one-electron coupling matrix elements and two-electron coupling matrix elements. However, most of the one-electron matrix elements and some of the two-electron matrix elements cancel out when evaluating the spin-independent coupling. This suggests that the final result for the spin-independent coupling is primarily determined by the remaining non-cancelled two-electron matrix elements. The second type also involves both one-electron coupling matrix elements and two-electron coupling matrix elements. However, unlike the spin-independent case, not all of these elements cancel out during the evaluation of spin-dependent coupling. This implies that both one-electron and two-electron matrix elements contribute to the final value of the spin-dependent coupling. In the third case, only the two-electron matrix terms are present.

Table 6.4: Coupling expression among three types of paired triplet giving triplet in context spatial orbitals. The spatial orbitals consists of frontier orbitals and all the all the electrons are unpaired.

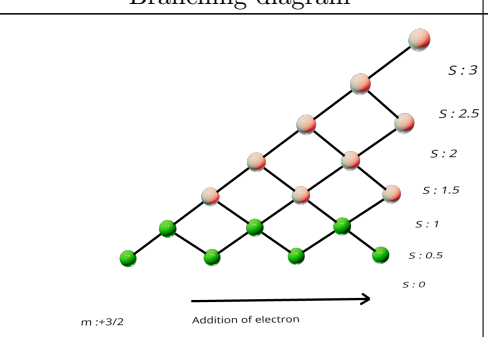
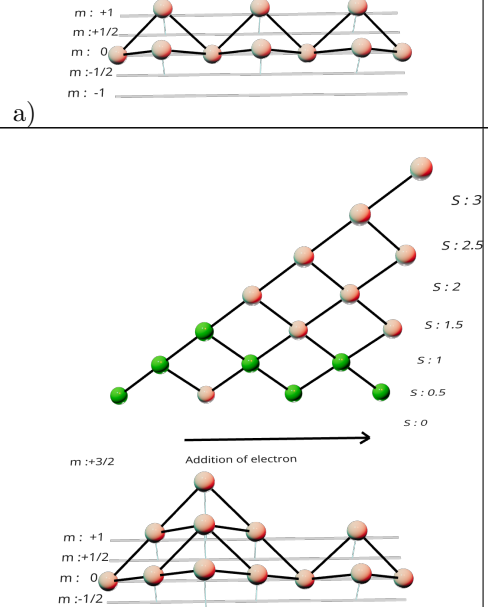
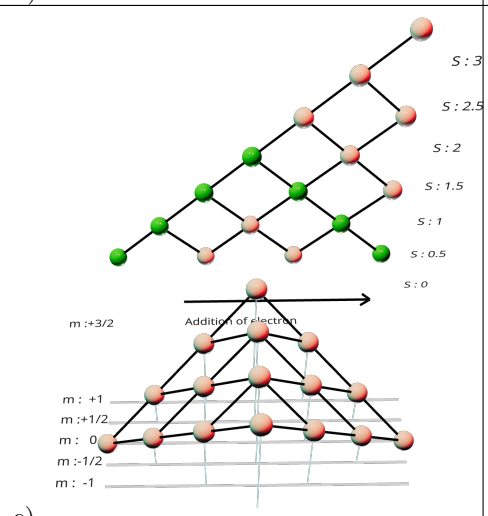
State Coupling	Two Electron Integrals	One electron Integrals
$\langle^{1:1:-1}TT \hat{H} ^{2:1:-1}TT\rangle$	$\sqrt{\frac{2}{3}}\langle l_n h_m h_m l_n \rangle - \sqrt{\frac{2}{3}}\langle l_n l_m l_m l_n \rangle$	$\frac{1}{\sqrt{24}}\langle h_{m\downarrow} \hat{h} h_{m\downarrow}\rangle - \frac{1}{\sqrt{24}}\langle h_{m\uparrow} \hat{h} h_{m\uparrow}\rangle = 0$ $+ \frac{1}{\sqrt{24}}\langle l_{m\uparrow} \hat{h} l_{m\uparrow}\rangle - \frac{1}{\sqrt{24}}\langle l_{m\downarrow} \hat{h} l_{m\downarrow}\rangle$
$\langle^{1:1:0}TT \hat{H} ^{2:1:0}TT\rangle$	$+\sqrt{\frac{2}{3}}\langle h_m l_n l_n h_m \rangle - \sqrt{\frac{2}{3}}\langle l_n l_m l_m l_n \rangle$	
$\langle^{1:1:1}TT \hat{H} ^{2:1:1}TT\rangle$	$\sqrt{\frac{2}{3}}\langle l_n h_m h_m l_n \rangle - \sqrt{\frac{2}{3}}\langle l_n l_m l_m l_n \rangle$	$\frac{1}{\sqrt{24}}\langle h_{m\uparrow} \hat{h} h_{m\uparrow}\rangle - \frac{1}{\sqrt{24}}\langle h_{m\downarrow} \hat{h} h_{m\downarrow}\rangle = 0$ $+ \frac{1}{\sqrt{24}}\langle l_{m\downarrow} \hat{h} l_{m\downarrow}\rangle - \frac{1}{\sqrt{24}}\langle l_{m\uparrow} \hat{h} l_{m\uparrow}\rangle$
$\langle^{1:1:-1}TT \hat{H} ^{3:1:-1}TT\rangle$	$\sqrt{\frac{2}{3}}\langle l_m l_n l_n l_m \rangle + \sqrt{\frac{2}{3}}\langle l_n l_m l_m l_n \rangle - \sqrt{\frac{8}{3}}\langle l_n h_n h_n l_n \rangle$	$\frac{1}{\sqrt{72}}\langle h_{m\downarrow} \hat{h} h_{m\downarrow}\rangle + \frac{1}{\sqrt{18}}\langle h_{n\uparrow} \hat{h} h_{n\uparrow}\rangle - \frac{1}{\sqrt{72}}\langle h_{m\uparrow} \hat{h} h_{m\uparrow}\rangle - \frac{1}{\sqrt{18}}\langle h_{n\downarrow} \hat{h} h_{n\downarrow}\rangle = 0$ $+ \frac{1}{\sqrt{72}}\langle l_{m\downarrow} \hat{h} l_{m\downarrow}\rangle - \frac{1}{\sqrt{72}}\langle l_{m\uparrow} \hat{h} l_{m\uparrow}\rangle$
$\langle^{1:1:0}TT \hat{H} ^{3:1:0}TT\rangle$	$\sqrt{\frac{2}{3}}\langle l_m l_n l_n l_m \rangle + \sqrt{\frac{2}{3}}\langle l_n l_m l_m l_n \rangle - \sqrt{\frac{8}{3}}\langle l_n h_n h_n l_n \rangle$	
$\langle^{1:1:1}TT \hat{H} ^{3:1:1}TT\rangle$	$\sqrt{\frac{2}{3}}\langle l_m l_n l_n l_m \rangle + \sqrt{\frac{2}{3}}\langle l_n l_m l_m l_n \rangle - \sqrt{\frac{8}{3}}\langle l_n h_n h_n l_n \rangle$	$\frac{1}{\sqrt{72}}\langle h_{m\uparrow} \hat{h} h_{m\uparrow}\rangle + \frac{1}{\sqrt{18}}\langle h_{n\downarrow} \hat{h} h_{n\downarrow}\rangle - \frac{1}{\sqrt{72}}\langle h_{m\downarrow} \hat{h} h_{m\downarrow}\rangle - \frac{1}{\sqrt{18}}\langle h_{n\uparrow} \hat{h} h_{n\uparrow}\rangle = 0$ $+ \frac{1}{\sqrt{72}}\langle l_{m\uparrow} \hat{h} l_{m\uparrow}\rangle - \frac{1}{\sqrt{72}}\langle l_{m\downarrow} \hat{h} l_{m\downarrow}\rangle$
$\langle^{2:1:-1}TT \hat{H} ^{3:1:-1}TT\rangle$	$\sqrt{\frac{3}{2}}\langle h_n h_m h_m h_n \rangle + \frac{1}{\sqrt{12}}\langle l_n h_m h_m l_n \rangle - \sqrt{\frac{3}{2}}\langle l_m h_n h_n l_m \rangle - \frac{1}{\sqrt{12}}\langle l_n l_m l_m l_n \rangle$	$\frac{1}{\sqrt{12}}\langle h_{m\downarrow} \hat{h} h_{m\downarrow}\rangle - \frac{1}{\sqrt{12}}\langle h_{m\uparrow} \hat{h} h_{m\uparrow}\rangle + \frac{1}{\sqrt{12}}\langle l_{m\uparrow} \hat{h} l_{m\uparrow}\rangle - \frac{1}{\sqrt{12}}\langle l_{m\downarrow} \hat{h} l_{m\downarrow}\rangle = 0$
$\langle^{2:1:0}TT \hat{H} ^{3:1:0}TT\rangle$	$\sqrt{\frac{3}{2}}\langle h_n h_m h_m h_n \rangle + \frac{1}{\sqrt{12}}\langle l_n h_m h_m l_n \rangle - \sqrt{\frac{3}{2}}\langle l_m h_n h_n l_m \rangle - \frac{1}{\sqrt{12}}\langle l_n l_m l_m l_n \rangle$	
$\langle^{2:1:1}TT \hat{H} ^{3:1:1}TT\rangle$	$\sqrt{\frac{3}{2}}\langle h_n h_m h_m h_n \rangle + \frac{1}{\sqrt{12}}\langle l_n h_m h_m l_n \rangle - \sqrt{\frac{3}{2}}\langle l_m h_n h_n l_m \rangle - \frac{1}{\sqrt{12}}\langle l_n l_m l_m l_n \rangle$	$\frac{1}{\sqrt{12}}\langle h_{m\uparrow} \hat{h} h_{m\uparrow}\rangle - \frac{1}{\sqrt{12}}\langle h_{m\downarrow} \hat{h} h_{m\downarrow}\rangle + \frac{1}{\sqrt{12}}\langle l_{m\downarrow} \hat{h} l_{m\downarrow}\rangle - \frac{1}{\sqrt{12}}\langle l_{m\uparrow} \hat{h} l_{m\uparrow}\rangle = 0$

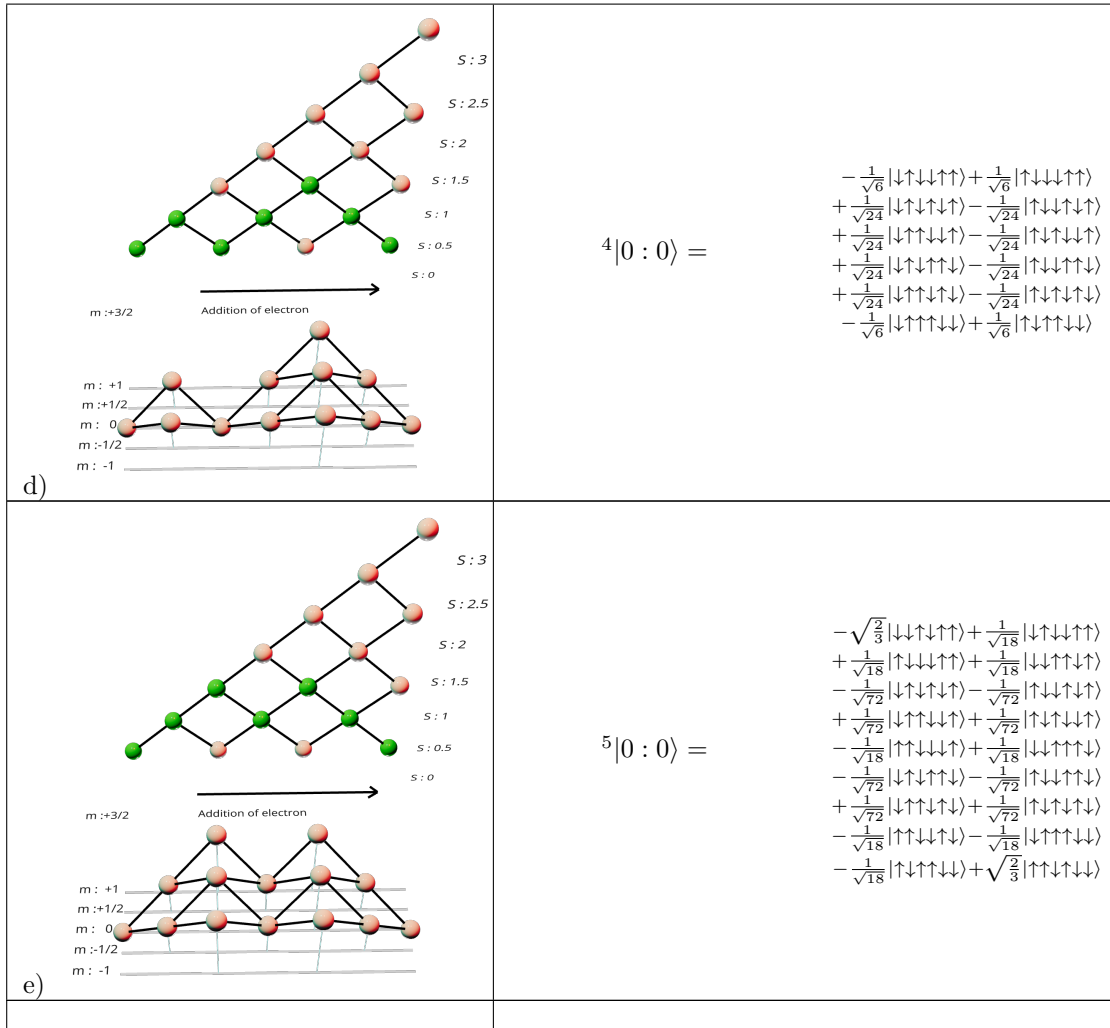
Table 6.5: Coupling expression among Three types of paired triplet giving triplet in context spatial orbitals. In state, ${}^{2:1:2m}S_0T$ first two electrons are in the same spatial orbitals next two electrons are unpaired.

State Coupling	Two Electron Integrals	One electron Integrals
$\langle {}^{2:1:-1}S_0T \hat{H} {}^{1:1:-1}TT \rangle$	$-\sqrt{\frac{8}{3}} \langle l_n l_m h_m l_n \rangle$	$\frac{1}{\sqrt{6}} \langle l_{m\uparrow} \hat{h} h_{m\uparrow} \rangle - \frac{1}{\sqrt{6}} \langle l_{m\downarrow} \hat{h} h_{m\downarrow} \rangle = 0$
$\langle {}^{2:1:0}S_0T \hat{H} {}^{1:1:0}TT \rangle$	$-\sqrt{\frac{8}{3}} \langle l_n l_m h_m l_n \rangle$	
$\langle {}^{2:1:1}S_0T \hat{H} {}^{1:1:1}TT \rangle$	$-\sqrt{\frac{8}{3}} \langle l_n l_m h_m l_n \rangle$	$\frac{1}{\sqrt{6}} \langle l_{m\downarrow} \hat{h} h_{m\downarrow} \rangle - \frac{1}{\sqrt{6}} \langle l_{m\uparrow} \hat{h} h_{m\uparrow} \rangle = 0$
$\langle {}^{2:1:-1}S_0T \hat{H} {}^{2:1:-1}TT \rangle$	$2 \langle h_m l_m h_m h_m \rangle + 2 \langle l_m h_n h_m h_n \rangle + 2 \langle l_n l_m l_n h_m \rangle - \langle l_m h_n h_n h_m \rangle - \langle l_n l_m h_m l_n \rangle$	$\langle l_{m\uparrow} \hat{h} h_{m\uparrow} \rangle + \langle l_{m\downarrow} \hat{h} h_{m\downarrow} \rangle = 2 \langle l_m \hat{h} h_m \rangle$
$\langle {}^{2:1:0}S_0T \hat{H} {}^{2:1:0}TT \rangle^0 =$	$2 \langle h_m l_m h_m h_m \rangle + 2 \langle l_m h_n h_m h_n \rangle + 2 \langle l_n l_m l_n h_m \rangle - \langle l_m h_n h_n h_m \rangle - \langle l_n l_m h_m l_n \rangle$	$\langle l_{m\uparrow} \hat{h} h_{m\uparrow} \rangle + \langle l_{m\downarrow} \hat{h} h_{m\downarrow} \rangle = 2 \langle l_m \hat{h} h_m \rangle$
$\langle {}^{2:1:1}S_0T \hat{H} {}^{2:1:1}TT \rangle$	$2 \langle h_m l_m h_m h_m \rangle + 2 \langle l_m h_n h_m h_n \rangle + 2 \langle l_n l_m l_n h_m \rangle - \langle l_m h_n h_n h_m \rangle - \langle l_n l_m h_m l_n \rangle$	$\langle l_{m\uparrow} \hat{h} h_{m\uparrow} \rangle + \langle l_{m\downarrow} \hat{h} h_{m\downarrow} \rangle = 2 \langle l_m \hat{h} h_m \rangle$
$\langle {}^{2:1:-1}S_0T \hat{H} {}^{3:1:-1}TT \rangle$	$-\frac{\sqrt{3}}{\sqrt{3}} \langle h_n l_m h_m h_n \rangle - \frac{1}{\sqrt{3}} \langle l_m l_n l_n h_m \rangle$	$\frac{1}{\sqrt{3}} \langle l_{m\uparrow} \hat{h} h_{m\uparrow} \rangle - \frac{1}{\sqrt{3}} \langle l_{m\downarrow} \hat{h} h_{m\downarrow} \rangle = 0$
$\langle {}^{2:1:0}S_0T \hat{H} {}^{3:1:0}TT \rangle$	$-\frac{\sqrt{3}}{\sqrt{3}} \langle h_n l_m h_m h_n \rangle - \frac{1}{\sqrt{3}} \langle l_n l_m h_m l_n \rangle$	
$\langle {}^{2:1:1}S_0T \hat{H} {}^{3:1:1}TT \rangle$	$-\frac{\sqrt{3}}{\sqrt{3}} \langle h_n l_m h_m h_n \rangle - \frac{1}{\sqrt{3}} \langle l_n l_m h_m l_n \rangle$	$\frac{1}{\sqrt{3}} \langle l_{m\downarrow} \hat{h} h_{m\downarrow} \rangle - \frac{1}{\sqrt{3}} \langle l_{m\uparrow} \hat{h} h_{m\uparrow} \rangle = 0$

6.3.4 Trimer Spin Chain

Table 6.6: Trimer Spin addition system

Branching diagram	Spin only wave functions
 a)	$^1 0:0\rangle =$ $-\frac{1}{\sqrt{8}} \downarrow\uparrow\downarrow\uparrow\downarrow\uparrow\rangle + \frac{1}{\sqrt{8}} \uparrow\downarrow\downarrow\uparrow\downarrow\uparrow\rangle$ $+ \frac{1}{\sqrt{8}} \downarrow\uparrow\uparrow\downarrow\downarrow\uparrow\rangle - \frac{1}{\sqrt{8}} \uparrow\downarrow\uparrow\downarrow\downarrow\uparrow\rangle$ $+ \frac{1}{\sqrt{8}} \downarrow\uparrow\downarrow\uparrow\downarrow\uparrow\rangle - \frac{1}{\sqrt{8}} \uparrow\downarrow\downarrow\uparrow\downarrow\uparrow\rangle$ $- \frac{1}{\sqrt{8}} \downarrow\uparrow\downarrow\uparrow\downarrow\uparrow\rangle + \frac{1}{\sqrt{8}} \uparrow\downarrow\uparrow\downarrow\uparrow\downarrow\rangle$
 b)	$^2 0:0\rangle =$ $-\frac{1}{\sqrt{6}} \downarrow\downarrow\uparrow\uparrow\uparrow\uparrow\rangle + \frac{1}{\sqrt{24}} \downarrow\uparrow\uparrow\uparrow\uparrow\uparrow\rangle$ $+ \frac{1}{\sqrt{24}} \uparrow\downarrow\uparrow\uparrow\uparrow\uparrow\rangle + \frac{1}{\sqrt{24}} \downarrow\uparrow\uparrow\downarrow\downarrow\uparrow\rangle$ $+ \frac{1}{\sqrt{24}} \uparrow\downarrow\uparrow\downarrow\downarrow\uparrow\rangle - \frac{1}{\sqrt{6}} \uparrow\uparrow\downarrow\downarrow\uparrow\uparrow\rangle$ $+ \frac{1}{\sqrt{6}} \downarrow\downarrow\uparrow\uparrow\uparrow\downarrow\rangle - \frac{1}{\sqrt{24}} \downarrow\uparrow\uparrow\uparrow\uparrow\downarrow\rangle$ $- \frac{1}{\sqrt{24}} \uparrow\downarrow\uparrow\uparrow\uparrow\downarrow\rangle - \frac{1}{\sqrt{24}} \downarrow\uparrow\uparrow\downarrow\downarrow\downarrow\rangle$ $- \frac{1}{\sqrt{24}} \uparrow\downarrow\uparrow\downarrow\downarrow\downarrow\rangle + \frac{1}{\sqrt{6}} \uparrow\uparrow\downarrow\downarrow\downarrow\downarrow\rangle$
 c)	$^3 0:0\rangle =$ $-\frac{1}{2} \downarrow\downarrow\downarrow\uparrow\uparrow\uparrow\rangle + \frac{1}{6} \downarrow\downarrow\uparrow\uparrow\uparrow\uparrow\rangle$ $+ \frac{1}{6} \downarrow\uparrow\downarrow\uparrow\uparrow\uparrow\rangle + \frac{1}{6} \uparrow\downarrow\downarrow\uparrow\uparrow\uparrow\rangle$ $+ \frac{1}{6} \downarrow\downarrow\uparrow\uparrow\uparrow\uparrow\rangle + \frac{1}{6} \downarrow\uparrow\uparrow\uparrow\uparrow\uparrow\rangle$ $+ \frac{1}{6} \uparrow\downarrow\uparrow\uparrow\uparrow\uparrow\rangle - \frac{1}{6} \uparrow\uparrow\downarrow\uparrow\uparrow\uparrow\rangle$ $- \frac{1}{6} \uparrow\uparrow\downarrow\uparrow\uparrow\uparrow\rangle - \frac{1}{6} \uparrow\uparrow\uparrow\downarrow\uparrow\uparrow\rangle$ $+ \frac{1}{6} \downarrow\downarrow\uparrow\uparrow\uparrow\downarrow\rangle + \frac{1}{6} \downarrow\uparrow\uparrow\uparrow\uparrow\downarrow\rangle$ $+ \frac{1}{6} \uparrow\downarrow\uparrow\uparrow\uparrow\downarrow\rangle - \frac{1}{6} \uparrow\uparrow\uparrow\uparrow\uparrow\downarrow\rangle$ $- \frac{1}{6} \uparrow\uparrow\uparrow\downarrow\uparrow\downarrow\rangle - \frac{1}{6} \uparrow\uparrow\downarrow\uparrow\downarrow\downarrow\rangle$ $- \frac{1}{6} \downarrow\uparrow\uparrow\uparrow\downarrow\downarrow\rangle + \frac{1}{2} \uparrow\uparrow\uparrow\uparrow\downarrow\downarrow\rangle$



In a trimer system with 6 electrons distributed across 6 sites. There are 5 singlet states with singlet multiplicity, corresponding to 5 different electron addition paths. Among these one state is a combination of all singlets. The two-path state involves one singlet and two triplets combining to form a triplet, resulting in one singlet and two triplets. This is illustrated in table 6.6. Another state requires 3 excited electrons, involving an unfactorizable triplet and a dimer combining with a triplet from a single monomer, forming a complete triplet. Additionally, a state arises from a combination of three triplets that form a singlet, where the triplets are factorisable in monomer states. Furthermore, there are 27 triplet states in the trimer system. These 27 triplet states are formed from 9 different electron addition sequences, each leading to triplet states, resulting in a total of 27 states. Moreover, the trimer system comprises 25 quintet states. These quintet states originate from 5 electron addition sequences, each of which gives rise to 5 quintet states, resulting in a total of 25 states. Finally, there are 7 septet states present in the trimer system.

In Table 6.6 row a), all electron pairs within the molecular fragments combine to form a singlet state, requiring 3 to 6 spatial orbitals. This spin configuration can occur with different numbers of spatial orbitals, ranging from 3 to 6. In row b), the first two electrons form a triplet, and the subsequent ones combine to result in a net singlet state. row c) depicts the reverse, with the first two electrons forming a singlet and the rest forming triplets, leading to a net singlet state. In row d), the first three electrons form a quartet, transitioning to a singlet as the next three interact. This electron addition sequence can occur in systems with a minimum of 6 spatial orbitals to accommodate the spin interactions. row e) showcases dynamic changes in spin multiplicities, from triplets to doublets and back to triplets, eventually leading to a singlet state. This sequence also requires a minimum of 6 spatial orbitals.

These electron addition sequences provide a detailed understanding of how electron spins and multiplicities evolve in complex molecular systems. Such insights are important for describing singlet fission processes, where the transformation between different spin states plays a central role

	$ S_0^m S_1^n S_0^o\rangle$	$ S_0^m S_0^n S_1^o\rangle$	$ C^m A^n S_0^o\rangle$	$ S_0^m C^n A^o\rangle$	$ A^m S_0^n C^o\rangle$	$ A^m C^n S_0^o\rangle$
$\langle S_1^m S_0^n S_0^o $	$-(h_m h_n l_n l_m) + 2(h_m l_m l_n h_n)$	$-(h_m h_o l_o l_m) + 2(h_m l_m l_o h_o)$	$\langle l_m \mathbf{F} l_n \rangle + 2(h_m l_m l_n h_m) - (h_m h_m l_m l_n)$	$2(h_m l_m l_o h_n) - 1(h_m h_n l_o l_m)$	$-\langle h_m \mathbf{F} h_o \rangle + 2(h_m l_m l_m h_o) - (h_m h_o l_m l_m)$	$-\langle h_m \mathbf{F} h_n \rangle + 2(h_m l_m l_m h_n) - (h_m h_n l_m l_m)$
$\langle S_0^m S_1^n S_0^o $	E		$-\langle h_n h_o l_o l_n \rangle + 2(h_n l_n l_o h_o) - (h_n h_m l_n l_n)$	$\langle l_n \mathbf{F} l_o \rangle + 2(h_n l_n l_n h_n) - (h_n h_n l_n l_o)$	$2(h_n l_n l_m h_o) - 1(h_n h_o l_m l_n)$	$\langle l_n \mathbf{F} l_m \rangle + 2(h_n l_n l_m h_n) - (h_n h_n l_n l_m)$
$\langle S_0^m S_0^n S_1^o $		E	$2(h_o l_o l_n h_m) - 1(h_o h_m l_n l_o)$	$-\langle h_o \mathbf{F} h_n \rangle + 2(h_o l_o l_o h_n) - (h_o h_o l_o l_o)$	$\langle l_o \mathbf{F} l_m \rangle + 2(h_o l_o l_m h_o) - (h_o h_n l_m l_o)$	$2(h_o l_o l_m h_n) - 1(h_o h_n l_m l_o)$
$\langle C_0^m A_0^n S_0^o $			E	$-(h_m h_n l_o l_n) + 2(h_m l_n l_o h_n)$	$-(h_m h_o l_m l_n) + 2(h_m l_n l_m h_o)$	$-(h_m h_n l_n l_m) + 2(h_m l_m l_n h_n)$
$\langle S_0^m C_0^n A_0^o $				E	$-(h_n h_o l_m l_o) + 2(h_n l_o l_m h_o)$	$\langle l_o \mathbf{F} l_m \rangle - (h_n h_n l_m l_o) + 2(h_n l_o l_m h_n)$
$\langle A_0^m S_0^n C_0^o $					E	$-\langle h_o \mathbf{F} h_n \rangle - (h_o h_n l_m l_m) + 2(h_o l_m l_m h_n)$

	$ S_0^m A^n C^o\rangle$	$ C^m S_0^n A^o\rangle$	$ T^m T^n S_0^o\rangle$	$ S_0^m T^n T^o\rangle$	$ T^m S_0^n T^o\rangle$
$\langle S_1^m S_0^n S_0^o $	$2(h_m l_m l_n h_o) - 1(h_m h_o l_n l_m)$	$\langle l_m \mathbf{F} l_o \rangle + 2(h_m l_m l_o h_m) - (h_m h_m l_m l_o)$	$\sqrt{\frac{3}{2}} \left(\begin{array}{c} (l_n l_m h_n l_n) \\ -(h_m l_m h_n h_m) \end{array} \right)$	0	$\sqrt{\frac{3}{2}} \left(\begin{array}{c} (l_o l_m h_o l_o) \\ -(h_m l_m h_o h_m) \end{array} \right)$
$\langle S_0^m S_1^n S_0^o $	$-\langle h_n \mathbf{F} h_o \rangle + 2(h_n l_n l_o h_o) - (h_n h_o l_n l_n)$	$2(h_n l_n l_o h_m) - 1(h_n h_m l_o l_n)$	$\sqrt{\frac{3}{2}} \left(\begin{array}{c} (l_m l_n h_m l_m) \\ -(h_n l_n h_m h_n) \end{array} \right)$	$\sqrt{\frac{3}{2}} \left(\begin{array}{c} (l_o l_n h_o l_o) \\ -(h_n l_n h_o h_n) \end{array} \right)$	0
$\langle S_0^m S_0^n S_1^o $		$\langle l_o \mathbf{F} l_m \rangle + 2(h_o l_o l_o h_m) - (h_o h_m l_o l_o)$	0	$\sqrt{\frac{3}{2}} \left(\begin{array}{c} (l_n l_o h_n l_n) \\ -(h_o l_o h_n h_o) \end{array} \right)$	$\sqrt{\frac{3}{2}} \left(\begin{array}{c} (l_m l_o h_m l_m) \\ -(h_o l_o h_m h_o) \end{array} \right)$
$\langle C_0^m A_0^n S_0^o $	$-\langle h_m \mathbf{F} h_o \rangle - (h_m h_o l_n l_n) + 2(h_m l_n l_n h_o)$	$\langle l_n \mathbf{F} l_o \rangle - (h_m l_m l_o l_n) + 2(h_m l_n l_o h_m)$	$\sqrt{\frac{3}{2}} \left(\begin{array}{c} (l_m \mathbf{F} h_n) \\ +(h_m l_m l_n l_n) \\ -(l_m h_n h_m h_m) \end{array} \right)$	$-\sqrt{\frac{3}{2}} (h_o h_m h_n l_o)$	$\sqrt{\frac{3}{2}} (h_o l_m l_n l_o)$
$\langle S_0^m C_0^n A_0^o $	$-(h_n h_o l_o l_n) + 2(h_n l_n l_o h_o)$	$-\langle h_n \mathbf{F} h_m \rangle - (h_n h_m l_o l_o) + 2(h_n l_o l_o h_m)$	$\sqrt{\frac{3}{2}} (h_m l_n l_o l_m)$	$\sqrt{\frac{3}{2}} \left(\begin{array}{c} (l_n \mathbf{F} h_o) \\ +(h_o l_n l_o l_o) \\ -(l_n h_o h_n h_n) \end{array} \right)$	$-\sqrt{\frac{3}{2}} (h_m h_n h_o l_m)$
$\langle A_0^m S_0^n C_0^o $	$\langle l_m \mathbf{F} l_n \rangle - (h_o h_o l_n l_m) + 2(h_o l_m l_n h_o)$	$-(h_o h_o l_m l_o) + 2(h_o l_o l_m h_m)$	$-\sqrt{\frac{3}{2}} (h_n h_o h_m l_n)$	$\sqrt{\frac{3}{2}} (h_n l_o l_m l_n)$	$\sqrt{\frac{3}{2}} \left(\begin{array}{c} (l_o \mathbf{F} h_m) \\ +(h_m l_o l_m l_m) \\ -(l_o h_m h_o h_o) \end{array} \right)$

	$ S_0^m A^n C^o\rangle$	$ C^m S_0^n A^o\rangle$	$ T^m T^n S_0^o\rangle$	$ S_0^m T^n T^o\rangle$	$ T^m S_0^n T^o\rangle$
$\langle A_0^m C_0^n S_0^o $	$-(h_n h_o l_n l_m) + 2(h_n l_m l_n h_o)$	$-(h_n h_m l_o l_m) + 2(h_n l_m l_o h_m)$	$\sqrt{\frac{3}{2}} \left(\begin{array}{c} (l_n \mathbf{F} h_m) \\ +(h_m l_n l_m l_m) \\ -(l_n h_m h_n h_n) \end{array} \right)$	$\sqrt{\frac{3}{2}} (h_o l_n l_m l_o)$	$-\sqrt{\frac{3}{2}} (h_o h_n h_m l_o)$
$\langle S_0^m A_0^n C_0^o $	E	$-(h_m h_n l_m l_o) + 2(h_m l_o l_m h_n)$	$-\sqrt{\frac{3}{2}} (h_m h_o h_n l_m)$	$\sqrt{\frac{3}{2}} \left(\begin{array}{c} (l_o \mathbf{F} h_n) \\ +(h_n l_o l_n l_n) \\ -(l_o h_n h_o h_o) \end{array} \right)$	$\sqrt{\frac{3}{2}} (h_m l_o l_n l_m)$
$\langle C_0^m S_0^n A_0^o $		E	$\sqrt{\frac{3}{2}} (h_n l_m l_o l_n)$	$-\sqrt{\frac{3}{2}} (h_n h_m h_o l_n)$	$\sqrt{\frac{3}{2}} \left(\begin{array}{c} (l_m \mathbf{F} h_o) \\ +(h_o l_m l_o l_o) \\ -(l_m h_o h_m h_m) \end{array} \right)$
$\langle T^m T^n S_0^o $			E	$2(h_m h_o l_o l_m)$	$2(h_n h_o l_o l_n)$
$\langle S_0^m T^n T^o $				E	$2(h_m h_n l_n l_m)$
$\langle T^m S_0^n T^o $					E

Figure 6.4: Diabatic Hamiltonian of the trimer system, considering the HOMO and LUMO of monomers. The diabatic states involve 3 Singlet exciton states 6 Charge transfer states and 3 correlated triplet states as illustrated in Fig. 1. The matrix elements are represented in terms of the Fock operator and electron repulsion integrals in molecular orbital basis.

in the overall dynamics.

In a trimer system, CT states can couple with other CT states through various mechanisms, each involving the movement of cations and anions across different fragments. 1. Cation on different fragment: When the cation moves to a different fragment, it results in different configurations of cations and anions across the fragments. These coupling terms include both one-electron integrals and two-electron integrals. The one-electron integrals typically involve the HOMO. 2. Anion on Different Fragment: Similarly, when the anion moves to a different fragment, it leads to different configurations of cations and anions. The coupling expressions in this case also include both one-electron and two-electron integrals. The one-electron integrals often involve the LUMO. 3. Exchange of Cation and Anion: When both the cation and anion exchange places, it changes the arrangement of charges on the fragments. In this scenario, the coupling expressions involve only two-electron integrals centred on spatial orbitals from 2 monomers. 4. If both the cation and anion change their positions while involving three spatial orbitals, the coupling expressions contain two-electron integrals centred on the orbitals of 3 monomers.

In a trimer system, CT states and ${}^1\text{TT}$ states can interact with each other through three distinct mechanisms: 1. When both the cation and anion are located on the same fragments of two triplets, the coupling expression involves both one-electron integrals and two-electron integrals.

The one-electron integrals include contributions from HOMO and LUMO, with a factor of $\sqrt{\frac{3}{2}}$. 2. In this case, a ${}^1(\text{TT})$ state is formed on fragments with a cationic fragment and a ground state fragment. The coupling expression includes only one two-electron integral with a factor of $-\sqrt{\frac{3}{2}}$. 3. Similarly, when a ${}^1(\text{TT})$ state is formed on fragments with an anionic and a ground state fragment, the coupling expression contains only one two-electron integral with a factor of $\sqrt{\frac{3}{2}}$.

The coupling expression between one paired triplet and another paired triplet in the trimer system is solely composed of a single two-electron integral term. This particular two-electron integral describes the simultaneous movement of a hole and an electron from the monomer where the initial triplet state was located to the monomer where the triplet state has been transferred.

6.4 Conclusion

This chapter is dedicated to the development of a diabatic model for singlet fission in trimers and higher aggregates. The primary focus of this chapter revolves around the creation and annihilation operators in the Jordan-Wigner representation, which are crucial for describing the states involved in singlet fission. In the course of this chapter, we formulate a spin-independent Hamiltonian and employ a branching diagram approach to analytically construct the wave functions for LE, CT, and TT states.

One significant advantage of this approach is the ability to selectively choose the states of interest and construct their wave functions, without the need to diagonalize matrices related to the total spin operator (\mathbf{S}) and its component along the z-axis (S_z). This selective construction of wave functions reduces the computational requirements of the analysis, making it more efficient and manageable. To avoid redundancy calculation involved in diagonalisation of \mathbf{S}^2 and S_z matrix to obtain the electronic configuration as eigenvectors. The wave function was obtained using a branching diagram. This work elucidates the algorithm to implement the generation of a branching diagram and extraction of wavefunction from the branching diagram in section Some. The complete wave function of given multiplicity in the desired frontier orbital is derived for dimer and trimer. In this chapter, the wave function of all the multiplicity for the dimer has been reported. This spin configuration can be used to make states such as 1S_nS_n , 3S_nT_n , 1T_nT_n , 3T_nT_n and 5T_nT_n . Depending on the fragment orbitals filled by the electron, the wave function of the charge transfer state is created. Although wave functions of all the multiplicity can be generated for a trimer system. The trimer wave function with singlet multiplicity has been shown. This generate state 1S_nS_nS_n , 1T_nS_nT_n , 1T_nT_nS_n , 1S_nT_nT_n , 1T_nS_nT_n and 1T_nT_nT_n .

The study involved an analysis of the coupling expressions among various states within a dimer, focused on the interactions within the frontier orbitals of each monomer. This thorough investigation encompassed the derivation of coupling expressions for singlet states formed by combining singlet monomers, charge transfer states in dimers, and paired triplets ${}^1(\text{TT})$. Additionally, the study was extended to derive expressions for coupling among three distinct types of paired triplets ${}^3(\text{TT})$. While the former analysis has been previously conducted by numerous scientists and researchers, the latter study, which delves into the coupling among different ${}^3\text{TT}$ pairs, has been explored by only a select few and didn't involve the analysis of coupling. ${}^3(\text{TT})$ shed's some light on nature of ${}^3(\text{TT})$ couplings. Continuing in this chapter, we dive into a detailed discussion of wave functions that are relevant for the generation of multiexcitons in the trimer system. We explore the complexities and qualitative aspects of the couplings between LE, CT, and ${}^1(\text{TT})$ states in the trimer. Subsequently, we construct the diabatic Hamiltonian and perform diagonalization to obtain the adiabatic energy levels of the system. This energy analysis provides valuable information about the states and trends necessary to proceed with the study. These methods and insights are further applied in the next chapter, where we specifically investigate singlet fission in a PBI (Perylene Bisimide) trimer. In this context, we analyze 64 pathways, shedding light on the generation of ${}^1(\text{TT})$ and ${}^1(\text{T...T})$ states through CT mediated processes, discussed in the next chapter. The model's future work and extensions encompass several promising avenues. Firstly, there is the prospect of expanding the model to encompass a completely spin-adapted system. This would enable the study of the impact of spin-orbit coupling on singlet fission, especially concerning charge-transfer states. The inclusion of spin-orbit coupling can yield valuable insights into electronic structure and dynamics. Secondly, extending the model to higher aggregates offers the opportunity to investigate bulk effects related to singlet fission and charge resonance phenomena.

This could be particularly relevant when examining singlet fission in solid-state materials or larger molecular assemblies. Thirdly, implementing perturbation corrections for adiabatic wave functions in the diabatic basis is essential for determining the energy levels of excited states from the context of property-specific states such as TT. The benefit of this method of evaluating the matrix element of the Hamiltonian over some previous works, such as Wick's theorem or using a diagrammatic approach, is that the matrix implementation can utilize preexisting computational libraries. Since parallelization on CPU and GPU is implemented in these libraries, this implementation of Hamiltonian evaluation takes advantage of higher performance.

Such corrections can substantially enhance the model's precision in describing electronic transitions. Additionally, the creation of diabatic wave functions for molecular aggregates, despite its computational complexity, holds the promise of simplifying the description of electronic transitions and couplings in complex systems, offering a valuable avenue of exploration. Lastly, the use of linear combinations of atomic orbitals to construct molecular orbitals, coupled with the importance of spin matrices in describing electron spin states and adhering to the Pauli exclusion principle, highlights the continuing importance of these foundational principles in quantum mechanics.

6.5 Appendix

6.5.1 Creation Operators

$$\begin{bmatrix} 0 & \cdots & & \cdots & \cdots & 0 \\ \vdots & & & & & \vdots \\ 0 & \cdots & & \cdots & \cdots & 0 \\ |h_{1\uparrow}\rangle & 0 & \cdots & \cdots & \cdots & 0 \\ 0 & |h_{1\uparrow}\rangle & 0 & \cdots & \cdots & 0 \\ \vdots & & \ddots & & & \vdots \\ 0 & \cdots & 0 & |h_{1\uparrow}\rangle & 0 & \cdots \cdots 0 \\ 0 & \cdots & \cdots & 0 & |h_{1\uparrow}\rangle & 0 \end{bmatrix} \quad (6.29)$$

$$\begin{bmatrix} 0 & \cdots & & \cdots & \cdots & & 0 \\ \vdots & & & & & & \vdots \\ 0 & \cdots & & \cdots & \cdots & & 0 \\ |h_{1\downarrow}\rangle & 0 & \cdots & \cdots & \cdots & & 0 \\ 0 & |h_{1\downarrow}\rangle & 0 & \cdots & \cdots & & 0 \\ \vdots & & \ddots & & & & \vdots \\ 0 & \cdots & 0 & |h_{1\downarrow}\rangle & 0 & \cdots \cdots & 0 \\ 0 & \cdots & \cdots & 0 & |h_{1\downarrow}\rangle & 0 & \cdots & 0 \\ 0 & \cdots & \cdots & 0 & 0 & 0 & \cdots & 0 \\ \vdots & & & & \ddots & & & \vdots \\ 0 & \cdots & \cdots & & 0 & 0 & 0 & \cdots & 0 \\ 0 & \cdots & \cdots & & 0 & -|h_{1\downarrow}\rangle & 0 & \cdots \cdots & 0 \\ 0 & \cdots & \cdots & & & 0 & -|h_{1\downarrow}\rangle & 0 & \cdots \cdots 0 \\ \vdots & & & & & & \ddots & & \vdots \\ 0 & \cdots & \cdots & & & & 0 & -|h_{1\downarrow}\rangle & 0 \cdots \cdots 0 \\ 0 & \cdots & \cdots & & & & \cdots & 0 & -|h_{1\downarrow}\rangle & 0 \cdots \cdots 0 \end{bmatrix} \quad (6.30)$$

$$\begin{bmatrix}
 0 & \dots & & \dots & & \dots & & 0 \\
 \vdots & & & & & & & \vdots \\
 8\text{times} & & & & & & & \\
 \vdots & & & & & & & \vdots \\
 0 & \dots & \dots & \dots & \dots & & & 0 \\
 |l_{1\uparrow}\rangle & 0 & \dots & \dots & \dots & & & 0 \\
 0 & \ddots & 0 & \dots & \dots & & & 0 \\
 \vdots & & 8\text{times} & & & & & \vdots \\
 \vdots & & & \ddots & & & & \vdots \\
 0 & \dots & \dots & 0 & |l_{1\uparrow}\rangle & 0 & \dots & 0 \\
 0 & \dots & \dots & 0 & 0 & 0 & \dots & 0 \\
 \vdots & & & & \ddots & & & \vdots \\
 \vdots & & & & & 8\text{times} & & \vdots \\
 \vdots & & & & & \ddots & & \vdots \\
 0 & \dots & \dots & & 0 & -|l_{1\uparrow}\rangle & 0 & \dots & \dots & \dots & 0 \\
 \vdots & & & & & \ddots & & \vdots \\
 \vdots & & & & & & & \vdots
 \end{bmatrix} \quad (6.31)$$

$$\begin{bmatrix}
 0 \\
 4\text{times} \\
 \vdots \\
 |l_{1\downarrow}\rangle & 0 \\
 0 & \ddots \\
 \vdots & 4\text{times} \\
 0 & \dots & 0 & 0 & 0 \\
 \vdots & & & \ddots & \\
 \vdots & & & & 4\text{times} \\
 \vdots & & & 0 & -|l_{1\downarrow}\rangle & 0 \\
 \vdots & & & & \ddots & \\
 \vdots & & & & & 4\text{times} \\
 \vdots & & & 0 & 0 & 0 \\
 \vdots & & & & \ddots & \ddots & \ddots
 \end{bmatrix} \quad (6.32)$$

$$\left[\begin{array}{ccccccc} 0 & \cdots & & & & & \\ 0 & \cdots & & & & & \\ |h_{2\uparrow}\rangle & 0 & \cdots & & & & \\ 0 & |h_{2\uparrow}\rangle & 0 & \cdots & & & \\ \vdots & 0 & 0 & 0 & \cdots & & \\ \vdots & 0 & 0 & 0 & \cdots & & \\ \vdots & 0 & -|h_{2\uparrow}\rangle & 0 & \cdots & & \\ \vdots & 0 & -|h_{2\uparrow}\rangle & 0 & \cdots & & \\ \vdots & 0 & 0 & 0 & \cdots & & \\ \vdots & 0 & 0 & 0 & \cdots & & \\ \vdots & 0 & -|h_{2\uparrow}\rangle & 0 & \cdots & & \\ \vdots & 0 & -|h_{2\uparrow}\rangle & 0 & \cdots & & \\ \vdots & 0 & 0 & 0 & \cdots & & \\ \vdots & 0 & 0 & 0 & \cdots & & \\ \vdots & 0 & |h_{2\uparrow}\rangle & 0 & \cdots & & \\ \vdots & 0 & |h_{2\uparrow}\rangle & 0 & \cdots & & \\ \ddots & \ddots & \ddots & \ddots & \ddots & \ddots & \ddots \end{array} \right] \quad (6.33)$$

$$\left[\begin{array}{ccccccc} 0 & \cdots & & & & & \\ |h_{2\uparrow}\rangle & 0 & \cdots & & & & \\ 0 & 0 & 0 & \cdots & & & \\ \vdots & 0 & -|h_{2\uparrow}\rangle & 0 & \cdots & & \\ \vdots & 0 & 0 & 0 & \cdots & & \\ \vdots & 0 & -|h_{2\uparrow}\rangle & 0 & \cdots & & \\ \vdots & 0 & 0 & 0 & \cdots & & \\ \vdots & 0 & |h_{2\uparrow}\rangle & 0 & \cdots & & \\ \vdots & 0 & 0 & 0 & \cdots & & \\ \vdots & 0 & -|h_{2\uparrow}\rangle & 0 & \cdots & & \\ \vdots & 0 & 0 & 0 & \cdots & & \\ \vdots & 0 & 0 & 0 & \cdots & & \\ \vdots & 0 & -|h_{2\uparrow}\rangle & 0 & \cdots & & \\ \vdots & 0 & \ddots & \ddots & \ddots & \ddots & \ddots \end{array} \right] \quad (6.34)$$

6.5.2 Operations to Obtain Hamiltonian

$$\langle c_{\uparrow h_1} | \mathbf{T} | c_{\uparrow h_1}^\dagger \rangle = \begin{bmatrix} |h_{1\downarrow}\rangle\langle h_{1\downarrow}| & 0 & 0 & 0 & 0 & \dots \\ 0 & |h_{1\downarrow}\rangle\langle h_{1\downarrow}| & |h_{2\downarrow}\rangle\langle h_{2\uparrow}| & 0 & |h_{2\downarrow}\rangle\langle l_{1\downarrow}| & \dots \\ 0 & |h_{2\uparrow}\rangle\langle h_{2\downarrow}| & |h_{1\downarrow}\rangle\langle h_{1\downarrow}| & 0 & |h_{2\uparrow}\rangle\langle l_{1\downarrow}| & \dots \\ 0 & 0 & 0 & |h_{1\downarrow}\rangle\langle h_{1\downarrow}| & 0 & \dots \\ 0 & |l_{1\downarrow}\rangle\langle h_{2\downarrow}| & |l_{1\downarrow}\rangle\langle h_{2\uparrow}| & 0 & |h_{1\downarrow}\rangle\langle h_{1\downarrow}| & \dots \\ \vdots & \vdots & \vdots & \vdots & \vdots & \ddots \end{bmatrix} \quad (6.36)$$

$$\langle c_{\downarrow l_1} c_{\uparrow h_1} | \mathbf{T} | c_{\uparrow h_1}^\dagger c_{\downarrow l_1}^\dagger \rangle = \begin{bmatrix} |l_{1\downarrow}\rangle\langle l_{1\downarrow}| & 0 & 0 & 0 & 0 & \dots \\ +|h_{1\uparrow}\rangle\langle h_{1\uparrow}| & |l_{1\downarrow}\rangle\langle l_{1\downarrow}| & +|h_{1\uparrow}\rangle\langle h_{1\uparrow}| & |h_{2\downarrow}\rangle\langle h_{2\uparrow}| & 0 & 0 & \dots \\ 0 & +|h_{2\downarrow}\rangle\langle h_{2\downarrow}| & |h_{2\uparrow}\rangle\langle h_{2\downarrow}| & |l_{1\downarrow}\rangle\langle l_{1\downarrow}| & 0 & 0 & \dots \\ 0 & |h_{2\uparrow}\rangle\langle h_{2\downarrow}| & +|h_{1\uparrow}\rangle\langle h_{1\uparrow}| & +|h_{2\uparrow}\rangle\langle h_{2\uparrow}| & |h_{2\downarrow}\rangle\langle h_{2\downarrow}| & 0 & \dots \\ 0 & 0 & 0 & +|l_{1\downarrow}\rangle\langle l_{1\downarrow}| & +|h_{1\uparrow}\rangle\langle h_{1\uparrow}| & 0 & \dots \\ 0 & 0 & 0 & +|h_{2\uparrow}\rangle\langle h_{2\uparrow}| & +|h_{2\downarrow}\rangle\langle h_{2\downarrow}| & 0 & \dots \\ \vdots & \vdots & \vdots & \vdots & \vdots & \ddots & \vdots \end{bmatrix} \quad (6.37)$$

$$\langle c_{\downarrow h_2} c_{\downarrow l_1} c_{\uparrow h_1} | \mathbf{T} | c_{\uparrow h_1}^\dagger c_{\downarrow l_1}^\dagger c_{\uparrow h_2}^\dagger \rangle = \begin{bmatrix} |l_{1\downarrow}\rangle\langle l_{1\downarrow}| & & & & & \\ +|h_{1\uparrow}\rangle\langle h_{1\uparrow}| & 0 & 0 & 0 & 0 & \dots \\ +|h_{2\uparrow}\rangle\langle h_{2\uparrow}| & & & & & \\ 0 & |h_{2\downarrow}\rangle\langle h_{2\downarrow}| + |l_{1\downarrow}\rangle\langle l_{1\downarrow}| & 0 & 0 & 0 & \dots \\ 0 & +|h_{1\uparrow}\rangle\langle h_{1\uparrow}| + |h_{2\uparrow}\rangle\langle h_{2\uparrow}| & & & & \\ 0 & 0 & 0 & 0 & 0 & \dots \\ 0 & 0 & 0 & 0 & 0 & \dots \\ 0 & 0 & 0 & 0 & 0 & \dots \\ \vdots & \vdots & \vdots & \vdots & \vdots & \ddots \end{bmatrix} \quad (6.38)$$

$$\langle c_{\downarrow h_2} c_{\downarrow h_2} c_{\downarrow l_1} c_{\uparrow h_1} | \mathbf{T} | c_{\uparrow h_1}^\dagger c_{\downarrow l_1}^\dagger c_{\uparrow h_2}^\dagger c_{\uparrow h_2} \rangle = \begin{bmatrix} |h_{2\downarrow}\rangle\langle h_{2\downarrow}| + |l_{1\downarrow}\rangle\langle l_{1\downarrow}| & 0 & 0 & 0 & 0 & \dots \\ +|h_{1\uparrow}\rangle\langle h_{1\uparrow}| + |h_{2\uparrow}\rangle\langle h_{2\uparrow}| & 0 & 0 & 0 & 0 & \dots \\ 0 & 0 & 0 & 0 & 0 & \dots \\ 0 & 0 & 0 & 0 & 0 & \dots \\ 0 & 0 & 0 & 0 & 0 & \dots \\ 0 & 0 & 0 & 0 & 0 & \dots \\ \vdots & \vdots & \vdots & \vdots & \vdots & \ddots \end{bmatrix} \quad (6.39)$$

Chapter 7

Formation Pathways of the Spin-Correlated, Spatially Separated ${}^1(T...T)$ State in the Singlet Fission Process of Perylene Diimide Stacks

7.1 Abstract

For the theoretical screening of Singlet Fission (SF) rates in molecular aggregates, commonly dimer model systems are employed. However, there is experimental evidence, that the SF process proceeds from the ${}^1(TT)$ state via an triplet-triplet energy transfer process to a further intermediate: a ${}^1(T...T)$ state with two non-adjacent, spin-correlated triplets, which cannot be captured by the dimer models. In this work, we extend Michl's diabatic frontier orbital model to trimer systems, for which we automatically generate the diabatic two and three-center couplings using symbolic algebra. We apply this method to study the packing dependence of the ${}^1(T...T)$ formation in the perylene diimide (PDI) trimer stack. We find that efficient triplet-triplet energy transfer is facilitated by structural motifs for which also significant excimer character can be observed. Furthermore, the coupling shows a local maximum for the structural motif that has been assigned to efficient ${}^1(TT)$ population. Employing second order perturbation theory, we study the interference of the individual electronic pathways that arise in the PDI trimer system, allowing us to reproduce the packing dependence of the SF rates derived from previous Redfield theory simulations.

7.2 Introduction

Singlet fission (SF) is a process occurring in molecular systems, in which a singlet exciton is converted into two triplets.[28] As SF offers the opportunity to overcome the thermalization loss in solar energy technologies, the design of efficient SF materials is an active field of research that crucially builds on the understanding how multiexcitons can be generated and controlled.[298, 299] It is commonly accepted that the SF process proceeds from an initially excited singlet exciton state via the transient formation of a correlated triplet exciton pair ${}^1(TT)$ intermediate with an overall singlet spin multiplicity, either via a direct or a charge transfer mediated pathway, however, the fate of the spin-correlated triplets is far less explored. [56, 300, 301] The populated ${}^1(TT)$ state has been commonly assumed to disentangle by spin decoherence effects, forming two independent triplets $T + T$.[55] However, Pensack et. al. reported on a femtosecond transient absorption study of the SF process in pentacene, providing evidence that the intermediate ${}^1(TT)$ state further evolves to a second intermediate, forming a specially separated, spin correlated triplet exciton pair ${}^1(T...T)$.[280] Based on their findings, they established a three-step kinetic scheme of the SF process:



The ${}^1(T...T)$ state can be considered as an electronically uncorrelated, but yet spin entangled triplet pair on non-adjacent molecules, that can be formed from a ${}^1(TT)$ state upon a triplet-triplet energy (Dexter) transfer mechanism. [178, 281] For deeper information, we refer the reader to the review by

Zhu and coworkers[56]. We wish to emphasize that the introduced three-step mechanism offers a so far unexplored strategy in the design of an efficient SF process: that is, the harvesting of the $^1(T\ldots T)$ state in order to steer the kinetics of the process. Interestingly, He et. al. have recently reported on the direct harvesting of a bound triplet pair.[302] Furthermore, in the computational screening of new SF materials, the transfer integral for the $^1(TT)$ to $^1(T\ldots T)$ transition should be taken into account as well as its packing dependence. However, this aspect is underexplored from theoretical side. Abraham et. al. have delivered an expression of the respective triplet-triplet energy transfer integral derived from the Spin Hamiltonian in the Heisenberg picture and studied its dependence on the packing motif in tetracene employing *ab – initio* calculations. [303] Taffet et. al. carried out highly accurate single-point computations of the noninteracting $^5(TT)$ state in the dimer that can be considered as a proxy for the spatial product of the $^1(T\ldots T)$ state, studying tetracenes as well as carotenoids. [304]

The existence of the described intermediates has already been proposed in the 70s by Frankevich et. al. based on the Reaction Yield Detected Magnetic Resonance Spectra, they recorded for the tetracene crystal, [305] while Chan et. al. has formulated a similar kinetic scheme upon the observation of two distinct multiexciton states in a pentacene/fullerene bilayer system using femtosecond nonlinear spectroscopies.[306] The formation of an $^1(T\ldots T)$ state in pentacene was also studied by others [307, 282] and has been further observed in crystalline rubrene [308], polycrystalline hexacene [309] as well as in linear oligomers and linked dimers of perylene[310, 88], each representing well-established SF molecules. Another prominent candidate for studying SF effects is perylene diimide (PDI), that offers the appealing possibility to effectively control its packing arrangement in thin films introducing different functional groups at their imide positions,[227, 260] while the introduction of linkers on these positions allows for the production of well-defined model compounds of stacked dimer and trimer oligomers that have provided valuable insights into the packing structure dependence of SF efficiency and underlying mechanisms.[311, 263, 265] Studies suggest a CT-mediated mechanism promoted by intermolecular orbital effects, while the role of a (transient) excimer formation is under debate.[26, 121, 263] A recent combined theoretical and experimental study on a linked trimer stack of PDIs revealed two SF channels that depend on the chosen wavelength of the initial excitation: a fast pathway that has been assigned to proceed via a virtual CT coupling, initiated by the excitation of a red band, and a (slower) pathway that is assumed to proceed via transient formation of the excimer, initialized upon the excitation of the main absorption band.[265] However, to the best of our knowledge, no experimental (and theoretical work) has targeted the mutual role of the specially separated $^1(T\ldots T)$ state in the SF process of PDIs. In this work, we deliver a theoretical study on the formation pathways and their packing dependence of the specially separated, spin-correlated triplet pair $^1(T\ldots T)$ state in the PDI trimer system, with the aim to stimulate further both experimental and theoretical studies in this field to fully explore the role of the $^1(T\ldots T)$ state in the SF process.

In the past, theoretical studies of the SF process and its packing dependence have often focused on molecular dimers. [12, 312, 15, 72, 313, 314, 315, 1, 287] In this regard, the diabatic frontier orbital (FO) model as introduced by Michl [28], in which the local excitation (LE), Charge Transfer (CT) as well as the singlet-correlated triplet pair excitation in the basis of the monomer HOMOs and LUMOs are considered is of frequent use. Approximating the couplings between these quasi-diabatic states by expressions of the Fock matrix, the model has been proven particularly suitable for the fast screening of the packing dependence of the SF process in molecular dimer systems. [316, 287] Berkelbach et. al. delivered an *ab – initio* parametrized implementation of the FO model and carried out periodic calculations in order to study the SF process in the crystalline phase, accounting for couplings between next neighbor molecules,[57, 58, 59], Li et al. delivered an ab-initio parametrized, extended exciton model for SF that considers the FMO model and couplings between adjacent molecules, studying pentacene clusters, while Nakano et. al. constructed linear aggregates with defined extended size based on the dimer parametrization.[317] Miryani et.al. screened the packing dependence of the SF rate by Redfield simulations, in which the FO dimer model is coupled to a bath, in order to account for the crystal environment. However, all these implementations are inherently insufficient for the investigation of the formation of the $^1(T\ldots T)$ state as for such studies, three-center couplings have to be considered. For such studies, an explicit trimer system, in which couplings between all monomers are taken into account, has to be employed as a minimal model.

In this work, we generalize the FO model for the description of molecular trimer systems, accounting for couplings between all monomers and employ second order perturbation theory to derive the Transition Probability of the formation of the correlated triplet pair state, which we scan along a vertical and a longitudinal slipping mode and study the electronic pathways of the $^1(T\ldots T)$ formation. We further determine the relative importance of the electronic pathways that arise in the trimer system and study the packing structure dependence of the individual formation pathways, identifying optimal stacking geometries for the SF process. In our algorithm, matrix elements are automatically generated using symbolic algebra, allowing an efficient calculation of products of matrix elements.

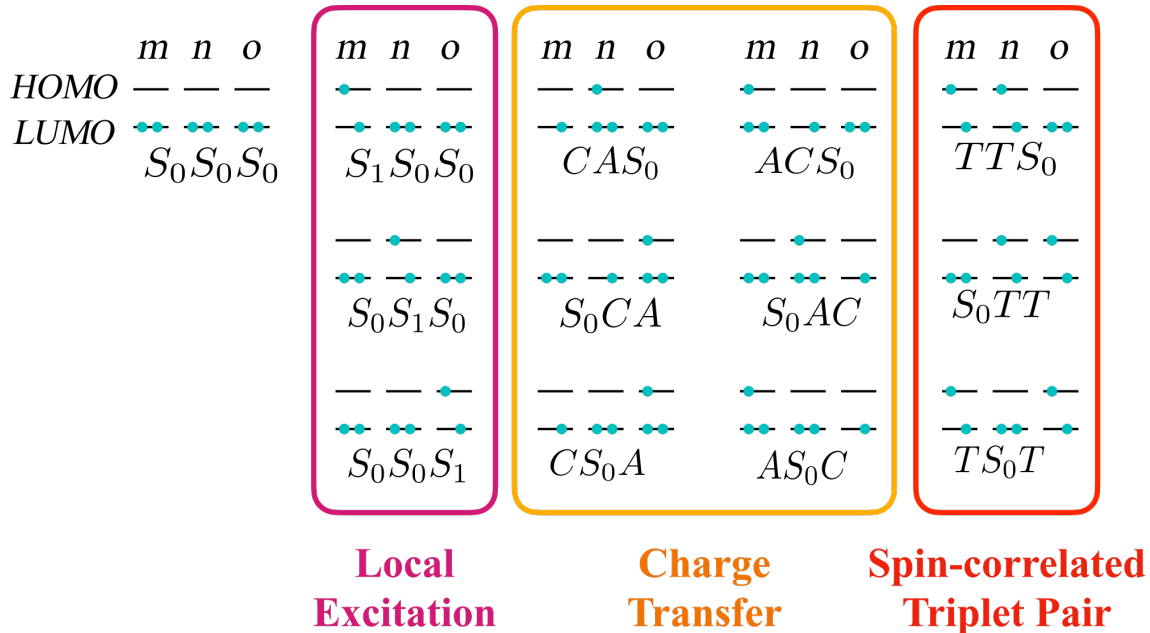


Figure 7.1: Diabatic states considered in the trimer model Hamiltonian.

7.3 Method

In the following, the details of the model are presented: We construct a stack consisting of three monomers m, n and o . Considering the highest occupied molecular orbitals (HOMO) and lowest unoccupied molecular orbitals (LUMO) on each monomer, the model describes a system with 6 electrons in the 6 orbitals h_m, l_m, h_n, l_n, h_o and l_o , where h and l represent HOMO and LUMO, respectively, and their subscripts represent the monomer they belong to. The orbitals are considered to be real, normalized and orthogonal to each other. Each monomer $I=m, n, o$ has 5 states, the ground state S_0^I , the singlet excited state S_1^I , a cationic state C^I , an anionic state A^I , and a triplet state T^I . Assuming an overall singlet multiplicity of the system, we construct 13 diabatic states of the trimer, giving rise to one ground state (GS), three locally excited singlet states (LE), six charge transfer states (CT) and three correlated paired triplet states ${}^1(TT)$ with overall singlet multiplicity, as illustrated in figure 8.1. Notice, that the doubly excited state (1S_1S_1) is excluded from further consideration, as the energy of this configuration is expected to be significantly higher. It is emphasised, that in contrast to a dimer system, in the trimer system configurations arise, in which the cation-anion pair as well as the spin-correlated triplets, are spatially separated by an "innocent" monomer. The resulting diabatic Hamiltonian of the model-CI system is then generated, for which the expressions for the matrix elements are derived employing our program given in ref [296]. In the implementation, the second quantization formalism is applied, leading to the following expression for the Hamiltonian:

$$\hat{H} = \sum_{i,j=1}^d \sum_{s_i, s_j = \alpha, \beta} h_{ij} c_{i,s_i}^\dagger c_{j,s_j} + \frac{1}{2} \sum_{i,j,k,l=1}^d \sum_{s_i, s_j, s_k, s_l = \alpha, \beta} V_{ijkl} c_{i,s_i}^\dagger c_{j,s_j}^\dagger c_{k,s_k} c_{l,s_l} \quad (7.2)$$

where h and V represent the one electron and 2-electron integrals respectively and c^\dagger and c are the creation and annihilation operators.

In that way the matrix elements of the Hamiltonian can be generally expressed as

$$\begin{aligned} \langle \Psi_m | \hat{H} | \Psi_n \rangle &= \sum_{i,j=1}^d \sum_{s_i, s_j = \alpha, \beta} h_{ij} \langle \Psi_m | c_{i,s_i}^\dagger c_{j,s_j} | \Psi_n \rangle \\ &+ \frac{1}{2} \sum_{i,j,k,l=1}^d \sum_{\substack{s_i, s_j, s_k, s_l \\ = \alpha, \beta}} V_{ijkl} \langle \Psi_m | c_{i,s_i}^\dagger c_{j,s_j}^\dagger c_{k,s_k} c_{l,s_l} | \Psi_n \rangle \end{aligned} \quad (7.3)$$

A crucial aspect of our algorithm is the choice of the Jordan-Wigner representation [175] of the fermionic creation and annihilation operators in order to automatically generate the model CI-Hamiltonian matrix and provide analytic expressions for the latter. The second-quantized operators are constructed by symbolic Kronecker products of the Pauli spin matrices corresponding to the spin orbitals, and the matrix elements are generated using the symbolic algebra programs. The Jordan-Wigner representation of the fermionic operators is given by:

$$c^\dagger = \sigma_z \otimes \dots \otimes \sigma_z \otimes \sigma^- \otimes \mathbb{1} \otimes \dots \otimes \mathbb{1} \quad (7.4)$$

$$c = \sigma_z \otimes \dots \otimes \sigma_z \otimes \sigma^+ \otimes \mathbb{1} \otimes \dots \otimes \mathbb{1} \quad (7.5)$$

where σ_z is the Pauli spin matrix corresponding to the z-component of the spin and $\sigma^\pm = \sigma_x \pm i\sigma_y$. Using these basic operators, spin adapted combinations of the fermionic operators can be constructed.

Using the operators formed as matrix of symbols, the one- and two-electron operators are obtained by performing tensor products of the basic operators. In this way, analytic expressions for the matrix elements involving configurations with arbitrary excitation level can be symbolically generated and utilized both for theoretical analysis of the couplings as well as for their numerical evaluation.

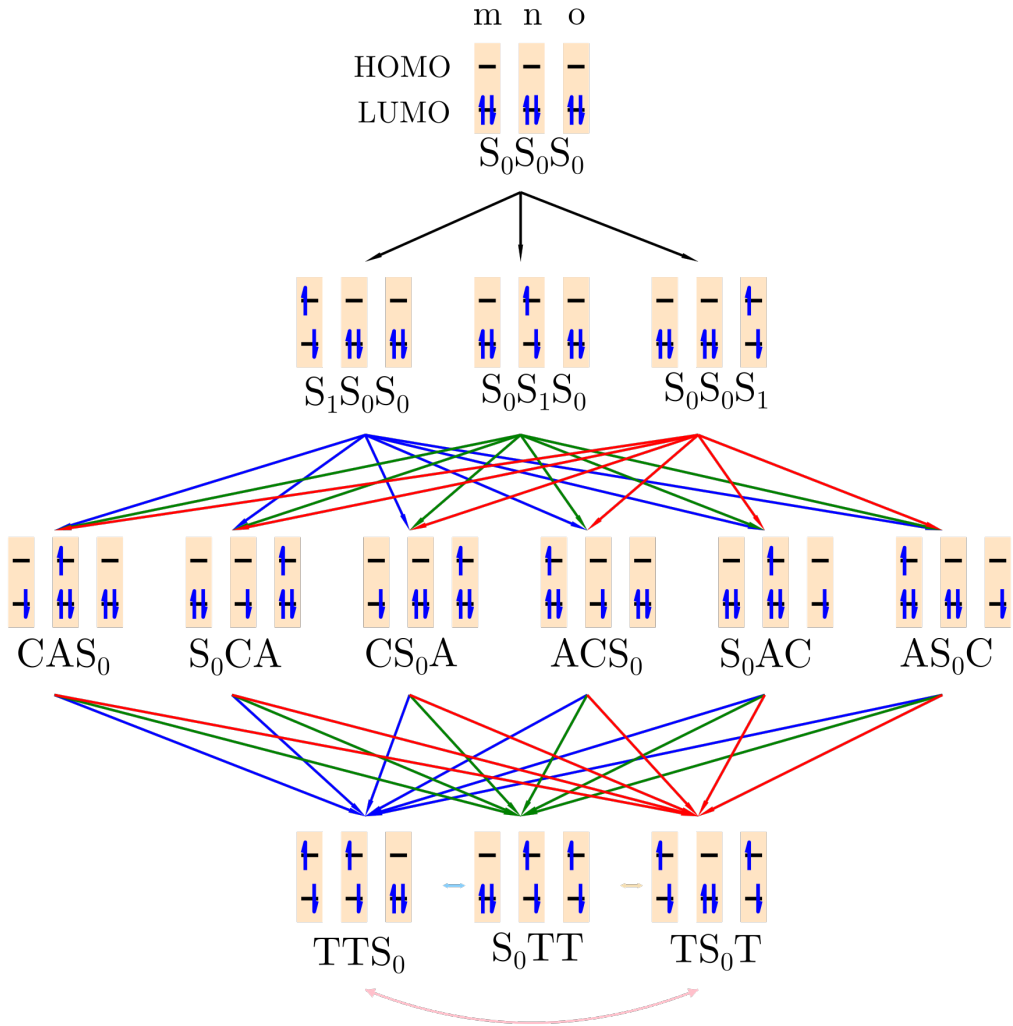


Figure 7.2: b) CT mediated pathways of ${}^1(TT)$ and ${}^1(T\ldots T)$ states formation.

In this work, we approximate the formation rate from a chosen initial diabatic state to the chosen final state by Fermi's golden rule, employing second-order perturbation theory. In that way, a transition probability can be calculated according to.

$$P_{a \rightarrow b} = \left| \sum_{a \neq b} \sum_{q \neq b} \sum_a \frac{\langle a | W_t | q \rangle \langle q | W_t | b \rangle}{(E_b - E_a)(E_q - E_b)} \right|^2, \quad (7.6)$$

where a and b are the initial and final diabatic states, respectively, q is the intermediate diabatic state and W_t is the perturbing Hamiltonian. E_a, E_b and E_q are the energy of diabatic states a, b and q respectively.

	$ S_0^m S_1^n S_0^o\rangle$	$ S_0^m S_0^n S_1^o\rangle$	$ C^m A^n S_0^o\rangle$	$ S_0^m C^n A^o\rangle$	$ A^m S_0^n C^o\rangle$	$ A^m C^n S_0^o\rangle$
$\langle S_1^m S_0^n S_0^o $	$-(h_m h_n l_n l_m) + 2(h_m l_m l_n h_n)$	$-(h_m h_o l_o l_m) + 2(h_m l_m l_o h_o)$	$\langle l_m \mathbf{F} l_n \rangle + 2(h_m l_m l_n h_m) - (h_m h_n l_m l_n)$	$2(h_m l_m l_o h_n) - 1(h_m h_n l_o l_m)$	$-\langle h_m \mathbf{F} h_o \rangle + 2(h_m l_m l_m h_o) - (h_m h_o l_m l_m)$	$-\langle h_m \mathbf{F} h_n \rangle + 2(h_m l_m l_m h_n) - (h_m h_n l_m l_m)$
$\langle S_0^m S_1^n S_0^o $	E		$-\langle h_n h_o l_o l_n \rangle + 2(h_n l_n l_o h_o)$	$\langle l_n \mathbf{F} l_o \rangle + 2(h_n l_n l_o h_n) - (h_n h_n l_n l_o)$	$2(h_n l_n l_m h_o) - 1(h_n h_o l_m l_n)$	$\langle l_n \mathbf{F} l_m \rangle + 2(h_n l_p l_m h_n) - (h_n h_n l_m l_m)$
$\langle S_0^m S_0^n S_1^o $		E	$2(h_o l_o l_n h_m) - 1(h_o h_m l_n l_o)$	$-\langle h_o \mathbf{F} h_n \rangle + 2(h_o l_o l_o h_n) - (h_o h_n l_o l_o)$	$\langle l_o \mathbf{F} l_m \rangle + 2(h_o l_o l_m h_o) - (h_o h_o l_o l_m)$	$2(h_o l_o l_m h_n) - 1(h_o h_n l_m l_o)$
$\langle C_0^m A_0^n S_0^o $			E	$-(h_m h_n l_o n) + 2(h_m l_n l_o h_n)$	$-(h_m h_o l_m n) + 2(h_m l_n l_m h_o)$	$-(h_m h_n l_n m) + 2(h_m l_m l_n h_n)$
$\langle S_0^m C_0^n A_0^o $				E	$-\langle h_n h_o l_m l_o \rangle + 2(h_n l_o l_m h_o)$	$\langle l_o \mathbf{F} l_m \rangle - (h_n h_n l_m l_o) + 2(h_n l_o l_m h_n)$
$\langle A_0^m S_0^n C_0^o $					E	$\langle h_o \mathbf{F} h_n \rangle - (h_o h_n l_m l_m) + 2(h_o l_m l_m h_n)$

	$ S_0^m A^n C^o\rangle$	$ C^m S_0^n A^o\rangle$	$ T^m T^n S_0^o\rangle$	$ S_0^m T^n T^o\rangle$	$ T^m S_0^n T^o\rangle$
$\langle S_1^m S_0^n S_0^o $	$2(h_m l_m l_n h_o) - 1(h_m h_o l_n l_m)$	$\langle l_m \mathbf{F} l_o \rangle + 2(h_m l_m l_o h_m) - (h_m h_m l_m l_o)$	$\sqrt{\frac{3}{2}} \begin{pmatrix} (l_m l_m h_n l_n) \\ -(h_m l_m h_n h_m) \end{pmatrix}$	0	$\sqrt{\frac{3}{2}} \begin{pmatrix} (l_o l_m h_o l_o) \\ -(h_m l_m h_o h_m) \end{pmatrix}$
$\langle S_0^m S_1^n S_0^o $	$-\langle h_n \mathbf{F} h_o \rangle + 2(h_n l_n l_n h_o) - (h_n h_o l_n l_n)$	$2(h_n l_n l_o h_m) - 1(h_n h_m l_o l_n)$	$\sqrt{\frac{3}{2}} \begin{pmatrix} (l_m l_n h_m l_m) \\ -(h_n l_n h_m h_n) \end{pmatrix}$	$\sqrt{\frac{3}{2}} \begin{pmatrix} (l_o l_n h_o l_o) \\ -(h_n l_n h_o h_n) \end{pmatrix}$	0
$\langle S_0^m S_0^n S_1^o $	$\langle l_o \mathbf{F} l_n \rangle + 2(h_o l_o l_n h_o) - (h_o h_o l_n l_n)$	$-\langle h_o \mathbf{F} h_m \rangle + 2(h_o l_o l_o h_m) - (h_o h_m l_o l_o)$	0	$\sqrt{\frac{3}{2}} \begin{pmatrix} (l_o l_o h_n l_n) \\ -(h_o l_o h_n h_o) \end{pmatrix}$	$\sqrt{\frac{3}{2}} \begin{pmatrix} (l_m l_o h_m l_m) \\ -(h_o l_o h_m h_o) \end{pmatrix}$
$\langle C_0^m A_0^n S_0^o $	$-\langle h_m \mathbf{F} h_o \rangle - (h_m h_o l_n l_n) + 2(h_m l_n l_o h_n)$	$\langle l_n \mathbf{F} l_o \rangle - (h_m h_m l_o l_n) + 2(h_m l_n l_o h_m)$	$\sqrt{\frac{3}{2}} \begin{pmatrix} (l_m \mathbf{F} h_n) \\ +(h_m l_m l_n l_n) \\ -(l_m h_n h_m h_m) \end{pmatrix}$	$-\sqrt{\frac{3}{2}} (h_o h_m h_n l_o)$	$\sqrt{\frac{3}{2}} (h_o l_m l_n l_o)$
$\langle S_0^m C_0^n A_0^o $	$-(h_n h_o l_o l_n) + 2(h_n l_n l_o h_o)$	$-\langle h_n \mathbf{F} h_m \rangle - (h_n h_m l_o l_o) + 2(h_n l_o l_o h_m)$	$\sqrt{\frac{3}{2}} (h_m l_n l_o l_m)$	$\sqrt{\frac{3}{2}} \begin{pmatrix} \langle l_n \mathbf{F} h_o \rangle \\ +(h_o l_n l_o l_o) \\ -(l_n h_o h_n h_n) \end{pmatrix}$	$-\sqrt{\frac{3}{2}} (h_m h_n h_o l_m)$
$\langle A_0^m S_0^n C_0^o $	$\langle l_m \mathbf{F} l_n \rangle - (h_o h_o l_n l_m) + 2(h_o l_m l_n h_o)$	$-(h_o h_m l_m l_o) + 2(h_o l_o l_m h_m)$	$-\sqrt{\frac{3}{2}} (h_n h_o h_m l_n)$	$\sqrt{\frac{3}{2}} (h_n l_o l_m l_n)$	$\sqrt{\frac{3}{2}} \begin{pmatrix} \langle l_o \mathbf{F} h_m \rangle \\ +(h_m l_o l_m l_m) \\ -(l_o h_m h_o h_o) \end{pmatrix}$

	$ S_0^m A^n C^o\rangle$	$ C^m S_0^n A^o\rangle$	$ T^m T^n S_0^o\rangle$	$ S_0^m T^n T^o\rangle$	$ T^m S_0^n T^o\rangle$
$\langle A_0^m C_0^n S_0^o $	$-(h_n h_o l_n l_m) + 2(h_n l_m l_n h_o)$	$-(h_n h_m l_o l_m) + 2(h_n l_m l_o h_m)$	$\sqrt{\frac{3}{2}} \begin{pmatrix} \langle l_n \mathbf{F} h_m \rangle \\ +(h_m l_n l_m l_m) \\ -(l_n h_m h_n h_n) \end{pmatrix}$	$\sqrt{\frac{3}{2}} (h_o l_n l_m l_o)$	$-\sqrt{\frac{3}{2}} (h_o h_n h_m l_o)$
$\langle S_0^m A_0^n C_0^o $	E	$-(h_m h_n l_m l_o) + 2(h_m l_o l_m h_n)$	$-\sqrt{\frac{3}{2}} (h_m h_o h_n l_m)$	$\sqrt{\frac{3}{2}} \begin{pmatrix} \langle l_o \mathbf{F} h_n \rangle \\ +(h_n l_o l_n l_n) \\ -(l_o h_n h_o h_o) \end{pmatrix}$	$\sqrt{\frac{3}{2}} (h_m l_o l_n l_m)$
$\langle C_0^m S_0^n A_0^o $		E	$\sqrt{\frac{3}{2}} (h_m l_m l_o l_n)$	$-\sqrt{\frac{3}{2}} (h_n h_m h_o l_n)$	$\sqrt{\frac{3}{2}} \begin{pmatrix} \langle l_m \mathbf{F} h_o \rangle \\ +(h_o l_m l_o l_o) \\ -(l_m h_o h_m h_m) \end{pmatrix}$
$\langle T^m T^n S_0^o $			E	$2(h_m h_o l_o l_m)$	$2(h_n h_o l_o l_n)$
$\langle S_0^m T^n T^o $				E	$2(h_m h_n l_n l_m)$
$\langle T^m S_0^n T^o $					E

Figure 7.3: Diabatic Hamiltonian of the trimer system, considering the HOMO and LUMO of monomers. The diabatic states involve 3 Singlet exciton states 6 Charge transfer states and 3 correlated triplet states as illustrated in Fig. 1. The matrix elements are represented in terms of the Fock operator and electron repulsion integrals (ERI) in molecular orbital basis.

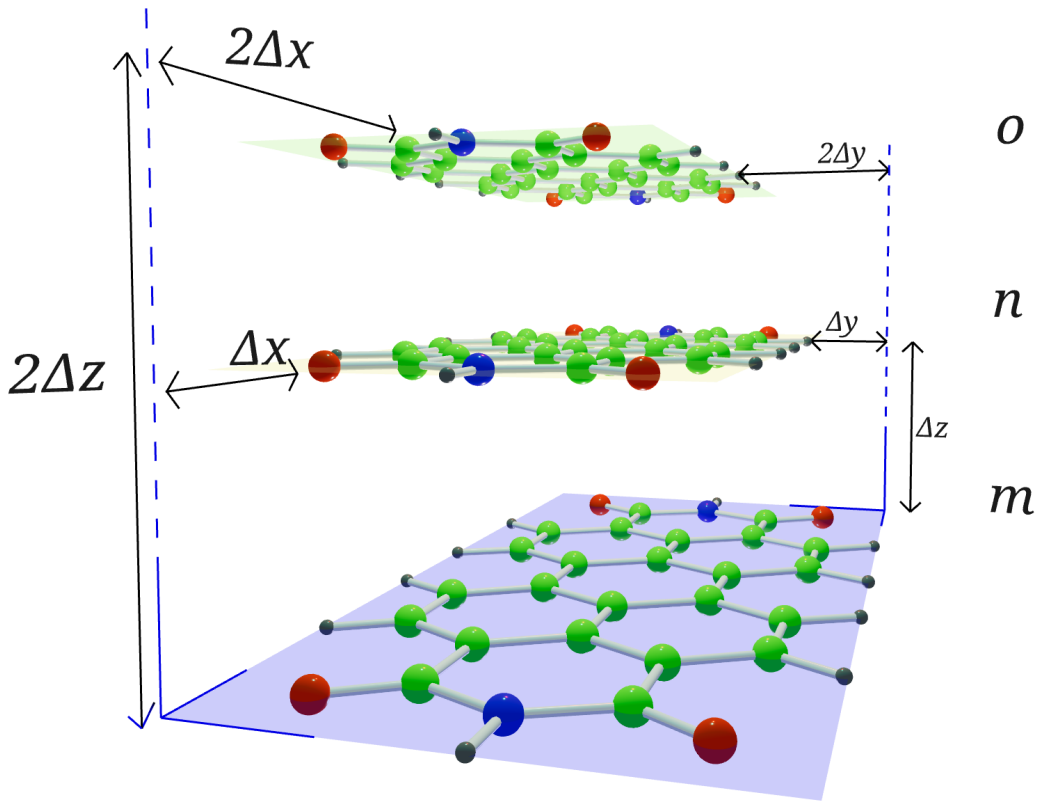


Figure 7.4: PDI trimer model.

$a)$	$ \text{S}_1\text{S}_0\text{S}_0\rangle$	$ \text{S}_0\text{S}_1\text{S}_0\rangle$	$ \text{S}_0\text{S}_0\text{S}_1\rangle$	$ \text{TS}_0\rangle$	$ \text{TS}_0\text{T}\rangle$
$ \text{CAS}_0\rangle$	0.300	0.642	-0.540		
$ \text{S}_0\text{CA}\rangle$		0.300	0.642	-0.550	
$ \text{AS}_0\text{C}\rangle$	0.001		0.005		-0.008
$ \text{AC}_0\text{S}\rangle$	0.642	0.300		0.550	
$ \text{S}_0\text{AC}\rangle$		0.642	0.300		0.540
$ \text{CS}_0\text{A}\rangle$	0.005		0.001		0.008

$b)$	$ \text{S}_1\text{S}_0\text{S}_0\rangle$	$ \text{S}_0\text{S}_1\text{S}_0\rangle$	$ \text{S}_0\text{S}_0\text{S}_1\rangle$	$ \text{TS}_0\rangle$	$ \text{TS}_0\text{T}\rangle$
$ \text{CAS}_0\rangle$	0.084	-0.112	0.010	0.241	
$ \text{S}_0\text{CA}\rangle$	-0.010	0.084	-0.112		0.241
$ \text{AS}_0\text{C}\rangle$	0.000	0.003	0.000	0.003	0.002 -0.153
$ \text{AC}_0\text{S}\rangle$	-0.112	0.084	-0.010	-0.269	
$ \text{S}_0\text{AC}\rangle$	0.010	-0.112	0.084		-0.269
$ \text{CS}_0\text{A}\rangle$	0.000	0.003	0.000	-0.002 -0.003	0.153

$c)$	$ \text{S}_1\text{S}_0\text{S}_0\rangle$	$ \text{S}_0\text{S}_1\text{S}_0\rangle$	$ \text{S}_0\text{S}_0\text{S}_1\rangle$	$ \text{TS}_0\rangle$	$ \text{TS}_0\text{T}\rangle$
$ \text{CAS}_0\rangle$	0.384	0.530	0.010	-0.299	
$ \text{S}_0\text{CA}\rangle$	-0.010	0.384	0.530		-0.308
$ \text{AS}_0\text{C}\rangle$	0.001	0.003	0.005	0.003 0.002	-0.161
$ \text{AC}_0\text{S}\rangle$	0.530	0.384	-0.010	0.281	
$ \text{S}_0\text{AC}\rangle$	0.010	0.530	0.384		0.271
$ \text{CS}_0\text{A}\rangle$	0.005	0.003	0.001	-0.002 -0.003	0.161

Figure 7.5: Matrix elements at $X=2.9 \text{ \AA}$, $Y=0.0 \text{ \AA}$, a) only Fock matrix values, b) Only the ERI values and c) Fock + ERI .

Notice, that the density of states, that depends on the vibrational structure, is neglected. For a given pathway of the SF process where the transition is occurring from any local exciton state LE_a to any final triplet pair state ${}^1(\text{TT})_b$, involving any charge transfer state CT_i , the transfer rate depends on the transfer probability ${}^i T_{LE_a \rightarrow {}^1(\text{TT})_b}$ according to equation 7.7.

$${}^i T_{LE_a \rightarrow {}^1(\text{TT})_b} = \frac{\langle LE_a | W | CT_i \rangle \langle CT_i | W | {}^1(\text{TT})_b \rangle}{(E_{{}^1(\text{TT})_b} - E_{LE_a})(E_{CT_i} - E_{{}^1(\text{TT})_b})} \quad (7.7)$$

Adding up ${}^i T_{LE_a \rightarrow {}^1(\text{TT})_b}$ for all possible CT states results in a total transfer probability $T_{LE_a \rightarrow {}^1(\text{TT})_b}$:

$$T_{LE_a \rightarrow {}^1(\text{TT})_b} = \sum_{CT_i} \frac{\langle LE_a | W | CT_i \rangle \langle CT_i | W | {}^1(\text{TT})_b \rangle}{(E_{{}^1(\text{TT})_b} - E_{LE_a})(E_{CT_i} - E_{{}^1(\text{TT})_b})} \quad (7.8)$$

We assume, that the energies of the individual CT states do not differ, as they are derived from the ionisation potential of the monomers. Thus, $E_{CT_i} - E_{{}^1(\text{TT})_b}$ are approximated to be same for all i . In that way, the expression reduces to

$$T_{LE_a \rightarrow {}^1(\text{TT})_b} \approx \sum_{CT_i} \langle LE_a | W | CT_i \rangle \langle CT_i | W | {}^1(\text{TT})_b \rangle \times c \quad (7.9)$$

where

$$c = \frac{1}{(E_{{}^1(\text{TT})_b} - E_{LE_a})(E_{CT_i} - E_{{}^1(\text{TT})_b})} \quad (7.10)$$

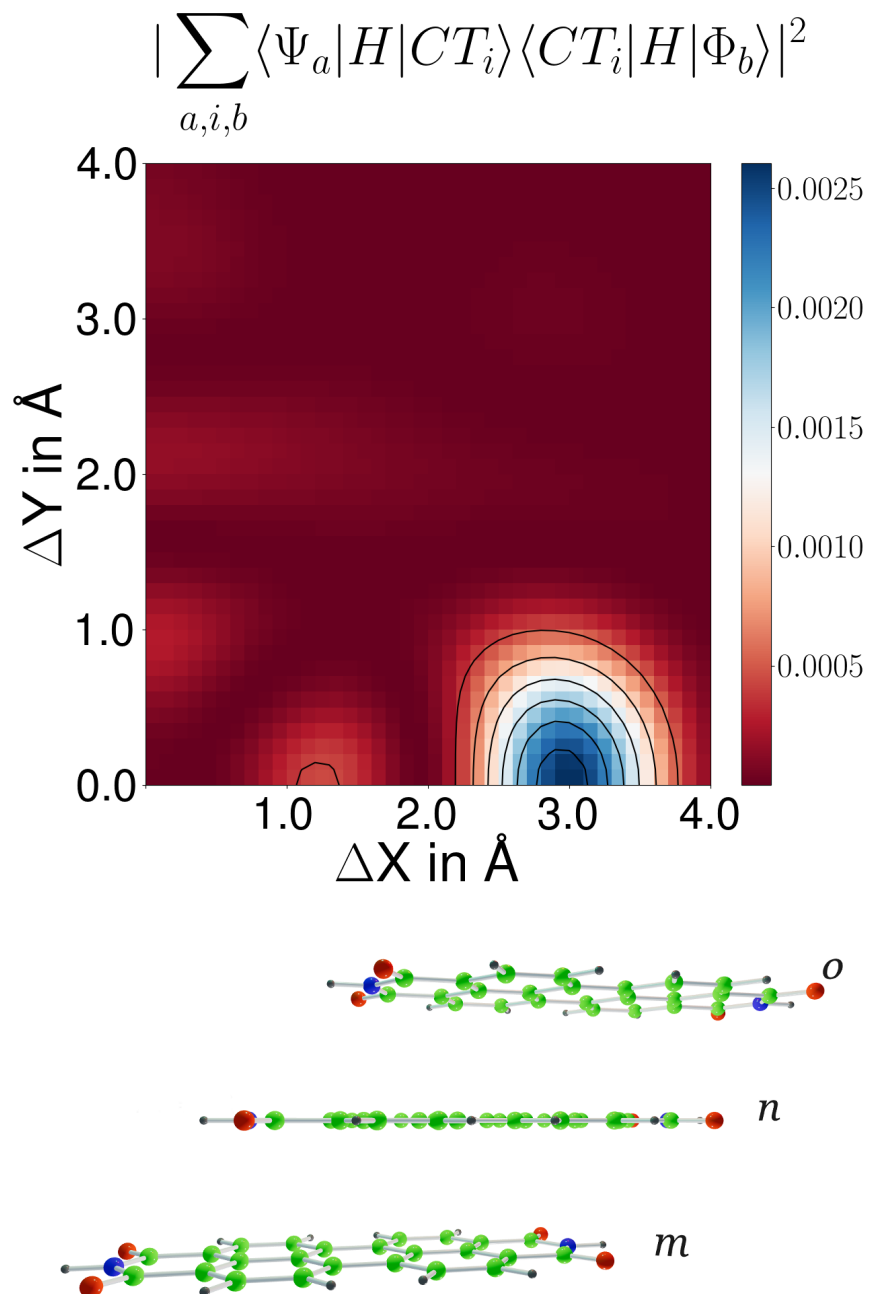


Figure 7.6: a) Scan of the Transition Probability for the $^1(\text{TT})$ formation (Sum over all transfer probabilities from LT (Ψ) to $^1(\text{TT})$ (Φ)). b) Packing motif of the trimer system at $\Delta X = 2.9 \text{\AA}$ and $\Delta Y = 0.0 \text{\AA}$

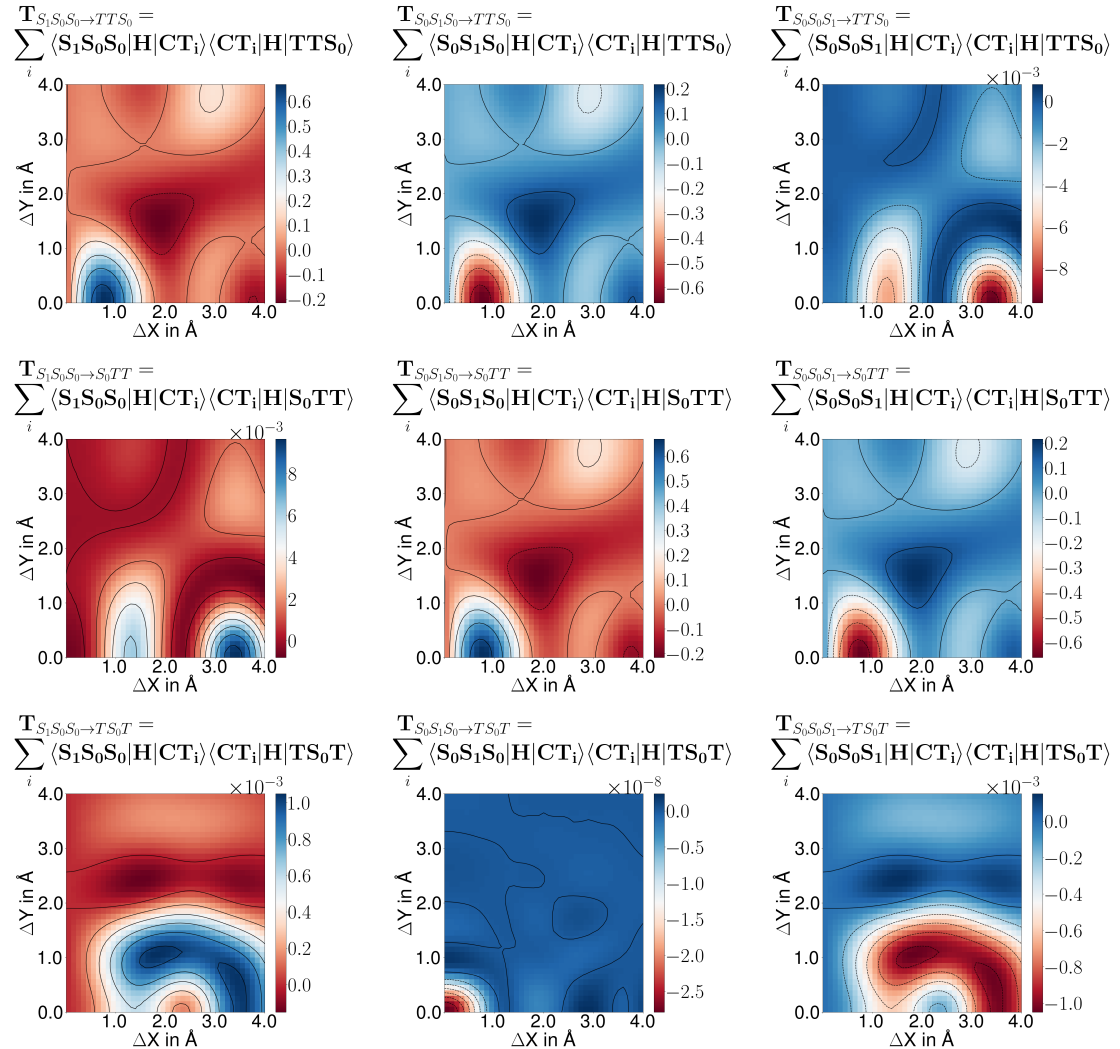


Figure 7.7: Plots of transfer probability from individual LE to individual ${}^1(\text{TT})$ or ${}^1(\text{T...T})$ state, summed over all intermediate CT states. Each column has common initial LE state and each row has common final ${}^1(\text{TT})$ state.

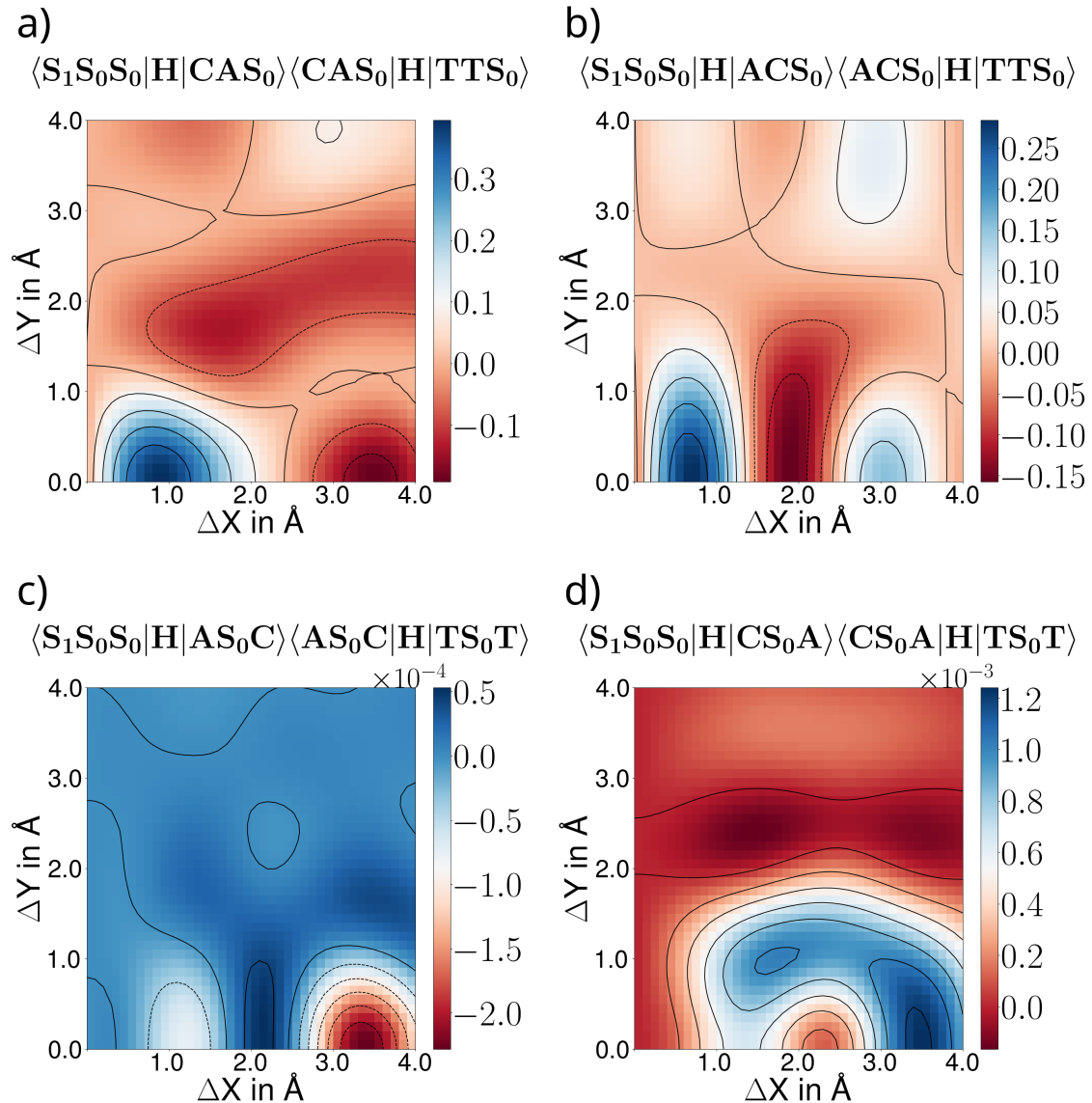


Figure 7.8: Scans of chosen individual CT-mediated pathways (in eV^2). For a) and b), CT and ${}^1(\text{T...T})$ are located on adjacent monomers. In c) and d), separated CT and ${}^1(\text{T...T})$ states are considered.

7.4 Computational Details

The molecular geometry of the PDI monomer has been optimised using DFT, employing the CAM-B3LYP functional and the 6-31g basis set. For the calculation of the Fock matrix for the trimer system in the atomic orbital basis (F^{AO}), the Hartree-Fock method along with the 6-31g and def2-svp basis set has been employed, as implemented in PYSCF. The coefficient matrix of the monomers were constructed from separate Hartree-Fock calculations. A combined coefficient matrix of the trimer has been generated with the monomer's coefficient matrices as diagonal elements. The Fock operator in molecular orbital basis F^{MO} , as it appears in the matrix elements given in figure 7.3 is calculated by transforming F^{AO} according to :

$$F_{a,b}^{MO} = \langle \psi_a | F | \psi_b \rangle = \langle C_a^\dagger | F^{AO} | C_b \rangle = \sum_j \sum_i C_i^a F_{i,j}^{AO} C_j^b \quad (7.11)$$

where C_a is the coefficient vector of molecular orbital a . The electron repulsion integrals (ERI) in the molecular orbital basis are calculated by transforming their counterparts in the AO basis as

$$\langle \psi_a \psi_b | \psi_c \psi_d \rangle = \sum_i \sum_j \sum_k \sum_l C_i^a C_j^b C_k^c C_l^d \langle ij | kl \rangle \quad (7.12)$$

The matrix elements of the diabatic Hamiltonian as given in Fig. 7.3 are derived using our code that uses SymPy, a Python library for symbolic mathematics [318].

To scan the diabatic coupling elements in the trimer system, we constructed a trimer stack of the three monomers, where consecutive monomers were stacked at an interplanar distance of 3.4 Å. The first monomer was kept stationary, and the second and third monomers were allowed to slip along both the longitudinal and transversal axes from 0 Å to 4.0 Å.

We performed the scanning in steps of 0.1 Å, where the slipping of the third monomer was twice that of the second monomer in each step. The slipping was performed in such a way that the consecutive monomers were slipped along the same vector. This ensured that each monomer felt the same interaction with its neighboring monomer.

By calculating the diabatic Hamiltonian in each step, we systematically explore the diabatic coupling elements as a function of the slipping mode.

7.5 Results

We generated the diabatic Hamiltonian for the trimer system, based on the procedure delineated in the "Methods" section. Notice, that our approach differs from Michl's Simple Model [319], since in the Simple Model, the coupling of the LE states with the $^1(TT)$ states is neglected, while our method specifically constructs these matrix elements. While in the SM, the matrix elements are essentially broken down to 1 electron integrals, we employ the full analytic expression derived for the individual matrix elements. Furthermore, in the trimer Hamiltonian we consider the configurations $^1|TS_0T\rangle$ as well as the $|AS_0C\rangle$ ($|CS_0A\rangle$, respectively), which might be defined as a charge separated state.

The derived equations for the individual matrix elements of the diabatic Hamiltonian are given in figure 7.3, expressed in terms of the Fock operator and electron repulsion integrals (ERI) in molecular orbital basis. The rows' labels correspond to the initial states, whereas the columns' labels represent the final states. In our trimer system, coupling terms emerge involving two-electron integrals that include orbitals from all three monomers, such as $\langle S_1 S_0 S_0 | \hat{H} | S_0 C A \rangle$ and $\langle C A S_0 | \hat{H} | S_0 T T \rangle$. We wish to emphasize that these terms do not appear in any dimer model or periodic system which is parametrized by dimer interactions.

The resulting matrix elements can be categorized in those describing the transfer of one electron, which leads to expressions that include both the Fock operator as well as the ERI terms, while the elements involving the transfer of two electrons have only ERI terms. Interestingly, the coupling of $^1(TT)$ states with LE and CT states have a negative factor $\sqrt{\frac{3}{2}}$, while the couplings within $^1(TT)$ states are positive. We then explicitly parametrized the diabatic Hamiltonian for the calculation of diabatic couplings in the considered PDI trimer stack employing quantum chemical procedure described in ("Computational Details").

In general, in molecular aggregates with increasing size, the number of electronic pathways grow exponentially. In the trimer system, in total six "direct" and 54 "CT mediated" pathways lead to one of the 2 $^1(TT)$ states that have triplet states on adjacent molecules as illustrated in Fig. 2. Following the scheme established by Scholes, in the SF process the transition would then further proceed to the $^1(T\ldots T)$ state. However, also an alternative route can be considered, in which the $^1(T\ldots T)$ intermediate is directly populated from the initial LE state (either in a CT mediated or direct pathway). To the best of our knowledge, such mechanism has not been considered so far. In order to estimate the efficiency and impact of the individual pathways as well as to determine the structural arrangements that promote the discussed transitions, we carried out 2D scans in the PDI trimer as described in detail in the "Methods" section.

7.5.1 Direct Pathway

As a first step, we studied the "direct" pathway, evaluating the diabatic matrix elements between the individual LE and the ${}^1(TT)$ states. The obtained scans are provided in the Appendix. Due to the symmetry of the chosen trimer system, all these scans appear similar, although with opposite signs, exhibiting an extremum located at $\Delta X=4.0 \text{ \AA}$ and $\Delta Y=0 \text{ \AA}$ with an absolute value of 0.025 eV. However, we wish to point out, that in the expression for the transition probability of the direct pathway, that follows from the first order perturbation theory, the denominator carries the energy difference between the respective diabatic states, leading to an overall negligible SF rate. The matrix elements between the individual LE states and the ${}^1(T\ldots T)$ state are particularly small, of the order of 10^{-6} eV and can be neglected. Notice, that the matrix element $\langle S_0S_1S_0 | \hat{H} | TS_0T \rangle$ is zero.

7.5.2 Charge Transfer Mediated Pathway

We subsequently shifted our attention to the CT mediated pathway that proceeds from an LE state via a virtual CT state to a ${}^1(TT)$ or ${}^1(T\ldots T)$ state. As worked out in the Methods part, according to equations 6 and 9, the Transition Probability of the mediated pathway in the trimer stack can be determined by summing over all individual pathways. The result of that scan is presented in 7.6 a). This plot indicates a highest SF transfer probability at the coordinates $\Delta X = 2.9 \text{ \AA}$ and $\Delta Y = 0.0 \text{ \AA}$ with an absolute value of 0.025. This rate is relatively low compared to the individual $T_{LE \rightarrow TT}$, which can be explained by the nullifying effect of the coupling terms of opposing sign in a homo trimer with symmetric slipped stacked geometry (see further discussion below). Consequently, a breaking of symmetry could potentially elevate the CT-mediated coupling. The obtained result clearly differs from the SF rate scan obtained for the dimer system (see [121, 1] and our work [198]) but resembles the results of the Redfield theory rate scan from Ref.[26]. However, it should be noticed that in the former cited studies, the resulting rates have been derived by evaluating the matrix elements of only one chosen pathway and therefore do not correspond to the expressions derived from second order perturbation theory.

In order to shed more light on the mechanistic details, we studied the individual pathways, focusing on their contribution and structural dependence. In particular, we considered the transition from a given LE state situated on one monomer proceeding via any CT state, to i) a given ${}^1(TT)$ state on adjacent monomers and ii) the separated ${}^1(T\ldots T)$ state. We then determined the transfer probability in accordance with equation 7.8. Applying these categorization resulted in 9 scans. The corresponding plots are shown in figure 7.7. Each scan in one row shares the same initial LE state, and each scan in a column shares the same final ${}^1(TT)$ or ${}^1(T\ldots T)$ state, respectively.

The investigated pathways can be further classified in those involving transfer of two electrons, in which one of the correlated triplets in the target state is localized on the monomer that is initially locally excited and in three-electron processes, in which the initially excited monomer does not contribute to the formation of the correlated triplet state.

For the plots illustrating transitions to ${}^1(TT)$ states (two upper rows in Fig. 7.7,) we make the observation, that the scan shape depicting two-electron processes appear remarkably alike, albeit with opposite signs: The coupling manifests an extremum at the coordinates $\Delta X = 0.7 \text{ \AA}$ and $\Delta Y = 0.0 \text{ \AA}$ with an absolute value of ± 0.65 as well as a local extremum of ± 0.2 , located at $\Delta X=1.8 \text{ \AA}$, $\Delta Y= 1.5 \text{ \AA}$. Interestingly, these plots strongly resemble the scan of the charge transfer mediated pathway in the PDI dimer system obtained with the Simple Model or ASD, as reported in our previous work. [198] The plots associated with the three-electron processes, specifically $T_{S_0S_0S_1 \rightarrow TTS_0}$, $T_{S_1S_0S_0 \rightarrow S_0TT}$ again present striking similarities but exhibit opposite signs. The transfer probability attains its extremum at $\Delta X = 3.4 \text{ \AA}$ and $\Delta Y = 0.0 \text{ \AA}$, however it worth noting that the absolute value of ± 0.008 is approximately two magnitudes smaller than those of the two-electron process. A further local extremum can be found at $\Delta X=1.2 \text{ \AA}$, $\Delta Y=0.0 \text{ \AA} (\pm 0.005)$.

We then studied the formation of the specially separated ${}^1(T\ldots T)$ state, considering the three possible pathways, in which the $|TS_0T\rangle$ state is formed via a charge transfer-mediated process from one of the three LE states. The resulting scans are shown in the figure 7.7 g), h) and i). $T_{S_0S_1S_0 \rightarrow TS_0T}$ has a negligible value of the order of 10^{-8} , bearing a maximum at position $\Delta X = 0.0 \text{ \AA}$ and $\Delta Y = 0.0 \text{ \AA}$. The other two pathways in which $|TS_0T\rangle$ is formed from those initial LE states, in which the edge fragments' electrons are excited, appear similar but with opposite signs due to the symmetry of the investigated system and exhibit considerable higher values. The scans have a broad extremum between $\Delta X=3 \text{ \AA}$ and $\Delta X = 4 \text{ \AA}$ with a center at $\Delta X = 3.4 \text{ \AA}$, and spanning from $\Delta Y = 0 \text{ \AA}$ $\Delta Y = 1 \text{ \AA}$ with an absolute value of $\pm 0.0010 \text{ eV}^2$. Interestingly, a second basin, located at $\Delta X=1.5 \text{ \AA}$ and $\Delta Y=1 \text{ \AA}$ shows an additional local maximum with the same value of about $\pm 0.0010 \text{ eV}^2$. Notice, that these values are about two magnitudes lower then those of the pathways targeting a ${}^1(TT)$ state.

Individual Pathways

Diving deeper into the details, we examined the role of individual CT states in the mediated pathways. These scans are discussed in detail in the Appendix. In general, we discovered that the pathways in which the CT states and the $^1(TT)$ or the $^1(T\ldots T)$ states, respectively, are not localised on the same molecules exhibit particularly low probabilities, of the order of 10^{-7} for the former and 10^{-9} for the latter.

Highest probabilities are found for those pathways, in which the LE, the CT and a final $^1(TT)$ state involve the same molecules. Those pathways can be further subcategorized into those where the Anion of the CT state is generated at the initially excited monomer and those where the Cation is located at these position.

For the former, we find a maximum absolute value of about 0.28, while the latter category, the scans exhibit higher values, indicating a maximum at position $\Delta X = 0.9 \text{ \AA}$ (abs. value 0.4), as illustrated in 7.8 a) and b). We find, that for these pathways, the initial position of the LE state, whether located at an "edge" molecule or the inner one, does not effect the resulting scans. Another category of pathways encompasses those two that involve an LE state on one of the outer molecules, a specially separated C...A state, that is located at the two edge molecules and a specially separated $^1(T\ldots T)$ state. In this type of pathways, the central monomer can be considered as "innocent" as it remains unexcited throughout the process. Again, the resulting scans depend on the position of the Anion (and therefore, also Cation): In case it is localized on the position of the previously locally excited molecule, the absolute probability is smaller, of the order of 10^{-4} , with an extremum at 3.4 \AA (-0.00020) eV. Conversely, for the Cation, the scan reveals a maximum at 0.0012, located at $\Delta X=3.4 \text{ \AA}$, that spans from $\Delta Y=0.0 \text{ \AA}$ to $\Delta Y=1.0 \text{ \AA}$ and a second basin at $\Delta X=1.8 \text{ \AA}$ and $\Delta Y=1.0 \text{ \AA}$. the overall motif of the scan is closely resembled in $T_{S_0 S_0 S_1 \rightarrow TS_0 T}$.

In the calculation of the individual transfer probabilities, we observe cancellation of matrix elements due to their different signs. As illustrated in Figure 7.4, the value of the Fock terms of couplings $\langle CAS_0 | \hat{H} | TTS_0 \rangle$ and $\langle S_0 AC | \hat{H} | S_0 TT \rangle$ have the same magnitude but opposite signs and so do the Fock terms of $\langle ACS_0 | \hat{H} | TTS_0 \rangle$ and $\langle S_0 CA | \hat{H} | S_0 TT \rangle$, while $\langle CAS_0 | \hat{H} | TTS_0 \rangle$ and $\langle ACS_0 | \hat{H} | TTS \rangle$ (as well as $\langle S_0 AC | \hat{H} | S_0 TT \rangle$ and $\langle S_0 CA | \hat{H} | S_0 TT \rangle$), in which CT and $^1(TT)$ state are located at the same dimer sub system, have different values. In the Transfer Probability, the sum of all products of the individual matrix elements of $\langle LE | \hat{H} | CT \rangle$ and $\langle CT | \hat{H} | ^1(TT) \rangle$ are calculated, in total the Fock terms of $\langle CT | \hat{H} | ^1(TT) \rangle$ couplings of the two equivalent dimer subsystems have equal value with opposite sign. Altogether the fock terms are canceled. In contrast, the ERI terms of the couplings located on one dimer subsystem, $\langle CAS_0 | \hat{H} | TTS_0 \rangle$ and $\langle ACS_0 | \hat{H} | TTS_0 \rangle$ (as well as $\langle S_0 AC | \hat{H} | S_0 TT \rangle$ and $\langle S_0 CA | \hat{H} | S_0 TT \rangle$ on the other dimer subsystem) exhibit the same value and sign, while equivalent couplings on the "different" dimers differ from each other in sign and values. Fock terms and ERI terms combined give a set of 4 different values of $\langle CT | \hat{H} | ^1(TT) \rangle$ couplings shown in figure 7.4 c. Summing up all the $\langle LE | \hat{H} | CT \rangle \langle CT | \hat{H} | ^1(TT) \rangle$ results in a value of 0.0028 eV².

7.5.3 Matrix Elements

We then studied the individual matrix elements between any LE and CT configuration. First we considered those matrix elements involving CT states on adjacent molecules that share a monomer with an "outer" LE state (in that way, one "edge" monomer remains innocent). The scans available in SI can be classified into two distinct motifs: for those involving a matrix element in which the LE state is situated on the same molecule as the cation of the CT state, we find a the overall highest absolute values, with a maximum of 0.8 eV, located at the origin, as well as two local extrema, located at $\Delta X=4 \text{ \AA}$ and $\Delta Y=0 \text{ \AA}$ (0.5 eV) and a broad band spanning from $\Delta X=0 \text{ \AA}$ to $\Delta X=4 \text{ \AA}$ and $\Delta Y=1.5 \text{ \AA}$ to $\Delta Y=2.5 \text{ \AA}$ with a center at $\Delta X=2 \text{ \AA}$, $\Delta Y=2 \text{ \AA}$ (-0.4 eV). For couplings in which the anion and the LE share the same monomer, the scan also exhibits a global extremum at the $\Delta X=0 \text{ \AA}$, $\Delta Y=0 \text{ \AA}$ position (-0.8 eV) as well as a local one at $\Delta X=2.5 \text{ \AA}$, $\Delta Y=0 \text{ \AA}$ (0.6 eV). Interestingly, for those transitions involving the LE state on the inner molecule and adjacent CT states, the scans exhibit the same motifs when the Anion or the Cation share the same molecule with the LE state, respectively. In general, the couplings between the individual LE states and the spatially separated $|AS_0C\rangle$ (or $|CS_0A\rangle$) state are weaker, of the order of 1×10^{-3} eV. A clear dependence on the position of the anion and cation can be observed: For the type of couplings with the LE on one of the outer molecules, which is also shared with the cation of the CT state, a maximum at $\Delta X=1.2 \text{ \AA}$, $\Delta Y=0.8 \text{ \AA}$, with a value of 0.011eV is observed. Furthermore, a significant region located between $\Delta X=3.1 \text{ \AA}$ and $\Delta X=3.9 \text{ \AA}$ extends in the y direction from 0 to 1 \AA reaching a value of 0.007eV. This motif is partly reflected in the scan for the individual CT-mediated pathway of the $^1(T..T)$ formation (see discussion above). In the case where LE and Anion share one monomer, the values of the matrix elements are of 1 magnitude lower, with the global extremum at $\Delta X=3.3 \text{ \AA}$, $\Delta Y=0.0 \text{ \AA}$ (0.0012 eV). The scans of the couplings between the "inner" LE state and a separated C...A exhibit their extremum located at $\Delta X=0 \text{ \AA}$, $\Delta Y=0 \text{ \AA}$ (-0.010 eV) and a local maximum spanning from $\Delta X=1.8 \text{ \AA}$ to $\Delta X=3.2 \text{ \AA}$ with a value of 0.002 eV.

We then proceeded by examining the individual matrix elements between the individual CA or C...A

and ${}^1(\text{TT})$ or ${}^1(\text{T...T})$ states, respectively. In general, we find that the couplings have significant values only when the Cation and Anion are situated at the same molecules as the two correlated triplets. Studying these class of matrix elements, we observe, that for the adjacent CT and ${}^1(\text{TT})$ states, all the scans exhibit almost similar patterns: A maximum between $\Delta X = 0.9 \text{ \AA}$ to 1.5 \AA , that spans from $\Delta Y = 0 \text{ \AA}$ to $\Delta Y = 0.8 \text{ \AA}$ (0.65 eV) and a local minimum between $\Delta X = 2.9 \text{ \AA}$ and $\Delta X = 3.8 \text{ \AA}$ and $\Delta Y = 0 \text{ \AA}$ and $\Delta Y = 0.5 \text{\AA}$. (-0.4 eV). Furthermore, a broad basin corresponding to a local maximum spanning from $\Delta Y = 3 \text{ \AA}$ (0.2 eV^2) and $3.6 \text{ (0.45 eV}^2)$. For the transition $\langle AS_0C|\hat{H}|TS_0T\rangle$, a broad maximum is found, with the center spread from at $\Delta X = 2.9 \text{ \AA}$ to $\Delta X = 4.0 \text{ \AA}$ and $\Delta Y = 0.0 \text{ \AA}$ to $\Delta Y = 1.0 \text{ \AA}$ with a value of 0.17 eV^2 .

Interestingly, our studies indicate that the regions of strongest LE/CT couplings and CT/ ${}^1(\text{TT})$ couplings do not overlap.

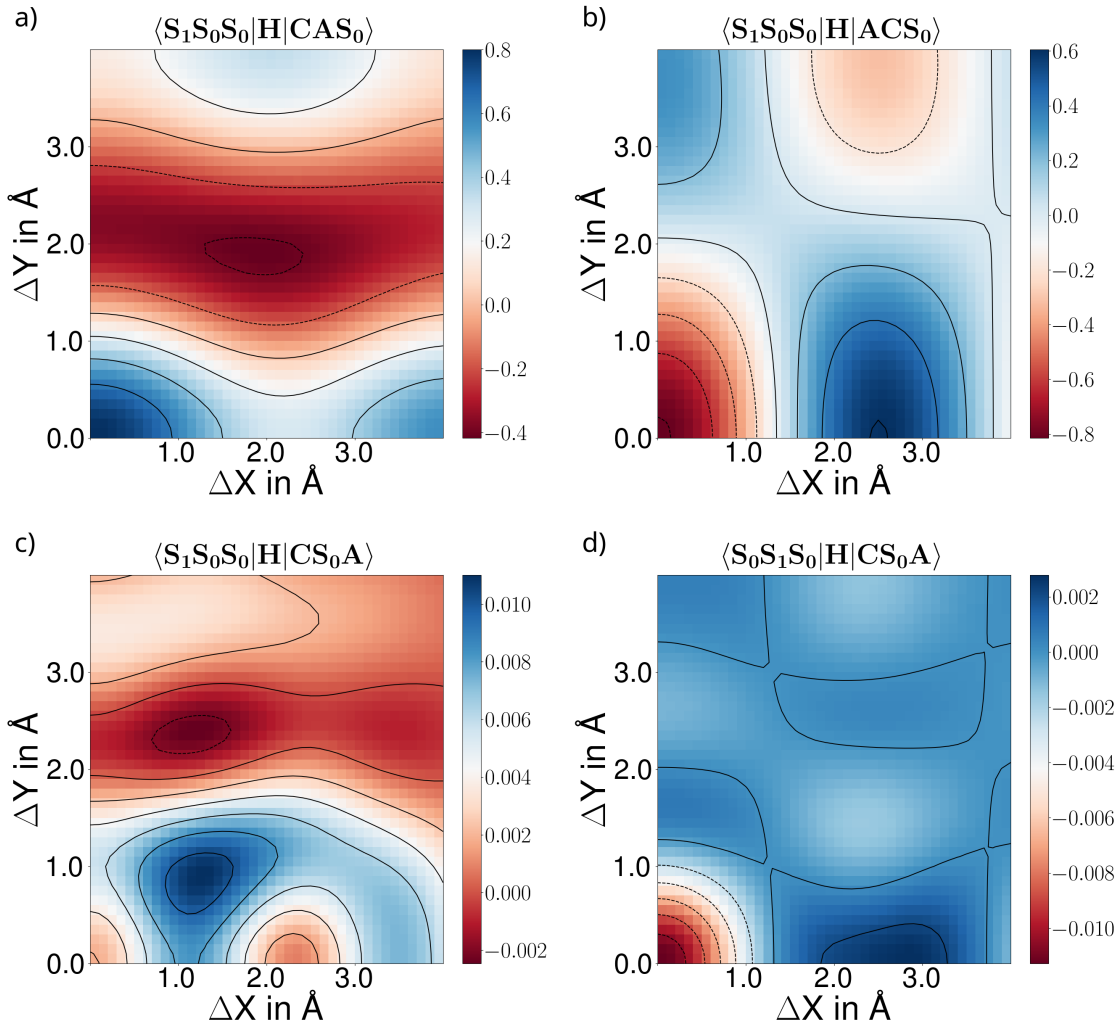


Figure 7.9: Plot of coupling among LE and CT states (in eV). a) and b) illustrate matrix elements between an "edge" LE state and CT states located on adjacent monomers. In c) and d) scans of the diabatic coupling between LE to a "separate" CT state.

7.5.4 ${}^1(\text{TT})$ to ${}^1(\text{T...T})$ State Transition

Finally, with the intend to elucidate the process of triplet delocalization and the generation of the ${}^1(\text{T...T})$ state, we performed 2D scans of the Matrix elements once between the two ${}^1(\text{TT})$ states and once between the individual ${}^1(\text{TT})$ and the ${}^1(\text{T...T})$ state. For the latter, the plot is presented in figure 7.11. The coupling between one conjoint triplet pair to the other conjoint triplet pair turns out to be very low, of the order 10^{-10} eV . In contrast, we find that the probability for the formation process from the ${}^1(\text{TT})$ intermediate to the ${}^1(\text{T...T})$ state based on the matrix elements $\langle TTS_0|\hat{H}|TS_0T\rangle$ and $\langle S_0TT|\hat{H}|TS_0T\rangle$ has significant values of the order 10^{-2} eV , with the broad maximum (0.0175 eV) centered at the perfectly stacked geometry. This motif has been previously assigned to the excimer structure in

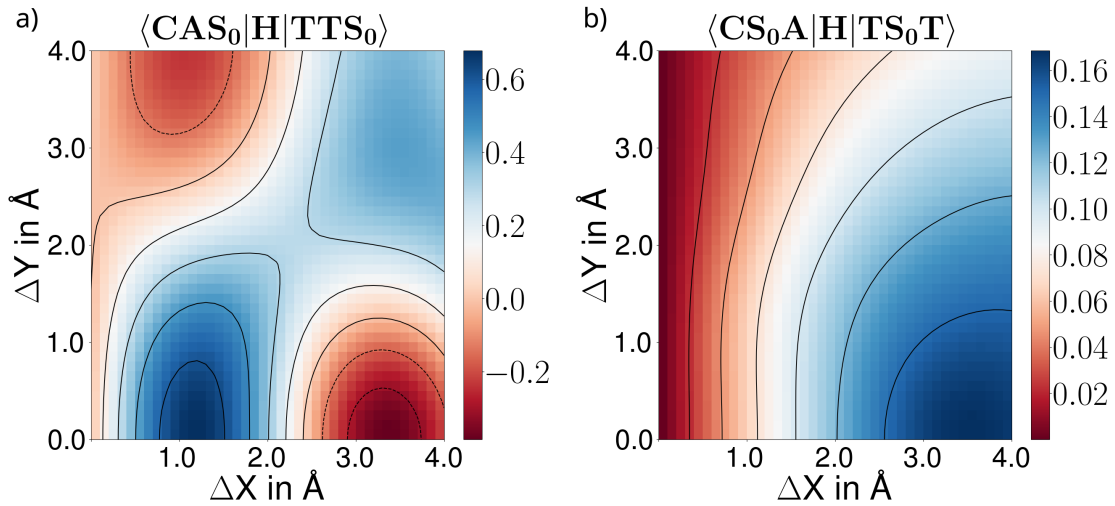


Figure 7.10: Plot of couplings (in eV) between "separate" CT state and a) joint triplet state and b) separated triplet state.

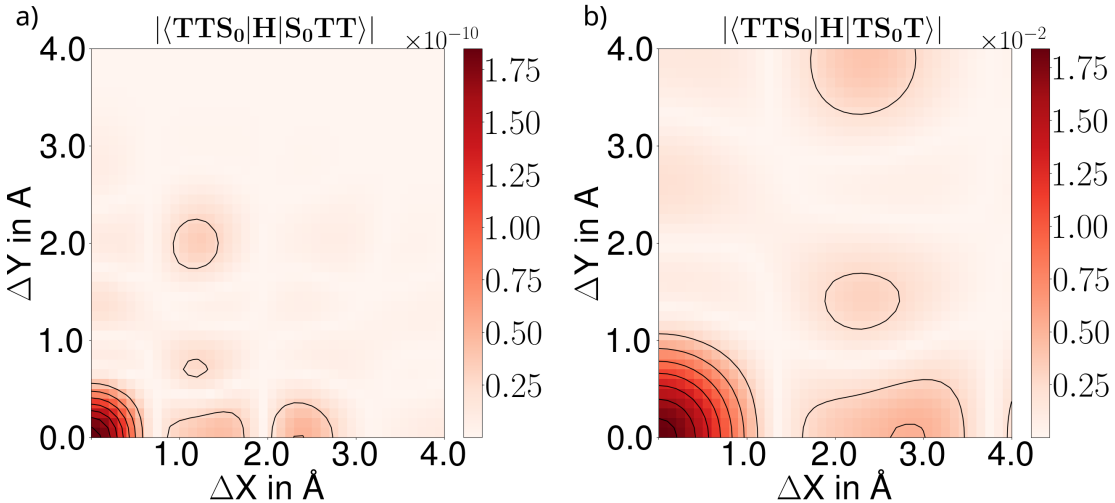


Figure 7.11: Scans of the absolute value of the coupling between a) the two ${}^1(\text{TT})$ states and b) between ${}^1(\text{TT})$ and ${}^1(\text{T...T})$ (in eV).

PDI.[320] While the excimer formation is accompanied with a significant structural relaxation leading to significantly shorter stacking distances[321], which we do not account for in the two-dimensional plots, by scanning the individual $\langle \text{LE}|\hat{H}|\text{CT} \rangle$ couplings, we have found that the corresponding matrix elements exhibit significant values for the particular structural motif. However, the scans of the $\langle \text{CT}|\hat{H}|{}^1(\text{TT}) \rangle$ and $\langle CS_0A|H|TS_0T \rangle$ matrix elements indicate a particularly weak coupling for the given structural motif, which would as a consequence hinder the process of SF. Further studying the scans of the matrix elements $\langle S_0TT|\hat{H}|TS_0T \rangle$, we find a further broad local minimum ranging from $\Delta X = 2.2 \text{ \AA}$ to $\Delta X = 3.0 \text{ \AA}$ with a value of 0.0075 eV. Interestingly, the plot of the absolute value clearly indicates its center located at $\Delta X = 2.9 \text{ \AA}$, $\Delta Y = 0.0 \text{ \AA}$ which has been also identified as the stacking coordinates corresponding to the maximum of the total Transition Probability for the CT mediated pathway of the ${}^1(\text{TT})$ state formation (see discussion above). This finding hints for an efficient ${}^1(\text{TT})$ formation. Again, for this region of stacking coordinates, we find significant values for the $\langle \text{LE}|\hat{H}|\text{CT} \rangle$ coupling, in particular for $\langle S_1S_0S_0|\hat{H}|ACS_0 \rangle$ and $\langle S_1S_1S_0|\hat{H}|CAS_0 \rangle$, that hint for the presence of a "local excimer". However, for this structure we find a narrow overlap between significant values of the respective $\langle \text{LE}|\hat{H}|\text{CT} \rangle$ couplings and the respective $\langle \text{CT}|\hat{H}|{}^1(\text{TT}) \rangle$ couplings for the structure with the stacking coordinates $\Delta X = 2.9 \text{ \AA}$, $\Delta Y = 0.0 \text{ \AA}$ which also exhibits significant coupling to ${}^1(\text{T...T})$. Notice, that for this coordinates, also a process via a "separated" C...A state shows overlap of the individual matrix elements. However, as discussed above, these couplings are in general of several magnitudes lower.

7.6 Conclusion

In this work, we have extended the widely applied diabatic frontier orbital model to the description of trimer systems in order to study the SF process in molecular trimer stacks. Our approach involves explicit parameterization of couplings between all monomers, incorporating also three-center couplings. This allows us to deliver a theoretical study of the formation pathways and their structure dependence of the separated, singlet-spin correlated triplet pair state, ${}^1(T\ldots T)$, that is discussed to play a decisive role in the SF process. We focused on the investigation of the trimer systems of cofacially stacked PDIs, that represent a prominent class of SF molecules, and evaluated the impact of the individual electronic pathways and diabatic matrix elements leading to ${}^1(T\ldots T)$ formation as well as their dependence on the packing motif by scanning along a longitudinal and a transversal slipping mode. We explored two possible mechanisms: the "two intermediates" scheme, as suggested by Scholes and others, in which a ${}^1(T\ldots T)$ is formed upon triplet energy transfer from the singlet spin coupled adjacent triplet pair state ${}^1(TT)$ and in addition, a so far unreported mutual pathway that proceeds in a CT mediated process from an initially excited LE state directly to the ${}^1(T\ldots T)$. For the latter, we find that the electronic pathway become significant only, when the process proceeds via a "charge separated" state, in which the cation and anion are separated and therefore located on the non-adjacent edge molecules. However, its transition probability is substantially lower compared to the competing ${}^1(TT)$ formation pathways. We have then studied the packing dependence of the $\langle {}^1(TT)|\hat{H}|{}^1(T\ldots T)\rangle$ coupling. Interestingly, the resulting scan shows similarities with the scan of matrix element $\langle S_0S_1S_0|\hat{H}|CS_0A\rangle$. The coupling is strongest at the perfectly stacked packing motif ($\Delta X=0.0 \text{ \AA}$, $\Delta Y=0.0 \text{ \AA}$), another region of significant coupling is found at $\Delta X=2.9 \text{ \AA}$, $\Delta Y=0.0 \text{ \AA}$, that matches the structural configuration, for which the highest ${}^1(TT)$ formation rate has been determined by Redfield theory simulations. Interestingly, we observe that the $\langle {}^1(TT)|\hat{H}|{}^1(T\ldots T)\rangle$ coupling is significant in regions of strong $\langle LE|\hat{H}|CT\rangle$ coupling corresponding to a "global" and a "local" excimer.

Additionally, employing second order perturbation theory, we screened the SF rate of the ${}^1(TT)$ formation in the trimer system, demonstrating that these simple approach reproduces the results of the advanced Redfield theory studies carried out by Miryani et. al.. We find, that the symmetry present in the system leads to cancellation of matrix elements and the total Transition Probability can be mainly broken down to contributions of the electron repulsion integrals, which are often neglected in the implementation of the FO dimer model. The simulations show, that the transfer probability of the ${}^1(TT)$ formation is highest if the process proceeds via a two-electron process located on a subset of adjacent dimers, in which the LE state and the Cation of the CT state share the same monomer. The $\langle LE|\hat{H}|CT\rangle$ coupling is strongest for the perfectly stacked structure which we assign to as "excimer". At this position, the $\langle CT|\hat{H}|{}^1(TT)\rangle$ coupling is particularly low, therefore the structural motif might be considered as a trap side hindering the SF process. A further "local excimer" region can be found for a longitudinally slipped structure between $\Delta X=2 \text{ \AA}$ and $\Delta X=3$ at $\Delta Y=0 \text{ \AA}$. With this study, we hope to motivate researchers from theory, synthesis and spectroscopy to further explore the formation pathways of the ${}^1(T\ldots T)$ state as well as a potential role of a separated CT state ($|AS_0C\rangle$).

7.7 Appendix

7.7.1 Individual Pathways

Highest probabilities are found for those pathways, in which the LE, the CT and a final ${}^1(TT)$ state involve the same molecules. Those pathways can be further subcategorized into those where the Anion of the CT state is generated at the initially excited monomer and those where the Cation is located at these position. For the former, a maximum absolute value of about 0.28 is reached at the position $\Delta X = 0.8 \text{ \AA}$ and $\Delta Y=0.0 \text{ \AA}$. Additionally, there are two further significant probabilities: an absolute value of 0.15 centered at $\Delta X=1.8 \text{ \AA}$, spanning from $\Delta Y=0.0 \text{ \AA}$ to $\Delta Y=1.0 \text{ \AA}$ and an absolute value of 0.10 at $\Delta X=3.1 \text{ \AA}$ $\Delta Y=0.0 \text{ \AA}$. For the latter category, the scans exhibit higher values, indicating a maximum at position $\Delta X = 0.9 \text{ \AA}$ (abs. value 0.4) and another significant probability of ± 0.2 located at $\Delta X = 3.5 \text{ \AA}$ $\Delta Y = 0.0 \text{ \AA}$. Furthermore, a broad basin reaching from $\Delta X=1.0 \text{ \AA}$ to $\Delta X=4 \text{ \AA}$ and $\Delta Y=1.5 \text{ \AA}$ to $\Delta Y=2.5 \text{ \AA}$ with a value of ± 1 can be observed, with its center located at $\Delta X=1.8 \text{ \AA}$ and $\Delta Y=1 \text{ \AA}$. This pattern can be partly detected in the scan of $T_{S_1S_0S_0 \rightarrow TTS_0}$. We find, that for these pathways, the initial position of the LE state, whether located at an "edge" molecule or the inner one, does not effect the resulting scans. The pathways characterized by a CT state located on the molecules involved in the ${}^1(TT)$ states, while in the LE configuration the third molecule is in the excited state, exhibit total transfer probability values of the order of 10^{-3} . Again, a clear impact of the position of the Anion and the Cation configuration in the CT state can be observed: The scans of those pathways proceeding via an Anion configuration on one of the edge molecules indicate an extremum at 3.4 \AA (absolute value 0.005) and another significant value for the structure with an offset of $\Delta X = 0.8 \text{ \AA}$ (absolute value 0.003). The latter closely resembles the motif of the extremum found in the Probabilities describing the 2 electron process from LE to TT, via any CT, such

as $T_{S_1 S_0 S_0 \rightarrow TTS_0}$. In case the Anion is located on the "inner" molecule, the highest value can be found for $\Delta X=1.0 \text{ \AA}$, 1.0 \AA (0.006) and another local extremum with a value at $\Delta X=3.4 \text{ \AA}$, $\Delta Y=1.0 \text{ \AA}$ (0.004) that finds resemblance with the patterns found in the transition probabilities of the 3 electron processes, for example, $T_{S_0 S_0 S_1 \rightarrow TTS_0}$. Another category of pathways encompasses those two that involve an LE state on one of the outer molecules, a specially separated C...A state, that is located at the two edge molecules and a specially separated ¹(T...T) state. In this type of pathways, the central monomer can be considered as "innocent" as it remains unexcited throughout the process. Again, the resulting scans depend on the position of the Anion (and therefore, also Cation): In case it is localized on the position of the previously locally excited molecule, the absolute probability is smaller, of the order of 10^{-4} , with an extremum at 3.4 \AA (-0.00020). Conversely, for the Cation, the scan reveals a maximum at 0.0012, located at $\Delta X=3.4 \text{ \AA}$, that spans from $\Delta Y=0.0 \text{ \AA}$ to $\Delta Y=1.0 \text{ \AA}$ and a second basin at $\Delta X=1.8 \text{ \AA}$ and $\Delta Y=1.0 \text{ \AA}$. the overall motif of the scan is closely resembled in $T_{S_0 S_0 S_1 \rightarrow TS_0 T}$.

7.7.2 $\langle \text{LE} | \hat{H} | \text{CT} \rangle$ and $\langle \text{CT} | \hat{H} | \text{CT} \rangle$ coupling

Further elucidating the $\langle \text{LE} | \hat{H} | \text{CT} \rangle$ coupling, we once considered a transition from a superposition of LE states to a given CT state, leading to expressions such as $|\sum \langle \text{LE} | \hat{H} | S_0 AC \rangle|$, that are then permuted over all CT configurations. The corresponding scans are provided in Fig. XY. For those CT states located on adjacent molecules, the scans appear similar, exhibiting a broad maximum with a center at $\Delta X=2.8 \text{ \AA}$, $\Delta Y=0.0 \text{ \AA}$ reaching a value of 0.8 eV. The scans for the pathways with the separated $|AS_0C\rangle$ or $|CS_0A\rangle$ target state show values that are about 3 magnitudes lower with the maximum at $\Delta X=1.2 \text{ \AA}$ and $\Delta Y=0.8 \text{ \AA}$ (0.00012 eV²). And two local maxima at the origin (0.00010 eV²) and $\Delta X=3.3 \text{ \AA}$, $\Delta Y=0.0 \text{ \AA}$ (0.00010 eV). Considering a possible competing process, we studied the couplings from a neighboring CT state to a separated $|CS_0A\rangle$ (or $|CS_0A\rangle$, respectively) state. Interestingly, for the respective 1-electron processes, the matrix elements hold significant values: For $\langle CAS_0 | \hat{H} | CS_0 A \rangle$, we found an extremum at $X=0 \text{ \AA}$ and $Y=0 \text{ \AA}$ with a value of 0.7 eV along with another noteworthy configuration (0.4 eV) at $X=4$, $Y=0 \text{ \AA}$ and a broad basin situated between $x=0 \text{ \AA}$ and $x=2.0 \text{ \AA}$ and $Y=1.8 \text{ \AA}$ and $Y=2.5 \text{ \AA}$ (-0.4 eV). In the case of $\langle ACS_0 | \hat{H} | AS_0 C \rangle$, an extremum is again detected at the origin (-0.85 eV) as well as a local extremum between $X=2.2 \text{ \AA}$ and $X=2.8 \text{ \AA}$, $Y=0 \text{ \AA}$ and $Y=0.5 \text{ \AA}$ (0.65 eV).

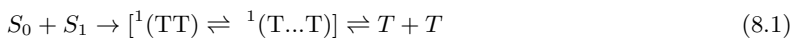
Chapter 8

Configuration Interaction in Frontier Molecular Orbital Basis for Screening the Spin-Correlated, Spatially Separated Triplet Pair State ${}^1(T\dots T)$ Formation

In the theoretical screening of Singlet Fission rates in molecular aggregates, often the frontier molecular orbital model for dimers is employed. However, the dimer approach fails to account for recent experimental findings that suggest singlet fission progresses through a further intermediate state featuring two spatially separated, spin-correlated triplets, specifically a ${}^1(T\dots T)$ state. We address this limitation by generalizing the often used frontier molecular orbital model for singlet fission by incorporation of both separated Charge Transfer (C...T) and ${}^1(T\dots T)$ states as well as mixed triplet-charge transfer states, delivering analytic expressions for the diabatic matrix elements. Applying the methodology to the perylene diimide trimer, we examine the packing dependence of competing formation pathways of the ${}^1(T\dots T)$ state by evaluation of diabatic matrix elements.

8.1 Introduction

Singlet fission (SF) is a process occurring in systems of electronically coupled molecules, in which a singlet exciton is converted into two triplet excitons that can subsequently dissociate producing two electron-hole pairs.[28] As SF offers the opportunity to overcome the thermalization loss in solar energy technologies, the design of efficient SF materials is an active field of research that crucially builds on the understanding how multiexcitons can be generated and controlled.[298, 299] It is commonly accepted that the SF process proceeds from an initially excited singlet exciton state via the transient formation of a correlated triplet exciton pair ${}^1(TT)$ intermediate with an overall singlet spin multiplicity, either via a direct or a charge transfer (CT) mediated pathway.[55] However, the fate of the spin-correlated triplets is far less explored. [56, 300, 301] The populated ${}^1(TT)$ state has been widely assumed to disentangle by spin decoherence effects, forming two independent triplet excitons ($T + T$), however, recent experimental studies indicate that the spin correlation remains for nanoseconds, in which the ${}^1(TT)$ state can undergo further processes.[322, 323]. On the one hand, population of the ${}^5(TT)$ state has been observed.[25, 324, 325, 326]. On the other hand, Pensack et al. reported on a femtosecond transient absorption study of the SF process in pentacene, indicating the transition to a further intermediate, which the authors interpret as a specially separated, spin-correlated triplet exciton pair ${}^1(T\dots T)$.[280] Based on their findings, they established a three-step kinetic scheme of the SF process:



Scholes has shown that the ${}^1(T\dots T)$ state is a spin entangled triplet pair on non-adjacent molecules, which can be formed from a ${}^1(TT)$ state upon a triplet-triplet energy (Dexter) transfer process. [178, 281] Chan et. al. has formulated a similar kinetic scheme upon the observation of two distinct multiexciton states in a pentacene/fullerene bilayer system using femtosecond nonlinear spectroscopies.[306] The formation of an ${}^1(T\dots T)$ state in pentacene was also experimentally detected by others. [307, 282] It has been further

observed in crystalline rubrene [308] and polycrystalline hexacene [309], each representing well-established SF molecules as well as in linear oligomers and linked dimers of perylene[310, 327]. Employing a model CI Hamiltonian, Ambrosio et al. investigated the energetics of the closely interacting ${}^1(\text{TT})$ ("bound" multiexciton, or ME state) and the more spatially separated ${}^1(\text{T...T})$ configurations within pentacene and tetracene trimers.[328] They discovered that the bound ME state is energetically favorable due to strong orbital overlap, providing stabilization, whereas the separated ${}^1(\text{T...T})$ state exhibits higher energy levels, akin to two independent triplets, attributed to its lesser stabilization from reduced orbital interaction. This variation in energy is interpreted as binding energy, acting as a critical barrier for efficient singlet fission (SF) and the dissociation of the triplet pairs. The authors propose a decay pathway bypassing the ${}^1(\text{TT})$ state, suggesting that the decay over the ${}^1(\text{T...T})$ configuration—potentially mediated by charge transfer (CT)—enables the generation of two free triplets without encountering this barrier, facilitating a more efficient SF process. Analytic energy expressions for paired triplets within a trimer have been also delivered by Tao and Tan.[286, 23] Taffet et. al. carried out highly accurate computations studying the orbital overlap-dependent contribution to the triplet–triplet exchange splitting for tetracene dimers.[304] However, little is known about the detailed mechanism of the ${}^1(\text{T...T})$ formation. Abraham et. al. have delivered an expression of the respective triplet–triplet energy transfer integral for an Dexter exchange mechanism derived from the Spin Hamiltonian in the Heisenberg picture and studied its dependence on the packing motif in tetracene employing ab-initio calculations. [303] Wang et. al. have recently presented an efficient diabatization approach relying on fragment particle-hole densities and applied their methodology to the investigation of the formation of the correlated ${}^1(\text{T...T})$ state in tetracene, finding significant influence of high-lying multiply-excited CT states. [329] A so far in this context unexplored, but prominent class of SF materials consists in stacked perylene diimides (PDIs).[26, 121, 263] This molecule offers the appealing possibility to effectively control its packing arrangement by introducing different functional groups at their imide positions,[227, 260] while the introduction of linkers on these positions allows for the production of well-defined model compounds of stacked dimer , trimer and oligomers that have provided valuable insights into the packing structure dependence of SF efficiency and underlying mechanisms.[311, 263, 265] However, to the best of our knowledge, no experimental or theoretical work has targeted the possible role of the underlying mechanisms of specially separated ${}^1(\text{T...T})$ state in the SF process of PDIs. In this work, we deliver a theoretical study on the formation pathways and their packing dependence of the spatially separated, spin-correlated triplet pair ${}^1(\text{T...T})$ state in the PDI trimer system, as a model system that follows a CT-mediated ${}^1(\text{TT})$ formation pathway. We consider a direct as well as a superexchange mechanism of the triplet energy transfer, and estimate their rates by evaluation of the respective squared diabatic couplings. Furthermore, we study an alternative route, in which the ${}^1(\text{T...T})$ state is populated from the initial local excitation (LE) in a process mediated either via a separated CT state ${}^1(\text{AS}_0\text{C})$ (A denoting Anion and C denoting cation configuration) or a mixed, doubly excited CT state of type ${}^1(\text{TCA})$ or ${}^1(\text{TAC})$, without the transient population of the ${}^1(\text{TT})$ state.

In the past, theoretical screenings of the packing dependence of SF rates have often focused on molecular dimers. [1, 287, 330, 331] In this regard, the diabatic frontier orbital (FO) model as introduced by Michl [28, 319], in which the local excitation (LE), Charge Transfer (CT) as well as the singlet-correlated triplet pair excitation in the basis of the monomer HOMOs and LUMOs are considered, is often used. Approximating the couplings between these quasi-diabatic states by orbital overlaps, the model has been proven particularly suitable for the fast screening of the packing dependence of the SF process in molecular dimer systems. [316, 287, 330] Berkelbach et. al. delivered an ab-initio parametrized implementation of the FO model and carried out periodic calculations in order to study the SF process in the crystalline phase, accounting for couplings between next neighbored molecules,[57, 58, 59] Li et al. implemented an ab-initio parametrized, extended exciton model for SF that considers the FO model and couplings between adjacent molecules, studying pentacene clusters, while Nakano et. al. constructed linear aggregates with defined extended size based on the dimer parametrization.[317]

Complementary, Morrison et al. proposed a fragment-based methodology for the ab initio implementation of the Frenkel–Davydov exciton model, employing singly excited monomer basis states. This approach enabled them to study long-lived coherence effects in the singlet fission (SF) process present in extended molecular aggregates.[332, 333, 334] Miryani et.al. screened the packing dependence of the SF rate by Redfield simulations, in which the dimer model is coupled to a bath, in order to account for the crystal environment[26]. However, all these implementations are inherently insufficient for the investigation of the formation of the ${}^1(\text{T...T})$ state, as for such studies, spatially separated state configurations of type ${}^1(\text{T...T})$ and ${}^1(\text{AS}_0\text{C})$, as well as mixed exciton states of type ${}^1(\text{TCA})$ and ${}^1(\text{TAC})$ have to be taken into account, for which an explicit trimer system has to be employed as a minimal model. This has been realized by Ambrosio et. al., who delivered a phenomenologically parameterized model CI Hamiltonian for linear chains of tetracene and pentacene[328].

In this work, we generalize the FO model for the description of systems comprising any number of molecules, deriving analytical expressions for the matrix elements through the utilization of symbolic algebra. This approach facilitates the efficient computation of rate expressions. We apply the methodology to the PDI trimer, studying competing formation pathways of the ${}^1(\text{T...T})$ state, for which we scan the

packing-dependence of the respective diabatic couplings and energies along a vertical and a longitudinal slipping mode. Notice that, as with all cluster approaches, using the trimer model to study charge transfer (CT) mediated processes in bulk or solvent neglects the dielectric polarization induced by interactions with the environment. However, this limitation can be addressed e.g. by incorporating state-specific solvation through a reaction-field operator. This operator describes the electrostatic interactions between the electronic states of the solute and the continuum solvent, as demonstrated in the work by Alam et al.[335]

8.2 Method

We construct a perylene diimide stack consisting of three monomers m , n and o . Considering the highest occupied molecular orbitals (HOMO) and lowest unoccupied molecular orbitals (LUMO) on each monomer, the model describes a system with 6 electrons in the 6 orbitals h_m , l_m , h_n , l_n , h_o and l_o , where h and l represent HOMO and LUMO, respectively, and their subscripts represent the monomer they belong to. Each monomer $I=m, n, o$ has 5 states, the ground state S_0^I , the singlet excited state S_1^I , a cationic state C^I , an anionic state A^I , and a triplet state T^I . Assuming an overall singlet multiplicity of the system, we construct 19 diabatic states of the trimer, giving rise to one ground state (GS), three locally excited singlet states (LE), 6 charge transfer states (CT) and 6 doubly excited, mixed CT-triplet states as well as three correlated paired triplet states (${}^1\text{TT}$) with overall singlet multiplicity, as illustrated in Figure 8.1. The resulting diabatic Hamiltonian for our model CI system is then generated using our program [296]. In the implementation, the second quantization formalism is applied, leading to the following expression for the Hamiltonian:

$$\hat{H} = \sum_{i,j=1}^d \sum_{s_i, s_j = \alpha, \beta} h_{ij} c_{i,s_i}^\dagger c_{j,s_j} + \frac{1}{2} \sum_{i,j,k,l=1}^d \sum_{s_i, s_j, s_k, s_l = \alpha, \beta} G_{ijkl} c_{i,s_i}^\dagger c_{j,s_j}^\dagger c_{k,s_k} c_{l,s_l} \quad (8.2)$$

where h and G denote the one-electron and two-electron integrals, respectively, while c^\dagger and c are the creation and annihilation operators.

These operators allow for the Hamiltonian matrix elements to be expressed as follows:

$$\langle \Psi_m | \hat{H} | \Psi_n \rangle = \sum_{i,j=1}^d \sum_{s_i, s_j = \alpha, \beta} h_{ij} \langle \Psi_m | c_{i,s_i}^\dagger c_{j,s_j} | \Psi_n \rangle + \frac{1}{2} \sum_{\substack{i,j,k, \\ l=1}}^d \sum_{\substack{s_i, s_j, \\ s_k, s_l \\ = \alpha, \beta}} G_{ijkl} \langle \Psi_m | c_{i,s_i}^\dagger c_{j,s_j}^\dagger c_{k,s_k} c_{l,s_l} | \Psi_n \rangle \quad (8.3)$$

A crucial aspect of our algorithm is the choice of the Jordan-Wigner representation [175] of the fermionic creation and annihilation operators facilitating automatic generation of the model CI-Hamiltonian matrix. This representation constructs the second-quantization operators through symbolic Kronecker products of the Pauli spin matrices for the spin orbitals, enabling the generation of matrix elements using symbolic algebra programs. The operators, represented as matrices of symbols, are combined through tensor products to obtain the one- and two-electron operators:

$$c^\dagger = \sigma_z \otimes \dots \otimes \sigma_z \otimes \sigma^- \otimes \mathbb{1} \otimes \dots \otimes \mathbb{1} \quad (8.4)$$

$$c = \sigma_z \otimes \dots \otimes \sigma_z \otimes \sigma^+ \otimes \mathbb{1} \otimes \dots \otimes \mathbb{1} \quad (8.5)$$

where σ_z is the Pauli spin matrix for the z-component of spin and $\sigma^\pm = \sigma_x \pm i\sigma_y$. Using these basic operators, spin adapted combinations can be constructed. The one-electron operator obtained is represented by \hat{h} , while the two-electron operator is denoted by \hat{G} in this paper. Using this set of operators, the equation

$$|\Psi_{(i_s)}\rangle = \sum_k CG_k c_{|s,m\rangle_j}^{\dagger \psi_i} c_{|s,m\rangle_j}^{\dagger \psi_i} \dots |-\rangle \quad (8.6)$$

describes the construction of a multi-particle quantum state $|\Psi_{(i_s)}\rangle$ with a given multiplicity i_s . In this expression, the summation over the index k indicates that the state is a superposition of various configurations. The term CG_k represents the Clebsch-Gordan coefficients. The creation operator $c_{|s,m\rangle_j}^{\dagger \psi_i}$ generates a particle in the quantum state with multiplicity s and high spin state m as $|s,m\rangle_j$ with the orbital ψ_i . The program is available on GitHub [296]. This approach not only facilitates the symbolic generation of analytic expressions for matrix elements involving configurations of any excitation level but also supports both theoretical analysis and numerical evaluation of couplings.

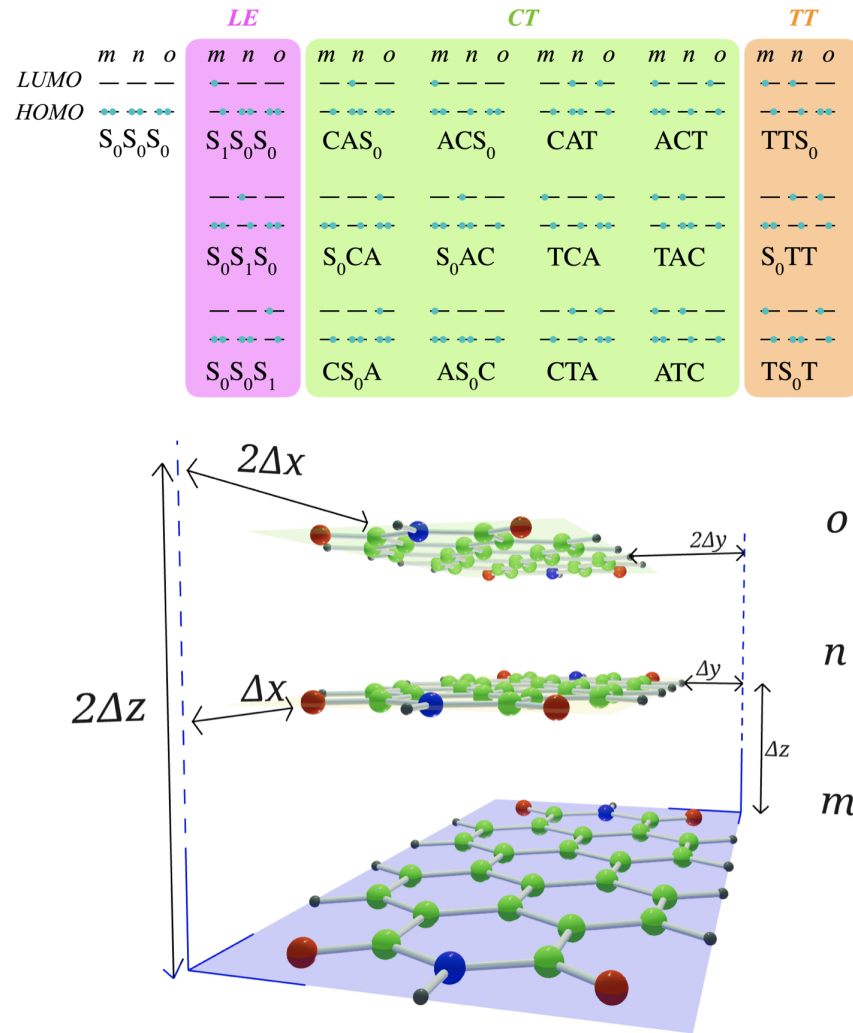


Figure 8.1: Top: Diabatic states considered in the trimer model Hamiltonian. Notice, that only singlet spin multiplicity is considered. Bottom: Structural model considered in the scans.

8.2.1 Rate Expression

The transition rate $T_{o \rightarrow m}$ from an initial state $|o\rangle$ with energy E_o to a final state $|m\rangle$ with energy E_m due to a perturbation \hat{V} is given by:

$$T_{i \rightarrow f} = \frac{2\pi}{\hbar} |\langle o | \hat{V} | m(\lambda) \rangle|^2 \rho(E_f) \quad (8.7)$$

where \hbar is the reduced Planck constant, $\langle o | \hat{V} | m(\lambda) \rangle$ is the matrix element of the perturbation \hat{V} between the initial and final states, and $\rho(E_f)$ is the density of final states at the energy E_f . In this work, the density of states is considered as one, while the prefactor is neglected.

The perturbation expansion of the state $|m(\lambda)\rangle$ is given by:

$$\begin{aligned} |m(\lambda)\rangle = & |m\rangle + \lambda \sum_{n \neq m} \frac{\langle n | \hat{V} | m \rangle}{E_m - E_n} |n\rangle \\ & + \dots \end{aligned} \quad (8.8)$$

Where $|m\rangle$ and $|n\rangle$ are the unperturbed states, and \hat{V} is the perturbing Hamiltonian, that accounts for the interaction of the monomers in the system. In the given expression, the perturbation of $|m(\lambda)\rangle$ consists of the unperturbed wave-function $|m\rangle$, the n^{th} -order perturbation with coefficient λ^n . Upon projection of an unperturbed state $|o\rangle$, we can obtain the matrix element of Fermi's golden rule.

Here, we consider the perturbed final state to incorporate and discuss various types of pathways and intermediate states that might be involved in the transition.

$$\begin{aligned} \langle o | \hat{V} | m(\lambda) \rangle = & \langle o | \hat{V} | m \rangle + \lambda \sum_{n \neq m} \frac{\langle n | \hat{V} | m \rangle}{E_m - E_n} \langle o | \hat{V} | n \rangle \\ & + \dots \end{aligned} \quad (8.9)$$

The term with coefficient λ is the first order correction to the matrix elements. It represents the transition strength of involving one intermediate step. Thus, the transition $T_{S_0\text{TT} \rightarrow TS_0\text{T}}$ via ACT is given by:

$$T_{S_0\text{TT} \rightarrow TS_0\text{T}} = \frac{\langle S_0\text{TT} | \hat{V} | \text{ACT} \rangle \langle \text{ACT} | \hat{V} | TS_0\text{T} \rangle}{E_{TS_0\text{T}} - E_{\text{ACT}}} \quad (8.10)$$

Similarly, the transition $T_{S_0\text{TT} \rightarrow TS_0\text{T}}$ via CAT is:

$$T_{S_0\text{TT} \rightarrow TS_0\text{T}} = \frac{\langle S_0\text{TT} | \hat{V} | \text{CAT} \rangle \langle \text{CAT} | \hat{V} | TS_0\text{T} \rangle}{E_{TS_0\text{T}} - E_{\text{CAT}}} \quad (8.11)$$

Furthermore, the transition $T_{S_1S_0S_0 \rightarrow TS_0\text{T}}$ is given by:

$$T_{S_1S_0S_0 \rightarrow TS_0\text{T}} = \frac{\langle S_1S_0S_0 | \hat{V} | \text{CS}_0\text{A} \rangle \langle \text{CS}_0\text{A} | \hat{V} | TS_0\text{T} \rangle}{E_{TS_0\text{T}} - E_{\text{CS}_0\text{A}}} \quad (8.12)$$

These equations describe transitions between diabatic states influenced by the perturbation operator \hat{V} , where $E_{TS_0\text{T}}$, E_{ACT} , and E_{CAT} denote their respective energies. The matrix elements $\langle S_0\text{TT} | \hat{V} | \text{ACT} \rangle$, $\langle S_0\text{TT} | \hat{V} | \text{CAT} \rangle$, and $\langle S_1S_0S_0 | \hat{V} | \text{CS}_0\text{A} \rangle$ quantify the transition couplings, reflecting the system's response to external influences. In the case where the perturbation is caused by monomers forming a trimer, \hat{V} represents the Hamiltonian of these monomers. Thus \hat{H} , constructed using operators described in previous subsections is used in this work as perturbing operator. The complete pathway for the formation of $TS_0\text{T}$ from a LE state involving CT states, as well as the interference of such pathways, has been discussed in the appendix.

8.3 Computational Details

The molecular geometry of the PDI monomer has been optimised using DFT, employing the CAM-B3LYP functional and the 6-31G basis set[336, 208]. To scan the diabatic coupling elements in the trimer system, we constructed a trimer stack of the three monomers, where consecutive monomers were stacked at an inter-planar distance of 3.4Å. The first monomer was kept stationary, and the second and third monomers were allowed to slip along both the longitudinal and transversal axes from 0Å to 4.0Å. The scanning was performed in steps of 0.1Å, where the slipping of the third monomer was twice that of the second monomer in each step, as shown in Figure 8.1. The slipping was executed in such a way that consecutive monomers were slipped along the same vector.

In the trimer system, one-electron and two-electron integrals are computed in the atomic orbital basis. The coefficient matrices (\mathbf{C}) for each monomer are obtained via Hartree-Fock calculations. These monomer coefficient matrices are then categorized into three groups: core containing molecular orbitals of the monomer lower than the HOMO, active containing the HOMO and LUMO of the monomers, and virtual orbitals made up of orbitals with higher energy than the LUMO. A collective coefficient matrix for the trimer is constructed, where the monomer's coefficient matrices serve as diagonal elements. The core orbitals' coefficients from each monomer are merged to form the core coefficient matrix, and similarly, the coefficients of the active and virtual orbitals of the monomers are grouped as active and virtual orbitals. Using the technique of multireference methods to incorporate the electron repulsion integrals (ERI) contribution of core electrons to calculate the couplings [337, 338, 339], the electron repulsion interaction term (\mathbf{G}_{core}) is determined by summing over specific core orbital indices in the expression involving the core density operator. The core density operator for the core orbitals is defined as:

$$\hat{\mathbf{D}}_{\text{core}} = 2\mathbf{C}_{\text{core}}\mathbf{C}_{\text{core}}^\dagger, \quad (8.13)$$

where \mathbf{C}_{core} represents the core orbital coefficient matrix, and $\mathbf{C}_{\text{core}}^\dagger$ denotes its transpose.

$$\mathbf{G}_{\text{core}} = \sum_{r,s} \hat{\mathbf{D}}_{\text{core}} [(pq|rs) - \frac{1}{2}(pr|sq)] \quad (8.14)$$

Here $(pq|rs)$ represents a two-electron integral in the atomic orbital basis. The core orbitals' ERI contributions are incorporated into the one-electron operator, making it an effective one-electron operator for active orbitals. The effective one-electron operator (\hat{h}_{act}) is then defined by adding \mathbf{G}_{core} to the one-electron operator (\hat{h}^{AO}) in the atomic orbital basis:

$$\hat{h}_{\text{act}} = \hat{h}^{\text{AO}} + \mathbf{G}_{\text{core}}. \quad (8.15)$$

The matrix element of the effective one-electron operator between two molecular orbitals ($\langle \psi_a | \hat{h}^{\text{MO}} | \psi_b \rangle$) is expressed in terms of the coefficients \mathbf{C}_a and \mathbf{C}_b^\dagger :

$$\langle \psi_a | \hat{h}^{\text{MO}} | \psi_b \rangle = \mathbf{C}_a^\dagger \hat{h}_{\text{act}} \mathbf{C}_b \quad (8.16)$$

Here, \mathbf{C}_a is the coefficient vector of molecular orbital a . The ERI in the molecular orbital basis are calculated by transforming their counterparts in the atomic orbital (AO) basis:

$$\langle \psi_a \psi_b | \psi_c \psi_d \rangle = \sum_p \sum_q \sum_r \sum_s C_p^a C_q^b C_r^c C_s^d (pq|rs) \quad (8.17)$$

Here, C_p^a is the coefficient of the p^{th} atomic orbital from a molecular orbital a . The expression for matrix elements of the diabatic Hamiltonian, as given in the appendix, is derived using our code [296]. The integrals used in this work are calculated using PYSCF [340, 341], which computes the integrals using libcint [342] and transforms them from the AO basis to the MO basis. The expressions of the diabatic energy of the states and the coupling discussed in this work are provided in the appendix.

8.4 Results

We categorize the several electronic pathways that can be considered for the formation of the spatially separated ${}^1(\text{T...T})$ state as follows: On the one hand, as suggested by Scholes, the formation can proceed via a Dexter type transfer from the preliminary populated ${}^1(\text{TT})$ state, in which the "inner" triplet gets transported, while the initial "edge" triplet acts as a spectator.[178] As FO models have been successfully employed for the description and evaluation of couplings of "conventional" triplet transfer[343], we are confident that the FO model chosen in this work is capable to predict reasonable couplings for the ${}^1(\text{TT})$ separation. Furthermore, Dexter Energy Transfer (DET) rates are well described by Fermi's golden rule, and therefore proportional to the square value of the involved couplings.[343] Therefore, screening the packing dependence of the relevant matrix elements provide insight in the structural preferences for the ${}^1(\text{TT})$ separation. In general, in DET, both an electron and a hole are transported, which results in a variety of optional mediation processes. [344] Here, we consider i) once the direct, two-particle transfer that originates from the short-range exchange interaction and ii) a (virtual) CT mediated process that can be understood as a super-exchange mechanism that proceeds via the coupling to a double excited, mixed CT -triplet state. Two pathways can be followed, in which initially either the hole is transported (in that case, the mediating configuration is of type ${}^1(\text{TAC})$) or an electron (via a state of type ${}^1(\text{TCA})$). Beside the DET mechanisms, in principle, a further pathway is conceivable that proceeds from an initially excited LE state via (virtual) CT state to the ${}^1(\text{T...T})$ state, bypassing the transient population of the ${}^1(\text{TT})$ state. We further scan the energy expressions that arise in the denominator of $T_{a \rightarrow b}$ as well as energy differences between ${}^1(\text{T...T})$ and ${}^1(\text{TT})$, as the energy difference between the initial and final states directly affects the density of states ρ , as ρ quantifies the number of states available at a given energy level for the system

Dexter direct transfer

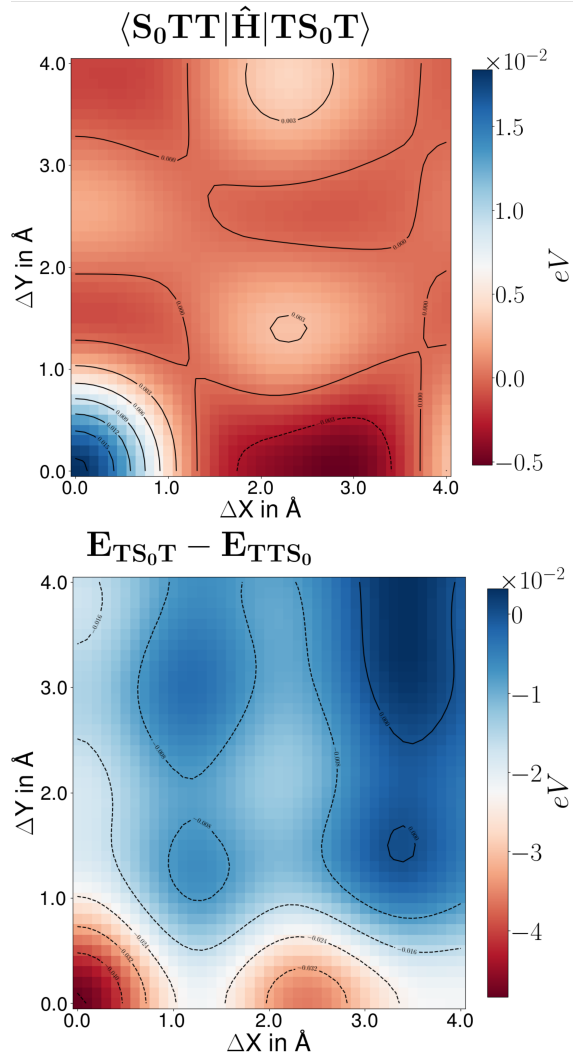


Figure 8.2: Top: Scan of transfer integral for the direct Dexter transfer mechanism. Bottom: Scan of the energy difference between ${}^1(\text{TT})$ state and ${}^1(\text{T...T})$ state.

to transition into. A large energy mismatch between the diabatic states and available energy levels can lead to a smaller ρ , hence influencing the transition rate. Notice that due to the minimal active space employed within our methodology, the total energies essentially lack dynamic correlation. However, the structural dependence of the energies might follow a realistic trend. The analytical expressions for the respective diabatic energies and scans of the resulting values are provided in the appendix, along with the adiabatic energies for the dimer systems. For the dimer, the three lowest adiabatic state energies lie between the values obtained with NOCI-CASPT2 and NOCI-CASSCF, as reported by Sousa et al.[212]. Our energy expressions are in line with those of Tan and Tao.[286, 23] Notice that our diabatic studies do not consider delocalization.

8.4.1 Dexter direct transfer:

In order to evaluate the Dexter exchange mechanism, we consider the matrix element $\langle S_0\text{TT}|\hat{H}|TS_0\text{T}\rangle$, corresponding to the simultaneous transfer of two electrons: one from the LUMO of fragment m to the LUMO of fragment n , and another from the HOMO of fragment n to the HOMO of fragment m . This transition is characterized by a two-electron integral or ERI term due to the interaction between these pairs of electrons, according to

$$\langle TS_0\text{T}|\hat{G}|S_0\text{TT}\rangle = 2(h_m h_n | l_m l_n) \quad (8.18)$$

The resulting scan presented in Figure 8.2 exhibits values of the order of 10^{-3} eV to 10^{-2} eV , highlighting a broad maximum (0.018 eV) for a perfectly stacked geometry ($\Delta X = 0.0\text{ \AA}$, $\Delta Y = 0.0\text{ \AA}$). Additionally, a local minimum of -0.005 eV is observed between $\Delta X = 2.2\text{ \AA}$ and $\Delta X = 3.0\text{ \AA}$ centering at $\Delta X = 2.9\text{\AA}$, $\Delta Y = 0.0\text{\AA}$. Further analysis was conducted on the energy difference between ${}^1(\text{TT})$ and ${}^1(\text{T...T})$ states (detailed analytical expressions provided in the appendix). The scan presented in Figure 8.2 (bottom) displays energy differences ranging from -0.04 eV to 0.0 eV. The largest energy gap of -0.04 eV occurs with a perfectly stacked packing motif at $\Delta X = 0\text{\AA}$, $\Delta Y = 0\text{\AA}$. Additionally, a local extremum with an energy gap of -0.03 eV is observed between $\Delta X = 2.0\text{\AA}$ and $\Delta X = 2.8\text{ \AA}$, $\Delta Y = 0.0\text{ \AA}$. As the offset in the Y direction increases, the energy gap decreases, reaching degeneracy at $\Delta X = 3.5\text{ \AA}$, $\Delta Y = 1.5\text{ \AA}$, and within the broad region of $\Delta X = 3.1\text{ \AA}$ to $\Delta X = 3.9\text{ \AA}$, $\Delta Y = 2.5\text{ \AA}$ to $\Delta Y = 4\text{ \AA}$. Apart from these specific extrema, the energy differences across broad regions are generally on the order of the thermal energy at room temperature (0.025 eV). This suggests that for the corresponding packing motifs, the ${}^1(\text{TT})$ to ${}^1(\text{T...T})$ transition can proceed barrierlessly and would mix in the adiabatic picture. Interestingly, for tetracene and pentacene, Ambrosio et al. observed energetically well-separated ${}^1(\text{TT})$ and ${}^1(\text{T...T})$ states, using their parameterized model CI Hamiltonian.[328]

8.4.2 Dexter superexchange mechanism:

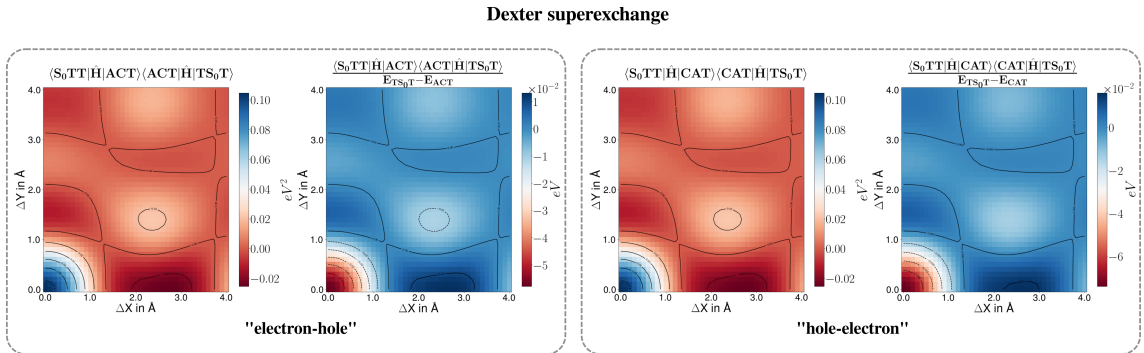


Figure 8.3: Scans of couplings and transition matrix elements enrolled in the Dexter super exchange mechanism. Left box: Pathway describing initial electron transfer, followed by the transport of the hole. Right box: Initial hole and subsequent electron transfer.

For the superexchange mechanism, we consider once the product of couplings $\langle S_0 \text{TT} | \hat{H} | \text{ACT} \rangle \langle \text{ACT} | \hat{H} | \text{TS}_0 \text{T} \rangle$ for initial hole transfer and once $\langle S_0 \text{TT} | \hat{H} | \text{CAT} \rangle \langle \text{CAT} | \hat{H} | \text{TS}_0 \text{T} \rangle$, describing initial electron transfer. One first sight, the respective scans appear similar, which can be explained by further analysis of the underlying analytic expressions, given in the appendix. In the transfer of states $\langle \text{ACT} | \hat{H} | \text{TS}_0 \text{T} \rangle$ and $\langle \text{CAT} | \hat{H} | \text{S}_0 \text{TT} \rangle$, electrons move from the HOMO of fragment m to the HOMO of fragment n and vice-versa. This occurs through the transfer of only one electron, leading to the presence of both one-electron integral terms (as shown in equations S.9 and S.11) and ERI terms (as shown in equations S.10 and S.12). When comparing the one-electron and two-electron contributions of both transitions, it can be noted that the one-electron part is equivalent, while the two-electron contributions show a difference in the terms $-(h_m h_n | l_n l_n)$ in $\langle \text{CAT} | \hat{H} | \text{S}_0 \text{TT} \rangle$ and $-(h_n h_m | l_m l_m)$ for $\langle \text{ACT} | \hat{H} | \text{TS}_0 \text{T} \rangle$. This discrepancy arises because the orbital l_m remains empty in the $\langle \text{CAT} | \hat{H} | \text{S}_0 \text{TT} \rangle$ transition, while l_n remains empty in the $\langle \text{ACT} | \hat{H} | \text{TS}_0 \text{T} \rangle$ transition. Accordingly, in the transfer of states $\langle \text{ACT} | \hat{H} | \text{S}_0 \text{TT} \rangle$ and $\langle \text{CAT} | \hat{H} | \text{TS}_0 \text{T} \rangle$, electrons move from the LUMO of fragment m to the LUMO of fragment n and vice-versa, leading to similar one-electron integral terms (as shown in equations S.13 and S.15) but differing ERI terms (as shown in equations S.14 and S.16). The global extremum at $\Delta X = 0\text{\AA}$, $\Delta Y = 0.0\text{ \AA}$ reaches a value of 0.1 eV eV^2 in both pathways. Further local extrema can be found at $\Delta X = 2.2\text{ \AA}$, $\Delta Y = 1.5\text{ \AA}$ and $\Delta X = 2.2\text{ \AA}$, $\Delta Y = 3.8\text{ \AA}$ (both with values of 0.03 eV^2) as well as for an offset of $\Delta X = 0.0\text{ \AA}$, $\Delta Y = 2.9\text{ \AA}$ (-0.02 eV^2). Notice, that the scans show the same features as the scan for the direct Dexter pathway. We further scanned the expression $T_{\text{S}_0 \text{TT} \rightarrow \text{TS}_0 \text{T}}$ for both pathways as presented in Figure 3. The topology of both scans appears similar, as the diabatic state energy differences in the denominator (see equation 8.11 and 8.10) are of the same order of magnitude and the respective energy plots, given in Figure S13, exhibit similar patterns. The diabatic state energies of ACT and CAT range from 7.4 eV to 7.9 eV and 7.0 eV to 7.6 eV, respectively, within the scanned conformational state (as presented in Figure S12 in appendix), and are therefore about 2 eV higher in energy as the ${}^1(\text{TT})$ states. The resulting transition matrix displays features comparable to those of the scan for the direct Dexter pathway, but with values that are about one order of magnitude higher in energy for the local extremum located between $\Delta X = 2.2\text{ \AA}$ and $\Delta X = 3.0\text{ \AA}$, $\Delta Y = 0.0\text{ \AA}$ due to the contributing one-electron integrals. Since both transition amplitudes have the same sign, the electronic

pathways constructively interfere.

8.4.3 "One step" mechanism

In addition to the Dexter processes of ${}^1(\text{TT})$ separation, we have studied an alternative pathway, in which the ${}^1(\text{T...T})$ is formed in a CT mediated process from the initially generated LE state, without the transient formation of a ${}^1(\text{TT})$ state. Within our model, such a mechanism only shows significant couplings when the involved charge transfer state is "separated" in the sense, that anion and cation are located at the same monomers as the paired triplets in the ${}^1(\text{T...T})$ state. Furthermore, when the cation resides on the same monomer as the LE, according to $\langle \text{S}_1\text{S}_0\text{S}_0|\hat{\mathbf{H}}|\text{CS}_0\text{A} \rangle \langle \text{CS}_0\text{A}|\hat{\mathbf{H}}|\text{TS}_0\text{T} \rangle$ the coupling values are significantly higher as shown in Figure S2 in the appendix.

In order to account for interference effects, we present and discuss the coupling scan for a chosen pathway that proceeds from a given LE state via any separated CT state to the final ${}^1(\text{T...T})$ state, which is shown in Figure 8.4 top left. The scan features a broad extremum between $\Delta X = 3 \text{ \AA}$ and $\Delta X = 4 \text{ \AA}$ with a center at $\Delta X = 3.4 \text{ \AA}$, and spanning from $\Delta Y = 0 \text{ \AA}$ to $\Delta Y = 1 \text{ \AA}$ with an absolute value of $\pm 0.001 \text{ eV}^2$. A second bulge, located at $\Delta X = 1.5 \text{ \AA}$ and $\Delta Y = 1 \text{ \AA}$ posses an additional local maximum with a value of $\pm 0.001 \text{ eV}^2$. The plot of the energy expression appearing in the denominator (see equation 8.12) of the corresponding transition matrix element is given in Figure S13 in the appendix and ranges between -0.5 eV and 0.2 eV , indicating that the energetic ordering of the involved diabatic states switches along the scanning modes. The plot of the transition matrix element exhibits strong variations in energy, ranging from 10^{-8} eV to 10^2 eV , caused by the (near-)degeneracy in the energies which appears as a difference in the denominator. The local near-degeneracy of the energies is reflected in the resulting scan, which exhibits a curved line ranging from $\Delta X = 0.0 \text{ \AA}$ and $\Delta Y = 2.4 \text{ \AA}$ to $\Delta X = 2.9 \text{ \AA}$ and $\Delta Y = 0.0 \text{ \AA}$, reaching values between 10^{-2} eV and 10^2 eV . For a meaningful evaluation of the significance of these pathway, we compare these values with those of a chosen competing "three step" mechanism that proceeds via the ${}^1(\text{TT})$ state and has to be treated by third order perturbation theory. The corresponding plots are shown in Figure 4 right. Again, We observe strong energy variations, ranging from 10^{-7} eV to 10^1 eV , which are driven by the (near-)degeneracy in the energy term in the denominator involving the energy difference between the two triplet pair states. The (near-)degeneracy is directly reflected in the scan as lines with high coupling values. A region of high values is located at $\Delta X = 0.0 \text{ \AA}$ and $\Delta X = 1.2 \text{ \AA}$, $\Delta Y = 0.0 \text{ \AA}$ and $\Delta Y = 1.0 \text{ \AA}$, with a value of 10^0 eV encompassing the local maxima at $\Delta X = 0.7 \text{ \AA}$ and $\Delta Y = 0.0 \text{ \AA}$. Interestingly, the plot of the "three step" mechanism shows higher coupling values than found for the "one step" mechanism. However, the latter becomes equally significant along the discussed curved line which captures also the packing motif with an offset of $\Delta X = 2.9 \text{ \AA}$ $\Delta Y = 0.0 \text{ \AA}$. It should be noted, that in both the "one step" and the "three step" mechanism, destructive electronic interference caused by opposite signs of the transition amplitudes of the individual CT-containing terms is observed, while the individual TAC/TCA terms lead to constructive interference. We further emphasize that symmetry-breaking would strongly influence the interference observed for the highly symmetric system studied in this work.

The presented findings for the "one step" mechanism can be contextualized within a recent combined experimental and theoretical study, in which we reported an efficient SF process in a defined PDI trimer stack in solution, achieved through the introduction of linkers [265]. Interestingly, the accompanying theoretical calculations suggested that the packing motif a displacement of about $\Delta X = 3 \text{ \AA}$, $\Delta Y = 0.0 \text{ \AA}$ leads to the cancellation of nearest-neighbor LE and CT couplings, resulting in a "null-aggregate", which is directly reflected in the experimental absorption spectrum. This molecular arrangement can be considered an isolated monomer sandwiched between a slightly coupled "outer dimer" system. Within the framework of the proposed "one step" mechanism, the formation of a separated CT state in such a system is conceivable. Our present findings support this result, as the transition matrix element for the "one step" mechanism becomes significantly large in the region of the discussed structural arrangement.

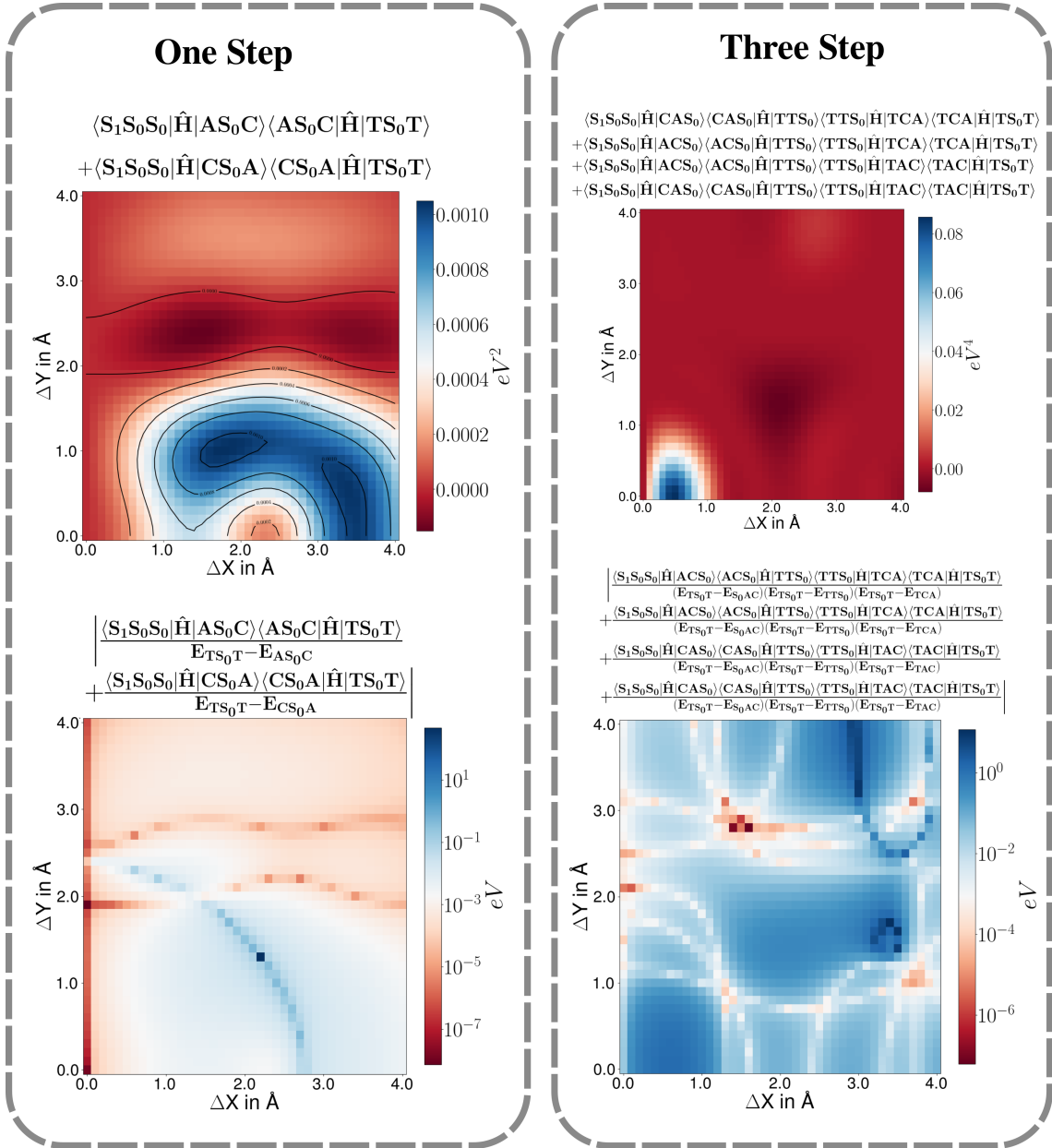


Figure 8.4: Top left: Scan of couplings involved in the "one step" mechanism. Bottom left: Scan of the respective transition rate expression with the energy term as arises in the denominator. The colors are shown in logarithmic scale. Top right: Scan of couplings involved in the "three step" mechanism proceeding via a CAS_0 and TCA mediated formation of $TS_0 T$. Bottom right: Scan of absolute third order perturbation term.

8.5 Conclusion

In this work, we have generalized the widely applied diabatic FO model for dimers to the description of extended aggregates with any number of molecules. Our implementation allows for the symbolic generation of matrix elements involving configurations with arbitrary excitation level employing symbolic algebra that can be utilized both for theoretical analysis of the couplings as well as for their numerical evaluation. This enabled us to study the packing dependence of the competing ${}^1(\text{T...T})$ formation pathways in a molecular trimer stack, that involve the spatially separated ${}^1(\text{T...T})$ and ${}^1(\text{A...C})$ state as well as mixed states of type ${}^1(\text{TAC})$. We explored three possible mechanisms: the "two intermediates" scheme, as suggested by Scholes and others, in which a ${}^1(\text{T...T})$ is formed upon Dexter type triplet energy transfer from the singlet spin coupled adjacent triplet pair state ${}^1(\text{TT})$, once via a direct and once via a superexchange pathway, and in addition, a so far unexplored "one step" pathway that proceeds in a separated-CT mediated process from an initially excited LE state directly to the ${}^1(\text{T...T})$. Our simulations indicate that the energy difference between the ${}^1(\text{T...T})$ and ${}^1(\text{TT})$ states is below thermal energy across a wide range of stacking configurations, suggesting that these states may mix in the adiabatic picture. We find that the transition matrix element for the Dexter superexchange "three step" mechanism generally yields higher values than for the "one step" mechanism. The latter pathway becomes significant only when the transfer occurs via (virtual) coupling to a "charge-separated" state, where the cation and anion are located on non-adjacent edge molecules. Evaluation of the transition matrix element suggests that ${}^1(\text{T...T})$ state formation can indeed proceed via this pathway for specific stacking motifs. A recent combined experimental and theoretical study reported efficient singlet fission in a "null-aggregate" trimer, where next-neighbor couplings are canceled [265]. In such a system, a separated CT state may play a significant role. In conclusion, our calculations indicate that the formation of the ${}^1(\text{T...T})$ state in stacked PDIs might follow different pathways, depending on the packing arrangement. While our primary motivation in this work was to provide the full analytic expressions of the minimal model for ${}^1(\text{T...T})$ formation, the capability of our implementation to automatically generate matrix elements for large aggregates will enable future model studies on the size effects of the ${}^1(\text{TT})$ separation, the underlying Dexter-type transport phenomenon, and the dependence of spin entanglement on system parameters and distances.

8.6 Appendix

8.6.1 Wave functions

Throughout this work, the three monomers of the trimer model use the following notation: first fragment is represented as m , the second fragment is represented as n , and the third fragment is represented as o . The wave functions shown in equations 8.19 and 8.20 represent a local exciton and a charge transfer state in the trimer. These wavefunctions describe only single excitations, with 5 electrons in the highest occupied orbitals (HOMO) and 1 electron in the lowest occupied orbitals (LUMO) of the three monomers. In equation 8.19, which represents the local exciton state $|\text{S}_1\text{S}_0\text{S}_0\rangle$, the electron from fragment m is excited. The excited fragment is highlighted with a yellow background. When the excited electron moves to fragment o , making m a cationic fragment and o an anionic fragment, it results in the wave function $|\text{CS}_0\text{A}\rangle$ (equation 8.20), where the label of the LUMO is changed to o .

$$|\text{S}_1\text{S}_0\text{S}_0\rangle = \begin{aligned} & -\frac{1}{\sqrt{8}} \begin{array}{|c|c|} \hline h_{m\uparrow} l_{m\downarrow} & h_{o\uparrow} h_{o\downarrow} h_{n\uparrow} h_{n\downarrow} \\ \hline \end{array} + \frac{1}{\sqrt{8}} \begin{array}{|c|c|} \hline h_{m\downarrow} l_{m\uparrow} & h_{o\uparrow} h_{o\downarrow} h_{n\uparrow} h_{n\downarrow} \\ \hline \end{array} \\ & + \frac{1}{\sqrt{8}} \begin{array}{|c|c|} \hline h_{m\uparrow} l_{m\downarrow} & h_{o\downarrow} h_{o\uparrow} h_{n\uparrow} h_{n\downarrow} \\ \hline \end{array} - \frac{1}{\sqrt{8}} \begin{array}{|c|c|} \hline h_{m\downarrow} l_{m\uparrow} & h_{o\downarrow} h_{o\uparrow} h_{n\uparrow} h_{n\downarrow} \\ \hline \end{array} \\ & + \frac{1}{\sqrt{8}} \begin{array}{|c|c|} \hline h_{m\uparrow} l_{m\downarrow} & h_{o\uparrow} h_{o\downarrow} h_{n\downarrow} h_{n\uparrow} \\ \hline \end{array} - \frac{1}{\sqrt{8}} \begin{array}{|c|c|} \hline h_{m\downarrow} l_{m\uparrow} & h_{o\uparrow} h_{o\downarrow} h_{n\downarrow} h_{n\uparrow} \\ \hline \end{array} \\ & - \frac{1}{\sqrt{8}} \begin{array}{|c|c|} \hline h_{m\uparrow} l_{m\downarrow} & h_{o\downarrow} h_{o\uparrow} h_{n\downarrow} h_{n\uparrow} \\ \hline \end{array} + \frac{1}{\sqrt{8}} \begin{array}{|c|c|} \hline h_{m\downarrow} l_{m\uparrow} & h_{o\downarrow} h_{o\uparrow} h_{n\downarrow} h_{n\uparrow} \\ \hline \end{array} \end{aligned} \quad (8.19)$$

$$|\text{CS}_0\text{A}\rangle = \begin{aligned} & -\frac{1}{\sqrt{8}} \begin{array}{|c|c|} \hline h_{m\uparrow} l_{o\downarrow} & h_{o\uparrow} h_{o\downarrow} h_{n\uparrow} h_{n\downarrow} \\ \hline \end{array} + \frac{1}{\sqrt{8}} \begin{array}{|c|c|} \hline h_{m\downarrow} l_{o\uparrow} & h_{o\uparrow} h_{o\downarrow} h_{n\uparrow} h_{n\downarrow} \\ \hline \end{array} \\ & + \frac{1}{\sqrt{8}} \begin{array}{|c|c|} \hline h_{m\uparrow} l_{o\downarrow} & h_{o\downarrow} h_{o\uparrow} h_{n\uparrow} h_{n\downarrow} \\ \hline \end{array} - \frac{1}{\sqrt{8}} \begin{array}{|c|c|} \hline h_{m\downarrow} l_{o\uparrow} & h_{o\downarrow} h_{o\uparrow} h_{n\uparrow} h_{n\downarrow} \\ \hline \end{array} \\ & + \frac{1}{\sqrt{8}} \begin{array}{|c|c|} \hline h_{m\uparrow} l_{o\downarrow} & h_{o\uparrow} h_{o\downarrow} h_{n\downarrow} h_{n\uparrow} \\ \hline \end{array} - \frac{1}{\sqrt{8}} \begin{array}{|c|c|} \hline h_{m\downarrow} l_{o\uparrow} & h_{o\uparrow} h_{o\downarrow} h_{n\downarrow} h_{n\uparrow} \\ \hline \end{array} \\ & - \frac{1}{\sqrt{8}} \begin{array}{|c|c|} \hline h_{m\uparrow} l_{o\downarrow} & h_{o\downarrow} h_{o\uparrow} h_{n\downarrow} h_{n\uparrow} \\ \hline \end{array} + \frac{1}{\sqrt{8}} \begin{array}{|c|c|} \hline h_{m\downarrow} l_{o\uparrow} & h_{o\downarrow} h_{o\uparrow} h_{n\downarrow} h_{n\uparrow} \\ \hline \end{array} \end{aligned} \quad (8.20)$$

The wave functions shown in equations 8.21, 8.22, 8.23, and 8.24 represent the electronic spin configuration of a triplet pair resulting in a singlet. Such a configuration requires 4 electrons. The fragments making up the system are shown with a yellow background. The electrons of the triplet are in different spatial orbitals, thus, the electrons reside in the HOMO and LUMO of the two fragments. In the state $|\text{S}_0\text{TT}\rangle$, the two fragments involved are n and o , whereas in the state $|\text{TS}_0\text{T}\rangle$, the two fragments involved are m and o .

In the state $|\text{S}_0\text{TT}\rangle$, the coefficients $\pm \frac{1}{\sqrt{6}}$ are also associated with terms where the electrons from fragments n and o are in opposite non-zero high spin states. Whereas the coefficients $\pm \frac{1}{\sqrt{24}}$ are also associated with terms where the electrons from fragments n and o are in zero high spin states. A similar arrangement of coefficients is present in the $|\text{TS}_0\text{T}\rangle$ wave function with fragments m and o .

When the LUMO electron in the state $|\text{TS}_0\text{T}\rangle$ from fragment m moves to the LUMO of fragment n , it results in the state $|\text{CAT}\rangle$, making m a cation and n an anion. The label referring to the fragment of the spatial orbital changes from m to n . Similarly, when the LUMO electron in the state $|\text{S}_0\text{TT}\rangle$ from fragment n moves to the LUMO of fragment m , it results in the state $|\text{ACT}\rangle$, making n a cation and m an anion. The label referring to the fragment of the spatial orbital changes from n to m .

$$|\text{S}_0\text{TT}\rangle = \begin{aligned} & -\frac{1}{\sqrt{6}} \begin{array}{|c|c|} \hline h_{n\downarrow} l_{n\downarrow} h_{o\uparrow} l_{o\uparrow} & h_{m\uparrow} h_{m\downarrow} \\ \hline \end{array} + \frac{1}{\sqrt{6}} \begin{array}{|c|c|} \hline h_{n\uparrow} l_{n\uparrow} h_{o\downarrow} l_{o\downarrow} & h_{m\downarrow} h_{m\uparrow} \\ \hline \end{array} \\ & -\frac{1}{\sqrt{6}} \begin{array}{|c|c|} \hline h_{n\uparrow} l_{n\uparrow} h_{o\downarrow} l_{o\uparrow} & h_{m\uparrow} h_{m\downarrow} \\ \hline \end{array} + \frac{1}{\sqrt{6}} \begin{array}{|c|c|} \hline h_{n\downarrow} l_{n\downarrow} h_{o\uparrow} l_{o\uparrow} & h_{m\downarrow} h_{m\uparrow} \\ \hline \end{array} \\ & + \frac{1}{\sqrt{24}} \begin{array}{|c|c|} \hline h_{n\uparrow} l_{n\downarrow} h_{o\uparrow} l_{o\downarrow} & h_{m\uparrow} h_{m\downarrow} \\ \hline \end{array} + \frac{1}{\sqrt{24}} \begin{array}{|c|c|} \hline h_{n\downarrow} l_{n\uparrow} h_{o\uparrow} l_{o\downarrow} & h_{m\uparrow} h_{m\downarrow} \\ \hline \end{array} \\ & + \frac{1}{\sqrt{24}} \begin{array}{|c|c|} \hline h_{n\uparrow} l_{n\downarrow} h_{o\downarrow} l_{o\uparrow} & h_{m\uparrow} h_{m\downarrow} \\ \hline \end{array} + \frac{1}{\sqrt{24}} \begin{array}{|c|c|} \hline h_{n\downarrow} l_{n\uparrow} h_{o\downarrow} l_{o\uparrow} & h_{m\uparrow} h_{m\downarrow} \\ \hline \end{array} \\ & - \frac{1}{\sqrt{24}} \begin{array}{|c|c|} \hline h_{n\uparrow} l_{n\downarrow} h_{o\uparrow} l_{o\downarrow} & h_{m\downarrow} h_{m\uparrow} \\ \hline \end{array} - \frac{1}{\sqrt{24}} \begin{array}{|c|c|} \hline h_{n\downarrow} l_{n\uparrow} h_{o\uparrow} l_{o\downarrow} & h_{m\downarrow} h_{m\uparrow} \\ \hline \end{array} \\ & - \frac{1}{\sqrt{24}} \begin{array}{|c|c|} \hline h_{n\uparrow} l_{n\downarrow} h_{o\downarrow} l_{o\uparrow} & h_{m\downarrow} h_{m\uparrow} \\ \hline \end{array} - \frac{1}{\sqrt{24}} \begin{array}{|c|c|} \hline h_{n\downarrow} l_{n\uparrow} h_{o\downarrow} l_{o\uparrow} & h_{m\downarrow} h_{m\uparrow} \\ \hline \end{array} \end{aligned} \quad (8.21)$$

$$\begin{aligned}
|\text{TS}_0\text{T}\rangle = & -\frac{1}{\sqrt{6}} [h_{m\uparrow}l_{m\uparrow}h_{o\downarrow}l_{o\downarrow} | h_{n\uparrow}h_{n\downarrow}] - \frac{1}{\sqrt{6}} [h_{m\downarrow}l_{m\downarrow}h_{o\uparrow}l_{o\uparrow} | h_{n\uparrow}h_{n\downarrow}] \\
& + \frac{1}{\sqrt{6}} [h_{m\uparrow}l_{m\uparrow}h_{o\downarrow}l_{o\downarrow} | h_{n\downarrow}h_{n\uparrow}] + \frac{1}{\sqrt{6}} [h_{m\downarrow}l_{m\downarrow}h_{o\uparrow}l_{o\uparrow} | h_{n\downarrow}h_{n\uparrow}] \\
& + \frac{1}{\sqrt{24}} [h_{m\uparrow}l_{m\downarrow}h_{o\uparrow}l_{o\downarrow} | h_{n\uparrow}h_{n\downarrow}] + \frac{1}{\sqrt{24}} [h_{m\downarrow}l_{m\uparrow}h_{o\uparrow}l_{o\downarrow} | h_{n\uparrow}h_{n\downarrow}] \\
& + \frac{1}{\sqrt{24}} [h_{m\uparrow}l_{m\downarrow}h_{o\downarrow}l_{o\uparrow} | h_{n\uparrow}h_{n\downarrow}] + \frac{1}{\sqrt{24}} [h_{m\downarrow}l_{m\uparrow}h_{o\downarrow}l_{o\uparrow} | h_{n\uparrow}h_{n\downarrow}] \\
& - \frac{1}{\sqrt{24}} [h_{m\uparrow}l_{m\downarrow}h_{o\uparrow}l_{o\downarrow} | h_{n\downarrow}h_{n\uparrow}] - \frac{1}{\sqrt{24}} [h_{m\downarrow}l_{m\uparrow}h_{o\uparrow}l_{o\downarrow} | h_{n\downarrow}h_{n\uparrow}] \\
& - \frac{1}{\sqrt{24}} [h_{m\uparrow}l_{m\downarrow}h_{o\downarrow}l_{o\uparrow} | h_{n\downarrow}h_{n\uparrow}] - \frac{1}{\sqrt{24}} [h_{m\downarrow}l_{m\uparrow}h_{o\downarrow}l_{o\uparrow} | h_{n\downarrow}h_{n\uparrow}]
\end{aligned} \tag{8.22}$$

$$\begin{aligned}
|\text{CAT}\rangle = & -\frac{1}{\sqrt{6}} [h_{m\uparrow}l_{n\uparrow}h_{o\downarrow}l_{o\downarrow} | h_{n\uparrow}h_{n\downarrow}] - \frac{1}{\sqrt{6}} [h_{m\downarrow}l_{n\downarrow}h_{o\uparrow}l_{o\uparrow} | h_{n\uparrow}h_{n\downarrow}] \\
& + \frac{1}{\sqrt{6}} [h_{m\uparrow}l_{n\uparrow}h_{o\downarrow}l_{o\downarrow} | h_{n\downarrow}h_{n\uparrow}] + \frac{1}{\sqrt{6}} [h_{m\downarrow}l_{n\downarrow}h_{o\uparrow}l_{o\uparrow} | h_{n\downarrow}h_{n\uparrow}] \\
& + \frac{1}{\sqrt{24}} [h_{m\uparrow}l_{n\downarrow}h_{o\uparrow}l_{o\downarrow} | h_{n\uparrow}h_{n\downarrow}] + \frac{1}{\sqrt{24}} [h_{m\downarrow}l_{n\uparrow}h_{o\uparrow}l_{o\downarrow} | h_{n\uparrow}h_{n\downarrow}] \\
& + \frac{1}{\sqrt{24}} [h_{m\uparrow}l_{n\downarrow}h_{o\downarrow}l_{o\uparrow} | h_{n\uparrow}h_{n\downarrow}] + \frac{1}{\sqrt{24}} [h_{m\downarrow}l_{n\uparrow}h_{o\downarrow}l_{o\uparrow} | h_{n\uparrow}h_{n\downarrow}] \\
& - \frac{1}{\sqrt{24}} [h_{m\uparrow}l_{n\downarrow}h_{o\uparrow}l_{o\downarrow} | h_{n\downarrow}h_{n\uparrow}] - \frac{1}{\sqrt{24}} [h_{m\downarrow}l_{n\uparrow}h_{o\uparrow}l_{o\downarrow} | h_{n\downarrow}h_{n\uparrow}] \\
& - \frac{1}{\sqrt{24}} [h_{m\uparrow}l_{n\downarrow}h_{o\downarrow}l_{o\uparrow} | h_{n\downarrow}h_{n\uparrow}] - \frac{1}{\sqrt{24}} [h_{m\downarrow}l_{n\uparrow}h_{o\downarrow}l_{o\uparrow} | h_{n\downarrow}h_{n\uparrow}]
\end{aligned} \tag{8.23}$$

$$\begin{aligned}
|\text{ACT}\rangle = & -\frac{1}{\sqrt{6}} [h_{n\uparrow}l_{m\uparrow}h_{o\downarrow}l_{o\downarrow} | h_{m\uparrow}h_{m\downarrow}] - \frac{1}{\sqrt{6}} [h_{n\downarrow}l_{m\downarrow}h_{o\uparrow}l_{o\uparrow} | h_{m\uparrow}h_{m\downarrow}] \\
& + \frac{1}{\sqrt{6}} [h_{n\uparrow}l_{m\uparrow}h_{o\downarrow}l_{o\downarrow} | h_{m\downarrow}h_{m\uparrow}] + \frac{1}{\sqrt{6}} [h_{n\downarrow}l_{m\downarrow}h_{o\uparrow}l_{o\uparrow} | h_{m\downarrow}h_{m\uparrow}] \\
& + \frac{1}{\sqrt{24}} [h_{n\uparrow}l_{m\downarrow}h_{o\uparrow}l_{o\downarrow} | h_{m\uparrow}h_{m\downarrow}] + \frac{1}{\sqrt{24}} [h_{n\downarrow}l_{m\uparrow}h_{o\uparrow}l_{o\downarrow} | h_{m\uparrow}h_{m\downarrow}] \\
& + \frac{1}{\sqrt{24}} [h_{n\uparrow}l_{m\downarrow}h_{o\downarrow}l_{o\uparrow} | h_{m\uparrow}h_{m\downarrow}] + \frac{1}{\sqrt{24}} [h_{n\downarrow}l_{m\uparrow}h_{o\downarrow}l_{o\uparrow} | h_{m\uparrow}h_{m\downarrow}] \\
& - \frac{1}{\sqrt{24}} [h_{n\uparrow}l_{m\downarrow}h_{o\uparrow}l_{o\downarrow} | h_{m\downarrow}h_{m\uparrow}] - \frac{1}{\sqrt{24}} [h_{n\downarrow}l_{m\uparrow}h_{o\uparrow}l_{o\downarrow} | h_{m\downarrow}h_{m\uparrow}] \\
& - \frac{1}{\sqrt{24}} [h_{n\uparrow}l_{m\downarrow}h_{o\downarrow}l_{o\uparrow} | h_{m\downarrow}h_{m\uparrow}] - \frac{1}{\sqrt{24}} [h_{n\downarrow}l_{m\uparrow}h_{o\downarrow}l_{o\uparrow} | h_{m\downarrow}h_{m\uparrow}]
\end{aligned} \tag{8.24}$$

8.6.2 Couplings

The transition $\langle \text{TS}_0\text{T} | \hat{H} | \text{S}_0\text{TT} \rangle$ corresponds to the simultaneous transfer of two electrons: one from the LUMO of fragment m to the LUMO of fragment n , and another from the HOMO of fragment n to the HOMO of fragment m . This transition is characterized by a two-electron integral or electron repulsion integral (ERI) term due to the interaction between these pairs of electrons.

$$\langle \text{TS}_0\text{T} | \hat{T} | \text{S}_0\text{TT} \rangle = 0 \tag{8.25}$$

$$\langle \text{TS}_0\text{T} | \hat{G} | \text{S}_0\text{TT} \rangle = 2(h_m h_n | l_m l_n) \tag{8.26}$$

In the transfer of states $\langle \text{ACT} | \hat{H} | \text{TS}_0\text{T} \rangle$ and $\langle \text{CAT} | \hat{H} | \text{S}_0\text{TT} \rangle$, electrons move from the HOMO of fragment m to the HOMO of fragment n and vice-versa. This occurs through the transfer of only one electron, leading to the presence of both one-electron integral terms (as shown in equations 8.27 and 8.29) and ERI terms (as shown in equations 8.28 and 8.30). The one-electron integral terms in both transitions are the same.

The ERI terms in both transitions are similar, except for the integral $-(h_m h_n | l_n l_n)$ in $\langle \text{CAT} | \hat{H} | \text{S}_0\text{TT} \rangle$ and $-(h_n h_m | l_m l_m)$ in $\langle \text{ACT} | \hat{H} | \text{TS}_0\text{T} \rangle$. This discrepancy arises because the orbital l_m remains empty in the $\langle \text{CAT} | \hat{H} | \text{S}_0\text{TT} \rangle$ transition, while l_n remains empty in the $\langle \text{ACT} | \hat{H} | \text{TS}_0\text{T} \rangle$ transition. Therefore, the terms involving empty orbitals are absent in their respective transitions.

In equations 8.28 and 8.30, the ERIs shown with a yellow background represent exchange integrals, while those with a green background represent Coulomb integrals.

$$\langle \text{ACT} | \hat{T} | \text{TS}_0\text{T} \rangle = -\langle h_n | \hat{h} | h_m \rangle \tag{8.27}$$

$$\begin{aligned}\langle \text{ACT} | \hat{G} | \text{TS}_0 \text{T} \rangle = & +\frac{3}{2}(h_n h_o | h_o h_m) + \frac{3}{2}(h_n l_o | l_o h_m) \\ & -(h_m h_m | h_n h_m) - (h_n h_m | h_n h_n) \\ & -(h_n h_m | h_o h_o) - (h_n h_m | l_m l_m) - (h_n h_m | l_o l_o)\end{aligned}\quad (8.28)$$

$$\langle \text{CAT} | \hat{T} | \text{S}_0 \text{TT} \rangle = -\langle h_m | \hat{h} | h_n \rangle \quad (8.29)$$

$$\begin{aligned}\langle \text{CAT} | \hat{G} | \text{S}_0 \text{TT} \rangle = & \frac{3}{2}(h_m h_o | h_o h_n) + \frac{3}{2}(h_m l_o | l_o h_n) \\ & -(h_m h_m | h_m h_n) - (h_m h_n | h_n h_n) \\ & -(h_m h_n | h_o h_o) - (h_m h_n | l_n l_n) - (h_m h_n | l_o l_o)\end{aligned}\quad (8.30)$$

In the transfer of states $\langle \text{ACT} | \hat{H} | \text{S}_0 \text{TT} \rangle$ and $\langle \text{CAT} | \hat{H} | \text{TS}_0 \text{T} \rangle$, electrons move from the LUMO of fragment m to the LUMO of fragment n . Similar to previous expressions they have both one-electron integral terms (as shown in equations 8.31 and 8.33) and ERI terms (as shown in equations 8.32 and 8.34). The different ERI terms are $2(l_m l_n | h_m h_m)$ in $\langle \text{ACT} | \hat{H} | \text{S}_0 \text{TT} \rangle$ and $2(l_m l_n | h_n h_m)$ in $\langle \text{CAT} | \hat{H} | \text{TS}_0 \text{T} \rangle$.

In equations 8.32 and 8.34, the ERIs shown with a yellow background represent exchange integrals with a coefficient of $\frac{1}{2}$ and have orbitals of the stationary triplet fragment, i.e., h_o and l_o . Those with a green background represent Coulomb integrals. The ERI terms with an orange background are Coulomb integrals involving the doubly occupied orbitals and have a coefficient of 2, while the ERI terms in pink are exchange integrals involving the fragments participating in the transition.

$$\langle \text{ACT} | \hat{T} | \text{S}_0 \text{TT} \rangle = \langle l_m | \hat{h} | l_n \rangle \quad (8.31)$$

$$\begin{aligned}\langle \text{ACT} | \hat{G} | \text{S}_0 \text{TT} \rangle = & +2(l_n l_m | h_m h_m) \\ & +\frac{1}{2}(l_n h_o | h_o l_m) + \frac{1}{2}(l_n l_o | l_o l_m) \\ & -(l_n h_m | h_m l_m) - (l_n h_n | h_n l_m) \\ & +(l_n l_m | h_n h_n) + (l_n l_m | h_o h_o) + (l_n l_m | l_o l_o)\end{aligned}\quad (8.32)$$

$$\langle \text{CAT} | \hat{T} | \text{TS}_0 \text{T} \rangle = \langle l_n | \hat{h} | l_m \rangle \quad (8.33)$$

$$\begin{aligned}\langle \text{CAT} | \hat{G} | \text{TS}_0 \text{T} \rangle = & +2(l_m l_n | h_n h_n) \\ & +\frac{1}{2}(l_m h_o | h_o l_n) + \frac{1}{2}(l_m l_o | l_o l_n) \\ & -(l_m h_m | h_m l_n) - (l_m h_n | h_n l_n) \\ & +(l_m l_n | h_m h_m) + (l_m l_n | h_o h_o) + (l_m l_n | l_o l_o)\end{aligned}\quad (8.34)$$

In the transfer of states $\langle \text{CS}_0 \text{A} | \hat{H} | \text{S}_1 \text{S}_0 \text{S}_0 \rangle$, electrons move from the LUMO of fragment m to the LUMO of fragment o . This occurs through the transfer of only one electron, resulting in the presence of both one-electron integral terms (as shown in equations 8.35) and electron repulsion integral (ERI) terms (as shown in equations 8.36). The one-electron integral terms in both transitions are the same. The color coding remains consistent with the previous system, with yellow background terms representing exchange integrals and green indicating Coulomb terms. The orange background terms depict Coulomb integrals involving double occupancy, with their corresponding exchange terms shown with a pink background. In this case, as the singly excited state transitions into another singlet excited state and the multiplicities of the fragments are also singlet, the ERI terms have a different set of coefficients.

$$\langle \text{CS}_0 \text{A} | \hat{T} | \text{S}_1 \text{S}_0 \text{S}_0 \rangle = \langle l_m | \hat{h} | l_o \rangle \quad (8.35)$$

$$\begin{aligned}\langle \text{CS}_0 \text{A} | \hat{G} | \text{S}_1 \text{S}_0 \text{S}_0 \rangle = & +(h_m l_m | l_o h_m) \\ & +(h_m h_m | l_o l_m) \\ & -(l_o h_n | h_n l_m) - (l_o h_o | h_o l_m) \\ & +2(h_n h_n | l_o l_m) + 2(h_o h_o | l_o l_m)\end{aligned}\quad (8.36)$$

8.6.3 Energy

This section contains expressions of Hamiltonian matrix elements where the states in the bra and ket are the same, thus representing the diabatic energy of the states. Equation 8.37 presents the one-electron integral expression of the energy of the $|\text{S}_0\text{TT}\rangle$ state. Equation 8.38 provides the ERI expression of the energy of the $|\text{S}_0\text{TT}\rangle$ state. Equation 8.39 shows the one-electron integral expression of the energy of the $|\text{TS}_0\text{T}\rangle$ state. Equation 8.40 depicts the ERI expression of the energy of the $|\text{TS}_0\text{T}\rangle$ state. Equation 8.39 and 8.37 have 5 terms, an expression for the doubly occupied orbital with a coefficient of 2, and 4 terms for singly occupied orbitals with a coefficient of 1.

In equations 8.39 and 8.37, the ERIs shown with a yellow background represent exchange integrals with a coefficient of $\frac{1}{2}$ and have orbital contributions of the triplet states. Those with a green background represent Coulomb integrals of previously mentioned orbitals. The ERI terms with an orange background are Coulomb integrals involving the doubly occupied orbitals and have a coefficient of 2, while the ERI terms in pink are exchange integrals, which also have contributions of the doubly occupied orbitals.

$$\langle \text{S}_0\text{TT} | \hat{T} | \text{S}_0\text{TT} \rangle = \langle h_o | \hat{h} | h_o \rangle + \langle l_o | \hat{h} | l_o \rangle + \langle h_n | \hat{h} | h_n \rangle + \langle l_n | \hat{h} | l_n \rangle + 2 \langle h_m | \hat{h} | h_m \rangle \quad (8.37)$$

$$\begin{aligned} \langle \text{S}_0\text{TT} | \hat{G} | \text{S}_0\text{TT} \rangle = & +\frac{1}{2}(h_n l_o | l_o h_n) + \frac{1}{2}(l_o l_n | l_n l_o) \\ & +\frac{1}{2}(h_o l_n | l_n h_o) + \frac{1}{2}(h_o h_n | h_n h_o) \\ & +(h_n h_n | l_o l_o) + (h_n h_n | l_n l_n) \\ & +(h_o h_o | l_o l_o) + (h_o h_o | l_n l_n) \\ & +(h_o h_o | h_n h_n) + (l_o l_o | l_n l_n) \\ & +2(h_m h_m | h_m h_m) + 2(h_m h_m | l_o l_o) + 2(h_m h_m | l_n l_n) \\ & +2(h_o h_o | h_m h_m) + 2(h_n h_n | h_m h_m) \\ & -(h_o h_m | h_m h_o) - (h_o l_o | l_o h_o) \\ & -(h_n h_m | h_m h_n) - (h_n l_n | l_n h_n) \\ & -(h_m l_o | l_o h_m) - (h_m l_n | l_n h_m) \end{aligned} \quad (8.38)$$

$$\langle \text{TS}_0\text{T} | \hat{T} | \text{TS}_0\text{T} \rangle = 2 \langle h_n | \hat{h} | h_n \rangle + \langle l_m | \hat{h} | l_m \rangle + \langle h_m | \hat{h} | h_m \rangle + \langle l_o | \hat{h} | l_o \rangle + \langle h_o | \hat{h} | h_o \rangle \quad (8.39)$$

$$\begin{aligned} \langle \text{TS}_0\text{T} | \hat{G} | \text{TS}_0\text{T} \rangle = & +\frac{1}{2}(h_m h_o | h_o h_m) + \frac{1}{2}(h_m l_o | l_o h_m) \\ & +\frac{1}{2}(h_o l_m | l_m h_o) + \frac{1}{2}(l_m l_o | l_o l_m) \\ & +(h_m h_m | h_o h_o) + (h_m h_m | l_m l_m) \\ & +(h_m h_m | l_o l_o) + (h_o h_o | l_m l_m) \\ & +(h_o h_o | l_o l_o) + (l_m l_m | l_o l_o) \\ & +2(h_n h_n | h_n h_n) + 2(h_m h_m | h_n h_n) + 2(h_o h_o | h_n h_n) \\ & +2(h_n h_n | l_m l_m) + 2(h_n h_n | l_o l_o) \\ & -(h_m h_n | h_n h_m) - (h_m l_m | l_m h_m) \\ & -(h_o h_n | h_n h_o) - (h_o l_o | l_o h_o) \\ & -(h_n l_m | l_m h_n) - (h_n l_o | l_o h_n) \end{aligned} \quad (8.40)$$

Equation 8.41 presents the one-electron integral expression of the energy of the $|\text{CAT}\rangle$ state, while Equation 8.42 provides the ERI expression of the energy of the $|\text{CAT}\rangle$ state. Equation 8.43 shows the one-electron integral expression of the energy of the $|\text{ACT}\rangle$ state. Equation 8.44 depicts the ERI expression of the energy of the $|\text{ACT}\rangle$ state. Equations 8.41 and 8.43 have 5 terms, an expression for the doubly occupied orbital with a coefficient of 2, and 4 terms for singly occupied orbitals with a coefficient of 1. The

difference from the previous system is that the anionic fragment has 3 electrons and the cationic fragment has one electron.

The ERI expressions are similar to those of the previous $|\text{S}_0\text{TT}\rangle$ state. The color codes to signify different types of ERI are the same. The difference arises from the occupancy of different fragments.

$$\langle \text{CAT} | \hat{\mathbf{T}} | \text{CAT} \rangle = 2\langle h_n | \hat{\mathbf{h}} | h_n \rangle + \langle h_m | \hat{\mathbf{h}} | h_m \rangle + \langle l_n | \hat{\mathbf{h}} | l_n \rangle + \langle l_o | \hat{\mathbf{h}} | l_o \rangle + \langle h_o | \hat{\mathbf{h}} | h_o \rangle \quad (8.41)$$

$$\begin{aligned} \langle \text{CAT} | \hat{\mathbf{G}} | \text{CAT} \rangle = & \frac{1}{2}(h_m h_o | h_o h_m) + \frac{1}{2}(h_o l_n | l_n h_o) \\ & + \frac{1}{2}(l_n l_o | l_o l_n) + \frac{1}{2}(l_o h_m | h_m l_o) \\ & +(h_m h_m | h_o h_o) + (h_m h_m | l_n l_n) \\ & +(h_m h_m | l_o l_o) + (h_o h_o | l_n l_n) \\ & +(l_n l_n | l_o l_o) + (l_o l_o | h_o h_o) \\ & +2(h_m h_m | h_n h_n) + 2(h_n h_n | h_n h_n) + 2(h_n h_n | h_o h_o) \\ & +2(h_n h_n | l_n l_n) + 2(h_n h_n | l_o l_o) \\ & -(h_m h_n | h_n h_m) - (h_m l_n | l_n h_m) \\ & -(h_n h_o | h_o h_n) - (h_n l_n | l_n h_n) \\ & -(h_n l_o | l_o h_n) - (h_o l_o | l_o h_o) \end{aligned} \quad (8.42)$$

$$\langle \text{ACT} | \hat{\mathbf{T}} | \text{ACT} \rangle = 2\langle h_m | \hat{\mathbf{h}} | h_m \rangle + \langle h_n | \hat{\mathbf{h}} | h_n \rangle + \langle l_m | \hat{\mathbf{h}} | l_m \rangle + \langle l_o | \hat{\mathbf{h}} | l_o \rangle + \langle h_o | \hat{\mathbf{h}} | h_o \rangle \quad (8.43)$$

$$\begin{aligned} \langle \text{ACT} | \hat{\mathbf{G}} | \text{ACT} \rangle = & +(h_o h_o | l_o l_o) + (l_m l_m | l_o l_o) \\ & +(h_n h_n | l_o l_o) + (h_o h_o | l_m l_m) \\ & +(h_n h_n | h_o h_o) + (h_n h_n | l_m l_m) \\ & \frac{1}{2}(h_n h_o | h_o h_n) + \frac{1}{2}(h_n l_o | l_o h_n) \\ & + \frac{1}{2}(h_o l_m | l_m h_o) + \frac{1}{2}(l_m l_o | l_o l_m) \\ & -(h_n l_m | l_m h_n) - (h_o l_o | l_o h_o) \\ & -(h_m l_m | l_m h_m) - (h_m l_o | l_o h_m) \\ & -(h_m h_n | h_n h_m) - (h_m h_o | h_o h_m) \\ & +2(h_m h_m | h_m h_m) + 2(h_m h_m | h_n h_n) \\ & +2(h_m h_m | h_o h_o) + 2(h_m h_m | l_m l_m) + 2(h_m h_m | l_o l_o) \end{aligned} \quad (8.44)$$

Equation 8.45 presents the one-electron integral expression of the energy of the $|\text{S}_1\text{S}_0\text{S}_0\rangle$ state, while Equation 8.46 provides the ERI expression of the energy of the $|\text{S}_1\text{S}_0\text{S}_0\rangle$ state. Equation 8.47 shows the one-electron integral expression of the energy of the $|\text{CS}_0\text{A}\rangle$ state. Equation 8.48 depicts the ERI expression of the energy of the $|\text{CS}_0\text{A}\rangle$ state.

Expressions highlighted in yellow represent Coulomb integrals of singly occupied orbitals with doubly occupied orbitals. Orange-colored expressions denote exchange integrals of singly occupied orbitals with doubly occupied orbitals. Green-colored background expressions represent Coulomb and exchange integrals for electrons between singly occupied orbitals. Blue-colored background expressions depict Coulomb and exchange integrals of electrons in doubly occupied orbitals with other doubly occupied orbitals. The expressions highlighted in emerald represent ERI of doubly occupied orbitals with themselves.

$$\langle \text{S}_1\text{S}_0\text{S}_0 | \hat{\mathbf{T}} | \text{S}_1\text{S}_0\text{S}_0 \rangle = \langle h_m | \hat{\mathbf{h}} | h_m \rangle + \langle l_m | \hat{\mathbf{h}} | l_m \rangle + 2\langle h_n | \hat{\mathbf{h}} | h_n \rangle + 2\langle h_o | \hat{\mathbf{h}} | h_o \rangle \quad (8.45)$$

$$\langle \text{CS}_0\text{A} | \hat{\mathcal{G}} | \text{CS}_0\text{A} \rangle = \langle h_m | \hat{\mathcal{H}} | h_m \rangle + \langle l_o | \hat{\mathcal{H}} | l_o \rangle + 2 \langle h_n | \hat{\mathcal{H}} | h_n \rangle + 2 \langle h_o | \hat{\mathcal{H}} | h_o \rangle \quad (8.47)$$

$$\begin{aligned}
\langle \text{CS}_0 \text{A} | \hat{G} | \text{CS}_0 \text{A} \rangle = & (h_m h_m | l_o l_o) + (h_m l_o | l_o h_m) \\
& \quad \boxed{\dots} \\
& + 2(h_m h_m | h_n h_n) + 2(h_m h_m | h_o h_o) \\
& + 2(h_o h_o | l_o l_o) + 2(h_n h_n | l_o l_o) \\
& \quad \boxed{\dots} \\
& - (h_m h_n | h_n h_m) - (h_m h_o | h_o h_m) \\
& - (h_n l_o | l_o h_n) - (h_o l_o | l_o h_o)
\end{aligned} \tag{8.48}$$

8.6.4 Singlet Fission Rate

The transition rate $T_{o \rightarrow m}$ from an initial state $|o\rangle$ with energy E_o to a final state $|m\rangle$ with energy E_m due to a perturbation \hat{V} is given by:

$$T_{i \rightarrow f} = \frac{2\pi}{\hbar} |\langle o | \hat{V} | m(\lambda) \rangle|^2 \rho(E_f) \quad (8.49)$$

where \hbar is the reduced Planck constant, $\langle o|\hat{V}|m(\lambda)\rangle$ is the matrix element of the perturbation \hat{V} between the initial and final states, and $\rho(E_f)$ is the density of final states at the energy E_f . The density of states is considered as one and the prefactor is neglected.

The perturbation expansion of the state $|m(\lambda)\rangle$ is given by:

$$\begin{aligned}
|m(\lambda)\rangle = & |m\rangle + \lambda \sum_{n \neq m} \frac{\langle n|\hat{V}|m\rangle}{E_m - E_n} |n\rangle \\
& + \lambda^2 \sum_{n \neq m} \sum_{q \neq m} \frac{\langle n|\hat{V}|q\rangle\langle q|\hat{V}|m\rangle}{(E_m - E_n)(E_m - E_q)} |n\rangle \\
& - \lambda^2 \sum_{n \neq m} \frac{\langle n|\hat{V}|m\rangle\langle m|\hat{V}|m\rangle}{(E_m - E_n)^2} |n\rangle \\
& - \frac{1}{2} \lambda^2 \sum_{n \neq m} \frac{\langle n|\hat{V}|m\rangle^2}{(E_m - E_n)^2} |m\rangle \\
& \frac{1}{\lambda^3} \left[- \sum_{n \neq m} \sum_{q \neq m} \sum_{r \neq m} \frac{\langle n|\hat{V}|q\rangle\langle q|\hat{V}|r\rangle\langle r|\hat{V}|m\rangle}{(E_n - E_m)(E_m - E_q)(E_m - E_r)} \right. \\
& + \sum_{n \neq m} \sum_{q \neq m} \frac{\langle m|\hat{V}|m\rangle\langle n|\hat{V}|q\rangle\langle q|\hat{V}|m\rangle}{(E_n - E_m)(E_m - E_q)} \left(\frac{1}{(E_m - E_n)} + \frac{1}{(E_m - E_q)} \right) \\
& - \sum_{n \neq m} \frac{|\langle m|\hat{V}|m\rangle|^2 \langle n|\hat{V}|m\rangle}{(E_n - E_m)^3} \\
& \left. + \sum_{n \neq m} \frac{|\langle m|\hat{V}|n\rangle|^2 \langle n|\hat{V}|m\rangle}{(E_n - E_m)(E_m - E_n)} \left(\frac{1}{(E_m - E_n)} + \frac{1}{2(E_m - E_n)} \right) \right] |n\rangle
\end{aligned}$$

$$\begin{aligned}
& + \left[\sum_{n \neq m} \sum_{q \neq m} - \frac{\langle m | \hat{V} | q \rangle \langle q | \hat{V} | n \rangle \langle n | \hat{V} | m \rangle + \langle q | \hat{V} | m \rangle \langle n | \hat{V} | q \rangle \langle m | \hat{V} | n \rangle}{2(E_m - E_q)^2(E_m - E_n)} \right. \\
& \quad \left. + \sum_{n \neq m} \frac{|\langle m | \hat{V} | n \rangle|^2 \langle m | \hat{V} | m \rangle}{(E_m - E_n)^3} \right] |m\rangle \tag{8.50} \\
& + \dots \tag{8.51}
\end{aligned}$$

Where $|m\rangle$, $|n\rangle$, $|q\rangle$, and $|r\rangle$ are the unperturbed states, and \hat{V} is the perturbing Hamiltonian, that accounts for the interaction of the monomers in the system. In the given expression, the perturbation of $|m(\lambda)\rangle$ consists of the unperturbed wave-function $|m\rangle$, the n^{th} -order perturbation with coefficient λ^n . Upon projection of an unperturbed state $|o\rangle$, we can obtain the matrix element of Fermi's golden rule.

Here, we consider the perturbed final state to incorporate and discuss various types of pathways and intermediate states that might be involved in the transition.

$$\begin{aligned}
\langle o | \hat{V} | m(\lambda) \rangle = & \langle o | \hat{V} | m \rangle + \lambda \sum_{n \neq m} \frac{\langle n | \hat{V} | m \rangle}{E_m - E_n} \langle o | \hat{V} | n \rangle \\
& + \lambda^2 \sum_{n \neq m} \sum_{q \neq m} \frac{\langle n | \hat{V} | q \rangle \langle q | \hat{V} | m \rangle}{(E_m - E_n)(E_m - E_q)} \langle o | \hat{V} | n \rangle \\
& - \lambda^2 \sum_{n \neq m} \frac{\langle n | \hat{V} | m \rangle \langle m | \hat{V} | m \rangle}{(E_m - E_n)^2} \langle o | \hat{V} | n \rangle \\
& - \frac{1}{2} \lambda^2 \sum_{n \neq m} \frac{\langle n | \hat{V} | m \rangle^2}{(E_m - E_n)^2} \langle o | \hat{V} | m \rangle \\
& \frac{1}{\lambda^3} \left[- \sum_{n \neq m} \sum_{q \neq m} \sum_{r \neq m} \frac{\langle n | \hat{V} | q \rangle \langle q | \hat{V} | r \rangle \langle r | \hat{V} | m \rangle}{(E_n - E_m)(E_m - E_q)(E_m - E_r)} \right. \\
& + \sum_{n \neq m} \sum_{q \neq m} \frac{\langle m | \hat{V} | m \rangle \langle n | \hat{V} | q \rangle \langle q | \hat{V} | m \rangle}{(E_n - E_m)(E_m - E_q)} \left(\frac{1}{(E_m - E_n)} + \frac{1}{(E_m - E_q)} \right) \\
& - \sum_{n \neq m} \frac{|\langle m | \hat{V} | m \rangle|^2 \langle n | \hat{V} | m \rangle}{(E_n - E_m)^3} \\
& + \sum_{n \neq m} \frac{|\langle m | \hat{V} | n \rangle|^2 \langle n | \hat{V} | m \rangle}{(E_n - E_m)^2} \left(\frac{1}{(E_m - E_n)} + \frac{1}{2(E_m - E_n)} \right) \Big] \langle o | \hat{V} | n \rangle \\
& + \left[\sum_{n \neq m} \sum_{q \neq m} - \frac{\langle m | \hat{V} | q \rangle \langle q | \hat{V} | n \rangle \langle n | \hat{V} | m \rangle + \langle q | \hat{V} | m \rangle \langle n | \hat{V} | q \rangle \langle m | \hat{V} | n \rangle}{2(E_m - E_q)^2(E_m - E_n)} \right. \\
& \quad \left. + \sum_{n \neq m} \frac{|\langle m | \hat{V} | n \rangle|^2 \langle m | \hat{V} | m \rangle}{(E_m - E_n)^3} \right] \langle o | \hat{V} | m \rangle \tag{8.52} \\
& + \dots \tag{8.53}
\end{aligned}$$

The term with coefficient λ is the first order correction to the matrix elements. It represents the transition strength of involving one intermediate step. In the case where the perturbation is caused by interaction between monomers forming a trimer, \hat{V} represents the Hamiltonian \hat{H} .

Thus, the transition $T_{S_0 \text{TT} \rightarrow TS_0 \text{T}}$ via ACT is given by:

$$T_{S_0 \text{TT} \rightarrow TS_0 \text{T}} = \frac{\langle S_0 \text{TT} | \hat{H} | \text{ACT} \rangle \langle \text{ACT} | \hat{H} | TS_0 \text{T} \rangle}{E_{TS_0 \text{T}} - E_{\text{ACT}}} \tag{8.54}$$

Similarly, the transition $T_{S_0 \text{TT} \rightarrow TS_0 \text{T}}$ via CAT is:

$$T_{S_0 \text{TT} \rightarrow TS_0 \text{T}} = \frac{\langle S_0 \text{TT} | \hat{H} | \text{CAT} \rangle \langle \text{CAT} | \hat{H} | TS_0 \text{T} \rangle}{E_{TS_0 \text{T}} - E_{\text{CAT}}} \tag{8.55}$$

Furthermore, the one step mediated transition $T_{S_1 S_0 S_0 \rightarrow TS_0 \text{T}}$ is given by:

$$T_{S_1 S_0 S_0 \rightarrow TS_0 \text{T}} = \frac{\langle S_1 S_0 S_0 | \hat{H} | \text{CS}_0 \text{A} \rangle \langle \text{CS}_0 \text{A} | \hat{H} | TS_0 \text{T} \rangle}{E_{TS_0 \text{T}} - E_{\text{CS}_0 \text{A}}} \tag{8.56}$$

8.6.5 Interference

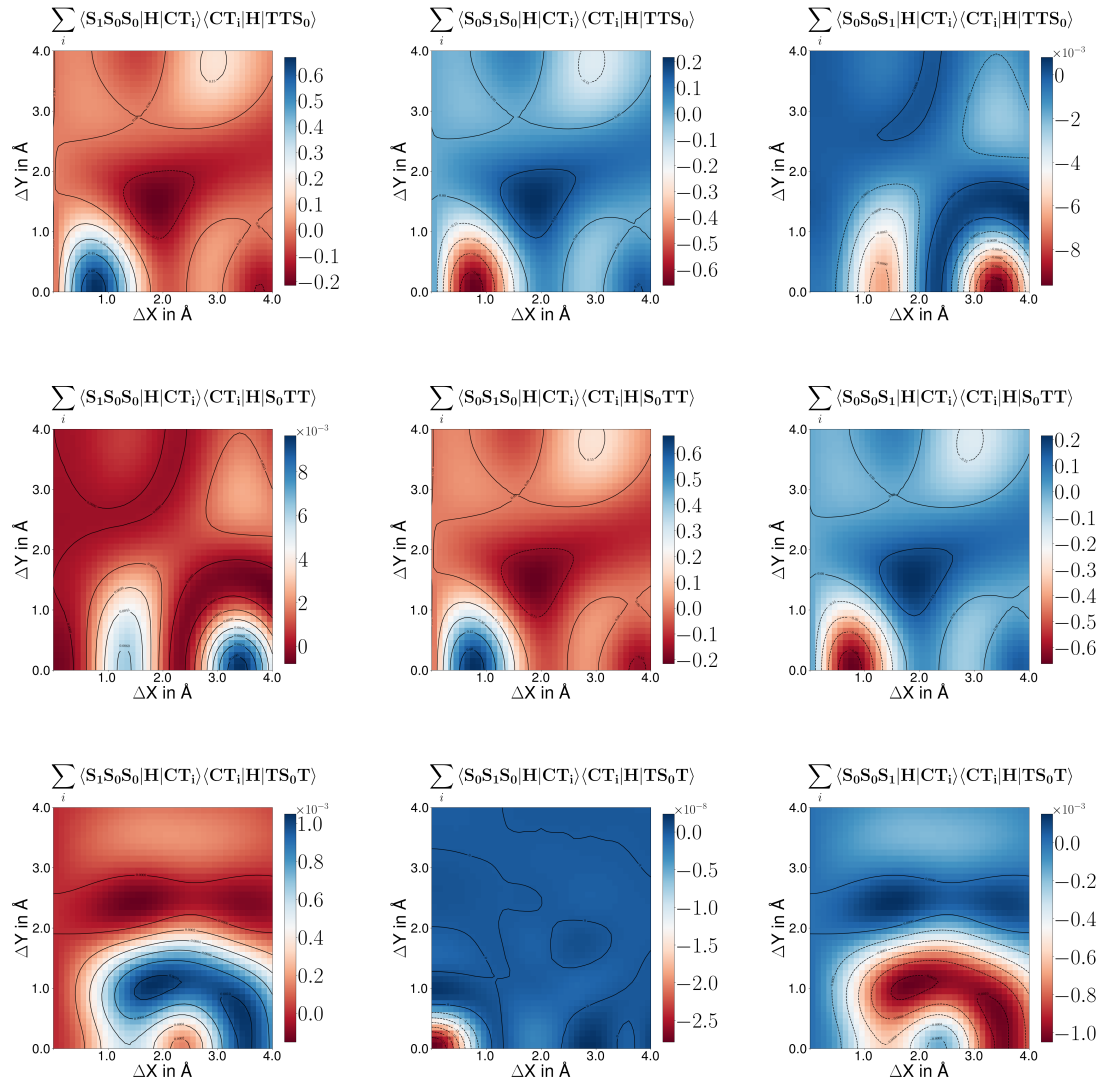


Figure S1: : Plots of $T_{LE_a \rightarrow {}^1TT_b}$ summed over all intermediate CT states. Each column has the same initial LE state and each row has the same final ${}^1\text{TT}$ state.

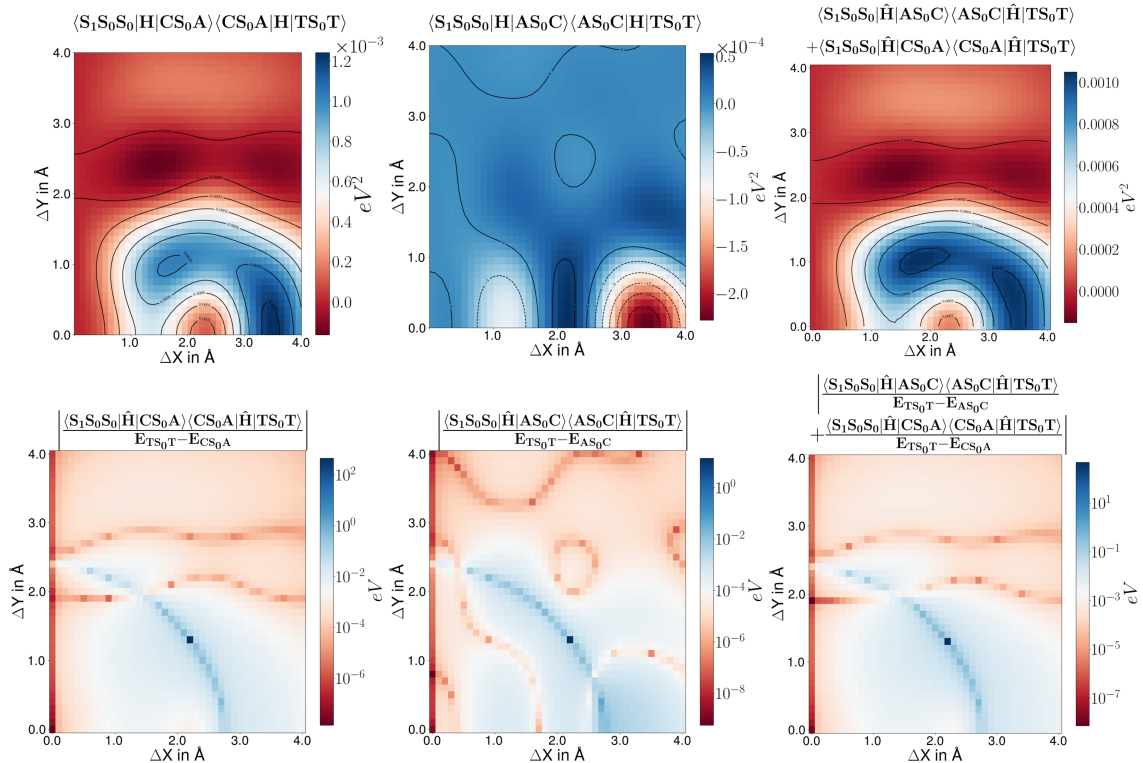


Figure S2: The first plot at the top shows the one-step coupling when the cation is formed on the LE, while the second plot at the top displays the one-step coupling when the anion is formed on the LE. The third plot at the top presents the sum of both couplings. Similarly, the first plot at the bottom shows the one-step perturbation term when the cation is formed on the LE, and the second plot at the bottom illustrates the one-step perturbation term when the anion is formed on the LE. The third plot at the bottom provides the sum of both perturbation terms. The plots at the bottom are shown on a logarithmic scale. To prevent numerical instability in calculations where energy differences ΔE_i are extremely small (e.g., $\Delta E_i < 10^{-16}$), we replace these problematic values with the smallest stable energy difference in the dataset. Specifically, if $\Delta E_i < \epsilon$ (with $\epsilon = 10^{-16}$), we substitute ΔE_i with ΔE_j , where $\Delta E_j = \min(\{\Delta E_k \mid \Delta E_k > \epsilon\})$. This approach ensures stable computations, particularly near points of near-degeneracy.

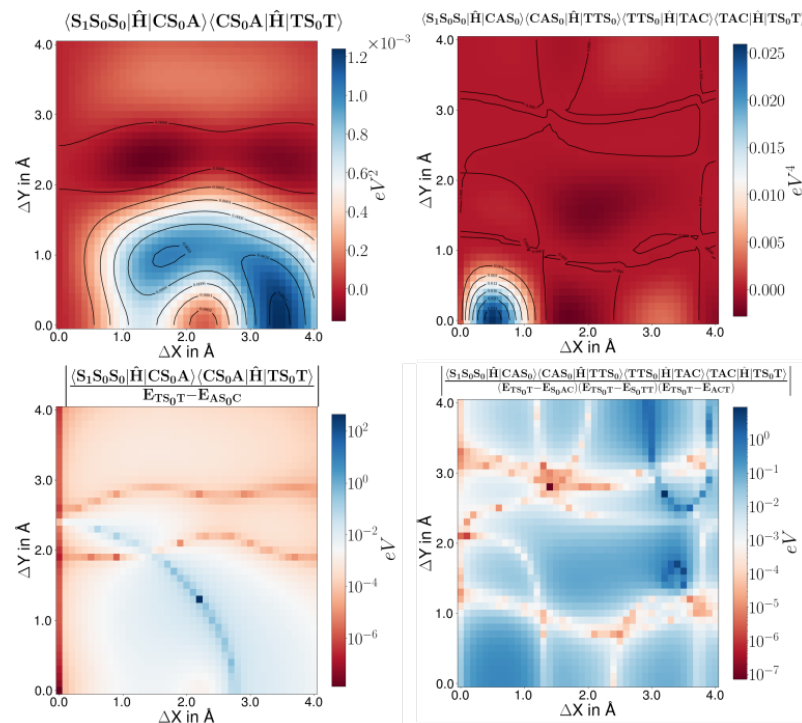


Figure S3: Top left: Scan of couplings involved in the "one-step" mechanism. Bottom left: Scan of the transition rate expression with the energy term as arises in the denominator. Top right: Scan of couplings involved in the "two step" mechanism proceeding via a CAS_0 and TCA mediated formation of $TS_0 T$. Bottom right: Scan of absolute third order perturbation term. The plot is shown in logarithmic scale.

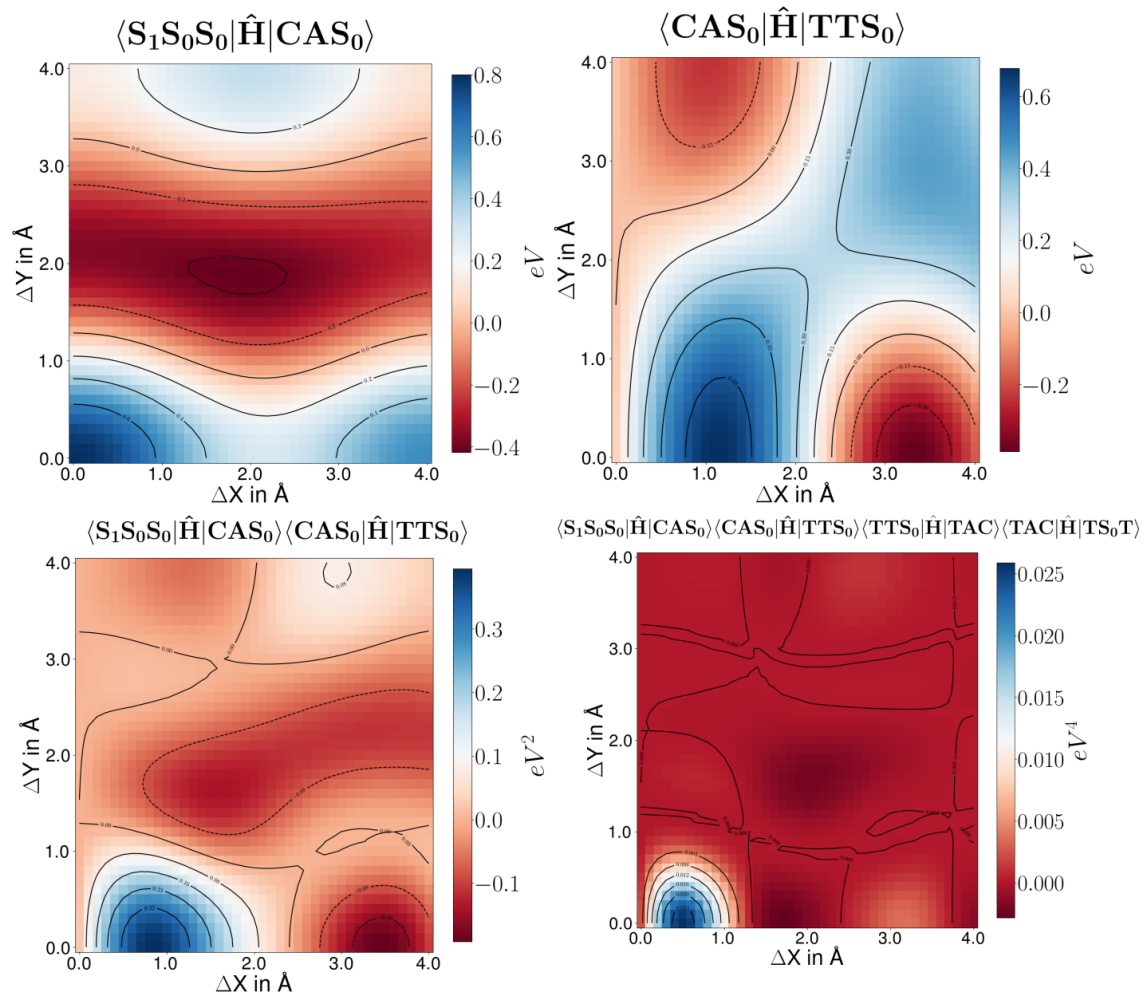


Figure S4: Couplings of the three-step mediated pathway $\text{S}_1\text{S}_0\text{S}_0 \rightarrow \text{CAS}_0 \rightarrow \text{TTS}_0 \rightarrow \text{TAC} \rightarrow \text{TS}_0\text{T}$.

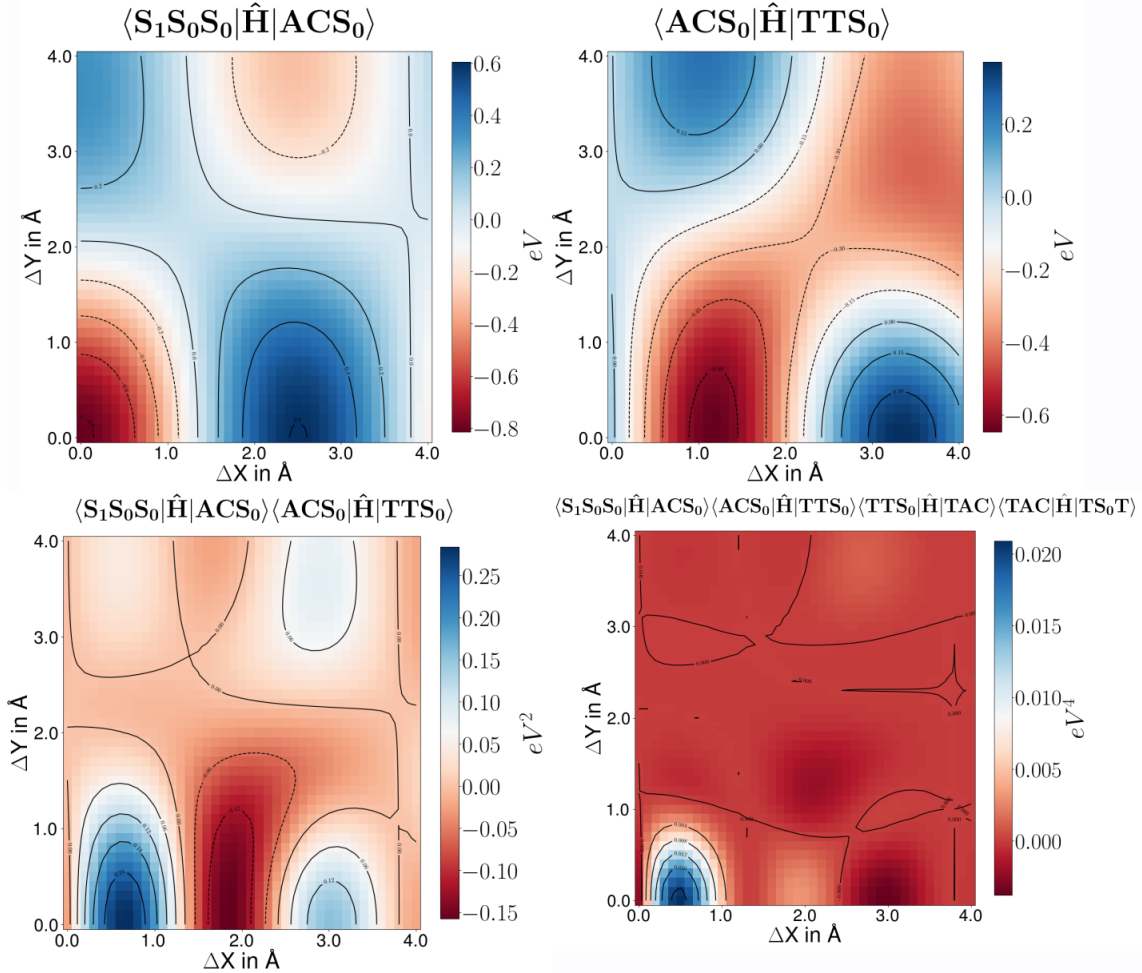


Figure S5: Couplings of the three-step mediated pathway $S_1S_0S_0 \rightarrow ACS_0 \rightarrow TTS_0 \rightarrow TAC \rightarrow TS_0T$.

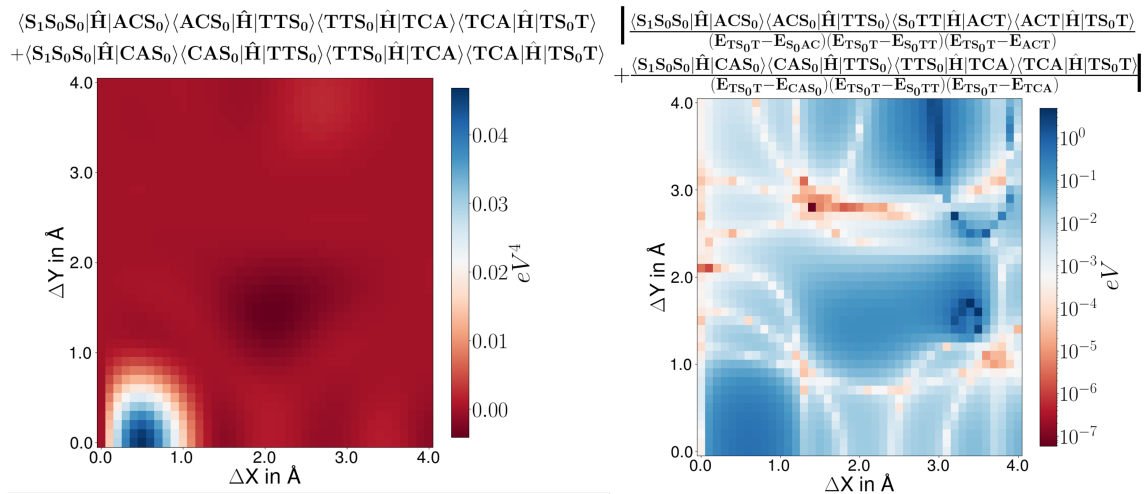


Figure S6: In the left plot, which shows the sum of the coupling terms for the three-step mediated pathway, the pathways exhibit the same signs. Upon summation, they yield a high value at $\Delta X = 0.7 \text{ \AA}$ and $\Delta Y = 0.0 \text{ \AA}$. This high value is also evident in the right plot, where a darker blue coloration is observed at $\Delta X = 0.7 \text{ \AA}$ and $\Delta Y = 0.0 \text{ \AA}$.

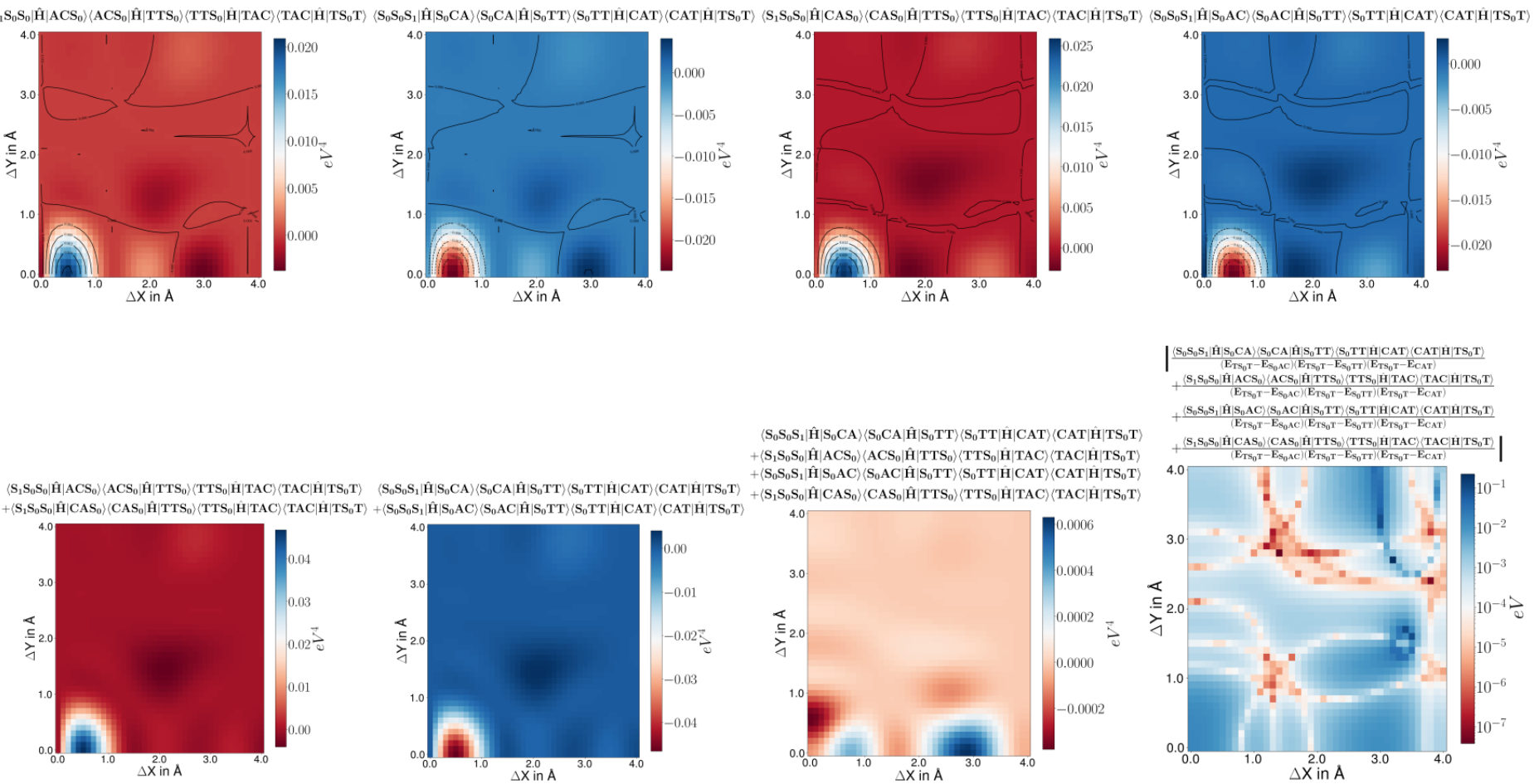


Figure S7: Superposition of pathways in the three-step $LE \rightarrow TS_0T$ transfer reveals that coupling terms originating from S_1 on the same monomer have the same sign. When these couplings, originating from the same LE source, are added together, the resulting plot resembles the one in Ref. [1]. While the couplings $\langle S_1S_0S_0|\hat{H}|ACS_0\rangle \langle ACS_0|\hat{H}|S_0TT\rangle \langle S_0TT|\hat{H}|TAC\rangle \langle TAC|\hat{H}|TS_0T\rangle$ and $\langle S_0S_0S_1|\hat{H}|S_0CA\rangle \langle S_0CA|\hat{H}|TTS_0\rangle \langle TTS_0|\hat{H}|CAT\rangle \langle CAT|\hat{H}|TS_0T\rangle$ exhibit opposite signs but similar features. This sign difference arises because $\langle CAS_0|\hat{H}|TTS_0\rangle$ and $\langle S_0AC|\hat{H}|S_0TT\rangle$ have opposite signs. Here, the cation has formed on the S_1 fragment. Similarly, pathways where the anion is formed on the S_1 fragment also show opposite signs. When the superposition of all four pathways is considered, the final plot shows the highest value at $\Delta X = 2.9 \text{ \AA}$ and $\Delta Y = 0 \text{ \AA}$, with other significant values observed at $\Delta X = 0.7 \text{ \AA}$ and $\Delta X = 0.0 \text{ \AA}$. The influence of these high values is evident in the perturbation term plot, where blue coloration appears near $\Delta X = 0.0 \text{ \AA}$ and $\Delta Y = 0 \text{ \AA}$, as well as near $\Delta X = 2.9 \text{ \AA}$ and $\Delta Y = 0 \text{ \AA}$.

In order to account for the interference of individual electronic pathways in the first order correction, one has to sum over all the considered intermediate states to obtain the total yield of the transition state:

$$T_{LE_a \rightarrow {}^1TT_b} = \sum_{CT_i} \frac{\langle LE | \hat{H} | CT_i \rangle \langle CT_i | \hat{H} | {}^1TT_b \rangle}{E_{{}^1TT_b} - E_{CT_i}} \quad (8.57)$$

In this expression, the total transition probability $T_{LE_a \rightarrow {}^1TT_b}$ is calculated by summing over all intermediate charge-transfer states CT_i . Each term in the sum represents the contribution of a specific intermediate state CT_i to the overall transition. Here, $\langle LE | \hat{H} | CT_i \rangle$ and $\langle CT_i | \hat{H} | {}^1TT_b \rangle$ are the matrix elements describing the transition probabilities between the states, and $E_{{}^1TT}$ and E_{CT_i} are their respective energies.

The triplet state can be formed by 54 pathways making three kinds of ${}^1\text{TT}$ states: $S_0\text{TT}$, TS_0 , and TS_0T . As shown in Figure S1, the transition amplitudes T_{AB} for TS_0 and $S_0\text{TT}$ have opposite signs, depending on their origin. For TS_0 originating from the source $S_1S_0S_0$, it has the opposite sign compared to $S_0\text{TT}$ originating from the source $S_0S_0S_1$, and they have nearly the same value. Similarly, TS_0 originating from $S_0S_1S_0$ has the opposite sign compared to TS_0 originating from $S_0S_1S_0$, and they have nearly the same value. Also, TS_0 originating from the source $S_0S_0S_1$ has the opposite sign compared to $S_0\text{TT}$ originating from the source $S_1S_0S_0$, and they have nearly the same value. TS_0T originating from $S_1S_0S_0$ has the opposite sign compared to TS_0T originating from $S_0S_0S_1$, and they have nearly the same value. As first-order perturbation theory dictates, terms with the same final states can be added. For instance, when considering the superposition of $S_0S_0S_1$ and $S_1S_0S_0$, and adding the matrix elements $\langle S_0S_0S_1 | \hat{H} | \text{TS}_0\text{T} \rangle$ and $\langle S_1S_0S_0 | \hat{H} | \text{TS}_0\text{T} \rangle$, the resulting overall value is zero.

To study the interference between TS_0 and $S_0\text{TT}$, we proceed with the three-step perturbation term. Here, TS_0T is formed from $S_0\text{TT}$ and TS_0 via a charge transfer state. The plot of the couplings is shown in Figures S4 and S5. The superposition of pathways to TS_0T from S_1 on different fragments is shown in Figure 8.6.5.

8.6.6 Comparison of basis sets

The plots of the line scan at $\Delta Y = 0\text{\AA}$ and $\Delta X = 0\text{\AA}$ to $\Delta X = 4\text{\AA}$ at $\Delta Z = 3.4\text{\AA}$ are shown in figure S8 and S9. Here, we changed the basis set and compared the values, observing low differences for the purpose of our work. The DEF2-SVP basis set estimates $E_{\text{TS}_0\text{T}} - E_{S_0S_0S_0}$ higher than the 6-31G basis set, with a maximum deviation of 0.096 eV. In contrast, it estimates $E_{S_0\text{TT}} - E_{S_0S_0S_0}$ lower than the 6-31G basis set, with a maximum deviation of 0.03 eV. For $E_{\text{CAT}} - E_{S_0S_0S_0}$, the DEF2-SVP basis set provides higher estimates than 6-31G, though their variations are consistent, with a maximum deviation of 0.09 eV. The estimates for $E_{\text{ACT}} - E_{S_0S_0S_0}$ are nearly identical between the DEF2-SVP and 6-31G basis sets, with a maximum deviation of 0.03 eV. Additionally, the DEF2-SVP estimates $E_{\text{TS}_0\text{T}} - E_{\text{CAT}}$ lower, with a deviation of 0.05 eV, and $E_{\text{TS}_0\text{T}} - E_{\text{ACT}}$ almost equal to the 6-31G basis set estimations, with a maximum deviation of 0.02 eV. Similarly the coupling terms shown in figure S9 homologous pattern.

8.6.7 Energies of the Dimer System

In order to evaluate and compare the energies obtained from the model CI methodology presented in this study, we studied the dimer system, as only dimer energies are available in the literature. We performed scans of both the diabatic and adiabatic energies. For the latter, we constructed the dimer Hamiltonian and diagonalized it to obtain the adiabatic energy levels. The diabatic energies are shown in Figure S11. The diabatic energy for the local excited (LE) states ranges between 4.06 and 4.08 eV, which is comparable to the monomer energies. The energy of S_1 PDI-EP monomer from CASSCF(8,8) calculation is 4.28 eV [212]. The charge transfer (CT) states range between 4.35 eV and 5.0 eV.

The adiabatic energies are shown in Figure S10. The resulting values for Ψ_1 to Ψ_4 lie energetically between the energies calculated by NOCI-CASSCF and NOCI-CASPT 2 – 0.25 [212], while the energy of Ψ_5 is overestimated. In our calculations for PDI-EP[281], which is stacked at $\Delta X = 3.2\text{\AA}$ and $\Delta Y = 0.4\text{\AA}$, we obtained the following energy values: $E_{\Psi_1} = 3.61\text{ eV}$, which lies between energies of NOCI-CASSCF (4.26 eV) and NOCI-CASPT2 (2.61 eV), $E_{\Psi_2} = 4.03\text{ eV}$, $E_{\Psi_3} = 4.35\text{ eV}$, and $E_{\Psi_4} = 5.32\text{ eV}$.

For PDI-C7[281], which has slipped stacking at $\Delta X = 3.0\text{\AA}$ and $\Delta Y = 1.2\text{\AA}$, the energy values are: $E_{\Psi_1} = 3.97\text{ eV}$ which lies between energies of NOCI-CASSCF (4.26 eV) and NOCI-CASPT2 (2.56 eV), $E_{\Psi_2} = 3.92\text{ eV}$, and $E_{\Psi_3} = 4.76\text{ eV}$.

8.6.8 Energy of the Trimer System

The diabatic energies obtained in this work are shown in Figures S11 and S11. The patterns observed in $E_{S_1S_0S_0} - E_{S_0S_0S_0}$, $E_{\text{TS}_0\text{T}} - E_{S_0S_0S_0}$, and $E_{S_0\text{TT}} - E_{S_0S_0S_0}$ are similar. This similarity is akin to the patterns observed in the diabatic energies of the dimer. In the trimer, $E_{\text{TS}_0\text{T}} - E_{S_0S_0S_0}$, and $E_{S_0\text{TT}} - E_{S_0S_0S_0}$

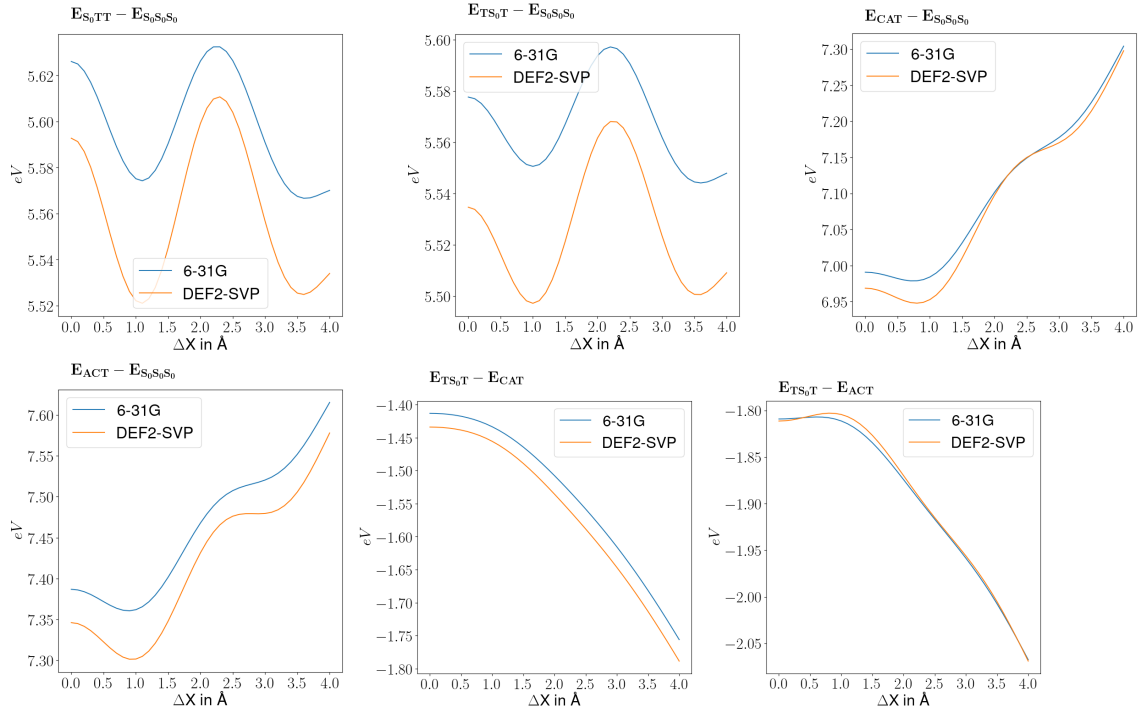


Figure S8: Comparison of the diabatic state energy difference obtained from the 6-31G and DEF2-SVP basis sets via a line scan at $\Delta Y = 0\text{\AA}$, $\Delta Z = 3.4\text{\AA}$, and varying ΔX from 0\AA to 4\AA for the trimer.

have lower energies than $E_{S_1\text{S}_0\text{S}_0} - E_{S_0\text{S}_0\text{S}_0}$. The energy of the charge transfer states $E_{\text{ACT}} - E_{S_0\text{S}_0\text{S}_0}$, $E_{\text{CAT}} - E_{S_0\text{S}_0\text{S}_0}$ and $E_{\text{CS}_0\text{A}} - E_{S_0\text{S}_0\text{S}_0}$ have similar patterns to the charge transfer states in the dimer.

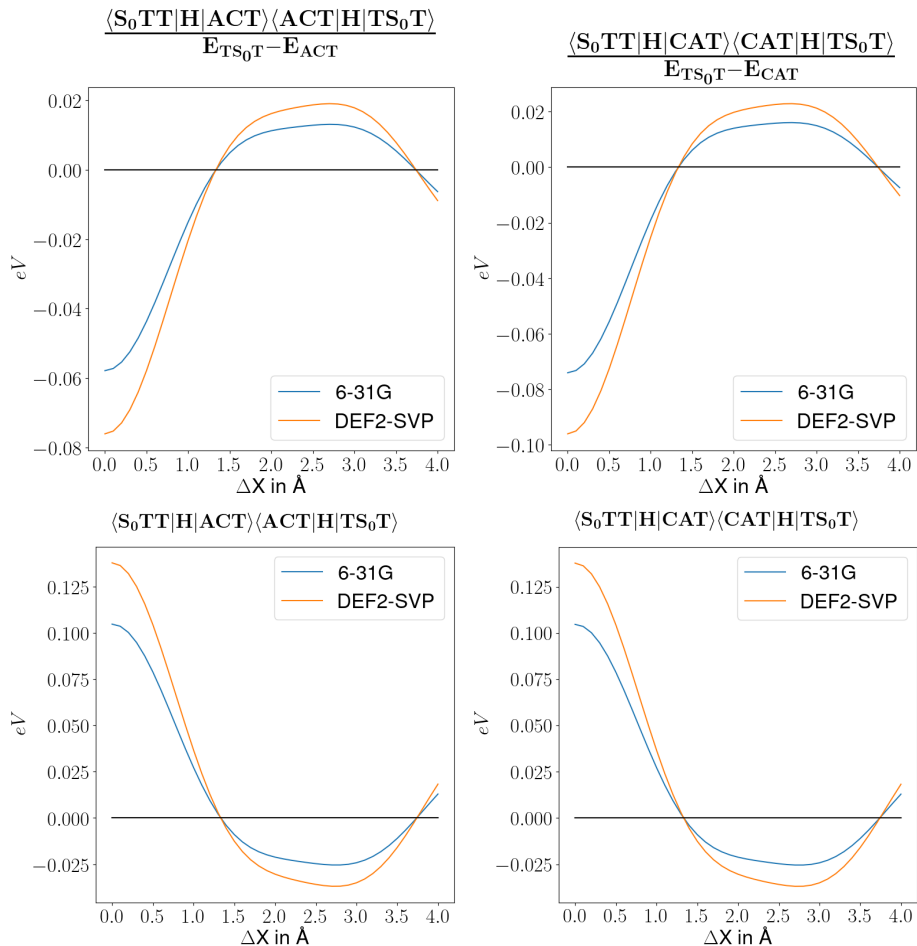


Figure S9: Comparison of coupling terms obtained from the 6-31G and DEF2-SVP basis sets via a line scan at $\Delta Y = 0 \text{ \AA}$, $\Delta Z = 3.4 \text{ \AA}$, and varying ΔX from 0 \AA to 4 \AA for the trimer.

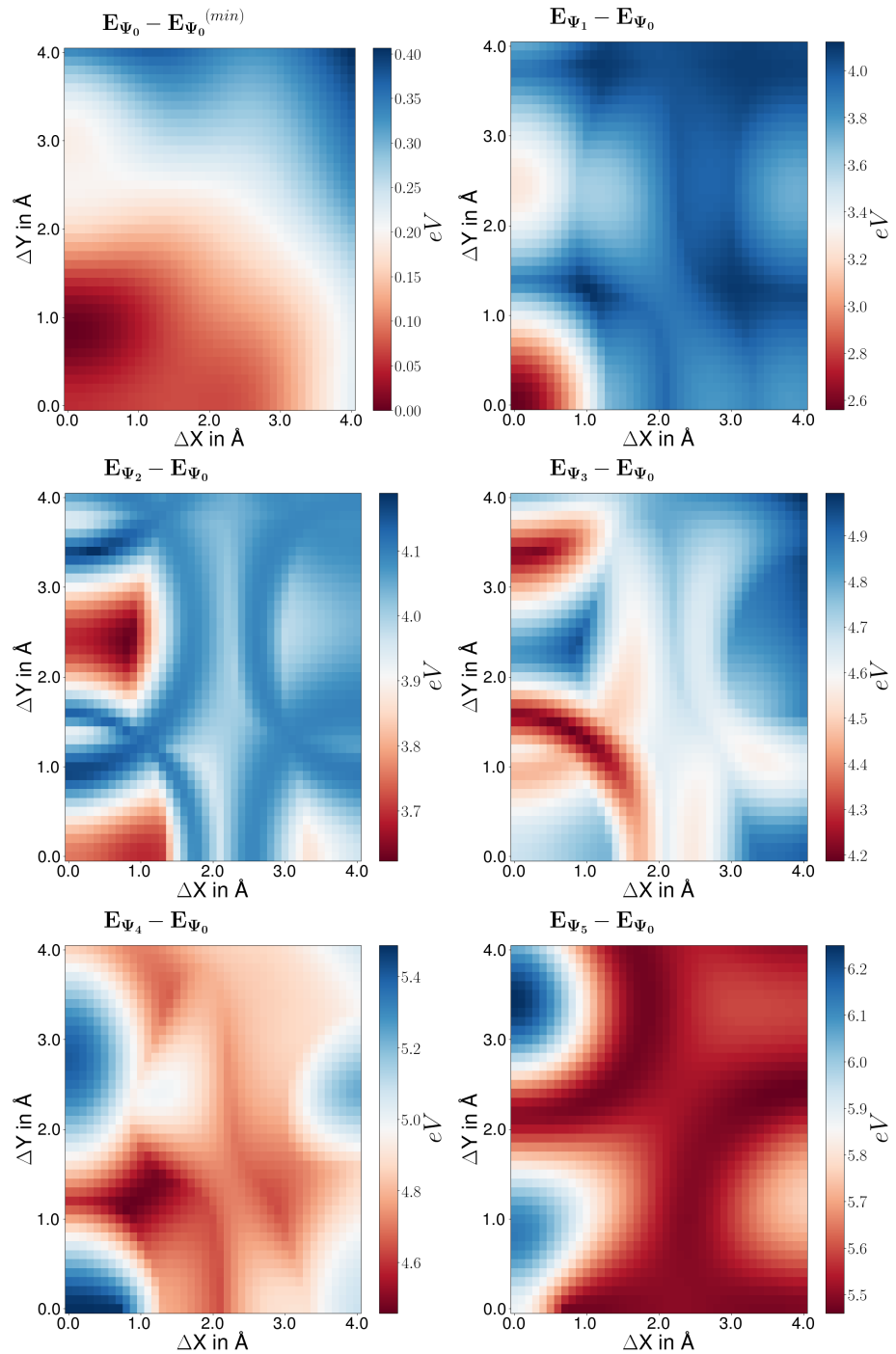


Figure S10: The adiabatic energies of states in the dimer formed by diagonalizing the diabatic Hamiltonian.

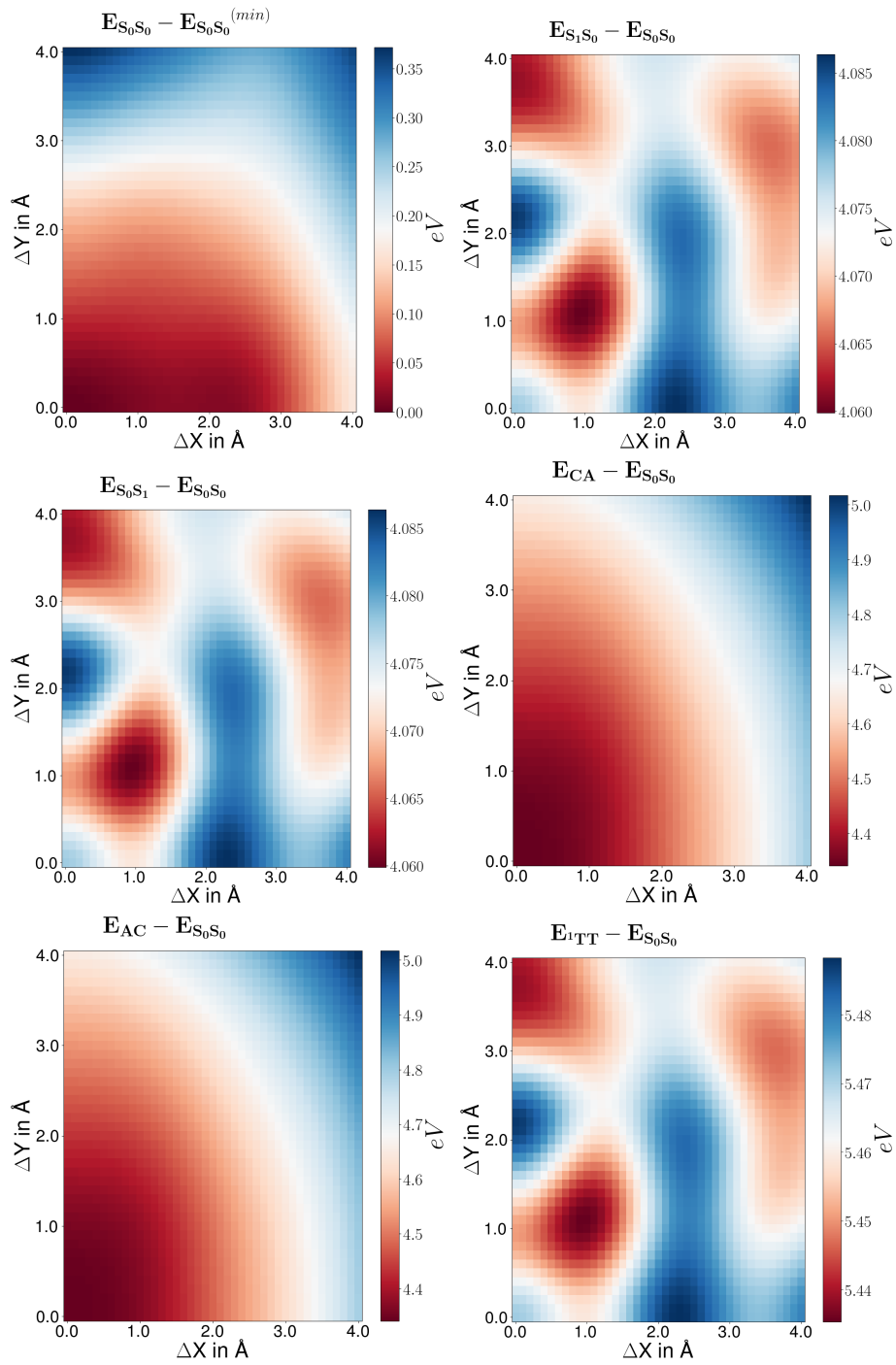
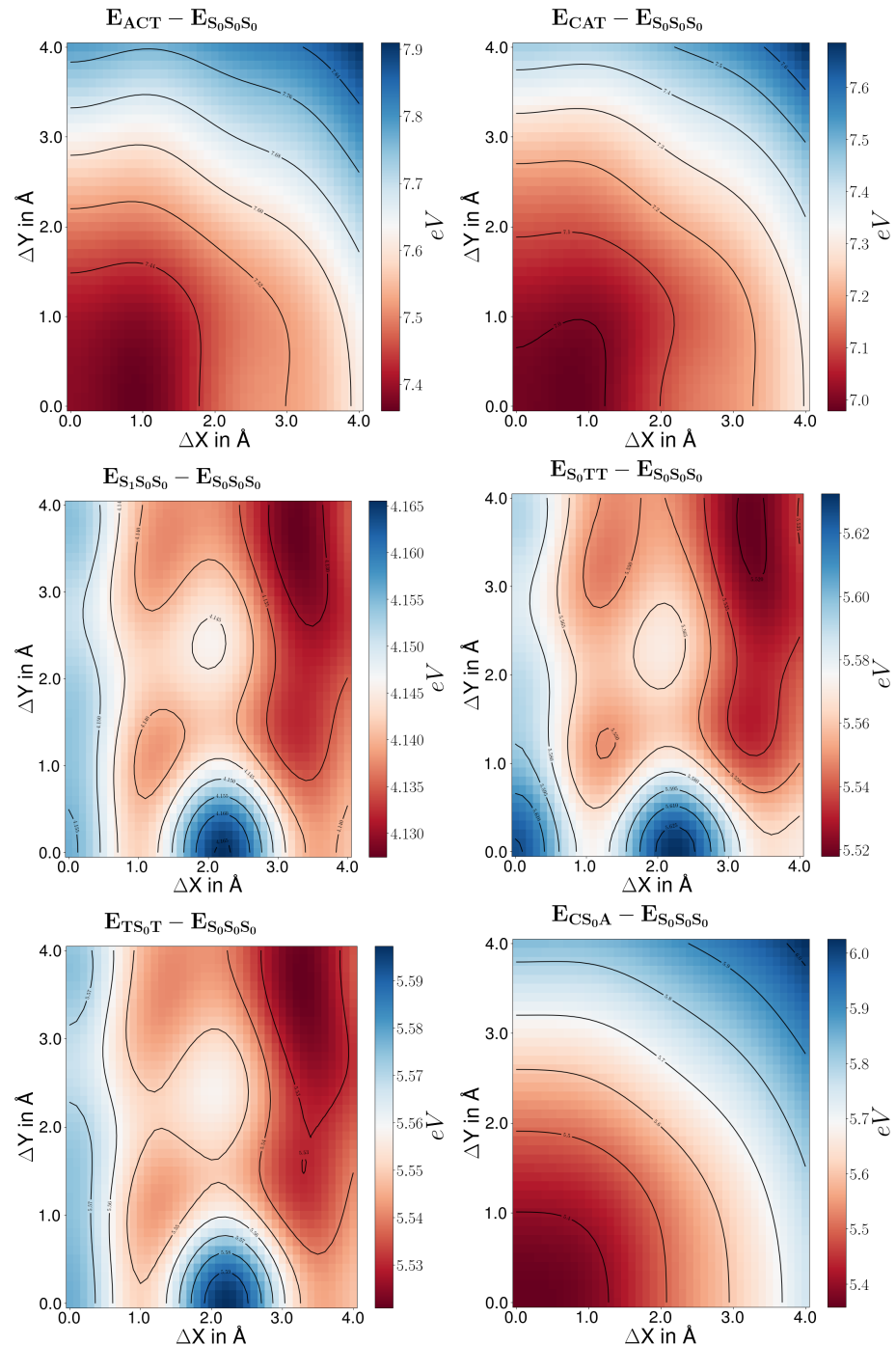


Figure S11: Diabatic energy of the dimer obtained by the model CI method presented in this work.



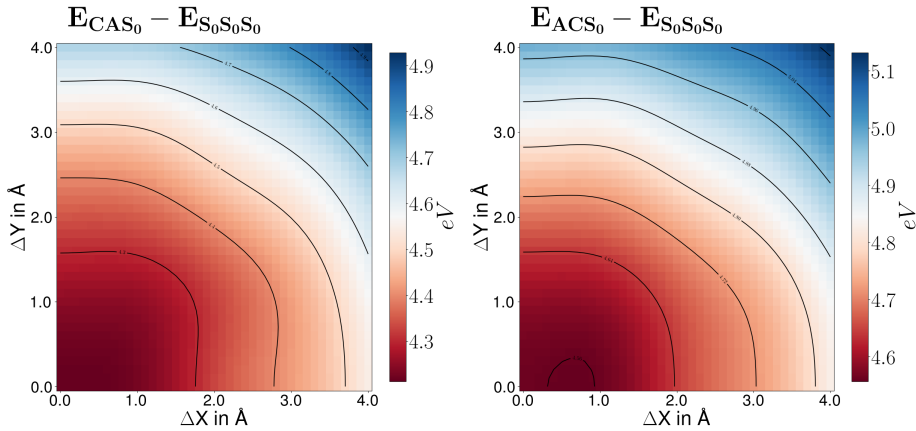
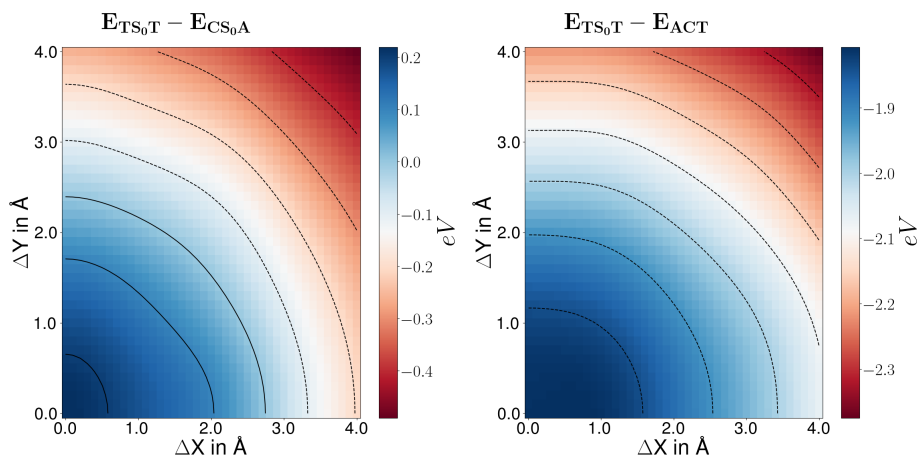


Figure S11: Diabatic state energies in the trimer relative to their respective ground states, obtained by the presented model CI methodology.



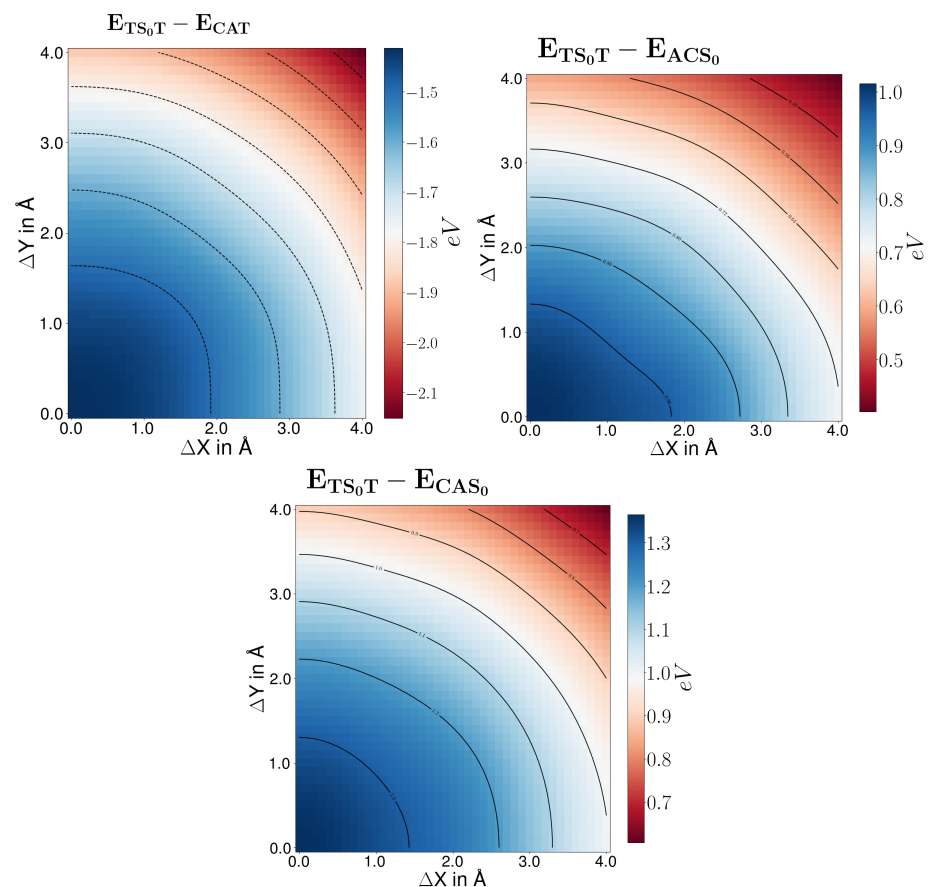


Figure S11: The diabatic energy differences of the intermediate states a) CS_0A , b) ACT , c) CAT , d) ACS_0 and e) CAS_0 from TS_0T of the trimer.

Chapter 9

Conclusion

9.1 Summary

The primary goal of this thesis was to develop a comprehensive and effective electronic structure method to describe spin-correlated triplet pair states in large molecular aggregates and to apply this method to the study of ${}^1(T\dots T)$ state formation, which is crucial in the singlet fission process. To achieve this, a rapid screening methodology was first established for assessing the packing dependence of singlet fission rates using model Hamiltonians within an adiabatic basis. This methodology was implemented in the algorithmic differentiation (AD) framework and thoroughly benchmarked. It proved effective for predicting new singlet fission molecules through isoelectronic substitution strategies and determining their optimal configurations. Additionally, the AD framework was further leveraged to introduce a functionality optimization technique that permits comprehensive screening of both intra- and intermolecular coordinate spaces in dimeric molecular systems. The theoretical insights obtained from this research have paved the way to the core of the thesis: the development of a generally applicable electronic structure methodology based on the Configuration Interaction approach. This methodology adeptly describes correlated states in extensive molecular aggregates. Its advanced implementation utilizes the Jordan-Wigner transformation and symbolic algebra to enhance computational efficiency.

Chapter 1 contains a brief summary of singlet fission, the contemporary state of research, and the questions regarding singlet fission that culminated in my motivation for this project.

Chapter 2 consists of a description of the background electronic structure theory and computational methods that have been utilized in the study of singlet fission in this thesis.

Chapter 3 reports on ASD calculations on PDI dimers. This included efforts to benchmark the "SFast" method for singlet fission analysis. This chapter explored the characteristics of LE, CT, and ${}^1(TT)$ states within adiabatic states of the dimers, leading to the construction of a quasi-diabatic Hamiltonian for analyzing couplings among these states. The continuity and differentiability of couplings and adiabatic states were also discussed, emphasizing their importance in the optimization process. The development of an efficient screening methodology in the adiabatic basis, relying on two semi-empirical models for estimating the SF rate as a function of molecular packing, is presented in Chapter 4. The first model is the "simple frontier orbital model," extensively used by the Michl group [162, 54, 28], while the second model treats singlet fission as a non-adiabatic transition and approximates the rate as the squared length of the non-adiabatic coupling vector between eigenfunctions of the diabatic Hamiltonian.

Doping of perylene with isoelectronic BN groups, where two adjacent carbon atoms are replaced by B–N, was explored as a means to enhance singlet fission. A dataset, comprising 276 molecules was analyzed. Among all perylene derivatives, the most suitable isomer for singlet fission was identified with the help of TD-DFT and CASPT2 calculations. In the best singlet fission isomer, boron substitutes the opposite carbon atoms in the bay position, and the adjacent carbon atoms in the ortho positions are replaced by nitrogen. The optimal relative disposition of the two monomer units in a co-facially stacked homo dimer was explored using two semi-empirical models.

In the 5th chapter, a comprehensive analysis of PDI molecules was performed, focusing on their behaviour under rotation of the z-axis and translation along with co-facial slipped stacking. These rotations were performed with the SFast and the ASD model Hamiltonian, to investigate how changes in molecular orientation affect its properties, particularly in the context of co-facial slipped stacking. High $|T_{RP}|^2$ was found at 0° of rotation and 60° of rotation. Variation of LE/CT coupling and CT/ ${}^1(TT)$ coupling upon rotation is also reported in the chapter. The molecular structure of the PDI dimer has been optimised for a high singlet fission rate with L-BFGS algorithms using objective functional fabricated with the rate. The obtained structure of the PDI dimer has a contorted structure.

The second phase of this thesis was development of electronic structure methodology, that captures biexcitonic states in larger aggregates. Chapter 6 showcases the techniques to go beyond the dimer model

of singlet fission. In this chapter, we developed algorithms based on the branching diagram approach to obtain wave functions for given many-body states with specified characteristics. This character consists of 1) multiplicity of the whole many-electron system 2) high spin state of the whole system 3) multiplicity of subsystems 4) high spin states of subsystems. The branching diagram approach derived the wavefunctions for unpaired electrons in completely degenerate orbitals. To account for the pairing of electrons in non-degenerate orbitals, creation and annihilation operators with symbolic specifiers for spatial orbital, based on Pauli's matrix, were constructed.

The formulations of couplings among singlet and triplet states, where electrons are distributed across different sets of spatial orbitals forming systems such as excitons, cations, and anions, were generated. This provides insight into electron transfer processes in the various states that can be formed by combining subsystems with different multiplicities (e.g., 1S_0S_1 , 1TT , 3S_0T , 3TT) and the separation of subsystems (e.g., CAS_0 , CS_0A , TTS_0 , TS_0T).

In Chapter 7, the developed method is applied to study singlet fission in trimer systems of cofacially stacked PDIs. This work uses the diabatic frontier orbitals of the monomers as subsystems to describe the trimer systems. We evaluated the impact of the individual electronic pathways (9 direct and 54 CT mediated pathways) and diabatic matrix elements leading to the formation of $^1(T...T)$, as well as their dependence on the packing motif by scanning along a longitudinal and a transversal slipping mode. The chapter described mechanisms for $^1(T...T)$ formation, one from $^1(TT)$ to $^1(T...T)$, and the other being CT-mediated process from an initially excited LE state directly to the $^1(T...T)$. Employing the pathway-based second-order perturbation theory model to screen the SF rate of $^1(TT)$ produced similar patterns as previous Redfield Theory studies. It shares very good agreement with the experimental results.

In Chapter 8, the widely used diabatic frontier orbital model for dimers is generalized to describe extended aggregates, allowing for symbolic generation of matrix elements for configurations with arbitrary excitation levels. The study finds that the transition matrix element for the Dexter superexchange "three-step" mechanism generally yields higher values compared to the "one-step" mechanism. The "one-step" pathway becomes significant only when the transfer occurs via coupling to a charge-separated state located on non-adjacent edge molecules. Higher-order perturbation theory is also employed to explore transfer processes involving singlet and paired triplet charge transfer states. An explicit trimer model is used to account for spatially separated configurations such as $(T...T)$, (AS_0C) , and mixed exciton states (TCA) and (TAC).

9.2 Outlook

In the course of this research, significant computational challenges were encountered, particularly the high demands of multi-reference methods required for an accurate description of singlet fission in molecular aggregates. A Configuration Interaction (CI) method was developed, capable of treating aggregates up to 10mers. However, this method still faces limitations due to the exponential increase in Hilbert space associated with larger systems, which comprise strongly entangled electronic states demanding extensive computational resources, especially in terms of dynamic memory. The presence of repeating subunits within the molecular aggregates presents an opportunity for computational efficiency. For instance, rylene dyes, constructed from linked naphthalene units, exemplify such repeating subunits. By recognizing and leveraging these repetitive patterns, future work could focus on developing algorithms that compress state and Hamiltonian matrices, thereby reducing both the storage and computational overhead. Such advancements would enable more efficient parallel computations across both CPU and GPU platforms, adapting seamlessly to technological improvements without significant programming alterations.

Though the idea of singlet fission is well established, the complexity around it is still being explored in theory as well as in experiments. As we know, $^1(TT)$ further forms separated triplet pairs $^1(T...T)$ and triplet pairs of higher multiplicities $^3(TT)$, $^5(TT)$, $^3(T...T)$ and $^5(T...T)$ [275]. Still, the mechanism for transformation is not clear. The spin combination of paired triplets, organized in spatial orbitals to form a mixture of charge transfer (CT) and $^1(TT)$ states, remains an area yet to be fully explored in various molecules, particularly as these systems are formed in trimer configurations. Such systems open up more mediated pathways for $^1(T...T)$ formation. Another future idea could be to study the coupling among $^3(TT)$, $^5(TT)$, $^3(T...T)$ and $^5(T...T)$ and get an optimised structure that would have high transfer probability between given pair of the states. The evolution of these states has potential in quantum computing and spintronics applications. Computational tools with perturbation theory such as CASPT2 and NEVPT2 that calculate accurate energies could be developed to examine states from the perspective of subsystem state combinations could be implemented in SYMBOLIC CI.

The analysis of differentiability and continuity for the function quantifying the transition of electrons among the states upon variation in the molecular structure opens avenues for optimisation of the desired process. Looking forward, the chosen AD framework will enable precise parametrization of Hamiltonian elements through machine learning or direct mapping to detailed electronic structure calculations. It also facilitates the direct optimization of electronic descriptors calculated by the method, streamlining

the design of molecular aggregates with specific functionalities without the need for complex gradient implementations. Moreover, the use of the Kronecker product formulation of second-quantized operators enables their mapping to qubits, thus allowing computations on a quantum computer.

Chapter 10

Schlussfolgerung

10.1 Zusammenfassung

Das Hauptziel dieser Arbeit bestand darin, eine umfassende und effektive elektronische Strukturmethode zur Beschreibung spin-korrelierter Triplet-Paarzustände in großen molekularen Aggregaten zu entwickeln und diese Methode auf die Untersuchung der Bildung des $^1(\text{TT})$ -Zustands anzuwenden, der im Singulett-Spaltungsvorgang entscheidend ist. Um dies zu erreichen, wurde zunächst eine schnelle Screening-Methodik zur Bewertung der Verpackungsabhängigkeit von Singulett-Spaltungs-Raten mithilfe von Modell-Hamiltonians innerhalb einer adiabatischen Basis etabliert. Diese Methodik wurde im Rahmen der algorithmischen Differentiation (AD) implementiert und gründlich benchmarkt. Sie erwies sich als wirksam bei der Vorhersage neuer Singulett-Spaltungs-Moleküle durch isoelektronische Substitutionsstrategien und bei der Bestimmung ihrer optimalen Konfigurationen. Zusätzlich wurde das AD-Framework weiter genutzt, um eine Funktionalitätsoptimierungstechnik einzuführen, die ein umfassendes Screening sowohl des intramolekularen als auch des intermolekularen Koordinatenraums in dimeren molekularen Systemen ermöglicht. Die theoretischen Erkenntnisse aus dieser Forschung haben den Weg zur Kernaussage der Arbeit geebnet: zur Entwicklung einer allgemein anwendbaren elektronischen Strukturmethodik auf Basis des Konfigurations-Interaktions-Ansatzes. Diese Methodik beschreibt geschickt korrelierte Zustände in umfangreichen molekularen Aggregaten. Ihre fortgeschrittene Implementierung nutzt die Jordan-Wigner-Transformation und symbolische Algebra, um die Recheneffizienz zu verbessern.

Kapitel 1 enthält eine kurze Zusammenfassung der Singulett-Spaltung, des gegenwärtigen Stands der Forschung und der Fragen zur Singulett-Spaltung, die Motivation für dieses Projekt geführt haben.

Kapitel 2 besteht aus einer Beschreibung des Hintergrunds der elektronischen Strukturtheorie und der Berechnungsmethoden, die bei der Untersuchung der Singulett-Spaltung in dieser Arbeit angewandt wurden.

Kapitel 3 berichtet über ASD-Berechnungen an PDI-Dimeren. Dies umfasste Bemühungen, die "SFast"-Methode für die Analyse der Singulett-Spaltung zu benchmarken. In diesem Kapitel wurden die Eigenchaften von LE-, CT- und $^1(\text{TT})$ -Zuständen innerhalb adiabatischer Zustände der Dimeren untersucht, was zur Konstruktion eines quasi-diabatischen Hamiltonians zur Analyse von Kopplungen zwischen diesen Zuständen führte. Die Kontinuität und Differenzierbarkeit von Kopplungen und adiabatischen Zuständen wurden ebenfalls diskutiert, wobei ihre Bedeutung im Optimierungsprozess betont wurde.

Die Entwicklung einer effizienten Screening-Methodik in der adiabatischen Basis, die auf zwei semiempirischen Modellen zur Abschätzung der SF-Rate als Funktion der molekularen Packung beruht, wird in Kapitel 4 vorgestellt. Das erste Modell ist das "einfache Frontorbitmodell", das umfangreich von der Michl-Gruppe verwendet wird [162, 54, 28], während das zweite Modell die Singulett-Spaltung als nichtadiabatische Übergang behandelt und die Rate als das Quadrat der Länge des nichtadiabatischen Kopplungsvektors zwischen Eigenfunktionen des diabatischen Hamiltonians approximiert.

Die Dotierung von Perylen mit isoelektronischen BN-Gruppen, bei der zwei benachbarte Kohlenstoffatome durch B-N ersetzt werden, wurde als Mittel zur Verbesserung der Singulett-Spaltung untersucht. Ein Datensatz mit 276 Molekülen wurde analysiert. Unter allen Perylen-Derivaten wurde mit Hilfe von TD-DFT- und CASPT2-Berechnungen der geeignete Isomer für die Singulett-Spaltung identifiziert. Im besten Singulett-Spaltungsisomer ersetzt Boron die gegenüberliegenden Kohlenstoffatome in der Bucht-Position, und die benachbarten Kohlenstoffatome in den Ortho-Positionen werden durch Stickstoff ersetzt. Die optimale relative Anordnung der beiden Monomereinheiten in einem homodimeren, ko-fazial gestapelten System wurde unter Verwendung von zwei semiempirischen Modellen untersucht.

Im 5. Kapitel wurde eine umfassende Analyse von PDI-Molekülen durchgeführt, wobei der Schwerpunkt auf ihrem Verhalten bei Rotation um die z-Achse und Translation sowie bei der ko-fazialen verschobenen Stapelung lag. Diese Rotationen wurden mit dem SFast- und dem ASD-Modell-Hamiltonian durchgeführt, um zu untersuchen, wie sich Änderungen der Molekülorientierung auf ihre Eigenschaften auswirken, ins-

besondere im Kontext der ko-fazialen verschobenen Stapelung. Es wurde festgestellt, dass hohe $|T_{RP}|^2$ bei einer Rotation von 0° und 60° gefunden wurden. In dem Kapitel wird auch über die Variation der LE/CT-Kopplung und der CT/ 1 (TT)-Kopplung bei Rotation berichtet. Die Molekülstruktur des PDI-Dimers wurde für eine hohe Singulett-Spaltungsrate mit L-BFGS-Algorithmen optimiert, die mit einem Ziel-Funktional konstruiert wurden, das auf der Rate basiert. Die erhaltene Struktur des PDI-Dimers weist eine verdrehte Struktur auf.

Die zweite Phase dieser Arbeit bestand in der Entwicklung einer Methodik für die elektronische Struktur, mit der biexzitonische Zustände in größeren Aggregaten erfasst werden können. In Kapitel 6 werden die Techniken vorgestellt, die über das Dimer-Modell der Singulett-Spaltung hinausgehen. In diesem Kapitel haben wir Algorithmen entwickelt, die auf dem Ansatz des Verzweigungsdiagramms basieren, um Wellenfunktionen für gegebene Vielteilchenzustände mit bestimmten Eigenschaften zu erhalten. Dieser Charakter besteht aus 1) der Multiplizität des gesamten Vielteilchensystems 2) dem Hochspinzustand des Gesamtsystems 3) der Multiplizität der Teilsysteme 4) den Hochspinzuständen der Teilsysteme. Der Verzweigungsdiagramm-Ansatz leitet die Wellenfunktionen für ungepaarte Elektronen in vollständig entarteten Orbitalen ab. Um die Paarung von Elektronen in nicht entarteten Orbitalen zu berücksichtigen, wurden Erzeugungs- und Vernichtungsoperatoren mit symbolischen Spezifizierern für räumliche Orbitale auf der Grundlage der Pauli-Matrix konstruiert.

Die Kopplung des Elektronentransfers zwischen verschiedenen Zuständen des Dimers und Trimers mit beliebigen Sätzen erlaubter Vielfachheiten des Subsystems wurde bewertet. Die Formulierungen der Kopplungen zwischen Singulettzuständen und Triplettzuständen, wenn verschiedene Sätze von räumlichen Orbitalen, die das System wie Exciton, Kation und Anion bilden, kombiniert werden, wurden untersucht. Dies gibt Einblicke in den speziellen Koeffizienten, der entsteht, wenn sich die Vielfachheit der Teilsysteme ändert (z. B. 1S_0S_1 , 1TT , 3S_0T , 3TT), die Trennung der Teilsysteme (z. B. $CAS_0 CS_0A$, $TTS_0 TS_0T$) und die Bewegung des Teilsystems von $S_1S_0S_0$ nach $S_0S_1S_0$.

Im Kapitel 7 wurde die entwickelte Methode verwendet, um die Singulett-Spaltung in den Trimer-Systemen der ko-fazial gestapelten PDIs zu untersuchen. In dieser Arbeit wurde das diabatische Frontorbit-Modell zur Beschreibung von Trimer-Systemen verwendet. Wir haben die Auswirkungen der einzelnen elektronischen Wege (9 direkte und 54 CT-vermittelte Wege) und diabatischen Matrixelementen, die zur Bildung von ${}^1(T...T)$, einen vom ${}^1(TT)$ zum ${}^1(T...T)$ und den anderen als CT-vermittelten Prozess von einem anfänglich angeregten LE-Zustand direkt zum ${}^1(T...T)$. Die Verwendung des modellbasierten Zweitordnungs-Störungstheorie-Modells zur Screening der SF-Rate von ${}^1(TT)$ ergab ein ähnliches Muster wie die Studien zur Redfield-Theorie. Es zeigt eine sehr gute Übereinstimmung mit den experimentellen Ergebnissen.

In Kapitel 8 wird das weit verbreitete diabatische Grenzorbitalmodell für Dimere verallgemeinert, um erweiterte Aggregate zu beschreiben, was die symbolische Erzeugung von Matrixelementen für Konfigurationen mit beliebigen Anregungsniveaus ermöglicht. Die Studie zeigt, dass das Übergangsmatrixelement für den „three-step“ Dexter-Superexchange-Mechanismus im Allgemeinen höhere Werte ergibt als der „one-step“ Mechanismus. Der „one-step“-Weg wird nur dann signifikant, wenn der Transfer über eine Kopplung an einen ladungstrennenden Zustand erfolgt, der sich auf nicht benachbarten Randmolekülen befindet. Die Störungstheorie höherer Ordnung wird auch eingesetzt, um Übertragungsprozesse zu untersuchen, an denen Singulett- und Triplett-Ladungstransferzustände beteiligt sind. Ein explizites Trimermodell wird verwendet, um räumlich getrennte Konfigurationen wie ($T...T$), (AS_0C) und gemischte Exzitonenzustände (TCA) und (TAC) zu berücksichtigen.

10.2 Ausblick

Im Verlauf dieser Forschung stießen wir auf bedeutende rechnerische Herausforderungen, insbesondere auf die hohen Anforderungen von Multireferenzmethoden, die für eine genaue Beschreibung der Singulett-Spaltung in molekularen Aggregaten erforderlich sind. Eine Konfigurationsinteraktionsmethode (CI) wurde entwickelt, die in der Lage ist, Aggregate bis zu 10 Mer-Einheiten zu behandeln. Diese Methode stößt jedoch weiterhin an Grenzen aufgrund des exponentiellen Anstiegs des Hilbertraums bei größeren Systemen, die stark korrelierte elektronische Zustände umfassen und umfangreiche Rechenressourcen erfordern, insbesondere in Bezug auf den dynamischen Speicher. Die Anwesenheit sich wiederholender Untereinheiten innerhalb der molekularen Aggregate bietet eine Möglichkeit zur Steigerung der rechnerischen Effizienz. Zum Beispiel illustrieren Rylene, die aus verbundenen Naphthaleneinheiten konstruiert sind, solche sich wiederholenden Untereinheiten. Durch Erkennen und Nutzen dieser wiederkehrenden Muster könnte sich zukünftige Arbeit auf die Entwicklung von Algorithmen konzentrieren, die Zustands- und Hamiltonmatrizen komprimieren, wodurch sowohl der Speicher- als auch der rechnerische Overhead reduziert werden. Solche Fortschritte würden effizientere parallele Berechnungen über sowohl CPU- als auch GPU-Plattformen ermöglichen und sich nahtlos an technologische Verbesserungen anpassen, ohne bedeutende Programmänderungen vornehmen zu müssen.

Obwohl das Konzept der Singulett-Spaltung gut etabliert ist, wird die damit verbundene Komplexität sowohl in der Theorie als auch in Experimenten weiterhin erforscht. Wie wir wissen, bilden ¹(TT)-Zustände weiterhin getrennte Triplett-Paare ¹(T...T) und Triplett-Paare höherer Vielfachheiten ³(TT), ⁵(TT), ³(T...T) und ⁵(T...T)[275]. Dennoch ist der Mechanismus für diese Transformation nicht klar. Die Spin-Kombination gepaarter Triplets, organisiert in räumlichen Orbitalen zur Bildung einer Mischung aus Ladungstransfer (CT) und ¹(TT)-Zuständen, bleibt ein Bereich, der noch vollständig in verschiedenen Molekülen erforscht werden muss, insbesondere da diese Systeme in Trimer-Konfigurationen vorliegen. Solche Systeme eröffnen mehr vermittelte Wege für die Bildung von ¹(T...T). Eine weitere zukünftige Idee könnte darin bestehen, die Kopplung zwischen ³(TT), ⁵(TT), ³(T...T) und ⁵(T...T) zu untersuchen und eine optimierte Struktur zu erhalten, die eine hohe Übertragungswahrscheinlichkeit zwischen einem gegebenen Paar dieser Zustände aufweisen würde. Die Entwicklung von Berechnungswerkzeugen mit Störungstheorien wie CASPT2 und NEVPT2, die genauen Energien berechnen, könnte dazu genutzt werden, Zustände aus der Perspektive von Kombinationen von Teilsystemzuständen zu untersuchen. Die Entwicklung dieser Zustände hat Potenzial in Anwendungen der Quantenberechnung und Spintronik.

Die Analyse der Differenzierbarkeit und Kontinuität für die Funktion, die den Übergang von Elektronen zwischen den Zuständen bei Variation der molekularen Struktur quantifiziert, eröffnet Möglichkeiten zur Optimierung des gewünschten Prozesses. In Zukunft wird das gewählte AD-Framework eine präzise Parametrisierung der Hamilton-Elemente durch maschinelles Lernen oder direkte Abbildung auf detaillierte elektronische Strukturberechnungen ermöglichen. Es erleichtert auch die direkte Optimierung elektronischer Deskriptoren, die von der Methode berechnet werden, und vereinfacht damit das Design von molekularen Aggregaten mit spezifischen Funktionalitäten, ohne dass komplexe Gradientenimplementierungen erforderlich sind. Darüber hinaus ermöglicht die Verwendung der Kronecker-Produktformulierung von Operatoren in der zweiten Quantisierung deren Abbildung auf Qubits, was Berechnungen auf einem Quantencomputer ermöglicht.

Acknowledgment

I am delighted to express my gratitude to my supervisor, Dr. Merle Insa Silja Röhr, for providing me with the opportunity to undertake this project. I sincerely thank her for offering valuable resources, guidance, and unwavering support, as well as for her constant motivation throughout the course of this research. I am also grateful for her assistance with bureaucratic matters, which significantly contributed to making my stay in Würzburg enjoyable.

I would like to thank Prof. Dr. Frank Würthner for the financial support and the healthy, intellectually stimulating work environment at the Center for Nanosystems Chemistry.

I extend my gratitude to Prof. Dr. Roland Mitric for the necessary resources, discussions, and the excellent working environment at the Institute of Theoretical Chemistry during my research.

I am grateful to Solar Technologies go Hybrid (SolTech) initiative and the Bayerisches Staatsministerium für Wissenschaft und Kunst for providing the necessary funding to conduct my research.

I would like to express my thanks to Dr. Alexander Humeniuk for collaborating on projects and providing valuable assistance in solving technical and scientific problems. Additionally, my appreciation goes to Dr. Jens Petersen, Dr. Joachim Lindner, Dr. Joscha Hoche, Dr. Matthias Wohlgemuth, Michael Wenzel, Dr. Kevin Issler, Michael Bühler, Richard Einsele, Johannes Greiner, Luca Nils Philipp, Xincheng Miao, Nikita Kavka, Lasse Kreimendahl, and Moritz Limbacher for engaging in numerous scientific discussions, fostering a friendly environment, and offering help for any challenges I encountered.

Special thanks to Michael Bühler, Richard Einsele, Johannes Greiner, Luca Nils Philipp, Xincheng Miao, and Nikita Kavka for reviewing the thesis and the codes.

I would also like to express my gratitude to my friends Dr. Suvendu Karak, Dr. Rahul Sharma, Pankaj Mandal, Lisa Keller and Sungat Mukhangali for providing an experimental perspective on the physics, computer science and chemistry of my ideas.

I am very thankful to my family and friends for their indispensable support throughout all these years.

Bibliography

- [1] Renaud, N.; Sherratt, P. A.; Ratner, M. A. Mapping the Relation between Stacking Geometries and Singlet Fission Yield in a Class of Organic Crystals. *The Journal of Physical Chemistry Letters* **2013**, *4*, 1065–1069, PMID: 26282022.
- [2] Global Warming of 1.5 xBA;C x2014; — ipcc.ch. <https://www.ipcc.ch/sr15/>, [Accessed 05-08-2023].
- [3] Shockley, W.; Queisser, H. J. Detailed Balance Limit of Efficiency of ip-n/i Junction Solar Cells. *Journal of Applied Physics* **1961**, *32*, 510–519.
- [4] Martí, A.; Araújo, G. L. Limiting efficiencies for photovoltaic energy conversion in multigap systems. *Solar Energy Materials and Solar Cells* **1996**, *43*, 203–222.
- [5] Henry, C. H. Limiting efficiencies of ideal single and multiple energy gap terrestrial solar cells. *Journal of Applied Physics* **1980**, *51*, 4494–4500.
- [6] Vos, A. D. Detailed balance limit of the efficiency of tandem solar cells. *Journal of Physics D: Applied Physics* **1980**, *13*, 839–846.
- [7] Brabec, C. J.; Sariciftci, N. S.; Hummelen, J. C. Plastic Solar Cells. *Advanced Functional Materials* **2001**, *11*, 15–26.
- [8] Park, S. H.; Roy, A.; Beaupré, S.; Cho, S.; Coates, N.; Moon, J. S.; Moses, D.; Leclerc, M.; Lee, K.; Heeger, A. J. Bulk heterojunction solar cells with internal quantum efficiency approaching 100%. *Nature Photonics* **2009**, *3*, 297–302.
- [9] Thompson, B.; Fréchet, J. Polymer–Fullerene Composite Solar Cells. *Angewandte Chemie International Edition* **2008**, *47*, 58–77.
- [10] Kippelen, B.; Brédas, J.-L. Organic photovoltaics. *Energy & Environmental Science* **2009**, *2*, 251.
- [11] Coakley, K. M.; McGehee, M. D. Conjugated Polymer Photovoltaic Cells. *Chemistry of Materials* **2004**, *16*, 4533–4542.
- [12] Zimmerman, P. M.; Zhang, Z.; Musgrave, C. B. Singlet fission in pentacene through multi-exciton quantum states. *Nature Chemistry* **2010**, *2*, 648–652.
- [13] Zimmerman, P. M.; Bell, F.; Casanova, D.; Head-Gordon, M. Mechanism for Singlet Fission in Pentacene and Tetracene: From Single Exciton to Two Triplets. *Journal of the American Chemical Society* **2011**, *133*, 19944–19952.
- [14] Greyson, E. C.; Stepp, B. R.; Chen, X.; Schwerin, A. F.; Paci, I.; Smith, M. B.; Akdag, A.; Johnson, J. C.; Nozik, A. J.; Michl, J.; Ratner, M. A. Singlet Exciton Fission for Solar Cell Applications: Energy Aspects of Interchromophore Coupling. *The Journal of Physical Chemistry B* **2009**, *114*, 14223–14232.
- [15] Greyson, E. C.; Vura-Weis, J.; Michl, J.; Ratner, M. A. Title of the Article (Please replace with the actual title). *J. Phys. Chem. B* **2010**, *114*, 14168.
- [16] Hanna, M. C.; Nozik, A. J. Solar conversion efficiency of photovoltaic and photoelectrolysis cells with carrier multiplication absorbers. *Journal of Applied Physics* **2006**, *100*.
- [17] Burdett, J. J.; Bardeen, C. J. Quantum Beats in Crystalline Tetracene Delayed Fluorescence Due to Triplet Pair Coherences Produced by Direct Singlet Fission. *Journal of the American Chemical Society* **2012**, *134*, 8597–8607.

- [18] Wakikawa, Y.; Ikoma, T. Radio-wave Effect on Singlet Fission in Polycrystalline Tetracene near Zero Magnetic Field. *The Journal of Physical Chemistry Letters* **2023**, *14*, 3907–3911.
- [19] Di, D.; Yang, L.; Richter, J. M.; Meraldi, L.; Altamimi, R. M.; Alyamani, A. Y.; Credgington, D.; Musselman, K. P.; MacManus-Driscoll, J. L.; Friend, R. H. Efficient Triplet Exciton Fusion in Molecularly Doped Polymer Light-Emitting Diodes. *Advanced Materials* **2017**, *29*.
- [20] Smyser, K. E.; Eaves, J. D. Singlet fission for quantum information and quantum computing: the parallel JDE model. *Scientific Reports* **2020**, *10*.
- [21] Collins, M. I.; Campaioli, F.; Tayebjee, M. J. Y.; Cole, J. H.; McCamey, D. R. Quintet formation, exchange fluctuations, and the role of stochastic resonance in singlet fission. *Communications Physics* **2023**, *6*.
- [22] Ladd, T. D.; Jelezko, F.; Laflamme, R.; Nakamura, Y.; Monroe, C.; O'Brien, J. L. Quantum computers. *Nature* **2010**, *464*, 45–53.
- [23] Tao, G.; Tan, Y. Modular Tensor Diagram Approach for the Construction of Spin Eigenfunctions: The Case Study of Exciton Pair States. *The Journal of Physical Chemistry A* **2020**, *124*, 5435–5443.
- [24] Chen, J.; Dou, W.; Subotnik, J. Active Spaces and Non-Orthogonal Configuration Interaction Approaches for Investigating Molecules on Metal Surfaces. *Journal of Chemical Theory and Computation* **2022**, *18*, 7321–7335.
- [25] Tayebjee, M. J. Y.; Sanders, S. N.; Kumarasamy, E.; Campos, L. M.; Sfeir, M. Y.; McCamey, D. R. Quintet multiexciton dynamics in singlet fission. *Nature Physics* **2016**, *13*, 182–188.
- [26] Mirjani, F.; Renaud, N.; Gorczak, N.; Grozema, F. C. Theoretical Investigation of Singlet Fission in Molecular Dimers: The Role of Charge Transfer States and Quantum Interference. *The Journal of Physical Chemistry C* **2014**, *118*, 14192–14199.
- [27] Kolomeisky, A. B.; Feng, X.; Krylov, A. I. A Simple Kinetic Model for Singlet Fission: A Role of Electronic and Entropic Contributions to Macroscopic Rates. *The Journal of Physical Chemistry C* **2014**, *118*, 5188–5195.
- [28] Smith, M. B.; Michl, J. Singlet fission. *Chemical reviews* **2010**, *110*, 6891–6936.
- [29] Ullrich, T.; Munz, D.; Guldi, D. M. Unconventional singlet fission materials. *Chemical Society Reviews* **2021**, *50*, 3485–3518.
- [30] Singh, S.; Jones, W. J.; Siebrand, W.; Stoicheff, B. P.; Schneider, W. G. Laser Generation of Excitons and Fluorescence in Anthracene Crystals. *The Journal of Chemical Physics* **1965**, *42*, 330–342.
- [31] Singh, S.; Stoicheff, B. P. Double-Photon Excitation of Fluorescence in Anthracene Single Crystals. *The Journal of Chemical Physics* **1963**, *38*, 2032–2033.
- [32] Swenberg, C.; Stacy, W. Bimolecular radiationless transitions in crystalline tetracene. *Chemical Physics Letters* **1968**, *2*, 327–328.
- [33] Merrifield, R.; Avakian, P.; Groff, R. Fission of singlet excitons into pairs of triplet excitons in tetracene crystals. *Chemical Physics Letters* **1969**, *3*, 386–388.
- [34] Geacintov, N.; Pope, M.; Vogel, F. Effect of Magnetic Field on the Fluorescence of Tetracene Crystals: Exciton Fission. *Physical Review Letters* **1969**, *22*, 593–596.
- [35] Merrifield, R. E. Theory of Magnetic Field Effects on the Mutual Annihilation of Triplet Excitons. *The Journal of Chemical Physics* **1968**, *48*, 4318–4319.
- [36] Johnson, R. C.; Merrifield, R. E. Effects of Magnetic Fields on the Mutual Annihilation of Triplet Excitons in Anthracene Crystals. *Physical Review B* **1970**, *1*, 896–902.
- [37] Suna, A. Kinematics of Exciton-Exciton Annihilation in Molecular Crystals. *Physical Review B* **1970**, *1*, 1716–1739.
- [38] Merrifield, R. E. Magnetic effects on triplet exciton interactions. *Pure and Applied Chemistry* **1971**, *27*, 481–498.
- [39] Klein, G.; Voltz, R. Formation and decay of superexcited states in dense organic matter under high energy radiation. *International Journal for Radiation Physics and Chemistry* **1975**, *7*, 155–174.

- [40] Rademaker, H.; Hoff, A. J.; Grondelle, R. V.; Duysens, L. N. Carotenoid triplet yields in normal and deuterated Rhodospirillum rubrum. *Biochimica et Biophysica Acta (BBA) - Bioenergetics* **1980**, *592*, 240–257.
- [41] Austin, R. H.; Baker, G. L.; Etemad, S.; Thompson, R. Magnetic field effects on triplet exciton fission and fusion in a polydiacetylene. *The Journal of Chemical Physics* **1989**, *90*, 6642–6646.
- [42] Friend, R. H.; Gymer, R. W.; Holmes, A. B.; Burroughes, J. H.; Marks, R. N.; Taliani, C.; Bradley, D. D. C.; Santos, D. A. D.; Brédas, J. L.; Lögdlund, M.; Salaneck, W. R. Electroluminescence in conjugated polymers. *Nature* **1999**, *397*, 121–128.
- [43] Garnier, F.; Hajlaoui, R.; Yassar, A.; Srivastava, P. All-Polymer Field-Effect Transistor Realized by Printing Techniques. *Science* **1994**, *265*, 1684–1686.
- [44] Dimitrakopoulos, C.; Malenfant, P. Organic Thin Film Transistors for Large Area Electronics. *Advanced Materials* **2002**, *14*, 99–117.
- [45] Peumans, P.; Yakimov, A.; Forrest, S. R. Small molecular weight organic thin-film photodetectors and solar cells. *Journal of Applied Physics* **2003**, *93*, 3693–3723.
- [46] Baldaccino, A. J.; Collins, M. I.; Nielsen, M. P.; Schmidt, T. W.; McCamey, D. R.; Tayebjee, M. J. Y. Singlet fission photovoltaics: Progress and promising pathways. *Chemical Physics Reviews* **2022**, *3*, 021304.
- [47] Einzinger, M.; Wu, T.; Kompalla, J. F.; Smith, H. L.; Perkinson, C. F.; Nienhaus, L.; Wieghold, S.; Congreve, D. N.; Kahn, A.; Bawendi, M. G.; Baldo, M. A. Sensitization of silicon by singlet exciton fission in tetracene. *Nature* **2019**, *571*, 90–94.
- [48] Wang, S.; Khafizov, M.; Tu, X.; Zheng, M.; Krauss, T. D. Multiple Exciton Generation in Single-Walled Carbon Nanotubes. *Nano Letters* **2010**, *10*, 2381–2386.
- [49] Johnson, J. C.; Nozik, A. J.; Michl, J. High Triplet Yield from Singlet Fission in a Thin Film of 1, 3-Diphenylisobenzofuran. *Journal of the American Chemical Society* **2010**, *132*, 16302–16303.
- [50] Wilson, M. W. B.; Rao, A.; Clark, J.; Kumar, R. S. S.; Brida, D.; Cerullo, G.; Friend, R. H. Ultrafast Dynamics of Exciton Fission in Polycrystalline Pentacene. *Journal of the American Chemical Society* **2011**, *133*, 11830–11833.
- [51] Ryasnyanskiy, A.; Biaggio, I. Triplet exciton dynamics in rubrene single crystals. *Physical Review B* **2011**, *84*.
- [52] Paci, I.; Johnson, J. C.; Chen, X.; Rana, G.; Popović, D.; David, D. E.; Nozik, A. J.; Ratner, M. A.; Michl, J. Singlet Fission for Dye-Sensitized Solar Cells: Can a Suitable Sensitizer Be Found? *Journal of the American Chemical Society* **2006**, *128*, 16546–16553.
- [53] Michl, J.; Nozik, A. J.; Chen, X.; Johnson, J. C.; Rana, G.; Akdag, A.; Schwerin, A. F. Toward singlet fission for excitonic solar cells. SPIE Proceedings. 2007.
- [54] Smith, M. B.; Michl, J. Recent Advances in Singlet Fission. *Annual Review of Physical Chemistry* **2013**, *64*, 361–386.
- [55] Casanova, D. Theoretical Modeling of Singlet Fission. *Chem. Rev.* **2018**, *118*, 7164–7207.
- [56] Miyata, K.; Conrad-Burton, F. S.; Geyer, F. L.; Zhu, X.-Y. Triplet Pair States in Singlet Fission. *Chemical Reviews* **2019**, *119*, 4261–4292.
- [57] Berkelbach, T. C.; Hybertsen, M. S.; Reichman, D. R. Microscopic theory of singlet exciton fission. I. General formulation. *The Journal of Chemical Physics* **2013**, *138*, 114102.
- [58] Berkelbach, T. C.; Hybertsen, M. S.; Reichman, D. R. Microscopic theory of singlet exciton fission. II. Application to pentacene dimers and the role of superexchange. *The Journal of Chemical Physics* **2013**, *138*, 114103.
- [59] Berkelbach, T. C.; Hybertsen, M. S.; Reichman, D. R. Microscopic theory of singlet exciton fission. III. Crystalline pentacene. *The Journal of Chemical Physics* **2014**, *141*, 074705.
- [60] Fuemmeler, E. G.; Sanders, S. N.; Pun, A. B.; Kumarasamy, E.; Zeng, T.; Miyata, K.; Steigerwald, M. L.; Zhu, X.-Y.; Sfeir, M. Y.; Campos, L. M.; Ananth, N. A Direct Mechanism of Ultrafast Intramolecular Singlet Fission in Pentacene Dimers. *ACS Central Science* **2016**, *2*, 316–324.

- [61] Damrauer, N. H.; Snyder, J. L. Symmetry-Directed Control of Electronic Coupling for Singlet Fission in Covalent Bis-Acene Dimers. *The Journal of Physical Chemistry Letters* **2015**, *6*, 4456–4462.
- [62] Alguire, E. C.; Subotnik, J. E.; Damrauer, N. H. Exploring Non-Condon Effects in a Covalent Tetracene Dimer: How Important Are Vibrations in Determining the Electronic Coupling for Singlet Fission? *The Journal of Physical Chemistry A* **2014**, *119*, 299–311.
- [63] Musser, A. J.; Liebel, M.; Schnedermann, C.; Wende, T.; Kehoe, T. B.; Rao, A.; Kukura, P. Evidence for conical intersection dynamics mediating ultrafast singlet exciton fission. *Nature Phys* **2015**, *11*, 352–357.
- [64] Tempelaar, R.; Reichman, D. R. Vibronic exciton theory of singlet fission. II. Two-dimensional spectroscopic detection of the correlated triplet pair state. *The Journal of Chemical Physics* **2017**, *146*.
- [65] Ehrler, B.; Musselman, K. P.; Böhm, M. L.; Friend, R. H.; Greenham, N. C. Hybrid pentacene/a-silicon solar cells utilizing multiple carrier generation via singlet exciton fission. *Applied Physics Letters* **2012**, *101*.
- [66] Fuemmeler, E. G.; Sanders, S. N.; Pun, A. B.; Kumarasamy, E.; Zeng, T.; Miyata, K.; Steigerwald, M. L.; Zhu, X.-Y.; Sfeir, M. Y.; Campos, L. M.; Ananth, N. A Direct Mechanism of Ultrafast Intramolecular Singlet Fission in Pentacene Dimers. *ACS Cent. Sci.* **2016**, *2*, 316–324.
- [67] Zeng, T.; Hoffmann, R.; Ananth, N. The Low-Lying Electronic States of Pentacene and Their Roles in Singlet Fission. *J. Am. Chem. Soc.* **2014**, *136*, 5755–5764.
- [68] Casanova, D. Electronic Structure Study of Singlet Fission in Tetracene Derivatives. *J. Chem. Theory Comput.* **2013**, *10*, 324–334.
- [69] Zimmerman, P. M.; Bell, F.; Casanova, D.; Head-Gordon, M. Mechanism for Singlet Fission in Pentacene and Tetracene: From Single Exciton to Two Triplets. *J. Am. Chem. Soc.* **2011**, *133*, 19944–19952.
- [70] Morrison, A. F.; Herbert, J. M. Evidence for Singlet Fission Driven by Vibronic Coherence in Crystalline Tetracene. *J. Phys. Chem. Lett.* **2017**, *8*, 1442–1448.
- [71] Tamura, H.; Huix-Rotllant, M.; Burghardt, I.; Olivier, Y.; Beljonne, D. First-Principles Quantum Dynamics of Singlet Fission: Coherent versus Thermally Activated Mechanisms Governed by Molecularmath mml:math xmlns:mml="http://www.w3.org/1998/Math/MathML" display="inline" mml:mi/mml:mi/mml:mathStacking. *Physical Review Letters* **2015**, *115*.
- [72] Berkelbach, T. C.; Hybertsen, M. S.; Reichman, D. R. Microscopic theory of singlet exciton fission. II. Application to pentacene dimers and the role of superexchange. *The Journal of Chemical Physics* **2013**, *138*, 114103.
- [73] Tao, G. Bath Effect in Singlet Fission Dynamics. *The Journal of Physical Chemistry C* **2014**, *118*, 27258–27264.
- [74] Renaud, N.; Grozema, F. C. Intermolecular Vibrational Modes Speed Up Singlet Fission in Perylenediimide Crystals. *The Journal of Physical Chemistry Letters* **2015**, *6*, 360–365.
- [75] Lee, J.; Small, D. W.; Epifanovsky, E.; Head-Gordon, M. Coupled-Cluster Valence-Bond Singles and Doubles for Strongly Correlated Systems: Block-Tensor Based Implementation and Application to Oligoacenes. *Journal of Chemical Theory and Computation* **2017**, *13*, 602–615.
- [76] Lengsfield, B. H.; Saxe, P.; Yarkony, D. R. On the evaluation of nonadiabatic coupling matrix elements using SA-MCSCF/CI wave functions and analytic gradient methods. I. *The Journal of Chemical Physics* **1984**, *81*, 4549–4553.
- [77] Saxe, P.; Lengsfield, B. H.; Yarkony, D. R. On the evaluation of non-adiabatic coupling matrix elements for large scale CI wavefunctions. *Chemical Physics Letters* **1985**, *113*, 159–164.
- [78] Tapavicza, E.; Bellchambers, G. D.; Vincent, J. C.; Furche, F. Ab initio non-adiabatic molecular dynamics. *Physical Chemistry Chemical Physics* **2013**, *15*, 18336.
- [79] Fatehi, S.; Alguire, E.; Shao, Y.; Subotnik, J. E. Analytic derivative couplings between configuration-interaction-singles states with built-in electron-translation factors for translational invariance. *The Journal of Chemical Physics* **2011**, *135*.

- [80] Zhang, X.; Herbert, J. M. Analytic derivative couplings for spin-flip configuration interaction singles and spin-flip time-dependent density functional theory. *The Journal of Chemical Physics* **2014**, *141*.
- [81] Jin, Z.; Subotnik, J. E. Localized diabatization applied to excitons in molecular crystals. *The Journal of Chemical Physics* **2017**, *146*.
- [82] Morrison, A. F.; You, Z.-Q.; Herbert, J. M. Ab Initio Implementation of the Frenkel–Davydov Exciton Model: A Naturally Parallelizable Approach to Computing Collective Excitations in Crystals and Aggregates. *J. Chem. Theory Comput.* **2014**, *10*, 5366–5376.
- [83] Sato, T.; Tokunaga, K.; Tanaka, K. Vibronic coupling in cyclopentadienyl radical: A method for calculation of vibronic coupling constant and vibronic coupling density analysis. *The Journal of Chemical Physics* **2006**, *124*.
- [84] Ito, S.; Nagami, T.; Nakano, M. Density Analysis of Intra- and Intermolecular Vibronic Couplings toward Bath Engineering for Singlet Fission. *J. Phys. Chem. Lett.* **2015**, *6*, 4972–4977.
- [85] Feng, X.; Luzanov, A. V.; Krylov, A. I. Fission of Entangled Spins: An Electronic Structure Perspective. *J. Phys. Chem. Lett.* **2013**, *4*, 3845–3852.
- [86] Feng, X.; Krylov, A. I. On couplings and excimers: lessons from studies of singlet fission in covalently linked tetracene dimers. *Physical Chemistry Chemical Physics* **2016**, *18*, 7751–7761.
- [87] Feng, X.; Krylov, A. I. On couplings and excimers: lessons from studies of singlet fission in covalently linked tetracene dimers. *Phys. Chem. Chem. Phys.* **2016**, *18*, 7751–7761.
- [88] Korovina, N. V.; Das, S.; Nett, Z.; Feng, X.; Joy, J.; Haiges, R.; Krylov, A. I.; Bradforth, S. E.; Thompson, M. E. Singlet Fission in a Covalently Linked Cofacial Alkynyltetracene Dimer. *Journal of the American Chemical Society* **2016**, *138*, 617–627.
- [89] Casanova, D.; Krylov, A. I. Quantifying local exciton, charge resonance, and multiexciton character in correlated wave functions of multichromophoric systems. *The Journal of Chemical Physics* **2016**, *144*.
- [90] Luzanov, A. V.; Casanova, D.; Feng, X.; Krylov, A. I. Quantifying charge resonance and multiexciton character in coupled chromophores by charge and spin cumulant analysis. *The Journal of Chemical Physics* **2015**, *142*.
- [91] Ni, W.; Gurzadyan, G. G.; Zhao, J.; Che, Y.; Li, X.; Sun, L. Singlet Fission from Upper Excited Electronic States of Cofacial Perylene Dimer. *The Journal of Physical Chemistry Letters* **2019**, *10*, 2428–2433.
- [92] Wu, T.; Ni, W.; Gurzadyan, G. G.; Sun, L. Singlet fission from upper excited singlet states and polaron formation in rubrene film. *RSC Advances* **2021**, *11*, 4639–4645.
- [93] Ni, W.; Gurzadyan, G. G.; Sun, L.; Gelin, M. F. Toward efficient photochemistry from upper excited electronic states: Detection of long S2 lifetime of perylene. *The Journal of Chemical Physics* **2021**, *155*.
- [94] Wan, Y.; Guo, Z.; Zhu, T.; Yan, S.; Johnson, J.; Huang, L. Cooperative singlet and triplet exciton transport in tetracene crystals visualized by ultrafast microscopy. *Nature Chemistry* **2015**, *7*, 785–792.
- [95] Köppel, H.; Domcke, W.; Cederbaum, L. S. *Advances in Chemical Physics*; John Wiley & Sons, Inc., 2007; pp 59–246.
- [96] Ichino, T.; Gauss, J.; Stanton, J. F. Quasidiabatic states described by coupled-cluster theory. *The Journal of Chemical Physics* **2009**, *130*.
- [97] Tamura, H.; Burghardt, I.; Tsukada, M. Exciton Dissociation at Thiophene/Fullerene Interfaces: The Electronic Structures and Quantum Dynamics. *The Journal of Physical Chemistry C* **2011**, *115*, 10205–10210.
- [98] Tamura, H.; Burghardt, I. Ultrafast Charge Separation in Organic Photovoltaics Enhanced by Charge Delocalization and Vibronically Hot Exciton Dissociation. *Journal of the American Chemical Society* **2013**, *135*, 16364–16367.
- [99] Aragó, J.; Troisi, A. Excitonic couplings between molecular crystal pairs by a multistate approximation. *The Journal of Chemical Physics* **2015**, *142*.

- [100] Pac, B.; Petelenz, P. Lowest Singlet Exciton in Pentacene: Modern Calculations versus Classic Experiments. *ChemPhysChem* **2014**, *15*, 2801–2809.
- [101] Yamagata, H.; Norton, J.; Hontz, E.; Olivier, Y.; Beljonne, D.; Brédas, J. L.; Silbey, R. J.; Spano, F. C. The nature of singlet excitons in oligoacene molecular crystals. *The Journal of Chemical Physics* **2011**, *134*.
- [102] Petelenz, P.; Pac, B. Is Dipole Moment a Valid Descriptor of Excited State's Charge-Transfer Character? *Journal of the American Chemical Society* **2013**, *135*, 17379–17386.
- [103] Cudazzo, P.; Sottile, F.; Rubio, A.; Gatti, M. Exciton dispersion in molecular solids. *Journal of Physics: Condensed Matter* **2015**, *27*, 113204.
- [104] Clark, A. E.; Davidson, E. R. Local spin. *The Journal of Chemical Physics* **2001**, *115*, 7382–7392.
- [105] Tretiak, S.; Mukamel, S. Density Matrix Analysis and Simulation of Electronic Excitations in Conjugated and Aggregated Molecules. *Chemical Reviews* **2002**, *102*, 3171–3212.
- [106] Hedin, L. New Method for Calculating the One-Particle Green's Function with Application to the Electron-Gas Problem. *Physical Review* **1965**, *139*, A796–A823.
- [107] Wong, B. M.; Hsieh, T. H. Optoelectronic and Excitonic Properties of Oligoacenes: Substantial Improvements from Range-Separated Time-Dependent Density Functional Theory. *Journal of Chemical Theory and Computation* **2010**, *6*, 3704–3712.
- [108] Luzanov, A. V.; Zhikol, O. A. Electron invariants and excited state structural analysis for electronic transitions within CIS, RPA, and TDDFT models. *International Journal of Quantum Chemistry* **2009**, NA–NA.
- [109] Plasser, F.; Aquino, A. J. A.; Hase, W. L.; Lischka, H. UV Absorption Spectrum of Alternating DNA Duplexes. Analysis of Excitonic and Charge Transfer Interactions. *The Journal of Physical Chemistry A* **2012**, *116*, 11151–11160.
- [110] Blancafort, L.; Voityuk, A. A. Exciton delocalization, charge transfer, and electronic coupling for singlet excitation energy transfer between stacked nucleobases in DNA: An MS-CASPT2 study. *The Journal of Chemical Physics* **2014**, *140*.
- [111] Bäppler, S. A.; Plasser, F.; Wormit, M.; Dreuw, A. Exciton analysis of many-body wave functions: Bridging the gap between the quasiparticle and molecular orbital pictures. *Physical Review A* **2014**, *90*.
- [112] Huang, J.; Du, L.; Hu, D.; Lan, Z. Theoretical analysis of excited states and energy transfer mechanism in conjugated dendrimers. *Journal of Computational Chemistry* **2014**, *36*, 151–163.
- [113] Wu, Q.; Voorhis, T. V. Direct optimization method to study constrained systems within density-functional theory. *Physical Review A* **2005**, *72*.
- [114] Head-Gordon, M.; Grana, A. M.; Maurice, D.; White, C. A. Analysis of Electronic Transitions as the Difference of Electron Attachment and Detachment Densities. *The Journal of Physical Chemistry* **1995**, *99*, 14261–14270.
- [115] Plasser, F.; Thomitzni, B.; Bäppler, S. A.; Wenzel, J.; Rehn, D. R.; Wormit, M.; Dreuw, A. Statistical analysis of electronic excitation processes: Spatial location, compactness, charge transfer, and electron-hole correlation. *Journal of Computational Chemistry* **2015**, *36*, 1609–1620.
- [116] Sun, M.; Kjellberg, P.; Beenken, W. J.; Pullerits, T. Comparison of the electronic structure of PPV and its derivative DIOXA-PPV. *Chemical Physics* **2006**, *327*, 474–484.
- [117] Ferguson, J. Absorption and Emission Spectra of the Perylene Dimer. *The Journal of Chemical Physics* **1966**, *44*, 2677–2683.
- [118] Birks, J. B. Excimers. *Reports on Progress in Physics* **1975**, *38*, 903–974.
- [119] Hartnett, P. E.; Margulies, E. A.; Mauck, C. M.; Miller, S. A.; Wu, Y.; Wu, Y.-L.; Marks, T. J.; Wasielewski, M. R. Effects of Crystal Morphology on Singlet Exciton Fission in Diketopyrrolopyrrole Thin Films. *The Journal of Physical Chemistry B* **2016**, *120*, 1357–1366.
- [120] Mauck, C. M.; Hartnett, P. E.; Margulies, E. A.; Ma, L.; Miller, C. E.; Schatz, G. C.; Marks, T. J.; Wasielewski, M. R. Singlet Fission via an Excimer-Like Intermediate in 3, 6-Bis(thiophen-2-yl)diketopyrrolopyrrole Derivatives. *Journal of the American Chemical Society* **2016**, *138*, 11749–11761.

- [121] Miller, C. E.; Wasielewski, M. R.; Schatz, G. C. Modeling Singlet Fission in Rylene and Diketopyrrolopyrrole Derivatives: The Role of the Charge Transfer State in Superexchange and Excimer Formation. *The Journal of Physical Chemistry C* **2017**, *121*, 10345–10350.
- [122] Walker, B. J.; Musser, A. J.; Beljonne, D.; Friend, R. H. Singlet exciton fission in solution. *Nature Chemistry* **2013**, *5*, 1019–1024.
- [123] Stern, H. L.; Musser, A. J.; Gelinas, S.; Parkinson, P.; Herz, L. M.; Bruzek, M. J.; Anthony, J.; Friend, R. H.; Walker, B. J. Identification of a triplet pair intermediate in singlet exciton fission in solution. *Proceedings of the National Academy of Sciences* **2015**, *112*, 7656–7661.
- [124] Nichols, V. M.; Rodriguez, M. T.; Piland, G. B.; Tham, F.; Nesterov, V. N.; Youngblood, W. J.; Bardeen, C. J. Assessing the Potential of Peroppyrene as a Singlet Fission Material: Photophysical Properties in Solution and the Solid State. *The Journal of Physical Chemistry C* **2013**, *117*, 16802–16810.
- [125] Feng, X.; Krylov, A. I. On couplings and excimers: lessons from studies of singlet fission in covalently linked tetracene dimers. *Physical Chemistry Chemical Physics* **2016**, *18*, 7751–7761.
- [126] Marciniaik, H.; Fiebig, M.; Huth, M.; Schiefer, S.; Nickel, B.; Selmaier, F.; Lochbrunner, S. Ultrafast Exciton Relaxation in Microcrystalline Pentacene Films. *Physical Review Letters* **2007**, *99*.
- [127] Marciniaik, H.; Pugliesi, I.; Nickel, B.; Lochbrunner, S. Ultrafast singlet and triplet dynamics in microcrystalline pentacene films. *Physical Review B* **2009**, *79*.
- [128] Tayebjee, M. J. Y.; Clady, R. G. C. R.; Schmidt, T. W. The exciton dynamics in tetracene thin films. *Physical Chemistry Chemical Physics* **2013**, *15*, 14797.
- [129] Born, M.; Oppenheimer, R. Zur Quantentheorie der Moleküle. *Annalen der Physik* **1927**, *389*, 457–484.
- [130] Andersson, K.; Malmqvist, P.-Å.; Roos, B. O. Second-order perturbation theory with a complete active space self-consistent field reference function. *The Journal of Chemical Physics* **1992**, *96*, 1218–1226.
- [131] Olsen, J. A direct method to transform between expansions in the configuration state function and Slater determinant bases. *The Journal of Chemical Physics* **2014**, *141*, 034112.
- [132] Finley, J.; Malmqvist, P.-; Roos, B. O.; Serrano-Andrés, L. The multi-state CASPT2 method. *Chemical Physics Letters* **1998**, *288*, 299–306.
- [133] Shiozaki, T.; Győrffy, W.; Celani, P.; Werner, H.-J. Communication: Extended multi-state complete active space second-order perturbation theory: Energy and nuclear gradients. *The Journal of Chemical Physics* **2011**, *135*, 081106.
- [134] Granovsky, A. A. Extended multi-configuration quasi-degenerate perturbation theory: The new approach to multi-state multi-reference perturbation theory. *The Journal of Chemical Physics* **2011**, *134*.
- [135] Shiozaki, T. BAGEL: Brilliantly Advanced General Electronic-structure Library. *WIREs Computational Molecular Science* **2018**, *8*, e1331.
- [136] Thomas, L. H. The calculation of atomic fields. *Mathematical Proceedings of the Cambridge Philosophical Society* **1927**, *23*, 542–548.
- [137] Teller, E. On the Stability of Molecules in the Thomas-Fermi Theory. *Reviews of Modern Physics* **1962**, *34*, 627–631.
- [138] Lieb, E. H.; Simon, B. The Thomas-Fermi theory of atoms, molecules and solids. *Advances in Mathematics* **1977**, *23*, 22–116.
- [139] Hohenberg, P.; Kohn, W. Inhomogeneous Electron Gas. *Physical Review* **1964**, *136*, B864–B871.
- [140] Kohn, W.; Sham, L. J. Self-Consistent Equations Including Exchange and Correlation Effects. *Physical Review* **1965**, *140*, A1133–A1138.
- [141] Bagayoko, D.; Zhao, G. L.; Fan, J. D.; Wang, J. T. *Ab initio* calculations of the electronic structure and optical properties of ferroelectric tetragonal. *Journal of Physics: Condensed Matter* **1998**, *10*, 5645–5655.

- [142] Becke, A. D. Density-functional thermochemistry. I. The effect of the exchange-only gradient correction. *The Journal of Chemical Physics* **1992**, *96*, 2155–2160.
- [143] Lee, C.; Yang, W.; Parr, R. G. Development of the Colle-Salvetti correlation-energy formula into a functional of the electron density. *Physical Review B* **1988**, *37*, 785–789.
- [144] Gilbert, T. L. Hohenberg-Kohn theorem for nonlocal external potentials. *Physical Review B* **1975**, *12*, 2111–2120.
- [145] Becke, A. D. A new mixing of Hartree–Fock and local density-functional theories. *The Journal of Chemical Physics* **1993**, *98*, 1372–1377.
- [146] Runge, E.; Gross, E. K. U. Density-Functional Theory for Time-Dependent Systems. *Physical Review Letters* **1984**, *52*, 997–1000.
- [147] Petersilka, M.; Gossmann, U. J.; Gross, E. K. U. Excitation Energies from Time-Dependent Density-Functional Theory. *Physical Review Letters* **1996**, *76*, 1212–1215.
- [148] van Leeuwen, R. Causality and Symmetry in Time-Dependent Density-Functional Theory. *Physical Review Letters* **1998**, *80*, 1280–1283.
- [149] Dewar, M. J. S.; Thiel, W. Ground states of molecules. 38. The MNDO method. Approximations and parameters. *Journal of the American Chemical Society* **1977**, *99*, 4899–4907.
- [150] Dewar, M. J. S.; Zoebisch, E. G.; Healy, E. F.; Stewart, J. J. P. Development and use of quantum mechanical molecular models. 76. AM1: a new general purpose quantum mechanical molecular model. *Journal of the American Chemical Society* **1985**, *107*, 3902–3909.
- [151] Stewart, J. J. P. Optimization of parameters for semiempirical methods V: Modification of NDDO approximations and application to 70 elements. *Journal of Molecular Modeling* **2007**, *13*, 1173–1213.
- [152] Zhou, G.; Nebgen, B.; Lubbers, N.; Malone, W.; Niklasson, A. M.; Tretiak, S. Graphics processing unit-accelerated semiempirical Born Oppenheimer molecular dynamics using PyTorch. *Journal of Chemical Theory and Computation* **2020**, *16*, 4951–4962.
- [153] Roothaan, C. C. J. New Developments in Molecular Orbital Theory. *Reviews of Modern Physics* **1951**, *23*, 69–89.
- [154] Thiel, W. Semiempirical quantum-chemical methods. *WIREs Computational Molecular Science* **2013**, *4*, 145–157.
- [155] Dewar, M. J. S.; Thiel, W. A semiempirical model for the two-center repulsion integrals in the NDDO approximation. *Theoretica Chimica Acta* **1977**, *46*, 89–104.
- [156] Badziag, P.; Solms, F. An improved SCF iteration scheme. *Computers Chemistry* **1988**, *12*, 233–236.
- [157] Pulay, P. Convergence acceleration of iterative sequences. the case of scf iteration. *Chemical Physics Letters* **1980**, *73*, 393–398.
- [158] Schrödinger, E. Quantisierung als Eigenwertproblem. *Annalen der Physik* **1926**, *385*, 437–490.
- [159] Soliverez, C. E. General theory of effective Hamiltonians. *Physical Review A* **1981**, *24*, 4–9.
- [160] Frasca, M. Duality in perturbation theory and the quantum adiabatic approximation. *Physical Review A* **1998**, *58*, 3439–3442.
- [161] Simon, B. Large orders and summability of eigenvalue perturbation theory: A mathematical overview. *International Journal of Quantum Chemistry* **1982**, *21*, 3–25.
- [162] Buchanan, E. A.; Havlas, Z.; Michl, J. Singlet fission: Optimization of chromophore dimer geometry. *Advances in Quantum Chemistry* **2017**, *75*, 175–227.
- [163] Squillante, L.; Ricco, L. S.; Ukpong, A. M.; Lagos-Monaco, R. E.; Seridonio, A. C.; de Souza, M. Grüneisen parameter as an entanglement compass and the breakdown of the Hellmann-Feynman theorem. *Physical Review B* **2023**, *108*.
- [164] Feynman, R. P. Forces in Molecules. *Physical Review* **1939**, *56*, 340–343.
- [165] Epstein, S. T. Time-Dependent Hellmann—Feynman Theorems for Variational Wavefunctions. *The Journal of Chemical Physics* **1966**, *45*, 384–384.

- [166] Hayes, E. F.; Parr, R. G. Time-Dependent Hellmann-Feynman Theorems. *The Journal of Chemical Physics* **1965**, *43*, 1831–1832.
- [167] Pulay, P. Ab initio calculation of force constants and equilibrium geometries in polyatomic molecules: I. Theory. *Molecular Physics* **1969**, *17*, 197–204.
- [168] Pulay, P. Ab initio calculation of force constants and equilibrium geometries in polyatomic molecules: II. Force constants of water. *Molecular Physics* **1970**, *18*, 473–480.
- [169] Helgaker, T.; Jørgensen, P. *Advances in Quantum Chemistry*; Elsevier, 1988; p 183–245.
- [170] Webb, S. P.; Iordanov, T.; Hammes-Schiffer, S. Multiconfigurational nuclear-electronic orbital approach: Incorporation of nuclear quantum effects in electronic structure calculations. *The Journal of Chemical Physics* **2002**, *117*, 4106–4118.
- [171] Tamayo-Mendoza, T.; Kreisbeck, C.; Lindh, R.; Aspuru-Guzik, A. Automatic Differentiation in Quantum Chemistry with Applications to Fully Variational Hartree–Fock. *ACS Central Science* **2018**, *4*, 559–566.
- [172] Samuelsson, B., Sohlman, M., Eds. *Nobel Lectures in Physics (1963–1970)*; Nobel lectures, including presentation speeches and laureates' biographies; 1998; Vol. 4; pp ix + 349.
- [173] Levi-Civita, M. d. T. Nozione di parallelismo in una varietà qualunque e conseguente specificazione geometrica della curvatura riemanniana. *Rendiconti del Circolo Matematico di Palermo* **1916**, *42*, 173–204.
- [174] Murnaghan, F. D. The Generalized Kronecker Symbol and its Application to the theory of Determinants. *The American Mathematical Monthly* **1925**, *32*, 233–241.
- [175] Jordan, P.; Wigner, E. Über das Paulische Äquivalenzverbot. *Zeitschrift für Physik* **1928**, *47*, 631–651.
- [176] Eckart, C. The Application of Group theory to the Quantum Dynamics of Monatomic Systems. *Reviews of Modern Physics* **1930**, *2*, 305–380.
- [177] Casanova, D. Bright Fission: Singlet Fission into a Pair of Emitting States. *Journal of Chemical Theory and Computation* **2015**, *11*, 2642–2650.
- [178] Scholes, G. D. Correlated Pair States Formed by Singlet Fission and Exciton–Exciton Annihilation. *The Journal of Physical Chemistry A* **2015**, *119*, 12699–12705.
- [179] Smith, M. B.; Michl, J. Singlet Fission. *Chem. Rev.* **2010**, *110*, 6891–6936.
- [180] Wang, R.; Zhang, C.; Zhang, B.; Liu, Y.; Wang, X.; Xiao, M. Magnetic dipolar interaction between correlated triplets created by singlet fission in tetracene crystals. *Nature Communications* **2015**, *6*.
- [181] Piland, G. B.; Burdett, J. J.; Dillon, R. J.; Bardeen, C. J. Singlet Fission: From Coherences to Kinetics. *J. Phys. Chem. Lett.* **2014**, *5*, 2312–2319.
- [182] Singh-Rachford, T. N.; Castellano, F. N. Photon upconversion based on sensitized triplet–triplet annihilation. *Coordination Chemistry Reviews* **2010**, *254*, 2560–2573.
- [183] Kollmar, C. Electronic structure of diradical and dicarbene intermediates in short-chain polydiacetylene oligomers. *The Journal of Chemical Physics* **1993**, *98*, 7210–7228.
- [184] Burdett, J. J.; Piland, G. B.; Bardeen, C. J. Magnetic field effects and the role of spin states in singlet fission. *Chemical Physics Letters* **2013**, *585*, 1–10.
- [185] Miyata, K.; Conrad-Burton, F. S.; Geyer, F. L.; Zhu, X.-Y. Triplet Pair States in Singlet Fission. *Chem. Rev.* **2019**, *119*, 4261–4292.
- [186] Folie, B. D.; Haber, J. B.; Refaelly-Abramson, S.; Neaton, J. B.; Ginsberg, N. S. Long-Lived Correlated Triplet Pairs in a -Stacked Crystalline Pentacene Derivative. *J. Am. Chem. Soc.* **2018**, *140*, 2326–2335.
- [187] Stern, H. L.; Cheminal, A.; Yost, S. R.; Broch, K.; Bayliss, S. L.; Chen, K.; Tabachnyk, M.; Thорley, K.; Greenham, N.; Hodgkiss, J. M.; Anthony, J.; Head-Gordon, M.; Musser, A. J.; Rao, A.; Friend, R. H. Vibronically coherent ultrafast triplet-pair formation and subsequent thermally activated dissociation control efficient endothermic singlet fission. *Nature Chem* **2017**, *9*, 1205–1212.

- [188] Lee, T. S.; Lin, Y. L.; Kim, H.; Pensack, R. D.; Rand, B. P.; Scholes, G. D. Triplet Energy Transfer Governs the Dissociation of the Correlated Triplet Pair in Exothermic Singlet Fission. *J. Phys. Chem. Lett.* **2018**, *9*, 4087–4095.
- [189] Johnson, J. C.; Akdag, A.; Zamadar, M.; Chen, X.; Schwerin, A. F.; Paci, I.; Smith, M. B.; Havlas, Z.; Miller, J. R.; Ratner, M. A.; Nozik, A. J.; Michl, J. Toward Designed Singlet Fission: Solution Photophysics of Two Indirectly Coupled Covalent Dimers of 1,3-Diphenylisobenzofuran. *J. Phys. Chem. B* **2013**, *117*, 4680–4695.
- [190] Herz, J.; Buckup, T.; Paulus, F.; Engelhart, J. U.; Bunz, U. H. F.; Motzkus, M. Unveiling Singlet Fission Mediating States in TIPS-pentacene and its Aza Derivatives. *J. Phys. Chem. A* **2015**, *119*, 6602–6610.
- [191] Pun, A. B.; Asadpoordarvish, A.; Kumarasamy, E.; Tayebjee, M. J. Y.; Niesner, D.; McCamey, D. R.; Sanders, S. N.; Campos, L. M.; Sfeir, M. Y. Ultra-fast intramolecular singlet fission to persistent multiexcitons by molecular design. *Nat. Chem.* **2019**, *11*, 821–828.
- [192] Le, A. K.; Bender, J. A.; Roberts, S. T. Slow Singlet Fission Observed in a Polycrystalline Perylenedimide Thin Film. *J. Phys. Chem. Lett.* **2016**, *7*, 4922–4928.
- [193] Jadhav, P. J.; Brown, P. R.; Thompson, N.; Wunsch, B.; Mohanty, A.; Yost, S. R.; Hontz, E.; Voorhis, T. V.; Bawendi, M. G.; Bulović, V.; Baldo, M. A. Triplet Exciton Dissociation in Singlet Exciton Fission Photovoltaics. *Adv. Mater.* **2012**, *24*, 6169–6174.
- [194] Zurek, W. H. Decoherence, einselection, and the quantum origins of the classical. *Rev. Mod. Phys.* **2003**, *75*, 715–775.
- [195] Yong, C. K. et al. The entangled triplet pair state in acene and heteroacene materials. *Nat Commun* **2017**, *8*.
- [196] Lukman, S.; Richter, J. M.; Yang, L.; Hu, P.; Wu, J.; Greenham, N. C.; Musser, A. J. Efficient Singlet Fission and Triplet-Pair Emission in a Family of Zethrene Diradicaloids. *J. Am. Chem. Soc.* **2017**, *139*, 18376–18385.
- [197] Thorsmølle, V. K.; Averitt, R. D.; Demsar, J.; Smith, D. L.; Tretiak, S.; Martin, R. L.; Chi, X.; Crone, B. K.; Ramirez, A. P.; Taylor, A. J. Morphology Effectively Controls Singlet-Triplet Exciton Relaxation and Charge Transport in Organic Semiconductors. *Phys. Rev. Lett.* **2009**, *102*.
- [198] Singh, A.; Humeniuk, A.; Röhr, M. I. S. Energetics and optimal molecular packing for singlet fission in BN-doped perylenes: electronic adiabatic state basis screening. *Physical Chemistry Chemical Physics* **2021**, *23*, 16525–16536.
- [199] source code for reproducing calculations. <https://github.com/roehr-lab/SFast-Singlet-Fission-adiabatic-basis-screening>.
- [200] Parker, S. M.; Shiozaki, T. Communication: Active space decomposition with multiple sites: Density matrix renormalization group algorithm. *The Journal of Chemical Physics* **2014**, *141*, 211102.
- [201] Parker, S. M.; Seideman, T.; Ratner, M. A.; Shiozaki, T. Communication: Active-space decomposition for molecular dimers. *The Journal of Chemical Physics* **2013**, *139*, 021108.
- [202] Felter, K. M.; Grozema, F. C. Singlet Fission in Crystalline Organic Materials: Recent Insights and Future Directions. *The Journal of Physical Chemistry Letters* **2019**, *10*, 7208–7214.
- [203] Mirjani, F.; Renaud, N.; Gorczak, N.; Grozema, F. C. Theoretical Investigation of Singlet Fission in Molecular Dimers: The Role of Charge Transfer States and Quantum Interference. *The Journal of Physical Chemistry C* **2014**, *118*, 14192–14199.
- [204] Farag, M. H.; Krylov, A. I. Singlet Fission in Perylenedimide Dimers. *The Journal of Physical Chemistry C* **2018**, *122*, 25753–25763.
- [205] Roos, B. O.; Taylor, P. R.; Sigbahn, P. E. A complete active space SCF method (CASSCF) using a density matrix formulated super-CI approach. *Chemical Physics* **1980**, *48*, 157–173.
- [206] Olsen, J.; Roos, B. O.; Jo/rsgensen, P.; Jensen, H. J. A. Determinant based configuration interaction algorithms for complete and restricted configuration interaction spaces. *The Journal of Chemical Physics* **1988**, *89*, 2185–2192.

- [207] Pipek, J.; Mezey, P. G. A fast intrinsic localization procedure applicable for ab initio and semiempirical linear combination of atomic orbital wave functions. *The Journal of Chemical Physics* **1989**, *90*, 4916–4926.
- [208] Yanai, T.; Tew, D. P.; Handy, N. C. A new hybrid exchange–correlation functional using the Coulomb-attenuating method (CAM-B3LYP). *Chemical Physics Letters* **2004**, *393*, 51–57.
- [209] Weigend, F.; Ahlrichs, R. Balanced basis sets of split valence, triple zeta valence and quadruple zeta valence quality for H to Rn: Design and assessment of accuracy. *Physical Chemistry Chemical Physics* **2005**, *7*, 3297.
- [210] Dunning, T. H.; Hosteny, R. P.; Shavitt, I. Low-lying π -electron states of trans-butadiene. *Journal of the American Chemical Society* **1973**, *95*, 5067–5068.
- [211] Dunning, T. H. Gaussian basis sets for use in correlated molecular calculations. I. The atoms boron through neon and hydrogen. *The Journal of Chemical Physics* **1989**, *90*, 1007–1023.
- [212] Sousa, C.; Sánchez-Mansilla, A.; Broer, R.; Straatsma, T. P.; de Graaf, C. A Nonorthogonal Configuration Interaction Approach to Singlet Fission in Perylenediimide Compounds. *The Journal of Physical Chemistry A* **2023**,
- [213] Japahuge, A.; Zeng, T. Theoretical Studies of Singlet Fission: Searching for Materials and Exploring Mechanisms. *ChemPlusChem* **2018**, *83*, 146–182.
- [214] Ito, S.; Nagami, T.; Nakano, M. Design Principles of Electronic Couplings for Intramolecular Singlet Fission in Covalently-Linked Systems. *The Journal of Physical Chemistry A* **2016**, *120*, 6236–6241, PMID: 27448100.
- [215] Akdag, A.; Havlas, Z.; Michl, J. Search for a Small Chromophore with Efficient Singlet Fission: Bi-radicaloid Heterocycles. *Journal of the American Chemical Society* **2012**, *134*, 14624–14631, PMID: 22876879.
- [216] Paci, I.; Johnson, J. C.; Chen, X.; Rana, G.; Popović, D.; David, D. E.; Nozik, A. J.; Ratner, M. A.; Michl, J. Singlet fission for dye-sensitized solar cells: Can a suitable sensitizer be found? *Journal of the American Chemical Society* **2006**, *128*, 16546–16553.
- [217] Zeng, T.; Ananth, N.; Hoffmann, R. Seeking Small Molecules for Singlet Fission: A Heteroatom Substitution Strategy. *Journal of the American Chemical Society* **2014**, *136*, 12638–12647, PMID: 25140824.
- [218] Zeng, T.; Ananth, N.; Hoffmann, R. Seeking small molecules for singlet fission: a heteroatom substitution strategy. *Journal of the American Chemical Society* **2014**, *136*, 12638–12647.
- [219] Pinheiro, M.; Machado, F. B. C.; Plasser, F.; Aquino, A. J. A.; Lischka, H. A systematic analysis of excitonic properties to seek optimal singlet fission: the BN-substitution patterns in tetracene. *J. Mater. Chem. C* **2020**, *8*, 7793–7804.
- [220] Zeng, T.; Mellerup, S. K.; Yang, D.; Wang, X.; Wang, S.; Stamplecoskie, K. Identifying (BN)2-pyrenes as a New Class of Singlet Fission Chromophores: Significance of Azaborine Substitution. *The Journal of Physical Chemistry Letters* **2018**, *9*, 2919–2927, PMID: 29763325.
- [221] Hatakeyama, T.; Hashimoto, S.; Seki, S.; Nakamura, M. *J. Am. Chem. Soc.* **2011**, *133*, 18614–18617.
- [222] Ishibashi, J. S. A.; Marshall, J. L.; Mazière, A.; Lovinger, G. J.; Li, B.; Zakharov, L. N.; Dargelos, A.; Graciaa, A.; Chrostowska, A.; Liu, S.-Y. Two BN Isosteres of Anthracene: Synthesis and Characterization. *Journal of the American Chemical Society* **2014**, *136*, 15414–15421, PMID: 25275460.
- [223] Ryerson, J. L.; Schrauben, J. N.; Ferguson, A. J.; Sahoo, S. C.; Naumov, P.; Havlas, Z.; Michl, J.; Nozik, A. J.; Johnson, J. C. Two thin film polymorphs of the singlet fission compound 1, 3-diphenylisobenzofuran. *The Journal of Physical Chemistry C* **2014**, *118*, 12121–12132.
- [224] Feng, X.; Kolomeisky, A. B.; Krylov, A. I. Dissecting the effect of morphology on the rates of singlet fission: Insights from theory. *The Journal of Physical Chemistry C* **2014**, *118*, 19608–19617.
- [225] Wang, L.; Olivier, Y.; Prezhdo, O. V.; Beljonne, D. Maximizing Singlet Fission by Intermolecular Packing. *The Journal of Physical Chemistry Letters* **2014**, *5*, 3345–3353, PMID: 26278443.
- [226] Nagami, T.; Ito, S.; Kubo, T.; Nakano, M. Intermolecular Packing Effects on Singlet Fission in Oligoylene Dimers. *ACS Omega* **2017**, *2*, 5095–5103.

- [227] Le, A. K.; Bender, J. A.; Arias, D. H.; Cotton, D. E.; Johnson, J. C.; Roberts, S. T. Singlet Fission Involves an Interplay between Energetic Driving Force and Electronic Coupling in Perylenediimide Films. *Journal of the American Chemical Society* **2018**, *140*, 814–826.
- [228] Hong, Y.; Kim, J.; Kim, D.; Kim, H. Theoretical Engineering of Singlet Fission Kinetics in Perylene Bisimide Dimer with Chromophore Rotation. *The Journal of Physical Chemistry A* **2021**, *125*, 875–884.
- [229] Buchanan, E. A. The Role of Molecular Packing in Singlet Fission. Ph.D. thesis, University of Colorado, Chemistry Department, 2019.
- [230] Parker, S. M.; Seideman, T.; Ratner, M. A.; Shiozaki, T. Model Hamiltonian analysis of singlet fission from first principles. *The Journal of Physical Chemistry C* **2014**, *118*, 12700–12705.
- [231] Sharifzadeh, S.; Darancet, P.; Kronik, L.; Neaton, J. B. Low-energy charge-transfer excitons in organic solids from first-principles: The case of pentacene. *The Journal of Physical Chemistry Letters* **2013**, *4*, 2197–2201.
- [232] Suarez, L. E. A.; de Graaf, C.; Faraji, S. Influence of the crystal packing in singlet fission: one step beyond the gas phase approximation. *Physical Chemistry Chemical Physics* **2021**, *23*, 14164–14177.
- [233] Matsika, S.; Feng, X.; Luzanov, A. V.; Krylov, A. I. What We Can Learn from the Norms of One-Particle Density Matrices, and What We Can't: Some Results for Interstate Properties in Model Singlet Fission Systems. *The Journal of Physical Chemistry A* **2014**, *118*, 11943–11955.
- [234] Parker, S. M.; Shiozaki, T. Communication: Active space decomposition with multiple sites: Density matrix renormalization group algorithm. *The Journal of Chemical Physics* **2014**, *141*, 211102.
- [235] Zaykov, A.; Felkel, P.; Buchanan, E. A.; Jovanovic, M.; Havenith, R. W.; Kathir, R.; Broer, R.; Havlas, Z.; Michl, J. Singlet fission rate: Optimized packing of a molecular pair. Ethylene as a model. *Journal of the American Chemical Society* **2019**, *141*, 17729–17743.
- [236] Saikia, D.; Sarma, R. Organic Light-Emitting Diodes with a Perylene Interlayer Between the Electrode–Organic Interface. *Journal of Electronic Materials* **2018**, *47*, 737–743.
- [237] Heo, J.-S.; Park, N.-H.; Ryu, J.-H.; Suh, K.-D. Novel Light-Emitting Diodes Using Organic Electroluminescent Nanocapsules. *Advanced Materials* **2005**, *17*, 822–826.
- [238] Clarke, R. H.; Hochstrasser, R. M. Location and assignment of the lowest triplet state of perylene. *Journal of Molecular Spectroscopy* **1969**, *32*, 309–319.
- [239] Birks, J. B.; Slifkin, M. A. -Electronic Excitation and Ionization Energies of Condensed Ring Aromatic Hydrocarbons. *Nature* **1961**, *191*, 761–764.
- [240] Ma, L.; Tan, K. J.; Jiang, H.; Kloc, C.; Michel-Beyerle, M.-E.; Gurzadyan, G. G. Excited-State Dynamics in an -Perylene Single Crystal: Two-Photon- and Consecutive Two-Quantum-Induced Singlet Fission. *The Journal of Physical Chemistry A* **2014**, *118*, 838–843, PMID: 24417598.
- [241] Ni, W.; Gurzadyan, G. G.; Zhao, J.; Che, Y.; Li, X.; Sun, L. Singlet Fission from Upper Excited Electronic States of Cofacial Perylene Dimer. *The Journal of Physical Chemistry Letters* **2019**, *10*, 2428–2433.
- [242] Giri, G.; Prodhan, S.; Pati, Y. A.; Ramasesha, S. A Model Exact Study of the Properties of Low-Lying Electronic States of Perylene and Substituted Perylenes. *The Journal of Physical Chemistry A* **2018**, *122*, 8650–8658, PMID: 30335382.
- [243] Stewart, J. MOPAC2016. "Stewart Computational Chemistry, Colorado Springs, CO, USA, HTTP://OpenMOPAC.net (2016)".
- [244] Doehnert, D.; Koutecky, J. Occupation numbers of natural orbitals as a criterion for biradical character. Different kinds of biradicals. *Journal of the American Chemical Society* **1980**, *102*, 1789–1796.
- [245] Flynn, C. R.; Michl, J. .pi., .pi.-Biradicaloid hydrocarbons. o-Xylylene. Photochemical preparation from 1, 4-dihydrophthalazine in rigid glass, electric spectroscopy, and calculations. *Journal of the American Chemical Society* **1974**, *96*, 3280–3288.
- [246] López-Carballera, D.; Zubiria, M.; Casanova, D.; Ruipérez, F. Improvement of the electrochemical and singlet fission properties of anthraquinones by modification of the diradical character. *Physical Chemistry Chemical Physics* **2019**, *21*, 7941–7952.

- [247] López-Carballeira, D.; Casanova, D.; Ruipérez, F. Theoretical design of conjugated diradicaloids as singlet fission sensitizers: quinones and methylene derivatives. *Physical Chemistry Chemical Physics* **2017**, *19*, 30227–30238.
- [248] Canesi, E. V.; Fazzi, D.; Colella, L.; Bertarelli, C.; Castiglioni, C. Tuning the Quinoid versus Biradicaloid Character of Thiophene-Based Heteroquaterphenoquinones by Means of Functional Groups. *Journal of the American Chemical Society* **2012**, *134*, 19070–19083.
- [249] Shen, L.; Wang, X.; Liu, H.; Li, X. Tuning the singlet fission relevant energetic levels of quinoidal bithiophene compounds by means of backbone modifications and functional group introduction. *Physical Chemistry Chemical Physics* **2018**, *20*, 5795–5802.
- [250] Perdew, J. P.; Burke, K.; Ernzerhof, M. Generalized Gradient Approximation Made Simple. *Physical Review Letters* **1996**, *77*, 3865–3868.
- [251] Frisch, M. J. et al. Gaussian~16 Revision C.01. 2016; Gaussian Inc. Wallingford CT.
- [252] Froeyen, M.; Herdwijn, P. Correct bond order assignment in a molecular framework using integer linear programming with application to molecules where only non-hydrogen atom coordinates are available. *Journal of chemical information and modeling* **2005**, *45*, 1267–1274.
- [253] Schäfer, A.; Horn, H.; Ahlrichs, R. Fully optimized contracted Gaussian basis sets for atoms Li to Kr. *The Journal of Chemical Physics* **1992**, *97*, 2571–2577.
- [254] Shao, Y.; Gan, Z.; Epifanovsky, E.; Gilbert, A. T.; Wormit, M.; Kussmann, J.; Lange, A. W.; Behn, A.; Deng, J.; Feng, X.; others Advances in molecular quantum chemistry contained in the Q-Chem 4 program package. *Molecular Physics* **2015**, *113*, 184–215.
- [255] Zhang, B.; Lyskov, I.; Wilson, L. J.; Sabatini, R. P.; Manian, A.; Soleimannejad, H.; White, J. M.; Smith, T. A.; Lakhwani, G.; Jones, D. J.; Ghiggino, K. P.; Russo, S. P.; Wong, W. W. H. FRET-enhanced photoluminescence of perylene diimides by combining molecular aggregation and insulation. *Journal of Materials Chemistry C* **2020**, *8*, 8953–8961.
- [256] Zhao, H.-M.; Pfister, J.; Settels, V.; Renz, M.; Kaupp, M.; Dehm, V. C.; Würthner, F.; Fink, R. F.; Engels, B. Understanding Ground- and Excited-State Properties of Perylene Tetracarboxylic Acid Bisimide Crystals by Means of Quantum Chemical Computations. *Journal of the American Chemical Society* **2009**, *131*, 15660–15668.
- [257] Hansen, M. R.; Graf, R.; Sekharan, S.; Sebastiani, D. Columnar Packing Motifs of Functionalized Perylene Derivatives: Local Molecular Order Despite Long-Range Disorder. *Journal of the American Chemical Society* **2009**, *131*, 5251–5256.
- [258] Würthner, F.; Saha-Möller, C. R.; Fimmel, B.; Ogi, S.; Leowanawat, P.; Schmidt, D. Perylene Bisimide Dye Assemblies as Archetype Functional Supramolecular Materials. *Chemical Reviews* **2015**, *116*, 962–1052.
- [259] Nowak-Król, A.; Würthner, F. Progress in the synthesis of perylene bisimide dyes. *Organic Chemistry Frontiers* **2019**, *6*, 1272–1318.
- [260] Eaton, S. W.; Shoer, L. E.; Karlen, S. D.; Dyar, S. M.; Margulies, E. A.; Veldkamp, B. S.; Ramanan, C.; Hartzler, D. A.; Savikhin, S.; Marks, T. J.; Wasielewski, M. R. Singlet Exciton Fission in Polycrystalline Thin Films of a Slip-Stacked Perylenediimide. *Journal of the American Chemical Society* **2013**, *135*, 14701–14712.
- [261] Mirjani, F.; Renaud, N.; Gorczak, N.; Grozema, F. C. Theoretical Investigation of Singlet Fission in Molecular Dimers: The Role of Charge Transfer States and Quantum Interference. *The Journal of Physical Chemistry C* **2014**, *118*, 14192–14199.
- [262] Masoomi-Godarzi, S.; Hall, C. R.; Zhang, B.; Gregory, M. A.; White, J. M.; Wong, W. W. H.; Ghiggino, K. P.; Smith, T. A.; Jones, D. J. Competitive Triplet Formation and Recombination in Crystalline Films of Perylenediimide Derivatives: Implications for Singlet Fission. *The Journal of Physical Chemistry C* **2020**, *124*, 11574–11585.
- [263] Hong, Y.; Kim, J.; Kim, W.; Kaufmann, C.; Kim, H.; Würthner, F.; Kim, D. Efficient Multiexciton State Generation in Charge-Transfer-Coupled Perylene Bisimide Dimers via Structural Control. *Journal of the American Chemical Society* **2020**, *142*, 7845–7857.

- [264] Williams, M. L.; Schlesinger, I.; Ramirez, C. E.; Jacobberger, R. M.; Brown, P. J.; Young, R. M.; Wasielewski, M. R. Effect of Crystallinity on Endoergic Singlet Fission in Perylenediimide Single Crystals and Polycrystalline Films. *The Journal of Physical Chemistry C* **2022**, *126*, 10287–10297.
- [265] Hong, Y.; Rudolf, M.; Kim, M.; Kim, J.; Schembri, T.; Krause, A.-M.; Shoyama, K.; Bialas, D.; Röhr, M. I. S.; Joo, T.; Kim, H.; Kim, D.; Würthner, F. Steering the multiexciton generation in slip-stacked perylene dye array via exciton coupling. *Nature Communications* **2022**, *13*.
- [266] Jadhav, S. D.; Sasikumar, D.; Hariharan, M. Modulating singlet fission through interchromophoric rotation. *Physical Chemistry Chemical Physics* **2022**, *24*, 16193–16199.
- [267] Miyata, K.; Kurashige, Y.; Watanabe, K.; Sugimoto, T.; Takahashi, S.; Tanaka, S.; Takeya, J.; Yanai, T.; Matsumoto, Y. Coherent singlet fission activated by symmetry breaking. *Nature Chemistry* **2017**, *9*, 983–989.
- [268] Schnedermann, C.; Alvertis, A. M.; Wende, T.; Lukman, S.; Feng, J.; Schröder, F. A. Y. N.; Turban, D. H. P.; Wu, J.; Hine, N. D. M.; Greenham, N. C.; Chin, A. W.; Rao, A.; Kukura, P.; Musser, A. J. A molecular movie of ultrafast singlet fission. *Nature Communications* **2019**, *10*.
- [269] Conrad-Burton, F. S.; Liu, T.; Geyer, F.; Costantini, R.; Schlaus, A. P.; Spencer, M. S.; Wang, J.; Sánchez, R. H.; Zhang, B.; Xu, Q.; Steigerwald, M. L.; Xiao, S.; Li, H.; Nuckolls, C. P.; Zhu, X. Controlling Singlet Fission by Molecular Contortion. *Journal of the American Chemical Society* **2019**, *141*, 13143–13147.
- [270] Sun, S.; Conrad-Burton, F. S.; Liu, Y.; Ng, F.; Steigerwald, M.; Zhu, X.; Nuckolls, C. Inducing Singlet Fission in Perylene Thin Films by Molecular Contortion. *The Journal of Physical Chemistry A* **2022**, *126*, 7559–7565.
- [271] Lindner, J. O.; Röhr, M. I. S.; Mitrić, R. Multistate metadynamics for automatic exploration of conical intersections. *Physical Review A* **2018**, *97*.
- [272] Lindner, J. O.; Röhr, M. I. S. Metadynamics for automatic sampling of quantum property manifolds: exploration of molecular biradicality landscapes. *Physical Chemistry Chemical Physics* **2019**, *21*, 24716–24722.
- [273] Smith, M. B.; Michl, J. Singlet fission. *Chemical reviews* **2010**, *110*, 6891–6936.
- [274] Dill, R. D.; Smyser, K. E.; Rugg, B. K.; Damrauer, N. H.; Eaves, J. D. Entangled spin-polarized excitons from singlet fission in a rigid dimer. *Nature Communications* **2023**, *14*.
- [275] Matsuda, S.; Oyama, S.; Kobori, Y. Electron spin polarization generated by transport of singlet and quintet multiexcitons to spin-correlated triplet pairs during singlet fissions. *Chemical Science* **2020**, *11*, 2934–2942.
- [276] Sanders, S. N.; Kumarasamy, E.; Pun, A. B.; Trinh, M. T.; Choi, B.; Xia, J.; Taffet, E. J.; Low, J. Z.; Miller, J. R.; Roy, X.; Zhu, X.-Y.; Steigerwald, M. L.; Sfeir, M. Y.; Campos, L. M. Quantitative Intramolecular Singlet Fission in Bipentacenes. *Journal of the American Chemical Society* **2015**, *137*, 8965–8972.
- [277] Lin, H.-H.; Kue, K. Y.; Claudio, G. C.; Hsu, C.-P. First Principle Prediction of Intramolecular Singlet Fission and Triplet Triplet Annihilation Rates. *Journal of Chemical Theory and Computation* **2019**, *15*, 2246–2253.
- [278] Wang, Z.; Liu, H.; Xie, X.; Zhang, C.; Wang, R.; Chen, L.; Xu, Y.; Ma, H.; Fang, W.; Yao, Y.; Sang, H.; Wang, X.; Li, X.; Xiao, M. Free-triplet generation with improved efficiency in tetracene oligomers through spatially separated triplet pair states. *Nature Chemistry* **2021**, *13*, 559–567.
- [279] Scholes, G. D. Correlated Pair States Formed by Singlet Fission and Exciton–Exciton Annihilation. *J. Phys. Chem. A* **2015**, *119*, 12699–12705.
- [280] Pensack, R. D.; Ostroumov, E. E.; Tilley, A. J.; Mazza, S.; Grieco, C.; Thorley, K. J.; Asbury, J. B.; Seferos, D. S.; Anthony, J. E.; Scholes, G. D. Observation of Two Triplet-Pair Intermediates in Singlet Exciton Fission. *The Journal of Physical Chemistry Letters* **2016**, *7*, 2370–2375.
- [281] Lee, T. S.; Lin, Y. L.; Kim, H.; Pensack, R. D.; Rand, B. P.; Scholes, G. D. Triplet Energy Transfer Governs the Dissociation of the Correlated Triplet Pair in Exothermic Singlet Fission. *The Journal of Physical Chemistry Letters* **2018**, *9*, 4087–4095.

- [282] Kandada, A. R. S.; Petrozza, A.; Lanzani, G. Ultrafast dissociation of triplets in pentacene induced by an electric field. *Phys. Rev. B* **2014**, *90*.
- [283] Kawata, S.; Kawata, Y. Three-Dimensional Optical Data Storage Using Photochromic Materials. *Chemical Reviews* **2000**, *100*, 1777–1788.
- [284] Mayhall, N. J. From Model Hamiltonians to ab Initio Hamiltonians and Back Again: Using Single Excitation Quantum Chemistry Methods To Find Multiexciton States in Singlet Fission Materials. *Journal of Chemical Theory and Computation* **2016**, *12*, 4263–4273.
- [285] Abraham, V.; Mayhall, N. J. Revealing the Contest between Triplet–Triplet Exchange and Triplet–Triplet Energy Transfer Coupling in Correlated Triplet Pair States in Singlet Fission. *The Journal of Physical Chemistry Letters* **2021**, *12*, 10505–10514.
- [286] Tan, Y.; Tao, G. Exploring the State Space Structure of Multiple Spins via Modular Tensor Diagram Approach: Going beyond the Exciton Pair State. *The Journal of Physical Chemistry A* **2021**, *125*, 1972–1980.
- [287] Zaykov, A.; Felkel, P.; Buchanan, E. A.; Jovanovic, M.; Havenith, R. W. A.; Kathir, R. K.; Broer, R.; Havlas, Z.; Michl, J. Singlet Fission Rate: Optimized Packing of a Molecular Pair. Ethylene as a Model. *Journal of the American Chemical Society* **2019**, *141*, 17729–17743.
- [288] Burton, H. G. A. Generalized nonorthogonal matrix elements: Unifying Wick’s theorem and the Slater–Condon rules. *The Journal of Chemical Physics* **2021**, *154*, 144109.
- [289] Burton, H. G. A. Generalized nonorthogonal matrix elements. II: Extension to arbitrary excitations. *The Journal of Chemical Physics* **2022**, *157*, 204109.
- [290] Li, Z.; Chan, G. K.-L. Spin-Projected Matrix Product States: Versatile Tool for Strongly Correlated Systems. *Journal of Chemical Theory and Computation* **2017**, *13*, 2681–2695.
- [291] Szalay, S.; Pfeffer, M.; Murg, V.; Barcza, G.; Verstraete, F.; Schneider, R.; Örs Legeza Tensor product methods and entanglement optimization for ab initio/i-quantum chemistry. *International Journal of Quantum Chemistry* **2015**, *115*, 1342–1391.
- [292] Keller, S.; Reiher, M. Spin-adapted matrix product states and operators. *The Journal of Chemical Physics* **2016**, *144*, 134101.
- [293] SILVI, P.; ROSSINI, D.; FAZIO, R.; SANTORO, G. E.; GIOVANNETTI, V. MATRIX PRODUCT STATE REPRESENTATION FOR SLATER DETERMINANTS AND CONFIGURATION INTERACTION STATES. *International Journal of Modern Physics B* **2012**, *27*, 1345029.
- [294] Knecht, S.; Keller, S.; Autschbach, J.; Reiher, M. A Nonorthogonal State-Interaction Approach for Matrix Product State Wave Functions. *Journal of Chemical Theory and Computation* **2016**, *12*, 5881–5894.
- [295] React App — roehr-lab.github.io. <https://roehr-lab.github.io/im1.html>, [Accessed 06-01-2024].
- [296] Singh, A. GitHub - roehr-lab/SymbolicCI — github.com. <https://github.com/roehr-lab/SymbolicCI>, 2023; [Accessed 31-07-2023].
- [297] Paldus, J. Group theoretical approach to the configuration interaction and perturbation theory calculations for atomic and molecular systems. *The Journal of Chemical Physics* **1974**, *61*, 5321–5330.
- [298] Lee, J.; Jadhav, P.; Reusswig, P. D.; Yost, S. R.; Thompson, N. J.; Congreve, D. N.; Hontz, E.; Van Voorhis, T.; Baldo, M. A. Singlet Exciton Photovoltaics. *Accounts of Chemical Research* **2013**, *46*, 1300–1311, Publisher: American Chemical Society.
- [299] Xia, J.; Sanders, S. N.; Cheng, W.; Low, J. Z.; Liu, J.; Campos, L. M.; Sun, T. Singlet Fission: Progress and Prospects in Solar Cells. *Advanced Materials* **2017**, *29*, 1601652, eprint: <https://onlinelibrary.wiley.com/doi/pdf/10.1002/adma.201601652>.
- [300] Sanders, S. N.; Pun, A. B.; Parenti, K. R.; Kumarasamy, E.; Yablon, L. M.; Sfeir, M. Y.; Campos, L. M. Understanding the Bound Triplet-Pair State in Singlet Fission. *Chem* **2019**, *5*, 1988–2005.
- [301] Hudson, R. J.; Stuart, A. N.; Huang, D. M.; Kee, T. W. What Next for Singlet Fission in Photovoltaics? The Fate of Triplet and Triplet-Pair Excitons. *The Journal of Physical Chemistry C* **2022**, *126*, 5369–5377, Publisher: American Chemical Society.

- [302] He, G.; Parenti, K. R.; Campos, L. M.; Sfeir, M. Y. Direct Exciton Harvesting from a Bound Triplet Pair. *Advanced Materials* **2022**, *34*, 2203974, eprint: <https://onlinelibrary.wiley.com/doi/pdf/10.1002/adma.202203974>.
- [303] Abraham, V.; Mayhall, N. J. Revealing the Contest between Triplet–Triplet Exchange and Triplet–Triplet Energy Transfer Coupling in Correlated Triplet Pair States in Singlet Fission. *The Journal of Physical Chemistry Letters* **2021**, *12*, 10505–10514, Publisher: American Chemical Society.
- [304] Taffet, E. J.; Beljonne, D.; Scholes, G. D. Overlap-Driven Splitting of Triplet Pairs in Singlet Fission. *Journal of the American Chemical Society* **2020**, *142*, 20040–20047, Publisher: American Chemical Society.
- [305] Frankevich, E. L.; Lesin, V. I.; Pristupa, A. Rate constants of singlet exciton fission in a tetracene crystal determined from the rydmr spectral linewidth. *Chemical Physics Letters* **1978**, *58*, 127–131.
- [306] Chan, W.-L.; Ligges, M.; Jailaubekov, A.; Kaake, L.; Miaja-Avila, L.; Zhu, X.-Y. Observing the Multiexciton State in Singlet Fission and Ensuing Ultrafast Multielectron Transfer. *Science* **2011**, *334*, 1541–1545.
- [307] Grieco, C.; Doucette, G. S.; Munro, J. M.; Kennehan, E. R.; Lee, Y.; Rimshaw, A.; Payne, M. M.; Wonderling, N.; Anthony, J. E.; Dabo, I.; Gomez, E. D.; Asbury, J. B. Triplet Transfer Mediates Triplet Pair Separation during Singlet Fission in 6, 13-Bis(triisopropylsilylithynyl)-Pentacene. *Advanced Functional Materials* **2017**, *27*, 1703929.
- [308] Baronas, P.; Kreiza, G.; Naimovičius, L.; Radiunas, E.; Kazlauskas, K.; Orentas, E.; Juršėnas, S. Sweet Spot of Intermolecular Coupling in Crystalline Rubrene: Intermolecular Separation to Minimize Singlet Fission and Retain Triplet–Triplet Annihilation. *J. Phys. Chem. C* **2022**, *126*, 15327–15335.
- [309] Qian, Y.; Huang-Fu, Z.-C.; Zhang, T.; Li, X.; Harutyunyan, A. R.; Chen, G.; Chen, H.; Rao, Y. Temperature-Dependent Recombination of Triplet Biexcitons in Singlet Fission of Hexacene. *The Journal of Physical Chemistry C* **2022**, *126*, 8377–8383.
- [310] Korovina, N. V.; Chang, C. H.; Johnson, J. C. Spatial separation of triplet excitons drives endothermic singlet fission. *Nature Chemistry* **2020**, *12*, 391–398.
- [311] Chen, M.; Bae, Y. J.; Mauck, C. M.; Mandal, A.; Young, R. M.; Wasielewski, M. R. Singlet Fission in Covalent Terrylenediimide Dimers: Probing the Nature of the Multiexciton State Using Femtosecond Mid-Infrared Spectroscopy. *Journal of the American Chemical Society* **2018**, *140*, 9184–9192.
- [312] Teichen, P.; Eaves, J. D. Title of the Article (Please replace with the actual title). *J. Phys. Chem. B* **2012**, *116*, 11473.
- [313] Feng, X.; Luzanov, A. V.; Krylov, A. I. Title of the Article (Please replace with the actual title). *J. Phys. Chem. Lett.* **2013**, *4*, 3845.
- [314] Casanova, D. Title of the Article (Please replace with the actual title). *J. Chem. Theory Comput.* **2014**, *10*, 324.
- [315] Zeng, T.; Hoffmann, R.; Ananth, N. Title of the Article (Please replace with the actual title). *J. Am. Chem. Soc.* **2014**, *136*, 5755.
- [316] Ryerson, J. L. et al. Structure and photophysics of indigoids for singlet fission: Cibalackrot. *Journal of Chemical Physics* **2019**, *151*, 184903.
- [317] Nakano, M.; Nagami, T.; Tonami, T.; Okada, K.; Ito, S.; Kishi, R.; Kitagawa, Y.; Kubo, T. Quantum Master Equation Approach to Singlet Fission Dynamics in Pentacene Linear Aggregate Models: Size Dependences of Excitonic Coupling Effects. *Journal of Computational Chemistry* **2019**, *40*, 89–104, eprint: <https://onlinelibrary.wiley.com/doi/pdf/10.1002/jcc.25539>.
- [318] Meurer, A. et al. SymPy: symbolic computing in Python. *PeerJ Computer Science* **2017**, *3*, e103.
- [319] Buchanan, E. A.; Havlas, Z.; Michl, J. *Advances in Quantum Chemistry*; Elsevier, 2017; pp 175–227.
- [320] Fink, R. F.; Seibt, J.; Engel, V.; Renz, M.; Kaupp, M.; Lochbrunner, S.; Zhao, H.-M.; Pfister, J.; Würthner, F.; Engels, B. Exciton Trapping in -Conjugated Materials: A Quantum-Chemistry-Based Protocol Applied to Perylene Bisimide Dye Aggregates. *Journal of the American Chemical Society* **2008**, *130*, 12858–12859, Publisher: American Chemical Society.

- [321] Hoche, J.; Schmitt, H.-C.; Humeniuk, A.; Fischer, I.; Mitić, R.; S. Röhr, M. I. The mechanism of excimer formation: an experimental and theoretical study on the pyrene dimer. *Physical Chemistry Chemical Physics* **2017**, *19*, 25002–25015, Publisher: Royal Society of Chemistry.
- [322] Folie, B. D.; Haber, J. B.; Refaeli-Abramson, S.; Neaton, J. B.; Ginsberg, N. S. Long-Lived Correlated Triplet Pairs in a -Stacked Crystalline Pentacene Derivative. *Journal of the American Chemical Society* **2018**, *140*, 2326–2335.
- [323] Kundu, A.; Dasgupta, J. Photogeneration of Long-Lived Triplet States through Singlet Fission in Lycopene H-Aggregates. *J. Phys. Chem. Lett.* **2021**, *12*, 1468–1474.
- [324] Basel, B. S. et al. Unified model for singlet fission within a non-conjugated covalent pentacene dimer. *Nat Commun* **2017**, *8*, 15171.
- [325] Lubert-Perquel, D.; Salvadori, E.; Dyson, M.; Stavrinou, P. N.; Montis, R.; Nagashima, H.; Kobori, Y.; Heutz, S.; Kay, C. W. M. Identifying triplet pathways in dilute pentacene films. *Nat Commun* **2018**, *9*, 4222.
- [326] Weiss, L. R.; Bayliss, S. L.; Krafft, F.; Thorley, K. J.; Anthony, J. E.; Bittl, R.; Friend, R. H.; Rao, A.; Greenham, N. C.; Behrends, J. Strongly exchange-coupled triplet pairs in an organic semiconductor. *Nature Phys* **2017**, *13*, 176–181.
- [327] Korovina, N. V.; Das, S.; Nett, Z.; Feng, X.; Joy, J.; Haiges, R.; Krylov, A. I.; Bradforth, S. E.; Thompson, M. E. Singlet Fission in a Covalently Linked Cofacial Alkynyltetracene Dimer. *J. Am. Chem. Soc.* **2016**, *138*, 617–627.
- [328] Ambrosio, F.; Troisi, A. Singlet fission in linear chains of molecules. *J. Chem. Phys.* **2014**, *141*.
- [329] Wang, Y.-C.; Feng, S.; Kong, Y.; Huang, X.; Liang, W.; Zhao, Y. Electronic Couplings for Singlet Fission Processes Based on the Fragment Particle-Hole Densities. *J. Chem. Theory Comput.* **2023**, *19*, 3900–3914.
- [330] Buchanan, E. A.; Havlas, Z.; Michl, J. Optimal Arrangements of Tetracene Molecule Pairs for Fast Singlet Fission. *BCSJ* **2019**, *92*, 1960–1971.
- [331] Wang, L.; Olivier, Y.; Prezhdo, O. V.; Beljonne, D. Maximizing Singlet Fission by Intermolecular Packing. *J Phys Chem Lett* **2014**, *5*, 3345–3353.
- [332] Morrison, A. F.; You, Z.-Q.; Herbert, J. M. Ab Initio Implementation of the Frenkel–Davydov Exciton Model: A Naturally Parallelizable Approach to Computing Collective Excitations in Crystals and Aggregates. *J. Chem. Theory Comput.* **2014**, *10*, 5366–5376.
- [333] Morrison, A. F.; Herbert, J. M. Low-Scaling Quantum Chemistry Approach to Excited-State Properties via an ab Initio Exciton Model: Application to Excitation Energy Transfer in a Self-Assembled Nanotube. *J. Phys. Chem. Lett.* **2015**, *6*, 4390–4396.
- [334] Morrison, A. F.; Herbert, J. M. Evidence for Singlet Fission Driven by Vibronic Coherence in Cocrystalline Tetracene. *J. Phys. Chem. Lett.* **2017**, *8*, 1442–1448.
- [335] Alam, B.; Jiang, H.; Zimmerman, P. M.; Herbert, J. M. State-specific solvation for restricted active space spin-flip (RAS-SF) wave functions based on the polarizable continuum formalism. *J. Chem. Phys.* **2022**, *156*, 194110.
- [336] Ditchfield, R.; Hehre, W. J.; Pople, J. A. Self-Consistent Molecular-Orbital Methods. IX. An Extended Gaussian-Type Basis for Molecular-Orbital Studies of Organic Molecules. *J. Chem. Phys.* **1971**, *54*, 724–728.
- [337] Aquilante, F.; Pedersen, T. B.; Lindh, R.; Roos, B. O.; Sánchez de Merás, A.; Koch, H. Accurate ab initio density fitting for multiconfigurational self-consistent field methods. *J. Chem. Phys.* **2008**, *129*.
- [338] Hohenstein, E. G.; Luehr, N.; Ufimtsev, I. S.; Martínez, T. J. An atomic orbital-based formulation of the complete active space self-consistent field method on graphical processing units. *J. Chem. Phys.* **2015**, *142*.
- [339] Chaban, G.; Schmidt, M. W.; Gordon, M. S. Approximate second order method for orbital optimization of SCF and MCSCF wavefunctions. *Theoretical Chemistry Accounts* **1997**, *97*, 88–95.
- [340] Sun, Q. et al. Recent developments in the PySCF program package. *J. Chem. Phys.* **2020**, *153*.

- [341] Sun, Q.; Berkelbach, T. C.; Blunt, N. S.; Booth, G. H.; Guo, S.; Li, Z.; Liu, J.; McClain, J. D.; Sayfutyarova, E. R.; Sharma, S.; Wouters, S.; Chan, G. K. PySCF: the Python-based simulations of chemistry framework. *WIREs Comput Mol Sci* **2017**, *8*.
- [342] Sun, Q. Libcint: An efficient general integral library for Gaussian basis functions. *J Comput Chem* **2015**, *36*, 1664–1671.
- [343] Bai, S.; Zhang, P.; Beratan, D. N. Predicting Dexter Energy Transfer Interactions from Molecular Orbital Overlaps. *J. Phys. Chem. C* **2020**, *124*, 18956–18960.
- [344] Skourtis, S. S.; Liu, C.; Antoniou, P.; Virshup, A. M.; Beratan, D. N. Dexter energy transfer pathways. *Proceedings of the National Academy of Sciences* **2016**, *113*, 8115–8120.